Karlsruhe Institute of Technology

Development of a Rear Wall for the KATRIN Rear Section and investigation of tritium compatibility of Rear Section components

Zur Erlangung des akademischen Grades eines
DOKTOR DER NATURWISSENSCHAFT
von der Fakultät für Physik
des Karlsruher Instituts für Technologie
genehmigte
DISSERTATION
von

Diplom-Physikerin
Kerstin Schönung
ausgearbeitet am Institut für Experimentelle Kernphysik und dem
Tritiumlabor Karlsruhe des Instituts für Technische Physik

Referent:	Prof. Dr. Guido Drexlin Institut für Experimentelle Kernphysik, KIT
Koreferent:	Prof. Dr. Bernhard Holzapfel Institut für Technische Physik, KIT

Tag der mündlichen Prüfung: 15.01.2016

Declaration of authorship

I declare that I have developed and written the enclosed thesis completely myself and have not used sources or means without declaration int the text.

Erklärung zur Selbstständigkeit

Hiermit versichere ich, die vorliegende Arbeit selbständig angefertigt, alle dem Wortlaut oder Sinn nach entnommenen Inhalte anderer Werke an den entsprechenden Stellen unter Angabe der Quellen kenntlich gemacht und keine weiteren Hilfsmittel verwendet zu haben.

Karlsruhe, den 15.01.2016

.....
Kerstin Schönung

Some of the cited sources are not available in published form, but details of interest may be requested via electronic mail to kerstin.schoenung@googlemail.com

Abstract

Neutrinos are elementary particles of the standard model of particle physics which were assumed to be massless. But since the discovery of neutrino oscillation it has been proven that the neutrino mass is not zero. The determination of this mass is of great interest not only for particle physicists but also for cosmologists and astronomers. However, until now only an upper limit of $2.05\,\mathrm{eV/c^2}$ (95 % C.L.) could be determined by a model-independent investigation of the kinetics of the tritium β-decay. Improving this limit to $0.2\,\mathrm{eV/c^2}$ (90 % C.L.) is the aim of the KArlsruhe TRItium Neutrino experiment (KATRIN).

To achieve this sensitivity a precise knowledge and monitoring of the measurement parameters is required. Hence, KATRIN is equipped with the Calibration and Monitoring System (CMS). One part of the CMS is the so called Rear Section. Among other instruments it will provide an angular selective electron gun based on the photoelectric effect, which can be used for several monitoring and calibration tasks. In addition, the Rear Section provides the gold surface of the so called Rear Wall, which might determine the plasma potential of the tritium source by its work function.

In spite of great effort made in the development of the Rear Section, some open questions remain. This includes the proof of suitability of several components for a tritium atmosphere of $10^{-5}\,\mathrm{mbar}$ to $10^{-8}\,\mathrm{mbar}$ partial pressure. In addition, an optical design for the e-gun must be developed and the resulting electron rate must be calculated. Also, a final Rear Wall is neither developed nor characterized yet. These open questions are covered in the scope of the thesis in hand.

For this purpose a custom made piezo motor was qualified. A mechanism driven by this motor enables the e-gun beam to pass through the Rear Wall and to provide a complete gold surface in the intervening time of two e-gun beams. The motor can perform more than twice of the required 100 000 driving cycles in a tritium atmosphere and withstands bake-outs at 150 °C. The tritium leak rate of a fiber feed-through installed at a vacuum flange was determined to be $L = (3.65 \pm 0.08) \cdot 10^{-13}\,\mathrm{mbar\,l\,s^{-1}}$ if the tritium partial pressure difference at the feed-through is about $10^{-1}\,\mathrm{mbar}$. That means, that fiber feed-troughs meet the safety requirements of tritium containing components. In addition, it has been ruled out that the transmission of ultraviolet (UV) light is reduced by tritium exposure. Based on the qualified fibers and fiber feed-through an optical setup for the e-gun has been designed. Using this optical setup, an electron rate of up to $7.26 \cdot 10^5\,\mathrm{s^{-1}}$ is expected at the design wavelength of 275 nm.

The impact of bake-outs and UV irradiation on the Rear Wall work function was found to be sample specific. For that reason an individual characterization for each Rear Wall candidate is required. During this characterization process a final Rear Wall for the Rear Section is found based on a stainless steel substrate. After a bake-out, it provides a work function homogeneity over the whole surface of the Rear Wall of $\overline{\sigma}_{\mathrm{RMS,surface}} = 9.4 \pm 0.2\,\mathrm{mV}$ with a stability $\leq 7.3\,\mathrm{mV}$ in one week. The distribution of the work function after the bake-out is found to be a combination of a radial distribution and a distribution over the complete surface. Further long-term stability investigations on the work function suggest a stability of below 18.5 mV over 3 weeks.

Zusammenfassung

Neutrinos sind Elementarteilchen des Standardmodels der Teilchenphysik, die als masselos angenommen wurden. Seit der Entdeckung der Neutrinooszillation ist jedoch klar, dass Neutrinos eine Masse besitzen. Die Bestimmung dieser Masse ist von großem Interesse nicht nur für Teilchenphysiker, sondern auch für Kosmologen und Astronomen. Allerdings wurde bisher nur eine Obergrenze von $2.05\,\mathrm{eV/c^2}$ (95 % C.L.) durch die Untersuchung der Kinematik des Tritium-β-Zerfalls bestimmt. Diese Obergrenze auf $0.2\,\mathrm{eV/c^2}$ (90 % C.L.) zu reduzieren ist Ziel des KArlsruhe TRItium Neutrino Experiments (KATRIN).

Um diese Sensitivität zu erreichen, müssen alle Messparameter genau bekannt sein und überwacht werden. Für diese Aufgabe ist KATRIN mit dem Calibration and Monitoring System (CMS) ausgestattet. Ein Teil dieses Systems ist die sogenannte Rear Section. Diese stellt neben anderen Überwachungsinstrumenten eine auf dem photoelektrischen Effekt beruhende, winkelselektive Elektronenkanone zur Verfügung, die unterschiedliche Kalibrier- und Überwachungsaufgaben erfüllt. Zudem ist die Goldoberfläche der sogenannten Rear Wall Teil der Rear Section, die unter bestimmten Umständen das Potential der Tritiumquelle mit ihrer Austrittsarbeit definiert.

Trotz großer Anstrengungen bei der Entwicklung der Rear Section sind einige Fragen noch ungeklärt. Diese beinhalten den Tauglichkeitsnachweis unterschiedlicher Komponenten in Tritiumatmosphären von $10^{-5}\,\mathrm{mbar}$ bis $10^{-8}\,\mathrm{mbar}$ Partialdruck. Außerdem muss ein optisches System für die Elektronenkanone entwickelt und die daraus resultierende Elektronenrate abgeschätzt werden. Auch die Entwicklung und Charakterisierung der Rear Wall ist noch nicht erfolgt. Diese Fragen zu klären, ist Ziel der vorliegenden Arbeit.

Dazu wurde zunächst ein speziell entwickelter Piezomotor qualifiziert. Der Mechanismus, der von diesem Motor betätigt wird, ermöglicht es dem Elektronenstrahl durch die Rear Wall zu gelangen und zwischen zwei Elektronenstrahlen eine geschlossene Goldoberfläche bereitzustellen. Der Motor kann mehr als die doppelte Anzahl der benötigten 100 000 Fahrzyklen in einer Tritiumatmosphäre ausführen und bis 150 °C ausgeheizt werden. Die Leckrate einer in einem Vakuumflansch installierten Glasfaserdurchführung wurde zu $L = (3.65 \pm 0.08) \cdot 10^{-13}\,\mathrm{mbar\,l\,s^{-1}}$ bestimmt. Damit erfüllen derartige Durchführungen die Sicherheitsanforderungen tritiumführender Systeme. Weiterhin konnte ausgeschlossen werden, dass eine Tritiumexposition die Transmissionseigenschaften von Glasfasern für ultraviolettes (UV) Licht beeinträchtigt. Basierend auf der Qualifikation der Glasfasern und der Glasfaserdurchführung konnte ein optisches System für die Elektronenkanone entwickelt werden. Mit diesem werden mit der Designwellenlänge von 275 nm Elektronenraten von bis zu $7.26 \cdot 10^5\,\mathrm{s^{-1}}$ erwartet.

In Bezug auf die Auswirkungen von Ausheizvorgängen und Bestrahlung mit UV Licht auf die Austrittsarbeit konnte ein individueller Zusammenhang mit der jeweiligen Probe nachgewiesen werden. Dieser fand bei der individuellen Charakterisierung der Rear Wall Kandidaten Berücksichtigung. Es wurde eine finale Rear Wall für die Rear Section gefunden, beruhend auf einem Edelstahlsubstrat. Diese weist nach einer Ausheizdauer von über einer Woche eine Austrittsarbeitshomogenität von $\overline{\sigma}_{\mathrm{RMS,surface}} = 9.4 \pm 0.2\,\mathrm{mV}$ und eine Stabilität von $\leq 7.3\,\mathrm{mV}$ auf. Die Austrittsarbeitsverteilung nach dem Ausheizen setzt sich dabei aus einer radialen und einer über die gesamte Oberfläche der Rear Wall verlaufenden Komponente zusammen. Weitere Langzeituntersuchungen zur Austrittsarbeitsstabilität legen nahe, dass die Fluktuationen innerhalb von 3 Wochen unter 18.5 mV liegen.

Contents

List of Figures

List of Tables

Introduction

Since its postulation in 1930 [Pau64] and its experimental discovery in 1953 [Rei53] the neutrino is part of the standard model of particle physics, which describes the properties of the elementary particles and their interactions. Within the standard model neutrinos are predicted to be massless as they, unlike all other elementary particles, are unable to get their mass by coupling to the vacuum expectation value of the Higgs field [Zub11]. The discovery of the neutrino oscillation [Dav79, Fuk98, Ahm01] implied that the neutrino masses must not be zero, though. This is a result of the dependence of the neutrino oscillation on the differences $\Delta m_{ij}^2 = m_i^2 - m_j^2$ of the participating neutrino mass eigenstates [Oli14].

A knowledge of the neutrino mass is of great interest not only in particle physics to investigate physics beyond the Standard Model and the origin of the neutrino mass, but also in cosmology and astrophysics. To take a single example, the neutrino mass is one of the parameters of the models that describe the formation of structures in the universe. If this parameter can be fixed the models are simplified and improved. But in spite of great efforts to measure the neutrino mass, only an upper limit for the neutrino mass of about $2.0\,\mathrm{eV\,c^{-2}}$ (see [Oli14] and references therein) could be established so far.

The improvement of this limit is the aim of the KArlsruhe TRItium Neutrino experiment (KATRIN). Its measurement method is based on a model-independent investigation of the kinematics during the tritium β-decay at the endpoint of the spectrum. The design sensitivity is $350\,\mathrm{meV\,c^{-2}}$ with 5σ significance or $200\,\mathrm{meV\,c^{-2}}$ at 90 % confidence level [Ang05] if the result is compatible with zero. Therefore, the current limit will be lowered by 1 order of magnitude. To reach this sensitivity requires not only a tritium source of high activity in the order of 10^{11} Bq and a spectrometer with very good energy resolution below 1 eV, but also a precise knowledge and monitoring of the measurement parameters. In case of the tritium source this task is accomplished by the Calibration and Monitoring System (CMS) which includes different measurement techniques to monitor the source parameters [Bab12, Bab14].

One part of the CMS is the so-called Rear Section, which is placed at the rear end of the KATRIN experiment. It provides the ability to measure the source activity by beta-induced x-ray spectrometry (BIXS) with a precision of 0.1 %. In addition, an angular selective e-gun with rates in the order of $10^4\,\mathrm{s^{-1}}$ and an energy resolution of 0.2 eV enables the measurement of the column density of the tritium source. The e-gun is also used to determine the transmission and response function of the spectrometer for calibration purposes. The so called Rear Wall, a gold coated plate which is also part of the Rear Section, is a possible candidate as determinant of the plasma potential. In case of a suitably chosen voltage applied on the Rear Wall, it determines the source potential. For that reason its surface potential must be homogeneous and long-term stable below

20 meV. Otherwise, its contribution to the systematic uncertainties of KATRIN exceeds the acceptable amount and hence could cause KATRIN to not achieve its sensitivity aim.

In the work of the past years the mechanical design of the Rear Section, as provider of these components, and of the components itself has been finalized. It has been proven by experiment as well as simulations that the BIXS technique achieves the required sensitivity [Pri13a, Röl13]. Furthermore, the basic operability of the e-gun has been demonstrated with a prototype by the collaborators at the University of California Santa Barbara (UCSB). But there still remain some open questions concerning the e-gun and the Rear Wall which must be answered before a fully functional Rear Section can be provided to KATRIN:

1. Are all components, which are planed to be used, tritium compatible concerning safety and their performance? Here the performance of a piezo motor and fibers are experimentally investigated and the tritium permeation through a fiber feed-through is calculated based on literature values and measured.
2. How can the optical setup, used to produce the electrons at the e-gun, be designed to prevent misalignment of optical components inside of a glove box and to meet the required electron rate of at least $10^4\,\mathrm{s}^{-1}$ with an energy distribution of 0.2 eV? This question not only includes the design of the optical setup, but also a calculation of the resulting e-gun rate.
3. What is the most suitable design of the Rear Wall to achieve a homogeneous and long-term stable surface potential, how is the surface potential effected by a bake-out or UV irradiation and how large is the resulting inhomogeneity of a final Rear Wall? To answer this question, diverse investigations are performed on factors influencing the work function of a gold layer.

Answering these questions was the objective of the thesis in hand.

The structure of the thesis is the following: Chapter 1 summarizes the basic neutrino properties and the experiments, on which our knowledge of these is based, are described. The working principle of KATRIN and its experimental setup are described in chapter 2. The end of this chapter focuses on the Rear Section and its components to establish a basis of knowledge about their requirements. In chapter 3 the investigation of the tritium compatibility of three different components relating to the Rear Section, is addressed. As two of these components are main components of the optical design of the Rear Section e-gun, this design and the calculation of the expected electron rate is also part of this chapter. Chapter 4 deals with the development of the Rear Wall. Three different experimental setups used during this development are introduced. Their results lead to a final Rear Wall and its characterization. The thesis is completed by chapter 5 where the obtained results are summarized. Here we refer back to this introduction by answering the questions that were posed above and discussing further steps which are necessary to provide the final Rear Section for KATRIN.

Chapter 1

Overview of neutrino physics

After its postulation by Pauli in 1930 [Pau64] and its experimental discovery by Cowan and Reines in 1956 [Cow56] many experiments have revolved around the properties of the neutrino. These experiments have not only investigated the basic neutrino properties but also enabled a look beyond the Standard Model of particle physics [Oli14] and a clearer understanding of the processes of mass generation and structure formation in our universe.

In the following sections a selection of these experiments and their implications on physics is presented, starting with some basic facts concerning the neutrino in section 1.1. While investigating the basic properties of the neutrino, discrepancies between the expected and measured neutrino fluxes were detected and finally explained by neutrino oscillation as described in section 1.2. Due to the fact that this oscillation is only possible if the neutrino is not massless (as it is in the Standard Model), different theoretical models explaining the origin of the neutrino mass were constructed. Some of these models are presented in section 1.3. As the non-zero neutrino mass not only affects the Standard Model and particle physics but also cosmology and astrophysics, the impact of the neutrino mass on these fields of research is discussed in section 1.4. The chapter is completed by section 1.5, where several approaches and resulting experiments are described, which make great efforts to measure the neutrino mass directly or indirectly.

1.1 Neutrino basics: discovery, properties and sources

The first indications of the existence of the neutrino were found by Chadwick in 1914 during his investigation of the β^--decay of ^{214}Pb and ^{214}Bi [Cha14]:

$$\begin{aligned} {}^{214}_{82}\mathrm{Pb} &\rightarrow {}^{214}_{83}\mathrm{Bi} + e^- + \overline{\nu}_\mathrm{e} \\ {}^{214}_{83}\mathrm{Bi} &\rightarrow {}^{214}_{84}\mathrm{Po} + e^- + \overline{\nu}_\mathrm{e}. \end{aligned} \tag{1.1}$$

Based on previous knowledge, the β-decay was expected to be a two body decay, where the mother nucleus decays into an electron and a daughter nucleus. Following this, a discrete energy spectrum was expected which conserves energy and momentum during the decay. But Chadwick measured a continuous energy spectrum of the electron apparently violating the established conservation rules.

To preserve the conservation of energy and momentum, in 1930 Pauli postulated a previously undetected new particle which carries away the missing energy by making the

β-decay a three body process [Pau64]. This new particle is the neutrino. Pauli also postulated certain properties of the neutrino: it must be stable, electrically neutral and must have a spin of 1/2 [Pau64]. Following this postulation, Fermi formulated a complete theoretical description of the β-decay as a weak, point-like interaction in which a neutrino with either zero or very small mass is produced [Fer34]. Bethe and Peierls followed this theoretical approach and arrived at an estimate of the interaction cross section of the neutrino with matter of $\sigma \approx 10^{-44}\,\mathrm{cm}^2$ [Bet34].

This small cross section is the reason why it took more than 25 years to experimentally detect the electron neutrino [Cow56]. The other 2 neutrinos of the Standard model (compare figure 1.1), the muon and tau neutrino, needed even more time to be detected: 6 years after the electron neutrino the muon neutrino [Dan62] could be experimentally observed. And, it took another 40 years to detect the tau neutrino [Kod01].

After the first signs of a possible electron neutrino detection were published by Cowan and Reines in 1953 [Rei53], the final confirmation of the detection was provided by project Poltergeist performed by the same experimenters in 1956 [Cow56]. In this experiment a nuclear fission reactor was used as a neutrino source. Two tanks filled with 200 l of water with 40 kg dissolved $CdCl_2$ were used as a detector. According to the inverse β-decay process [Pov13]

$$\overline{\nu}_\mathrm{e} \; + \; p \; \rightarrow \; e^+ \; + \; n, \tag{1.2}$$

the incident anti-neutrinos from the fission reactor interact with protons in the water tank into a positron and a neutron. The characteristic signal of this reaction is a delayed coincidence signal: the produced positron annihilates with an electron into two 511 keV photons, which are emitted in opposite directions. In addition, a few microseconds later a MeV-gamma ray is emitted by the exited $CdCl_2$, which has captured the produced neutron of the inverse β-decay [Rei97]. The neutrino cross section which was measured by this coincidence was $\sigma = 6.3 \cdot 10^{-44}\,\mathrm{cm}^2$ [Cow56] in good agreement with the estimated cross section by Bethe and Peierls.

The detection of the muon neutrino by Ledermann, Schwartz and Steinberger [Dan62] was based on the pion decay

$$\pi^+ \; \rightarrow \; \mu^+ \; + \; \nu_\mu \qquad \text{and} \qquad \pi^- \; \rightarrow \; \mu^- \; + \; \overline{\nu}_\mu \tag{1.3}$$

into muons and neutrinos. The required pions were produced by bombarding a beryllium target with 15 GeV protons produced by the Brookhaven Alternating Gradient Synchrotron. The neutrino detection was performed by a characteristic straight track in a spark chamber containing 10 tons of aluminum.

Finally, the DONUT experiment [Kod01] at the Fermilab Tevatron detected the tau neutrino by producing taus in the decay of D_S-mesons

$$D_\mathrm{S} \; \rightarrow \; \tau \; + \; \overline{\nu}_\tau. \tag{1.4}$$

The required D_S-mesons are produced in the interaction of high energetic protons with a tungsten target. The tauons are detected by their decay in alternating stainless-steel sheets and emulsion plates: within 2 mm after the tau is produced it decays in the detector, resulting in a characteristic kink in the trajectory.

As evidenced by these three neutrino detection experiments not just one neutrino, but three different flavors of neutrinos exist, ν_e, ν_μ and ν_τ. Each of these neutrino flavors also has an anti-particle partner, $\overline{\nu}_\mathrm{e}$, $\overline{\nu}_\mu$ and $\overline{\nu}_\tau$. The experimental proof that ν_e is not the

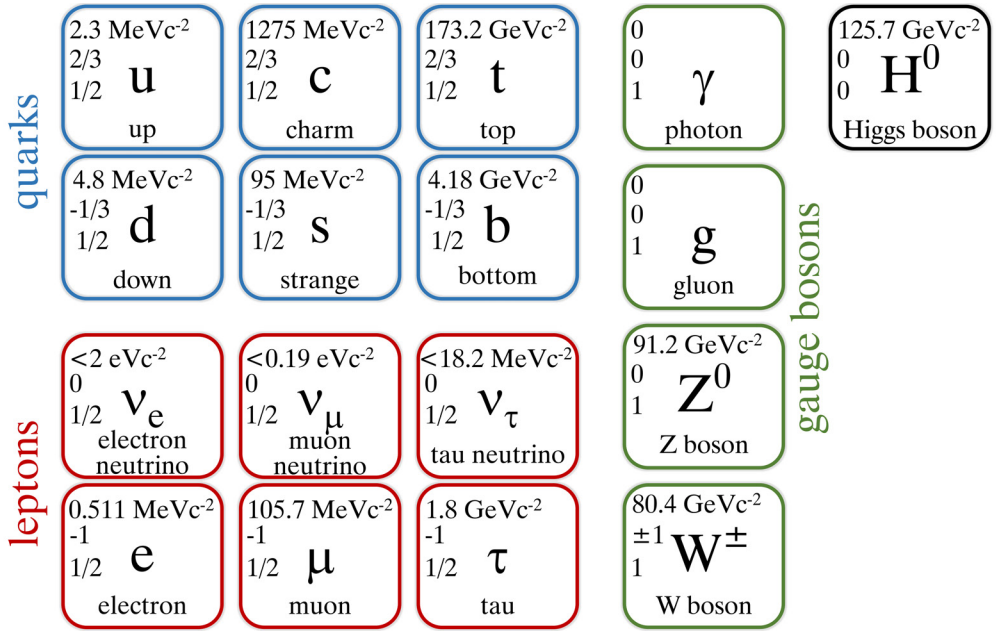

Figure 1.1: Standard model of particle physics. The Standard Model consists of the fermionic leptons (red) and quarks (blue) as well as the gauge bosons (green) and the Higgs boson (black). For simplicity the anti-leptons and anti-quarks are not shown in this figure. Both quarks and leptons are divided into three generations each forming a doublet of two particles (columns in the figure). For each particle mass, charge and spin are given (from top to bottom) in the respective boxes. All values are taken from [Oli14].

same particle as $\overline{\nu}_e$ was given by Davis in [Dav55]. Both neutrinos and anti-neutrinos are spin 1/2 fermions of the Standard Model of particle physics (see figure 1.1), electrically neutral and have a lepton number of $L = +1$ in case of the neutrino and $L = -1$ in case of the anti-neutrino [Akh99].

All neutrinos are weakly interacting, meaning that the neutrino interacts with matter with a very small cross section [Bet34]. This can be exemplified by the fact, that the mean free path of a 1 MeV neutrino in lead is about 1 light year [Akh99]. Due to the weak interaction of the neutrino which maximally violates parity as consequence of the V-A theory [Fey58, Sud58], the neutrino was assumed to be massless. For the same reason it was also assumed, that only left-handed neutrinos and right-handed anti-neutrinos exist. The experimental proof that neutrinos are left-handed was given by Goldhaber [Gol58]. A further consequence of the weak interaction is that the neutrino participates in reactions mediated by the Z^0 bosons and the $W^\pm$ bosons. In these reactions the $W^\pm$ decay

$$\begin{aligned} W^+ &\rightarrow l_a^+ + \nu_a \\ W^- &\rightarrow l_a^- + \overline{\nu}_a \end{aligned} \tag{1.5}$$

is the so-called charged current (CC), while the Z^0 decay into a neutrino and an anti-neutrino of the same flavor

$$Z^0 \rightarrow \nu_a \overline{\nu}_a \tag{1.6}$$

is the so-called neutral current (NC) [Akh99].

The latter decay channel of the Z^0 boson is also used to determine the number of neutrino flavors: in the ALEPH experiment the width of the Z^0 resonance was measured. This

resonance is composed of the neutrino, the quark and the charged lepton decay channel. In contrast to the later two, the contribution to the resonance by the neutrino can not be detected. Therefore, the total width minus the width of the visible decay channels gives the width caused by the neutrino channel. This way the number of neutrino flavors can be calculated to [Sch06]

$$N_\nu = 2.9840 \pm 0.0082. \tag{1.7}$$

This result is supported by calculations based on the big bang nucleosynthesis, which limits the number of light neutrinos[1] to less than 3.3 [Sar96, Wal91], and measurements performed at the LEP e^+e^- collider at CERN, where no fourth generation with masses below $104\,\mathrm{GeV\,c^{-2}}$ was found [Sch06].

The 3 neutrino flavors are generated in different decays: the electron-type neutrino production is based on the nuclear β-decay [Akh99]

$$\begin{aligned} A\,(Z,N) &\rightarrow A\,(Z+1,N-1) + e^- + \overline{\nu}_\mathrm{e}, \\ A\,(Z,N) &\rightarrow A\,(Z-1,N+1) + e^+ + \nu_\mathrm{e}. \end{aligned} \tag{1.8}$$

The elementary process behind both decays is the transition of an up quark into a down quark and vice versa

$$\begin{aligned} u &\rightarrow d + e^+ + \nu_\mathrm{e}, \\ d &\rightarrow u + e^- + \overline{\nu}_\mathrm{e}, \end{aligned} \tag{1.9}$$

which is also shown in figure 1.2. In addition, electron neutrinos are produced in neutron, muon and pion decays

$$\begin{aligned} n &\rightarrow\ p\ +\ e^-\ +\ \overline{\nu}_\mathrm{e}, \\ \mu^\pm &\rightarrow\ e^\pm\ +\ \overline{\nu}_\mathrm{\mu}(\nu_\mathrm{\mu})\ +\ \nu_\mathrm{e}(\overline{\nu}_\mathrm{e}), \\ \pi^\pm &\rightarrow\ e^\pm/\mu^\pm\ +\ \nu_\mathrm{e}(\overline{\nu}_\mathrm{e})/\nu_\mathrm{\mu}(\overline{\nu}_\mathrm{\mu}), \end{aligned} \tag{1.10}$$

of which the latest is subdominant. As one can see, muon neutrinos are also produced in the two last decays. Tau neutrinos are produced in tau decays [Pov13]

$$\begin{aligned} \tau^- &\rightarrow\ e^-\ +\ \overline{\nu}_\mathrm{e}\ +\ \nu_\tau, \\ \tau^- &\rightarrow\ \mu^-\ +\ \overline{\nu}_\mu\ +\ \nu_\tau, \\ \tau^- &\rightarrow\ \pi^-\ +\ \nu_\tau. \end{aligned} \tag{1.11}$$

These production processes take place at different sources. Sources of neutrinos detectable on the earth are the sun, the freeze-out after the big bang, cosmic showers, supernovae, natural radioactivity, nuclear power plants and neutrino accelerators. Each of these sources is briefly discussed in the following:

Neutrino accelerators
Dedicated neutrino beams are produced at proton accelerators [Zub11, Kop07]. To produce the neutrinos, a high energy proton beam is guided to a target usually made of beryllium or graphite. Among others this also produces pions and kaons. These particles are focused by a magnetic horn into decay tunnels selected by their charge. During the decay of the pions (compare equ. (1.10)), kaons and their secondaries a neutrino beam with mean energies from 0.5 to more than 250 GeV [Kop07] can be generated.

[1] In this context light neutrinos refer to neutrinos with masses of less than $1\,\mathrm{MeV\,c^{-2}}$.

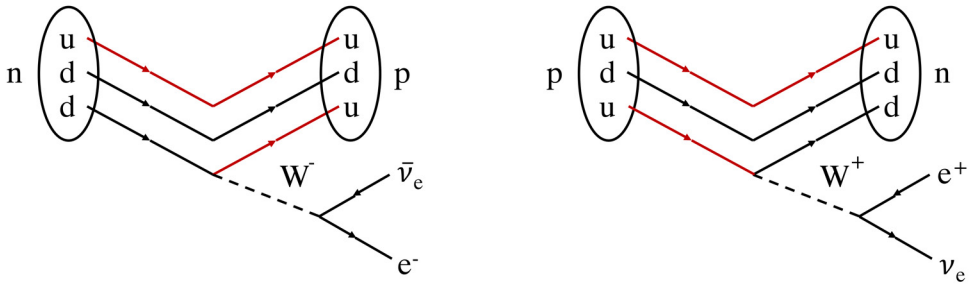

Figure 1.2: Feynman diagrams of the β^- and the β^+-decay. Left: in the β^--decay a down quark is decaying in an up quark and a W^- boson. The W^- again decays into an electron and an electron anti-neutrino. Right: in the β^+-decay a W^+ is generated by the decay of an up quark into a down quark. The latter decay of the W^+ results in the production of a positron and an electron neutrino.

Nuclear power plants

Nuclear power plants are the most intense electron anti-neutrino sources on earth [Zub11]. On average 6 neutrinos are produced by the β-decay of the daughter molecules generated by the fission reaction [Akh99]. That means that a 3 GW fission reactor isotropically emits about $7.7{\cdot}10^{20}$ neutrinos per second causing a neutrino flux of $6{\cdot}10^{11}\,\mathrm{cm}^{-2}\,\mathrm{s}^{-1}$ at 100 m distance to the reactor [Akh99]. The emitted neutrinos have energies up to 10 MeV.

Natural radioactivity

Due to radioactive nuclides like ^{40}K, ^{238}U and ^{232}Th and their natural decay chains a neutrino flux of about $6{\cdot}10^{6}\,\mathrm{cm}^{-2}\,\mathrm{s}^{-1}$ with energies of up to 1 MeV are produced on earth [Akh99]. These neutrinos can be used to obtain further information on the chemical composition of the interior of the earth [Ede66].

Supernovae

Supernovae type II are a huge but short-lived source of both neutrinos and anti-neutrinos of each flavor. Stars produce elements up to ^{56}Fe by nuclear fusion in their core which increases the mass of the core [Per09]. As long as the mass of the inner core of a star is below the Chandrasekhar limit of about $1.5\,M_\odot$ [Zub11] the electron degeneracy pressure balances the gravitational pressure of the core itself. But if this limit is passed the core of the star collapses. In case of a supernova type II up to 10^{58} neutrinos are produced by [Per09]

$$\begin{aligned} p \;+\; e^- &\rightarrow\; n \;+\; \nu_e \qquad \text{neutronization} \\ \gamma \;\rightarrow\; e^+ \;+\; e^- &\rightarrow\; \nu_\alpha \;+\; \overline{\nu}_\alpha \qquad \text{thermalization.} \end{aligned} \tag{1.12}$$

The neutronization takes place during the first milliseconds of the collapse and the pair production by thermalization during about 10 s after the beginning of the collapse [Sch97, Woo05, Jan07]. The mean energies of the neutrinos are 10 MeV to 15 MeV. During these processes the neutrinos carry away about 99 % of the energy released during the collapse [Bah87].

Cosmic showers generating atmospheric neutrinos

Atmospheric neutrinos are produced by the continuous bombardment of the atmosphere by high energetic particles [Zub11]. These particles interact with the molecules of the atmosphere giving rise to hadronic showers and a neutrino flux of $10^{-1}\,\mathrm{cm}^{-2}\,\mathrm{s}^{-1}$ at the surface of the earth [Akh99]. In these showers muon and electron neutrinos are generated

mostly by

$$\begin{aligned} p(\alpha,...) + \text{air} &\rightarrow \pi^{\pm}(K^{\pm}) + X \\ \pi^{\pm}(K^{\pm}) &\rightarrow \mu^{\pm} + \nu_{\mu}(\overline{\nu}_{\nu}) \\ \mu^{\pm} &\rightarrow e^{\pm} + \nu_{\mathrm{e}}(\overline{\nu}_{\mathrm{e}}) + \overline{\nu}_{\mu}(\nu_{\mu}) \end{aligned} \tag{1.13}$$

with a muon to electron neutrino ratio of roughly 2 and energies up to 1 TeV [Hir88].

Freeze-out after big bang generating relic neutrinos
Directly after the big bang at time $t \ll 0.1\,\mathrm{s}$ the temperature of the universe was $E \gg 1\,\mathrm{MeV}$. At this stage all fundamental particles were in a thermodynamic equilibrium. That means that the neutrino interacted with other particles via the weak interaction and the total energy density was dominated by radiation. With its expansion [Hub31, Sli15] the universe cooled down. At $E \approx 1\,\mathrm{MeV}$ and $t \approx 0.1\,\mathrm{s}$ the weak interaction rate dropped below the expansion rate of the universe. From this time on the neutrinos were decoupled [Les12] and not able to interact with the other particles anymore. Nevertheless, the neutrinos still had an influence on the processes during the evolution of our universe, namely as hot dark matter. The neutrinos carried away energy during the formation of structures and by that smeared out fluctuations on small scales. Overall it is expected that there is a cosmic neutrino background of about 112 relic neutrinos of each flavor per cm^3 [Oli14] with an energy distribution equal to that of a black body of temperature $T_{\nu} \approx 1.9\,\mathrm{K}$ [Oli14] and an average energy of $5{\cdot}10^{-4}\,\mathrm{eV}$ [Akh99, Oli14]. Due to the low energy of the neutrinos, this background is not yet experimentally confirmed.

Sun generating solar neutrinos
The sun emits about $2{\cdot}10^{38}$ electron neutrinos per second by thermonuclear reactions causing a neutrino flux of about $6{\cdot}10^{10}\,\mathrm{cm}^{-2}\,\mathrm{s}^{-1}$ with $E \leq 0.42\,\mathrm{MeV}$ and about $5{\cdot}10^{6}$ $\mathrm{cm}^{-2}\,\mathrm{s}^{-1}$ with $0.8\,\mathrm{MeV} \leq E \leq 15\,\mathrm{MeV}$ [Akh99]. These numbers are calculated in the standard solar model by Bahcall [Bah05]: the dominant process of neutrino generation in the sun is the pp cycle [Zub11]

$$2e^{-} + 4p \rightarrow {}^{4}\mathrm{He} + 2\nu_{\mathrm{e}} + 26.73\,\mathrm{MeV}. \tag{1.14}$$

Overall 6 reactions of this cycle produce neutrinos, 3 of them mono-energetic and 3 with continuous energy spectrum [Akh99], all with $E_{\nu,\mathrm{pp}} < 0.42\,\mathrm{MeV}$ [Zub11, Bah05]. To detect these low energetic neutrinos gallium experiments like GALLEX [Ans92] and SAGE [Abd94] are used. Neutrinos with energies $< 15\,\mathrm{MeV}$ [Zub11, Bah05] are produced in the reaction

$${}^{8}\mathrm{B} \rightarrow {}^{4}\mathrm{He} + {}^{4}\mathrm{He} + e^{+} + \nu_{\mathrm{e}}. \tag{1.15}$$

The higher energy enables the detection of the ${}^{8}B$-neutrinos by Cerenkov detectors like Kamiokande [Hir89]. The ^{7}B-neutrinos

$${}^{7}\mathrm{B} + e^{-} \rightarrow {}^{7}\mathrm{Li} + \nu_{\mathrm{e}} \tag{1.16}$$

and pep-neutrinos [Kla13]

$$p + e^{-} + p \rightarrow {}^{2}\mathrm{H} + \nu_{\mathrm{e}} \tag{1.17}$$

have monoenergetic energies of 0.862 MeV and 0.384 MeV or 1.44 MeV [Kla13], respectively. These neutrinos are detectable by radiochemical experiments like the Homestake experiment of Davis [Dav68] and the liquid scintillation experiment Borexino [Bel14].

The investigation of solar neutrinos by experiment lead to the so-called solar neutrino problem and its resolving by the discovery of the neutrino oscillation both described in the following section.

1.2 Neutrino oscillation

In the Homestake experiment R. Davis [Dav68] measured the flux of solar electron neutrinos by detecting ^{8}B- and ^{7}B-neutrinos in the reaction

$$\nu_e + {}^{37}\mathrm{Cl} \rightarrow {}^{37}\mathrm{Ar} + e^- . \tag{1.18}$$

The produced ^{37}Ar can be separated from the ^{37}Cl. To determine the amount of produced ^{37}Ar the number of decays are counted by a proportional counter [Dav68]. Note that the experiment is only sensitive to electron neutrinos. During the experiment on average about 0.48 events per day were detected over the course of 24 years [Cle98, Dav94].

The measured flux was compared to the flux predicted by the standard solar model of Bahcall [Bah64] with the result that the flux was too low by a factor of 3 to 4 [Bah76, Dav79]. This discrepancy between theory and experiment of 3/1 was also confirmed by GALLEX [Ham99], SAGE [Abd02] and GNO [Alt05], also based on chemical reactions. This incident was called the solar neutrino problem.

The experiments Kamiokande [Fuk96], Super-Kamiokande [Fuk98] and SNO [Ahm01] have also measured the flux of the neutrinos from the sun. These experiments are based on the detection of characteristic Cerenkov light cones with photo-multipliers, emitted by particles which move faster than the phase velocity of light in the dielectric medium. The method enables not only to measure the number of neutrinos moving through the detector volume but also to measure the energy, the direction of the neutrino and the arrival time. In addition, Cerenkov detectors are not only sensitive to electron neutrinos but to all flavors. The Cerenkov experiments also confirmed the deficit in the electron neutrino flux [Ahm01, Ahm02, Fuk98, Fuk94] and the existence of the solar neutrino problem.

SNO was also able to measure the absolute neutrino flux of all flavors using the neutral current, which is $(5.44 \pm 0.99) \cdot 10^6\,\mathrm{cm}^{-2}\,\mathrm{s}^{-1}$ [Ahm01]. This value is in good agreement with the fluxes predicted by the standard solar model [Bah01, Bru97, Bru98].

In combination with results provided by the Super-Kamiokande experiment about the atmospheric neutrino flux [Fuk98] this measurement solved the solar neutrino problem: The Super-Kamiokande experiment measured a deficit of the atmospheric muon neutrinos, which is called the atmospheric neutrino problem or the atmospheric neutrino anomaly. In addition to the deficit, Super-Kamiokande also verified the dependence of the deficit on the path length through matter and the energy of the neutrino [Fuk98, Akh99]. A smaller number of neutrinos was detected if the neutrinos had to move through the earth prior to detection. If the neutrino is produced directly above the detector the path length L is about 10 km, if the neutrino is produced at the other side of the earth $L \approx 10^4$ km [Zub11]. This allows determining the dependence of the deficit on L/E.

The solution to both problems, the solar and the atmospheric neutrino problem, is the neutrino oscillation. The neutrinos produced in a specific flavor change their flavor periodically. That the transformation of neutrinos of one flavor into another flavor is possible, has not only been proven by deficits but also by the appearance of flavors not previously produced in the respective experiments. For example in the long baseline neutrino accelerator experiment T2K the transformation of muon into electron neutrinos was demonstrated [Abe13] and in the OPERA experiment the transformations of muon neutrinos in tau neutrinos were observed [OPE14].

The first theoretical description of the neutrino oscillation was developed by Pontecorvo in [Pon58, Pon57] and further improved by him and Gribov [Pon68, Gri69] as well as Maki,

Nakagawa and Sakata [Mak62]. This theory is based on three weak flavor eigenstates $|\nu_\alpha\rangle$ ($\alpha = e, \nu, \tau$), which participate in weak interactions, and three mass eigenstates $|\nu_i\rangle$ ($i = 1, 2, 3$) with well-defined masses. Both, the flavor and the mass eigenstates are connected via the so-called Pontecorvo-Maki-Nakagawa-Sakata (PMNS) matrix U [Zub11]

$$|\nu_\alpha\rangle = \sum_i U_{\alpha i}|\nu_i\rangle \text{ and } |\nu_i\rangle = \sum_\alpha U^*_{\alpha i}|\nu_\alpha\rangle, \tag{1.19}$$

which is unitary, meaning $U^\dagger_{i\alpha} = U^*_{\alpha i}$, and given by

$$U = \begin{pmatrix} c_{12}c_{13} & s_{12}c_{13} & s_{13}e^{-i\delta} & \\ -s_{12}c_{23} - c_{12}s_{23}s_{13}e^{i\delta} & c_{12}s_{23} - s_{12}s_{23}s_{13}e^{i\delta} & s_{13}e^{i\delta} & s_{23}c_{13} \\ s_{12}s_{23} - c_{12}s_{23}s_{13}e^{i\delta} & -c_{12}s_{23} - s_{12}c_{23}s_{13}e^{i\delta} & s_{13}e^{i\delta} & c_{23}c_{13} \end{pmatrix} \cdot \begin{pmatrix} 1 & 0 & 0 \\ 0 & e^{\frac{i\alpha_{21}}{2}} & 0 \\ 0 & 0 & e^{\frac{i\alpha_{31}}{2}}. \end{pmatrix} \tag{1.20}$$

Here $c_{ij} = \cos(\vartheta_{ij})$ and $s_{ij} = \sin(\vartheta_{ij})$, which means that the mixing angle ϑ_{ij} describes the contribution of a certain mass eigenstate on a certain flavor eigenstate and the other way around. δ is the Dirac CP violating[2] phase and α_{ij} are the Majorana CP violating phases.

The mass eigenstates $|\nu_i\rangle$ satisfy the equation [Zub11][3]

$$H|\nu_i\rangle = E_i|\nu_i\rangle \tag{1.21}$$

where H is the Hamiltonian and E_i are eigenvalues. To describe the temporal propagation of $|\nu_i\rangle$ the Schrödinger equation

$$i\hbar\frac{\partial}{\partial t}|\nu_i(x,t)\rangle = H|\nu_i(x,t)\rangle \tag{1.22}$$

must be solved. The solution yields plane waves of the form

$$|\nu_i(x,t)\rangle = e^{-\frac{i}{\hbar}(E_i t - p_i x)}|\nu_i\rangle \tag{1.23}$$

But as only the flavor eigentstates $|\nu_\alpha\rangle$ take place in weak interactions the neutrino mass eigenstate $|\nu_i\rangle$ can neither be produced nor detected. This means that a primary produced pure flavor eigenstate $|\nu_\alpha\rangle$ transforms into a superposition

$$|\nu(x,t)\rangle = \sum_i U_{\alpha i}|\nu_i(x,t)\rangle = \sum_i U_{\alpha i}e^{-\frac{i}{\hbar}(E_i t - p_i x)}|\nu_i\rangle = \sum_{i,\beta} U_{\alpha i}U^*_{\beta i}e^{-\frac{i}{\hbar}(E_i t - p_i x)}|\nu_\beta\rangle \tag{1.24}$$

of the 3 flavor eigenstates.

With equation (1.24) the transition amplitude of a neutrino of the flavor α into a flavor β is

$$A(\nu_\alpha \to \nu_\beta)(x,t) = \langle\nu_\beta|\nu(x,t)\rangle = \sum_{i,\beta} U^*_{\beta i}U_{\alpha i}e^{-\frac{i}{\hbar}(E_i t - p_i x)}, \tag{1.25}$$

giving a transition probability of

$$P(\nu_\alpha \to \nu_\beta)(x,t) = |A(\nu_\alpha \to \nu_\beta)(x,t)|^2 = \sum_{i,j} U_{\alpha i}U^*_{\alpha j}U^*_{\beta i}U_{\beta j}e^{-\frac{i}{\hbar}(E_i t - p_i x)}e^{-\frac{i}{\hbar}(E_j t - p_j x)}. \tag{1.26}$$

[2] CP violation is the non-conservation of a simultaneous transformation of charge and parity. If CP is conserved a particle in a system is not distinguishable from its antiparticle in the mirrored system.

[3] If not differently stated all following formulas are taken from [Zub11].

If the neutrino is ultra-relativistic, meaning $v \approx c$ and $E \approx p_i c \gg m_i c^2$, the eigenvalues and the flight distance can be simplified to

$$\begin{aligned} E_i = \sqrt{p_i^2 c^2 + m_i^2 c^4} \approx p_i c + \frac{m_i^2 c^4}{2E} \text{ and } x = L = vt \approx ct \\ \Rightarrow E_i t - p_i x = \frac{m_i^2 c^3}{2} \frac{L}{E}, \end{aligned} \tag{1.27}$$

which changes equation (1.26) to

$$\begin{aligned} P(\nu_\alpha \to \nu_\beta)(x,t) &= \sum_{i,j} U_{\alpha i} U_{\alpha j}^* U_{\beta i}^* U_{\beta j} e^{-\frac{i}{\hbar}\frac{m_i^2 c^3}{2}\frac{L}{E}} \\ &= \sum_i |U_{\alpha i} U_{\beta i}^*|^2 + 2\mathrm{Re} \sum_{j<i} U_{\alpha i} U_{\alpha j}^* U_{\beta i}^* U_{\beta j} e^{-\frac{i}{\hbar}\frac{m_i^2 c^3}{2}\frac{L}{E}} \\ &= P(\nu_\alpha \to \nu_\beta)(L,E)(\geqslant 0) \end{aligned} \tag{1.28}$$

with $\Delta m_{ij}^2 = m_i^2 - m_j^2$. The first term in this equation describes the average probability that a flavor eigenstate ν_α oscillates into a flavor eigenstate ν_β and the second term contains the spatial and temporal dependence of the oscillation. If instead of the probability of measuring a new flavor the probability of measuring the initial flavor is of interest, it is given by

$$P(\nu_\alpha \to \nu_\alpha) = 1 - \sum_{\alpha \neq \beta} P(\nu_\alpha \to \nu_\beta)(\leqslant 1). \tag{1.29}$$

For a better understanding of the influence of the mixing angles on oscillation the simplified case of neutrino mixing of only two flavor eigenstates is considered now[4]. In that case the mixing matrix simplifies to

$$U = \begin{pmatrix} cos(\theta) & sin(\theta) \\ -sin(\theta) & cos(\theta) \end{pmatrix}, \tag{1.30}$$

where θ is the mixing angle between the flavor eigenstates. As one can see, U is independent from any CP violating phase in this simplification [Zub11]. With U the transition probability given in equation (1.26) simplifies to

$$\begin{aligned} P(\nu_\alpha \to \nu_\beta) = P(\nu_\beta \to \nu_\alpha) = P(\overline{\nu}_\alpha \to \overline{\nu}_\beta) = P(\overline{\nu}_\beta \to \overline{\nu}_\alpha) \\ = \sin^2(2\theta) \cdot \sin^2\left(\frac{\Delta m^2 c^3}{4\hbar}\frac{L}{E}\right) \\ = 1 - P(\nu_\alpha \to \nu_\alpha). \end{aligned} \tag{1.31}$$

The oscillation does neither depend on the absolute neutrino mass nor the Majorana phase and therefore these parameters are not observable by investigation of neutrino oscillation [Bil80]. In contrast to this the Dirac CP violating phase can cause a difference in the oscillation probability of neutrinos and anti-neutrinos which can be measured[5] [Zub11].

[4] As the mixing angle θ_{13} differs by more than one order of magnitude from the other mixing angles (compare table 1.1) this simplification is sufficiently describing reality.

[5] If CP invariance is violated by the neutrino oscillation, $P(\nu_\beta \to \nu_\alpha) \neq P(\overline{\nu}_\alpha \to \overline{\nu}_\beta)$. This difference could be measured in experiment.

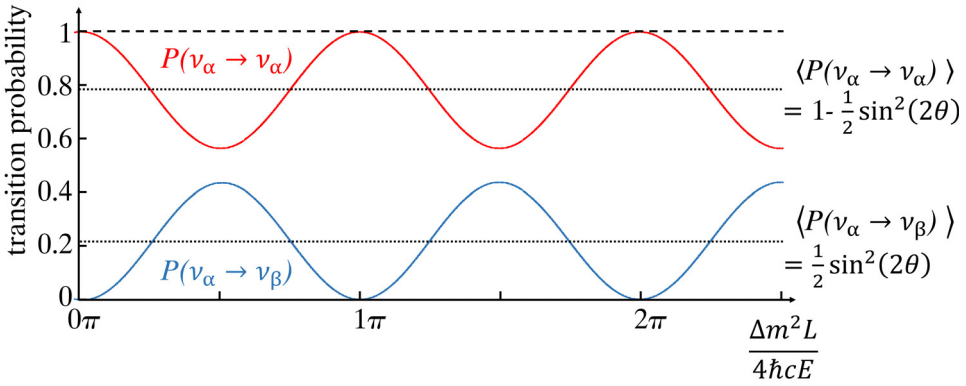

Figure 1.3: Transition probability of the neutrino oscillation $\nu_\alpha \to \nu_\beta$. The upper (red) curve is the probability that a neutrino produced with the flavor α is detected in the flavor α. This is called the disappearance channel. The lower (blue) curve is the appearance channel, where neutrinos of the flavor β are detected although neutrinos of the flavor α are produced.

As mentioned above the first term describes the oscillation amplitude which only depends on the mixing angle θ. The second term describing the spatial and temporal behavior of the oscillation is defined by the characteristic oscillation length

$$L_0 = \frac{4\pi\hbar}{c^3}\frac{E}{\Delta m^2} = 2.48\,\mathrm{m} \cdot \frac{E/\mathrm{MeV}}{\Delta m^2/\mathrm{eV}^2} \tag{1.32}$$

visualized in figure 1.3. As the transition probability given in equation (1.31) is zero only if both the mixing angle and the mass difference are zero, the neutrino cannot be massless due to the observation of neutrino oscillation.

In addition to depending on the energy E and the mass difference Δm the oscillation frequency also depends on the medium the neutrinos move through [Akh99]: if neutrinos move through matter, they can be elastically scattered without changing their momentum. In this process a mean potential V_a is created which is proportional to the number densities of the scatterers. This potential affects the oscillation, but only if the potential is as large as or larger than the quotient $\Delta m^2/2E$. Then the effect, the so-called the Mikheyev-Smirnov-Wolfenstein (MSW) effect [Mik85, Wol78], has a significant impact. This was experimentally verified by the dependence of the neutrino flux on the direction by Super-Kamiokande [Fuk98]. For that reason, the MSW effect is part of the solution of the atmospheric neutrino problem. Another experimental proof of the existence of this effect was found by the Borexino experiment [Bel10] by investigating the reduction of the survival probability of high-energetic electron neutrinos.

The determination of the oscillation parameters θ_{12} and Δm_{21} is associated with solar neutrino oscillation. They are measured by Kamiokande[Fuk96], Super-Kamiokande [Fuk01] and SNO [Aha07, Aha08], by the reactor experiment KamLand [Abe08] and the accelerator experiments K2K [Ahn06] and MINOS [Ada13b]. θ_{23} and Δm_{32} are linked to atmospheric neutrino oscillation. They are measured by Super-Kamiokande [Abe11], K2K [Ahn06] and MINOS [Ada13b]. The mixing angle θ_{13} is determined by accelerator experiments and reactor experiments as Double Chooz [Abe12], RENO [Ahn12] and Daya Bay [An13]. A summary of current values of the 3 mixing angles and the 2 mass differences are given in table 1.1.

Table 1.1: Selected experimental results of the oscillation parameters. As the results of the experiments depend on the hierarchy of the neutrino mass (compare figure 1.4) multiple results are given for some experiments. Results expecting a normal hierarchy are marked by n.h., those expecting an inverted hierarchy are marked by i.h.

parameter	result	unit	experiment	source
Δm^2_{21}	$7.59^{+0.21}_{-0.19}$	$10^{-5}\,\mathrm{eV}^2\,\mathrm{c}^{-4}$	solar data+KamLAND+ Borexino+SNO	[Aha13]
	7.53 ± 0.18	$10^{-5}\,\mathrm{eV}^2\,\mathrm{c}^{-4}$	solar data+KamLAND	[Oli14]
Δm^2_{13}	2.48±0.10	$10^{-3}\,\mathrm{eV}^2\,\mathrm{c}^{-4}$	T2K (i.h.)	[Abe14]
Δm^2_{32}	2.51±0.10	$10^{-3}\,\mathrm{eV}^2\,\mathrm{c}^{-4}$	T2K (n.h.)	[Abe14]
$\lvert\Delta m^2_{32}\rvert$	$2.28 - 2.46$ $(2.32 - 2.53)$	$10^{-3}\,\mathrm{eV}^2\,\mathrm{c}^{-4}$	MINOS n.h. (i.h.)	[Ada14]
$\tan^2(\theta_{12})$	$0.47^{+0.05}_{-0.04}$		solar data+KamLAND+ Borexino+SNO	[Aha13]
	$0.436^{+0.029}_{-0.025}$		solar data+KamLAND	[Oli14]
$\sin^2(\theta_{13})$	0.023 ± 0.002		solar data+KamLAND	[Oli14]
$\sin^2(2\theta_{13})$	$0.090^{+0.008}_{-0.009}$		Daya Bay	[An14]
	$0.100^{+0.010}_{-0.012}$		RENO	[Oli14]
	$0.109^{+0.030}_{-0.025}$		Double Chooz	[Abe12]
$\sin^2(\theta_{23})$	$0.514^{+0.055}_{-0.056}$ (0.511 ± 0.055)		T2K n.h. (i.h.)	[Abe14]
	$0.35 - 0.65$ $(0.34 - 0.67)$		MINOS n.h. (i.h.)	[Ada14]

As mentioned above accessing the Majorana CP violating phases is not possible for the neutrino oscillation experiments. Therefore, no information about this phase is currently available [Oli14]. In contrast to this, access to the Dirac phase is possible for long-baseline experiments with baselines of about 1 000 km [Alb04, Bar00]. An example for such an experiment is the accelerator experiment NOνA [Ayr04]. But even with such experiments the Dirac phase can only be determined if the MSW effect is fully understood.

The absolute mass of the neutrino is also not measurable by oscillation experiments as only the mass difference between two mass eigenstates contributes to the oscillation. Therefore, three different hierarchy scenarios are still possible:

- Normal hierarchy with $m_1 \ll m_2 < m_3$
- Inverted hierarchy with $m_3 \ll m_1 < m_2$
- Quasi-degenerated case with $m_1 \cong m_2 \cong m_3$

In future experiments based on accelerator neutrinos [Pat12, Ada13a, Rub13], reactor neutrinos [Zha08, Zha09, Li14] and atmospheric neutrinos [Aar14] the question about the hierarchy will be addressed and hopefully answered. However, the fact that the neutrino oscillates, makes it impossible for the neutrino to be massless as predicted by the Standard Model. Some models that try to explain how the neutrino mass is generated, are discussed in the following section.

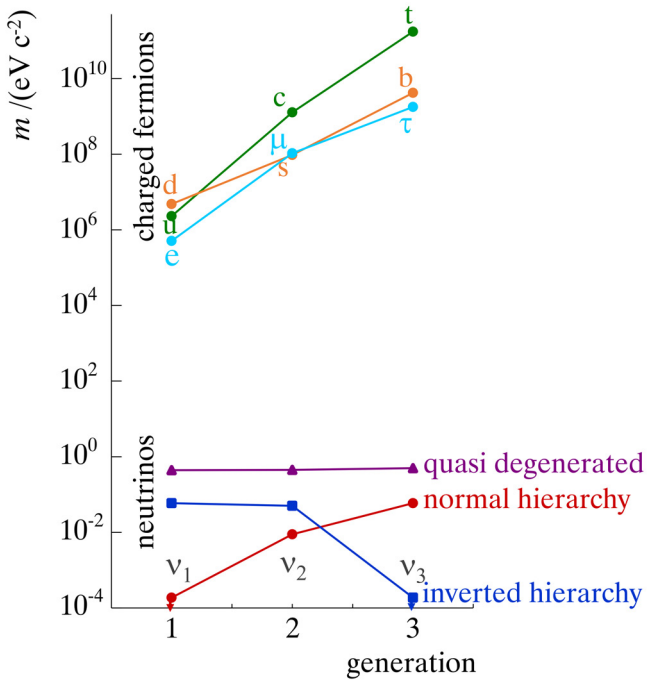

Figure 1.4: The masses in the Standard Model and the neutrino mass hierarchy. The mass of the fermionic particles of the Standard Model is plotted against their generation. The quark and charged lepton masses are several orders of magnitude larger than the neutrino masses. In addition, the masses within the quark generations only differ by up to 2 orders of magnitude which is by far exceeded in case of the leptonic generations. This can be stated although the absolute neutrino masses are not known yet. That means the hierarchy of the 3 neutrinos is not yet known either. The 3 possible hierarchies are shown in the lower part of the plot.

1.3 The mass of the neutrino

The fact that neutrino oscillations have been observed proves that at least 2 of the neutrino mass eigenstates ν_1, ν_2 and ν_3 have a non-zero mass. The charged fermions of the Standard Model with non-zero mass obtain their mass by a spontaneous symmetry breaking and the Higgs mechanism [Hig64, Kib67]: a doublet of scalar Higgs fields $(H^+, H^0)^T$ can couple to doublets of a left-handed and a right-handed singlet due to a non-zero vacuum expectation. This specific type of coupling is called the Yukawa coupling, which is described by the Lagrangian [Zub11]

$$\mathfrak{L}_{\mathrm{Yuk}} = -\frac{c_\mathrm{e} v}{\sqrt{2}}(\overline{\nu}_\mathrm{R}\nu_\mathrm{L} + \overline{\nu}_\mathrm{L}\nu_\mathrm{R}) = -\frac{c_\mathrm{e} v}{\sqrt{2}}\overline{\nu}\nu = -m_\nu \overline{\nu}\nu. \tag{1.33}$$

In this Lagrangian c_e is the coupling constant of the Yukawa coupling, v is the Higgs field vacuum expectation value, ν is the spinor of the electron and $\overline{\nu}$ is the adjoined spinor. The fact that both left- and right-handed neutrinos are needed to generate mass by this coupling, but the V-A theory [Sch95] prohibits the existence of right-handed neutrinos [Zub11], is the reason why the neutrino was expected to be massless.

One approach to explain the neutrino mass generation is to extend the Standard Model by the required right-handed neutrino. In that case a Dirac mass term [Zub11]

$$\mathfrak{L} = -m_\mathrm{D}\overline{\nu}\nu. \tag{1.34}$$

must be added to the Lagrangian given in equation (1.33). But to explain the smallness of the neutrino mass the coupling constant must be in the order of $c_e \lesssim 3 \cdot 10^{-11}$ [Akh99]. Compared to the coupling constants of the electron for example it is about 5 orders of magnitude smaller [Akh99]. This is in principle possible, but it seems to be unrealistic. Especially as the difference of the masses within the three quark generations is about 1 to 2 orders of magnitude and in case of the lepton generations would need to be more than 10 orders of magnitude (compare figure 1.4). This issue could be fixed by the seesaw mechanism [Rod11] explained later in this section.

Another approach is to also superinduce a Majorana mass term. This is possible since the neutrino is a neutral particle and therefore it could in principle be its own anti-particle. In that case the Lagrangian would be [Zub11]

$$\mathfrak{L} = -\frac{1}{2}\left[\left(\overline{\nu}_{\mathrm{L}}\,\overline{N}^{c}_{L}\right)\begin{pmatrix} m_{\mathrm{L}} & m_{\mathrm{D}} \\ m_{\mathrm{D}} & m_{\mathrm{R}} \end{pmatrix}\begin{pmatrix} \nu^{c}_{\mathrm{R}} \\ N_R \end{pmatrix} + \mathrm{h.c.}\right], \tag{1.35}$$

where N is the heavy sterile neutrino which is not weakly interacting, the superscription ^{c} marks charge conjugated particles, h.c. means hermitian conjugated and m_{D} is the Dirac mass. m_{L} and m_{R} are the left- or the right-handed Majorana masses, respectively. The mass eigenstates of the neutrino are therefore a superposition of the Dirac and Majorana masses calculable by the diagonalization of the mass matrix [Zub11]

$$\begin{aligned} \nu_{1\mathrm{L}} &= \cos(\theta)\nu_{\mathrm{L}} - \sin(\theta)N^{c}_{\mathrm{L}} \qquad & \nu^{c}_{1\mathrm{R}} &= \cos(\theta)\nu^{c}_{\mathrm{R}} - \sin(\theta)N_{\mathrm{R}} \\ \nu_{2\mathrm{L}} &= \sin(\theta)\nu_{\mathrm{L}} + \cos(\theta)N^{c}_{\mathrm{L}} \qquad & \nu^{c}_{1\mathrm{R}} &= \sin(\theta)\nu^{c}_{\mathrm{R}} + \cos(\theta)N_{\mathrm{R}} \end{aligned} \tag{1.36}$$

The corresponding mass eigenvalues are

$$\tilde{m}_{1,2} = \frac{1}{2}\left[(m_{\mathrm{L}} + m_{\mathrm{R}}) \pm \sqrt{(m_{\mathrm{L}} - m_{\mathrm{R}})^2 + 4m^2_{\mathrm{D}}}\right] \tag{1.37}$$

and the mixing angle is

$$\tan(2\theta) = \frac{2m_{\mathrm{D}}}{m_{\mathrm{R}} - m_{\mathrm{L}}}. \tag{1.38}$$

In addition to this general solution 4 different special cases can be considered [Zub11]:

- If the Majorana masses are vanishing ($m_{\mathrm{L}} = m_{\mathrm{R}} = 0$), the mass eigenvalues are equal to the Dirac mass $\tilde{m}_{1,2} = m_{\mathrm{D}}$.
- If the Dirac mass is much larger than both Majorana masses ($m_{\mathrm{D}} \gg m_{\mathrm{L}}, m_{\mathrm{R}}$) the mass eigenvalues are almost degenerated. The resulting neutrinos are called pseudo-Dirac neutrinos.
- If the left-handed Majorana mass is vanishing ($m_{\mathrm{L}} = 0$) and the right-handed is much larger than the Dirac mass ($m_{\mathrm{R}} \gg m_{\mathrm{D}}$) the two mass eigenvalues become

$$\tilde{m}_1 = \frac{m^2_{\mathrm{D}}}{m_{\mathrm{R}}} \ll m_{\mathrm{D}} \tag{1.39}$$

$$\tilde{m}_2 = m_{\mathrm{R}}\left(1 + \frac{m^2_{\mathrm{D}}}{m^2_{\mathrm{R}}}\right) \ll m_{\mathrm{R}}. \tag{1.40}$$

  As $m_{\mathrm{R}} \gg m_{\mathrm{D}}$, the mass eigenvalue $\tilde{m}_1$ becomes small and $\tilde{m}_1 \ll m_{\mathrm{D}}$. The mass eigenvalue $\tilde{m}_2$ is approximately equal to m_{R}. This special case is the so-called type I seesaw mechanism [Moh80, Moh81] which explains the smallness of the neutrino mass by the existence of a heavier neutrino. Due to its heaviness, $\tilde{m}_2$ is out of the range of current experiments for most theoretical models.

- If the right-handed Majorana mass is again much larger than the Dirac mass ($m_{\mathrm{R}} \gg m_{\mathrm{D}}$) and the left-handed Majorana masses are much larger than the right-handed one ($m_{\mathrm{L}} \ll m_{\mathrm{R}}$) a second contribution to the neutrino mass must be added. This contribution represents a coupling to the Higgs field [Zub11]. This coupling causes an almost degenerated neutrino mass and the corresponding effect is the so-called type II seesaw mechanism.

There are also approaches based on R-parity violating supersymmetric models [Hir04] and Higgs triplets added to the Higgs doublet [Zub11] explaining the origin of the neutrino mass.

The variety of different approaches to the neutrino mass illustrates that understanding the origin of the neutrino mass is of high interest. The origin of this interest is discussed in the following section.

1.4 Impact of neutrino mass on physics

The neutrino mass has a large influence on different aspects of physics, namely particle physics, astrophysics and cosmology [Akh99].

In particle physics the investigation of physics beyond the Standard Model by itself is sufficient motivation for investigations into the nature and the value of the neutrino mass. If the neutrino mass is known a new, yet unexplored mass scale could be found. In addition, a better understanding of mass generation could be reached.

In case of cosmology and astrophysics there are several reasons why knowledge of the neutrinos mass is important: neutrinos contribute to the overall amount of matter and energy in the universe. As they are not participating in the electromagnetic interactions and as they are relativistic [Per09], they are part of the so-called hot dark matter. The contribution of this hot dark matter on the overall dark matter is determined by the mass of the neutrino. In addition, the neutrino has influenced the structure formation of the early universe by smearing out density inhomogeneities which are caused by quantum fluctuations [Per09]. That is why today the universe is isotropic and homogeneous at long scales above 100 Mpc ($3.1 \cdot 10^{18}$ m) [Zub11]. Current concepts of the structure formation at this early stage of the universe are based on the neutrino mass as one parameter [Aga11]. If this parameter is known, a more precise concept of the structure formation can be obtained. Another reason for the importance of the neutrino mass is the role of the neutrino in baryogenesis, the process by which an excess amount of baryons compared to anti-baryons exists in the universe. This could be caused by the decay of Majorana neutrinos with large mass.

To measure the neutrino mass several approaches are possible. The most important are discussed in the following section.

1.5 Measurement of the neutrino mass

The measurement techniques used to determine the neutrino mass can be divided into direct and indirect methods. Direct methods are characterized by the fact that kinematics, the conservation of momentum and the momentum-energy relation are used to determine the neutrino mass. Because of this, direct methods are purely dependent on accepted theory and called model-independent. In contrast to that indirect methods rely on assumptions and models made by the analysis of data. These methods are therefore susceptible to systematic uncertainties and highly dependent on the correctness of the used model. For both methods exemplary experiments are given in the following (note that different experiments may have different observables).

1.5.1 Indirect measurement method

Cosmological observations
With the help of cosmological observations the neutrino mass can be determined indirectly. Such observations are the distribution of galaxy clusters or the cosmic microwave background. The calculation of the neutrino mass is then based on the fact that neutrinos contribute most to the fermionic matter in the universe. Their contribution Ω_ν to the overall energy density of the universe is dependent on the sum of the neutrino masses and the Hubble parameter[6] $h = H_0/(100\,\mathrm{km\,s^{-2}\,Mpc^{-1}})$ [Win11, Oli14]:

$$\sum_i m_i = 93\Omega_\nu h^2\,\mathrm{eV}. \tag{1.41}$$

Taking advantage of this an upper limit on the neutrino mass can be calculated by assuming a neutrino dominated ($\Omega_\nu = \Omega_\mathrm{tot}$), flat universe $\Omega_\mathrm{tot} = 1$:

$$\sum_i m_i \lesssim 51\,\mathrm{eV}. \tag{1.42}$$

Of course, a more realistic upper limit can be calculated if the energy densities of matter Ω_m and dark energy Ω_Λ are also taken into account [Ade14]. Combining the results of the Planck measurements on the cosmic microwave-background [Ade14], the WMAP measurements [Hin13] and surveys of baryon acoustic oscillations [Beu11] the upper limit on the sum off all neutrino masses becomes

$$\sum_i m_i \lesssim 0.23\,\mathrm{eV}\ (95\,\%\ \mathrm{C.L.}). \tag{1.43}$$

Neutrinoless double β-decay
Another indirect method is the investigation of the neutrinoless double β-decay ($0\nu\beta\beta$). To understand this decay the double β-decay ($2\nu\beta\beta$) is discussed first: the $2\nu\beta\beta$-decay is a second order process in the weak interaction [Akh99]. It takes place if the normal β-decay is energetically forbidden (compare figure 1.5). During the $2\nu\beta\beta$-decay reaction

$$A(Z,N) \rightarrow A(Z \pm 2, N \mp 2) + 2e^{\mp} + 2\overline{\nu}_\mathrm{e}(2\nu_\mathrm{e}) \tag{1.44}$$

the daughter nucleus, two electrons and two neutrinos are produced. The existence of the $2\nu\beta\beta$-decay is experimentally confirmed for different isotopes like ^{76}Ge, ^{136}Xe and ^{100}Mo in [Alb14, Ago13, Fla11, Bar11].

[6] The Hubble constant is $H_0 = (73.8 \pm 2.4)\,\mathrm{km\,s^{-1}\,Mpc^{-1}}$ [Win11] or $H_0 = (67.3 \pm 1.2)\,\mathrm{km\,s^{-1}\,Mpc^{-1}}$ [Ade14].

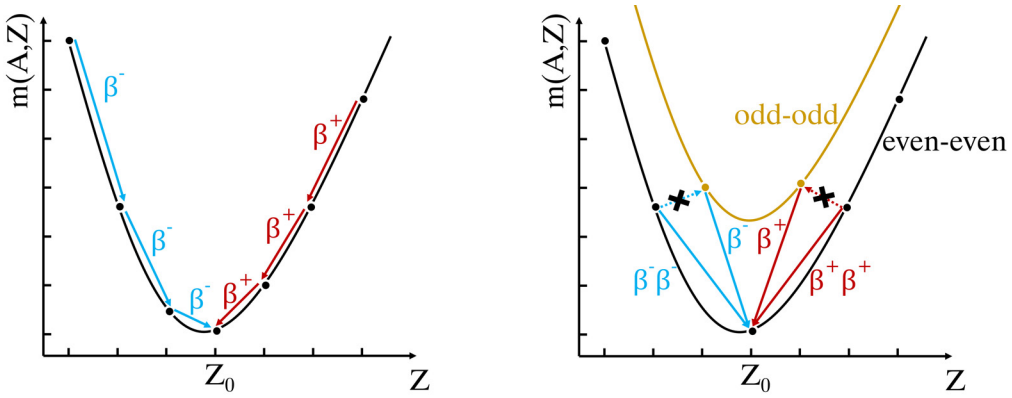

Figure 1.5: Mass parabola and the β-decay. Left: the mass of the nucleus is plotted against the proton number Z. By β^--decay (marked in blue) the minimal mass can be reached from the left and by β^+-decay (marked in red) from the right side. As the energy of the nucleus is minimal where the mass is minimal, it is stable at this point. Right: in case of an even-even nucleus, with even proton number Z and even neutron number N, the $\beta^\pm$-decay can be energetically prohibited. This is a result of the spin coupling in the pairing term of the semi-empirical Bethe-Weizsäcker mass formula [Wei35], which makes the even-even nuclei more stable than odd-odd ones. Such nuclei can decay by double β-decay.

If the lepton number and the chirality are not conserved and the neutrino is a Majorana particle (meaning $\nu = \overline{\nu}$ and the Majorana mass must be non-zero), it is also possible that instead of a $2\nu\beta\beta$-decay a $0\nu\beta\beta$-decay happens (compare figure 1.6). That would mean that in the decay reaction [Akh99]

$$A(Z, N) \rightarrow A(Z \pm 2, N \mp 2) + 2e^{\mp} \tag{1.45}$$

only the daughter nucleus and 2 electrons are produced. The anti-neutrino produced in the first decay is absorbed by inverse β-decay as a neutrino in the second decay. Therefore, no neutrino is emitted [Doi85]. This is the reason why the neutrino needs to be a Majorana particle to make the $0\nu\beta\beta$-decay possible and why the lepton number is violated by 2 [Doi85]. The required change in chirality (by a spin-flip), which enables the absorption of the neutrino by the inverse β-decay, is only possible if either the neutrino has mass[7] and 2 helicity components [Sch95] or not yet observed right-handed gauge bosons $W_R^\pm$ are present at the vertex [Bog85]. However, $0\nu\beta\beta$-decays are strongly suppressed as their probability is proportional to $\langle m_{\nu_e} \rangle^2_{\text{eff}} / E_0^2$ [Akh99]. The energy spectrum of the produced electrons is a discrete line at the endpoint energy as the recoil energy of the daughter nucleus is negligible [Akh99].

By the detection of a $0\nu\beta\beta$-decay the effective Majorana mass of the neutrino

$$m_{\text{ee}} = \left| \sum_{i=1}^{3} U_{ei}^2 m_i \right| \tag{1.46}$$

can be measured. But the GERDA experiment searching for the $0\nu\beta\beta$-decay has not yet detected a single decay. This leads to an upper limit of [Ago13]

$$m_{\text{ee}} < (0.2 - 0.4)\,\text{eV}\,\text{c}^{-2} \tag{1.47}$$

[7] To enable a spin-flip, the neutrino must be slower than light. This is only possible if the neutrino is not massless.

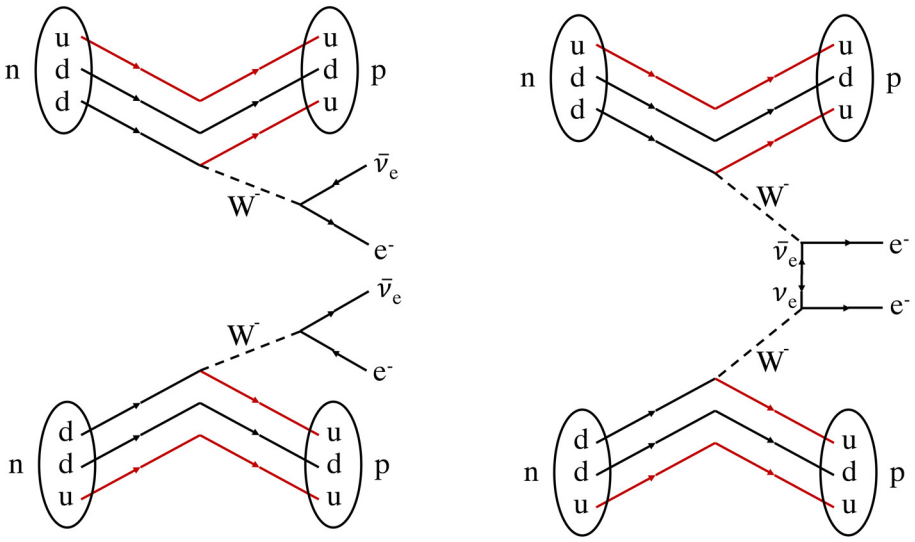

Figure 1.6: Feynman diagrams of the 2νββ and the 0νββ-decay. Left: here the Feynman diagram of the 2νββ-decay is shown. Two single β-decays happen at the same time. Right: the Feynman diagram of the 0νββ-decay is drawn. The electron neutrino produced at the lower β-decay is absorbed at the upper β-decay as an anti-neutrino.

on the Majorana mass. Therefore a lower limit on the half-life time of the studied ^{76}Ge of $2.1{\cdot}10^{25}$ y (90 % C.L.) is found. These results are contradictory to those of the Heidelberg-Moskau-experiment, which reported the detection of 0νββ-decays resulting in an upper limit on the Majorana mass of [Kla04, Kla06, Kla06]

$$m_{ee} = (0.32 \pm 0.03)\,\mathrm{eV\,c^{-2}} \tag{1.48}$$

Due to the conflicting results several other experiments also try to detect the 0νββ-decay such as CUORE [Arn04], KamLAND-Zen[Gan13], MAJORANA [Phi12] and SNO+ [Har12].

1.5.2 Direct measurement methods

Time-of-flight (ToF) measurement of Supernova neutrinos

A cosmological approach to the more or less direct determination[8] of the neutrino mass is the measurement of the time-of-flight t_{tof} of core-collapse supernovas which were discussed in section 1.1. The time the emitted neutrino needs to reach the earth is given by [Zub11]

$$t_{\mathrm{tof}} = \frac{L}{v} = \frac{L}{c}\frac{E_\nu}{p_\nu c} = \frac{L}{c}\frac{E_\nu}{\sqrt{E_\nu^2 - m_\nu^2 c^4}} \approx \frac{L}{c}\left(1 + \frac{m_\nu^2 c^4}{2E_\nu^2}\right), \tag{1.49}$$

where L is the distance between earth and a supernova and $m_\nu c^2 \ll E_\nu$ has been used. From this the time spread of neutrinos with different energies can be calculated to

$$\Delta t_{\mathrm{tof}} = t_{\mathrm{tof},1} - t_{\mathrm{tof},2} = \Delta t_0 + \frac{L m_\nu^2}{2c}\left(\frac{1}{E_1^2} - \frac{1}{E_2^2}\right). \tag{1.50}$$

[8]The ToF method is not completely independent from models and assumptions as parameter needed for the calculation of the neutrino mass can only be determined by astrophysical observations (e.g. the distance L and the point in time, when the neutrinos are emitted). Nevertheless, the principle approach is only based on kinematics which is the characterization of the direct methods. For that reason the tof-method is counted as a direct method.

By using equation (1.50) the neutrino mass can be calculated.

The first and up to now only supernova detected is SN1987A. The neutrinos of this supernova have been detected by IMB [Bio87] and Kamiokande [Hir88]. Due to their data an upper limit on the neutrino mass of

$$m_\nu < 30\,\mathrm{eV\,c^{-2}} \tag{1.51}$$

could be found. An improved analysis reduced this value further to [Lor02]

$$m_\nu < 5.7\,\mathrm{eV\,c^{-2}}\ (95\,\%\mathrm{C.L.}). \tag{1.52}$$

Investigation of the pion and tauon decay
The kinematic investigation of the pion and tau-decay also enables the measurement of the neutrino mass. The pion-decay

$$\pi^+ \rightarrow \mu^+ + \nu_\mu \tag{1.53}$$

is a two-body decay in which the pion is assumed to be at rest. If the masses of the pion and of the muon are known and the momentum of the muon is measured, the mass of the muon neutrino can be calculated by

$$m_{\nu_\mu}^2 = m_\pi^2 + m_\mu^2 - 2m_\pi\sqrt{m_\mu^2 + |\overrightarrow{p}_\mu|^2}. \tag{1.54}$$

An upper limit on the muon neutrino mass by this decay is [Ass96]

$$m_{\nu_\mu} < 0.17\,\mathrm{MeV\,c^{-2}}\ (90\,\%\ \mathrm{C.L.}). \tag{1.55}$$

A similar kinematic investigation of the tau decay channels

$$\tau^- \rightarrow \nu_\tau + 2\pi^- + \pi^+ \text{ and } \tau^- \rightarrow \nu_\tau + 3\pi^- + 2\pi^+(+\pi^0), \tag{1.56}$$

which are studied by the ALEPH experiment, gives an upper limit on the tau neutrino mass of [Bar98]

$$m_{\nu_\tau} < 18.2\,\mathrm{MeV\,c^{-2}}\ (95\,\%\ \mathrm{C.L.}). \tag{1.57}$$

Due to the high upper limits of these approaches an improvement to the sub-eV-range is not expected in the near future.

Investigation of β^- and β^+-decays
This sub-eV-range can be reached by the investigation of β^- and β^+-decays and the electron capture process. Of these the β^- decay is the most investigated process which is why the following description is concentrating on this decay: by investigating the β^- decay a measurement of the squared neutrino mass [Ott08, Dre13]

$$m_{\nu_\mathrm{e}}^2 = \sum_i |U_{\mathrm{e}i}|^2\, m_i^2 \tag{1.58}$$

is possible. The energy released during the decay is given by the Q-value [Zub11]

$$Q = (m(Z,A) - m(Z+1,A))c^2 \tag{1.59}$$

dependent on the mass of the mother and daughter nucleus. As the decay is a three-body process, the produced electron has a continuous energy spectrum. Close to the endpoint energy of the spectrum

$$E_0 = Q - E_\mathrm{rec}, \tag{1.60}$$

with the recoil energy E_{rec} of the daughter nucleus, the dependence on the neutrino mass becomes visible [Ott08] (compare also chapter 2, section 2.1.1, page 23ff).

The measurement of the electron energy spectrum is possible in several ways: in Project 8 [Mon09, For12] it is planned to use the synchrotron radiation in the radio frequency range emitted in the presence of magnetic fields to measure the electron energy spectrum of tritium[9]. The suitability of this approach is tested at the moment. Also, low temperature microcalorimeters [Gat01, Boo96] in which a radioactive isotope is implanted, can be used to measure the differential energy spectrum of the electron capture process. This measurement is performed by the detection of a change either in resistance [Vac08], in temperature [KB08] or in magnetization [Gas09, Ran12]. Microcalorimeter experiments using ^{187}Re as electron capture material have already published upper limits on the electron neutrino mass of $m_{\nu_{\mathrm{e}}} < 26\,\mathrm{eV\,c^{-2}}$ (95 % C.L.) in case of MANU [Gat01] and $m_{\nu_{\mathrm{e}}} < 15\,\mathrm{eV\,c^{-2}}$ (90 % C.L.) in case of the MIBETA experiment. Although improvement of the detectors [Fle05, Gas09, RG13] and production methods for the probably more suitable ^{163}Ho isotope [Eng13] are being investigated, it seems to be unlikely that the sub-eV-range can be achieved in the near future.

But another kind of experiment which is currently under construction and which is based on the β^--decay of tritium aims for this energy range: the KArlsruhe TRItium Neutrino experiment (KATRIN) [Ang05]. This experiment is based on a high intensity tritium source and a spectrometer based on the Magnetic Adiabatic Collimation combined with an Electrostatic Filter (MAC-E filter) principle [Lob85] with an energy resolution below 1 eV. With its challenging setup KATRIN will achieve a sensitivity on the neutrino mass of 0.2 eV (90 % C.L.) [Ang05]. The working principles, components and the technical realization are discussed in detail in the following chapter.

[9] Tritium is ^{3}H, so-called super-heavy hydrogen, consisting of 1 proton and 2 neutrons in the nucleus and 1 electron in the electron shell. It decays via β^- decay into ^{3}He.

Chapter 2

The Karlsruhe tritium neutrino experiment and its Rear Section

The aim of the KArlsruhe TRItium Neutrino experiment (KATRIN) [Ang05] is the measurement of the neutrino mass. The measurement is performed model-independently by the investigation of the kinematics of the tritium β-decay. The end of the electron spectrum at high kinetic energies is of particular interest. There the sensitivity is increased by a factor of 10 compared to previous experiments in Mainz and Troitsk: the measured upper limits are $2.3\,\mathrm{eV\,c^{-2}}$ (95 % C.L.) at Mainz [Kra05] and $2.05\,\mathrm{eV\,c^{-2}}$ (95 % C.L.) at Troitsk [Ase11]. On the other hand KATRIN will be able to measure a mass of $0.35\,\mathrm{eV\,c^{-2}}$ with 5σ significance. If the measured neutrino mass is compatible with zero an upper limit of $0.2\,\mathrm{eV\,c^{-2}}$ can be achieved with 90 % C.L.. As the experiment does not measure the neutrino mass itself but the square of the neutrino mass, a sensitivity improvement by a factor of 10 requires an improvement of the experimental precision by a factor of 100, which is a huge challenge.

Before each component of KATRIN and its contribution to meet this challenge is described in detail in section 2.2, the general working principles of KATRIN are explained in 2.1. In section 2.3 the main components and the physics objectives of the Rear Section are described since they concern the objectives of this thesis. Those objectives themselves are then discussed in the last section of this chapter, section 2.4.

2.1 Working principles and systematic uncertainties of KATRIN

2.1.1 The impact of the neutrino mass on the tritium β-spectrum

The energy spectrum of β-electrons provides the opportunity for a model-independent, direct measurement of the neutrino mass, since it only rests on the energy and momentum conservation during the decay. In case of KATRIN, the decay of the super-heavy hydrogen isotope tritium is utilized for the investigation of the neutrino mass. Tritium decays into a positively charged helium ion, an electron and an electron anti-neutrino

$$^3\mathrm{H} \;\rightarrow\; ^3\mathrm{He}^+ \;+\; e^- \;+\; \overline{\nu}_e. \tag{2.1}$$

More precisely KATRIN investigates not the electron anti-neutrino mass itself but the average electron neutrino mass as the method sums up all the mass states contributing to the electron neutrino [Dre13]:

$$m(\nu_\mathrm{e})^2 = \sum_i |U_{ei}^2| m(\nu_i)^2. \tag{2.2}$$

Here U_{ei} are the elements of the unitary matrix, which describes the neutrino oscillation, and $m(\nu_i)$ are the masses of the three neutrino mass eigenstates. This is the case since the resolution even of modern spectrometers (e.g. 0.93 eV at the KATRIN main spectrometer [Ang05]) is much larger than the difference between mass states (e.g. $0.05\,\mathrm{eV\,c^{-2}}$ in case of $|\sqrt{m_{23}^2}|$ [Abe14, Ada14]).

In the following the formulas to describe the tritium β-spectrum are established. If no other source is given, the sources are [Wei05] and [Ott08].

According to Fermi's Golden Rule the transition rate of the β-decay

$$\frac{\mathrm{d}^2 N}{\mathrm{d}t\mathrm{d}E} = \frac{2\pi}{\hbar} |M^2| \varrho(E) \tag{2.3}$$

is proportional to the transition matrix element M and the density of final states $\varrho(E)$. The number of final states $\mathrm{d}n$ in the normalization volume V, in the solid angle $\mathrm{d}\Omega$ and in the momentum range from p to $p + \mathrm{d}p$ is

$$\mathrm{d}n = \frac{V p^2 \mathrm{d}p \mathrm{d}\Omega}{2\pi^2\hbar^3} = \frac{p E_\mathrm{tot} V \mathrm{d}E_\mathrm{tot} \mathrm{d}\Omega}{2\pi^2\hbar^3 c^2}. \tag{2.4}$$

In the right part of this equation the energy-momentum relation is used. Using the simplification that the nucleus absorbs no energy but balances all momenta the density of states of electron and neutrino are independent from each other. Therefore, the density of states per energy interval and solid angle is

$$\varrho(E) = \frac{\mathrm{d}n_\mathrm{e}}{\mathrm{d}E_\mathrm{e}\mathrm{d}\Omega_\mathrm{e}} \frac{\mathrm{d}n_\nu}{\mathrm{d}E_\nu \mathrm{d}\Omega_\nu} = \frac{p_\mathrm{e} E_\mathrm{e} p_\nu E_\nu V^2}{4\pi^4\hbar^6 c^4}. \tag{2.5}$$

As the energy of the neutrino can be calculated from the total energy of the decay E_0 and the kinetic energy of the electron E by

$$E_\nu = E_0 - E \tag{2.6}$$

equation (2.5) simplifies to

$$\varrho(E) = \frac{p_\mathrm{e}(E + mc^2)\sqrt{(E_0 - E)^2 - m^2(\nu_\mathrm{e})c^4}\,(E_0 - E)\,V^2}{4\pi^4\hbar^6 c^5}. \tag{2.7}$$

The transition matrix M is composed of the leptonic M_lep and the hadronic M_had matrix elements

$$M^2 = G_\mathrm{F}^2 \cos^2(\theta_\mathrm{C})\, M_\mathrm{lep}^2 M_\mathrm{had}^2, \tag{2.8}$$

where θ_C is the Cabbibo angle and G_F is the Fermi coupling constant. The leptonic transition matrix is given by

$$|M_\mathrm{lep}^2| = \frac{1}{V^2} F(E, Z+1). \tag{2.9}$$

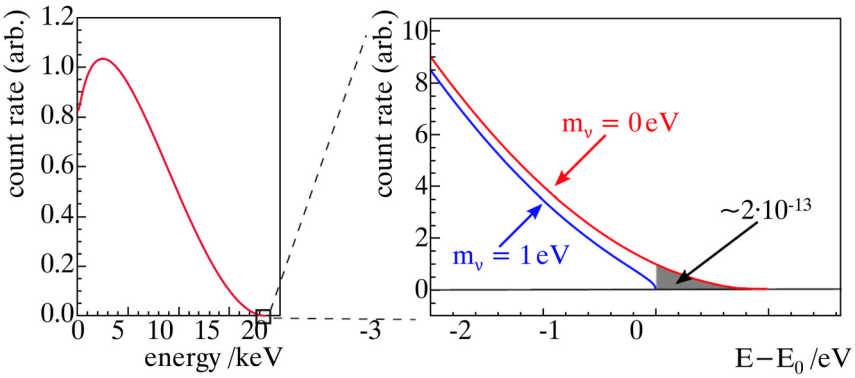

Figure 2.1: Impact of the neutrino mass on the tritium β-spectrum. In the left diagram the whole energy spectrum of the β-electrons is plotted. The right diagram shows a magnification of the endpoint region of the left diagram but dependent on the energy difference of the endpoint energy E_0 and the electron energy E. The red (upper) line is the spectrum in case of a neutrino mass consistent with $0\,\mathrm{eV\,c^{-2}}$. The blue (lower) line visualizes the curve shape in case of a neutrino mass of $1\,\mathrm{eV\,c^{-2}}$. A comparison of both lines and their shape makes it obvious that the impact of a non-zero neutrino mass is largest at the endpoint of the spectrum (figure adapted from [Ang05]).

Here $F(E, Z+1)$ is the Fermi function describing the Coulomb interaction between the electron and the daughter nucleus with charge $Z+1$. Differently from the leptonic transition matrix the hadronic one is independent of the kinetic energy of the electron. This results from the super-allowed decay of tritium. M^2_{had} is

$$|M^2_{\mathrm{had}}| = 5.55. \tag{2.10}$$

Using these equations the spectrum of equation (2.3) can be described by

$$\begin{aligned}\frac{\mathrm{d}^2N}{\mathrm{d}t\mathrm{d}E} =& \frac{G_{\mathrm{F}}^2\cos^2(\theta_{\mathrm{C}})}{2\pi^3\hbar^7c^5}|M^2_{\mathrm{had}}|F(E,Z+1)p(E+mc^2)(E_0-E) \\ &\times\sqrt{(E_0-E)^2-m_\nu^2c^4}\,\Theta(E_0-E-m_\nu c^2).\end{aligned} \tag{2.11}$$

The Heaviside function $\Theta(E_0 - E - m_\nu c^2)$ takes into account that the sum of the kinetic energy of the electron E and the energy needed to generate the neutrino mass never exceeds E_0. In order to consider the sudden change of charge during the decay, it is necessary to sum up all possible states of excitation after the decay for all neutrino mass eigenstates

$$\begin{aligned}\frac{\mathrm{d}^2N}{\mathrm{d}t\mathrm{d}E} =& \frac{G_{\mathrm{F}}^2\cos^2(\theta_{\mathrm{C}})}{2\pi^3\hbar^7c^5}|M^2_{\mathrm{had}}|F(E,Z+1)p(E+mc^2)\sum_j W_j(E_0-V_j-E) \\ &\times\left(\sum_i|U_{ei}|^2\sqrt{(E_0-V_j-E)^2-m_{\nu_j}^2c^4}\,\Theta(E_0-V_j-E-m_{\nu_i}c^2)\right).\end{aligned} \tag{2.12}$$

Here W_j is the probability that the daughter system is exited by the excitation energy V_j. This equation can be simplified with equation (2.2) to

$$\begin{aligned}\frac{\mathrm{d}^2N}{\mathrm{d}t\mathrm{d}E} =& \frac{G_{\mathrm{F}}^2\cos^2(\theta_{\mathrm{C}})}{2\pi^3\hbar^7c^5}|M^2_{\mathrm{had}}|F(E,Z+1)p(E+mc^2) \\ &\times\sum_j W_j(E_0-V_j-E)|U_{ei}|^2\sqrt{(E_0-V_j-E)^2-m_{\nu_j}^2c^4}\,\Theta(E_0-V_j-E-m_{\nu_i}c^2).\end{aligned} \tag{2.13}$$

The resulting spectrum can be found in figure 2.1. As the effect of the neutrino mass on the spectrum is the strongest close to the endpoint energy,

- a source of high intensity
- an efficient electron transport
- a spectrometer with resolution in the sub-eV region at the endpoint of the spectrum
- small systematic and statistical uncertainties

are needed to resolve the neutrino mass impact on the spectrum. The working principles of the source and the spectrometer used in the KATRIN experiment are discussed in the following sections.

2.1.2 Concept of a Windowless Gaseous Tritium Source and the transport of the electrons

KATRIN uses an isotropic tritium source with high luminosity and small systematic uncertainties which is called Windowless Gaseous Tritium Source (WGTS) [Ang05]. This concept was previously employed by the LANL neutrino mass experiment [Wil88, Rob91] and the Troitsk experiment [Ase11]. In this context windowless means that there is no barrier that contains the tritium in a source [Kaz08]: it is injected into the source and pumped out at the ends of the source again [Wil88]. In this process of circulation a non-linear column density profile develops. For the case of KATRIN this profile is shown in figure 2.2. Using a gas column as a source instead of condensed films offers the advantage that it mainly behaves like undisturbed tritium gas. As a consequence, gaseous sources feature smaller systematic effects than condensed thin films. For that reason energy loss inside of the film as well as a charging of the film and the excitation of neighbor molecules in the lattice of the film are not present [Ang05].

In addition to the cross section of the source A_S and the tritium purity ε_T the column density ϱd defines the number of tritium molecules by [Ang05]

$$N(T_2) = A_\mathrm{S} \cdot \varepsilon_\mathrm{T} \cdot \varrho d. \tag{2.14}$$

The column density is the density of atoms in a cross-sectional area of the source.

Tritium is particularly suitable due to its low endpoint energy E_0 of $(18\,571.8 \pm 1.2)\,\mathrm{eV}$ [Ott08]. Because of this, the portion of the spectrum sensitive to the neutrino mass is extended. In addition, tritium is characterized by a high specific activity due to its short half-life of about 12.32 years [Luc00]. A further advantage of tritium is the super-allowed decay which makes the nuclear matrix element constant and its simple composition of the atomic shell which enables the calculation of the final states [Ott08].

The electrons produced in the WGTS are adiabatically transported towards a spectrometer (the working principle of the KATRIN spectrometer is explained in the next section) by a magnetic field [Ang05]. The magnetic flux in which this transport takes place is given by

$$\Phi = \int B \cdot \mathrm{d}A \tag{2.15}$$

and conserved not only in the WGTS but over the entire way of the electrons through the experiment. The largest flux tube provided in the WGTS is $229\,\mathrm{T\,cm},^2$ but it is not transported completely to the detector. Only the inner flux tube of $191\,\mathrm{T\,cm}^2$ [Bab14] is completely transported through the experiment. To enable a scatter-free transport of the

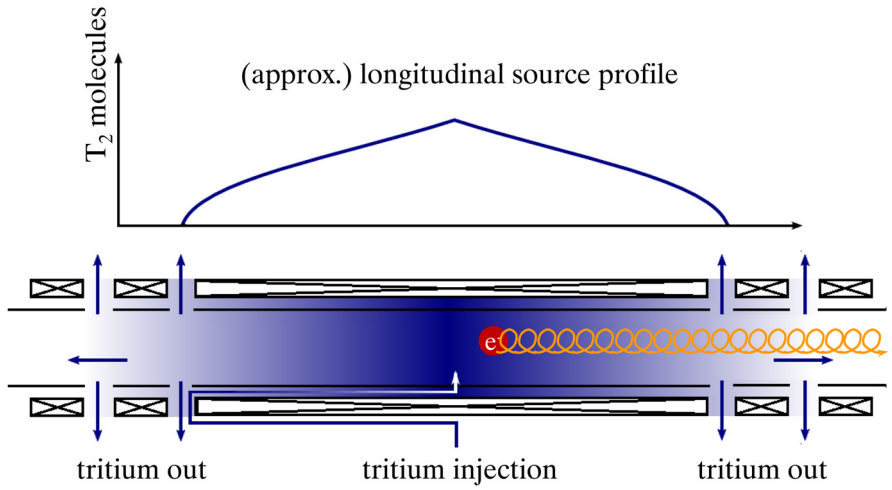

Figure 2.2: Sketch of the KATRIN Windowless Gaseous Tritium Source (WGTS). The lower part of the picture shows the beam line of the WGTS and the solenoids surrounding it. In the middle of the beam tube tritium is injected and at both ends it is pumped out again. In addition, a sample electron and its cyclotron motion caused by the magnetic field of the magnets is drawn in the beam tube. As the source is isotropic, half of the produced electrons are moving towards and the other half is moving away from spectrometer. The declining coloration indicates the density distribution of the gas in the source tube. For a more detailed visualization the upper part of the drawing shows the density profile in the longitudinal direction in simplified terms. As one can see the number of molecules is largest at the center and decreasing to both ends of the WGTS. Therefore, the density distribution also reaches its maximum at the center. If the pumping speed at both ends is equal, the density distribution is symmetric with regard to the center as shown in the diagram (own drawing according to [Ang05]).

electrons, a pressure below 10^{-6} mbar is required everywhere in the setup except for the tritium source itself [Bab14].

Nevertheless, even with a WGTS there are source-related systematic effects which have to be considered:

- **Doppler broadening:** the motion of a decaying tritium molecule in the source causes an increase or a decrease in the energy of the β-electron in the laboratory frame due to the Doppler effect. This can be reduced if the temperature of the source is decreased. As tritium starts clustering and freezing at the walls of the WGTS below a temperature of about 27 K [Höt12] a good balance can be found in the temperature range from 27 K to 33 K [Höt12].
- **Final state distribution:** the daughter molecules of the decay can retain energy if they remain in rotational, vibrational or electric excitation states after the decay. The excitation energy is missing from the kinetic energy of the electrons. These excitations are dependent on the kind of tritium isotopologue decaying (HT, DT or T_2). Therefore, the effect of the final state distribution depends on the gas composition in the tritium source [Höt12].
- **Inelastic scattering:** the electrons can be scattered on their way towards the spectrometer by striking molecules of the source. These scattering processes cause an energy loss of the electrons. With the help of electron emitter measurements the effect of inelastic scattering can be calculated [Ang05].

- **Activity fluctuations:** the activity of the source is affected by tritium purity ε_T and the column density. The fluctuations of the column density itself depend on the pressure gradient between the pressure at the tritium inlet (p_{in}) and at the position of the pumps (p_{out}), the geometry affecting the flow rate, and the temperature T. For that reason a stabilization or at least a monitoring of these parameters is needed to achieve the sensitivity aim of KATRIN [Bab12].

2.1.3 Measurement principle of a MAC-E filter

As mentioned before, the electrons produced in the WGTS are magnetically guided towards a spectrometer. In case of KATRIN the working principle of that spectrometer is based on a Magnetic Adiabatic Collimation combined with an Electrostatic filter, commonly abbreviated as a MAC-E filter. It enables the required high energy resolution of 0.93 eV [Ang05].

A MAC-E filter is an integrating high pass filter which works in the following way (compare also figure 2.3): the isotropically emitted electrons move in cyclotron cycles from the source to the spectrometer guided by magnetic field lines. This magnetic field drops by several orders of magnitude from the outside of the spectrometer to its center. The resulting gradient in the magnetic field transforms most of the perpendicular energy from the cyclotron motion $E_\perp$ of the electrons into a longitudinal motion. If the change in the magnetic field during one cyclotron cycle is sufficiently small, the magnetic moment

$$\mu = \frac{E_\perp}{B} \tag{2.16}$$

is conserved [Pic92]. In that case the motion is called adiabtic (at least in the first order): an adiabatically moving electron, which starts in a homogeneous magnetic field and passes varying electric and magnetic fields, returns to its starting values of energy and momentum, if a homogeneous magnetic field is reached again. Therefore, the adiabatic motion is required at KATRIN to transport the electrons from the source to the analyzing plane of the spectrometer without losing the information about their kinetic energy.

In addition to the magnetic field an electrostatic potential is applied to the spectrometer. This potential acts as a retarding potential. The highest potential is reached at the so-called analyzing plane at the center of the spectrometer [Dre13]. Here the magnetic field has its minimum. Only if the longitudinal energy of the electrons exceeds the potential in the analyzing plane, the electrons pass the spectrometer. Otherwise, they are reflected. The passing electrons are again re-accelerated after the analyzing plane. If the magnetic field strengths at both ends of the spectrometer are equal, the initial value of $E_\perp$ is also restored.

If ΔE is the energy resolution of the spectrometer, the relative sharpness of the MAC-E filter is given by the ratio of the minimum and maximum magnetic field [Pic92]

$$\frac{\Delta E}{E} = \frac{B_{min}}{B_{max}}, \tag{2.17}$$

where B_{min} is the magnetic field in the analyzing plane. Therefore, the transmission function T, which describes if an electron with a certain energy E is reflected ($T = 0$) or transmitted ($T = 1$), is not a perfect step function. The transition from $T = 0$ to

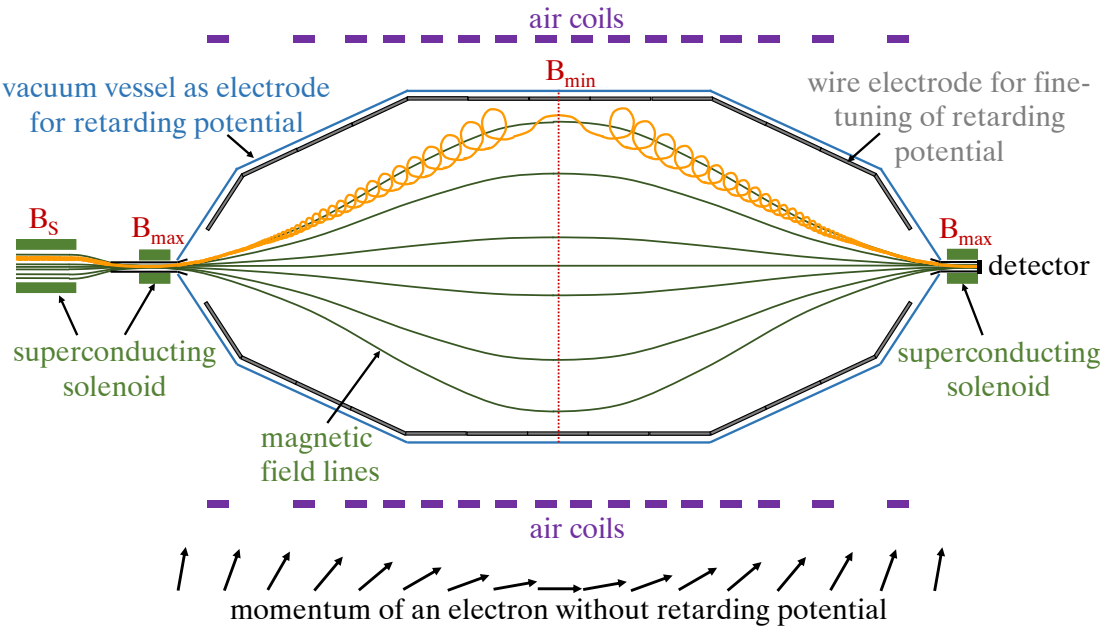

Figure 2.3: Schematic drawing of the MAC-E filter working principle. The electrons emitted in the source at the magnetic field B_S are magnetically transported in the flux tube to the spectrometer. At both ends of the spectrometer the superconducting solenoids produce a magnetic field B_{max} which is larger than that at the source. In the analyzing plane the magnetic field drops to B_{min}. In case of KATRIN an air coil system surrounding the spectrometer improves the symmetry of the magnetic field and its gradient. Through the drop of the field the transversal energy of the electron is transformed into longitudinal motion. This is visualized by the arrows at the bottom of the figure. The electrons which are isotropically emitted from the source are altered into a broad electron beam mostly parallel to the magnetic field lines at the analyzing plane. An electrostatic retarding potential, which is applied in the case of KATRIN to the vessel of the tank and wire electrodes inside of the tank, allows only electrons with high enough energy to pass and hence hit the detector. By the increase of the magnetic field at the detector end the initial angular and energy distribution is restored (own drawing according to [Lob85] and [Ang05]).

$T = 1$ has the width ΔE. For that reason the normalized transmission function is given by [Ang05]

$$T(E, qU) = \begin{cases} 0 & \text{if } E - qU < 0 \\ \dfrac{1-\sqrt{1-\frac{E-qU}{E}\frac{B_S}{B_{max}}}}{1-\sqrt{1-\frac{\Delta E}{E}\frac{B_S}{B_{max}}}} & \text{if } 0 \leq E - qU \leq \Delta E \\ 1 & \text{if } E - qU > \Delta E, \end{cases} \tag{2.18}$$

where B_S is the magnetic field in the source region.

The kinetic energy E of the electron can be changed by scattering processes on the way towards the spectrometer. As a consequence of the scattering, electrons need more energy to pass the spectrometer at a certain retarding potential than without scattering. This effect cannot be neglected in case of KATRIN as only 41.3 % of all electrons are unscattered at normal conditions but 29.3 % are scattered once and 16.7 % are even scattered twice [Bab12]. This effect is described by the so-called response function given by

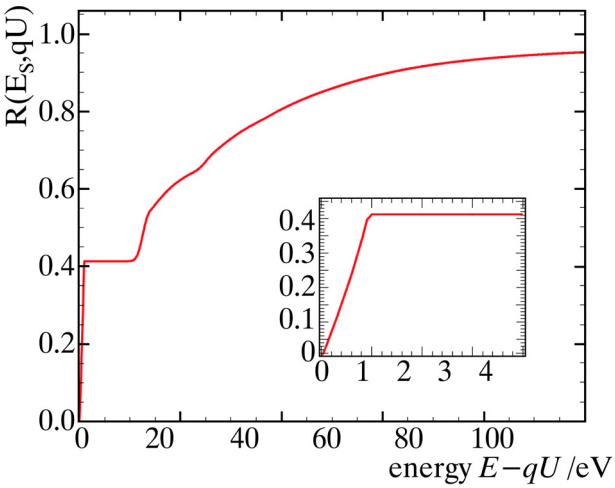

Figure 2.4: Diagram of the response function. The transmission probability at the MAC-E filter is plotted against the so-called surplus energy $E - qU$ of the electrons relative to the retarding potential. The first sharp increase to 41.3 % and the plateau afterwards is the transmission function of unscattered electrons. An enlarged version of this transmission function is again plotted in the inlet. Roughly at 20 eV and 30 eV the influence of electrons scattered once or twice can be seen [Ang05, Mer12b].

[Mer12a, Ang05]

$$R(E_\mathrm{S}, qU) = \int_0^E T(E_\mathrm{S} - \varepsilon, qU)(P_0\delta(\varepsilon) + P_1 f(\varepsilon) + P_2(f \otimes f)(\varepsilon) + ...)\mathrm{d}\varepsilon, \tag{2.19}$$

where the energy loss by the scattering is ε, the probability of a scattering with this energy loss is $f(\varepsilon)$ and E_S is the starting kinetic energy of the electron. The probability that an electron is scattered i-times is described by the factor P_i. The resulting shape of the response function is shown in figure 2.4.

For that reason the overall count rate detectable after the MAC-E filter in a measurement time t_U is [Mer12a]

$$N(qU, E_0, m_\nu) = N_\mathrm{tot} t_\mathrm{U} \int_0^{E_0} \frac{\mathrm{d}N}{\mathrm{d}E}(E_0, m_\nu) R(E, qU)\mathrm{d}E, \tag{2.20}$$

which is a convolution of the response function with the differential spectrum described in section 2.1.1. In this equation N_tot is the number of tritium atoms in the source and t_U is the measurement time at a certain retarding potential.

The systematic uncertainties of KATRIN are discussed in the following section.

2.1.4 Systematic uncertainties

To achieve the targeted sensitivity of $0.2\,\mathrm{eV\,c^{-2}}$ (90 % C.L.) on the neutrino mass measurement, the total uncertainty must be about [Ang05]

$$\sigma_{\mathrm{tot}} = \sqrt{\sigma^2_{\mathrm{sys,tot}} + \sigma_s tat} \approx 0.025\,\mathrm{eV^2c^4}. \tag{2.21}$$

This total uncertainty is composed of systematic and statistical uncertainties, which should both contribute equally to the total uncertainty. Therefore, the total systematic uncertainty on the observable m^2_ν must not exceed

$$\sigma_{\mathrm{sys,tot}} \leq 0.017\,\mathrm{eV^2c^4} \tag{2.22}$$

and the statistic uncertainty after 3 years of effective KATRIN measurement time is limited to

$$\sigma_{\mathrm{sys,tot}} \leq 0.018\,\mathrm{eV^2c^4}. \tag{2.23}$$

Assuming that there are at most 5 dominant systematic uncertainties, these uncertainties must be lower than [Ang05]

$$\Delta m^2_\nu = 0.0075\,\mathrm{eV^2c^4}. \tag{2.24}$$

Otherwise the requirement on $\sigma_{\mathrm{sys,tot}}$ cannot be met.

As discussed already in section 2.1.2 there are several systematic effects related to the WGTS or more precisely to the column density and the gas composition. Therefore, a stabilization and monitoring of the source parameters is required [Ang05, Bab12]:

- The targeted tritium inlet pressure is p_{in} =$3.368 \cdot 10^{-3}$ mbar with a required relative stability of 0.1 %.
- The outlet pressure must be p_{out} =(0.03 - 0.05)$\cdot p_{\mathrm{in}}$ with a relative stability of 3 %.
- The tritium purity must be higher than 95 % (composed of more than 90 % T_2, less than 10 % DT and traces of HT) monitored with a relative stability of 0.1 % and an accuracy of 1 %.
- The source temperature T must be stabilized at about 30 K over the whole beam tube with a relative stability of 0.1 % and a trueness of 0.5 K.
- The source activity must be monitored with a precision of 0.1 %.

In addition to the stabilization and monitoring of these individual parameters, the inelastic scattering probability and the column density itself will be determined by an electron emitter (in the following called e-gun).

Further systematic uncertainties of KATRIN are related to the potentials of the setup, both at the MAC-E filter and at the tritium source. In case of the retarding potential of the MAC-E filter the stability must be better than 60 mV[1] to not exceed the maximum allowed individual systematic uncertainty. The potential variations in the source are limited to about 10 mV [Ang05]. Potential variations of this order cause a systematic uncertainty of

$$\Delta m^2_{\nu\,\mathrm{WGTS\,potential}} < 2 \cdot 10^{-4}\,\mathrm{eV^2c^4}. \tag{2.25}$$

How the KATRIN experiment is designed and built up to meet all these requirements on the systemic uncertainties is described in the following section.

[1] The absolute stability of 60 mV is equal to a relative stabilization of 3 ppm.

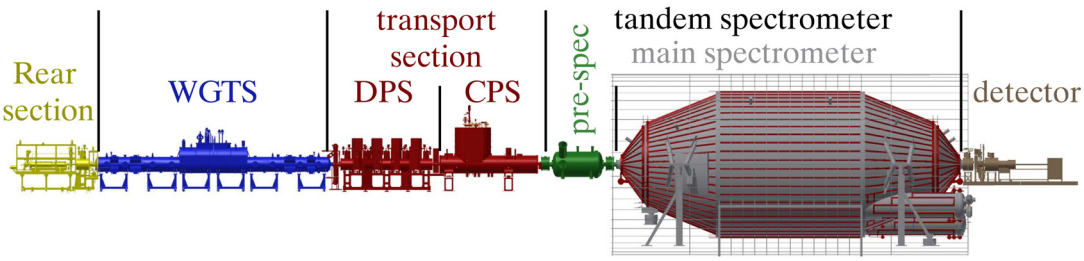

Figure 2.5: Overview of the experimental setup of KATRIN. From left to right the Rear Section, the tritium source WGTS, the transport section including DPS and CPS, the tandem spectrometer, consisting of the pre-spectrometer and the main spectrometer, and the detector section are shown.

2.2 Overview of the KATRIN experiment

At KATRIN most of the tritium decays take place in the WGTS [Bab12, Ang05]. The produced β-electrons are then magnetically guided towards the main spectrometer. On their way they pass the differential pumping section (DPS) [Kos12], the cryogenic pumping section (CPS) [Gil10] and the pre-spectrometer [Pra12]: the function of the DPS is to remove the tritium out of the beam line and to pump it into the tritium loop system [Stu10a]. The task of the tritium loop is to purify the gas and feed it into the WGTS again. The CPS further decreases the tritium gas flow before the electrons reach the pre-spectrometer. The pre-spectrometer acts as a pre-filter to reduce the number of electrons reaching the main spectrometer. All electrons with a kinetic energy below a certain value are reflected here. The main spectrometer reflects all electrons with an energy which is to low to pass the analyzing potential. Both spectrometers' working principle is based on the MAC-E filter. All passing electrons reach the Focal Plane Detector (FPD) [Ams15]. To achieve the sensitivity aim of KATRIN a calibration and monitoring system (CMS) consisting of several components is integrated in the setup. Several of them are installed in the Rear Section [Bab14] which is placed at the rear end of the WGTS.

As up to 40 g of tritium are cycled through the tritium source per day [Pri15], the tritium related components of KATRIN are built up at the Tritium Laboratory Karlsruhe (TLK) of the Karlsruhe Institute of Technology (KIT). The tandem spectrometer and the detector section are not located in the TLK directly, but next to it.

The setup is also shown in figure 2.5. The main components are described in more detail in the following. If not stated otherwise, the sources of the given information are [Ang05, Dre13] or the individual sources given in the first paragraph of this section.

2.2.1 Windowless Gaseous Tritium Source and tritium loops

The main part of the WGTS is a 10 m long cylindrical stainless steel beam tube with 90 mm diameter. The tritium gas is injected at the middle of this tube (5 m from each end of the tube). The injection rate is 1.853 mbar l s^{-1} (at STP[2]) [Ang05] resulting in a column density of $\varrho d = 5 \cdot 10^{17}$ molecules cm^{-2} and a source activity of $1.7 \cdot 10^{11}$ Bq [Pri15]. At both ends of the WGTS the gas is pumped differentially out of the source reducing the

[2]STP is an abbreviation for Standard Temperature and Pressure. Depending on the definition, the temperature is T =273.15 K and the pressure is p =101.325 kPa [Cal90] or T =293.15 and p =101.325 kPa [ISO96]

gas flow by 3 orders of magnitude. The injected gas is provided by the KATRIN tritium loops [Pri15]. The gas, which is pumped out of the source, is again fed back into the loops. The task of these loops is to provide a stable injection rate, to clean the gas and measure the gas composition by a Laser Raman system [Fis11, Stu10b]. At the rear side of WGTS the so-called Rear Wall completes the beam tube. The objectives of the Rear Wall itself are discussed in section 2.3.3.

The beam tube is surrounded by superconducting magnets which produce a magnetic flux density of maximum $B_S = 3.6\,\mathrm{T}$ or [Ang05]

$$\frac{B_S}{B_{max}} = 0.6 \tag{2.26}$$

in relation to the maximum magnetic field B_{max} of KATRIN. The smaller magnetic field in the source suppresses electrons with a long path to the spectrometer which have a high scatter probability as the maximum acceptance angle is [Ang05]

$$\theta_{max} = \arcsin\left(\sqrt{\frac{B_S}{B_{max}}}\right) = 51^\circ. \tag{2.27}$$

All electrons with larger starting angles do not reach the spectrometer.

The following requirements on the WGTS related systematic effects described in section 2.1.4 are already met:

- The injection rate is stable within $120 \pm 0.5\,\mathrm{sccm}$ meaning almost 1 order of magnitude better than the required stability [Pri15].
- The monitoring of the gas composition is performed in-situ with a Laser Raman system which reaches the 0.1 % precision with a detection limit of $5{\cdot}10^{-3}$ in an acquisition time of 60 s [Fis14].
- The WGTS is cooled down by the usage of two-phase neon [Gro13]. To test the stability of the temperature, a 12 m long demonstrator was built [Gro13]. With the help of this demonstrator it was found that the stability over 1 week is 8 mK at 30 K, which is about a factor of 20 below the required value.

In addition, there is the possibility to monitor the column density directly with an electron gun and to monitor the activity of the source with a β-induced X-ray detector (or BIXS system for short) at the Rear Section. These two monitoring techniques are discussed in detail in section 2.3.2 or 2.3.1, respectively.

The WGTS was transported to the TLK in September 2015 where the integration into the TLK infrastructure is now ongoing.

2.2.2 Transport section consisting of DPS and CPS

The objectives of the Transport Section is to transport the electrons adiabatically towards the spectrometer and to reduce the tritium flow. The reduction must be by about 14 orders of magnitude to achieve a tritium partial pressure of about 10^{-22} mbar in the main spectrometer [Dre13]. In so doing the tritium related background is less than 10^{-4} cps. To achieve this reduction two separate sections are needed, the active pumping DPS and the passive pumping CPS.

The DPS performs active differential pumping with turbo molecular pumps. In addition to the reduction of the tritium flow the DPS supplies diagnostics for measurement of

the composition and suppression of ions produced in the WGTS and transported by the magnetic field. The first one is performed by two Fourier Transform-Ion Cyclotron Resonance devices by measuring the cyclotron frequency of the ions in the magnetic field of DPS. The suppression takes place by an electrostatic dipole field at the ring electrode at the end of DPS. The construction of the system is ongoing.

The CPS is a large cryo-sorption pump to reduce the tritium flow by 7 orders of magnitude [Dre13]. It removes traces of tritium still remaining in the beam tube. The main working principle is that tritium is trapped at a surface of 3 K temperature [Gil10]. To enlarge this surface argon frost is prepared on the inner surface of the CPS. After 60 days, the CPS will be regenerated to remove the tritium. Similar to the DPS, the CPS also has objectives in addition to the reduction of the tritium flow. It supplies a condensed krypton source (^{83m}Kr produced by electron capture from ^{83}Rb) for monitoring of the retarding potential of the spectrometer and a Si-diode which can be moved in the flux tube to monitor the source intensity. The CPS was delivered to the TLK at the end of July 2015. The integration in the TLK infrastructure is ongoing.

2.2.3 Tandem spectrometer consisting of Pre- and Main Spectrometer

The energy analysis of the electrons is performed by a tandem spectrometer consisting of 2 MAC-E filters, the pre-spectrometer and the main spectrometer. The pressure inside of both spectrometers is 10^{-11} mbar [Ang05].

The pre-spectrometer has two main objectives: on the one hand it works as a pre-filter for the main spectrometer at a fixed retarding potential of 18.3 kV to reduce the electron flux by 6 orders of magnitude to $10^4\,\mathrm{s}^{-1}$. This helps to minimize the background from ionization of residual gas molecules in the main spectrometer. On the other hand the pre-spectrometer is a small copy of the main spectrometer, which acted as a small prototype at which the vacuum and high voltage design could be tested. In so doing new backgrounds caused by Penning traps and radon were found [Pra12].

The pre-spectrometer tank is 3.38 m long with a 1.68 m inner diameter and the hull of the vessel acts as a high voltage electrode. It can be supplied with up to 35 kV. Inside of the vessel a nearly massless electrode system is installed. This inner electrode system decouples the high voltage from electrical noise of other electrical components installed at the spectrometer and therefore allows a fine-tuning of the retarding potential.

The main spectrometer is 23.28 m long and has an inner diameter of 9.8 m. By the reduction of the magnetic field to $B_\mathrm{A} = 3$ Gauss at the analyzing plane, the flux tube is increased to 9 m in diameter. To compensate for disturbing magnetic fields (e.g. the earth's magnetic field) and for general improvement horizontal and vertical current loops as well as Helmholtz-like coils are added around the main spectrometer [Dre13]. Like the pre-spectrometer the vessel itself is supplied with high voltage acting as a guard electrode for a more accurate high voltage supplied to an inner wire electrode system.

The stability of the voltage supplied to the electrode system must be better than 60 mV and is measured by two independent methods. The first one is based on 2 custom made high voltage dividers. Their relative stability is 10^{-6} per month and the dependence on temperature or voltage is negligible [Thü09]. The second method is the comparison with a nuclear standard realized by ^{83m}Kr. ^{83m}Kr emits mono-energetic electrons at 17.8 keV. These electrons are detected at the detector of the so-called monitor spectrometer [Erh14]. The monitor spectrometer is the upgraded former Mainz spectrometer also based on the

MAC-E-filter principle. In contrast to the tandem spectrometer the retarding potential is not supplied to the hull of the spectrometer vessel but to an electrode system of cylindrical and conical full-metal electrodes and wire electrodes in the inside of the vessel. These electrodes can be supplied with high voltage from a local controller or by a galvanic connection with the retarding potential of the main spectrometer. The later case enables the monitoring of the high voltage of the main spectrometer. This monitoring technique is performed with a stability of 50 mV [Erh14]. In section 4.6 the monitor spectrometer is used as a spectrometer for photo-electron spectroscopy as well.

2.2.4 Focal plane detector

The pinch magnet of the detector section completes the MAC-E-filter of the main spectrometer. It has the highest magnetic field of the beam line. In the center of a second magnet the detector is placed. Operating the magnet at 3.3 T optimizes the performance of the detector as it strikes a balance between back-scattering and detector background.

Although the electrons are re-accelerated by the MAC-E filter after the analyzing plane a further increase of their energy by up to 12 keV is possible. The advantage being that the energy is increased to a range at which the background rate of the detector is lower. An additional radiation shield and a veto system reduces the background.

The Focal Plane Detector (FPD) itself is a silicon PIN-diode detector on a single silicon wafer with <111> crystal orientation with 148 detector pixels. The diameter of the active area is 90 mm covering the 191 T cm^2 flux tube with a 10 % safety margin. The pixels are separated by 50 µm boundaries, so that the resistance between two pixels is larger than 1 GΩ. The area of each of the 148 pixels is 44 mm^2. The pixels are positioned in 12 concentric rings with 15° displacement at alternating rings. The arrangement of all pixels in rings allows the correction of radial magnetic and electrical inhomogeneities. In the center of these rings 4 pixels are placed.

The detector system was constructed by the University of Washington in Seattle, USA, and delivered to Karlsruhe in summer 2011, where the commissioning took place.

2.2.5 Rear Section

Completing the setup on the rear side of the WGTS, there is the so-called Rear Section. The Rear Section provides calibration and monitoring sources and is part of the Calibration and Monitoring System (CMS) of KATRIN. It provides an angular selective electron gun for monitoring and calibration purposes and a detector for source activity measurements. In addition, the Rear Section houses the so-called Rear Wall. The Rear Wall is one possible candidate as determinant of the potential of the tritium source. In addition, it has the option to be irradiated by UV light. During the UV irradiation electrons are produced that could compensate a possible charging of the source. Due to their importance for both, KATRIN and this thesis, the physical objectives of these components are discussed in detail in the section 2.3.1, 2.3.3 and 2.3.2. This paragraph continues the technical discussion of the Rear Section.

The Rear Section primary system[3] is divided in three main parts (compare figure 2.6): the Rear Wall, the mid and the e-gun chamber. The Rear Wall chamber is connected

[3]The primary system is the vacuum system of an experiment or facility which safely contains the tritium [Man93].

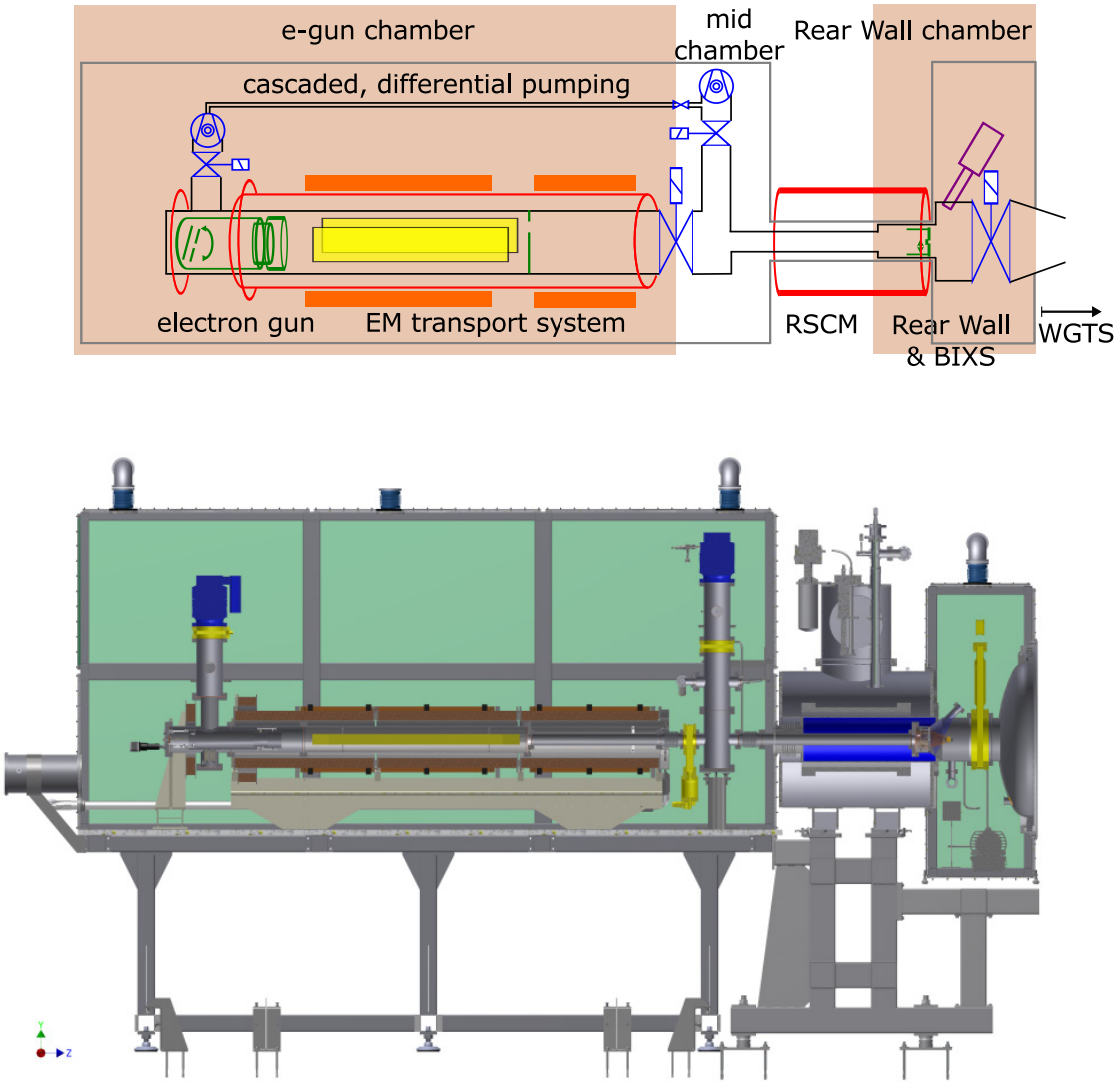

Figure 2.6: Scheme and CAD of the Rear Section. At the top the basic components of the Rear Section are shown. In the large second containment the e-gun chamber and the mid chamber are located and divided from the small second containment with the Rear Wall chamber by the re-condenser superconducting magnet (RSCM). The green parts at the left side are the e-gun cathode and the post-acceleration electrodes. The beam tube is surrounded by the normal conducting magnets (red line) and the magnetic dipoles (orange rectangles). The electric dipoles inside the beam tube (yellow rectangles) enable shifting the beam through the off-axis aperture (green line). The component marked green at the right side is the Rear Wall, at which the double-sided arrow indicates a piezo-motor with which the Rear Wall hole (needed to transport the e-gun beam) can be closed. One of the two SDD detectors facing the Rear Wall is shown in violet. The blue components are vacuum related components like pumps and valves. At the bottom a CAD drawing of the Rear Section is presented. The setup is cut at the center of the beam tube to illustrate how the Rear Section will look like after assembly (the scheme and CAD are adapted from [Bab14]).

to the DPS1-R of the WGTS, with a valve enabling the detachment. It houses the Rear Wall in a chamber with 4 access ports. At 2 of these silicon drift detectors are installed (compare 2.3.1). A further port is equipped with a UV transparent window for Rear Wall irradiation. The last one houses electrical feed-throughs and sensors. The Rear Wall chamber is separated from the mid chamber by a superconducting re-condenser magnet of the same type as those installed at DPS. The connection between the chambers is established by a pipe through the borehole of the magnet. The mid chamber's main task is to provide pumping. In addition, it houses a gate valve enabling the disconnection of the e-gun in the furthest part of the Rear Section from the rest. As its name implies the e-gun chamber houses the main components of the e-gun, namely the e-gun cathode and the electromagnetic transport section. Additionally, normal conducting magnets, beam steering coils and dipole coils completing the transport section of the e-gun are placed around the primary system of the e-gun chamber. Furthermore, all mechanical, optical and electrical feed-troughs necessary for the operation of the e-gun are attached to this chamber. At the rear end of the mid chamber a small aperture with an offset to the z-axis is installed. This aperture prohibits the direct motion of ions from the WGTS through the central hole of the Rear Wall to the e-gun cathode.

The pressure in the e-gun chamber is expected to be $1.9{\cdot}10^{-8}$ mbar calculated from the pressure in the Rear Wall chamber which is equal to that of DPS1-R, namely 10^{-5} mbar (for the detailed calculation see [Bab14]). This pressure is good enough to transport the electron beam to the WGTS. The activity caused by the tritium partial pressure is about 14.8 MBq in the Rear Wall chamber, about 5.2 kBq in the mid chamber and about 32.8 kBq in the e-gun chamber. These activities are low enough that no second containment[4] would be required as the limit is 10^{10} Bq and a fume hood would be sufficient. But in the foreline of the turbo pumps an activity exceeding this limit could be reached. For that reason a second containment is required. This second containment is realized by two glove boxes, one smaller box surrounding the Rear Wall chamber and the very end of DPS1-R and a large box surrounding the mid and the e-gun chamber. Both boxes are connected via a pipe through the borehole of the superconducting magnet. The installation of both, the primary system and the second containment, in the borehole of the solenoid offers the advantage of easy access to the magnet for cryogenic fillings and maintenance in case of malfunction.

After this rather technical description of the Rear Section the physics objectives of its main components are discussed in the following section.

2.3 Main components of the Rear Section and their physics objectives

The main components of the Rear Section with regard to the physics involved are the Rear Wall, the silicon drift detectors (SDD-detectors) looking at the Rear Wall and the angular selective electron gun. The following three sections discuss, why these components are needed. In addition, their working principles and their implementation in the Rear Section are elaborated.

[4] A second containment is a safety device required at TLK if the handled activity is higher than 10^{10} Bq. It is an air tight box, e.g. a glove box, which encapsulates tritium containing components [Man93]. In case of leakage no flowing tritium can reach a human operator of the laboratory. A second containment has a slight under pressure with regard to the laboratory pressure to enable a flow into the box in case of a failure of the second containment.

2.3.1 SDD-detectors as activity monitor of the tritium source

As mentioned in section 2.1.4 the source activity must be either adjusted or monitored with a relative stability of 0.1 %. Two different detectors are used for this purpose, the Forward Beam Monitor (FBM) [Bab12] and SDD-detectors for β-induced X-ray spectrometry (BIXS) (compare [Röl13],[Pri13b] and [Bab12]). If not stated differently all information given in the following are taken from these sources. In addition to these methods another one was investigated by the University of California Santa Barbara to measure the source activity with help of the Rear Wall: a direct current measurement of the decay electrons impinging on the Rear Wall which acts as a Faraday cup. But this method is postponed to an eventual upgrade. The reason for that is that no working prototype meeting all requirements could be manufactured yet (compare section 2.3.3).

The FBM is a silicon detector installed at CPS which can be moved directly in the flux tube measuring the electron flux with a precision of 0.1 % in 30 s [Bab12]. That means that the FBM covers part of the flux tube during measurement. In contrast to that BIXS measures the source activity directly at the rear end of the source. It does not interfere with the flux tube or the plasma in general. In addition, BIXS is not led astray by other secondary charges present in the source.

BIXS is based on the generation of X-rays by the inverse photoelectric effect. The X-rays are produced on the Rear Wall gold surface by impinging tritium β-electrons. In contrast to those the low energetic secondary electrons and ions produced in the source by ionization of the gas molecules do not produce X-rays. The resulting spectrum is a combination of bremsstrahlung and characteristic lines of gold and the other materials surrounding the Rear Wall. The intensity of the produced X-rays is given by Kramer's law [Kra23]

$$I(\lambda)\mathrm{d}\lambda = \frac{KiZ}{\lambda^2}\left(\frac{\lambda}{\lambda_{\min}} - 1\right), \tag{2.28}$$

where K is the Kramer constant and $\lambda_{\min}$ is the minimum wavelength produced. The intensity is therefore proportional to the incoming electron current i, the atomic number of the target Z, which is 79 in case of gold, and the wavelength of the produced X-rays λ. As the incoming electron current is proportional to the source activity and the count rate at the SDD-detector is also proportional to the activity, a monitoring of the produced X-rays enables the monitoring of the source activity.

The SDD-detectors offer two main advantages if they are used at KATRIN compared to other radiation or electron detectors: generally the detector can be self-calibrated by the characteristic lines of gold in the spectrum. Therefore, a drift of the calibrated energy scale can be compensated. In addition, in the specific case of KATRIN the minimum energy of the X-rays produced at the Rear Wall in direction of the detector is larger than the energy threshold of the detector. That means, that a systemic effect on the count rate due to a shift of the energy of the primary electrons or of the detector threshold is rather unlikely [Bab14]. But the system also has a drawback as the expected rate of X-rays impinging on one of the detectors is comparatively small with (7155 ± 218) cps [Röl15]. Therefore, the measurement time for one spectrum must be about 100 s to reach the 0.1 % precision. However, KATRIN requires the monitoring within an acquisition time of at maximum 1 000 s [Ang05]. This requirement is met with BIXS.

A proof of concept experiment called TriRex [Pri13b] has shown that a monitoring of the source activity with 0.1 % precision is possible with this technique. In the TriRex setup

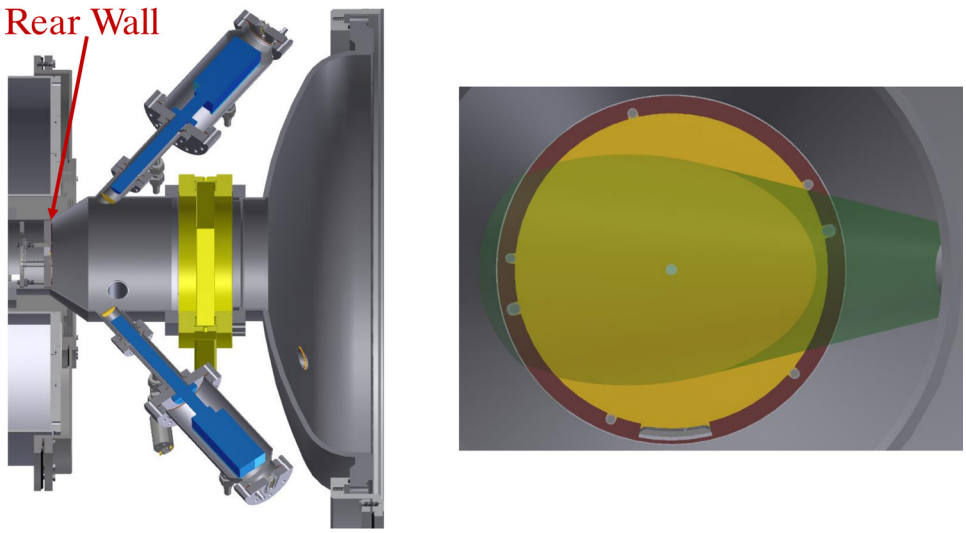

Figure 2.7: Implementation of the BIXS detectors at the Rear Wall chamber. On the left side a sliced-through view in the inner part of the Rear Wall chamber can be seen. The blue components above and below the beam tube are the SDD detectors looking at the Rear Wall. On the right side the Rear Wall (gold circle in the middle) is shown. The green cone marks the viewing area of one of the SDD detectors (adapted from [Bab14])

the 0.1 % precision goal was reached in less than 70 s. But due to the different geometries the count rate will be lower at KATRIN [Bab12].

To detect the X-rays a detector must be placed close to the Rear Wall. As the low energetic X-rays can not penetrate through the Rear Wall, it is not possible to install the detectors directly behind the Rear Wall. Therefore, the detectors must be placed in front of the Rear Wall but without disturbing the flux tube. For that reason 2 ports are added at the chamber which houses the Rear Wall. These ports enable a direct line of sight on the Rear Wall gold surface, without reducing the space available for the flux tube (see figure 2.7). This is possible as the produced X-rays have a broad angular distribution. This distribution is dependent on the energy of the electron. At non relativistic electron energies the intensity of emitted X-rays is of the same order at 0° and 90° [Koc59]. The detectors itself are separated from the Rear Wall chamber and the plasma by a gold coated beryllium window. These windows enable a protection of the detectors from direct electron irradiation as well as a transmission of the X-rays since beryllium is almost completely transparent for X-rays.

The detectors used at the Rear Section are SDD-detectors of the kind Axas M SDD from KETEK[5] with 100 mm^2 sensitive area. SDDs are chosen as they combine a large sensitive area and a good energy resolution of below 200 eV FWHM at 5.9 keV [Lec01]. For more details on the working principle of SDDs and their performance see [Lec01].

[5]KETEK GmbH, Hofer Str. 3, 81737 München, Germany.

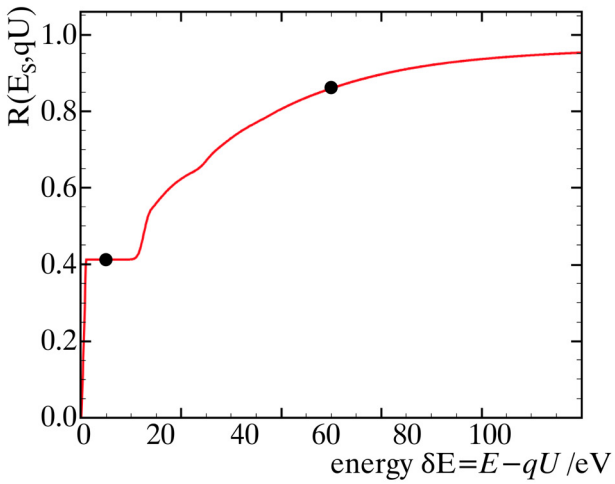

Figure 2.8: Measurement of the column density with the Rear Section e-gun. The curve shows two suitable positions for the column density measurement with the Rear Section e-gun (marked by the dots). By decoupling the rate and the response function one can calculate the column density [Ang05].

2.3.2 Electron gun as calibration and monitoring tool

A further monitoring instrument available at the Rear Section is the angular selective e-gun based on the photoelectric effect. The e-gun is an electron source with a narrow beam with less than 1 mm diameter at the position of the e-gun[6] and adjustable energy and momentum. With the help of the e-gun several effects of the electrons emitted in the source can be reproduced.

The main tasks of the Rear Section e-gun are given in the following. In table 2.1 the e-gun measurement parameters of these tasks are summarized.

- **Column density monitoring:** a precise knowledge of the column density inside of the WGTS is of high importance for the KATRIN sensitivity aim as discussed already. The monitoring of the column density with the e-gun is performed by measuring the electron rates at different retarding potentials. The measurement is repeated at different analyzing potentials $q\Delta U = E_e - \delta E$ by varying the retarding potential, where E_e is the energy of the e-gun electrons. δE is the surplus energy of the electrons with energy E_e compared to the required energy to pass the retarding potential. The measurement is performed at $\delta E = 5\,eV$ and $\delta E = 50\,eV$ (compare figure 2.8). Then the column density ϱd can be calculated as a fraction of $\varrho d_{\mathrm{free}}$, the mean free column density with $\varrho d_{\mathrm{free}} = (2.94 \pm 0.06) \cdot 10^{17}\,\mathrm{cm}^{-2}$ [Ang05]. The required electron rate is in the order of $10^4\,\mathrm{s}^{-1}$ or higher, as a higher rate reduces the measurement time needed to achieve the statistical accuracy of $1{\cdot}10^{-3}$ to $2{\cdot}10^{-3}$ (compare [Ang05]). The measurement is planned to be repeated periodically but not more often than every 2 hours [Ang05].
- **Energy loss function measurement:** the probability of an electron hitting the detector and not being scattered on its way is only 41.3 %. For that reason a precise knowledge of the inelastic scattering cross sections, described by the energy loss function, is required [Ang05]. As the energy loss function depends mainly on the

[6] The e-gun beam size is initially defined by the spot size of the incident light. But on the way through the experiment, the diameter is changed according to the conservation of the magnetic flux.

column density, the electron rate is measured at different column densities. Once measured for a certain column density, the probability to scatter should not change during the whole KATRIN life-time. If a radial dependence or other spatial effects occur, the measurement can also be performed at various angles or by scanning over the whole flux tube, but in normal operation it is planned to be performed on-axis.

- **Transmission function measurement:** the transmission function depends on the fields and the potential applied to the MAC-E-filter [Ang05]. For that reason the measurement of the transmission function is also performed with the Rear Section e-gun. During these measurements the count rate at the detector dependent on the voltage differences $U_{\mathrm{gun}} - U$ between the e-gun voltage U_{gun} and the analyzing voltage U_0 is of interest. The rate is measured at several voltage differences and for each of the 148 detector pixels individually. To enable an electron transport through the source without scattering, the WGTS is not filled during the measurement. When the energy loss function, the column density and the transmission function are measured, the response function of the spectrometer is also known.
- **Work function calibration:** the absolute potential seen by the electron at the analyzing plane is not solely defined by the supplied spectrometer voltage but also by the work function[7] of the surface with the most negative potential. The most negative potential is applied to the inner wire layer. The work function of this layer Φ_{MS} can be measured by the electron gun, if the voltage applied on the e-gun cathode U_{C}, the kinetic energy of the e-gun electrons E_{ph}, the punch through voltage U_{pt}, and the work function of the e-gun cathode $\Phi_{\mathrm{e-gun}}$ are known:

$$|\Phi_{\mathrm{MS}}| = |\Phi_{\mathrm{e-gun}}| + |E_{\mathrm{ph}}| - |\Delta U_{\mathrm{C}}| + |U_{\mathrm{pt}}| \tag{2.29}$$

  The cathode work function can be determined by measuring the rate at the detector related to the wavelength of the UV-light used to emit the electrons. If the rate at several wavelengths is measured, the resulting spectrum behaves like a Fowler function [Fow31]. Fitting this function to the data gives the work function of the material.
- **Spectrometer trap testing:** during the KATRIN measurements it could be possible that the residual gas in the main spectrometer is ionized by the electrons from the source. The produced ions could be trapped in the spectrometer and cause an additional background. If this trapping of ions occurs, it can be tested with the e-gun. This is done by emitting at least 10^6 electrons per second. Due to the high density of electrons in such an electron beam the probability to ionize a sufficient number of residual gas atoms in the main spectrometer is much larger than during normal operation of the WGTS[8]. To check for the dependence of the trapping probability of the spectrometer on the radial position the polar angle is varied between 0° and 51°. The specific conditions during the measurements must be adapted to each test individually.

To meet the requirements for each of these measurements an e-gun based on the photoelectric effect was designed. The UV-light from a light source must be filtered and transported into the primary system, where the UV-light transmits through a thin gold layer which acts as a cathode (compare figure 2.9). The emitted electrons are accelerated

[7] The work function is the difference between the Fermi level of a material and the vacuum potential. For more information see chapter 4.1.

[8] There are admittedly 10^{11} electrons per second emitted in the WGTS. Of these electrons 20 % are reaching the pre-spectrometer [Pra12]. But at the pre-spectrometer most of the electrons are reflected so that only about $10^4\,\mathrm{s}^{-1}$ electrons reach the main spectrometer. The exact number of electrons reaching the main spectrometer therefore depends on the retarding potential of the pre-spectrometer.

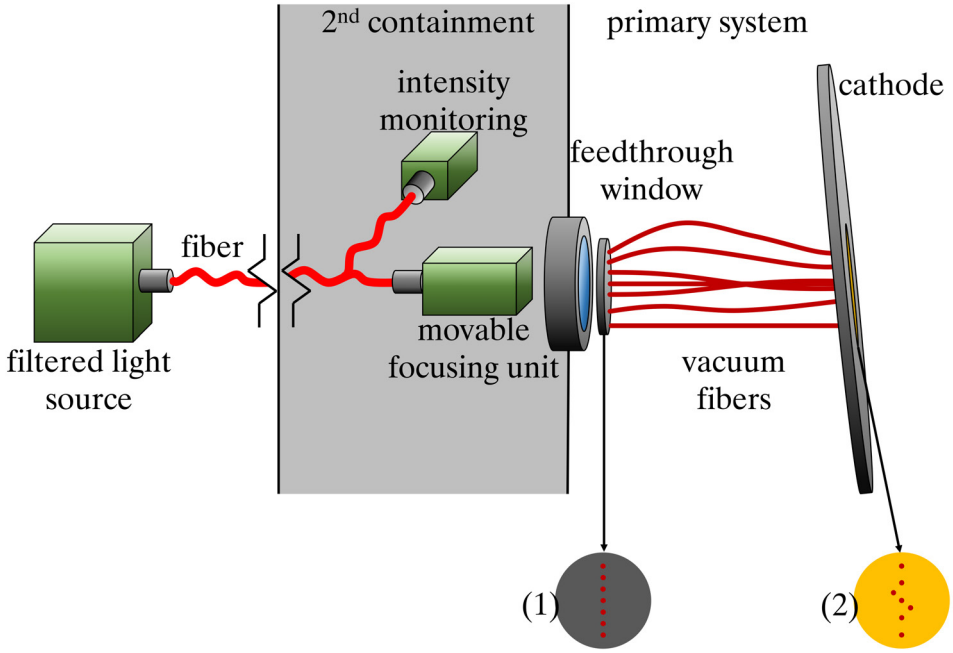

Figure 2.9: Schematic drawing of the basic optical setup of the Rear Section e-gun. Outside of the second containment there is only the filtered light source. The light is transported by fibers via a not yet specified interface into the second containment (marked gray). In the second containment an intensity monitoring is required. In addition, an optical setup which focuses the light through a feed-through window into the primary system is needed. To be able to focus the light into each of the 7 fibers installed in the primary system, the focusing unit must be movable. Neither of the components colored green is specified in detail yet (in the scope of the thesis in hand the design of the optical setup is fixed, compare section 3.2.1.1). Directly behind the feed-through window a plate is placed, in which the vacuum fibers are glued. The positioning of the fibers on this plate is shown in (1). The fibers transport the light to the cathode of the e-gun, where the electrons are produced. At the cathode the fibers are arranged differently to the plate at the feed-through window (see (2)). The positions are a result of the simulations presented in [Hei15].

by the acceleration electrodes to the required energy. The main spectrometer potential acts as reference potential for this acceleration [Bab14]. Only an additional offset, possible in both directions, is generated by its own voltage supply. The adiabatic transport of the electron through the Rear Section is ensured by the electromagnetic transport section of the Rear Section. The components of this transport section are shown in figure 2.10.

The optical setup including the gold cathode defines many parameters of the e-gun, namely the energy distribution of the electrons, the rate, the rate stability and the beam size: the width of the energy distribution is mainly defined by the difference between the photon energy and the work function of the cathode. For that reason it is necessary that the wavelength of the UV-light source can be changed to adapt the photon energy to the work function. In addition, a tunable width of the wavelength distribution is needed to adjust the energy distribution for the purpose of the measurement. In doing so one has to take into account, that the requirement of a small energy distribution is contradictory to the rate requirements. But the rate is not only dependent on the light impinging on the cathode but also on the material specific quantum efficiency and the free mean path of

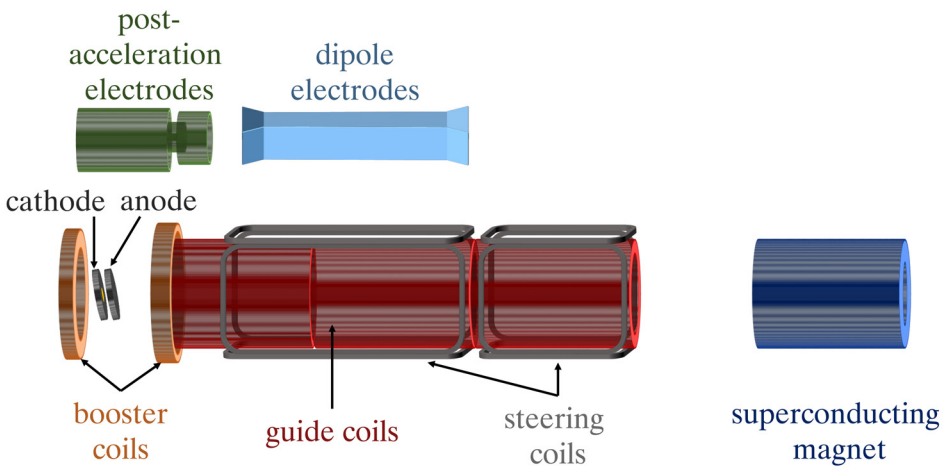

Figure 2.10: Components of the electromagnetic transport section of the Rear Section e-gun. The electrodes shown at the top of the picture are placed inside of the magnets and only drawn outside of the magnets for clarity. The electrodes of the electromagnetic transport section of the Rear Section e-gun consist of the cathode, the anode, the three-part post-acceleration electrodes and the dipole electrode. Electrons emitted at the cathode are accelerated by the anode at first and afterwards by the post-acceleration electrodes. The tube walls of the vacuum system, which is inside of the coils surrounding the electrodes, are grounded. For that reason the negatively applied voltages with the highest negative potential at the electrode surrounding the cathode cause the acceleration on the electrons. The dipole electrodes make a shifting of the beam possible. The magnetic components are the booster coils, the guide coils, the steering coils and the superconducting magnet. The function of the booster coils is to increase the magnetic field at the position of the e-gun cathode and in doing so to improve the adiabaticity of the electron transport during the acceleration process. The steering coils enable the passing through the off-axis aperture inserted in the beam line to prevent ions from hitting the e-gun cathode. The guiding coils and the superconducting magnets ensure the adiabatic transport of the electrons into the WGTS.

the electrons in the gold cathode (for a more precise description see section 3.2.1.2). The beam size is defined by the light spot impinging on the gold cathode at first. As the light is transported by 200 nm fibers to the gold cathode, the required beam size of less than 1 mm with 99 % of the light intensity [Bab14] is achieved. Later the beam size changes with the magnetic flux tube on its way through KATRIN.

The angle of the e-gun beam towards the magnetic field line is changed by tilting the cathode. In addition, the beam can be shifted by the Rear Section dipole fields. Dipoles, which are installed at the WGTS for that purpose, are needed as well to fully cover the flux tube. The angular distribution is defined by the transport of the electrons through KATRIN: the magnetic moment depends on the energy perpendicular to the field lines and this energy is defined by the kinetic energy and the polar angle of the electrons. If the transport of the electrons is not adiabatic the magnetic moment is not conserved and the angular distribution is broadened. Furthermore, the angular and positional distribution depends on the quality of the cathode's surface.

Table 2.1: Summary table of e-gun measurement parameters. In this table the measurement parameters and, if defined, their allowed uncertainties are given. In addition the conditions in the WGTS during the different measurements are added.

Electron beam parameters		column density measurement	Energy loss function	Transmission function	Work function calibration	Trap measurements
Energy:	absolute energy E /eV	18 600	18 600	18 600	18 600	0 - 18 600
	σE /eV	< 2	< 2	< 0.2	< 0.2	< 2
Polar angle in WGTS:	absolute angle θ /°	0	0 or 51	0 - 51	0	0 - 51
	σ_θ /°	<4	<4	<4	<4	<4
Rate:	absolute /s^{-1}	O(10^4)	O(10^4)	O(10^4)	O(10^4)	O(10^6)
	relative stability	0.1 % over minutes	0.1 % over hours	0.1 % over minutes	1 % over minutes	not important
Spatial:	Axial	yes	yes	yes	yes	yes
	beam shifted off-axis	no	on request	yes	yes	on request
	Flux tube coverage	no	on request	on request	on request	on request
Gas in WGTS:		^{3}H	^{3}H	None	with and without ^{3}H	with and without ^{3}H
Gas pressure in WGTS:		normal run pressure	modified pressure	evacuated	normal run pressure	dependent on request
Frequency:		periodic	once at the beginning for calibration	on request	on request	on request

2.3.3 Rear Wall as possible determinant of WGTS plasma potential

The Rear Wall is installed at the rear end of the beam tube. It is the main neutralizer of charges in the WGTS: electrons, which are emitted in rear direction, and those, which are reflected at the tandem spectrometer, impinge on the Rear Wall. To reduce the number of electrons, which are reflected at the Rear Wall, the electron absorption of the Rear Wall is maximized [Bab14]. This is required, as reflected electrons can reach the spectrometer again with changed energy: it is expected that about 57.5 % of the impinging electrons are absorbed [Bab14]. The reflected electrons are moving through the WGTS towards the spectrometer. The probability that the entire WGTS is passed without scattering is 15.3 % [Höt12]. That means that 8.8 % of the primary electrons, which hit the Rear Wall, emerges from the WGTS towards the spectrometer. In addition, the neutralization of ions at the Rear Wall is one of the three main ion removal processes besides the recombination with electrons and the removal through the electric dipole at the DPS [Ang05]. Nonetheless, a charging of the Rear Wall is prevented by the connection to a power supply [Bab14].

However, the main objective of the Rear Wall is to expose a well defined, temporally and spatially stable electrostatic potential towards the magnetically confined plasma of the tritium source. In the tritium source a neutral gas coexists with a cold plasma which arises from the ionization of the gas molecules (on average 15 secondary electrons per original β-electron are produced [Höt12]). The particles forming the plasma have a small kinetic energy in the order of the gas temperature[9] of the tritium source [Ang05]. For that reason small potential variations in the source in the order of several 10 meV have a large impact on the neutrino mass measurement already. This is caused by the fact, that the source potential acts as a reference potential for the electrons at the moment of their formation: a change in the source potential causes a linear offset of the kinetic energy of the electrons. Therefore, the energy filtering at the tandem spectrometer is also affected, as a MAC-E-filter uses the difference of the potentials at the source and analyzing plane for energy filtering.

The transport of electrostatic potentials through the source is defined by the mobility of the charged particles. The movement of the charged particles towards the tube walls is, in contrast to the longitudinal movement, reduced by the transverse magnetic confinement of the plasma [Bab14]: the electrons dominate the longitudinal conductivity. Conversely, in the transverse direction the electron conductivity is negligible due to their cyclotron motion. For that reason, ions dominate the transverse conductivity as they can also move towards the walls after scatter processes. But the perpendicular ion conductivity is about 7 orders of magnitude smaller than the longitudinal electron conductivity. That means that potentials and external voltages can be shielded by or conducted through the plasma depending on their position: the potential of the walls has only a small impact on the potential of the source. But it must be considered that the impact is not negligible and it increases along the beam tube. In contrast to this the Rear Wall potential is transported through the whole tritium source (compare figure 2.11).

Previous calculations presented in [Bab14] confirm this dominance of the Rear Wall potential and the increasing impact of the tube walls' potential on the potential in the tritium source. As this calculation neglects gas flows, densities, charge generation and annihilation an improved simulation with COMSOL multi-physics is performed. Its main result concerning the Rear Wall is, that the Rear Wall defines the plasma potential of the

[9] A gas temperature of 27 K corresponds to a kinetic energy of 2.4 meV.

source as long as the difference between the Rear Wall potential Φ_{RW} and the tube wall potential Φ_{tube} is within the limits:

$$-50\,\mathrm{mV} \leq \Phi_{\mathrm{RW}} - \Phi_{\mathrm{tube}} \leq 100\,\mathrm{mV}. \tag{2.30}$$

A detailed description can be found in [Kuc16].

To check the importance of the Rear Wall on the source potential during operation, a monitoring of the Rear Wall impact is planned. This monitoring is also needed for the adjustment of the potential difference between Rear Wall and beam tube walls. The monitoring is done by changing the potential applied to the Rear Wall combined with a scanning through the spectrometer potential. During this, the electron rate measured at the detector is changing depending on applied potentials. To increase the statistics by a higher electron rate the measurement takes place about 1 000 V below the endpoint. If the electron rate at the detector is changed for all pixels, the plasma potential is also shifted over the entire source cross section. That means, the potential is fully defined by the Rear Wall. The opposite result, that no detector pixel is affected, means the Rear Wall has no impact. If both, the tube walls and the Rear Wall, influence the plasma potential the count rate should change at the inner pixels and not at the outer ones. This effect can be removed or at least reduced by applying a suitable voltage on the Rear Wall.

To make sure that the potential of the Rear Wall is suitable, an additional voltage of $\pm 10\,\mathrm{V}$ compared to the WGTS tube walls potential can be applied with the connected power supply. But there is always an aspect of the Rear Wall potential that is completely independent of the supplied voltage and determined only by the difference between the vacuum level and the Fermi level of the Rear Wall material: the work function [Lan71]. If the work function varies over the surface of the Rear Wall these variations are transported along the plasma in so-called plasma tubes. These plasma tubes are shielded among others by a double layer structure [Alf81], if their diameter is larger than the Debye length [Ina10]

$$\lambda_{\mathrm{D}} = \sqrt{\frac{\varepsilon_0 k_{\mathrm{B}} T_{\mathrm{e}}}{n_{\mathrm{e}} e^2}} = 3.78 \cdot 10^{-4}\,\mathrm{m}. \tag{2.31}$$

Here $\varepsilon_0 = 8.9 \cdot 10^{-12}\,\mathrm{F\,m^{-1}}$ is the vacuum permittivity, $k_{\mathrm{B}} = 1.4 \cdot 10^{-23}\,\mathrm{J\,K^{-1}}$ is the Boltzmann constant, $e = 1.6 \cdot 10^{-19}\,\mathrm{C}$ [Moh15] is the elementary charge, $T_{\mathrm{e}} = 30\,\mathrm{K}$ is the electron temperature and $n_{\mathrm{e}} = 10^{11}\,\mathrm{m^{-3}}$ is the charge density close to the Rear Wall [Ott12]. If the plasma tubes are smaller, variations in the potential are averaged out.

This means that an unrecognized change of the Rear Wall work function, whether spatial or temporal, causes a systematic uncertainty on the neutrino mass measurement. For that reason the basic design of the Rear Wall must pass a test on long-term stability of its work function. Each Rear Wall candidate[10] must be tested on work function homogeneity in general. Both of these tests must be passed with a standard deviation of $\sigma_{\mathrm{WF}} \leq 20\,\mathrm{meV}$ [Bab13] in the area of each detector pixel[11]. For the latter test the absolute value of the work function does not matter as it only causes a shift of the electron energy in total, which is one of the fit parameters in the KATRIN analysis.

[10] Rear Wall candidates are parts which are fabricated identically to a Rear Wall. But the work function of these candidates is not characterized yet. After a successful characterization procedure a Rear Wall candidate can be installed as a Rear Wall (compare also chapter 4).

[11] The requirement on the work function stability is established per pixel as the data of each pixel will be analyzed individually.

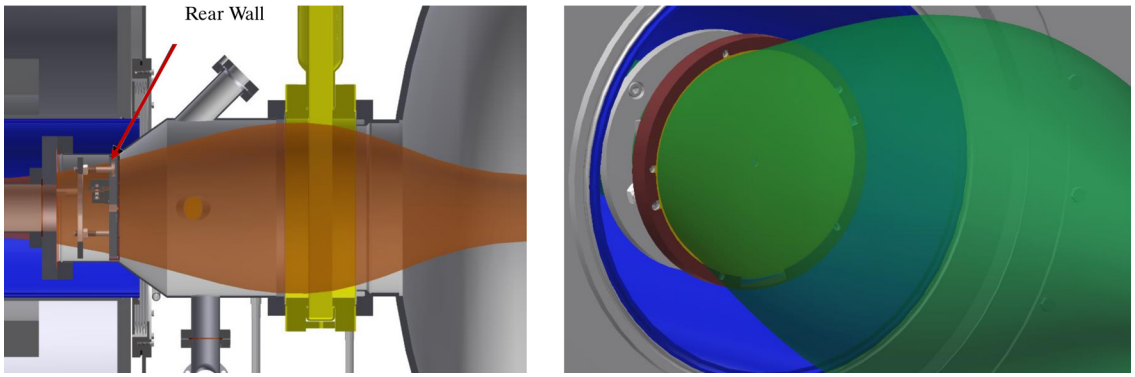

Figure 2.11: Flux tube impinging on the Rear Wall. On the left side a side-view of the Rear Wall with the outer flux tube of 229 T cm^2 is shown which can be transported through the Rear Wall chamber without contacting the walls. On the right side a front view of the Rear Wall and the technical flux tube of 210 T cm^2 is presented. This flux tube impinges on the Rear Wall with a safety margin of 1.3 mm (adapted from [Bab14]).

2.4 Objectives of this thesis

The setup and the main working principles of the Rear Section and its main components have been presented in the last section. However, there are still some open questions which must be answered before a fully functional Rear Section can be provided to KATRIN. These questions are discussed in the following.

The Rear Section and its components need to withstand the KATRIN conditions preferably for the whole KATRIN lifetime of at least 5 calendar years. During this time all components are exposed to a tritium atmosphere. The performance and properties of the components must be unchanged or at least not changed in a way that impedes on the required performance of the components. This is especially true for the components that are part of or inside of the tritium containing primary system.

Due to the long-standing experience with tritium containing systems at TLK this poses no risk for components like pressure sensors, vacuum chambers and pumps (KATRIN related pumps have been tested in [Pri13b]). But there are other components where no experience concerning their reliability in a tritium atmosphere is available either at TLK or in the literature: piezo motors, fiber feed-throughs and fibers. The piezo motor is needed to close the center hole at the Rear Wall if it is not crossed by an e-gun beam. When closed, a complete gold surface faces the tritium plasma. As the piezo motor is installed at the back side of the Rear Wall (which itself is installed at one end of the superconducting magnet), exchanging the motor in case of a failure would be a huge effort. The fiber feed-through is planned to be used to inject light into the second containment. But as there are safety requirements on the leak tightness of the second containment the fiber feed-through can only be used if the leak tightness and the tritium permeation rate meet the TLK requirements. Otherwise, the fiber feed-through cannot be used. The mentioned fibers are planned to be used inside of the primary system transporting the UV light to the gold cathode of the e-gun. As the e-gun should be stable within 0.1 % and a monitoring of the intensity is not possible inside the primary system, the optical properties of the fibers must not be affected by the tritium atmosphere, at least not within several hours. Otherwise, it would be possible to not reach the required rate stability of the different e-gun measurements.

In addition, a complete optical setup of the e-gun is not yet existing. It is established

that the electrons are produced by the photoelectric effect by UV-light, most likely a laser driven light source (LDLS). But it is not yet specified in detail how the broadband light of the light source is filtered and focused into the fiber feed-through and later into the fiber in the primary system. Also, a monitoring detector must be specified as well as the position of this detector in the optical setup. In addition, it is yet unclear if an optical design based on fibers can transport light of sufficiently high intensity to the gold cathode to achieve the required rates of up to 10^6 electrons per second.

The design of the Rear Wall is also not yet specified in detail. While there is the known requirement for a gold coating to enable the production of bremsstrahlung for the activity monitoring of the tritium source, the substrate and potential intermediate layers like diffusion barriers or adhesion layers are not yet defined. The main requirement on which the design depends is the spatial and temporal work function stability of at least 20 mV. But other criteria like a good adhesion of the gold layer on the underlying layers for easier handling and the possibility of a bake-out without damaging the gold surface must also be met.

From these open questions and still missing designs the three main objectives of this thesis are derived:

Investigation of tritium compatibility of components for the Rear Section
All three components, the piezo motor, the fiber feed-through and the fiber itself, must be tested in a tritium atmosphere for possible degradation. Suitable test experiments must be designed, built up and performed. Depending on the results of these experiments the consequences on the Rear Section and its design are identified and if necessary the design of the component must be changed.

Development of the optical design for the Rear Section e-gun and calculation of the resulting electron rate
First the specific components are selected and their exact positions to each other is optimized. Then the expected electron rate must be calculated. This needs to take into account all losses calculable with geometrical optics and the efficiency of the electron emission depending on the energy of the incident photons. Furthermore, the probability that an electron can leave the gold layer must be considered depending on its starting position in the gold layer. If the rates are lower than the required rates, further improvements of the optical setup are also part of the objective.

Development of a Rear Wall for the Rear Section
The quality of the gold layers coated on different materials must be tested for their work function homogeneity and stability dependent also on the surface treatment of the substrate before coating. For this the work function measurement should not only take place at ambient air but also at a vacuum of 10^{-5} mbar which will be the pressure at the Rear Wall of KATRIN. In addition, the effect of bake-outs, UV light and electron irradiation must be tested. If a suitable design is found, the manufacturing and characterization of several Rear Wall candidates is also part of this objective.

The first two objectives are treated in the following chapter 3 in section 3.1,3.2.2 and 3.2.3 or 3.2.1, respectively. All measurements concerning the Rear Wall development can be found in chapter 4.

Chapter 3

Investigation of the tritium compatibility of Rear Section components

As the Rear Section is one of the tritium carrying parts of the KATRIN experiment the tritium compatibility of all used components has to be ensured. This is especially the case for parts which can only be replaced making huge efforts[1] and safety relevant components. This makes tritium compatibility tests with materials that have not yet been deployed in a tritium atmosphere essential prior to an installation at the Rear Section. This includes a fiber feed-through as well as optical fibers which both are needed for the electron gun and a piezo based motor. The latter is placed at the backside of the Rear Wall. For these components the following questions must be answered:

1. Is a piezo based motor suitable for the KATRIN experiment, meaning that it can perform more than 100 000 driving cycles in a tritium atmosphere without failure even after multiple bake-outs at 150 °C?
2. Is the tritium leak rate through an optical fiber feed-through below $10^{-9}\,\mathrm{mbar\,l\,s^{-1}}$ that the feed-through poses no safety risk when installed as part of a tritium containing system?
3. Are the optical transmission properties of a fiber affected when installed inside of a tritium containing system?

The fiber feed-through and the fibers itself are planned to be used at the optical setup of the Rear Section e-gun. Therefore, it is required to answer another question before a fiber feed-through is installed at the second containment or a fiber is used in the tritium containing system:

4. Is the electron rate produced by the planned optical system high enough to meet the requirement of at least 10^4 electrons per second and of an electron energy spread of $\sigma_\mathrm{E} < 0.2\,\mathrm{eV}$?

Due to the variety of the tested components three completely different tritium compatibility tests are required. These are described in this chapter. The first section (3.1) deals with the so-called Piezotest. The goal of this test is to demonstrate the suitability of a piezo based motor for an operation in tritium atmosphere. The second part of the

[1] In this context huge effort means expenditure of time of about 3 to 6 months.

chapter (section 3.2) deals with the performance of the optical setup of the e-gun and its electron rate. In addition, the leak tightness of fiber feed-throughs concerning tritium and the effect that tritium will have on the fiber's optical properties are investigated. In the last section of the chapter (section 3.3) the consequences of the results of these tritium compatibility tests regarding the Rear Section are discussed.

3.1 Piezotest: measurement of the life expectancy of a piezo motor in a tritium atmosphere

As discussed in chapter 2 the main tasks of the Rear Section are to provide an angular selective electron gun and a Rear Wall with homogeneous as well as temporally and spatially stable work function over the area of the whole flux tube. To ensure that the Rear Wall covers the whole flux tube area, the e-gun has to be placed behind the Rear Wall (compare figure 3.1). For that reason, the Rear Wall has a centered hole where the electron beam can pass through. But if the hole cannot be closed, the plasma potential of the tritium source is not homogeneous anymore. The electromagnetic field lines cross the Rear Wall and impinge on a not gold coated surface behind the Rear Wall, which has a undefined work function.

To solve this problem a moving mechanism on the back side of the Rear Wall is needed (compare figure 3.2). This mechanism moves a cover which is gold plated on the side facing towards WGTS. It can be placed in 2 different positions: the hole in the Rear Wall is completely covered or is uncovered. In the latter position, the electron beam can pass through the Rear Wall. In principle there are different moving mechanisms conceivable, like stepper, servo, linear and piezo motors. These would be installed directly at the backside of the Rear Wall. A mechanical feed-through for the control of the cover position from the outside of the vacuum system could also be an option. Regardless of the choice of moving mechanism the following general requirements must be met (compare [Bab14]):

- A travel range of at least 5 mm is needed in order to open and close the 5 mm hole at the Rear Wall.
- The moving mechanism must be as small as possible since mechanical access is only possible from the backside of the Rear Wall. The circumference must not exceed 192 mm. The space for electrical feed-throughs is also restricted.
- The moving mechanism must be able to work in a magnetic field of more than 1 T as the Rear Wall is placed inside the superconducting magnet. That also means that the motor must be built out of non-magnetic materials.
- The maximum load should be ≥ 2 N as the cover has to be mounted on the moving mechanism. To match the work function of the Rear Wall as closely as possible, the same materials and manufacturing procedures must be used. This means the cover is built out of gold plated stainless steel (for more detailed information about the Rear Wall design see chapter 4).
- The operating temperature range will be between 10 °C and 50 °C. The upper temperature that the motor can withstand while not moving must be higher, namely up to 150 °C. This is required to make a bake-out of the vacuum system possible.
- The mean time before failure must be at least 100 000 driving cycles[2]. This number results from the fact that the electron beam has to pass through the Rear Wall twice

[2]One driving cycle implies that the motor moves from one end of the travel range to the other end and back again.

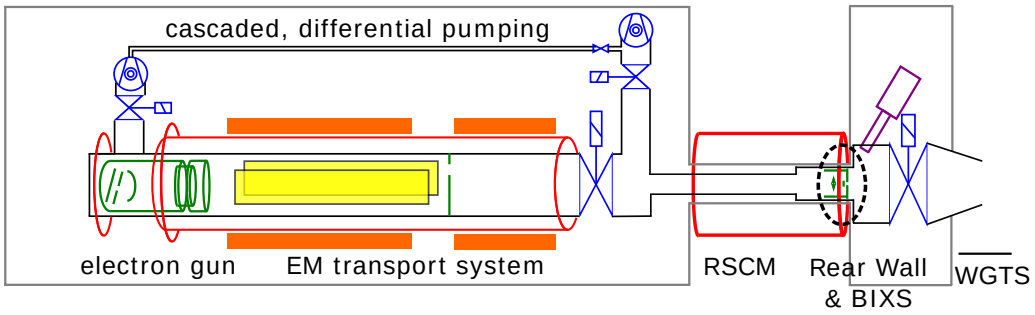

Figure 3.1: Integration of a movable cover in the Rear Section setup. The sketch shows the basic setup of the Rear Section (compare figure 2.6). The dotted circle marks the place where the movable, gold plated cover is needed. It enables that the electron beam can pass the Rear Wall if it is moved away from the hole. If it covers the hole, a continuous gold plated surface is presented to the plasma of the WGTS. To avoid electromagnetic field lines, electrons and ions impinging on the moving meachnism, it is installed on the backside of the Rear Wall.

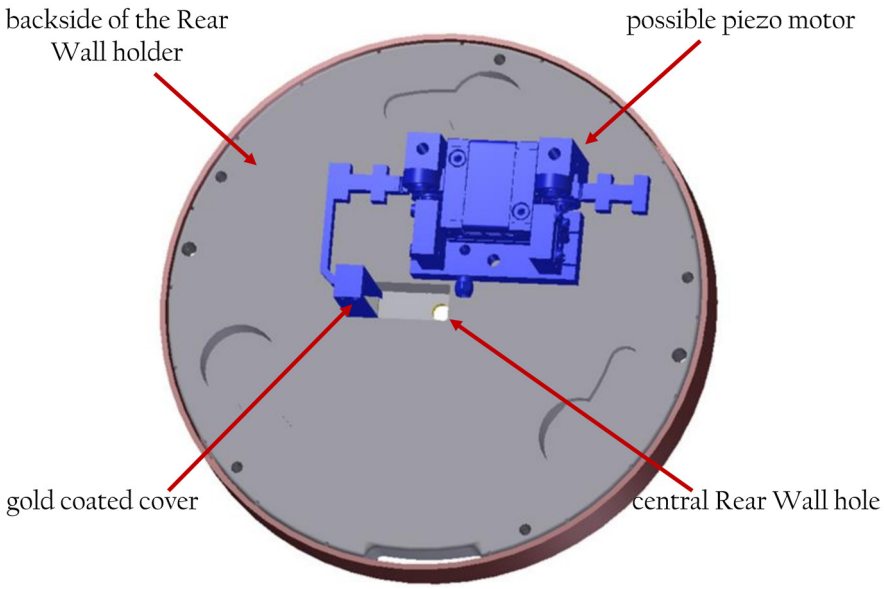

Figure 3.2: CAD-drawing of the integration of a possible piezo motor on the backside of the Rear Wall holder in the Rear Section setup. On the moving part of the piezo motor a gold coated cover is installed. This cover can be moved in front of the central hole of the Rear Wall. In doing so, a complete gold surface is facing the tritium plasma.

each hour over three years of measurement time. Including a safety factor of about 2 this results in about 100 000 driving cycles. It is necessary that the motor does not fail during the KATRIN measurement time as a replacement is very difficult due to the position of the motor inside the superconducting magnet.
- Some kind of position sensor should be installed if possible, e.g. limit switches. Especially in case of a motor failure a position sensor would be very helpful in finding the cause.

Due to space restrictions, it is not possible to use mechanical feed-throughs and the magnetic fields exclude all electromotors. Therefore, a piezo motor is the only viable option.

Aside from the above requirements, certain tritium specific requirements also have to be taken into account when selecting a suitable piezo motor:

- The motor should be UHV compatible as outgassing must be as low as possible to minimize the impact on the tritium purity of the gas. Therefore, the outgassing rate should in the order of or below the outgassing rate of stainless steel, which is about $10^{-11}\,\mathrm{mbar\,l\,s^{-1}\,cm^{-2}}$ [Avd12].
- Halogens are not allowed at all [TLK13] as corrosive liquids or acids can be produced by their reaction with tritium [Wea99]. This restriction also includes common insulators like Teflon[3] or Viton[4] and applies to cables and electronics inside the tritium containing vacuum system as well.
- Lubricants must be avoided to minimize the possibility of unintended reactions with the tritium gas.

A motor which meets all the above mentioned requirements could in principle be used for the KATRIN experiment. Nevertheless, there remains the risk of a motor failure due to the tritium atmosphere. Up to now, only tests of piezoelectric valves[5] in a tritium atmosphere have already been performed. During these the valves are tested concerning β-induced charge leakage from the piezoelectric crystal to the ground which would cause a degradation of the valve performance [Gil83]. In fact some gas discharge activities as evidenced by a discoloration of the piezo crystal were observed [Gil83]. However, the valve did not show any significant degradation ($> 5\,\%$) of performance [Cof88, Gil83]. For all KATRIN intents and purposes, a piezo motor, especially one which must be able to perform 100 000 driving cycles without failure, has never been tested in a tritium atmosphere before. Therefore, two tests of different piezo motors are performed, the so-called Attotest (described in detail in [Bab14]) and the Piezotest.

The results of the Attotest are briefly summarized in section 3.1.2. The Piezotest is then discussed in detail in sections 3.1.3 to 3.1.5. Finally, a summary and discussion of the results of the performed tests concludes the parts of this chapter that deal with the tritium compatibility of piezo motors. Before that the general mode of operation of piezo motors is explained in the following section.

[3] Teflon is a registered trademark of the company E. I. du Pont de Nemours and Company, 1007 Market Street, Wilmington, DE 19898, USA. The chemical compound is Polytetrafluorethylen or shortened PTFE.

[4] Viton is also a registered trademark of the company E. I. du Pont de Nemours and Company, 1007 Market Street, Wilmington, DE 19898, USA. It is an umbrella term for different fluoropolymer elastomers.

[5] The operating principle of such valves is based on a piezo crystal which opens and closes the valve.

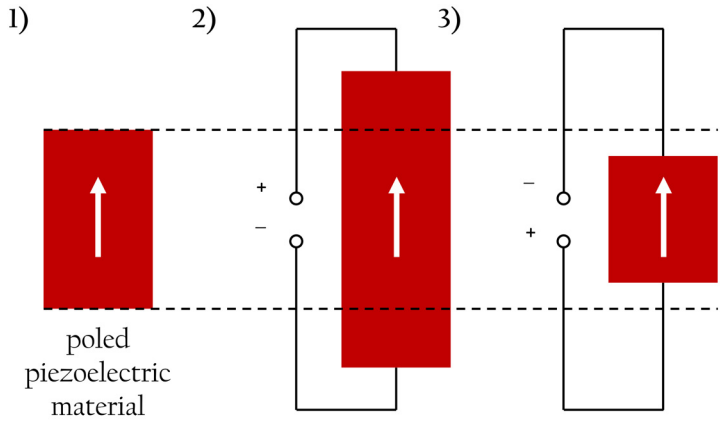

Figure 3.3: Visualization of the inverse piezoelectric effect. In 1) an already poled piezoelectric material is shown. The length of the crystal without applied external field is marked with the two dotted lines. If a voltage with the same polarity is applied, as it was used to pole the crystal, the piezoelectric material gets extended. This can be seen in 2). In 3) the polarity of external voltage is reversed compared to the one in 2). Therefore, the crystal is compressed. The deformation in both cases is directly proportional to the strength of the applied voltage (own figure in accordance with [Vij12]).

3.1.1 Working principle of piezo motors

The working principle of piezo motors is based on the transformation of electrical energy to mechanical motion using the inverse piezoelectric effect [Hii10]. If piezoelectric materials are subjected to an external field the anions and cations in the piezo material are asymmetrically displaced. This microscopic displacement of charge causes a macroscopic deformation of the crystal [Vij12] which is used in piezo motors (see figure 3.3).

There is a large variety of piezo motor designs, many of them described in [Spa06]. Common to all piezo motors are the extremely fine resolution down to the sub-nanometer [Hii10], a fast response time [Mar09], large generated torques and a simple construction [Mor03]. In the following two different piezo motors both based on a clamping-type design are presented in more detail as these are the designs tested in the Attotest and the Piezotest.

The Attotest examines a piezo motor which is based on two principles: the inertia of the slider and the friction between a piezoelectric crystal and the slider (compare figure 3.4 1)). Due to a slowly increased applied voltage the piezoelectric material extends. During this phase the slider sticks to the piezoelectric material due to friction. Once the piezoelectric material is extended as far as possible, it is very quickly compressed. Due to inertia the slider is not following the quick motion of the piezoelectric material [Spa06, Mar09, Sch00, Mor03] and sticks to the rod. This motion approach is also-called stick-slip mechanism [Hii10]. It is also described in detail in figure 3.4. The main advantages of this motor design are the simple design itself, the fast response and the comparatively high velocities of several mm/s. In addition, large workspaces of several mm^3 are possible [Sch00]. However, there are some drawbacks to this design as well: motors are restricted to horizontal movement unless a clamping mechanism is added [Hii10] and the design relies on friction and inertia of the slider [Mar09].

The motor tested during the Piezotest is working with the Piezo Walk Drive design.

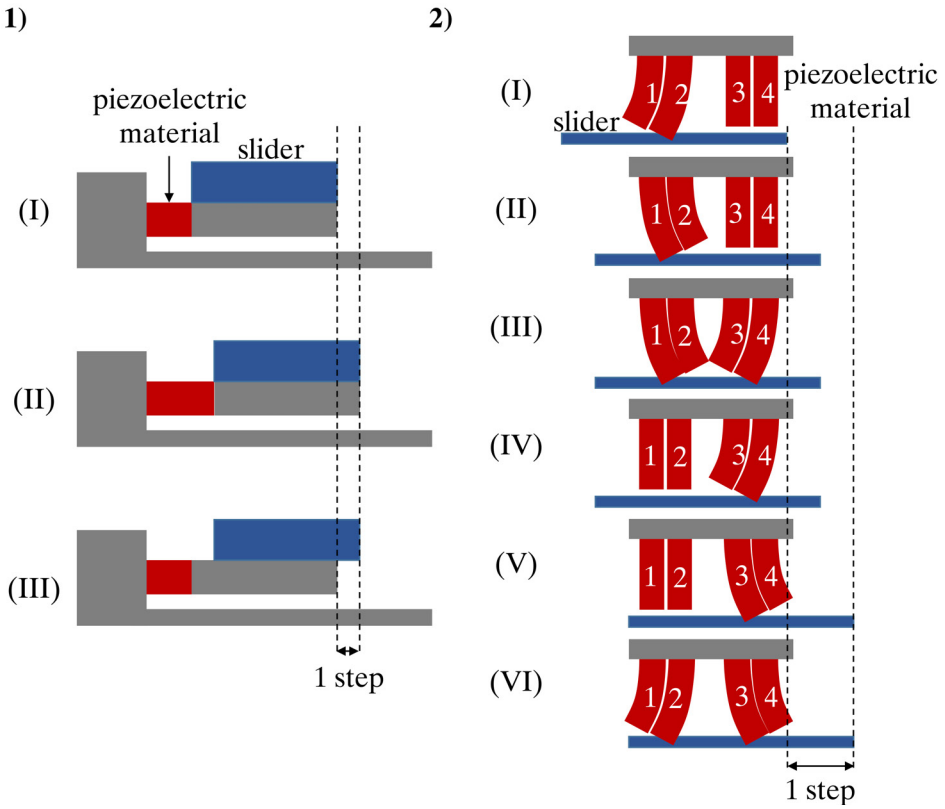

Figure 3.4: Visualization of typical approaches for piezo actuators. In 1) the working principle of a stick-slip motor is shown. A slider is placed on top of a driving rod which is directly attached to the piezoelectric material. In (I) the piezoelctric material is relaxed, in (II) the piezoelectric material is extended slowly (slider remains on rod because of friction) and in (III) it is quickly shrunk again (slider stays at its position because of interia). If the position of the slider in the top and bottom pictures are compared (dashed lines) the slider moved towards the right side. The difference between both positions is one step width of the motor [Mor03]. In 2) the motion of Piezo Walk Drive based motors is shown. For simplicity only two bimorph legs are shown here. The four piezo materials are tagged with numbers from 1 to 4 from left to right to be able to distinguish between them. In (I) and (II) piezo 1 and 2 are expanded simultaneously, thereby moving the slider to the right side. Now piezo 4 is also expanded and the second leg is pressed against the slider (III). As the slider is fastend by the second leg, the first leg can be removed from the slider (IV). By releasing piezo 4 and expanding piezo 3 at the same time the slider is moved rightwards (V). In (VI) piezo 2 is expanded again and the process starts over again with picture (I). The distance between the two dashed lines marks the starting and end position of the motor. This is one step width of the motor [Glö04] (own figures in accordance with [Mor03, Glö04].)

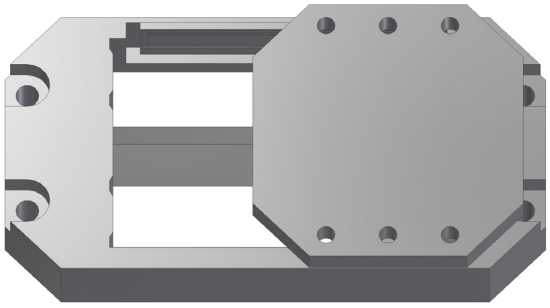

Figure 3.5: CAD drawing of the ANPx101eXT20/RES tested during the Attotest. The motor consists of three main parts: motor body, axis and platform. Once the motor body is fixed to another surface, the only movable part is the platform. The platform enables the attachment of a Rear Wall hole cover by six screw holes [Bab14].

In this design four legs each consisting of a bimorph piezo are pressed against a slider. Bimorph piezos consist of two piezo materials with different polarity [Sch11] which are electrically isolated and bonded to each other. By that both piezo materials can be controlled independently [Glö04]. By applying a voltage at one part of the bimorph piezo the whole leg is bent. As the four legs are successively bent and released again, the slider is moved forwards (see figure 3.4 2)). Similar to the stick-slip design high velocities of up to 20 mm/s [Mar09] and a very compact setup can be realized [Mar09]. Although it is not necessary[6], the forces developed by this design are much higher, namely 1 kN compared to usually just a few 10 N [Mar09].

In principle both motor types should be equally suitable for a tritium atmosphere if the requirements mentioned in the last section, especially the material restrictions, are met. None of them has been used in a tritium atmosphere before. That is why their tritium suitability must be demonstrated in a test before usage. The test of the stick-slip based motor in the Attotest was part of [Bab14]. The result of this test are presented briefly in the following section.

3.1.2 Result of a previous experiment: the Attotest

During the so-called Attotest (for details see [Bab14]), a commercially available stick-slip based motor, ANPx101eXT20/RES, from Attocube[7] was tested (see figure 3.5). The specifications of the motor are given in table 3.1. By comparing these specifications with the requirements given in section 3.1 it can be seen that the motor meets almost all requirements. There is no information regarding the mean time before failure from the manufacturer. Therefore, the non-tritium related specifications of the motor met the KATRIN requirements. But a proof of the tritium compatibility was required.

The procedure to test the tritium suitability of the motor was as follows: the motor was constantly moved to randomly chosen positions. Each of these movements was called a driving operation. Once the motor stopped, the current position was measured by the positioning sensor and compared with the intended position. If both values deviated by more than 10 µm from each other the driving operation was considered erroneous. That

[6] Even the weight of a Rear Wall is less than 400 g.

[7] Attocube systems AG, Koeniginstrasse 11a, 80539 München, Germany

Table 3.1: Summary of manufacturer specifications of the piezo motor ANPx101eXT20/RE. Requirements for the KATRIN experiment are shown in the third column. All specifications meet the requirements except for the mean time before failure which was not specified by the manufacturer [Att13].

parameter	specified	KATRIN requirement
travel range	20 mm	$\geqslant$ 5 mm
maximum footprint size	24 mm x 48 mm	$\leqslant$ 48 mm x 48 mm
magnetic field range	0 T to 31 T	at least 1 T
maximum load	2 N	$\geqslant$ 2 N
operation temperature range	-273 °C to 100 °C	10 °C to 50 °C
maximum bake-out temperature	150 °C	up to 150 °C
mean time before failure	not specified	100 000
position sensor	absolute resistive position sensor	required if possible
UHV compatibility	fulfilled	required
used materials	piezo material: zirconate titanate; motor body: titanium; wires: KAPTON isolated copper	no halogens, no lubricants or coatings

way the performance of the motor could be monitored by its error rate. At the beginning of the Attotest, the error rate was below 3 %.

Before the actual test in a tritium atmosphere was started, an initial functional testing was performed in ambient air. In the course of this first test, experience with the motor and its operation was supposed to be gained. During this time frequency and voltage were adjusted in a way that an operation free from error was possible and re-polarization in case of multiple errors was tested. Afterwards the motor was installed in a vacuum system, where it moved for about 11 000 driving operations in an ambient air atmosphere of $2{\cdot}10^{-3}$ mbar to 13 mbar. Towards the end of this test, the performance of the motor worsened with the error rate rising up to about 30 %. This error rate was reduced to less than 15 % by re-polarization of the motor before the vacuum system was filled with 0.08 mbar gas and a tritium fraction of more than 90 %. After about two and a half days and 3 500 driving operations the error rate started to steadily rise again. Finally, the test was unintentionally stopped after 4 days and about 5 500 driving operations in a tritium atmosphere when the motor got completely stuck.

The most likely cause of this failure are abrasion-like effects of an organic coating needed to ensure ideal friction and inertia for the stick-slip mechanism (see figure 3.6). The existence of this coating was not mentioned in the data sheet of the motor. This extends to the necessity of regular maintenance after about 10 000 end-to-end cycles. However, once the motor is exposed to tritium a maintenance is only possible with huge efforts. This is caused by the position of the motor inside of the borehole of the superconducting magnet: both the primary system and the second containment must be disassembled to exchange the motor. This work would be further complicated by the safety restrictions after the tritium exposure. Concluding, the required mean time before failure of 100 000 driving operations cannot be met with this motor. This means that the ANPx101eXT20/RES

Table 3.2: Summary of manufacturer specifications of custom made piezo motor N-310K176. Requirements for the KATRIN experiment are shown in the third column. All requirements are met [Phy15, Phy13].

parameter	specified	KATRIN requirement
travel range	20 mm	$\geqslant$ 5 mm
maximum circumference	192 mm	$\leqslant$192 mm
magnetic field range	not specified, but non-magnetic materials used	at least 1 T
maximum load	10 N	$\geqslant$ 2 N
operation temperature range	10 °C to 50 °C	10 °C to 50 °C
maximum bake-out temperature	150 °C	0 °C to 150 °C
mean time before failure	$\geqslant$ 100 000 without maintenance	100 000
position sensor	limit switches	required if possible
UHV compatibility	specified	required
used materials	ball bearings: ceramics no lubricants	no halogens, no lubricants or coatings

motor is not suitable for the KATRIN experiment.

Nevertheless, the reason for disqualification of the motor from Attocube is not a failure caused by the tritium atmosphere but general problems with the slip-stick approach. For this reason a piezo motor based on another motion approach which does not depend on friction might be viable. To this end a custom adapted N-310K176 motor based on the piezo walk drive approach was developed in cooperation with the company Physik Instrumente[8]. The performance test of this motor is the so-called Piezotest which is described in the following sections.

3.1.3 Experimental setup of the Piezotest

The Piezotest is designed to test the custom adapted motor N-310K176 from Physik Instrumente (see figure 3.7) for its tritium suitability. The drive of this motor is taken from the NEXACT[9] and the technical implementation from the NEXLINE N-216[10]. All specifications of this motor meet the requirements including the mean time before failure (see table 3.2).

The vacuum chamber used for the Piezotest is a stainless steel DN100-63 CF[11] reduction cross (see figure 3.8). This is not only a vacuum chamber but also the primary system of

[8]Physik Instrumente (PI) GmbH & Co. KG, Auf der Römerstraße 1, 76228 Karlsruhe, Germany

[9]The NEXACT motor is a piezo linear motor based on the piezo walk drive and a registered trademark of the company Physik Instrumente

[10]The NEXLIME motor is a piezo linear motor based on the piezo walk drive and a registered trademark of the company Physik Instrumente

[11]CF is an abbreviation for ConFlat, a standard for vacuum flanges. ConFlat is a registered trade mark of the company Varian, Inc., 5301 Stevens Creek Blvd. Santa Clara, CA, 95051 USA.

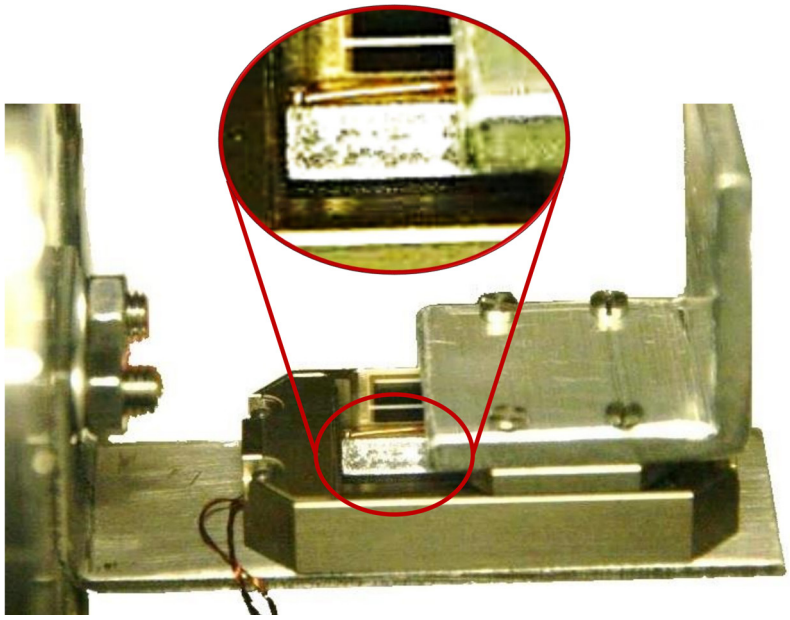

Figure 3.6: Photography of the Attocube motor after its complete failure. The dark spots visible at the axis of the motor (shown also in the enlarged part of the picture) might be destroyed organic coating. This would explain why the motor got completely stuck after about 20 000 driving operations [Bab14].

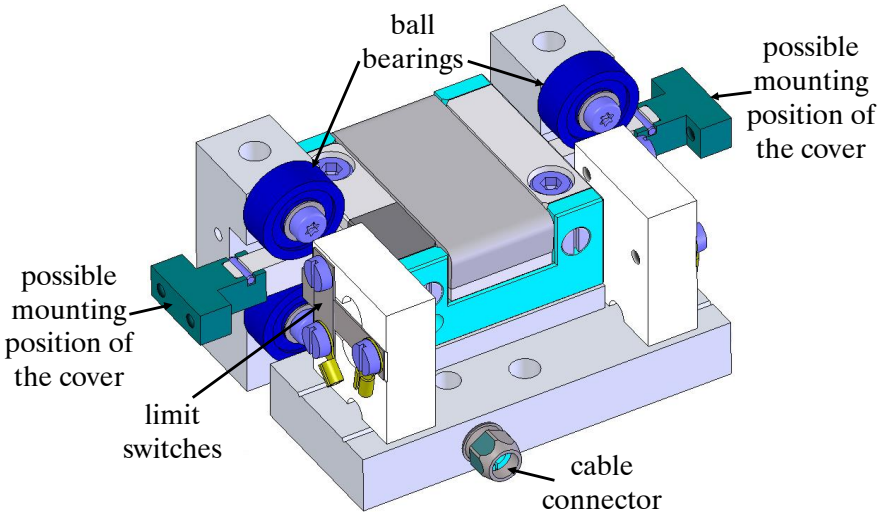

Figure 3.7: CAD drawing of the N-310K176 tested during the Piezotest. The motor axis is stabilized by ball bearings (marked in dark blue). The axis is the only part of the motor which is moved once the motor body is screwed down to another surface. The cover can be attached to the T-shaped parts of the axis (marked in green). Inside of the central box (marked in light blue) the piezo walk drive mechanism is installed. At the left side of the motor the contact plates of the limit switches can be seen.

the Piezotest, the system where the tritium gas is safely stored. Therefore, the reduction cross has to meet all requirements mentioned in [TLK13]. The motor is installed in the vacuum chamber with an angle piece to which the motor is bolted. This angle piece is bolted to one of the DN100 CF flanges sealing the vacuum chamber. At the opposite flange a viewport is installed. This viewport enables a position measurement of the motor with a Bosch[12] GLM150 Professional [Rob15] laser rangefinder which is fixed at the viewport. As it would be difficult to hit the small moving axis with the laser rangefinder, a stainless steel plate is bolted on the axis. This plate also simulates the load due to the cover at the KATRIN experiment.

At one of the smaller DN63 CF flanges two pressure sensors are installed, namely a MKS[13] 902-1213, a piezo pressure sensor, and a MKS 626B02TBE, a Baratron[14] pressure sensor. Both pressure sensors are gas type independent. Overall a pressure range from 10^{-5} mbar to 1 000 mbar is covered. At the same port there is also the possibility to connect a test gas cylinder. By expanding the gas from the test gas cylinder into the vacuum system, the experiment is filled with tritium. At the opposite DN63 CF flange the electrical feedthroughs for the motor controller (a NEXACT controller from Physik Instrumente) are placed.

For safety reasons the Piezotest is installed in the TRAP fume hood. The already existing infrastructure of this specific fume hood can be used, namely a backing pump and a turbopump. These pumps are connected to the TLK infrastructure. With this combination of pumps a pressure of less than 10^{-5} mbar can be achieved in the Piezotest setup. The connection to the primary system is realized at the same port where the pressure sensors are installed. Due to the installation of the experiment in a fume hood, the activity in the experiment is limited to 10^{10} Bq. This also limits the tritium partial pressure to about 10^{-2} mbar. However, this partial pressure exceeds the partial pressure at the Rear Wall by three orders of magnitude.

Outside of the TRAP fume hood the motor controller and the measurement computer are located. A LabView[15] software is used for motor control and pressure sensors read out. Additionally, the LabView Software automatically controls the motor during the test procedure. A detailed description of the measurement procedure can be found in the next section.

3.1.4 Measurement procedure

By using the previously described setup the piezo motor N-310K176 is tested for its tritium suitability. To this end the primary system of the Piezotest is filled with a tritium gas mixture with a gas mixture which contains as much tritium as possible. This usually means $> 90\,\%$. As the motor will not just be exposed to tritium but also be baked out at the Rear Section, this has to be tested as well. According to its specifications the motor cannot be moved during bake-out and while the temperature is above 50 °C. Since the only way to determine, if the motor has been damaged, is by observing it in motion, the motor cannot be controlled for damage during the bake-out. So, to ensure that the motor

[12] Robert Bosch GmbH, Robert-Bosch-Platz 1, 70839 Gerlingen-Schillerhöhe, Germany

[13] MKS, 2 Tech Drive, Suite 201 Andover, MA 01810, USA

[14] Baratron pressure sensors are capacitance based sensors and the name Baratron is a registered trade mark of MKS.

[15] LabView is a system design software of National Instruments Corporation (NI), 11500 N MoPac Expwy, Austin, Texas, USA

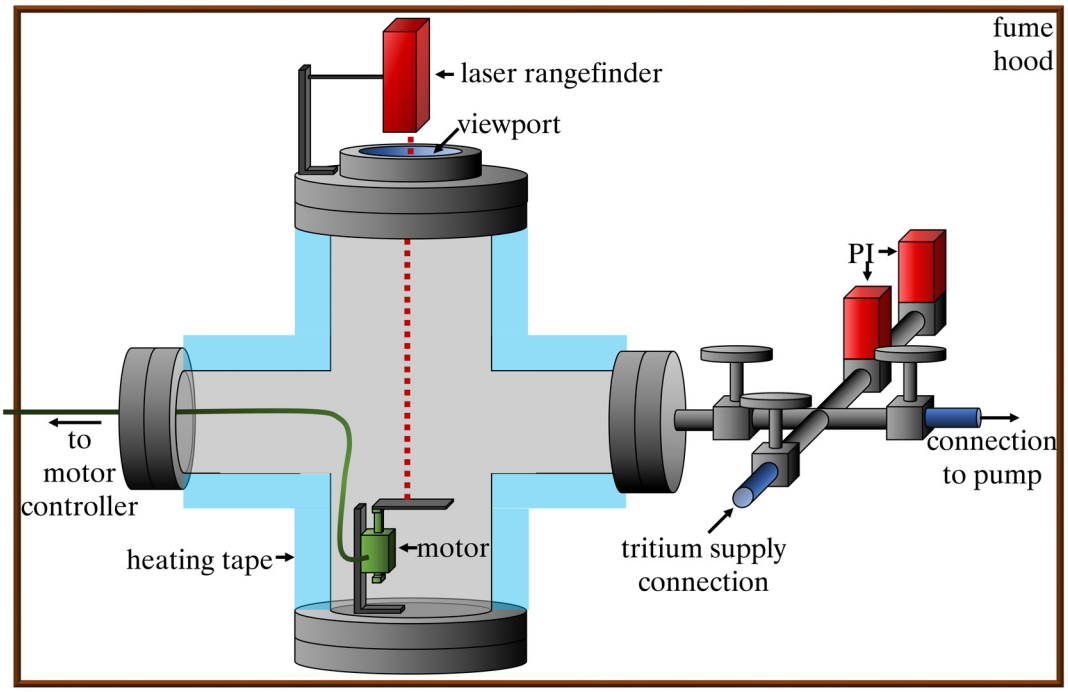

Figure 3.8: Sketch of the experimental setup of the Piezotest. The motor is placed inside of a primary system which is sourrounded by a heating tape needed for bake-outs. Two pressure sensors (PI) are connected to the system via a hand valve and a crossed pipe. Tritium is injected and evacuated at the other available ports of the cross pipe. The laser rangefinder is placed outside of the primary system but inside of the fume hood.

can perform the required 100 000 driving cycles, the first bake-out will not take place until this milestone has been reached. Otherwise, it would be impossible to determine if the motor is suitable to perform as many driving operations in a tritium atmosphere.

Over the course of the experiment, the performance of the motor is monitored. In the precursor experiment Attotest (see section 3.1.2) a change in performance was detected by comparing the position of the intended motor targets with the position where the motor actually stops. However, the N-310K176 is not equipped with position sensors but only limit switches. Therefore, a completely different measurement procedure is necessary in the case of the Piezotest: two different methods of how to register a performance change have been developed. One of these is based on limit switches, called automatic measurements, and one is based on the laser range finder, called manual measurement. Both measurement techniques are performed on the same motor and are needed to ensure optimal data gathering about its performance. They are described in detail in the following.

Automatic measurements are used to continuously gather data about the functioning of the motor accumulated over the entire travel range, but not about detailed positional failures. During this measurement the motor is automatically moved from one limit switch to the other. One cycle is completed when the motor moved once the hole travel range and back again. After a certain number of cycles a calibration run occurs: these are cycles where the needed steps in both directions are counted. Therefore, the measured quantity in this measurement technique is the number of steps needed to cover the entire travel

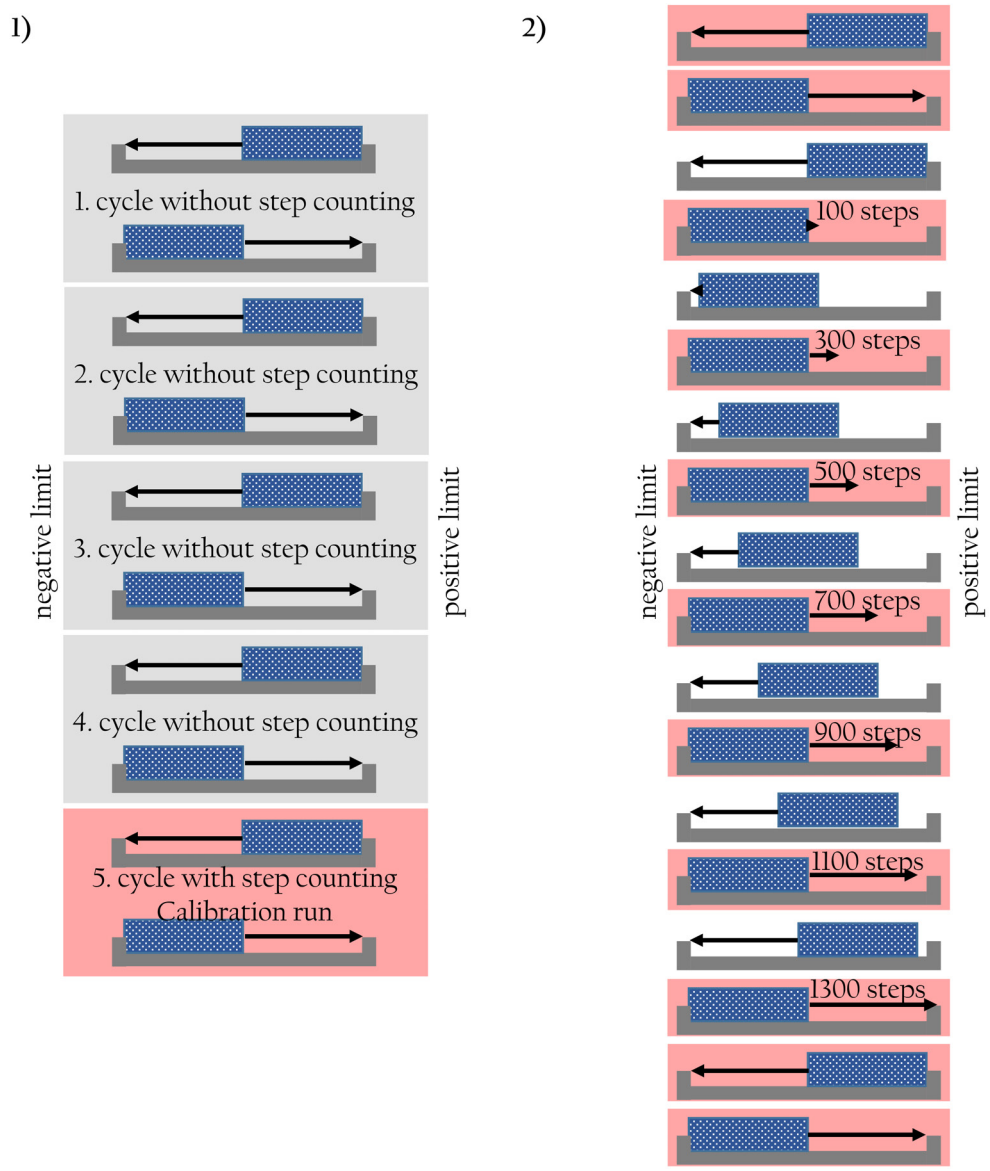

Figure 3.9: Visualization of the measurement procedures of the Piezotest. In both parts of the figure the positions that involve step counting are highlighted with a rose box. On the left side automatic measurements (1) are shown: here the motor is driving from one end to the other end and back again. Only after every fifth cycle are the steps counted. Most of the measurements are taken exactly with this sequence of counted and uncounted cycles. The measurements are performed with an accuracy of 10 steps meaning that after every 10th step it is checked whether the slider has reached the end of the travel range. In general this check could be done with an accuracy of 1 step. However, this would be too time consuming. As an acceptable compromise accuracy is downgraded to multiples of 10 steps to speed up measurements. Due to the fact, that this measurement procedure is automated, it is performed almost 24/7. Since both measurement techniques are performed on the same motor, the automatic measurements are suspended to perform measurements with a laser range finder. These manual measurements are shown at the right side of the sketch (2): the measurement procedure starts with a movement to negative limit and back to positive limit. Afterwards the motor is driven back to the negative limit again to achieve a reference position. From this reference position the motor is moved 100, 500, 700, 900, 1 100 and 1 300 steps each time moving back to the reference position after the allotted number of steps. It should be noted that the 1 300 steps are only ever reached if there is already a drop in performance. The measurement procedure is finished by a movement to negative and positive limit.

range. If the performance of the motor remains unchanged, the number of steps remains unchanged as well (see also figure 3.9 1)).

Manual measurements are used to gather data about positional effects on the performance of the motor over the travel range, e.g. to see if the motor looses performance only at one particular point or over the whole travel range. As manual measurements cannot be automated they are performed only once a workday and do not give a continuous picture of the motor's performance.

During the manual measurements the laser range finder is used to measure the distance of the motor from the range finder after a certain number of steps (0, 100, 300, 500, 700, 900, 1100, 1300 from negative limit and 0 from positive limit) with an accuracy of ± 1 mm (a more detailed description of the test sequence can be found in figure 3.9 2)). The distance is always measured from the upper end of the laser range finder to the plate bolted onto the moving axis of the piezo motor. If the distance after a certain number of steps decreases this is evidence that the performance of the motor is getting worse. Another important piece of information that can be gained is that of positional effects: if distances are plotted against the number of steps one can see if there is just one position the motor gets stuck at or if a change of travel distance is homogeneous over the whole travel range.

3.1.5 Execution of measurements

Before being exposed to tritium the motor is moved in ambient air for a few driving cycles (in the order of 1 000) to make sure that it is moving without any problems. Afterwards the system is filled with tritium gas mixtures twice: as the measurement with the Piezotest must be interrupted to perform another experiment in the TRAP fume hood, the tritium gas is pumped out of the system. After the other experiment is finished, the Piezotest is filled with tritium gas again. In addition, after about 186 000 driving cycles the system was baked out three times at 150 °C, 180 °C and 180 °C. During the last bake-out the system is connected to the pump again. By doing so the system is evacuated to $\leq 10^{-5}$ mbar for the rest of the measurements. For more details about the actions performed during the Piezotest see table 3.3.

Over the whole measurement time automatic and manual measurements are performed to monitor the performance of the piezo motor. Exemplary sample data of these measurements can be seen in figures 3.10 and 3.11. The remaining data can be found in appendix A.3 on pages 198ff. In figure 3.10 one can see a change in performance after about 83 000 cycles: the motor needs an increased number of steps to get to a specified position. But the motor still reaches the limits. About 11 000 cycles later steady degradation in performance reaches some kind of plateau after which the performance no longer or just slightly worsens. By this time the motor needs approximately 1.6 times the number of steps from one limit to the other compared with its starting value.

After about 186 000 driving cycles and 119 days of tritium exposure two short bake-outs are performed. Afterwards the motor seems to regenerate and performance remains stable at a level similar to that at the beginning of the Piezotest. Finally, the third, longer bake-out is performed which worsens the performance of the motor extremely. The number of steps increases by a factor of 6 - 7. The steady increase in steps is stopped and reversed

Table 3.3: Summary of actions performed during the Piezotest. For each action the absolute pressure at its beginning and end as well as the action's duration are given. Note, that the absolute pressure in the system rose due to outgassing and the leak rate of the vacuum system. In addition, the absolute number of driving cycles is noted.

action	absolute pressure in mbar	duration in days	driving cycles after action
system filled with 0.1 mbar tritium gas with purity of 90 %	0.1 - 0.3	16	23 149
system filled with 0.1 mbar tritium gas with purity of 90 %	0.1 - 0.75	103	217 558
bake-out at 150 °C	0.77 - 1.58	0.25	∼ 186 000
bake-out at 180 °C	1.58 - 2.8	0.25	∼ 186 000
bake-out at 180 °C	$< 10^{-5}$	3.2	217 558
filling system with ambient air	1 000	∼ 21	∼ 220 650

immediately when the system is filled with ambient air. After that, the number of steps needed to reach the other limit is again back to its starting value.

From cycle 233 236 on the number of steps reaches negative, nonsensical values (only positive positions are defined) randomly at every 5th to 200th calibration run with increasing frequency. The motor is therefore retroactively declared damaged starting at the first occurrence of this behavior and the Piezotest is stopped.

The same effects on performance can be seen in figure 3.11 where the data of the manual measurements are plotted against time. In figure 3.12 the same data is plotted against the number of steps. The motor seems to homogeneously change its performance over the whole travel range.

In the next section possible reasons for the observed performance changes are discussed.

3.1.6 Results of the Piezotest experiment and discussion

The piezo motor N-310K176 has shown performance changes during the course of the measurement runs. Those reasons are discussed in the following.

Degradation of performance after about 83 000 driving cycles and reaching a plateau of performance after about 94 000 driving cycles - The degradation expresses itself in the increasing number of steps needed to move from one end of the travel range to the other. It can be explained by a slight depolarization of the piezo crystals. According to the manufacturer the fact that the performance degrades is expected for this kind of piezo actuator. The number of driving cycles performed before the degradation takes place is also common for that kind of motor. However, the fact that the degradation saturates is rather unusual and cannot be explained exactly. Due to the smaller polarization the motion of the piezo legs is smaller. This can have two different impacts: either the legs do not completely leave the slider anymore or the bending of the legs becomes smaller. Both has the consequence that the slider is no longer moved in the same way as it was before the depolarization.

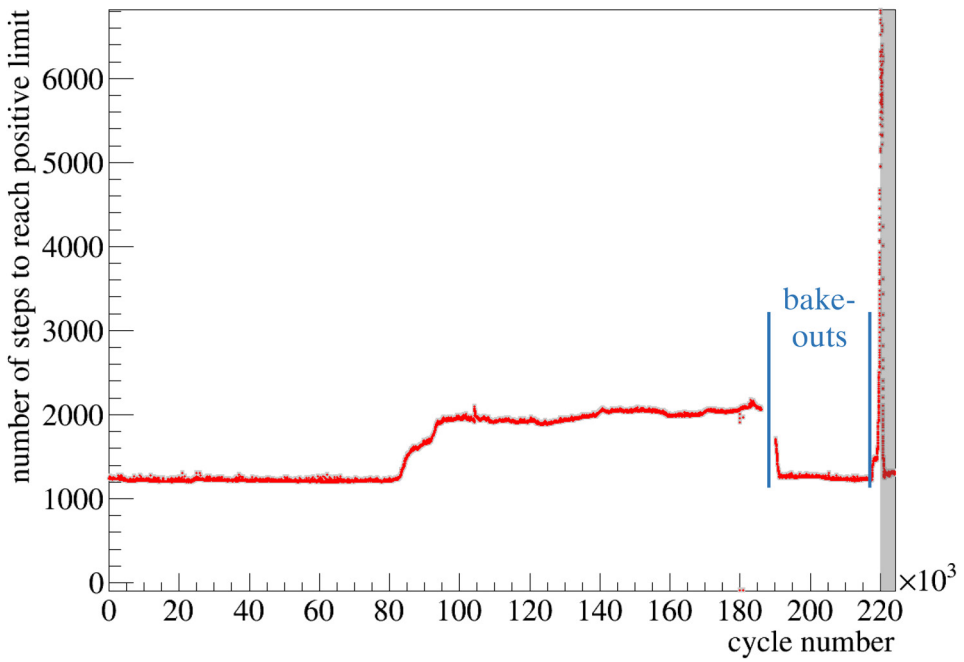

Figure 3.10: Plot of the data taken during the automatic measurements. The number of steps is plotted against the cycles. Points in the range from about 185 000 to 190 000 are missing because of a malfunction of the data acquisition. The first two short bake-outs and the third long bake-out are each marked by a vertical line. The grey area beginning at about 220 600 cycles marks the time when system was filled with ambient air again.

Improvement of performance after short bake-outs of about 6 hours at 150 °C or 180 °C respectively - At elevated temperatures a repolarization of the motor is possible. This repolarization causes an improvement of the performance. The fact that the motor does not yet degrade from the temperature of 180 °C is most likely due to the short bake-out time: the outside of the primary system had a temperature of 180 °C for 6 hours. But the motor is not installed directly at the wall of the primary system. Therefore, the motor temperature was probably not that high.

Degradation of Performance by more than a factor of 6 in steps after long bake-out of more than 3 days at 180 °C - The temperature of 180 °C is higher than the specified bake-out temperature of the motor. Above this temperature a depolarization of the piezo material starts: the oriented dipoles are evenly distributed in the crystal again and therefore the crystal looses its piezoelectric properties.

Improvement of performance after filling the system with ambient air - According to the manufacturer the fact that the motor performance is improved by filling the system with ambient air again can be explained by an improvement of its friction properties.

Damage after 233 236 driving cycles - While the motor can be moved to the end of the travel range manually, it cannot do so automatically. The limit switches to not work properly anymore. This indicates that the connection to the limit switches is damaged. This is also supported by the microscopic examination of the slider after the experiment is finished. The pictures taken during this examination can be found in figure 3.13.

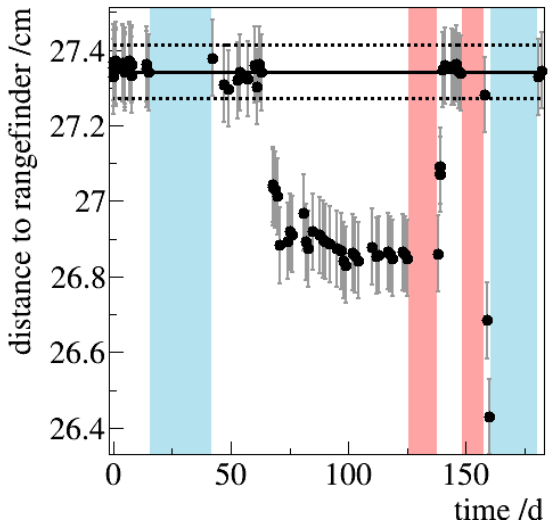

Figure 3.11: Plot of data taken during manual measurements with 700 steps. Each point represents one measurement. The straight and dotted line represent the mean and error of the reference data before the tritium exposure. At first the measured distance is stable. From day 15 to 42 there is no measurement as the TRAP fume hood is needed for other experiments at that period of time (marked blue). The Piezotest is filled with ambient air during that time. About 20 days after filling the system with tritium again performance starts to decrease until an almost stable level is reached. The break afterwards is caused by preparations to bake-out the system (marked red). Directly after the short bake-outs the travelled distance is similar to the reference again. The next break is caused by the long bake-out (marked red) as is the following decrease in performance. During the blue colored time duration from day 160 to day 180 no manual measurements are performed. Data taken from day 180 on are performed at ambient air.

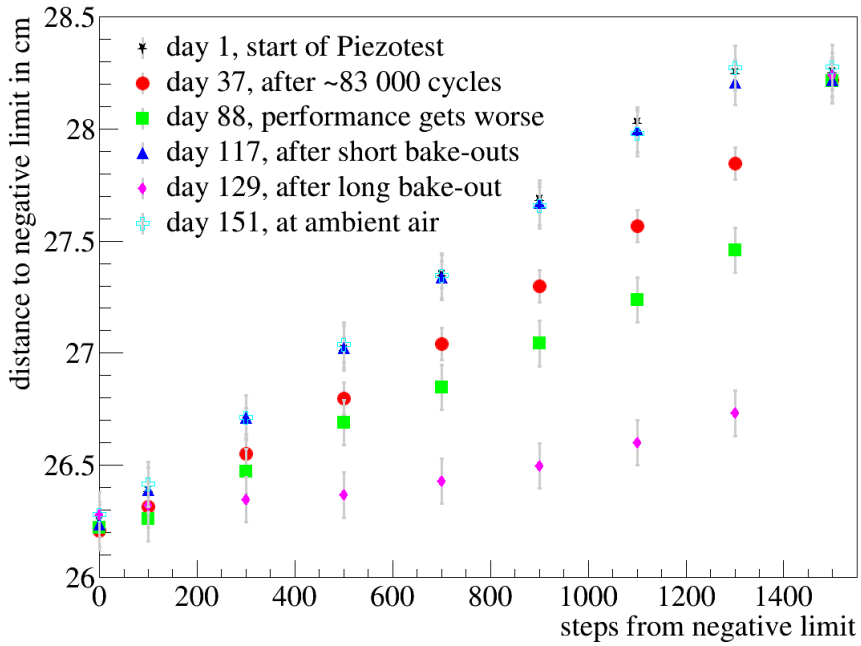

Figure 3.12: Plot of data taken during manual measurements plotted against number of steps. Data taken at six manual measurements are plotted against steps the motor has to travel. NL and PL are abbreviations for negative limit and positive limt. At all times the limit switches are reached.

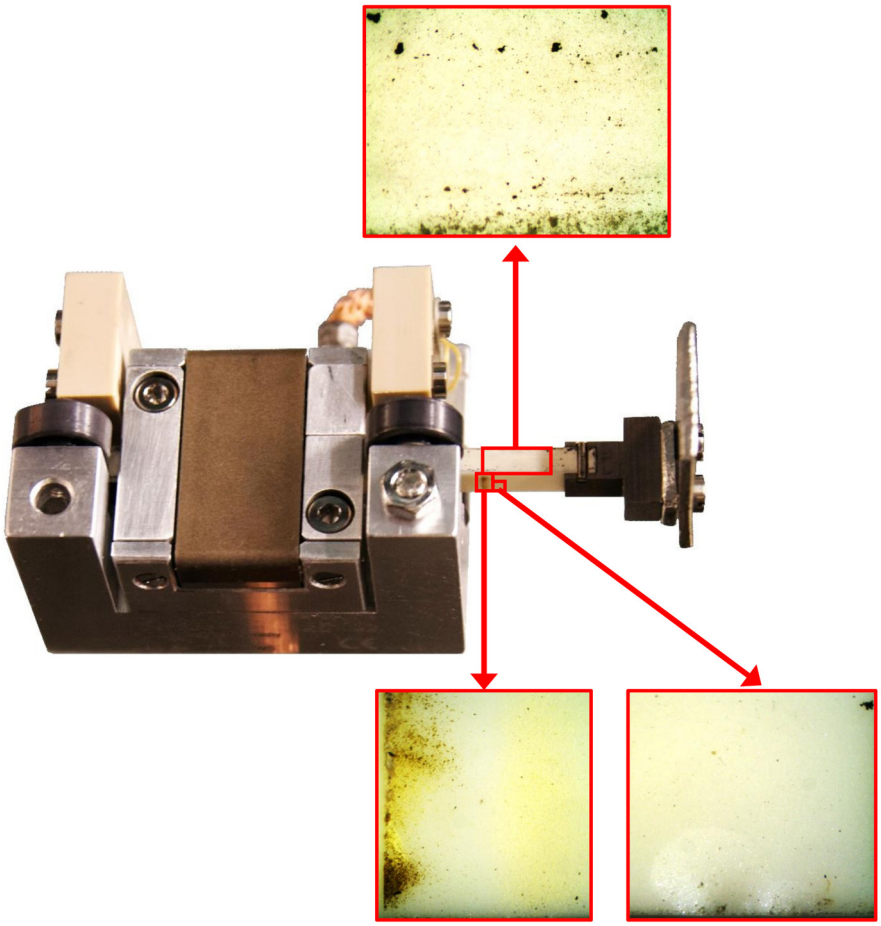

Figure 3.13: Photographies of the motor slider after the experiment is finished. In the middle the motor is shown with those positions marked where the magnified pictures were taken. At the top the upper side of the slider is magnified. The contaminated surface is probably caused by abrasion due to the high number of driving cycles of the motor. At the bottom modifications caused by the degradation of the motor performance can be seen (left): the motor got caught at this position and caused higher abrasion there. This a characteristic artifact if the motor moves to the same position all the time. At the right side a modification of unknown origin is found.

3.2 Fibertest: investigation of performance characteristics of fiber components in a tritium atmosphere

The angular selective electron gun discussed in section 2.3.2 is based on the photoelectric effect [Her87, Ein05]: UV light in the range of approximately 260 nm to 300 nm[16] is used to emit electrons out of a gold cathode. Since the electron gun is integrated in a tritium filled primary system the optical setup for UV irradiation is constrained by the following factors:

- The materials allowed in the primary system are highly restricted by [TLK13].
- (Re-)alignment and replacement in case of damage of all optical components must be possible at all times.
- Space both in the primary system and the second containment is limited.

Because of these restrictions the optical setup is placed outside of the second containment and the light is coupled in by a fiber and a fiber feed-through inside of the second containment. Inside of the second containment a fiber coupled splitter enables the intensity monitoring of the light. The injection into the primary system is done through two lenses. Inside of the primary system several vacuum compatible fibers are staggered fixed in which the light of the lenses is injected. These fibers guide the light towards the gold cathode which is coated at the end of the fibers (for a more detailed description of the optical setup see section 3.2.1).

However, questions which must be answered before using are (compare beginning of chapter 3):

1. Is the electron rate that is emitted with this optical setup high enough to meet the KATRIN requirements?
2. Is a fiber feed-through leak-tight concerning tritium?
3. Are the optical properties of a fiber affected by a tritium atmosphere?

To answer the first question a detailed analysis of the respective intensity, losses and rate is conducted. This analysis is described in section 3.2.1. The answers to question 2 and 3 are given by the so-called Fibertest. This experiment is divided into two parts: Fibertest I which deals with the leak tightness of a fiber feed-through; and Fibertest II in which the effects of tritium on the optical properties of fibers are tested. Both experiments are described in detail in section 3.2.2 and section 3.2.3 respectively.

3.2.1 Calculation of the electron rate of a fiber based optical system for the electron gun of the Rear Section

In this section question 1 from section 3.2 is dealt with: is the electron rate achievable with the planned optical setup high enough? To answer the question the optical setup used at the electron gun and its design considerations are discussed in more detail first (see section 3.2.1.1). With the knowledge of the optical properties of the components the expected electron rate can be calculated. These calculations and its results are discussed in the subsection 3.2.1.2. To test the calculations without the final e-gun setup, the same calculations were successfully performed for the test setup of the e-gun which was used at UCSB. The results of these calculations can be found in appendix B.2.

[16] The work function of gold once exposed to ambient air is in the range of 4.0 eV to 4.2 eV (compare chapter 4).

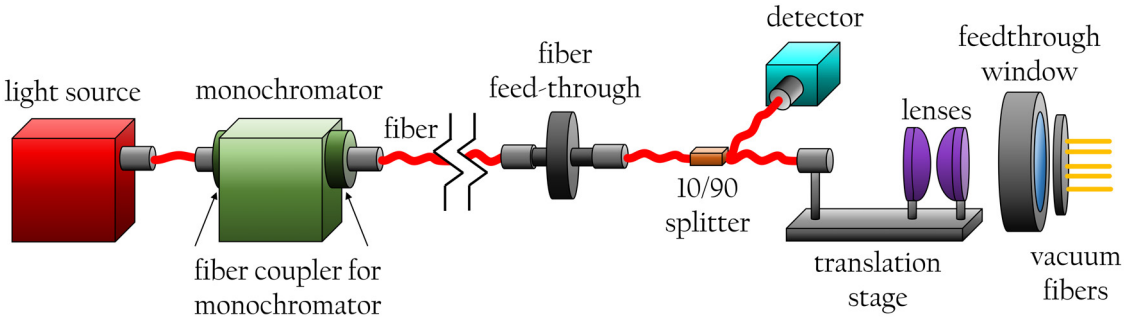

Figure 3.14: Scheme of the optical setup used at the e-gun. The light source should be able to provide a high enough intensity needed for an electron rate of at least 10^4 electrons s^{-1} and a tunable wavelength. The tunable wavelength is important as the energy spread of the produced electrons is dependent on the difference between the incident light energy and the work function of the gold cathode. As the work function could shift over time, a wavelength tunable light source is necessary. To meet this requirement a laser driven light source with high broadband spectral radiance in the order of 150 mW in combination with a monochromator is used. Through a fiber and a fiber feed-through the light is guided into the second containment. To minimize the number of optical components not monitored by the detector, it is installed inside of the second containment. Therefore, the fiber splitter is connected to the fiber feed-through inside of the second containment. The usage of a fiber splitter avoids the need for the light to be ejected from the fiber, focused by lenses into a stand-alone beamsplitter and re-injected into another fiber. To focus the light through the feed-through window into the fibers inside of the primary system two lenses are used. To be able to inject the light in any of the 7 fibers inside of the primary system a translation stage is used. In principle a Y stage would be suitable to inject the light in each of the fibers as they are arranged in a vertical line. But to compensate potential variations from this vertical line, e.g. by production tolerances, an XYZ translation stage is used.

3.2.1.1 The optical setup

For the optical setup commercially available parts are used where ever possible in order to minimize the development time. In addition, separate optical components like lenses and beamsplitters are replaced by fixed parts, e.g. a fiber splitter. In doing so the effort to align the setup and make it ready for use is minimized and aligning of the setup is simplified.

An overview of the complete optical setup is given in figure 3.14. The specifications of each optical component is discussed piece by piece in the following:

- **Light source:** the light source is the laser driven light source EQ-99XFC from Energetiq[17]. The light source is directly coupled to a 1 m long fiber with an FC/PC[18] connector at the end. The diameter of the fiber is 450 µm and its NA[19] is 0.22. The spectral radiance of the light source at the end of the fiber is shown in figure 3.15. To make the spectral radiance of the light source as stable as possible a temperature stabilization is added.

[17] Energetiq Technology, Inc. 7 Constitution Way, Woburn, MA 01801 USA
[18] FC and PC are acronyms. FC stands for fiber channel and PC for physical contact.
[19] NA is an acronym for numerical aperture. It is a dimensionless number describing the beam width of a beam of light.

- **Monochromator:** the monochromator is of the type DK240 from Spectral Products[20]. The working principle of this monochromator is based on the Czerny-Turner principle [Mes08]. The gratings itself are inserted into a turret. The grating whose peak transmission best fits our needs is the AG1200-00250-686 grating with 1200 g/mm, a peak transmission wavelength of 250 nm and a peak transmission of 70 % and the AG1200-00300-686, also with 1200 g/mm, a peak wavelength of 300 nm and a peak transmission of 72 % [Spe09] (see figure 3.15 for the transmission curves of both gratings). The wavelength accuracy of the monochromator is ± 0.30 nm [Spe09]. The slit width can be changed between 10 µm and 3 mm corresponding to a wavelength width of 0.032 nm to 9.6 nm. Both, the wavelength and the slit width, can be changed automatically via software control.
  To focus the light from the fiber into the monochromator and to inject it into the fiber after passing the monochromator again, two matching fiber adapters of the type AFDK240-L-FC [Spe09] are used. These adapters contain UV lenses with transmissions better than 90 %. For better adjustment the adapters provide the opportunity to manually change the X and Y positions by 10 mm and the Z position of the fibers by 5 mm.
- **Fiber outside of second containment:** the fiber used outside of the second containment is a 1.5 m long AVA FC-UV600-1,5-SR-FC from Avantes[21]. It is a solarization resistant 400 µm fiber with transmission of about 95 % after more than 80 hours of irradiation with light at 275 nm [Ava15]. To further improve the transmission properties of the fiber it is pre-irradiated by the manufacturer for 8 hours. The attenuation is given in figure 3.15. At both ends of the fiber FC/PC connectors are fitted.
- **Fiber feed-through:** the fiber feed-through is custom made and manufactured by VACOM[22]. The solarization resistant 400 µm multimode fiber with NA of 0.22 is fitted in a threaded flange which can be screwed to the wall of the second containment. The connector type of the feed-through is FC/PC at both sides. The insertion loss of the fiber feed-through at 850 nm is less than 0.5 dB.
- **Splitter fiber:** the splitter fiber is manufactured by FONT[23]. All used fibers are solarization resistant multimode fibers with 400 µm core diameter. The insertion losses are expected to be less than 0.5 dB. The length of the input arm is 0.5 m. The length of the two output arms is 0.25 m and 0.5 m, respectively. The splitting ratio is 10/90, where 10 % of the intensity is injected into the longer output fiber. The excess losses at the splitter are less than 0.7 dB. At all fiber ends FC/PC connectors are installed.
- **Lenses:** the lenses used to focus the light into the fibers in the primary system are two lenses of the type 48-537 of Edmund Optics[24]. Theses lenses are aspherically shaped, to improve the performance of the focusing system, as light entering the lens at the center and off-axis is refracted to the same focal point. The diameter of the lenses is 25 mm with a clear aperture of 90%. The focal length of the lenses is 27.8 mm at the design wavelength of 275 nm. The transmission curve of the lenses is shown in 3.15. To enable an easy alignment of the lenses and also of the splitter fiber, they are installed in the cage system of Edmund. The splitter fiber and the second lens are both positioned at the focal point of the first lens but at opposite

[20] Spectral Products, 111 Highland Drive, Putnam, CT 06260, USA
[21] Avantes BV, Oude Apeldoornseweg 28, NL-7333 NS Apeldoorn, The Netherlands, Europe
[22] VACOM Vakuum Komponenten & Messtechnik GmbH, Gabelsbergerstraße 9, 07749 Jena, Germany
[23] Fiber Optic Network Technology Co., 2242 - 173 Street, Surrey, British Columbia, V3Z 9Z7 Canada
[24] Edmund Optics, 101 East Gloucester Pike, Barrington, NJ 08007, USA

sides of the lens. The cage system is then mounted to the XYZ translation stage.

- **XYZ translation stage:** the translation stage is used to position the focusing system in a way that its focus is at the end of a certain fiber inside of the primary system. It is of the type PT3/M-Z8 from Thorlabs[25]. The XYZ translation stage is built by stacking 3 PT1/M-Z8 motors, each with a travel range of 25 mm. As the 7 fibers in the primary system are placed in a line of about 8 mm this travel range is more than sufficient. The resolution of one motor is 29 nm[26] with a repeatability of < 1.5 µm. The integrated servo actuator Z825B DC enables the automatic approach of a certain position.
- **Feed-through window:** the feed-through window is of the type VPCF16UVS-L from Vacom. It consists of a sapphire window bonded into a CF16 flange. The transmission curve is shown in figure 3.15.
- **Fibers inside of primary system:** the fibers are #57-074 fibers from Edmund Optics, have a core size of 200 µm and a length of 16.4 cm. The attenuation caused by the length of the fiber is wavelength dependent and is given in figure 3.15.
- **Detector:** the detector used to monitor the stability of the light source and part of the optical components is an AD421 from Spectral Products. It is a silicon detector with a size of 5.8 mm x 5.8 mm and a sensitivity of 0.4 A/W at 720 nm. The dark current of the detector is 20 pA [Spe09].
- **Titanium and gold layer:** the gold layer of the photo cathode is not really a part of the optical setup. Nevertheless, these layers contribute to the losses of the light on its way into the gold by reflection and absorption. Both contributions are discussed in more detail in section 3.2.1.2. The thickness of the titanium layer is 3 nm and the thickness of the gold layer is 37 nm. Both are applied by sputtering performed at UCSB.

As the properties of each optical component are now known, the overall performance of the optical setup can be calculated. The knowledge of this enables the calculation of the e-gun rate. This calculation and its results is presented and discussed in the following subsection.

3.2.1.2 E-gun rate calculations

The calculation of the electron flux has two main parts: the spectral flux $\Phi(\lambda)$ reaching the gold layer of the cathode and the probability $\Gamma(\lambda)$ to produce an electron which leaves the gold layer. By integration of the product of both parts the electron rate Ξ of the e-gun can be calculated

$$\Xi = \int_{-\infty}^{+\infty} \Phi(\lambda) \cdot \Gamma(\lambda)\, d\lambda. \tag{3.1}$$

The spectral flux $\Phi(\lambda)$ can be calculated by multiplying the spectral flux of the light source with all losses at the components of the optical setup:

$$\Phi(\lambda) = F(\lambda) \cdot T_{\mathrm{a}}^2 \cdot T_{\mathrm{m}}(\lambda) \cdot \mathfrak{A}_{\mathrm{f1}}(\lambda) \cdot \mathfrak{A}_{\mathrm{t}}(\lambda) \cdot (A)_{\mathrm{s}}(\lambda) \cdot T_{\mathrm{l}}^2(\lambda) \cdot \mathfrak{L}_{\mathrm{l}}(\lambda) \cdot T_{\mathrm{w}}(\lambda) \cdot \mathfrak{A}_{\mathrm{f2}}(\lambda) \cdot R(\lambda). \tag{3.2}$$

All factors of this equation are explained in the following:

[25] Thorlabs Inc, 56 Sparta Avenue, Newton, New Jersey 07860, USA

[26] The resolution is calculated by the encoder counts per motor revolution and the gear transformation ratio: as there are 512 encoder counts per revolution and the gear transformation ratio is 67:1 the resolution is 1 mm /(512 encoder counts · 67)

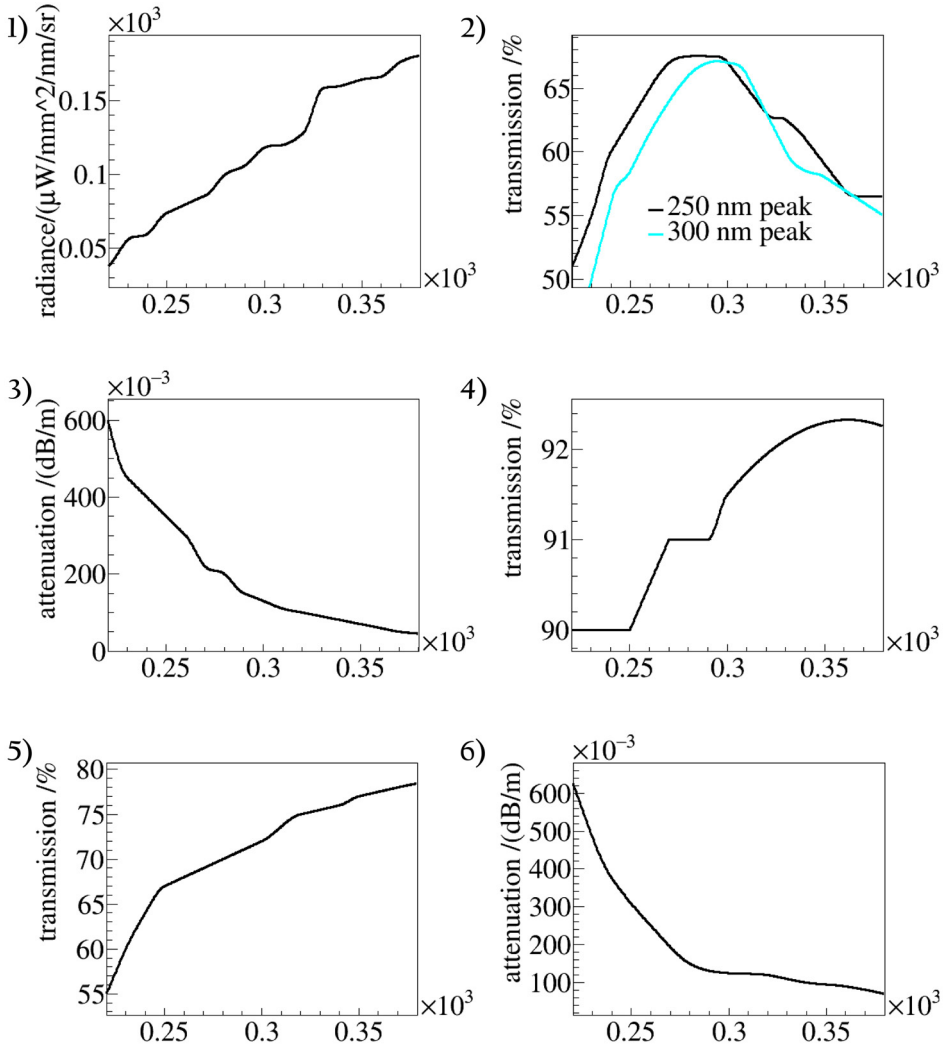

Figure 3.15: Properties of the optical components. The optical properties of the light source, of the two different gratings, of the fiber outside and inside of the primary system, of the lenses and of the feedthrough window are shown. The diagram (1) shows the spectral radiance of the light source, at the position of the fiber end. The graph is interpolated from data points taken from a diagram provided by the manufacturer [Ene14]. In (2) the transmission through the grating AG1200-00250-686 and AG1200-00300-686 are shown (interpolation on data points taken from a transmission plot provided by the manufacturer). (3) shows the attenuation of the fiber outside of the vacuum system. The attenuation is interpolated from data points taken from a diagram provided by the manufacturer. In (4) the transmission curve of the lenses is shown (interpolated from data given by the manufacturer [Tho15b]). Diagramm (5) shows the transmission through the feed-through window interpolated from data points taken from a diagram provided by the manufacturer [MDC15]. In (6) the attenuation of the fiber inside of the primary system can be found. The graph is an interpolation of data points taken from a graph provided by the manufacturer.

- $F(\lambda)$ is the spectral radiance of the light source emitted at the end of the fiber mounted to the light source (compare figure 3.15).
- T_a is the transmission through the lenses of the fiber adapters at the monochromator. The adapters focus the light into the monochromator and after the monochromator into the fiber. The value of T_a is given by the manufacturer as less than 90 % without wavelength dependence.
- $T_\mathrm{m}(\lambda)$ describes the transmission through the monochromator. In principle the transmission curves $T_\mathrm{grating}(\lambda)$ of possible gratings are given in figure 3.15. However, the bandwidth b, dependent on the slit width, must be taken into account to really get the wavelength dependent transmission. Therefore, $T_\mathrm{grating}(\lambda)$ must be multiplied with a Gaussian peak with a mean value λ_peak and the standard deviation

$$\sigma = \frac{\mathrm{FWHM}}{2 \cdot \sqrt{2 \cdot \ln(2)}}, \tag{3.3}$$

  where FWHM is equal to the bandwidth b of the grating. Therefore, $T_\mathrm{m}(\lambda)$ is given by

$$T_\mathrm{m}(\lambda) = T_\mathrm{grating}(\lambda) \cdot \exp\left(-\frac{(\lambda - \lambda_\mathrm{peak})^2}{2 * \left(\frac{b}{2 \cdot \sqrt{2 \cdot \ln(2)}} \right)^2} \right). \tag{3.4}$$

- $\mathfrak{A}_\mathrm{f1}(\lambda)$ describes the losses at the fiber. It is composed of the attenuation over the length of the fiber, $\mathfrak{A}_\mathrm{f1,attenuation}$, the insertion losses when light is injected into the fiber, $\mathfrak{A}_\mathrm{f1,insertion}$, and the losses caused by a bigger fiber diameter at the entrance than at the exit of the monochromator, $\mathfrak{A}_\mathrm{f1,spot}$:

$$\mathfrak{A}_\mathrm{f1}(\lambda) = \mathfrak{A}_\mathrm{f1,attenuation} \cdot \mathfrak{A}_\mathrm{f1,insertion} \cdot \mathfrak{A}_\mathrm{f1,spot}\,. \tag{3.5}$$

  The insertion loss is expected to be 0.5 dB, which is a conservative assumption [Gha98]:

$$\mathfrak{A}_\mathrm{f1,insertion} = \frac{1}{10^{\frac{0.5}{10}}}. \tag{3.6}$$

  The value of att in

$$\mathfrak{A}_\mathrm{f1,attenuation} = \frac{1}{10^{\frac{att \cdot l}{10}}} \tag{3.7}$$

  can be found in figure 3.15 and l is the length of the fiber. As the different fiber radii before and after the monochromator are $r_\mathrm{fiber1} = 0.225\,\mu\mathrm{m}$ and $r_\mathrm{fiber2} = 0.2\,\mu\mathrm{m}$ the losses are given by

$$\mathfrak{A}_\mathrm{f1,spot} = \frac{r^2_\mathrm{fiber2}}{r^2_\mathrm{fiber1}}\,. \tag{3.8}$$

- $\mathfrak{A}_t(\lambda)$ takes into account the insertion losses at the fiber feed-through, namely

$$\mathfrak{A}_\mathrm{t,insertion} = \frac{1}{10^{\frac{0.5}{10}}} \tag{3.9}$$

  or 0.5 dB, and the attenuation over the length of the fiber, which is 5 cm:

$$\mathfrak{A}_\mathrm{t}(\lambda) = \mathfrak{A}_\mathrm{t,attenuation} \cdot \mathfrak{A}_\mathrm{t,insertion}. \tag{3.10}$$

- $\mathfrak{A}_\mathrm{s}(\lambda)$ describes the losses at the splitter and its fiber. Therefore, it is the product of the insertion loss, $\mathfrak{A}_\mathrm{s,fiberins}$, the attenuation over the length of the fiber, $\mathfrak{A}_\mathrm{s,fiberatt}$,

and the losses caused by splitting the light $\mathfrak{A}_{\mathrm{s,ratio}}$ itself and losses due to the splitting $\mathfrak{A}_{\mathrm{s,losses}}$:

$$\mathfrak{A}_{\mathrm{s}}(\lambda) = \mathfrak{A}_{\mathrm{s,fiberatt}} \cdot \mathfrak{A}_{\mathrm{s,fiberins}} \cdot \mathfrak{A}_{\mathrm{s,ratio}} \cdot \mathfrak{A}_{\mathrm{s,losses}}. \tag{3.11}$$

The insertion loss is expected to be 0.5 dB:

$$\mathfrak{A}_{\mathrm{s,fiberins}} = \frac{1}{10^{\frac{0.5}{10}}}. \tag{3.12}$$

The splitting ratio at the splitter is 90:10, meaning

$$\mathfrak{A}_{s,ratio} = 90\,\%, \tag{3.13}$$

and the losses directly at the splitter are less than 1 dB or

$$\mathfrak{A}_{\mathrm{s,losses}} = \frac{1}{10^{\frac{1}{10}}} \tag{3.14}$$

according to the manufacturer.

- $T_{\mathrm{l}}(\lambda)$ is the transmission through the lenses at a certain wavelength (see figure 3.15).
- $\mathfrak{L}_{\mathrm{l}}$ takes into account all losses due to geometrical optics considerations occuring at the two lenses which are focusing the light into the primary system (compare also figure 3.16):

$$\mathfrak{L}_{\mathrm{l}} = \mathfrak{L}_{\mathrm{lens1}} \cdot \mathfrak{L}_{\mathrm{lens2}} \cdot \mathfrak{L}_{\mathrm{NA}} \cdot \mathfrak{L}_{\mathrm{spot}}. \tag{3.15}$$

The first place losses is at the first lens, if the radius of the divergent light cone from the fiber end r_1 is larger than the diameter of the clear aperture of the lens r_{ca}. This loss is described by

$$\mathfrak{L}_{\mathrm{lens1}} = \Theta(r_1 - r_{\mathrm{ca}}) \cdot \frac{r_{\mathrm{ca}}^2}{r_1^2} + \Theta(r_{\mathrm{ca}} - r_1), \tag{3.16}$$

where $\Theta(x)$ is the Heaviside step function. The losses at the second lens are similarly caused if the radius of the light cone after the first lens r_2 is larger than the radius of the clear aperture of the second lens:

$$\mathfrak{L}_{\mathrm{lens2}} = \Theta(r_2 - r_{\mathrm{ca}}) \cdot \frac{r_{\mathrm{ca}}^2}{r_2^2} + \Theta(r_{\mathrm{ca}} - r_2). \tag{3.17}$$

During the insertion of the light into the fiber there are two possible reasons for losses: first an angle that is too large compared to the acceptance angle [Gha98] of the fiber. This loss is described by the formula

$$\mathfrak{L}_{\mathrm{NA}} = \Theta(\sin(\vartheta) - NA_{\mathrm{fiber}}) \cdot \frac{\left(\tan(\arcsin(NA_{\mathrm{fiber}}))x_{\mathrm{lens-fiber}}\right)^2}{\left(\tan(\vartheta)x_{\mathrm{lens-fiber}}\right)^2} + \Theta(NA_{\mathrm{fiber}} - \sin(\vartheta)), \tag{3.18}$$

where NA_{fiber} is 0.22, $x_{\mathrm{lens-fiber}}$ is the distance from the second lens to the end of the fibers inside of the primary system and ϑ is the angle of the light on its path from the second lens to the fiber. Second, a spot diameter that is too large at the position of the fibers inside of the primary system causes losses. The combination of both losses can be calculated by

$$\mathfrak{L}_{\mathrm{spot}} = \Theta(r_3 - r_{\mathrm{fiber3}}) \cdot \frac{r_{\mathrm{fiber3}}^2}{r_3^2} + \Theta(r_{\mathrm{fiber3}} - r_3), \tag{3.19}$$

with $r_{\text{fiber3}} = 0.2\,\mu\text{m}$ and $r_3 = \frac{f_2}{f_1} r_{\text{fiber2}}$ being the radius of the light cone at the position of the fibers.
For all these losses at the focusing system it is important to keep in mind that the design wavelength of the lens system is 275 nm. That means that the position of the fiber end inside of the second containment and the distance between the two lenses is optimized for this wavelength. The efficiency of the light injection into the fiber is not affected by a wavelength change, as the distance between the fiber and lens can be changed with the XYZ translation stage. The overall losses at the focusing lenses are 56.9 % mainly dominated by the fact that the light spot at the position of the fiber inside of the primary system is at least 400 nm since the magnification of two lenses with the same focal length is 1.

- $T_{\text{w}}(\lambda)$ describes the losses due to absorption and reflection at the feed-through window. The remaining transmission can be found in figure 3.15.
- $\mathfrak{A}_{\text{f2}}(\lambda)$ takes into account the losses at the fiber inside of the primary system due to attenuation and insertion losses:

$$\mathfrak{A}_{\text{f2}}(\lambda) = \mathfrak{A}_{\text{f2,fiberatt}} \cdot \mathfrak{A}_{\text{f2,fiberins}}. \tag{3.20}$$

  The insertion losses are conservatively expected to be 0.5 dB or

$$\mathfrak{A}_{\text{f2,fiberins}} = \frac{1}{10^{\frac{0.5}{10}}} \tag{3.21}$$

  and the attenuation can be found in figure 3.15.
- $R(\lambda)$ are the losses due to reflection at the sputtered titanium and gold layer:

$$R(\lambda) = (1 - R_{\text{Au}}) \cdot (1 - R_{\text{Ti}}). \tag{3.22}$$

The second factor of equation (B.3), $\Gamma(\lambda)$, describes the processes inside of the gold layer (compare [Jia98b])

$$\begin{aligned} \Gamma(\lambda) =& P_{\text{QY,Ti}}(\lambda, E_{\text{WF}}) \cdot \frac{\int_0^{x_{\text{Ti}}} I(x,\lambda) P_{\text{S}}(x,\lambda)\, dx}{x_{\text{Ti}}} \\ &+ P_{\text{QY,Au}}(\lambda, E_{\text{WF}}) \cdot \frac{\int_{x_{\text{Ti}}}^{x_{\text{Au}}} I(x,\lambda) \cdot P_{\text{S}}(x,\lambda)\, dx}{x_{\text{Au}}}, \end{aligned} \tag{3.23}$$

namely the probability to produce an electron $P_{\text{QY}}(\lambda, E_{\text{WF}})$, which is also-called the quantum yield, the absorption inside of the titanium and gold layer $I(x,\lambda)$ and the probability $P_{\text{S}}(x,\lambda)$ that an electron produced at position x in the layers reaches the surface and escapes there. The reason why both integrals are divided by the distances x_{Au} and x_{Ti}, is to arrive at a mean probability that a produced electron leaves the cathode.

The probability that an electron escapes out of the layers is equal to the probability that the electron does not scatter on its way to the surface [Jia98b]. This probabiltiy can be calculated by[27]

$$\begin{aligned} P_{\text{S}}(x,\lambda) &= \frac{(l-(t-x))^2 \cdot (3 \cdot l - (l-(t-x))}{4 \cdot l^3} && \text{if } t - x < l \\ P_{\text{S}}(x,\lambda) &= 0 && \text{if } t - x > l \end{aligned} \tag{3.24}$$

[27] The points reachable by the isotropically emitted electron are all within a sphere defined by the free mean path l which is the radius of this sphere. To derive equation (3.24) the volume of the spherical segment outside of the gold layer is divided by the overall volume. This is performed at each position x in the gold layer.

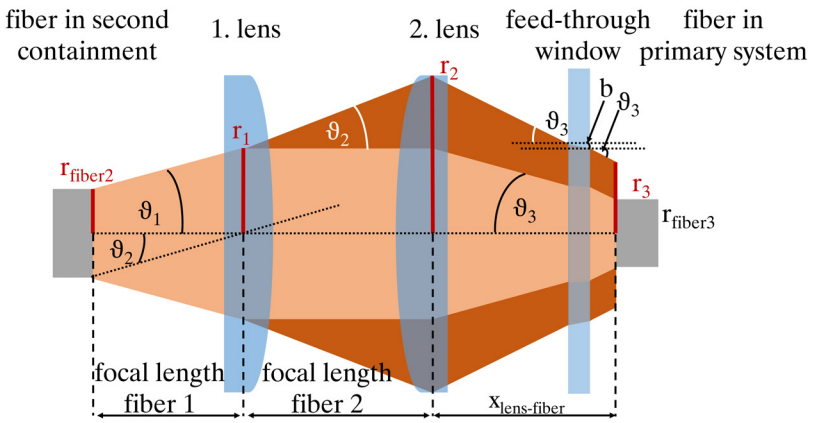

Figure 3.16: Geometry at the focusing lens system. The light ejected by the fiber positioned at the focal point of the first lens is propagating towards the first lens with a half angle of ϑ_1. Here the light is collimated. The half opening angle ϑ_2 of the light cone after the collimation is dependent on the radius of the fiber and the distance to the lens. The second lens is placed in a way that the focal point of the second lens is at the position of the first lens. In so doing the smallest spot size of the light cone after the second lens is at the focal point of the second fiber. As the light must pass the feed-through window as well, it is diffracted on its way to the fiber twice: first it is refracted towards, then off the horizontal line.

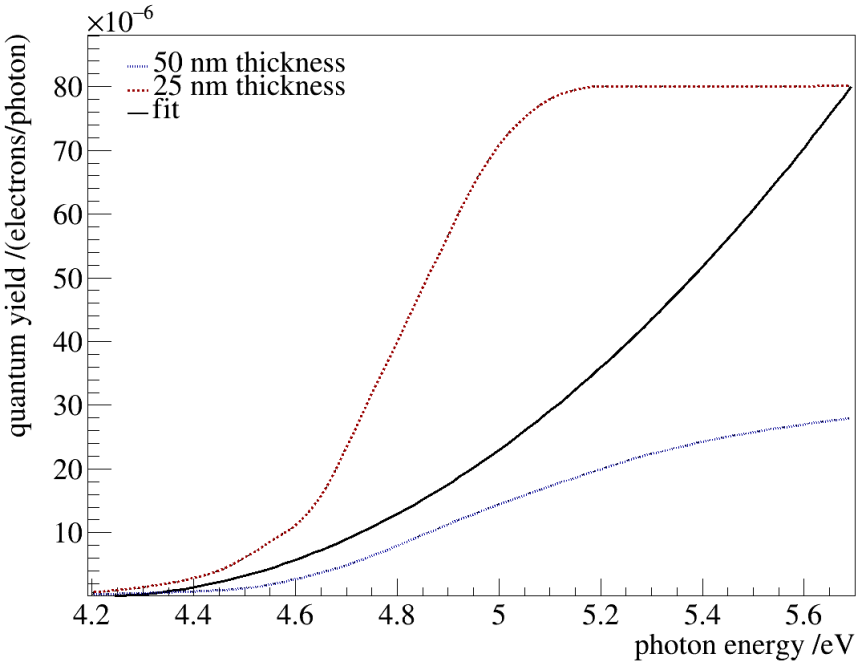

Figure 3.17: Quantum yield calculation by using experimental data. The calculated quantum yield of gold (black line) interpolated from data given by [Jia98b] for 25 nm (red dotted line) and 50 nm gold thickness (blue dotted line) is shown.

where l is the free mean path of an electron in the material, t is the thickness of the material and x is the position in the material at which the electron is produced. The energy dependent free mean path for gold and titanium can be found in [Sea79], which is

$$l_{\mathrm{Au}} = \frac{177}{E^2} + 0.054\sqrt{E} \tag{3.25}$$

in case of gold and

$$l_{\mathrm{Ti}} = \frac{143}{E^2} + 0.054\sqrt{E} \tag{3.26}$$

in case of titanium. That means, that the free mean path in titanium is shorter than the distance to the surface of the gold layer. Therefore, the first term in equation (3.23) vanishes.

The light absorption in the different layers is calculated by

$$I(x, \lambda) = \mathrm{e}^{(-\alpha(\lambda)\cdot x)}, \tag{3.27}$$

where $\alpha(\lambda)$ is the wavelength dependent absorption coefficient of the material. For the calculation this absorption coefficient is interpolated from data given by [Bab15] in case of gold. Both the light absorption and the probability of reaching the surface as well as their product is shown in figure 3.18.

The gold quantum yield is derived from data of Jiang et al. given in [Jia98b]. Jiang has determined the quantum efficiency P_{QY} of gold layers with different thickness if light is transmitting through the gold layer deposited on sapphire. The measured data is describable by

$$P_{\mathrm{QY}} = C(\lambda, \Phi)(\lambda, E_{\mathrm{WF}}) \cdot (1 - R_1(\lambda)) \cdot (1 - R_2(\lambda)) \cdot \left(\mathrm{e}^{(-x/l)} - \mathrm{e}^{(-\alpha\cdot x)}\right) \cdot (1 - 1/(\alpha \cdot l))^{-1}, \tag{3.28}$$

where $R_1(\lambda)$ and $R_2(\lambda)$ is the reflection at the air sapphire or the sapphire gold junction, α is the absorption coefficient in gold[28], l is the free mean path and $C(\lambda, \Phi)$ is the bulk quantum efficiency. As in [Jia98b] the measured gold layer thicknesses are 25 nm and 50 nm, but the thickness of the gold layer of the e-gun cathode is 37 nm, an interpolation between these two data sets must be performed. For this interpolation the fact is used that the quantum yield of gold can be described by

$$P_{\mathrm{QY}}(\lambda, E_{\mathrm{WF}}) = a \cdot (\lambda - b)^2, \tag{3.29}$$

as stated in [Mon91]. In this fit function a is a proportional constant and b is the work function of the material. In doing so, the available data sets are interpolated.

By using these equations the expected e-gun rate can be calculated. Unfortunately the work function of the cathode's gold layer is unknown, although the work function of gold exposed to ambient air is usually expected to be between 4.0 eV and 4.2 eV [Jia98b]. The work function could be roughly determined by a comparison of the electron rates achieved at the e-gun test setup at UCSB and the electron rate calculations for the optical setup used at this setup. But this comparison does not produce explicit results as no dedicated measurement runs are performed for that purpose (compare appendix B.2, page 213). That is why the results of the calculations are always dependent not only on the slit width and the peak wavelength set at the monochromator, but also on the gold work

[28] The absorption in the sapphire is neglected

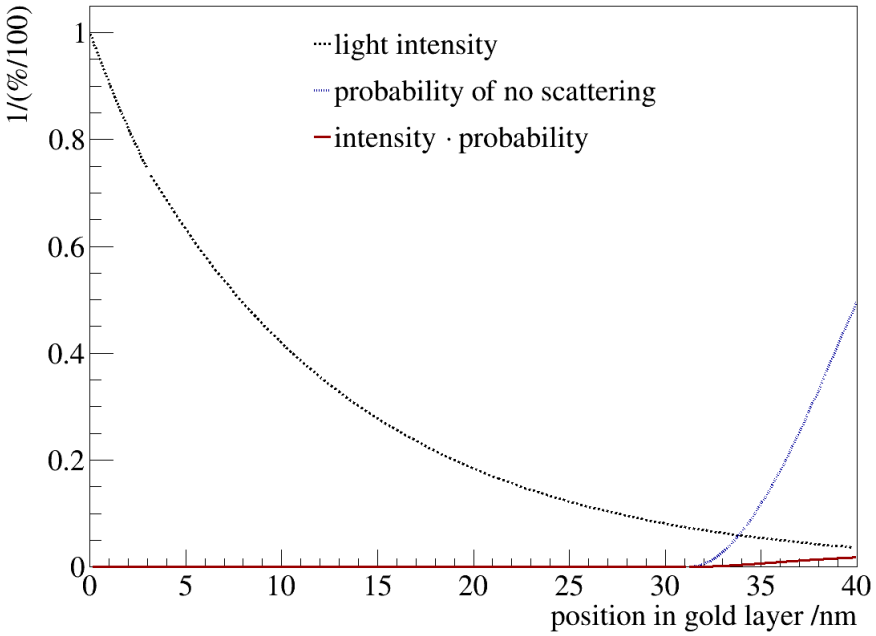

Figure 3.18: Plots of the light absorption as well as the quantum yield and the escape probability of electrons in the e-gun gold layer. The black dotted lines show the light absorption. In the range from 0 nm to 3 nm the absorbing material is titanium and between 3 nm and 40 nm it is gold. The light absorption lines show a continuous behavior without step but with a small kink at 3 nm as the light is continuously absorbed but with different absorption coefficients. The probability of no scattering is plotted by the blue dotted line. The curve is dependent on the free mean path in the specific material and the position in the material. If the distance to the surface is larger than the free mean path, the escape probability is 0. The red line is the product of the light intensity and the probability of no scattering.

function. Plots to visualize the dependence of the electron rate on these parameters can be found in figure 3.19.

If a gold work function of 4.2 eV and the design wavelength of 275 nm is assumed the required electron rate of at least $10^4\,\mathrm{s}^{-1}$ can be achieved even with a slit width of 0.05 mm. This slit width results in an energy distribution with $\sigma_\mathrm{E} \approx 0.0011\,\mathrm{eV}$, which is far below the required value of $\sigma_\mathrm{E} \leq 0.2\,\mathrm{eV}$. For the same work function and wavelength the electron rate at the maximum slit width of 3 mm is $7.26{\cdot}10^5\,\mathrm{s}^{-1}$. This maximum slit width results in $\sigma_\mathrm{E} \approx 0.07\,\mathrm{eV}$ which is still below the required value. If necessary the wavelength can be changed between 220 nm, the smallest wavelength which is included in this calculation, and 300 nm at maximum slit width.

Nevertheless, it must be taken into account, that there are some factors that can cause the electron rate to be smaller than calculated here:

- Neglect of Gaussian beam properties: as the calculation of the optical beam path is based on geometrical optics, bigger waste caused by the Gaussian profile of the beam is not taken into account. Especially at the fiber injections this can cause bigger losses than expected.
- Work function distribution of the cathode: for the calculation a sharp edge is assumed and if the energy of the incoming photon is larger than this edge an electron

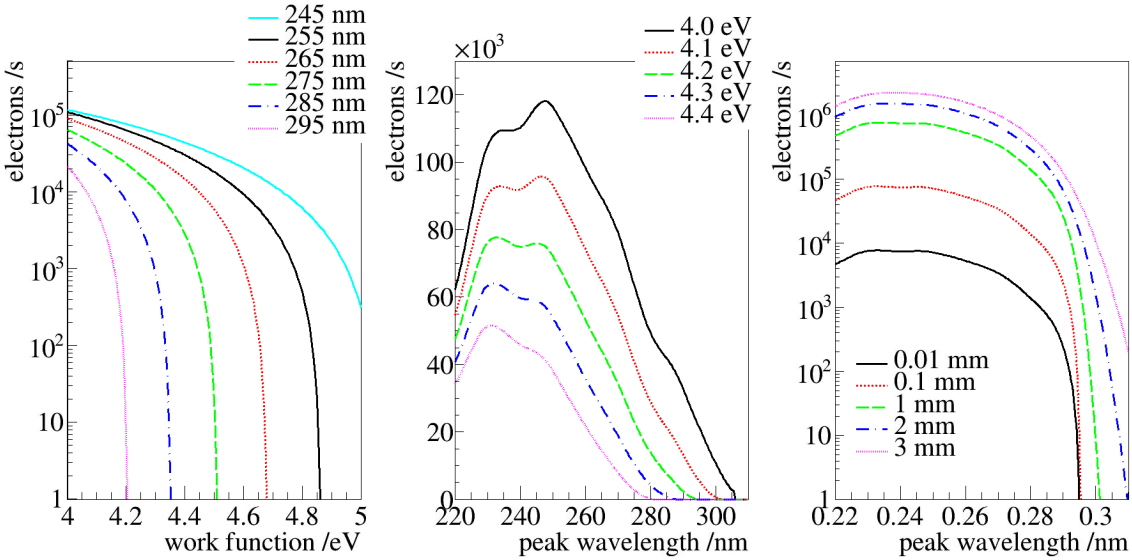

Figure 3.19: Calculated e-gun rates dependent on the peak wavelength set on the monochromator, the gold work function and the slit width. Left: here the dependence of the electron rate on the work function of the gold cathode is shown for 6 different peak wavelengths from 295 nm to 245 nm and a slit width of 0.1 mm. As expected the rate vanishes if the energy of the photon does not exceed the work function of the material. Middle: the electron rate is plotted for different gold work functions from 4.0 eV to 4.4 eV and a slit width of 0.1 mm against the peak wavelength, set at the monochromator. As expected the electron rate first increases with decreasing peak wavelength, but after a certain wavelength the rate starts to decrease again (see chapter 4 for more details). The maximum of the rate is wavelength dependent. Right: in this plot the dependence of the electron rate on the slit width of the monochromator is shown for a gold work function of 4.2 eV. A change of the slit width from its minimum to its maximum can change the electron rate by more than 2 orders of magnitude. If the work function of the gold cathode is 4.2 eV the maximum possible rate achievable with the optical setup described is $2.27 \cdot 10^6\ s^{-1}$ at 238 nm.

is produced. But in reality the edge usually has a certain width which can affect the calculations, especially close to the edge.

- Less than perfect aligned optics: in the calculation all the optical components are placed exactly at the perfect position and therefore the maximum possible intensity is transported to the cathode. In reality the alignment of the optics might not be that perfect. Therefore, it is very likely, that the intensity of the light is less than the calculated one.
- Solarization of the optical components: due to the irradiation of all optics with UV light the transmission of these optics could decrease. This is a commonly known effect especially for fused silica, the material most of the optical components are made of. Solarization is worst for wavelengths close to 214 nm and getting weaker for longer wavelengths. Therefore, the effect at the design wavelength of 275 nm is already reduced. In addition, all components are chosen in a way to further reduce the solarization losses. For example, the solarization losses of the fiber connecting the monochromator and the second containment are about 5 % at 275 nm according to the manufacturer. For more details on solarization see section 3.2.3.2.
- Volume effects of the photo effect: the calculated rate has a maximum at wavelengths of about 230 nm to 250 nm dependent on the work function of the material. But in contrast to the expectation, based on [Fre31, May57, Tho57] and measure-

ments presented in section 4.6, the rate is not decreasing enough towards lower wavelengths. This is probably caused by an insufficient consideration of volume effects. These volume effects are described in more detail in section 4.6.

These factors can reduce the measured electron rate at the final setup further. But the comparison of the calculations with the data at the test setup (compare appendix B.2) has shown, that the rate is underestimated by about a factor of 3 to 9 for most wavelengths at the estimated work function of 4.2 eV. This underestimation could be caused by the conservative estimates during the calculation. In addition σ_E is expected to be larger than calculated: the calculation only includes the distribution of the wavelength but not the distribution of the gold work function. However, the result of the presented calculations is, that the electron rate produced with the described setup can meet the KATRIN requirement.

3.2.2 Fibertest I: examination of tritium leak tightness of fiber feed-throughs

To inject the light from the optical setup of the Rear Section electron gun (which is outside of the second containment) into a fiber (which is inside of the second containment) a fiber feed-through is planned to be used. However, a fiber feed-through that does not meet the requirements on leaktightness standardized by the TLK (which is 10^{-9} mbar·l/s for single connections [TLK13]) cannot be used for safety reasons. Therefore the Fibertest I is performed which aims to determine if a fiber feed-through is leak-tight concerning tritium.

At first an estimation of the expected leak rate based on the available literature is given in the next section. It briefly introduces permeation theory and then goes on to calculate the permeation rates for tritium through silicondioxide (SiO_2), which is the material the fiber is made of, as well as epoxy, which is used to glue the fiber to the feed-through. Then the experimental setup, the measurements and the results of the Fibertest I are presented.

3.2.2.1 Literature based estimate of tritium leak rate through fiber feed-throughs

The permeation process of a gas through a homogeneous solid can be divided into three main parts [Hum98] (see also figure 3.20):

1. Dissolution of the gas at the high partial pressure side of the solid into the solid
2. Diffusion of the gas through the solid
3. Dissolution of the gas at the low partial pressure side of the solid into the gas phase.

The permeation process is driven by the concentration gradient measured normal to the cross section of the solid. In case of solution in polymers or glasses the saturation value of the gas concentration at the surfaces is directly proportional to the pressure [Nor57]. The gas concentration C is then given by Henry's Law [Ste83, Rog54]

$$C = p \cdot S, \tag{3.30}$$

where p is the partial pressure of the gas and S is the solubility of the gas in the solid. Both, solubility S and diffusivity D, are correlated with temperature by an Arrhenius

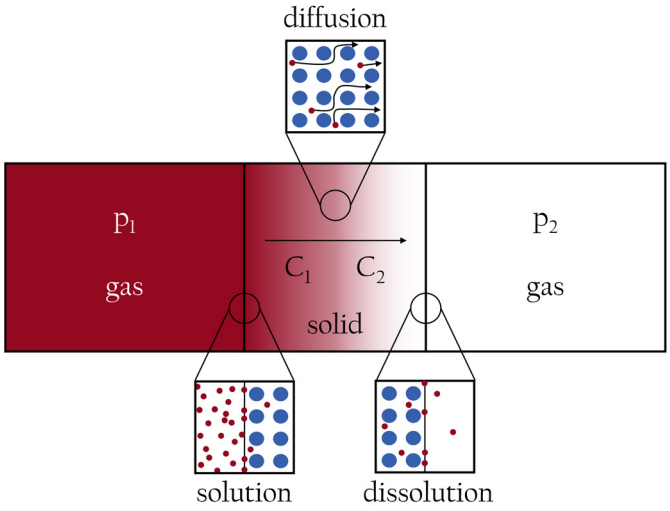

Figure 3.20: Schematic diagram illustrating the main steps of permeation. At the left side there is a high partial pressure p_1 of a gas, on the right side the partial pressure p_2 of the same gas is lower. Because of this, there is a gradient of concentration in the solid which is in the center between the two gases. Due to this gradient, the gas is solved at the left side of the solid, diffuses through the solid and is dissolved at right side of the solid (own figure in accord with [Sch08]).

equation [Hum98, Lee62]:

$$S = S_0 \cdot \exp\left(-\frac{E_s}{R \cdot T}\right) \tag{3.31}$$

$$D = D_0 \cdot \exp\left(-\frac{E_d}{R \cdot T}\right), \tag{3.32}$$

where S_0 and D_0 are coefficients, E_d and E_s are activation energies, $R = 8.314 \cdot 0.239 \frac{\text{cal}}{\text{mol K}}$ [Moh15] is the gas constant and T is the temperature.

As the dissolution process is much faster than the diffusion process, it is assumed that the concentration at the high partial pressure side is achieved immediately after the exposure to gas. The relation of the temporal and spatial change of the concentration during the diffusion process in one direction is given by Fick's second law [Bar41]:

$$\frac{\partial C}{\partial t} = D\frac{\partial^2 C}{\partial x^2} \ . \tag{3.33}$$

The general solution to this partial differential equation in case of permeation through a finite solid of length l is [Cra75]:

$$C = C_1 + (C_2 - C_1)\frac{x}{l} + \frac{2}{\pi}\sum_{n=1}^{\infty}\frac{C_2 cos(n\pi) - C_1}{n}\sin\left(\frac{n\pi x}{l}\right)\exp\left(-\frac{Dn^2\pi^2 t}{l^2}\right) \tag{3.34}$$
$$+ \frac{4C_0}{\pi}\sum_{m=1}^{\infty}\frac{1}{(2m+1)}\sin\frac{(2m+1)\pi x}{l}\exp\left(-\frac{D(2m+1)^2\pi^2 t}{l^2}\right).$$

In case of the feed-through with length l and no inner starting concentration C_0 which divides the inside of the second containment with tritium partial pressure p_1 and the

outside with $p_2 = 0\,\text{mbar}$, the following boundary conditions

$$C = C_0 = 0 \qquad \text{at } t = 0, \text{ and } 0 \leq x \leq l \tag{3.35a}$$
$$C(x = 0) = C_1 = p_1 \cdot S \qquad \text{at } t = 0, \tag{3.35b}$$
$$C(x = l) = C_2 = p_2 \cdot S = 0 \text{ at } t = 0, \tag{3.35c}$$
$$C = C(x) \qquad \text{for all } t > 0 \text{ and } 0 \leq x \leq l \tag{3.35d}$$

can be used to simplify formula 3.34 to [Bar41]

$$C = C_1 \left(1 - \frac{x}{l}\right) + \frac{2}{\pi} \sum_{n=1}^{\infty} \frac{-C_1}{n} \sin\left(\frac{n\pi x}{l}\right) \exp\left(-\frac{Dn^2\pi^2 t}{l^2}\right). \tag{3.36}$$

There are two helpful approximations for this formula, a short-term approximation and a long-term approximation. In case of the short-term approximation it is estimated that the concentration of the gas at the low partial pressure side has not yet significantly changed. Therefore, the finite solid can be approximated by a semi-infinite one (extending from $x = 0$ to $x \to \infty$). The solution of the diffusion equation is then given by [Cra75]

$$C(x,t) = C_1 \left(1 - \frac{2}{\sqrt{\pi}} \cdot \int_0^{x/2\sqrt{D\cdot t}} \cdot e^{-y^2}\,\mathrm{d}y\right) = C_1 \cdot (1 - \text{erf}(y)), \tag{3.37}$$

where $y = \frac{x'-x}{2\cdot\sqrt{D\cdot t}}$ and erf(y) is the Gaussian integral. This approximation can be used as long as the concentration at position $x = l$ is small. This is assumed to be the case as long as the concentration $C(x = l, t)$ is smaller than 1 % of C_1 [Cra75],

$$1 - \text{erf}\left(\frac{l}{2\sqrt{D \cdot t}}\right) \leq 0.01, \tag{3.38}$$

which is the case as long as

$$\Rightarrow t \leq \frac{l^2}{(2 \cdot \text{erf}^{-1}(0.99))^2 \cdot D}. \tag{3.39}$$

This also means that equation (3.39) gives an estimate of the time needed to get a non-negligible tritium concentration at the low partial pressure side of the fiber feed-through.

The long-term approximation is used to calculate the partial pressure at the low pressure side and the leak rate L through the material. In general the pressure change at the low partial pressure side is given by [Rog54]

$$\frac{dp}{dt} = \frac{A \cdot D \cdot S}{V \cdot l} \cdot p_1 \left(1 + \sum_{m=1}^{\infty} 2 \cdot \cos(\pi \cdot m) \exp\left(\frac{-m^2 \cdot \pi^2 \cdot D \cdot t}{l^2}\right)\right), \tag{3.40}$$

where V is the volume of the low pressure side and A is the surface area exposed to the gas. After a sufficiently long time the linear part of this equation is getting dominant and the exponential part can be neglected. In that case equation (3.40) becomes

$$\frac{dp}{dt} = \frac{A \cdot D \cdot S}{V \cdot l} \cdot p_1. \tag{3.41}$$

By multiplying this equation with V one gets the long-term approximation of the leak rate

$$L = \frac{dp}{dt} \cdot V = \frac{A \cdot D \cdot S}{l} \cdot p_1. \tag{3.42}$$

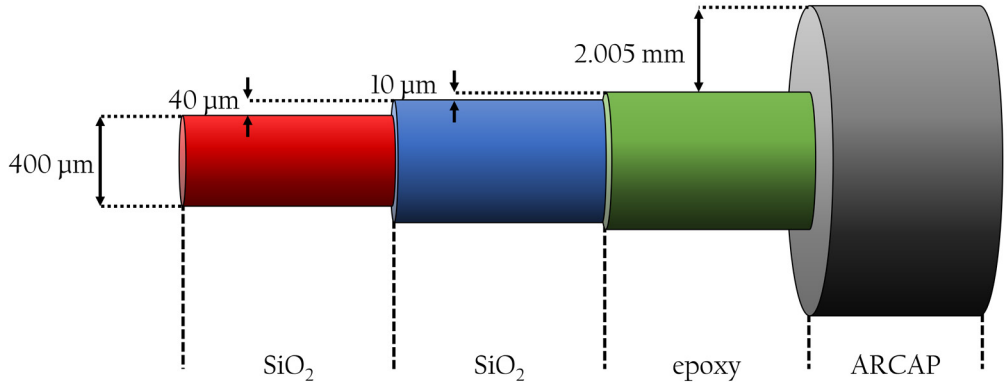

Figure 3.21: Schematic of the composition of a fiber feed-through. The inner core with a diameter of 400 µm consists of fused silica. Proximate to the core is the 40 µm thick cladding which also consists of fused silica but differently doped. To glue the silica parts of the feed-through in the surrounding jacket consisting of ARCAP (a non-magnetic copper alloy with high corrosion resistance) a layer of about 10 µm of epoxy is used.

By integrating the pressure at the low partial pressure side can be found to be

$$p = \frac{A \cdot D \cdot S}{V \cdot l} \cdot p_1(t - t_c), \tag{3.43}$$

where $t_c = \frac{l^2}{6 \cdot D}$ is the time needed to get a constant flow through the material.

The materials of interest in the case of a fiber feed-through are SiO_2 and epoxy resin (compare figure 3.21) both with $l = 4.1\,\text{cm}$. The copper alloy housing material ARCAP and the stainless steel flange are known to meet the requirements on leak tightness and are therefore not discussed further. In order to calculate the permeation and especially the diffusion length at a certain time the coefficients D_0 and S_0 as well as the activation energies E_d and E_s of tritium in the permeated material have to be known. Unfortunately, in case of tritium these values cannot be found in the literature directly, but in principle it should be possible to approximately calculate them by using the values of hydrogen and deuterium: the permeation and diffusion coefficient are inversely proportional to the square root of the mass of the permeating or diffusing hydrogen isotope [Mar07]:

$$\frac{D_H}{D_T} = \sqrt{\frac{m_T}{m_H}} \text{ bzw. } \frac{D_D}{D_T} = \sqrt{\frac{m_D}{m_H}}. \tag{3.44}$$

This implies that solubility is independent of the mass of the solved isotope[29]. In table 3.4 some literature values for D_0, E_d, S_0 and E_s for both SiO_2 and epoxy resin are given.

In the following the worst case scenario[30] is calculated to ensure the highest level of safety.

[29] The permeability K is defined as the product of solubility S and diffusivity D: $K = D \cdot S$.
[30] Worst case means the highest possible diffusivity and solubility at 300 K.

Table 3.4: Values of the diffusivity and solubility parameters D_0, E_d, S_0 and E_s in case of SiO_2 and diffusivity and solubility itself in case of epoxy resin. Additionally, the reference source and the temperature range in which the values were measured are given. *: in reference [Hum97] the parameters D_0, E_d, S_0 and E_s itself are not given. $^+$: in [Hum97] solubility is stated without unit and the given value is $4.4 \cdot 10^{-2}$. As described in [Rog54] a unitless solubility means cm^3 of gas/($cm^3 \cdot$ atm). By assuming STP conditions and using the ideal gas law[Cla34] the number of molecules per cm^3 can be calculated and by so doing the unitless solubility can be converted to the unit $\frac{\text{molecules}}{\text{cm}^3\text{atm}}$.

gas/solid	D_0 in $\frac{\text{cm}^2}{\text{s}}$	E_d in $\frac{\text{kcal}}{\text{mol}}$	S_0 in $\frac{\text{molecules}}{\text{cm}^3\text{atm}}$	E_s in in $\frac{\text{kcal}}{\text{mol}}$	T in °C	source
H_2/fused quartz	$5.65 \cdot 10^{-4}$	10.37	$8.01 \cdot 10^{16}$	-1.49	300-1000	[Lee62]
D_2/fused quartz	$5.01 \cdot 10^{-4}$	10.52	$7.76 \cdot 10^{16}$	-1.47	300-1000	[Lee62]
H_2/vitreous silica	$5.65 \cdot 10^{-4}$	10.37	$8.0 \cdot 10^{16}$	-1.48	300-1000	[Lee63]
H_2/vitreous silica	$5.65 \cdot 10^{-4}$	10.40	$9.4 \cdot 10^{16}$	-1.36	300-1000	[Lee63]
H_2/vitreous silica	$3.07 \cdot 10^{-4}$	9.68	$4.9 \cdot 10^{16}$	-2.46	45- 90	[Swa02]
H(atomic)/SiO_2	$1 \cdot 10^{-4}$	4.15	-	-	-	[Gri85]
H_2/epoxy resin*	$D^* = 3.2 \cdot 10^{-7} \frac{\text{cm}^2}{\text{s}}$		$S^{*+} = 1.18 \cdot 10^{18} \frac{\text{molecules}}{\text{cm}^3\text{atm}}$		20	[Hum97]

Therefore, diffusivity and solubility are set to the following values:

$$D_{\text{silica}} = \sqrt{\frac{m_H}{m_T}} \cdot D_{\text{H,silica}} = \sqrt{\frac{1}{3}} \cdot 5.65 \cdot 10^{-4} \cdot \exp\left(\frac{-10.40 \cdot 10^3}{R \cdot T}\right) \frac{\text{cm}^2}{\text{s}} \tag{3.45a}$$

$$S_{\text{silica}} = 9.4 \cdot 10^{16} \cdot \exp\left(\frac{1.36 \cdot 10^3}{R \cdot T}\right) \frac{\text{molecules}}{\text{cm}^3\text{atm}} \tag{3.45b}$$

$$D_{\text{epoxy}} = \sqrt{\frac{m_H}{m_T}} \cdot D_{\text{H}_2\text{,epoxy}} = \sqrt{\frac{1}{3}} \cdot \ 3.2 \cdot 10^{-7} \frac{\text{cm}^2}{\text{s}} \tag{3.45c}$$

$$S_{\text{epoxy}} = 1.18 \cdot 10^{18} \frac{\text{molecules}}{\text{cm}^3\text{atm}} \tag{3.45d}$$

With these values the permeation through the two materials can be calculated by solving equation (3.36) both at the Rear Section electron gun and at the Fibertest I using MuPAD[31]. For the first case, the electron gun, pressures[32] of $p_1 = 10^{-8}$ mbar and $p_2 = 0$ mbar and a fiber length of 4.1 cm is used. The results for permeation through SiO_2 and epoxy resin at different time steps are shown in figure 3.22.

In the diagram showing the permeation in SiO_2 one can see that the penetration depth even after 5 years is well below the 4.1 cm length of the fiber feed-through. Therefore, no permeation through this part of the feed-through is to be expected. Nevertheless, the calculations of the permeation through the epoxy resin does not look anything like the permeation through the SiO_2. After 1 year of exposure already, the concentration close to the low partial pressure end of the feed-through is only 1 order of magnitude lower than at the high partial pressure side. The reason that the concentration at 4.1 cm vanishes is the

[31] Multi Processing Algebra Data Tool developed by SciFace Software GmbH & Co. KG, Paderborn

[32] $p_1 \approx 10^{-8}$ mbar is the pressure expected in the Rear Section primary system at the position of the electron gun. Since usage of the fiber feed-through was initially also considered directly at the primary system, all calculations and experimental tests are performed in a way that an approval of the fiber feed-through for the primary system is possible. As the fiber feed-through is now only planned at the second containment the $p_1 \approx 10^{-8}$ mbar is used as a very conservative way of calculating the expected leak rate.

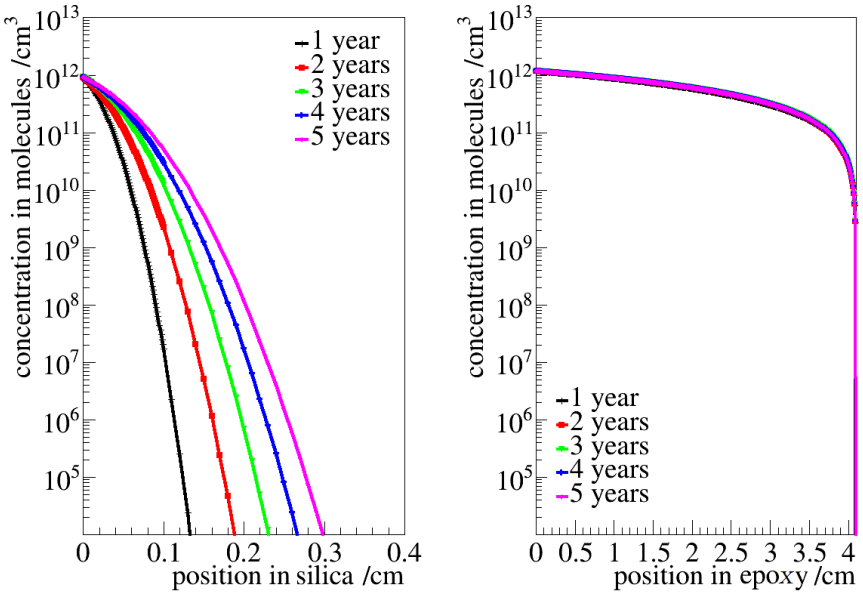

Figure 3.22: Permeation through SiO_2 and epoxy resin dependent on the position inside the permeated material under KATRIN conditions. Both diagrams show 5 graphs, each at another point in time after exposing the material to tritium. On the left diagram the permeation through SiO_2 and on the right side through epoxy resin after 1 to 5 years of exposure time are shown.

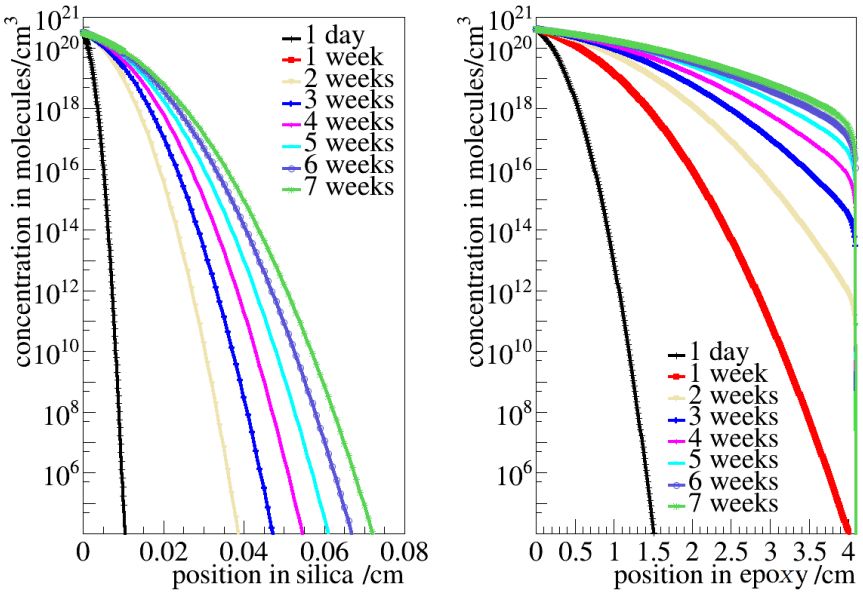

Figure 3.23: Permeation through SiO_2 and epoxy resin dependent on the position inside the permeated material under Fibertest I conditions. In the left diagram the permeation through SiO_2 and on the right side through epoxy resin after 1 day to 7 weeks of exposure time are shown.

boundary condition defined in equation (3.35c). The condition defines the concentration at the low partial pressure side as 0 at any time. By using equation (3.39) the time t when the concentration at the low partial pressure side is higher than 1 % of C_1 can be calculated as

$$t \lesssim 42.5\,\text{days}. \tag{3.46}$$

The expected leak rate through the fiber and the surrounding epoxy can be calculated by using the long-term approximation assuming a steady state inside of the fiber and the epoxy (see 3.41). It can be calculated by

$$L = \frac{dp}{dt} \cdot V = \frac{A_{SiO_2} D_{SiO_2} S_{SiO_2}}{l} p_1 + \frac{A_{epoxy} D_{epoxy} S_{epoxy}}{l} p_1 \tag{3.47a}$$

$$= (3.06 \cdot 10^{-27} + 6.22 \cdot 10^{-26}) \frac{\text{mbar} \cdot \text{l}}{\text{s}} \tag{3.47b}$$

$$= (6.52 \cdot 10^{-26}) \frac{\text{mbar} \cdot \text{l}}{\text{s}} \tag{3.47c}$$

where $A_{SiO_2} = \pi \cdot 440^2\,\mu\text{m}$ and $A_{epoxy} = \pi(450^2 - 440^2)\,\mu\text{m}$ are the areas of SiO_2 and epoxy facing the tritium gas (compare figure 3.21), $p_1 = 10^{-8}$ mbar is the pressure at the high tritium partial pressure side and solubility S is transferred into the dimensionless value by multiplying with $2.7 \cdot 10^{-19}$ [Rog54]. The calculated leak rate of the fiber feed-through is 16 orders of magnitude lower than the required leak rate.

However, since the calculation of tritium diffusivity from hydrogen diffusivity does not necessarily reflect reality (see [Lee62]), the theory must be confirmed by an experiment. That is why the so-called Fibertest I, which is described in the following section, was built up at the TLK.

3.2.2.2 Experimental setup of the Fibertest I

Figure 3.24 shows the experimental setup that is used to determine the leak rate through an optical fiber feed-through. It mainly consists of two vacuum vessels, one acting as the primary system containing the tritium gas and the other containing ambient air and acting as a measurement chamber. Both vessels are separated by a flange with an optical fiber feed-through produced by VACOM[33]. The flange is a standard flange of the type DN40 CF-MM400UV- FCPC-1 with minor modifications: the flange is produced out of 316L steel where possible and cutting edges as well as staggered tapped blind holes are placed on both sides of the flange. That way tritium can only get into the measurement chamber by permeating through the fiber feed-through.

The Fibertest I is installed in the TRAP fume hood for safety reasons. The infrastructure of this fume hood, such as the backing pump and the turbopump, can be used. Tritium sample cylinders prepared by the TLK infrastructure can be connected to the setup (compare figure 3.24) and the gas is expanded into the sample chamber. Evacuation is done by the TRAP pumping system. The tritium partial pressure inside of the primary system can be calculated from the partial pressure and the volume of the test gas cylinder and the volume of the primary system.

To measure the tritium permeated through the fiber feed-through an ionization chamber DT D-MLB of the company PREMIUM Analyse[34] is connected to the measurement

[33] VACOM Vakuum Komponenten & Messtechnik GmbH Gabelsbergerstraße 9, 07749 Jena, Germany
[34] PREMIUM Analyse, ZAC Euromoselle, 9 rue de la Fontaine Chaudron, 57140 norroy-le-veneur, France

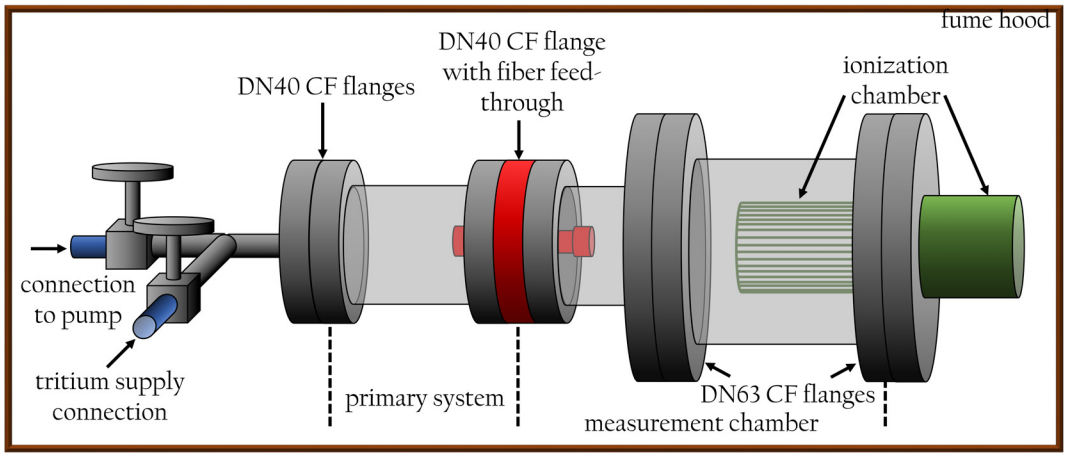

Figure 3.24: Experimental setup of the Fibertest I. The setup mainly consists of two vacuum vessels. The primary system vessel is built up from a standard DN40 CF pipe sealed by a DN40 CF flange with T-shaped pipe and a DN40 CF flange with a fiber feed-through. The measurement vessel is built out of a DN40 CF pipe installed at the feed-through flange and a DN63 CF pipe. The DN63 CF pipe is sealed by a flange in which the ionization chamber is installed. The whole setup must be placed in a fume hood for safety reasons.

chamber. Ionization chambers are gas-filled radiation detectors [May07] and which are commonly used in tritium analytic [Dem12]. Their measurement principle is based on the ionization of the gas in the chamber by, in this case, the electrons produced by the tritium beta decay and a measurement of the resulting anode current [Wor05, Hal12, Leh11] (compare figure 3.25). At that the measured signal not only depends on the activity in the chamber but also on the applied voltage between anode and cathode [May07, Ahm14]: at low voltages the number of electrons reaching the anode is relatively small as most of the electrons recombine with other ions. The number of electrons detected can be increased by increasing the voltage between the electrodes until it saturates at the saturation voltage. At this voltage, the measurement signal reaches a plateau as all produced electrons are collected. The region of this plateau is called the ionization chamber region [May07]. Usually the saturation voltage applied to get a current of the plateau is in the range from about 100 V to 200 V [Leh11]. If much higher voltages are applied between the electrodes, the energy of the electrons produced during the first ionization process is high enough to further ionize the gas and produce a lot of electrons and ions [Hal12].

Due to the fact that the average energy needed to ionize a gas is almost independent from the gas itself, basically any gas can be used to fill an ionization chamber [Ahm14]. For that reason ambient air, as it is used during the Fibertest I, is commonly used as the filling gas. The cylindrical geometry of the ionization chamber DT D-MLB is also one of the most common ones [Ahm14]: this geometry mainly consists of an outer metallic cylinder and a central anode. Due to this geometry the electrical field strength close to the anode is increased compared to the cathode. For that reason electrons reach the anode much faster than the positive ions reach the cathode, which increases the collection efficiency of the ionization chamber. The DT D-MLB consists of a cylindrical wire grid as a cathode with a volume of 100 cm^3 and a typical noise value of 0.01 fA. The reason why the cathode is built out of a wire grid is that the large surface of a solid electrode would increase the background signal of the measurement and probably affect the whole measurement due to surface contamination [Wor05].

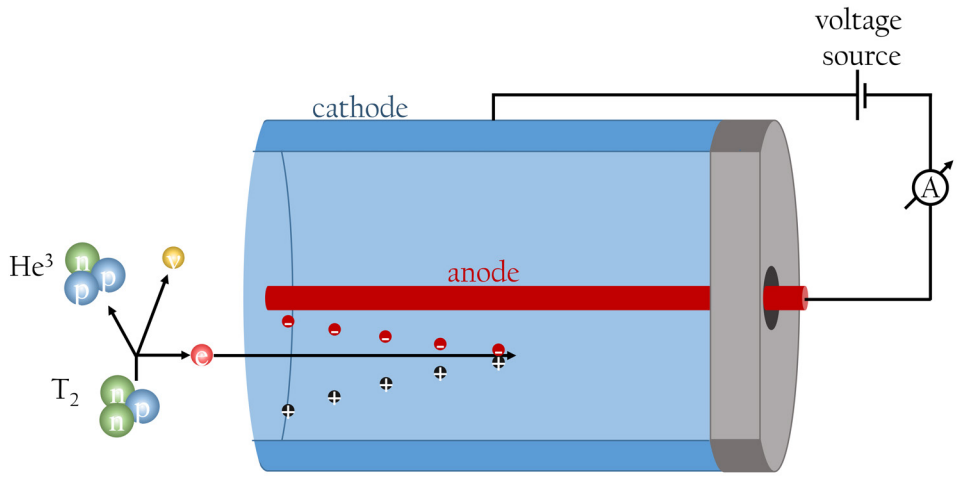

Figure 3.25: Cut-view of an ionization chamber. β-electrons produced in the tritium decay ionize the gas molecules in the volume between the cylindrical cathode and the anode in its center. The generated charges are divided by the electrical field between cathode and anode. The resulting current is the measurement signal of the ionization chamber which can be measured with an ammeter.

The ionization chamber DT D-MLB is connected to a feed-through seal DT PE-BTD installed in a DN63 CF flange. The preamplifier DTP-LN 1B8 is connected to the feed-through directly at the outside of the measurement chamber. The expected detection limit is calculated in the following: the measuring range of the preamplifier is 0.04 fA to 40 nA with a conversion factor of 380 kBq m^{-3} fA^{-1}. The sensitivity in this range is 2 aA and the accuracy is 0.5 % of the reading and ± 0.2 fA additionally. As the volume of the measurement chamber is V =0.00078 m^3, the lowest activity $\mathfrak{A}$ which can be detected with the preamplifier is

$$\mathfrak{A} = (11.9 \pm 59.3)\ \text{Bq}. \tag{3.48a}$$

The activity is given by [Mar13]

$$\mathfrak{A}_\text{o}(n = 1\,\text{mol}) = \lambda \cdot N = \lambda \cdot 2 \cdot N_\text{A} \cdot n = \lambda \cdot 2 \cdot N_\text{A} \cdot 1\,\text{mol} \tag{3.49}$$

and

$$\mathfrak{A} = \mathfrak{A}_\text{o} \frac{p \cdot V \cdot T_\text{STP}}{p_\text{STP} \cdot V_\text{1mol} \cdot T}, \tag{3.50}$$

where $\lambda = \frac{\ln(2)}{t_\text{halflife}}$ is the decay rate, $t_\text{halflife} = 4500$ days [Luc00] is the half-time of tritium, N is the particle number, $n = \frac{N}{2 \cdot N_\text{A}}$ is the amount of substances[35], $N_\text{A} = 6.02214082(18) \cdot 10^{23}\,\text{mol}^{-1}$ is the Avogadro constant [Moh15], $V_\text{1mol} = 22.710953(21) \cdot 10^{-3}\,\text{m}^3$ [Moh15] is the volume of 1 mol at STP conditions and p_STP and T_STP are standard temperature and pressure [Cox82]. The lowest detectable pressure can be calculated to

$$p = \frac{\mathfrak{A} \cdot t_\text{halflife}}{2 \cdot \ln(2) \cdot N_\text{A}} \frac{p_\text{STP} \cdot V_\text{1mol} \cdot T}{V \cdot T_\text{STP}} \tag{3.51a}$$

$$= (1.77 \pm 8.83) \cdot 10^{-10}\,\text{mbar}. \tag{3.51b}$$

That means that the ionization chamber is able to detect tritium at the latest if the tritium partial pressure in the measurement chamber exceeds the given pressure value.

[35] The factor 2 is necessary as tritium is present as a diatomic molecule.

After this pressure is reached it measures with a sensitivity in the order of 10^{-11} mbar. Therefore, it is possible to check whether the fiber feed-through meets the requirement on leak tightness of less than 10^{-9} mbar l/s with this experimental setup. How the measurements are performed is described in the next section in detail.

3.2.2.3 Measurement procedure and execution of measurements

The Fibertest I experiment mainly consists of two parts: the reference measurement and the tritium measurement. The data taken during the reference measurement functions as a comparative value, how the system behaves inside of the TRAP fume hood when it is connected to the TRAP infrastructure. This is important, since the temperature in the laboratory and also the local exhaust ventilation of the fume hood follows the alternation of day and night and a temperature change could affect the measurement as the ionization current is dependent on the temperature [Hec13]. In fact, the used ionization chamber already has a temperature sensor implemented which is used to correct for temperature effects, nevertheless it must be checked if and in which way temperature affects the measurement. Additionally, the vibrations produced by the pumps could influence the measurement and the system could show a drift.

One possible reason for a drift (in addition to a drift in the electronics of the ionization chamber itself) is that the grid of the ionization chamber was already exposed to tritium before. Although the grid was carefully decontaminated several times with the result that the surface contamination was in the order of the detection limit[36] of $0.02\,\mathrm{Bq/m^2}$, tritium which was diffused in the material of the grid could escape during the measurement.

In contrast to the tritium measurement during the reference measurements the primary system is pumped down continuously. Once the tritium is filled into the primary system, the tritium measurement starts.

The time tritium needs to permeate through the fiber feed-through can be estimated by using equation (3.39), which gives the time needed to increase the tritium concentration in the measurement chamber to 1% of the tritium concentration of the primary system. The time is

$$t \leq 79.25\,\mathrm{days}, \tag{3.52}$$

calculated with the diffusion coefficient of epoxy resin. If the tritium partial pressure in the primary system is 10^{-8} mbar and therefore comparable to the conditions we want to qualify the fiber feed-through for, this would mean, that even after about 80 days the pressure in the measurement chamber would be in the order of 10^{-10} mbar. As this pressure is in the order of the detection of the ionization chamber, even longer measurement times would be required to measure a significant permeation. Therefore, the fact that permeation is directly proportional to the partial pressure is used to shorten the needed measurement time during tritium measurement. The only restriction of the tritium partial pressure in the primary system is that the tritium activity in the fume hood must not exceed $10^{10}\,\mathrm{Bq}$. As the test gas cylinder has a volume of $(10 \pm 1)\,\mathrm{cm^3}$ its maximum allowed tritium partial pressure is (10.6 ± 1.1) mbar. If this pressure is expanded into the primary system with a volume of $(161.0 \pm 1.1)\,\mathrm{cm^3}$, the pressure in the primary system is about (0.6 ± 0.1) mbar.

[36] The surface contamination is measured with a wipe test, which is dissolved in a scintillation liquid. The analysis takes place in a liquid scintillation counter.

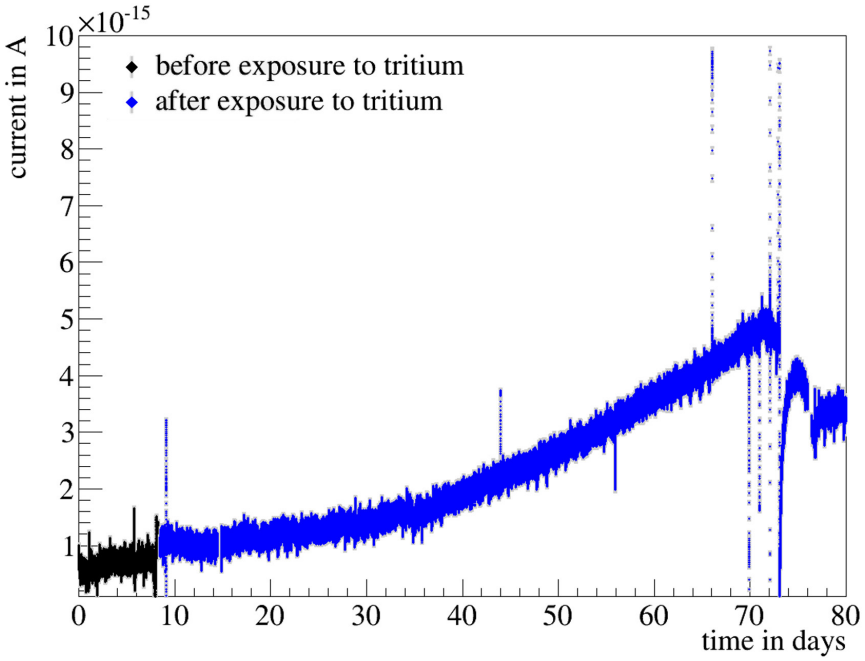

Figure 3.26: Plot of data taken during the Fibertest I. The reference data is shown in black, the tritium data is shown in blue. Each second one measurement was performed over the whole measurement time.

For these Fibertest I conditions again MuPAD calculations are performed before the experiment started. In figure 3.23 the results of these MuPAD calculations for Fibertest I conditions are shown. From the calculations of the permeation in silica it can be seen, that even after 7 weeks the penetration depth of tritium does not exceed 0.08 cm. However, tritium permeating through the epoxy resin reaches the low partial pressure side sometime between the first and the second week. Note that the faster timescale compared to the calculations under KATRIN conditions is only caused by the higher tritium partial pressure at the high partial pressure side. Due to these results, the data in the Fibertest I can be analyzed by assuming only one material the tritium permeates through, as no tritium should be able to permeate through the silica part of the fiber feed-through within the measurement time.

In the experiment the duration of the reference measurement was 9 days 1 hour and 43 minutes (compare figure 3.26). The system was then filled with a tritium gas mixture with a tritium purity of $95 \pm 5\,\%$. As the test gas cylinder was filled with 10 ± 0.5 mbar of this gas mixture the overall pressure in the primary system was 0.62 ± 0.07 mbar directly after the expansion of the gas. This leads to a tritium partial pressure of 0.59 ± 0.07 mbar. Note, that due to wall effects and exchange reactions the tritium partial pressure in the gas phase is decreasing with time. This decrease cannot be monitored during the measurement. After approximately 61 days of tritium exposure another experiment started in the TRAP fume hood in parallel. The vibrations caused by the work in the fume hood on this additional experiment disturbed the Fibertest I measurements so much, that the taken data cannot be used. Therefore, the data is cut off after 70 days and only data before the cut-off is analyzed. The analysis of this data is described in more detail and discussed in the following section.

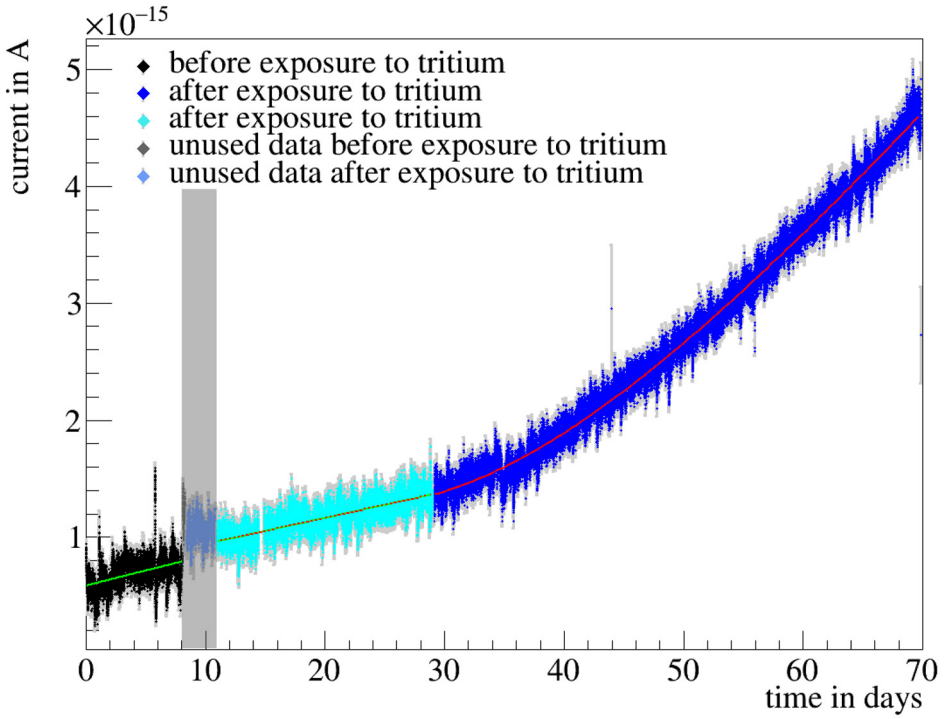

Figure 3.27: Plot of data used for data analysis of the Fibertest I. In black, azure and dark blue the data which is used for analysis and in gray and light blue the data which is not used for analysis is shown. For better visibility the range of unused data is shaded in gray additionally. The linear fits between day 0 and day 9 as well as between day 10.98 and 28.951 are drawn in with a green line. The exponential increase after day 28.951 is fitted with the red line.

3.2.2.4 Results of Fibertest I and discussion

Before a detailed analysis, the data is first cleaned up: in figure 3.26 all the data (one measurement each second) is shown. As already discussed in the last section data after day 70 are cut-off. In addition, one can see at 6 positions in figure 3.26 peaks in the current value in positive or negative direction (twice at about 9 days and one at about 44, 56, 66 and 70 days each). These peaks are caused by a power-up after the deactivation of the ionization chamber for data read-out and a kind of warming phase of about 5 minutes from power-up. This data is also not used for the data analysis. Furthermore, the data of each minute is averaged to one measurement point. This is done to reduce the memory requirements and to speed up the analysis. The error of the minute values is calculated by the RMS deviation of the second values and the systematic uncertainties of the measurement. The plot of the cleaned up data is shown in figure 3.27.

By looking at figure 3.27 some general observations can be made which are listed in the following:

- The current data of the reference measurements drifts towards higher currents. The drift seems to be linear.
- There is a sudden increase after 8 days and 2 and a half hours shortly before the tritium gas is filled in. It can be ruled out that there was a sudden increase of activity in the measurement chamber at that time as both measurement chamber and primary system are sealed and no tritium was filled into the primary system

Table 3.5: List of values of the fit parameters used to analyze the Fibertest I data. For reasons of clarity and comprehensibility additional to the fit parameter names the fit functions to which the parameters belong is given in the first column. The values and also the errors of these values, given in the fourth column, are calculated using ROOT.

fit function	parameter	value	error
f_1	c_1	$5.852{\cdot}10^{-16}$ A	$7.0{\cdot}10^{-19}$ A
	c_2	$2.554{\cdot}10^{-17}$ A d^{-1}	$1.5{\cdot}10^{-19}$ A d^{-1}
f_2	c_3	$6.635{\cdot}10^{-16}$ A	$2.0{\cdot}10^{-18}$ A
	c_4	$2.540{\cdot}10^{-17}$ A d^{-1}	$1.2{\cdot}10^{-19}$ A d^{-1}
f_3	c_5	$1.060{\cdot}10^{-16}$ A	$3.0{\cdot}10^{-19}$ A
	c_6	54.62 d	0.13 d
	c_7	$7.944{\cdot}10^{-15}$ A	$2.0{\cdot}10^{-17}$ A
	c_8	$3.754{\cdot}10^{-2}$ d^{-1}	$2.0{\cdot}10^{-4}$ d^{-1}

so far. This increase is most likely caused by the work at the fume hood during connection of the test gas cylinder to the Fibertest I experiment.

- There is no significant change in the current data visible directly after the tritium gas was filled into the primary system.
- After the sudden increase the current slowly decreases. As the increase and decrease in current does not seem to be caused by an activity change in the measurement chamber but by an instability of the ionization chamber this data is not used for data analysis.
- After the current decrease stops there is a slight drift in the data towards higher currents noticeable again. This drift also seems to be linear.

Due to these observations the data is analyzed by using

$$f_1(t) = c_1 + c_2 \cdot t \ , \ t < 8.103\,\text{days}, \tag{3.53}$$

$$f_2(t) = c_3 + c_4 \cdot t \ , \ 10.98\,\text{days} \leq t < 28.951\,\text{days and} \tag{3.54}$$

$$f_3(t) = (c_5 \cdot (t - c_6) + c_7 \cdot \exp(-c_8 \cdot t)) + f_2(t) \ , \ 28.951\,\text{days} \leq t < 70\,\text{days} \tag{3.55}$$

as functions which are fitted to the data in the given time ranges. The linear functions f_1 and f_2 are chosen as the current value seems to linearly increase in this particular field. f_3 is chosen since the pressure at the low pressure side before reaching the linear regime is given by the general formula[37] [Rog54]

$$p = \frac{A \cdot D \cdot S}{V \cdot l} \cdot p_1 \left(t - t_c - \frac{2 \cdot l^2}{\pi^2 \cdot D} \cdot \sum_{m=1}^{\infty} (-1)^m \frac{exp\left(\frac{-m^2 \cdot \pi^2 \cdot D \cdot t}{l^2}\right)}{m^2} \right) \tag{3.56}$$

plus drift with the fixed values from f_2.

The time range of f_1 is defined by the sudden increase. The ranges for f_2 and f_3 are found by calculating the mean residues per measurement point for each fit and by minimizing the sum of both mean residues per measurement point (for more information see appendix A.2 on page 199).

All fits are performed with ROOT[38] and the resulting fits are also shown in figure 3.27. In addition, in figure 3.28 the residues of the three fits are plotted. These three plots indicate,

[37] Note that the sum of formula (3.56) vanishes at large t, so that the formula changes to equation (3.43).

[38] ROOT is an object oriented data analysis framework for large scale data analysis developed at the European Organization for Nuclear Research Conseil Européen pour la Recherche CERN.

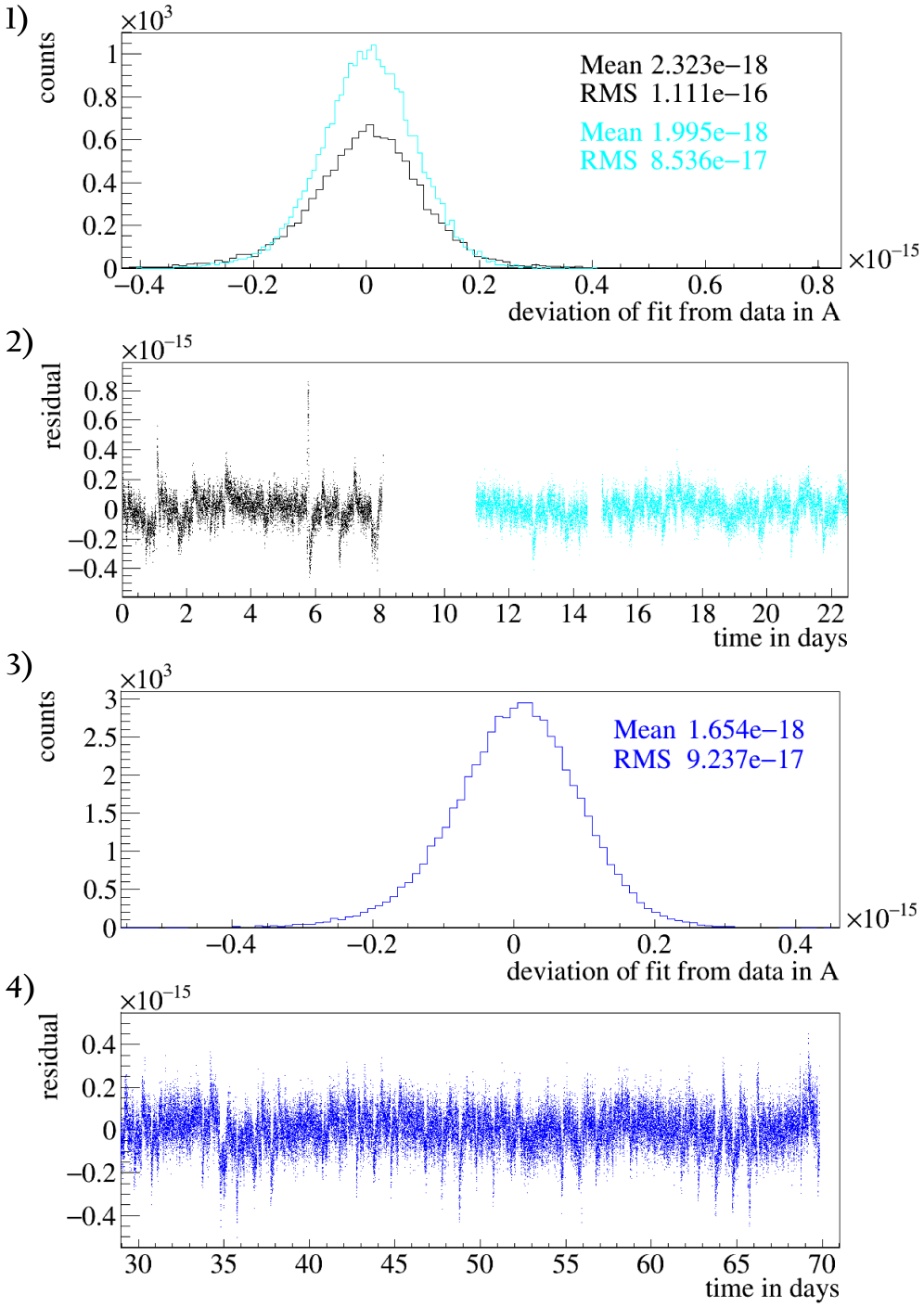

Figure 3.28: Residues of functions fitted on the Fibertest I data. In graph (1) the distribution of the reference data (black) and of the tritium data (azure) described by a linear increase is shown. Both distributions have their maximum close to 0. In addition, the mean and RMS deviation values for both distributions are given (reference data on top). In the graph below (2) the residues of both data sets (same colors as before) are plotted against the time. The residues are statistically fluctuating around zero deviation. In the two graphs below the distribution (including mean and RMS deviation values) of the residues (3) and the residues of the tritium data described by an exponential increase itself (4) are shown. As before the distribution maximum is close to 0 deviation and the residues are statistically fluctuating around 0, meaning that the chosen exponential fit seems to be suitable.

that the fit functions are suitably chosen. In table 3.5 the calculated fit parameters are given. It needs to be mentioned that within the errors the slopes of f_1 and f_2 are equal, but not the y intercepts. That might be an indication for a systematic drift of the ionization chamber. Therefore, the addition of f_2 to f_3 seems to be suitable as well.

By comparing equation (3.56) and the function f_3 one notices that parameter c_4 is equivalent to t_c, the time needed to get a linear behavior of the pressure. That means that after 54.62 days the activity in the measurement chamber should linearly increase with the value of parameter c_5 which is the gradient of the pressure increase. From the value of c_5 the increase of the tritium partial pressure inside of the measurement chamber can be calculated to

$$\frac{dp}{dt} = (4.68 \pm 0.09) \cdot 10^{-10} \, \frac{\text{mbar}}{\text{s}} \tag{3.57}$$

by using equation (3.51b). The theoretically expected pressure change, calculated by using equation (3.41), would be $\frac{dp}{dt} = (4.76 \pm 0.60) \cdot 10^{-18} \, \frac{\text{mbar}}{\text{s}}$. That means that the difference between the calculated and the experimentally determined value is 7 orders of magnitude. This can at least partially be explained by using diffusivity and solubility values for tritium which are extrapolated from hydrogen and deuterium. In the case of deuterium other measurements also found a difference between of experimentally determined and extrapolated diffusivity and solubility values [Lee62].

The leak rate measured with the ionization chamber is

$$L = (3.65 \pm 0.08) \cdot 10^{-13} \, \frac{\text{mbar} \cdot \text{l}}{\text{s}}, \tag{3.58}$$

which is already 4 orders of magnitude below the TLK requirement of $10^{-9} \, \frac{\text{mbar} \cdot \text{l}}{\text{s}}$. If a partial pressure of 10^{-8} mbar at the high partial pressure side is assumed, the leak rate would be even lower by about 7 orders of magnitude.

Even if a pressure difference of 1 bar between the high and low pressure side is assumed (which roughly means a pressure difference 3 orders of magnitudes higher than during the Fibertest I) as it is usually the case during helium leak tests, the leak rate would still be below the requirement as permeation is linear to the partial pressures. Due to this the decrease in tritium partial pressure in the gas phase caused by wall effects and exchange reactions, which is not expected to decrease the tritium partial pressure by several orders of magnitude, should not significantly change the results of the Fibertest I.

In conclusion the tested fiber feed-through implemented in a DN40 CF flange meets the requirements of the TLK and can be used to seal at least the second containment. The usage of such a fiber feed-through at the primary system of a tritium facility seems to be feasible as well. Nevertheless, a dedicated experiment similar to the Fibertest I demonstrating the feasibility at higher tritium partial pressures would be needed.

3.2.3 Fibertest II: Investigation of influence of low pressure tritium atmosphere on optical properties of UV fibers

In this section question 3) from the beginning of chapter 3 is answered: what influence do the tritium exposure and radiochemical effects caused by it have on the optical properties of optical fibers optimized for the UV light range? Finding an answer to this question is important since the e-gun rate and its stability is affected directly by changes in the optical properties of the fibers which guide the UV light towards the gold cathode were the

electrons are produced. The Fibertest II experiment is designed to answer this question by measuring the transmission properties of fibers during a tritium exposure.

Before the Fibertest II experiment and its results are discussed in more detail in subsections 3.2.3.3 to 3.2.3.7 the requirements for the optical components itself are deduced from those for the Rear Section e-gun as presented in subsection 3.2.3.1. The e-gun operating parameters which can affect the optical properties of a fiber in general are discussed in subsection 3.2.3.2.

3.2.3.1 Stability requirements on the e-gun and its optics under KATRIN conditions

The stability of the Rear Section e-gun rate is of importance for monitoring the operation parameters of both the WGTS and the spectrometer. As mentioned in section 2.3.2, the e-gun electron rate of about $10^4\,\mathrm{s}^{-1}$ must be stable within 0.1 % over several minutes (during the column density measurements at the WGTS, the transmission function measurement and the work function calibration at the main spectrometer). For measurements of the energy loss function the same level of stability has to be maintained for several hours.

There are four factors which can affect the e-gun rate stability. These are the work function and the thickness of the gold layer, the intensity of the light source and transmission properties of the optical setup:

- A change in the gold work function changes the energy of the light needed to get electrons out of the gold layer. That means, that it directly affects the electron rate. This effect is further increased by the fact, that the absorption and reflection as well as the light intensity are wavelength dependent. In addition, the mean free path of the electrons inside of the gold layer changes with the work function (compare 3.2.1.2). However, it is not expected that the gold work function of the cathode changes. Jiang et al. measured the quantum efficiency of gold films irradiated by UV light at 257 nm at a pressure of about 10^{-7} mbar in [Jia98b]. After a degradation in the first 3 weeks by a factor of 3 the quantum efficiency remained stable for more than 10 days. As the quantum efficiency is connected to the work function this result implicates that after an initial measurement time of about 3 weeks the work function should remain stable as well.
- A change in the thickness of the gold layer changes both the possibility of emitting an electron and the possibility of producing an electron that reaches the surface of the cathode without scattering. This is caused by the fact that the path of the light and of the electron through the layer is decreased. A reduction of the gold layer thickness can only occur through ion bombarding caused by the attractive potential of the cathode with negative potential. This should effectively be prevented by the usage of the dipole electrodes of the Rear Section [Bab14].
- A change in the intensity of the light source directly affects the electron rate. However, it is possible to detect intensity fluctuations of the light source using the detector that is installed at one of the splitter fibers (compare figure 3.14 at page 68). The monitoring of the light source intensity effectively allows eliminating the influence of an unstable light source.
- A change in the transmission properties of the optical setup also changes the amount of photons available to eject electrons. Part of the transmission properties are monitored with the detector, just as the stability of the light source is. However, since the detector is not installed directly at the entrance position of the light

into the gold layer but rather behind the splitter in the second containment, the transmission of the focusing lenses, the feed-through window and the fibers inside of the primary system are not monitored by the detector.

Due to all these factors, the 0.1 % stability requirement of the e-gun can only be met, if the transmission of the system consisting of the focusing lenses, the feed-through window and the fibers inside of the primary system also meet this requirement. However, the fibers are exposed to tritium which might cause a significantly different transmission behavior during the e-gun operation. To make sure that the tritium environment is not preventing the e-gun from achieving the intended stability it must be tested if the transmission of the fibers is affected by tritium.

The theoretical changes in a fiber caused by tritium are discussed in the next section together with all the other possible changes caused by the operating parameters of KATRIN.

3.2.3.2 KATRIN measurement conditions affecting the optical properties of fibers

Before discussing possible causes of a degradation of the optical properties of fibers that are used inside of the primary system, some general remarks on those fibers and the structure of the fiber material are necessary [Gha98]: the fibers used at the e-gun are so-called step index fibers. They consist of a core with refractive index n_1 and a surrounding cladding with refractive index n_2. Light which is injected into the fiber is guided through the fiber by total refraction as long as the angle between the perpendicular and the light path is more than

$$\Phi_{\mathrm{C}} = \sin^{-1}\left(\frac{n_2}{n_1}\right) \tag{3.59}$$

(compare figure 3.29). That implies that the maximum acceptance angle of a fiber is given by

$$\vartheta_{\max} = \sin^{-1}\left(\frac{1}{n_0}\cdot\sqrt{n_1^2 - n_2^2}\right). \tag{3.60}$$

As the fibers used at the e-gun are made of fused silica and the refractive index of fused silica is wavelength dependent [Mal65] it is quite evident that both Φ_{C} and $\vartheta_{\max}$ are also wavelength dependent. The transmission characteristic of the fibers is dependent on the difference of the refractive indices of core and cladding.

Fused silica itself is an amorphous material with a short range order which dominates its general properties [O'R83]. Therefore, the structure of fused silica is called an ideal continuous random network [Gri85] (see figure 3.30). In this structure point defects can be incorporated (described in detail in [Sal11]): one of the best known point defects is the E' center, where a silicon atom is bonded to 3 oxygen atoms leaving an unpaired electron in the network (compare figure 3.31). Overall there a 4 different types of E' centers, all with an absorption band in the energy range above 5.2 eV. Therefore, this kind of defect is not really important for the e-gun. A more important defect might be the non-bridging oxygen hole center (NBOHC), where one oxygen has a dangling bond [Dev90]. Its absorption band is at 4.8 eV with a FWHM of 1.07 eV [Pac00]. Another defect with an absorption band in the energy range of interest is the peroxy radical [O'R83]. This defect is characterized by a silicon with only three bonds to oxygen atoms in combination with an oxygen-oxygen bond at another silicon atom. For this defect an absorption band of 5.4 eV with FWHM of 1.3 eV at the surface of SiO_2 is found [Pac00]. More point defects in fused silica can be found in [Gri91, Sal11, O'R83]. Overall the absorption coefficient

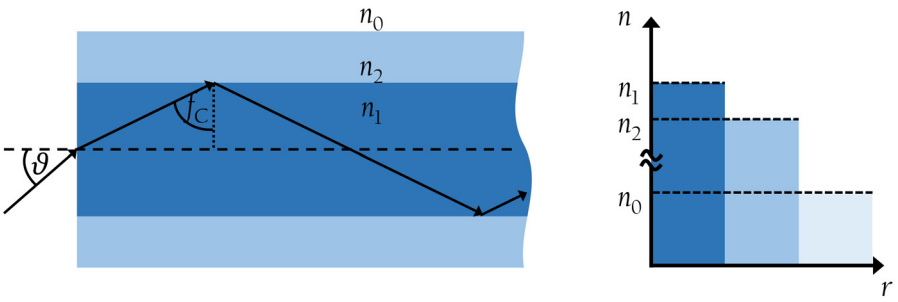

Figure 3.29: Design of step-index fibers with cylindrical central core. Left: a fiber consists of a core with refractive index n_1 and a cladding with refractive index n_2. Light with an angle ϑ to the horizontal smaller than $\vartheta_{\max}$ is guided by total reflection through the fiber, as the angle to the perpendicular at the core cladding junction inside of the core is always larger than the angle of total reflection Φ_C. Right: here a diagram with the refractive index as y-axis and the distance to the center of the fiber on the x-axis is shown. To enable the total reflection at the core cladding junction the refractive index of the core n_1 must be larger than the refractive index n_2 of the cladding. In case of the fibers used at the e-gun the values $n_1 = 1.458$, $n_2 = 1.441$, $r_{\text{core}} = 100\,\mu\text{m}$ and $r_{\text{cladding}} = 10\,\mu\text{m}$ measured from the outside of the core are given by the manufacturer Edmund optics GmbH.

of fused silica with its natural defects is about $10^{-3}\,\text{cm}^{-1}$ between 200 nm and 300 nm whereas it is about $10^{-5}\,\text{cm}^{-1}$ between 500 nm and 700 nm [Gri91].

The absorption as well as the density and the refraction index of fused silica fibers can be changed by any kind of irradiation [Hir05] as point defects of the described kind and others are created [Gri91]. In addition, a vacuum is known to have an effect on the transmission properties of SiO_2. The fibers of the primary system are exposed to UV light of maximum 82 µW at 275 nm and ionizing radiation of less than $2{\cdot}10^5\,\text{Bq}$[39] or $1.6{\cdot}10^{-7}\,\text{Gy/s}$[40]. In addition, the fibers are also exposed to a vacuum of about 10^{-8} mbar, where the remaining gas is mostly composed of hydrogen isotopes. All these KATRIN measurement conditions can have an effect on the optical properties of the fibers. These effects are discussed in more detail in the following:

In case of **UV light** irradiation of silica, it is known that defects are generated that cause both solarization and densification of the glass [Mar97]. E. A. Nevis has reported in his work [Nev85] that the irradiation of different all-silica fibers with a pulsed UV laser causes a sharp decay of the transmission with a quasi exponential behavior at short exposures and a linear behavior with low slope at longer exposures regardless of the fiber size. The decay time and the amount of decay is dependent on the intensity of the light, but a significant effect can already be observed at pulses with an energy of 0.001 of the surface damage-threshold energy. The loss in transmission is caused by an absorption peak at 260 nm. After a time period of 2 to 3 weeks the transmission recovers again to 10 % of its initial value. Nevis assigns the formation of color centers, which are related to point defects [Cou67] like E' and NBOHC [Nat04] in the silica, as the reason for the transmission losses. W. Primak and R. Kampwirth also observed this effect. They were

[39] $2{\cdot}10^5$ Bq is the acitivity in the e-gun chamber as given in the Rear Section Technical Design Report for the primary vacuum system, second containment and support structures.

[40] This dose rate is calculated by multiplying the mean electron energy of the tritium decay, 5.7 eV, with the activity in the e-gun chamber of $2{\cdot}10^5$ Bq divided by the mass of the fiber. The mass is calculated with the density of UV fused silica of $2.202\,\text{g cm}^{-3}$ given by Newport [Cor15], the diameter of 200 µm and the length of the fibers of 16.4 cm.

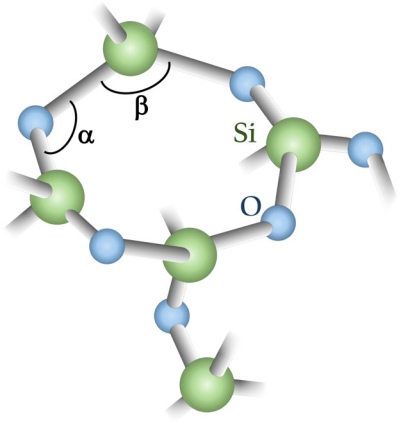

Figure 3.30: Visualization of the basic structure of amorphous SiO_2. The basic building block of amorphous SiO_2 is an SiO_4 tetrahedron with an O-Si-O bond angle of β =109.5° and a Si-O-Si angle of α =120° - 180°. The tetrahedrons are joined in rings of variable amount of tetrahedrons. The smallest possible ring is built out of 3 tetrahedrons, but the most common one is a 4 membered ring also shown in this figure [Dev94].

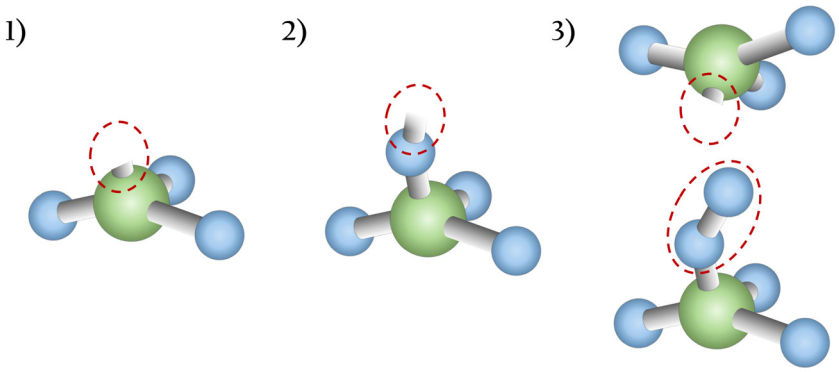

Figure 3.31: Visualization of the E' defect, NBOHC and peroxyl radical 1) shows the E' defect. The red dashed circle marks the dangling bond at the silicon atom. In 2) the NBOHC is shown. In case of this defect the dangling bond is at an oxygen atom, which is also marked by a dashed circle. In 3) the two parts of the peroxyl radical are drawn. This defect is characterized by an oxygen vacancy and an oxygen-oxygen bonding (own figures according to [Sal11]).

not able to find a threshold energy for the production of color centers in SiO_2.

In addition to the production of color centers, the density and as a result the refraction index of fused silica can also be changed by UV irradiation [Nat04]. The change in density is found to be possible in both directions, meaning compaction at high to medium and compaction combined with rarefaction at low doses of irradiation. The first one causes an increase, the second one a decrease of the refractive index. The largest measured changes are in the order of 10^{-5} in case of increase and about 10^{-6} in case of decrease. As the refraction index of the core and the cladding of the fiber are optimized to each other for a certain wavelength, this can cause a change in the properties of the fiber. But due to the small changes in the refractive index the effects on the acceptance angle $\vartheta_{\max}$ and Φ_C are only in the order of at maximum 10^{-4} degree or -10^{-4} degree, respectively (compare B.2). Besides the fibers, the lenses are also affected by the UV light or more precisely their focal length. However, the change of the focal length is very small, meaning several 10 nm. That means the change in refraction would not cause further losses.

A third effect caused by the UV irradiation of fibers is hydrogen consumption. During the irradiation hydrogen is absorbed by the generated E' defects and NBOHC. The consumption adds up to about 70 % of the initial hydrogen content of the fiber [Nat04]. If this is also true for tritium the incorporated tritium could decay directly as part of the network. This might enhance the effect of the ionizing radiation further. The effects on fused silica caused by **ionizing radiation** are in general similar to those of UV irradiation: it can cause the generation of defects with absorption bands, a densification and as a result a change in the refraction index as well as a possible change in the trapping probability and the diffusion coefficient of hydrogen isotopes.

The defect generation under radiation can be divided in three basic processes [Gri85]: radiolysis, which is the atomic rearrangement induced by any kind of radiation; the displacement damage, resulting from the transfer of momentum and energy from the incident particle usually in the range from 4 eV to 25 eV to an atom of the network by which bonds are broken; and the electron rearrangement at already existing defects. Especially in case of the first and the second processes the generated defects, like oxygen vacancy centers as E' centers, are known to induce absorption in the range of 200 nm to 400 nm [Dec04, Mar97, Leo09], which rapidly reduces the transmission in that region [GM00]. The number of generated defects is dependent on the precursor density, especially in case of E' centers implanted in the network during manufacturing [Leo09]. Therefore, the manufacturing parameters such as temperature and drawing speed, the composition (how is the material doped, what is the OH-content and how many impurities does the material have?) and also a possible preconditioning by hydrogen-loading, annealing or pre-irradiation can make a fiber more resistant to radiation [Dec04]. This is especially important as radiation effects are enhanced at fibers compared to windows due to the longer optical length [Dec04].

Another very important effect of ionizing radiation is the volume compaction of the irradiated fused silica [Bus10, Gri85, Boi03]. This compaction is the result of two effects [Nor74]: the knock-on displacement and a polyamorphic transformation [Bus09, Pfe85]. The latter is the result of a reorganization through rebonding whereby almost all initial Si-O bonds are renewed. The new formed network has a larger number of members per basic rings (mostly 3)[Dev94, Dev90, Boi03], a smaller β angle between Si-O-Si and an increased Si-O-bonding length [Bus09]. This densification can reach a saturation value of up to 3 % [Dev94, Gri85], but in case of electron radiation the required dose to reach this saturation value is 2 orders of magnitude higher than for proton irradiation [Hir05].

Nevertheless, there is no electron energy threshold for a compaction onset found by the irradiation with electrons above 2.2 keV [Nor74]. Just like the compaction due to UV irradiation causes a change in the refraction index so does the compaction due to ionizing radiation [Dev94], but in the order of 1 %. A change in this order of magnitude could cause a maximum reduction of the acceptance angle $\vartheta_{\max}$ of almost 9° and an increase in Φ_C of almost 5° if only the refraction index of the cladding is changed. The assumption that only the cladding is affected by the radiation seems to be reasonable as the free mean path of the tritium beta decay electrons is at maximum about 14 nm [Sea79] and the thickness of the cladding is several micrometers. The change in the optical properties of the fiber could increase the losses at the fiber injection by 37 % (for a more detailed calculation see appendix B.2). If both the refractive indices of the cladding and the core are changed, there are no further losses expected.

Concerning the densification of fused silica due to irradiation with low energy electrons from 0.05 keV to 30 keV J. Pitts and A. Czanderna have found that the O/Si ratio is reduced from initially 2 to values from 0.59 to 0.91 by a stimulated desorption process at the surface[Pit86]. This accelerated desorption implies that the irradiation with electrons can change the permeability characteristics of fused silica. A similar statement is possible by looking at the results of A. Ibarra et a. who found that the diffusion coefficients and the trapping probability of deuterium in fused silica is increased by irradiation with electrons [Iba07]. The exact impact of these results on the properties of fibers at the Rear Section e-gun is not known.

Another effect which has to be considered at the e-gun of the Rear Section is the **vacuum environment** in which the fibers are used. The effect of vacuum on fused silica can be divided into 2 processes: at first a kind of cleaning which increases the transmission followed by a decrease in transmission. This was observed at a fused silica window irradiated with UV light by Stephen et al. This degradation finds expression in a decrease of transmission [Ste93] mostly caused by an increased absorbance but also by a change of reflectance from 0.5 % to 1.1 % [Bur00]. The degradation only occurs if the pressure in the chamber is below 1 torr. If it is filled with higher pressures again the transmission returns to 80 % of its initial value [Ste93]. The damage is more quickly increasing in a vacuum [SZ08]. The explanation for the degradation is an accumulation of point defects and the formation of silica with a O/Si ratio of less than 2 [SZ08, Bur00]. Especially the reduction of oxygen in the network is increased at vacuum conditions compared to air [SZ08]. Due to the higher number of defects the damage threshold is also decreased in a vacuum by 10 $\mathrm{J \cdot m^{-2}}$ [Bur00].

All the discussed effects are known and can be found in the literature. However, the literature just deals with one or at the maximum two of these effects at once. But the effects could further enhance each other. Therefore, the Fibertest II is essential not only with regard to the tritium compatibility of fibers but also as a first test of fibers under KATRIN-like conditions. However, the main aim of the Fibertest II remains to qualify the fibers for the tritium atmosphere. The setup which is used for that is presented in the following section.

3.2.3.3 Experimental setup

The experimental setup of the Fibertest II can roughly be divided into two parts, namely the optical system outside and the tritium containing primary system inside of the TRAP fume hood (compare section 3.2.2.2, page 85).

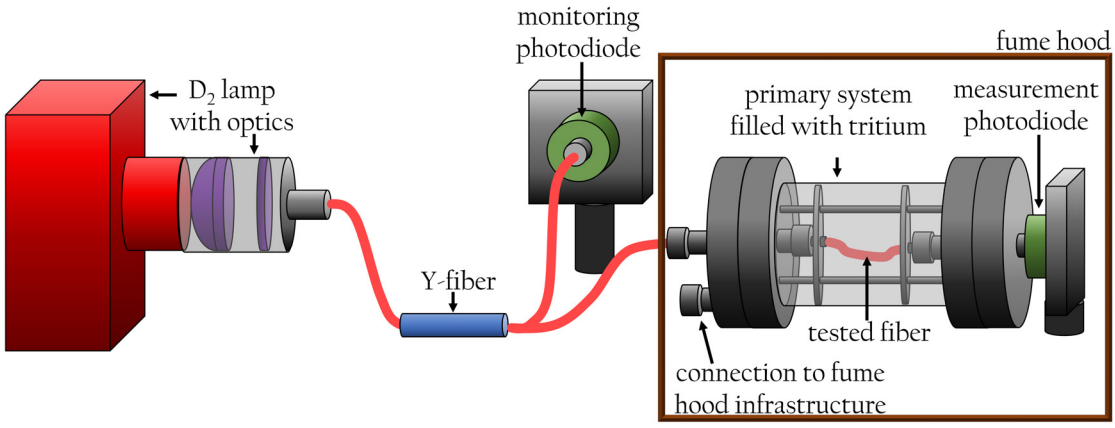

Figure 3.32: Experimental setup of the Fibertest II. In contrast to the later setup at the e-gun a deuterium lamp is used as a light source with an intensity that is about a factor of 100 lower. Instead of the monochromator of the e-gun the wavelength selection at the fiber test is done by a filter optimized for 232 nm. This is also the wavelength the whole setup is optimized for which in case of the e-gun is 275 nm. To split the light into two fibers a Y-fiber instead of a real splitter is used. In a Y-fiber 3 fibers are simply glued together. Therefore, spatial fluctuations in the intensity over the radius of the fiber cause a change in the splitting ratio, whereas a splitter acts like a beamsplitter dividing all the light spatially independent in a well defined ratio into the 2 output fibers. In spite of these facts the Y-fiber is installed as no company was found that was able to built a splitter optimized for 232 nm.

The optical system was planned in a way that it optimally represents the conditions in the later optical setup of the e-gun. But as the optical setup of the e-gun has changed in many ways since the design phase of the Fibertest II not all components are still the same (compare figure 3.32). Therefore, the broadband light source of the setup is a deuterium lamp of the type 63163 by Newport[41]. To collimate the light the lens assembly 60006 is used and the wavelength selection is done by a filter of the type 10BPF10-232 both also manufactured by Newport. The filter has a peak transmission of at least 12 % at (232 ± 2) nm matching the gold work function of 5 eV to 5.5 eV[42]. The FWHM of the filter is (11 ± 3) nm. After the filter the light is focused by a Newport lens of the type 6198 into the input fiber of a Y-fiber custom-produced out of a solarization resistant fiber by SEDI·ATI[43]. The Y-fiber divides the light into two output fibers, one of them connected to the so-called monitoring photodiode. The second output fiber is laid into the TRAP fume hood where the tritium containing parts of the Fibertest II are placed.

The tritium containing primary system is a DN40 CF bellow leak-tight closed on both sides by two flanges with fiber feed-throughs produced by Vacom. One of these flanges is customized by an additional VCR connector which is added to the flange. This connector enables the connection of the primary system with the infrastructure of the TRAP fume hood and the filling with tritium by the expansion method. The output fiber of the Y-fiber is connected to this modified flange. To the other flange the so-called measurement photodiode is fastened. The fiber, which is exposed to tritium, is mounted inside of the

[41] Newport Corporation, 1791 Deere Avenue, Irvine, CA 92606, USA

[42] The given values for the work function are those directly after production and without exposure to air. The exact value is depending on whether it is amorphous or crystalline and on the crystal orientation [Hay14].

[43] SEDI·ATI Fibres Optiques, 8 rue Jean Mermoz, Z.A. de Saint Guénault, 91080 Courcouronnes, France

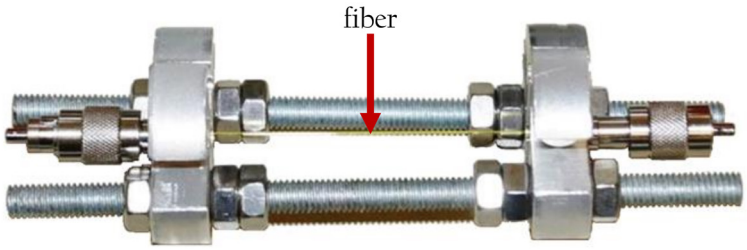

Figure 3.33: Photography of a fiber in its holder. The fiber is clamped into a holder to simplify the handling of the fiber. As the length of the holder can manually be adjusted by screws to each of the three fibers a bending of the fiber and possible damage is prevented.

bellow (see also figure 3.33). The bellow as the primary system is needed to make the installation possible without damage to the fiber. Overall there are three fibers which are tested.

In addition to the Fibertest II which directly monitors the transmission properties of the fibers during tritium exposure a microscope of the type EXPERT-DN from Groß- und Einzelhandel Müller GmbH[44] is used to make microscopic pictures of the fibers. This microscope provides a magnification of 7 to 90, reflected and transmitted light irradiation and a camera. To enable the investigation of the contaminated fibers after the tritium exposure the microscope is placed in a glove box. The microscopic investigation before and after exposure are taking place for reasons of reproducibility.

With both the Fibertest II and the microscope a thorough investigation of the fibers before, during and after the tritium exposure is possible. The measurement procedure of this investigation is described in detail in the following section.

3.2.3.4 Measurement procedure

As the Fibertest II setup not only investigates the fibers with regard to their transmission properties but also using a microscope, the whole measurement procedure includes 8 main steps (compare figure 3.34). A more detailed description of the steps is given in the following:

1. The new fiber, which is already installed in its holder, is loaded into the glove box, where the microscope is mounted. From this moment on the fiber is considered to be contaminated and is handled that way. After the microscopic pictures are taken, the fiber is unloaded again.
2. The fiber is installed into the primary system of the Fibertest II in a fume hood. The handling of the fiber in the fume hood is necessary as the fiber is considered to be contaminated. To make sure that the bellow of which the primary system consists is not leaky due to the extension needed to close the primary system, a helium leak test is performed inside of the fume hood to assure that the leak rate is below $10^{-9}\,\mathrm{mbar\,l\,s^{-1}}$.
3. The primary system is installed inside of the TRAP fume hood and connected to the TRAP infrastructure and the optical setup of the Fibertest II. To make sure

[44] Groß- und Einzelhandel Müller GmbH, Hohenwindenstraße 13 Haus 3A, 99086 Erfurt, Germany

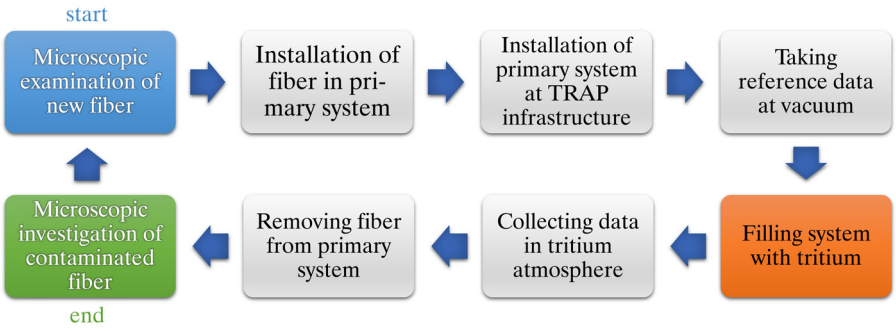

Figure 3.34: Measurement procedure for the investigation of tritium exposed fibers. Each of the 8 boxes represents one of the main steps of the experiment for a single fiber. The procedure starts in the upper left corner and ends in the bottom left corner. This procedure is repeated for each of the three tested fibers.

that the connection between the TRAP infrastructure and the primary system is also leak tight an isolation test is performed.

4. For reference, transmission measurements are performed before exposing the fiber to tritium. These measurements are performed at a vacuum of less than 10^{-5} mbar.
5. When a sufficient amount of reference data is taken (at least 1 week) the system is filled with tritium gas. Due to the restricted activity of 10^{10} Bq which can be handled in a fume hood the tritium partial pressure in the primary system does not exceed 0.6 mbar.
6. The tritium measurements are performed for at least a week.
7. To remove the fiber from the primary system again, the primary system is evacuated, disconnected from the TRAP infrastructure and transported to another fume hood which enables a more convenient handling of the system.
8. The fiber is loaded into the glove box where the microscope is mounted again and the pictures of the fiber after exposure are taken.

These steps are performed for each of the 3 fibers which are tested in a tritium atmosphere. However, before the experiment can be performed as described it must be ensured that the Fibertest II produces reliable results if the light source is turned on once and not turned off again during the measurement. To this end long-term measurements of the ratio of measurement photodiode signal and monitoring photodiode signal are performed. As one can see in figure 3.35 the ratio never settles down but is monotonically non-decreasing with time following a rapid increase of the ratio immediately after turning on the light source. The rapid increase, which cannot be explained by a change in intensity of the light source as the ratio is calculated, is caused by different intensities reaching the photodiodes. The intensities differ as the Y-cable splits the light not perfectly into a 50:50 ratio. As the light intensity at the monitoring photodiode is larger, the formation of color centers is also faster. That means that the intensity measured by the monitoring photodiode is decreasing faster than the one measured by the measurement photodiode. As the rate of color center formation is dependent on the light intensity, after a certain time the increase in ratio decelerates. But it is not possible to predict how the ratio is exactly behaving over time and a reliable comparison of data before tritium exposure with data during or after is impossible.

For that reason the attempt was made to find the measurement interval with the smallest deviation between the measurements, where each measurement has a well defined period

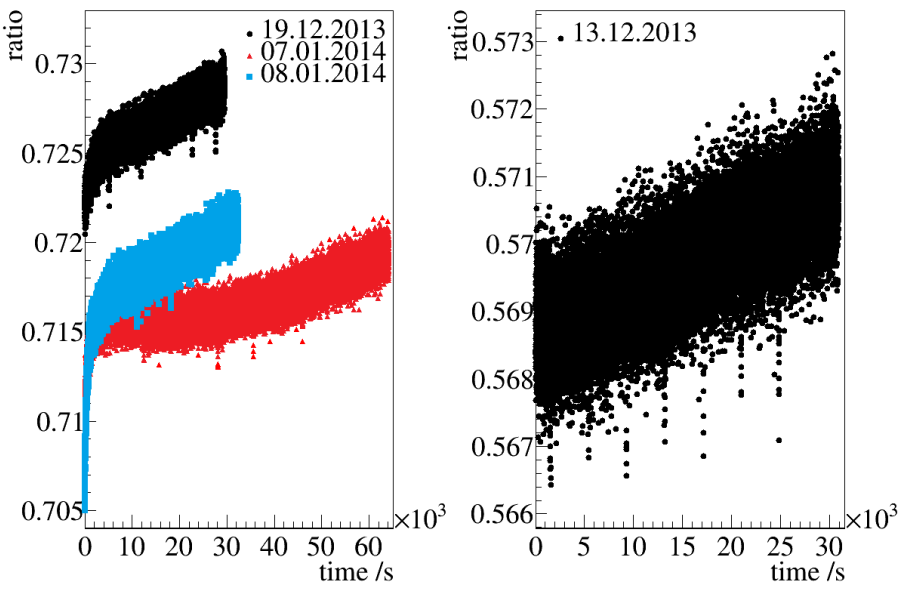

Figure 3.35: Long-term measurements with the Fibertest II setup. The error bars are not plotted, as the shape of the curve is more noticeable that way. Left: the ratio of the measurement signal of the measurement photodiode to the measurement signal of the monitoring photodiode is plotted against the time for 2 measurements of about 8 hours and 1 measurement of about 17 hours. After a rapid increase at the beginning of the measurement, when the light is turned on, the ratio changes to a monotonically non-decreasing behavior. In addition, by comparing the data from the 19th of December and the 8th of January with the data from the 7th of January one can see that the monotonically non-decreasing period is not behaving in the same way for different measurements. Right: here the data of a measurement of about 8 hours is shown again but the lamp has already been turned on for more than 2 days before the data acquisition. Even then the ratio is still monotonically non-decreasing.

of time for which the lamp is turned on and off. The decision whether the measurements give reproducible results is made by fitting the function

$$f(x) = a \cdot \mathrm{e}^{-\frac{x}{\tau}} + y_0 \tag{3.61}$$

to the data after the rapid increase. This function is used since the color center formation is following a quasi exponential function, at least at pulsed UV irradiation [Nev85]. The comparison of the parameters a and τ for the same intervals results in the interval which is chosen for the tritium measurements. In table 3.6 the relative RMS deviation of these fit parameters for each kind of interval measurement are listed together with the results of the fit parameters. Furthermore, a diagram of each fit parameter result is shown in figure 3.36.

Overall there are 8 different intervals each tested with at least 2 measurements. The shortest time the light source was turned on for is 30 minutes and the longest 90 minutes. No shorter periods are used, since only the part of the measurement that occurs after the rapid increase is used for analysis. Longer measurements would immoderately increase the time to get a sufficient number of measurements and therefore are not tested. The period of time the light is turned off lasts from 15 minutes to 90 minutes.

By looking at figure 3.36 one can see, that the values of the y intercept y_0 is not stable over the measurements but decreasing. That behavior can be explained by the formation

Table 3.6: Relative RMS deviation of the fit parameters a and τ used to find the best measurement interval. In addition to this, the period of time the light source is turned off and on and the number of measurements performed with a given interval procedure are listed. For measurements marked with * the fit is done from time values above 900 s until the end of the measurement and for those marked with † from 2 500 s onwards.

light off /min	light on /min	measurements	$\sigma_{\mathrm{RMS,a}}$ /%	$\sigma_{\mathrm{RMS},\tau}$ /%
15*	30	4	37.0	7.0
45*	30	3	28.8	5.6
30*	30	3	49.0	12.1
60*	30	4	25.6	8.7
70*	30	8	14.7	6.1
60,70*	70	2	20.9	7.4
40†	40	2	20.9	7.9
90†	90	5	11.6	23.8
90†	90	53	9.1	11.2

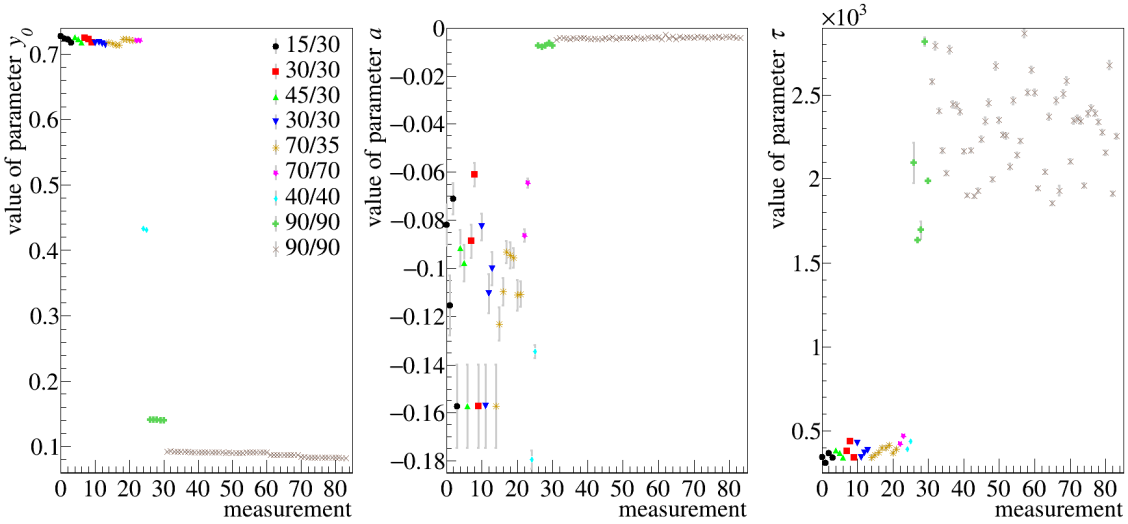

Figure 3.36: Diagram of the fit results of the interval measurements for the Fibertest II. In each diagram the fit parameter value is plotted against the measurement number consisting of one period of time where the light source was both off and on. For all diagrams the large difference between the first and the latest measurement is conspicuously. On the one hand this difference is caused by several modifications to the setup during the commissioning phase including the exchange of a photodiode as it became untransparent for UV light due to being irradiated with the light of the unfiltered deuterium lamp. On the other hand more and more color centers are already produced on both photodiodes from measurement to measurement. The left diagram shows the values of the y intercept y_0. The diagram in the middle shows the factor a. The diagram on the right shows the time-constant τ values. Note that except for the second 90/90 and the 70/70 measurements there is always one measurement where the light source is turned off for a much longer time than the usual interval duration, e.g. over night.

of color centers. If the irradiation stops, color centers form back within a time period of 2 to 3 weeks [Nev85]. If the same time constant of regeneration for the light path to the monitoring and to the measurement photodiode can be expected (which seems to be reasonable as it is the same defect in the same material) the regeneration is larger in case of the light path to the monitoring photodiode due to the larger starting value of color centers. Therefore, the ratio is decreasing from measurement to measurement. In addition, it can be expected that the decrease in the ratio shows an exponential behavior due to the saturation of the color center concentration (see also section 3.38). Therefore, a and τ are used for comparing the different intervals, but not y_0.

As the fit parameters a and τ of the different kinds of intervals also vary in their value the relative RMS deviation of the fit parameters is used to find the best interval. The deviations for these fit parameters are given in table 3.6. As one can see the measurements with intervals of 70 min off / 30 min on and 90 min off / 90 min on are the most suitable intervals according to this criterion. As the 90 min interval has the advantage of more data points which can be used to fit the exponential function this interval is used for all the following measurements. The way how the data is analyzed which is collected during the interval measurements with the Fibertest II, is described in detail in the following section.

3.2.3.5 Analysis method for Fibertest II

In this section the analyzing procedure of the interval measurements is described. To make all the data independent of fluctuations of the light source the ratio of the signals of the measurement and the monitoring photodiode is calculated and used as the main measurement parameter. As it was already described in the last section, the data of each interval follows (after a first, sharp increase) an exponential behavior due to the formation of color centers in the optical materials described by [Nev85] (see also equation (3.61)). To find a comparable point from which the exponential fit starts the slope of the data is used: if the slope of the following 88 ratio values is less than $1.647 \cdot 10^{-7}$ the fit is started from this ratio value. That this function describes the data well can be seen in figure 3.37, where an exemplary fit, its residues and the statistics of the residues can be found.

The results of the fit parameters a and τ stay stable over time. Therefore, a change in the parameters after the fiber is exposed to tritium can be seen directly if the values after exposure leave the 5σ error range of the data before exposure. In case of the y intercept y_0 the analysis is different. This parameter is decreasing with time: the light path from the y-cable to the monitoring photodiode and the photodiode itself are irradiated with more intensity than the light path to the measurement photodiode and the photodiode itself. Therefore, the formation of color centers is faster in case of the monitoring photodiode. That can be seen in the data as the ratio increases from the time the light source is turned on until it is turned off again. The moment it is turned off there are more color centers on the part of the setup leading to the monitoring photodiode. As it is known that color centers produced by UV irradiation recover with time [Nev85], it can be assumed that there is also a regeneration of the transmission in case of the Fibertest II as soon as the light source is turned off. If an exponential recovery of the color centers and the same time constant is assumed, the absolute number of color centers decreases faster in case of the light path to the monitoring photodiode. For that reason the signal of the monitoring photodiode is more regenerated than that of the measurement photodiode, meaning that the ratio is decreased. It is expected that y_0 behaves as described until the saturation of

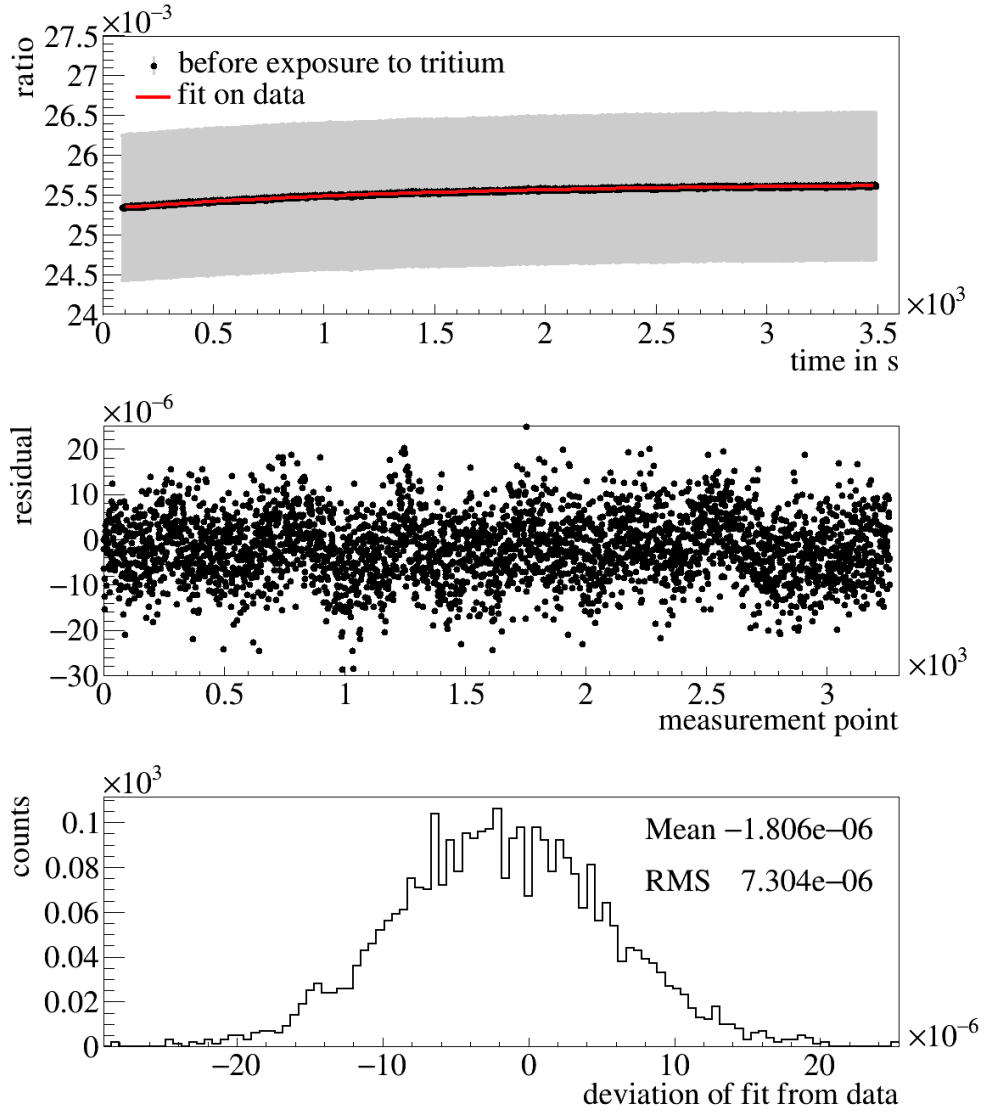

Figure 3.37: Exemplary fit on Fibertest II data, its statistics and residues. In all three diagrams data and the corresponding analysis of the 35^{th} measurement before tritium of the third fiber are shown. In the diagram at the top the measured ratio is shown. The rapid increase at the beginning of the measurement is already cut off. The time is corrected in a way, that it starts at 0. In addition, the fit adapted to the data is shown. In the middle the residues of each measurement point is plotted. The residues are evenly distributed around zero and the values of the residues are all below $3{\cdot}10^{-5}$. The statistic of the corresponding residues are plotted in the diagram at the bottom of this figure. The histogram has the shape of a normal curve. The mean value and the RMS deviation of the data are also given in the histogram. According to these values the mean deviation of the fit with the ratio data is compatible with zero. Overall one can conclude that neither the plot of the residues itself nor its statistics imply a misacception of the fit function.

color centers in the material is reached. A formula describing such a behavior is

$$y_0(x) = e^{-\tau_1 \cdot x} + y_1. \tag{3.62}$$

As a result a comparison between the y_0 value before the exposure to tritium with those during the exposure can be achieved by comparing the parameters of an exponential fit with the formula given in equation (3.62) or more precisely by the time constant τ_2 of this exponential fit. The fit is performed in blocks of 5 measurement points at a time in case of fiber 1 and 2 and 8 measurement points in case of fiber 3 and the values of the fit parameters are used to detect a change caused by the tritium exposure. To improve the low statistics of these fits the so-called bootstrap method is used [Efr94]: during bootstrapping 5 or 8 pairs of y_0 values and measurement number are drawn with replacement from a certain block. The fit is now performed on this "new" data set. This procedure is performed not only once but 100 000 times. From these 100 000 fit parameters the weighted mean and the RMS deviation are calculated and used for further analysis. To attach the greatest importance to the time constant of the fit, the bootstrap procedure is performed on all the data before tritium first. Then the mean value of the parameter y_1 is calculated and used for a second fit iteration. In this way all changes in the behavior of the decrease in y_0 are represented by changes in τ_1. All the steps of the analysis are illustrated in figure 3.38.

Before the results obtained with this analysis method are shown, the execution of the measurements is described in detail.

3.2.3.6 Execution of measurements

All the measurements with the microscope and the Fibertest II setup are performed as described in section 3.2.3.4. Before a new fiber is installed in the primary system the bellow and the two flanges with the fiber feed-throughs are decontaminated to values below $20\,\mathrm{Bq\,cm^{-2}}$. In so doing it is ensured that the fibers are not exposed to tritium gas emerging from the walls of the primary system during the reference measurements before the actual exposure.

The pressure in the primary system during the reference measurements before exposure is less than the lowest pressure detectable with the installed pressure sensor, meaning below 10^{-5} mbar. The tritium partial pressure during the exposure to tritium is almost the same for all fibers, as the same test gas cylinder with a volume of about $10\,\mathrm{cm^3}$ is filled with about 10 mbar gas and this gas is expanded into the evacuated system. The time periods of the measurements before and during tritium exposure vary widely. Both the pressures and the time periods are summarized in table 3.7.

In addition to the measurements before and during tritium exposure there are also measurements after the tritium exposure in case of fiber 3. These measurements are preformed in an evacuated system, which means that the pressure inside of the primary system is below 10^{-5} mbar. As the tritium emerging from the walls of the primary system is pumped out immediately it can be assumed that no further exposure to tritium takes place. Therefore, the conditions of these measurements are comparable to those during the measurements before exposure.

In the following section the results of both of the Fibertest II, executed as described here, and the microscopic examination of the three fibers are shown.

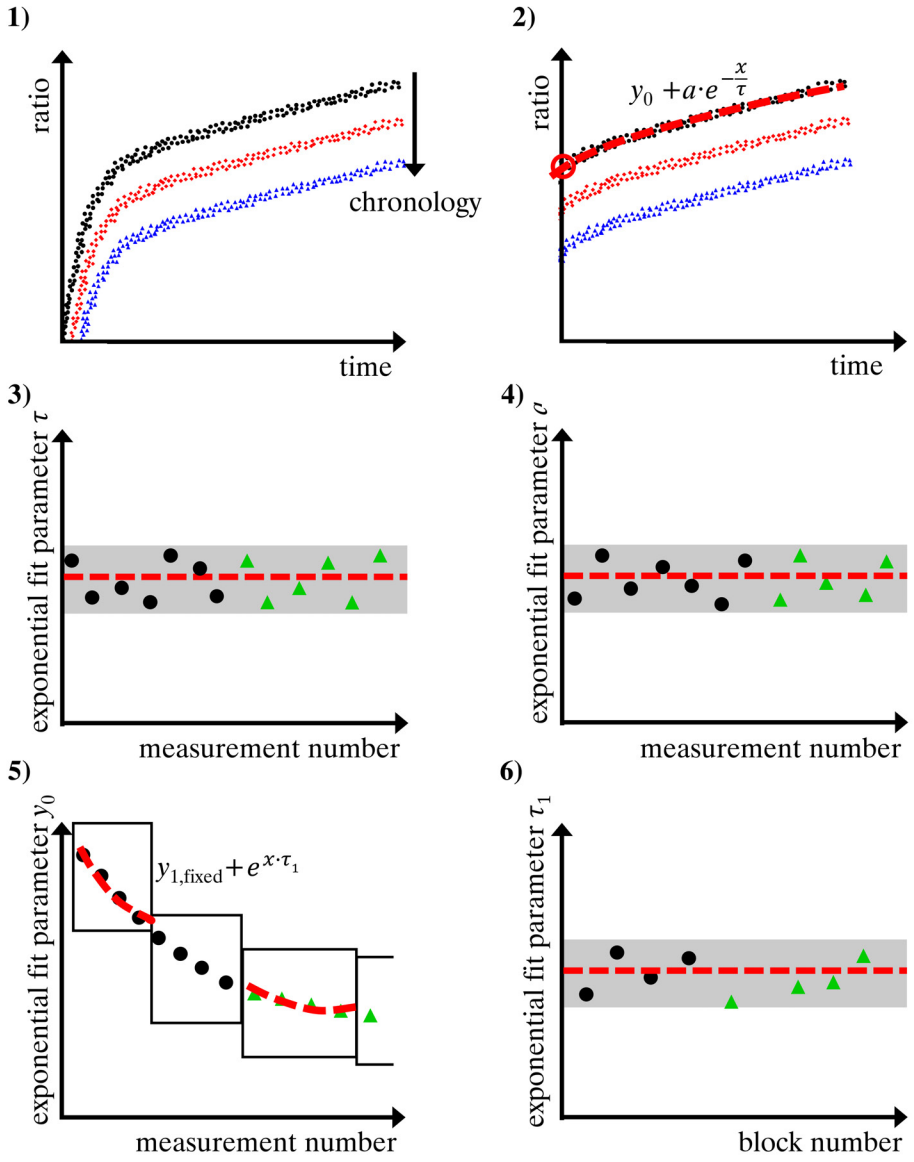

Figure 3.38: Scheme explaining the analysis method of the Fibertest II. 1) Here it is shown what the raw data of the ratio looks like when it is plotted against time. Each interval has a lower ratio than the one before. 2) The data after the cut off at the beginning is shown. The time is also adjusted to this cut off, so that the time of each interval starts at 0. To this data a line with the given function is fitted. 3) and 4) The fit parameters τ and a are plotted in a diagram. In addition, the mean value and the standard deviation of the measurements before tritium are calculated and plotted in the same diagram. If the data during the tritium exposure does not significantly differ from this mean value no change in these parameters due to the tritium exposure is detectable. 5) The decreasing values of the y intercept y_0 are shown. To check if the decrease is the same before and during the exposure the given equation is fitted to the data. Note that the y intercept of the fit is fixed, so that the only fit parameter is the time constant τ_1. The fit is always performed at blocks of 5 or 8 data points depending on the fiber. 6) The values of the fit parameter τ_1 are plotted against the block number. Just like in diagrams 3) and 4) the mean value and the standard deviation of the measurements before tritium are plotted in the diagram as well. If the parameter values are not changing after the exposure to tritium the transmission properties are also unchanged. Diagrams like those shown in 3), 4) and 6) are given in section 3.2.3.7 for each of the fibers.

Table 3.7: Summary of the measurements performed during the Fibertest II. In addition to the time periods measured before, during and after the tritium exposure the pressure in the primary system is given. By mistake the pressure in the system is much higher in case of fiber 2 as an intermediate piece was not evacuated before the gas was expanded from the test gas cylinder into the primary system. Therefore, the pressure in the system was much larger than the tritium partial pressure. The pressure due to the gas expansion from the test gas cylinder is assumed to be about (0.55 ± 5) mbar as the test gas cylinder was filled with 10 mbar gas just like it was for the other fibers. Since the gas that the test gas cylinders are filled with is not 100% pure tritium gas, a gas chromatography of the gas is performed. The tritium content measured is given in the fifth column.

fiber	measurement time in vaccum	measurement time in tritium	pressure in system	tritium content	measurement time after tritium
1	4 days	21 days	0.55 mbar	84 ± 5 %	-
2	7 days	7 days	> 3.4 mbar/ 0.55 ± 5 mbar	94 ± 5 %	-
3	13 days	26 days	0.61 mbar	95 ± 5 %	27 days

3.2.3.7 Results of Fibertest II

In this section, first the effect of tritium on the transmission of fibers is investigated and afterwards the results of the microscopic examination are presented.

The results of the fit parameters of the first fiber are plotted in the diagrams of figure 3.39. In case of parameter a one can see a slight increase of the values both before and after the tritium filling but the points do not leave the $5\,\sigma$ range of the fit. For the τ fit parameter no significant change of the values after the exposure is visible either. Even a slight change or a drift cannot be detected. Concerning the parameter y_0 one first has to notice that the general curve shape looks as expected. The ratio decreases before and after the tritium exposure in a similar way. But the more precise analysis with the exponential fit and the bootstrap method gives an increase in the time constant of the exponential fit.

The results of the fits performed for the data of the second fiber are shown in the figures 3.40 and 3.41. In contrast to the results of the first fiber those of the second neither show a change in the parameter a nor in the parameter τ. In addition, there are more outliers especially before the tritium exposure. In case of the y-intercept the two main finds are prominent: the parameter values seem to fluctuate around a general curve shape and there is a sudden rise of the y-intercept directly after filling the system with tritium. As this rise is caused by the filling of the system with a pressure of more than 3.4 mbar (compare appendix A.3 on page 200 and [Ste93, Bur00]) the data is corrected for the difference caused by the pressure change. After the correction the data before and after the exposure roughly follows the same curve shape again. With the corrected data the second exponential fit and the bootstrap method are performed. The results of these analyses are also presented in figure 3.40. Due to the fluctuation of the y_0 parameters around a general behavior, the error bars of the time constants of the fit on this data are very large meaning that the minimum error is in the order of twice the value itself. Due to the large error bars the values of each block both of the data before and during tritium exposure are easily compatible with each other.

For the third fiber figure 3.42 shows not only the values of the fit parameters before

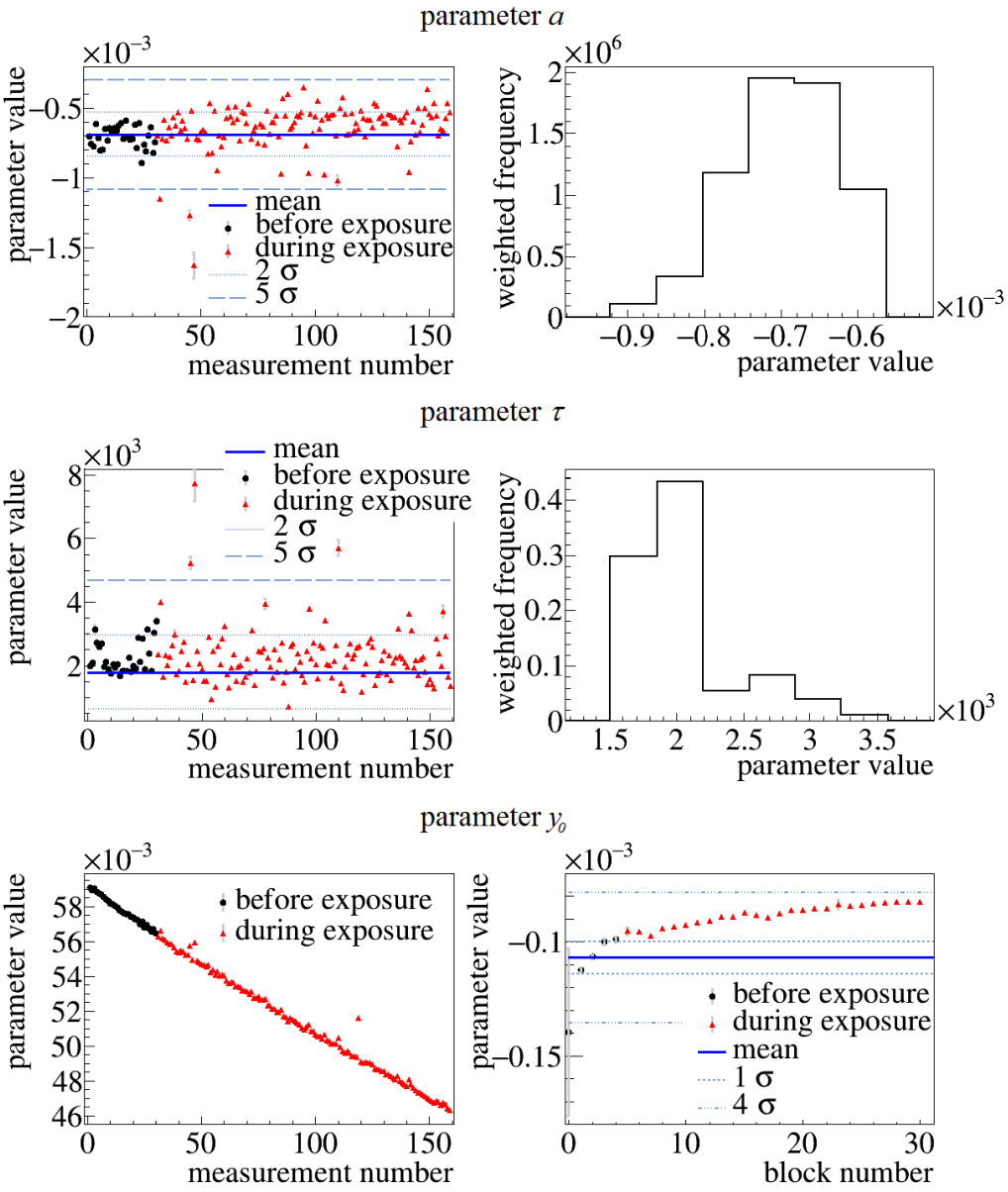

Figure 3.39: Diagrams for the parameters a, τ, y_0 and τ_1 of fiber 1. In all scatter diagrams the black dots are values before and the red triangles are values during the tritium exposure. If the error bars are not visible, they are smaller than the marks. Top row: on the left side a diagram of the parameter a against the measurement number is shown. The data during the tritium exposure slightly increases with the measurement number. In addition, the mean value as well as the $2\,\sigma$ and $5\,\sigma$ interval are shown. In the histogram on the right side the distribution of the data before tritium is presented. The distribution looks similar to a normally distributed data set. As only 30 measurements before tritium are performed the statistics is not high enough for a clear statement. Middle row: on the left side again the parameter τ is plotted against the measurement number and on the right side the weighted frequency against the parameter value. It is remarkable that there are only data points with greater variance at values above the mean value. The data during exposure also has a slight tendency towards higher values, but there is neither a significant change nor a drift clearly visible. Bottom row: the left diagram presents the values of the parameter y_0. Except for 3 to 4 outliers among the points during tritium exposure no unexpected behavior can be found. In the diagram at the right side the results of the parameter τ_2 of the exponential fitting and bootstrapping is plotted against the block number. One block combines 5 measurement points of the diagram on the left. During all blocks, meaning both the values before and during tritium exposure, there is an increase in the value noticeable.

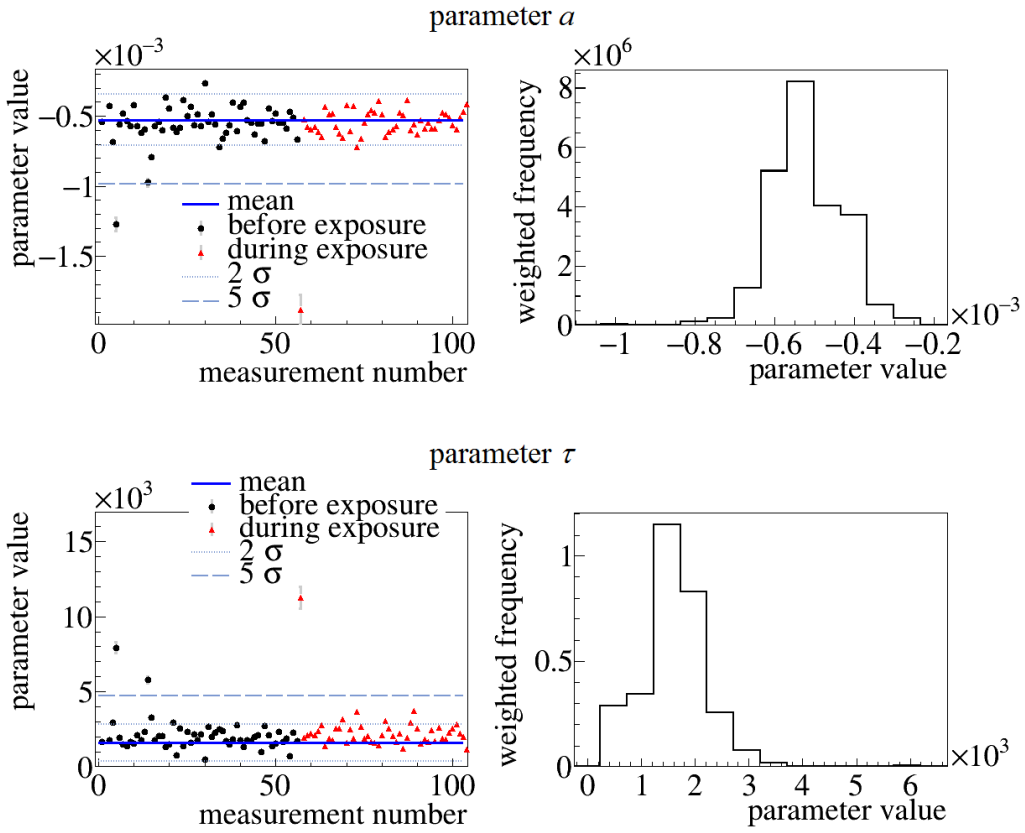

Figure 3.40: Diagrams of the parameters a and τ of fiber 2. The black dots in the diagrams mark the data before and the red triangles the data during the tritium exposure. The blue solid lines in the scatter plots indicate the mean value of the data points and the dashed and dotted lines different σ intervals before tritium. All data points are plotted with their errors, if the error bars are not visible they are smaller than the markers. Top row: here the results of fit parameter a is presented. Both, the data before and during exposure, are statistically distributed around the mean value of the data before tritium (left diagram). The statistical distribution of the data before tritium can also be seen in the histogram on the right side, where the weighted frequency of parameter a is plotted against the parameter value. Bottom row: the scatter plot at the left side shows the parameter τ plotted against the measurement number and in the histogram at the right side the weighted frequency of τ is plotted against the parameter value. In both diagrams the statistical distribution of the data before tritium is noticeable. In addition, one can see that the data during the tritium exposure does not show a significant change from the reference data. It must just be mentioned that there is a slight tendency of the parameter values towards values which are higher than the mean value.

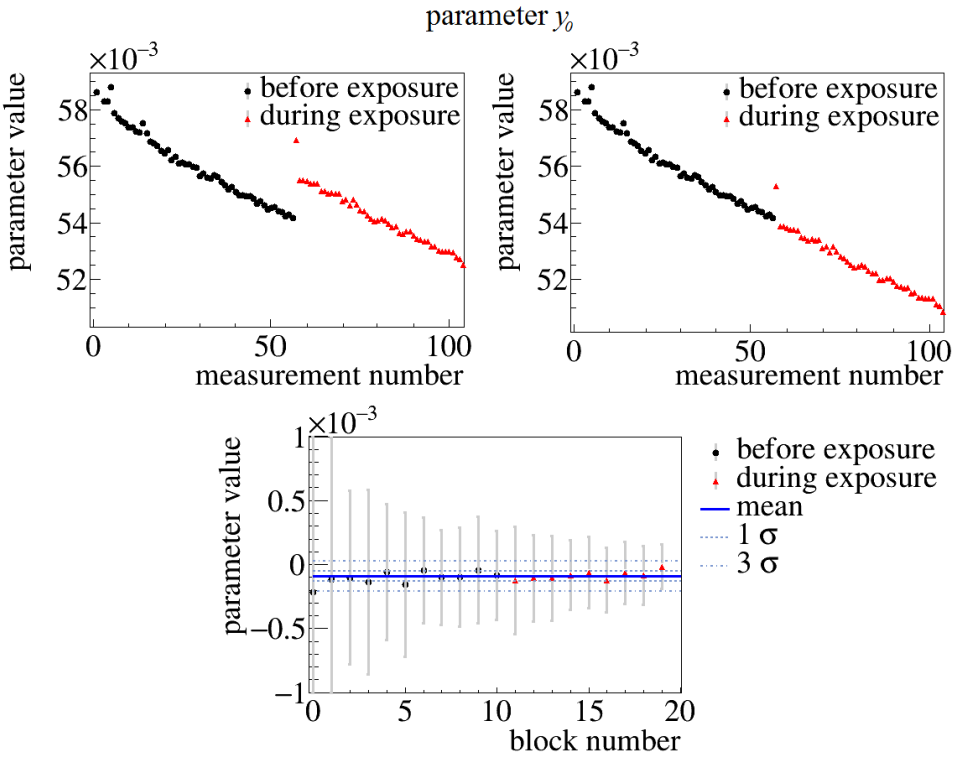

Figure 3.41: Diagrams of the parameters y_0 and τ_1 of fiber 2. In each diagram the black dots mark the data before and the red triangles the data during the tritium exposure. In addition, in the diagram at the bottom the mean value (blue solid line) and the $1\,\sigma$ and $3\,\sigma$ intervals (dotted or dotted and dashed blue line) are plotted. In case that the error bars of the data points are not visible, they are smaller than the marker. Top row: in both diagrams the parameter y_0 is plotted against the measurement number. The difference between the two diagrams is, that the data in the right diagram is corrected for the sudden rise caused by the filling of the system with a pressure of more than 3.4 mbar. Bottom: here the parameter τ_1, which is the result of bootstrapping and exponentially fitting the data of the corrected parameter y_0, is plotted against the block number. Each block consists of 5 measurements. Due to the large error bars, which are most likely caused by the small fluctuation of the data points also visible in the two diagrams above, all data points are compatible with each other. Therefore, no change in the parameter can be detected.

and during the tritium exposure but also the fit parameters of measurements after the tritium exposure at vacuum. By looking at the diagram of the parameter a one can see that about the first half of the data during tritium exposure is consistent with the data before tritium. Afterwards there is a slight drift of the parameter towards larger values. However, the change is only in the order of $3\,\sigma$. A change in the values of the parameter τ is not observable. The y_0 parameter again shows the expected decay with time. But directly after the tritium exposure the value of y_0 first decreases followed by an increase. The analysis with the bootstrap method and additional exponential fitting gives fluctuant time constants τ_1. After a rapid decrease of the value in case of the first three blocks the value increases again and stabilizes in the $1\,\sigma$ interval around the mean value of $(-2.22 \pm 0.07)\cdot 10^{-5}$. After the tritium injection the parameter stays inside of the $1\,\sigma$ interval for 11 blocks before it leaves out. The parameter saturates again at a value of $(-2.112 \pm 0.005)\cdot 10^{-5}$. The first block after the tritium is pumped off again is also at this saturation point. But then the τ_1 value decreases for 8 blocks to increase again until

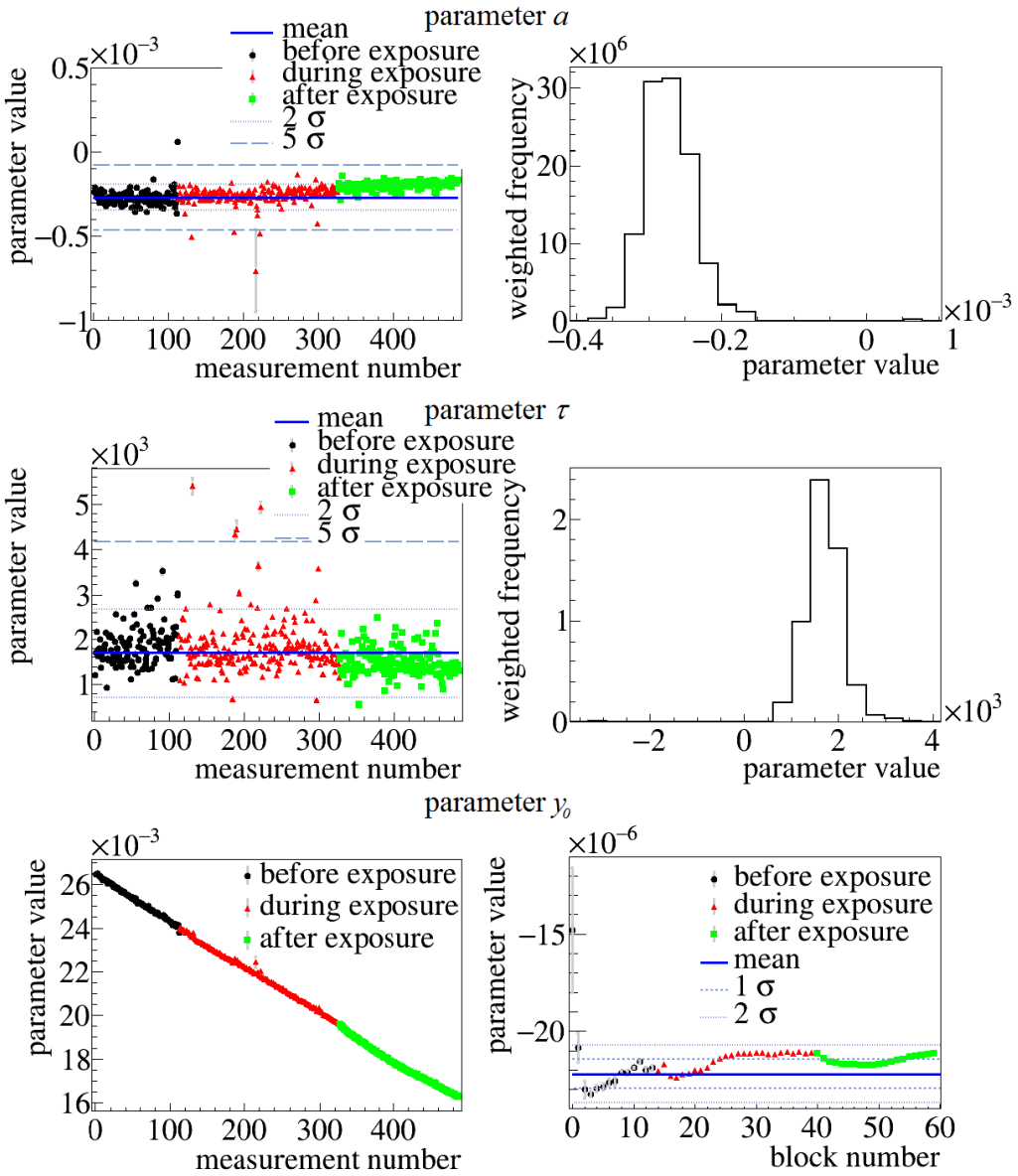

Figure 3.42: Diagrams of the parameters a, τ, y_0 and τ_1 of fiber 3. In the scatter plots at the left side of this figure the respective parameter is plotted against the measurement number. In all scatter plots of this figure the black points mark the data before, the red triangles the data during and the green squares the data after tritium exposure. As every data point is plotted together with its error, the error is smaller than the marker if the error is not visible. Top row: in this row the data of parameter a is plotted. As one can conclude from the histogram at the right side, where the weighted frequency is plotted against the parameter value, the data points before the exposure are normally distributed around their mean value. Up to about half of the data during exposure shows the same behavior. Afterwards the parameter value slightly increases, which also continues in the data after the tritium exposure. Mid row: in the scatter plot of parameter τ two outliers are not shown for better visualization of the remaining data points, one before the tritium exposure with a value of $-3\,057 \pm 122$ and one during the exposure of $24\,040 \pm 8\,999$. The data before tritium is normally distributed (see histogram) and the data after tritium exposure has a slight tendency towards lower values. A significant change of the data during tritium is not noticeable. Bottom row: the values of the parameter y_0 plotted at the right diagram show a slight drop after the primary system is evacuated again. The values of the parameter τ_1 which are plotted in the right diagram against the block number show a similar variation in each time period of the experiment: first the data decreases after which it increases and finally saturates. This happens within the $2\,\sigma$ interval around the mean of the reference data.

the saturation value is reached at the last measurement block again. Therefore, it is not possible to predict, if the parameter saturates again at that value or further increases.

The microscopic examination yields similar observations for all fibers before the exposure to tritium:

- There is a great number of small points at the surface of the fiber. Most of these points are dust particles but the possibility that some of these points are also small damage points cannot be excluded.
- There are some cracks at the fibers most likely caused by the mechanical stress during manufacturing, transport and installation in the fiber holder.
- The first and the second fiber have some features, which can also be seen in figure 3.43 among others. But purely based on the microscopic examination it is hard to say, if these features are imperfections of the fiber or inclusions in the material.

When examining the fibers after exposure special attention is paid to a possible change of the three observations made before the exposure, especially to cracks and scratches as tritium can enter the fiber more easily here: the number of small points is almost 0 after the exposure, which makes it possible to conclude, that these points really were dust particles which have been removed by the evacuation of the primary system. In contrast to the number of small points the number of cracks is further increased after the exposure. But this is most likely caused by the mechanical stress during the installation of the fiber in the primary system and the later disassembling as well as the transport in the glove box from the lock to the microscope. No significant change to the cracks before and after exposure is observable. The special features of the first and third fiber also show no change after the exposure to tritium (compare 3.43).

In addition, attention is paid to new small spots which do not look like dust particles and which could indicate damage caused by the tritium. However, all of those new points were revealed by a shadow to be scratches or deposits.

The results presented in this section are discussed and interpreted the following section.

3.2.3.8 Discussion of the results of Fibertest II

Before the results of the Fibertest II are discussed in detail some general remarks on the tritium exposure and transferability to the KATRIN experiment are addressed. The activity, dose rate and overall doses during the Fibertest II experiment are given for each fiber in table 3.8. In case of the overall dose a maximum value is given in the table. This is the case, since a small part of the tritium diffuses into the walls of the primary system due to wall exchange reactions [Mor77]. Nevertheless, the overall tritium content is assumed to change by no more than 1 % or 2 %. A similar decrease was measured in [Fis11] in which the composition of gas filled in a stainless steel primary system was monitored over more than 22 days. During this time the content of tritiated hydrogen isotopologues HT, DT and T_2 changed but the overall tritium content stayed almost the same. The overall dose during the 3 years of measurement time of KATRIN is in the order of 10 Gy to 20 Gy. For that reason the overall dose during the exposure of the Fibertest II is about 2 to 3 orders of magnitude larger. Therefore, the compaction due to the irradiation with low energy electrons should be larger in the Fibertest II compared with KATRIN as well, as it follows an almost linear dose dependence at low doses [Nor74]. Even if the tritium which is diffused into the fiber material has a larger impact, the effects during KATRIN are simulated with the Fibertest II, as the diffusion is also proportional to the partial

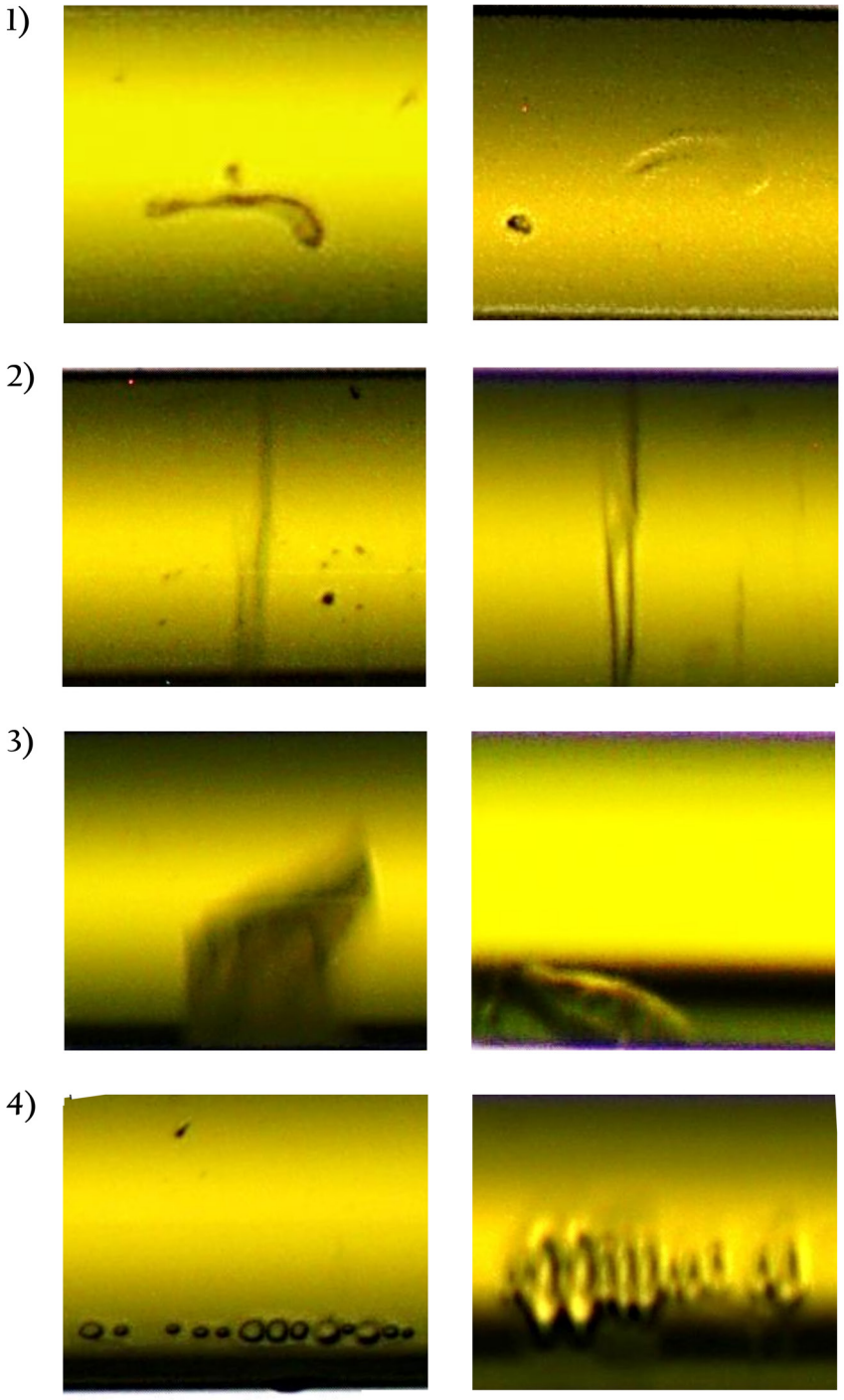

Figure 3.43: Microscopic view on the fibers before and after tritium exposure. The left column shows the fibers before and the right column after the exposure to tritium. In (1) a feature of the first fiber is shown and no change is visible (the different colors are caused by a different irradiation of the fiber). In (2) one can see pictures of the second fiber. Both the small points and a crack can be seen before the exposure. Afterwards the points are removed, but there are additional smaller cracks. (3) and (4) show features of the third fiber but from a different viewing angle. The exposed fiber shown in (4) is turned by 180°. In addition the fiber is rotated in a way that the feature can be seen directly from above. No change in the features is noticeable after the exposure.

Table 3.8: Summary of the activity, dose rate and overall dose the fibers are exposed to during the Fibertest II.

fiber	activity in Bq	dose rate in $\mathrm{Gy\,s^{-1}}$	dose in Gy
1	$(7.9 \pm 0.5) \cdot 10^9$	$(6.4 \pm 0.4) \cdot 10^{-3}$	$\leq (1.2 \pm 0.7) \cdot 10^4$
2	$(8.9 \pm 0.5) \cdot 10^9$	$(7.2 \pm 0.4) \cdot 10^{-3}$	$\leq (4.4 \pm 0.2) \cdot 10^3$
3	$(9.0 \pm 0.5) \cdot 10^9$	$(7.2 \pm 0.4) \cdot 10^{-3}$	$\leq (1.6 \pm 0.9) \cdot 10^4$

pressure, which is more than 4 orders of magnitude higher during the Fibertest II than during KATRIN. In summary it can be stated, that an exposure time of about 1 hour under conditions as they are at during the Fibertest II simulates the exposure during the whole KATRIN experiment[45].

Concerning the fit parameter a there are only small changes observable for all fibers, especially in the case of the second fiber where no change can be found at all. The values of fiber 1 increase with a slope of $(8.1 \pm 2.2) \cdot 10^{-7}$ per measurement point if the outliers of the measurement, meaning points 32, 45 and 47, are not taken into account. The slope of the parameter values of fiber 3 are even lower with $(1.5 \pm 0.2) \cdot 10^{-7}$ per measurement point during the exposure. This change in the parameter value means that the $1\,\sigma$ deviation of the measurement points before exposure of $7.9 \cdot 10^{-5}$ (fiber 1) and $3.7 \cdot 10^{-5}$ (fiber 3) are reached after 98 days or 247 days exposure on average. Converted to KATRIN conditions this is equivalent to an exposure time of at least 294 years or 741 years. An increase of the negative parameter a means that the exponential part of equation (3.61) is getting smaller and therefore the increase of the ratio especially at the beginning of the interval measurement is not as steep anymore. This might be evidence of saturation of the color center formation. In that case the exponential shape of the curve after the start period should be less important and the curve should change to a stable value. This theory is supported by the fact that the measurements after the exposure of fiber 3 show the same increase with a compatible slope of $(1.7 \pm 0.3) \cdot 10^{-7}$ per measurement point.

That the time constant τ of the exponential fit stays the same in case of all fibers is evidence that the tritium exposure does not change the characteristics of the color center formation during tritium exposure. If that was the case a change of τ during the measurement would have been expected.

Similar to parameter a the fit parameter τ_2 of the exponential fit on the values of y_0 only shows a detectable change in case of the first and the second fiber. The change of the first fiber seems to follow an exponential behavior again, but since the values already increase for the blocks before the tritium exposure, it is unlikely that this is caused by the tritium. Nevertheless, the specific parameters of the change could be effected by the tritium exposure. To check if this is the case an exponential fit of the kind in equation (3.61) is fitted to both the data before and during the exposure. The two fit functions are then given by:

$$f(x)_{\text{before}} = (-9.20 \pm 0.83) \cdot 10^{-5} + (-3.05 \pm 0.49) \cdot 10^{-5} \cdot e^{-\frac{x}{2.6 \pm 1.7}}, \tag{3.63}$$

$$f(x)_{\text{during}} = (-7.76 \pm 0.17) \cdot 10^{-5} + (-2.48 \pm 0.10) \cdot 10^{-5} \cdot e^{-\frac{x}{18.0 \pm 3.8}}. \tag{3.64}$$

By comparing these functions one can see that the largest difference of the fit parameters can be found in the time constants (the factor in front of the exponential function is

[45] This is correct even if the more than 10 % of the tritium is absorbed in the walls of the primary system.

compatible within the errors, the y-intercept is compatible within $1.5\,\sigma$ and the time constant within $2.8\,\sigma$). During the exposure the time constant is larger than before. Overall the parameter τ_1 described by the function $f(x)_{\text{during}}$ also reaches higher values than with the function $f(x)_{\text{before}}$. In the context of the Fibertest II this means that the y-intercepts are decreasing more slowly and if this is the case the transmission through the fiber is also decreasing more slowly. So, one can conclude that there is a slight change in the specific behavior of the decrease of the y-intercepts detectable, which would even improve the performance of the fibers.

Concerning the τ_2 parameters of the third fiber an explanation as to why it shows the same behavior for the data before, during and after the exposure is hard to come by. As the data points are not normally distributed, it is assumed that a systematical effect of the measurement parameters is noticeable in the data. As the measurement was performed exactly like the measurements with the other two fibers before and those fibers have not shown the same behavior no explanation can be given. Nevertheless, as the parameter does not decrease but rather increases after the tritium exposure a negative effect of the tritium on the transmission can be excluded in case of this parameter as well.

Overall the measurements with the Fibertest II show that the transmission of the fibers in a tritium atmosphere is definitely not worsened. This is also supported by the results of the microscopic examination: no evidence of damage caused by the tritium could be found not even at those positions of the fiber which were already mechanically damaged before the installation in the primary system.

For that reason one can say that the Fibertest II and the microscopic examination have demonstrated that the usage of these kinds of fibers in a tritium atmosphere is possible without degradation of their optical properties.

3.3 Consequences for the Rear Section

In the previous sections the answers to the four questions concerning tritium compatibility and general suitability of components stated at the beginning of this chapter are given:

Is a piezo based motor suitable for the KATRIN experiment, meaning that it can perform more than 100 000 driving cycles without failure even after multiple baked-outs at 150 °C? - Not every piezo motor is suitable for a tritium atmosphere and the KATRIN requirements. The tested N-310K176 meets all the requirements. In the case of the minimum number of possible driving cycles it exceeds the requirement by more than a factor of 2 and the performance after a bake-out is also sufficient. Therefore, the motor is suitable for the usage at the Rear Section. The hole of the Rear Wall can be opened if the e-gun beam must pass the Rear Wall and be closed again to provide a closed gold surface to the source plasma. Its later position at the backside of the Rear Wall is, as it was already shown in figure 3.2. Due to its large dimensions the motor must be placed at the Rear Wall in exactly the position shown in this figure. The new motor is on site already. As it is possible to place the motor behind the Rear Wall as planned another question must be asked now: does the plasma see a homogeneous surface potential if the hole is closed and is there a deviation at the edges of the hole? This question is addressed in the next chapter.

Is the electron rate produced by the planned optical system high enough to meet the requirements of at least 10^4 electrons per second and of an electron energy spread of

$\sigma_E < 0.2\,eV$? - Partially based on the experience made during the Fibertest II the optical setup for the e-gun of the Rear Section has been designed. The resulting e-gun rate was calculated: the rate is at maximum 1 orders of magnitude higher than the required rate (at slit width 3 mm, with a gold work function of 4.2 eV and a design wavelength of 275 nm). The corresponding σ_E is found to be about 0.07 eV, if only the wavelength distribution of the incident light and not the distribution of the gold work function is taken into account. That means that even if the transmission decreases due to the UV irradiation the required e-gun rate seems to be feasible. Nevertheless, due to the experience with the Fibertest experiment it is recommended to carefully monitor the light intensity as described above. In addition, the rate is calculated in dependence of the wavelength of the light, the work function of the gold layer and the slit width of the monochromator. Due to these results the design of the e-gun optics is fixed and will be used at the e-gun as described.

Is the tritium leak rate through an optical fiber feed-through below $10^{-9}\,mbar\,l\,s^{-1}$ that the feed-through poses no safety risk when installed as part of a tritium containing system? - The optical fiber feed-through of the manufacturer VACOM was successfully qualified for the usage as part of the second containment. The leak rate of the component is found to be more that 4 orders of magnitude lower than the required value. For that reason the fiber feed-through will be used at the final optical setup of the e-gun irradiation.

Are the optical transmission properties of a fiber affected when installed inside of a tritium containing system? - UV fibers were successfully qualified by the Fibertest II as well. The fibers were found to show no degradation in transmission. Therefore, the fiber irradiation of the gold cathode in the primary system will be implemented as planned. In addition, helpful experience was gained as the fiber was tested under similar conditions as is the case during the e-gun operation at the Rear Section: the transmission of the fiber can be affected not only by the tritium environment but also by the vacuum and UV irradiation. Especially the UV irradiation and the losses caused by it have to be taken into account: an investigation of the light intensity stability is recommended as part of the commissioning of the optical setup. If the light intensity decreases with too large gradient ($\geq 0.1\,\%$ within several minutes), a test of the individual components and, if necessary, an replacement of the most affected components is required. Furthermore, a precise monitoring of the intensity with a detector is necessary. Among other things, that is the reason why a detector, monitoring the light intensity, is placed as close to the cathode as possible. The parts not monitored by that detector are the focusing system, the feed-through window and the fiber in the primary system. The monitoring of those parts must be performed directly by the electron rate: during commissioning the electron rates at all parameter settings, needed for the usual measurements with the e-gun, must be measured, so that the electron rate can be estimated by the monitored intensity at all times. If the electron rate deviate from the estimated value significantly, the unmonitored components must be assumed to be damaged. In addition, it is recommended to have at least some optics as spare parts available locally. This is why a second focusing system is aligned already at the commissioning of the optical system to make an easy and fast exchange possible. Also, the fiber system installed at the primary system is planned to be manufactured several times for the same reason.

In the following chapter the development of the Rear Wall occupies center stage. Most of the open questions related to the Rear Wall are addressed there.

Chapter 4

Development of a Rear Wall for the Rear Section

If the potential difference between the Rear Wall and the tube walls is between -50 mV and 100 mV, the Rear Wall may significantly influence the potential of the tritium source (compare 2.3.3). For that reason, it is required, that the Rear Wall surface potential is not only homogeneous but also temporally and spatially stable. In addition to the voltage applied to the Rear Wall, the surface potential has a material specific component which is not changeable by the experimentalists in any way: the work function Φ.

This chapter is dealing with the development of a Rear Wall which meets the requirements both on homogeneity and long-term stability of the work function. Concerning a suitable layer design, it is already known, that the surface layer must be gold. But the substrate and potential intermediate layers were not defined prior to this thesis. This also extends to the surface treatment before coating and the coating procedure itself. Promising designs concerning homogeneity were further investigated regarding their long-term stability and the effects of bake-outs and UV irradiation. To enable the passing of the electron beam produced by the Rear Section e-gun, the Rear Wall needs a central hole with 4 mm diameter. The manufacturing of this hole must be possible without damaging the substrate. In addition, a change in the work function close to the hole due to the manufacturing process must be minimized, or optimally excluded. The importance of this is emphasized by the fact, that the hole itself could affect the work function. It is known, that the work function can be changed by steps in the surface [Jia97, Jia98a]. Once the optimal layer design is found, final Rear Wall candidates which could in principle be installed in the Rear Section as a final Rear Wall must be characterized.

In summary, the following questions must be answered to find a suitable design and the final Rear Wall:

1. Which Rear Wall layer design is most qualified for KATRIN?
2. Is the work function and its distribution stable over several weeks?
3. How does a bake-out or UV light irradiation affect the work function and its homogeneity?
4. How does a central hole affect the work function at the center region of the flux tube?
5. How large are the work function deviations of final Rear Wall candidates and how is the work function distributed over the sample?

To answer these questions several samples are produced. An overview of these samples is given in section 4.2. A first visual investigation of some of these samples is performed by a scanning electron microscope (see section 4.3). For the investigation of the work function a large variety of techniques is available. The most commonly used techniques are presented in section 4.4. Two of these techniques are suitable and available for the Rear Wall development: the Kelvin Probe technique and photoelectron spectroscopy. Three different setups, an ambient air Kelvin Probe, a vacuum Kelvin Probe and a setup at the monitor spectrometer of KATRIN, enable to obtain the required results. The setups, the performed measurements and the results are presented in the sections 4.5, 4.7 and 4.6. Prior to this, the requirements on the work function homogeneity are recapped in the following section 4.1.

4.1 Requirements on homogeneity and stability of the surface potential of the Rear Wall

The importance of the Rear Wall for KATRIN results from its interaction with the charged particles of the tritium source: due to the β-decay and subsequent ionization processes a mixture of plasma and neutral gas is formed in the source. The particles of this plasma are confined along the z-axis due to strong axially symmetric magnetic fields. For that reason the potential of the Rear Wall, on which the magnetic field lines impinge, is dominantly transported through the tritium source. This is the case as long as the difference between the Rear Wall potential and the potential of the tube walls is between -50 mV and 100 mV [Kuc16]. In that case, the electrostatic potential of the Rear wall defines the plasma potential of the source subsequently (compare section 2.3.3).

As the Rear Wall must define the plasma potential over the whole cross sectional area of the source, it is important that the whole technical flux tube[1] impinges on the Rear Wall surface. In principle electrons are generated over the whole outer flux tube. However, the outer flux tube is not transported through the whole KATRIN setup. Therefore, the technical flux tube is defined as the cross sectional area each component must completely transport towards the spectrometer instead. A magnetic field of 1.6 T is required at the position of the Rear Wall. By that, the cross sectional area of the technical flux tube is equal to or smaller than the gold surface provided by the Rear Wall. In that case the clearance between the end of the Rear Wall's gold surface and the technical flux tube is 1.3 mm. To compensate for manufacturing uncertainties, the magnetic field and as a consequence the clearance can be increased by adjusting the z-position of the Rear Wall inside of the recondenser magnet (compare [Bab14]).

The electrostatic potential of the Rear Wall can be shifted by an applied voltage source. This voltage source enables the adjustment of the Rear Wall potential with regard to the potential of the tube walls. Overall a shift of ± 10 V is possible. But the material specific work function of the Rear Wall cannot be controlled by this. Therefore, inhomogeneities and instabilities of the work function also cause inhomogeneities and instabilities in the source potential. As a consequence, the endpoint of the measured β-spectrum is shifted unnoticed (compare figure 4.1). This is caused by the fact, that the minimum electron energy which is needed to pass the spectrometer is determined by the potential difference between spectrometer and source. As the endpoint is one of the fit parameters in the final

[1] Overall there are 3 different flux tubes defined, namely the outer flux tube of 229 T cm^2, the technical flux tube of 210 T cm^2 and the inner flux tube of 191 T cm^2.

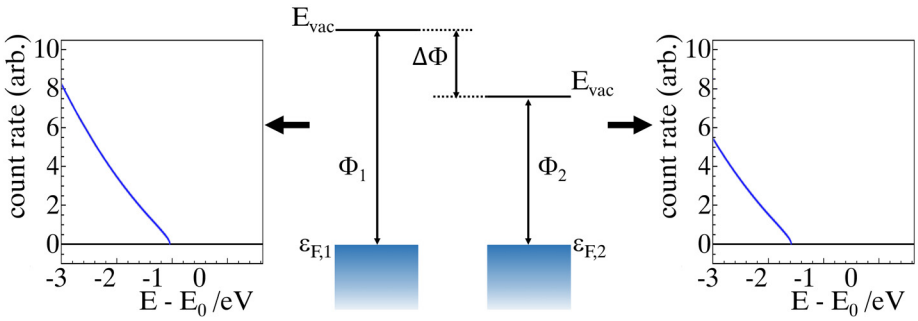

Figure 4.1: Influence of different work functions on the β-spectrum. In the center of the figure so-called energy level diagrams of two materials with different work functions are shown. The Fermi levels $\varepsilon_{F,1}$ and $\varepsilon_{F,2}$, the work functions Φ_1 and Φ_2 and the resulting vacuum potentials are drawn with respect to each other. The larger work function on the left side also causes a higher vacuum potential. Therefore, a β-electron with the kinetic energy $E_{\mathrm{kin,decay}}$, emitted on the left side, would seem to have a higher kinetic energy at the spectrometer than an electron with the same $E_{\mathrm{kin,decay}}$ at the right side. This leads to a shift in the spectrum at the detector (see corresponding diagrams of this figure).

analysis of the KATRIN data, variations in both the spectrometer high voltage and the plasma potential cause systematic uncertainties [Ang05].

For that reason strict requirements on the work function of the Rear Wall surface are imposed: the work function fluctuations must be [Bab13]

$$\sigma_{\mathrm{RMS,pixel}} < 20\,\mathrm{mV} \tag{4.1}$$

within the projected area of each of the 148 focal plane detector pixels of the focal plane detector on the surface of the Rear Wall[2]. The limitation on the detector pixels is possible, as each detector pixel is analyzed on its own. Due to the fact that the plasma smears out fluctuations which are at least smaller than the Debye length of about 0.4 mm (see 2.3.3), microscopic fluctuations are not included in this requirement.

In addition, the fluctuations over the whole Rear Wall must also be

$$\sigma_{\mathrm{RMS,surface}} < 20\,\mathrm{mV}. \tag{4.2}$$

This requirement enables an easier comparison of the data of the different pixels. But note that this requirement is not as absolute as the requirement for $\sigma_{\mathrm{RMS,pixel}}$. That means: if a Rear Wall passes the $\sigma_{\mathrm{RMS,pixel}}$ requirement but fails the $\sigma_{\mathrm{RMS,surface}}$ requirement, it can be considered suitable. This is the case, if the mean work function and $\sigma_{\mathrm{RMS,pixel}}$ values of the detector are regularly distributed over the surface, e.g. radially distributed or increasing from one side to the other.

The samples which are tested concerning these requirements are presented in the following section.

[2]The projected area is 0.86 cm^2 at the design z-position of the Rear Wall and a magnetic field of 1.6 T at the position of the Rear Wall.

4.2 Produced Rear Wall candidates

The samples produced for the Rear Wall development are, with exception of a gold foil, all based on a multilayer structure, which usually consists of the following layers:

1. **Top layer:** this layer is the only one which is in direct contact with the flux tube and the tritium atmosphere in the source. It must consist of gold for several reasons: gold has a high Z value of 79 which is needed to generate the required Bremsstrahlung for the monitoring of the source activity by BIXS. Besides that, gold is in general characterized by a high chemical inertness and a small degradation of the surface. Both is associated with a stable work function. In addition, it does not catalytically react with hydrogen molecules and has a small tritium adsorption of maximum (0.68 ± 0.10) monolayer at room temperature [Röl15]. For that reason gold outperfomrs most other elements.
   The gold used for the Rear Wall must be as pure as possible to minimize work function variations due to impurities. The possible coating methods are various, e.g. galvanization, chemical or physical vapor deposition. Important for the choice of the deposition technique is, that it results in a homogeneous work function.
2. **Intermediate layer:** an intermediate layer is not necessarily required. But the usage of a diffusion barrier can avoid the diffusion of the gold into the substrate or vice versa. An adhesion layer can improve the robustness of the Rear Wall if the gold does not stick well to the substrate. In case that a Rear Wall should also act as source activity monitoring tool by measuring the current of high energetic primary electrons an insulation layer with thickness in the order of a few nanometers is required. This layer must have an electric resistance above $10^6\,\Omega$ to prevent the low energetic secondary electrons from reaching the substrate of the Rear Wall. Otherwise the current measurement at the substrate is not linearly correlated with the source activity. In any case the selection of a suitable or even required intermediate layer depends on the substrate material.
3. **Substrate:** the substrate gives the Rear Wall the stability required during handling. Its surface must be flat and homogeneous to prevent a possible impact of flatness imperfections of the surface on the work function [Jia97, Jia98a]. The first generation of Rear Wall samples were produced with substrates of α-aluminum oxide ("corrundum" or sapphire), beryllium, silicon and copper: sapphire is tested as it is possible to epitaxially grow mono-crystalline gold layers on it [Käs02]. The test of beryllium is historically accounted for by former setup requirements. These have required, that the produced Bremsstrahlung could penetrate through the Rear Wall which is possible in case of beryllium. Silicon benefits from its wide availability in chip grade quality. In addition, it is the preferred substrate for a current measuring Rear Wall. The testing of copper is motivated by the successful production of a gold coated copper electrode [Kon11, Sch12] at the *a*SPECT experiment [Zim00].
   The second generation of Rear Wall samples concentrates more on widely available materials, which are easily processed: copper, aluminum and stainless steel. In addition, copper and stainless steel are commonly used at the tritium laboratory and also at KATRIN. So no further materials with possibly unknown effects on the source are integrated into the setup. Furthermore, the principle feasibility of gold coatings, which can be baked-out without affecting the gold layer, has already been shown at the tritium laboratory in case of these materials.

Rear Wall samples of smaller scale (mostly 3 inch) have been fabricated for the first development steps. Later 6 inch samples and so-called Rear Wall candidates are also

Table 4.1: Overview on stainless steel samples produced during the Rear Wall development. The name of each sample can be split in four parts: first a consecutive numbering of those samples which are similarly produced, then the substrate material followed by the polishing technique of the substrate and last the size of the sample. If there is a yes in the column "hole" this means, that the sample has a hole. Note that this hole does not necessarily need to be placed in the center of the sample. If the yes is additionally marked by * the sample has all the holes and recesses needed to install it at the Rear section. These specific samples are the so-called Rear Wall candidates.

name	substrate	ø /"	hole	polishing	coating type	layers	coating company
1-SS-ep-3	1.4307 steel	3	no	electro.	sputtered	100 nm Ti, 1 µm Au	Siegert TFT
2-SS-ep-3	1.4307 steel	3	no	electro.	galvanic	1 µm Ni, 2 µm Au	Galvano
3-SS-ep-3	1.4307 steel	3	yes	electro.	sputtered	100 nm Ti, 1 µm Au	Siegert TFT
4-SS-ep-3	1.4307 steel	3	yes	electro.	sputtered	100 nm Ti, 1 µm Au	Siegert TFT
5-SS-ep-3	1.4307 steel	3	yes	electro.	sputtered	100 nm Ti, 1 µm Au	Siegert TFT
6-SS-ep-3	V4A steel	3	no	electro.	sputtered	100 nm Ti, 1 µm Au	Siegert TFT
7-SS-ep-3	V4A steel	3	yes	electro.	sputtered	100 nm Ti, 1 µm Au	Siegert TFT
8-SS-ep-3	V4A steel	3	yes	electro.	sputtered	100 nm Ti, 1 µm Au	Siegert TFT
1-SS-ep-68	V4A steel	5,7	no	electro.	sputtered	100 nm Ti, 1 µm Au	Siegert TFT
2-SS-ep-68	V4A steel	5,7	no	electro.	sputtered	100 nm Ti, 1 µm Au	Siegert TFT
1-SS-ep-6	1.4571 steel	6	yes	electro.	sputtered	100 nm Ti, 1 µm Au	Siegert TFT
2-SS-ep-6	1.4571 steel	6	yes	electro.	sputtered	100 nm Ti, 1 µm Au	Siegert TFT
3-SS-ep-6	V4A steel	6	yes*	electro.	sputtered	100 nm Ti, 1 µm Au	Siegert TFT
4-SS-ep-6	V4A steel	6	yes*	electro.	sputtered	100 nm Ti, 1 µm Au	Siegert TFT
5-SS-ep-6	V4A steel	6	yes*	electro.	sputtered	100 nm Ti, 1 µm Au	Siegert TFT
6-SS-ep-6	V4A steel	6	yes*	electro.	sputtered	100 nm Ti, 1 µm Au	Siegert TFT
1-SS-mp	1.4571 steel	3	no	mech.	galvanic	2 µm Ni, 2 µm Au	Galvano
2-SS-mp	1.4571 steel	3	no	mech.	sputtered	100 nm Ti, 1 µm Au	Siegert TFT
3-SS-mp	1.4571 steel	3	no	mech.	sputtered	100 nm Ti, 1 µm Au	Siegert TFT

Table 4.2: Overview on non-stainless steel samples produced during the Rear Wall development. With exception of the gold sheet, the copper mirror, the sapphire and SiO_2 samples, the other samples are named by the same system as described in table 4.1. The copper mirror was not purposely produced for the KATRIN experiment. If there is a "q" in the size column, the sample is not round but quadratic. Note that none of these samples has been produced with a hole as one can see in column 4.

name	substrate	ø /"	hole	polishing	coating type	layers	coating company
Sapphire-5	sapphire	2	no	unknown	unspecified	10 nm TiN 90 nm Au	UCSB
Sapphire-6	sapphire	2	no	unknown	unspecified	10 nm TiN 90 nm Au	UCSB
SiO_2-3	unknown	6	no	unknown	evaporated	10 nm TiN 90 nm Au	UCSB
SiO_2-4	unknown	6	no	unknown	evaporated	10 nm TiN 90 nm Au	UCSB
SiO_2-5	unknown	3	no	unknown	evaporated	10 nm TiN 90 nm Au	UCSB
SiO_2-6	unknown	3	no	unknown	evaporated	10 nm TiN 90 nm Au	UCSB
Cu mirror	unknown	q	no	unknown	evaporated	unknown	KIT - IMT
goldsheet	-	q	no	-	-	-	-
1-Co-ep-3	Cu (Al99,5)	3	no	electro.	evaporated	unknown	KIT - IMT
1-Co-ep-3	Cu (Al99,5)	3	no	electro.	galvanic	1 µm Ni, 2 µm Au	Galvano
2-Co-mp-3	E-Cu F20	3	no	mech.	evaporated	unknown	KIT - IMT
2-Co-mp-3	E-Cu F20	3	no	mech.	galvanic	1 µm Ni, 2 µm Au	Galvano
3-Co-mp-3	E-Cu F20	3	no	mech.	sputtered	10 nm Ti, 1 µm Au	SiegertTFT
1-Co-LTU	OFHC Cu	3	no	unknown	sputtered	10 nm Ti, 1 µm Au	SiegertTFT
2-Co-LTU	OFHC Cu	3	no	unknown	evaporated	unknown	KIT - IMT
1-Al-ep-3	AlMgSi	3	no	electro.	galvanic	3-5 µm Ni, 2 µm Au	Galvano
2-Al-ep-3	AlMgSi	3	no	electro.	evaporated		KIT - IMT
3-Al-ep-3	AlMgSi	3	no	electro.	evaporated	15 nm Cr, 100nm Au	KIT - IMT
4-Al-ep-3	AlMgSi	3	no	electro.	sputtered	100 nm Ti, 1 µm Au	SiegertTFT
1-Al-mp-3	AlMgSi19	3	no	mech.	evaporated	unknown	KIT - IMT
2-Al-mp-3	AlMgSi19	3	no	mech.	galvanic	3-5 µm Ni, 2 µm Au	Galvano
3-Al-mp-3	AlMgSi19	3	no	mech.	sputtered	10 nm Ti, 1 µm Au	SiegertTFT

produced. The latter can in principle be installed in the Rear Section after successful qualification. An overview of the produced samples using a stainless steel substrate is given in table 4.1. Samples with other substrates are summarized in table 4.2. The names given in these tables are used in the following to distinguish the samples. As one can see, not only different materials are tested to find the most suitable Rear Wall design but also different surface treatments and coating techniques.

The dependence of the work function homogeneity on the surface treatment and the corresponding roughness before coating is investigated by testing different polishing qualities. For that reason some samples are mechanically polished by the Institute of Microstructure Technology (IMT)[3] of the Karlsruhe Institute of Technology (KIT) and some electropolished by Poligrat[4]. In addition copper mirrors produced by LTUltra[5] were used as a substrate.

The tested coating procedures are galvanization by Adler Galvano[6], sputtering by Siegert TFT[7] and vapor deposition by the IMT. The companies Adler Galvano and Siegert TFT have been chosen due to good earlier experiences with the work of these companies: Adler Galvano already produced gold layers with high work function uniformity for the aSPECT experiment and gold layers of Siegert TFT have already been used at Tritium Laboratory Karlsruhe several times without any problems concerning adhesion.

In addition to the samples already mentioned, the following samples have been tested in earlier investigations by M. Babutzka [Bab14]:

- A 3-inch silicon wafer of 100 nm thickness, on which silicon dioxide is grown by thermal oxidation and atomic layer deposition. On top of this titanium nitride with a thickness < 10 nm and 50 nm of gold are sputtered.
- A 2-inch sapphire sample produced by CrysTec[8] which is coated by epitaxially grown gold. The coating technique is not specified. The resulting gold layer is polycrystalline with grain sizes of about 1 mm^2 and a dominant (>90 %) (111)-surface orientation [Bab14].
- A Triade beryllium window from Materion[9] installed in a CF-flange and coated by Siegert TFT.
- Two 1-inch beryllium samples coated by sputtering at University of California, Santa Barbara (UCSB).
- An *a*SPECT sample coated with galvanized gold. The copper substrate is first mechanically polished and later electropolished.
- Platinized stainless steel of the sample holder used as a reference at the photoelectron measurements.

A first purely visual examination of samples produced in the course of this thesis is performed by scanning electron microscopy. The results of this investigation are presented in the following section.

[3]Institute of Microstructure Technology, Karlsruhe Institute of Technology, Campus North, Hermann-von-Helmholtz-Platz 1, 76344 Eggenstein-Leopoldshafen, Germany

[4]POLIGRAT GmbH, Valentin-Linhof-Straße 19, 81829 München, Germany

[5]LTUltra Precision Technology GmbH , Aftholderberg, Wiesenstrasse 9 88634 Herdwangen-Schönach, Germany

[6]Adler Galvano Metall-Veredelung GmbH, Friedrich-Koenig-Str. 21, 55129 Mainz, Germany

[7]Siegert Thinfilm Technology GmbH, Robert-Friese-Straße 3, 07629 Hermsdorf, Germany

[8]CrysTec GmbH, Köpenicker Str. 325, 12555 Berlin, Germany

[9]Materion Brush Beryllium & Composites, 14710 W. Portage River South Road, Elmore, OH, USA

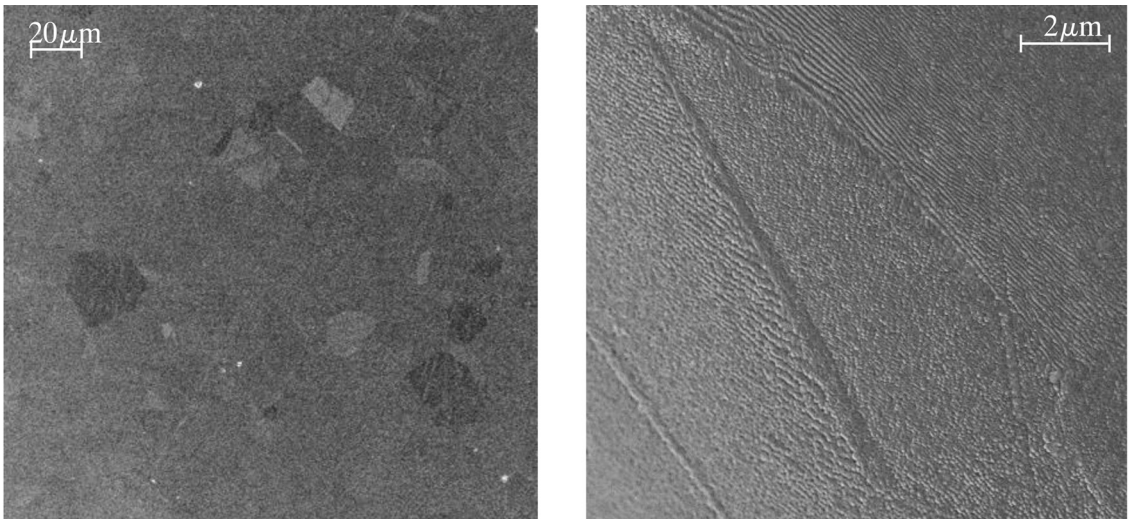

Figure 4.2: Scanning electron microscope picture of patterned gold surface. Both pictures show the gold surface of sample 7-SS-ep-3, but sample 8-SS-ep-3 exhibits the same structures. Left: there are lighter and darker areas visible, which are most likely caused by grains in the gold. Right: on closer examination a lamellar structure within the grains is visible. The lamellae of the grains are differently orientated.

4.3 Electron-microscopic investigation of Rear Wall candidates

The samples 7-SS-ep-3 and 8-SS-ep-3 are examined at the Laboratory for Electron Microscopy (LEM)[10], which is part of the KIT. The examination is performed by a scanning electron microscope [Rei98].

The first observation during this examination is the patterned surface of the samples. Two exemplary pictures with different magnification of the surface are shown in figure 4.2. It seems that the gold layer is built out of grains of sizes in the order of 10 µm. The higher magnification makes a lamellar structure within these grains visible. An examination of the back side, which is not gold coated and therefore pure stainless steel, gives similar results. A plausible assumption is, that the grains existing in the steel could be transferred to the gold coating. But due to the low contrast and the high noise level of the pictures, a statistical analysis of the grains concerning their size is not possible. Therefore, neither the correctness nor the falseness of this assumption can be verified.

In addition, features of different sizes from about 1 µm to several 10 µm can be found on the surface. One feature found on each of the examined samples is exemplarily shown in figure 4.3. It is not possible to say if these features were taken up by defects already existing at the substrate. However, the features cause a height change in the surface of the gold layer and therefore can affect the work function of the gold layer at this position. Jia et al. have found that the work function of gold coated copper is reduced on surface irregularities. For instance at irregularities with a height of 6.5 ± 1Å they measured a change in the work function of 0.9 ± 0.3 eV [Jia98a]. Indeed, it is not expected, that these features cause a significant variation of the work function due to their smallness. This

[10]Laboratory for Electron Microscopy, Karlsruhe Institute of Technology, Kaiserstraße 12, 76131 Karlsruhe, Germany

is a result of the fact, that the plasma averages out work function variations on scales smaller than the Debey length of 0.4 mm. But it might be possible that protruding parts at the inner surface of the hole wall could affect the work function. The size of such parts is found to be larger than the Debey length (compare 4.4).

This examination does not directly give any indication regarding the work function homogeneity. Nevertheless, it implies that the surface quality affects the structural homogeneity of the gold layer. In addition, processing of the samples must even more carefully be performed, to prevent defects and protruding parts at the central hole and their effect on the work function. The most common techniques which enable the measurement of the work function are described in the following section.

4.4 Techniques of work function measurements

In principle the work function measurement techniques can be divided into absolute and relative techniques [Pan12]. Absolute techniques are based on the ejection of electrons by temperature, electric field emission or photon absorption and the spectroscopy of these electrons. Relative techniques do not directly measure the work function but the so-called contact potential difference (CPD) [Lüt14]

$$U_{\mathrm{CPD}} = -(\Phi_{\mathrm{S}} - \Phi_{\mathrm{T}}) \tag{4.3}$$

between the work function of a sample (Φ_{S}) and that of a reference electrode, the so-called tip (Φ_{T}). Techniques which are commonly used are static and vibrating capacitors, the diode method and thermionic-, photoelectric and field emission [Hol66, Kna73]. These techniques are described in the following divided into absolute and relative techniques.

Absolute techniques

The **Diode method** is based on the thermic emission of electrons out of the sample which is placed in a diode [Kor13]. The emitted electrons are captured by an electrode on which high positive potential is applied. The saturation current of the diode is given by [Kor13]

$$I = A_{\mathrm{rich}} \cdot T^2 \mathrm{e}^{(-\Phi/(k_{\mathrm{B}} \cdot T))}, \tag{4.4}$$

where T is the temperature of the sample, A_{rich} is the Richardson constant and k_{B} is the Boltzmann constant. By varying T the work function of the material can be measured within $\pm\,1\,\mathrm{mV}$ [Kna73]. Advantages of this technique are the simplicity of the setup and the little or non-existing disturbance of the sample surface. Drawbacks are that measurements are only possible at pressures below $10^{-3}\,\mathrm{mbar}$ to $10^{-4}\,\mathrm{mbar}$ and that reactions at the hot surface may take place.

The **field emission retarding potential technique** utilizes the increased tunneling probability of electrons through the surface potential barrier in presence of strong accelerating fields (compare figure 4.5). By measuring the current density j of the emitted electrons in dependence of the field strength E [Fow28, Dom74]

$$j = \frac{C_1 E^2}{\Phi} \exp\left(\frac{-C_2 \Phi^{3/2}}{E}\right), \tag{4.5}$$

where C_1 and C_2 are constants, the work function can be found. The accuracy of this measurement is $\pm\,10\,\mathrm{mV}$ [Hol66] to $\pm\,20\,\mathrm{mV}$ [Str73]. It also enables the possibility to

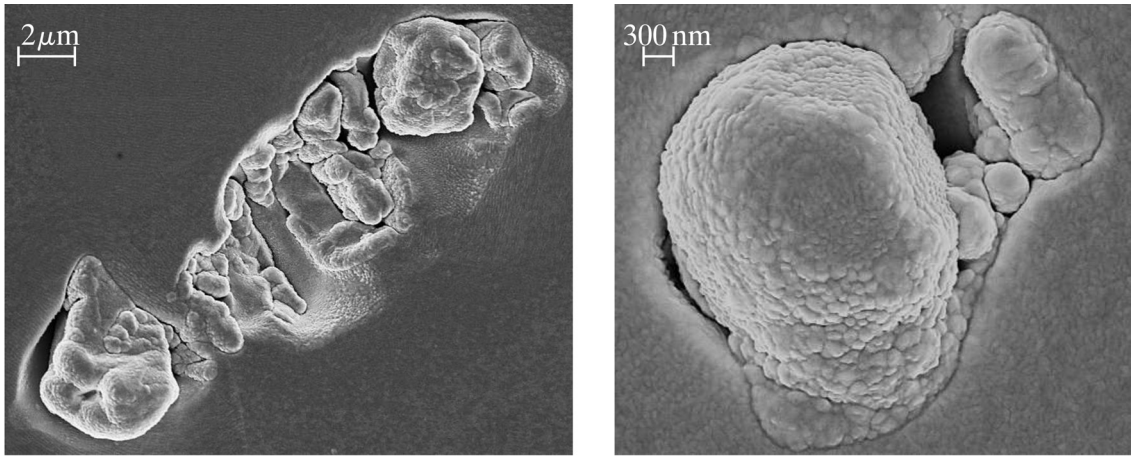

Figure 4.3: Scanning electron microscope picture of defects on the gold surface. Left: a defect on the surface of sample 8-SS-ep-3 is shown, the defect is about 20 µm long and about 5 µm wide. Right: an exemplary defect in the gold layer of sample 7-SS-ep-3 is shown. The length of this defect is about 5 µm and the width about 4 µm. The height of the defects cannot be specified.

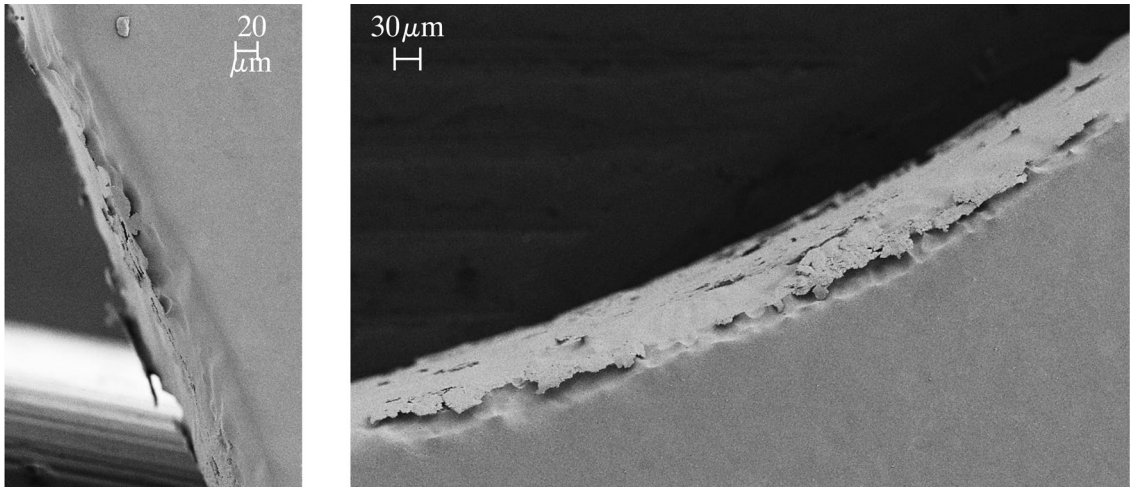

Figure 4.4: Scanning electron microscope picture of protruding parts at the inner surface of the hole wall. Left: the hole of sample 7-SS-ep-3 is shown in this picture. Right: here sample 8-SS-ep-3 is shown. Overall the protruding part has a length of more than 0.6 mm.

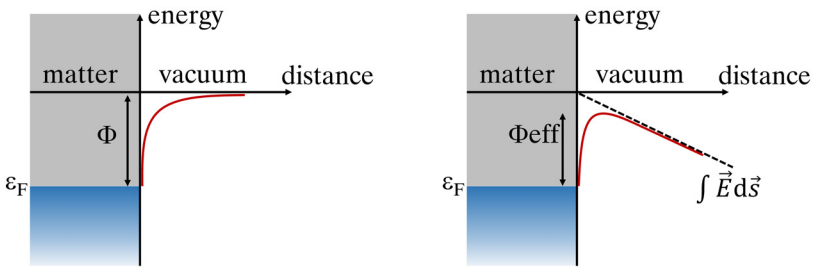

Figure 4.5: Surface barrier and work function in the presence of accelerating fields. Left: the surface potential barrier is shown without accelerating field. To eject an electron out of the material (gray area) at least the difference between the vacuum potential and the Fermi energy ε_F is needed, which is exactly the work function Φ. Right: here an accelerating field $\vec{E}$ is present. By this field the potential barrier is lowered which means that an energy of $\Phi_{eff} < \Phi_F$ is needed to eject an electron. In addition, the probability that an electron tunnels through the narrowed surface barrier is increased.

measure the work function of different crystallographic orientations within one material [Dom74]. The fact, that a static field of about 10^7 V/cm is applied to the tip makes the work function measurement independent of adsorption [Hol66]. A drawback of this method is, that it only can be used in a non-destructive way if the pressure does not exceed 10^{-6} torr [Hol66].

Photoelectron spectroscopy is based on the photoelectric emission of electrons by UV light or more generally by electromagnetic radiation with energy below 100 eV [Pan12]. There are several kinds of photoelectron spectroscopy, like X-ray photoelectron spectroscopy [Hol70], X-ray photoelectron diffraction [Hub95] and Ultraviolet photoelectron spectroscopy [Gos78], to name but a few. In the following the attention is focused on the Ultraviolet photoelectron spectroscopy. The emission takes place if the energy of the photon is higher than the potential difference between the Fermi sea and the vacuum potential (see also section 3.2 on page 67 and especially subsection 3.2.1 within it). To prevent the ejected electrons from returning to the surface of the sample a negative potential must be applied to the sample. It must be ensured that the potential does not generate an electric field which bends the potential barrier as shown in figure 4.5. In that case not the real but a smaller effective work function would be measured.

One method to determine the work function is performed with a spectrometer which measures the kinetic energy of the emitted electrons. This is possible as the kinetic energy of the electrons is linked to the surplus energy of the photons and by that also to the work function of the material: the rate is plotted in dependence of the surplus energy. But the surplus energy is not only dependent on the work function, but also on the variance of the spectrometer and broadness of the wavelength distribution of the optical setup. However, the broadness of the rate spectrum is used to determine the work function. If the rate spectrum is measured at several wavelengths an extrapolation to the point of 0 eV kinetic energy gives the work function of the material. This method is particularly suitable for measuring of the lowest work function in the area of the light spot. This is caused by the fact that the main parameter is not the emission rate but the broadening of the surplus energy. But there is another method, which can be used to determine the work function with a wavelength-selective UV-light source: as soon as the photon energy exceeds the work function, electrons are emitted. The increase with

the wavelength at energies close to the work function is exponential (at least within the first electron volt above the work function). The shape of the increase is described by the so-called Fowler function [Fow31]

$$\begin{aligned} f(\mu) &= \frac{\pi^2}{6} + \frac{1}{2}\mu^2 - \left(\mathrm{e}^{-\mu} - \frac{\mathrm{e}^{-2\mu}}{2^2} + \frac{\mathrm{e}^{-3\mu}}{3^3} - ...\right) && \text{for } \mu \geq 0, \\ f(\mu) &= \mathrm{e}^{\mu} - \frac{\mathrm{e}^{2\mu}}{2^2} + \frac{\mathrm{e}^{3\mu}}{3^3} - ... && \text{for } \mu \leq 0, \end{aligned} \tag{4.6}$$

with

$$\mu = e^{\frac{E_\gamma - \Phi}{k_\mathrm{B} T}}. \tag{4.7}$$

Here E_γ is the energy of the photon, k_B is the Boltzmann constant and T is the temperature. Fitting this function to the data enables the calculation of the work function.

Although the photoelectron spectroscopy enables work function measurements with relatively high sensitivity and high resolution [Hüf03] the accuracy of the measurement is limited. This is caused by a splitting of the Fermi sea into complex surface states at the surface of a material [Feu76, Güd05] and a smearing of the Fermi-Dirac function due to thermodynamic effects. This smearing effect is described by the probability $f(\varepsilon)$ [Roy01]

$$f(\varepsilon) = \frac{1}{\exp^{(\varepsilon-\mu)/(k_\mathrm{B}T)} + 1} \tag{4.8}$$

that a state in the material is occupied. This probability depends on the energy ε of a single particle state, the temperature T and the chemical potential μ. Only if there is neither thermal broadening nor an electrical field applied, μ becomes equal to the work function. By using equation (4.8) the smearing at 20 °C can be estimated by using $k_\mathrm{B}T = 25\,\mathrm{meV}$ [Bab14]. Also, adsorbates can have an impact on the measured work function [Hec12].

Due to the sensitivity of photoelectron spectroscopy on the minimal work function this method is microscopic: as soon as the photon energy is sufficiently high electrons are emitted from any crystalline surface. But as any used light spot has a non-vanishing dimension the measurement can also be called macroscopic. Due to the propagation of the light into the material photoelectron spectroscopy is sensitiv not only to the surface itself but also to the underlying layers up to to 20 nm thickness [Pan12].

Relative techniques

Examples of **vibrating capacitor methods** are Scanning Kelvin Probe Force Microscopy [Pan12, Ono01, Non91, Yas96] and the Kelvin Probe method[11] [Kel98, Zis32, Bai99]. As the latter is one of the most commonly used techniques of CPD measurement [Woo88], the following description focuses on this technique.

The **Kelvin Probe method** was developed by W. T. Kelvin in [Kel98] and further improved by W. A. Zisman in [Zis32]. It measures the CPD by a vibrating metal reference tip which together with the stationary sample forms a capacitor [Bai01, Bai99] (see also figure 4.6): two not electrically connected materials (in this case sample and tip) usually

[11] Although the Scanning Kelvin Probe Force Microscopy and the Kelvin Probe method are based on the vibrating capacitor methods, they have a different observable: the Scanning Kelvin Probe Force Microscopy measures the electrostatic forces on the tip, while the Kelvin Probe method measures the voltage. That is why both are named.

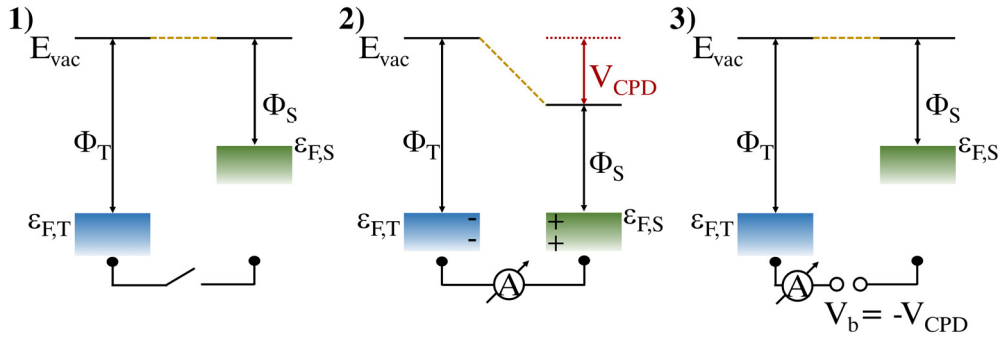

Figure 4.6: Energy level diagrams and the contact potential difference. In (1) the non-connected materials with different work function but same vacuum potential are shown. In (2) the materials are electrically connected and the Fermi levels are equalized by a charge exchange. Resulting from that, the vacuum potentials are shifted to each other. The magnitude of the shift is determined by the CPD. At the surface of the material surface charges arise. In (3) an additional backing potential is applied between sample and tip. If this backing potential is of the same value as the CPD but with negative sign the vacuum potentials and Fermi levels are bend (to the position of unconnected materials), while the vacuum potential is equalized again.

have Fermi levels of different energy ε_F and different work functions Φ. If the materials are connected, the potentials influence each other. Electrons move from the material with higher Fermi level to the material with lower Fermi level to compensate the potential gradient. Once the Fermi levels are equal [Lüt14]

$$\varepsilon_{\mathrm{F,S}} = E_{\mathrm{vac,S}} - e\Phi_\mathrm{S} = E_{\mathrm{vac,T}} - e\Phi^\mathrm{T} = \varepsilon_{\mathrm{F,T}} \tag{4.9}$$

the motion of the electrons stops. During this process the vacuum potentials are shifted and surface charges are induced which shield the field inside of the material and generate the potential gradient. That means that sample and tip form a capacitor with a charge Q [Lüt14]

$$Q = C\left(-\left(\Phi_\mathrm{S} - \Phi_\mathrm{P}\right)\right) \tag{4.10}$$

and capacitance C of approximately [Dem14]

$$C = \varepsilon_0 \frac{A}{d}, \tag{4.11}$$

where ε_0 is the vacuum permittivity, A is the area of the smaller surface (usually the tip area) and d is the distance between sample and tip. Note that the given formula of C is only an approximation which neglects stray fields and non-parallelism and which uses $\sqrt{A} \gg d$. If now sine-like vibrations of the tip are induced the distance d and therefore the capacity C of the capacitor are constantly changed. This cause a continuous charge exchange between sample and tip describable by the current [Lüt14]

$$I = \frac{\mathrm{d}Q}{\mathrm{d}t} = \left(-\left(\Phi_\mathrm{S} - \Phi_\mathrm{P}\right)\right)\frac{\mathrm{d}C(t)}{\mathrm{d}t} \propto \frac{\mathrm{d}}{\mathrm{d}t}\frac{1}{d + \Delta d\sin(\omega t)}, \tag{4.12}$$

with the variation of the distance $d = d + \Delta d\sin(\omega t)$.

In order to measure the CPD an external voltage U_b can be applied between sample and tip which affects the output signal (compare figure 4.7 (1)). If

$$U_\mathrm{b} = \Phi_\mathrm{S} - \Phi_\mathrm{P} = -U_\mathrm{CPD}, \tag{4.13}$$

the output signal vanishes. This method of measuring the CPD is called the null method [Rom15, Chu09]. To improve the measurement usually a lock-in amplifier is added to the setup which is adjusted to the vibration frequency of the tip. But still the measurement remains sensitive to noise as noise becomes dominant at a vanishing signal [Gri14, Bai91]. In addition a lock-in amplifier can only filter out noise with a frequency different from the vibration frequency, but stray capacities generate noise with the same frequency.

A less noise-sensitive method of measuring the CPD is the so-called off-null technique (compare figure 4.7 (2)). Here two or more different voltages are applied between sample and tip differing from -CPD (e.g. $\pm 1\,\mathrm{V}$ in case of CPD values in the order of $\pm 0.5\,\mathrm{V}$ [Bab14]). In doing so large signals with large signal to noise ratios are generated. By using the linear dependence between signal and U_b a linear fit through the measured points followed by a calculation of the x-intercept of this fit gives the negative CPD value. A side effect of this method is that the distance between sample and tip is reflected by the Gradient G of the fit line in a non-trivial manner.

With the Kelvin Probe technique the CPD of both metals and semiconductors [Bai89] can be measured in a non-invasive way [Bai01]. The measurements can be performed in a broad range of temperatures and pressures including ultra high vacuum (UHV). If translation stages are added to the system scans over almost any area size are possible. As the Kelvin Probe averages the CPD value over the surface area of the tip, it determines the arithmetic mean of the CPD value of the outermost layer of the sample surface [Bai89, Bai99]. That way a resolution of 1 meV and an accuracy in the meV range are possible [Bai99]. But the accuracy depends on any change in the work function of the tip, e.g. by degradation, due to the relative character of the measurement. For that reason the most common tip materials are gold and stainless steel. Despite the relative measurement, changes in the work function and long-term stability measurements are feasible, if the tip work function remains stable.

A **static capacitor** also uses the connection of two materials with different work functions: it monitors the current which results from the connected materials forming a capacitor (compare figure 4.6 (1) and (2)). During the connection of the materials a backing potential V_B is applied until there is no current anymore. This must be done with a very short response time t_R. In this context short means that the time constant RC of the circuit must be much larger than t_R (the overall response time is typically in the order of 0.5 s) [Bac85]. If the ratio t_R/RC is smaller than 0.01 the accuracy of the work function measurement is $\pm 1\,\%$ [Woo88]. The sensitivity can reach values of 0.25 mV [Bac85].

The Kelvin Probe method is used to develop the final Rear Wall, as it combines a high possible resolution and accuracy with the possibility to scan over the whole Rear Wall surface. In addition, a Kelvin Probe is available at the KATRIN collaborator Johannes Gutenberg University of Mainz. Of particular interest is the fact that a Kelvin Probe averages the CPD over the tip surface. This represents the smearing effect of the plasma. The measurements with the Kelvin Probe method are completed by photoelectron spectroscopy at the monitor spectrometer of KATRIN. In addition to the measurement of absolute work function values, investigations of the impact of the hole area are possible with this method. The monitor spectrometer is also based on the MAC-E filter principle. Therefore a measurement of Rear Wall samples at the monitor spectrometer also tests the performance of the Rear Wall in a MAC-E filter prior to its installation at the Rear Section. The results obtained by the Mainz Kelvin Probe are presented in the following section.

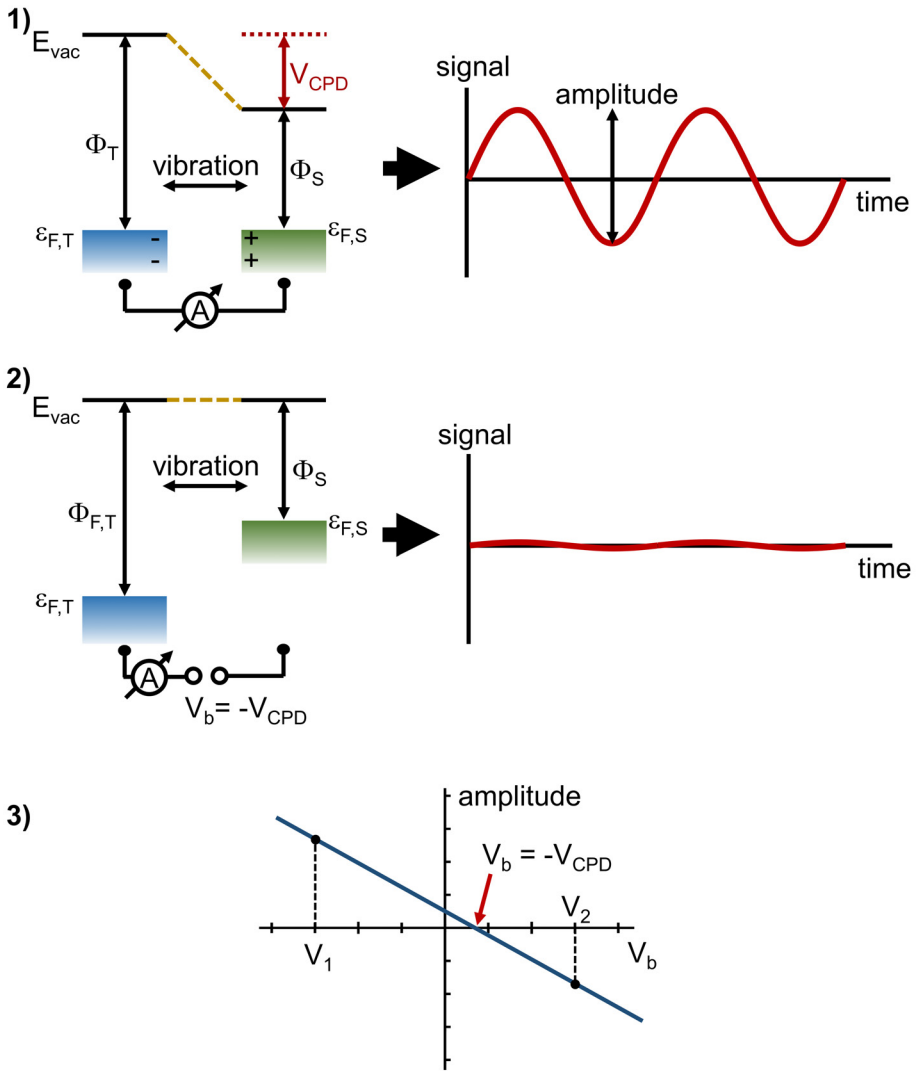

Figure 4.7: Measurement principles of a Kelvin Probe. On the left side of (1) the energy level diagram of two electrically connected materials is shown. If the distance between these materials is periodically changed a signal as shown in the right part of this figure can be measured. The amplitude of the signal is dependent on the CPD of the two materials. In (2) the energy level diagram is again shown on the left side and the resulting signal on right side. But now a backing potential is applied between sample and tip. If the backing potential is equal to the negative CPD value - the situation presented in this figure - the vacuum potentials are equalized again and the resulting signal vanishes. This is the measurement principle of the on-null method. In (3) the off-null method is shown. Here the amplitude of the signal is measured in dependence of the applied backing potential. At least two different backing potentials V_1 and V_2 are used. The x-intercept of the resulting line through the measured points is equal to the negative CPD value.

4.5 Relative Work function measurements by an ambient air Kelvin Probe

In this section the results of a Kelvin Probe, which is available at the Johannes Gutenberg University of Mainz are presented. This Kelvin Probe setup was implemented in late 2011 to investigate the work function of electrodes used at KATRIN or *a*SPECT [Sch12]. At the time of the measurements the system was already fully commissioned [Sch12]. Note that the measurements with the particular Kelvin Probe are performed at ambient air conditions which is why it is called an ambient air Kelvin Probe in the following. Nevertheless, two important questions concerning the Rear Wall and its work function can be addressed with the measurement using the ambient air Kelvin Probe, namely:

1. Is the homogeneity of the CPD dependent on the treatment of the sample surface before coating?
2. Which is the most suitable substrate material and coating technique?

In addition, at least a first assessment of the dependence of the CPD homogeneity on time and bake-outs can be given.

An overview on the ambient air Kelvin Probe setup is given in the subsequent section 4.5.1. The procedure during the measurements and the analysis of the data taken during the measurements is described in section 4.5.2. Earlier results of the Rear Wall development also generated with this ambient air Kelvin Probe are summarized in section 4.5.3. The execution of the measurements and the results concerning surface quality dependence, work function homogeneity of different samples, long-term stability and bake-out effects are presented in the sections 4.5.4 and 4.5.5. Finally these sections about the ambient air Kelvin Probe are completed by a discussion concentrating on first discoveries and necessary further steps in section 4.5.6.

4.5.1 Experimental setup of the ambient air Kelvin Probe

The Kelvin Probe at Mainz is of the model ASKP150150 from KP Technologies LTD[12]. By positioning the Kelvin Probe above stacked linear stages scans over an area of 150 mm $\times$ 150 mm are possible. On top of these stages the sample stage with the samples is installed. The adjustment of the tip position relative to the sample is realized by two methods: For a rough height positioning a linear stage driven by a stepper motor is used. The fine adjustment is done by the coil inside of the Kelvin Probe head which also produces the vibration of the tip. A static offset voltage is applied to the coil in addition to the periodic supply voltage. The tip which is installed at the Kelvin Probe head is exchangeable. The available tips differ by their diameter. As the capacity linearly depends on the tip area, different tip sizes result in different signal strengths and sensitivities. For all measurements in this thesis a 2 mm gold coated stainless steel tip is used. To enable not only a relative but also an absolute measurement of the work function, two reference sample surfaces are available at the sample stage: a gold and an aluminum surface.

To stabilize the conditions under which the Kelvin Probe measures, it is installed in an optical enclosure. Influences on the measurement by light, humidity and temperature are therefore reduced. But even with this enclosure the Kelvin Probe is not completely independent of the ambient measurement conditions. To find correlations between CPD

[12]KP Technologies, Burn Street, Wick Caithness KW1 5EH, Scotland

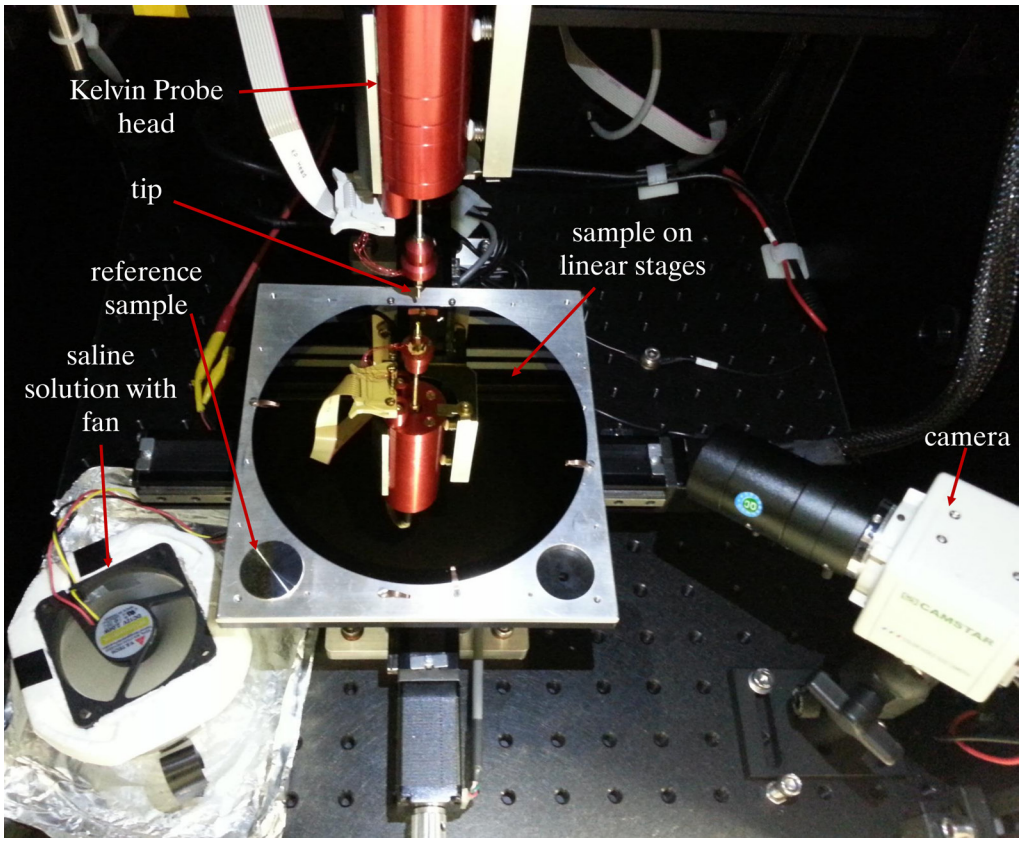

Figure 4.8: The ambient air Kelvin Probe setup. The photography shows a view inside of the enclosure which surrounds the setup.

and the conditions inside of the enclosure ,temperature and humidity sensors are installed. Especially the humidity was found to have a large impact on the CPD values as it can cause drifts larger than 20 mV [Sch12, Bab14]. For that reason the humidity is stabilized with a saline solution of the salt complex $MgCl_2{\cdot}6H_6O$ which dries off the air. In equilibrium at 25 °C this solution has a relative humidity of 32.3 %. To improve and speed up the drying of the air, a fan continuously blows air on the saline solution. The time until the equilibrium is reached is about 12 to 24 hours. This period of time is always waited for prior to measurements. A camera and an LED installed in the enclosure enable the visual control of the Kelvin Probe. Both are controlled by the KP software. The photography of the complete setup inside of the optical enclosure is shown in figure 4.8.

This setup is completed by dedicated motor controllers outside of the enclosure for the motorized linear stages moving the sample stage and the z-stage. The measurement signal is also further processed outside of the enclosure. For that the measurement signal is split and routed into an oscilloscope for visual monitoring of the measurement signal and into an ADC. The controlling of all components is performed by the KP software on a PC which is connected with the controllers by a National Instruments[13] 6025E data acquisition system. Limitations in this supplied software cause that only rectangular shaped areas with limited number of points can be measured.

A precise description of the necessary steps to perform a measurement is given in the following section.

[13]National Instruments Corporation, 11500 N MoPac Expwy, Austin, TX 78759-3504, USA

4.5.2 Measurement procedure and analysis method

A sample which is planned to be measured with the ambient air Kelvin Probe must first be installed on the sample stage in the optical enclosure. For a good electrical connection between the Kelvin Probe and the sample, the samples are fixed to the stage by clamps. Afterwards the optical enclosure is closed. After about 12 to 24 hours, when the humidity in the enclosure and the saline solution reach the equilibrium, the samples can be measured.

To perform an automatic scan controlled by the KP software the starting position as well as the length and width of the area which should be scanned must be found manually. Afterwards the work function of the gold reference sample is measured 50 times. For that the tip is manually moved close to the surface with the z-stage. The fine adjustment is performed automatically by the KP software by adjusting the Gradient G to a certain value[14] (compare section 4.4). The mean value of these measurements can be used to detect drifts of the system during the scan. The next step is to again move the tip to the starting position of the scan. The height is adjusted in the same procedure as at the reference electrode. When the Kelvin Probe is in the correct position above the sample, the scan can be started. Now the KP software automatically moves the sample under the tip and adjusts the height by tracking the Gradient. During the scan the sample is only moved 1 mm from measurement point to measurement point in case of the 2 mm tip. In doing so the measurement points overlap which makes sure that in spite of the round surface of the tip each position within the scan area is measured. After the scan the Kelvin Probe is manually moved to the reference sample again, where an additional 50 measurements are performed.

The analysis of the data is performed by calculating the mean CPD value and its RMS deviation $\sigma_{\mathrm{RMS,surface}}$ over the whole scan area. With these values it can be checked, if the CPD value of the reference sample before and after the scan are compatible within the errors. In case of the measurements presented in the thesis in hand this was true with exception of only 6 measurements. But in case of these 6 measurements the CPD values of the reference sample before and after the scan are also compatible within 3σ. For that reason and for increased clarity the results of the reference sample measurements are not discussed in the following.

The CPD and $\sigma_{\mathrm{RMS,surface}}$ give some indication of the overall homogeneity of the sample. If $\sigma_{\mathrm{RMS,surface}} < 20\,\mathrm{mV}$, one of the two KATRIN requirements is met. In addition, a comparison of $\sigma_{\mathrm{RMS,surface}}$ of different measurements of the same sample, e.g. before and after bake-out, makes effects on the homogeneity of the sample work function and its stability visible. Note, that for these comparisons only the $\sigma_{\mathrm{RMS,surface}}$ and not the CPD value itself can be used, as the CPD value is not comparable under ambient conditions. To check for the spatial distribution the CPD value is plotted in a diagram dependent on its x- and y-position. These diagrams are called CPD maps in the following.

Previous measurements with the ambient air Kelvin Probe by M. Babutzka were also based on the measurement procedure and analysis method presented in this section. Their results are summarized in the following section.

[14] The exact value of the Gradient is dependent on the Kelvin Probe itself and the amplification of the measurement signal. In case of measurements performed with the ambient air Kelvin Probe in the course of this thesis the Gradient is set to a value of 300.

4.5.3 Previous results of measurements at the ambient air Kelvin Probe

The measurements described in [Bab14] were executed during one week. In general the strong dependence of the measurement on humidity and dust under ambient conditions could be verified at the Kelvin Probe in Mainz during this time. Work function changes of more than 50 mV have been detected and the correlation with the atmosphere in the enclosure was shown.

In addition, 5 different samples have been measured with the ambient air Kelvin Probe. The results of these measurements were:

- 3-inch silicon wafer: 171 ± 7 mV
- 2-inch sapphire: 279 ± 6 mV
- Triade window (beryllium substrate): -12 ± 26 mV
- 1-inch beryllium 1: 154 ± 10 mV
- 1-inch beryllium 2: 181 ± 8 mV

As one can see, all samples with exception of the Triade window clearly have a work function homogeneity of less than 20 mV. The difference in homogeneity between the Triade window and the beryllium samples can most likely be explained by the insertion of the beryllium foil in the CF flange in case of the window. Due to this the surface of the beryllium is curved. This might either induce stress in the beryllium and the above gold layer causing the inhomogeneity or it might disturb the measurement of the Kelvin Probe.

The results imply that silicon, sapphire and beryllium could be suitable as a substrate for the Rear Wall. But as each sample was measured just once, long-term effects cannot be excluded. To further investigate samples with these substrates, but also with other substrates such as aluminum, copper and stainless steel, additional measurements were performed with more samples and over a longer time. The execution of these measurements and their results are presented in the following section.

4.5.4 Execution of measurements with the ambient air Kelvin Probe

During the measurements which are performed over a period of 3 months overall 20 different samples are measured at least once but mostly several times. In each scan a rectangular area (or in case of the 6-inch sample a cross-like area[15]) is measured which differs in position and size from scan to scan. The same surface cannot be measured, for several reasons: the scan area is dependent on the mounting of the samples on the sample stage, the sample is fixed by clamps and by the position of a possible hole. However, it is assumed, that the work function homogeneity is more or less equal over the whole surface so that the $\sigma_{\mathrm{RMS,surface}}$ values are comparable for different measurements of the same sample.

During the measurements, the impact of the surface quality of the substrate on the work function homogeneity is investigated in more detail. Therefore, the samples 2-Al-mp-3, 1-Al-ep-3, 1-SS-ep-3 and 3-SS-mp-3 are measured before and after the coating process. The samples with same substrate but different surface treatment can be compared. In addition, the gold coated Cu of mirror quality is measured. This mirror is of the same

[15] As the KP software does not allow measurements with unlimited number of points it was not possible to measure the surface of the sample in one scan. Therefore, the scan is split in three to four parts.

type as the copper mirror of the samples 1-Co-LTU and 2-Co-LTU. Therefore, a scan of these uncoated mirrors is compared with the results of the coated Cu mirror sample. Also, the impact of the substrate, the consequent layer design and the coating technique is investigated by measuring differently produced samples. As some samples are measured up to 5 times within the measurement period of 3 months, the long-term stability of the homogeneity can be investigated.

In addition, the effect of a bake-out is tested on 6 samples: SiO_2-6, 1-SS-ep-3, 2-SS-ep-3, 1-SS-mp, 2-SS-mp and 3-Co-mp-3. These samples are measured about 2 weeks before the bake-out for comparison. As a reference the samples SiO_2-5 and 3-SS-mp-3 are not baked but also measured before and after the bake-out of the other samples. As these samples are identically manufactured as the samples SiO_2-6 and 2-SS-mp, a possible change in the homogeneity of the baked samples but not in the reference samples is traceable to the bake-out. Due to the fact that no heatable vacuum chamber is available at Mainz at the time of the measurements, the bake-out is performed at the KIT. The samples are installed in sample holders for the bake-out to avoid any damage. After the bake-out, the samples are transported to the University of Mainz. During the approximately 4 hours between the extraction of the samples out of the vacuum chamber and the closing of the optical enclosure of the Kelvin Probe the samples are directly exposed to uncontrolled and un-monitored ambient air.

An overview of all measured samples, the number of performed scans and the scanned areas are given in table 4.3. Furthermore, it is stated if they are used to determine the effect of the surface quality or of a bake-out on the CPD homogeneity. The results of these measurements are given in the following section.

4.5.5 Results of the measurements with the ambient air Kelvin Probe

For reasons of clarity and comprehensibility the results of the measurements performed with the ambient air Kelvin Probe are divided in 4 parts: the effect of the substrate surface on the $\sigma_{\mathrm{RMS,surface}}$, the homogeneity of differently produced samples, the long-term stability of $\sigma_{\mathrm{RMS,surface}}$ and the impact of a bake-out on $\sigma_{\mathrm{RMS,surface}}$.

4.5.5.1 Dependence of the homogeneity on the surface quality before coating

A copper mirror, mechanically polished and electropolished samples are measured before and after coating. The results of these measurements are given in table 4.4. Before the coating the mirror and 1-SS-ep-3 have a good homogeneity clearly lower than 20 mV, 3-SS-mp-3 and 1-Al-ep-3 have a barely to high inhomogeneity above 20 mV and 2-Al-mp-3 has a $\sigma_{\mathrm{RMS,surface}}$ value of clearly more than 20 mV. After the coating the homogeneity is generally improved by a factor between 1.19 and 4 for all samples with exception of the mirror. The $\sigma_{\mathrm{RMS,surface}}$ of the mirror is increased by a factor of more than 6.

The stainless steel samples have (independent from the surface treatment prior to the coating) $\sigma_{\mathrm{RMS,surface}}$ values below 10 mV. In case of the aluminum samples the relative improvement of the mechanically polished sample is higher but the absolute $\sigma_{\mathrm{RMS,surface}}$ value is worse: in case of sample 1-Al-ep-3 the requirement on $\sigma_{\mathrm{RMS,surface}}$ is barely met, sample 2-Al-mp-3 failed the requirement.

Table 4.3: Overview on measurements performed with the ambient air Kelvin Probe. Areas which are marked by † are performed at the bare substrate prior to the coating process. Areas marked by * are performed after the bake-out. Note, that the measurements of samples SiO_2-3 and SiO_2-4 are all performed on one day but at different positions of the sample. This is necessary because of the size of these samples.

sample	measured before coating	baked	performed scans after coating	scaned area /cm^2					
goldsheet	-	-	3	2.30 × 0.96	2.30 × 0.86	1.73 × 1.82			
Cu mirror	yes	-	1	3.74 × 4.13†	7.01 × 4.70				
Sapphire-5	-	-	2	2.28 × 2.67	2.38 × 2.97				
Sapphire-6	-	yes	5	2.97 × 3.17	2.97 × 3.17	2.97 × 3.17	2.28 × 2.67	2.38 × 2.97*	
SiO_2-3	-	-	2	2.59 × 9.60	2.59 × 2.98				
SiO_2-4	-	-	4	4.61 × 9.79	4.61 × 2.50	4.03 × 1.06	3.07 × 1.06		
SiO_2-5	-	-	2	3.56 × 5.25	4.46 × 4.16				
SiO_2-6	-	yes	6	3.07 × 5.84	3.07 × 5.84	3.07 × 5.84	3.56 × 5.25	4.46 × 4.16*	4.46 × 4.16*
1-Al-ep-3	yes	-	1	3.65 × 5.38†	3.27 × 5.64				
4-Al-ep-3	-	-	2	4.36 × 3.96	3.47 × 4.75				
2-Al-mp-3	yes	-	1	3.65 × 2.98†	4.95 × 4.16				
3-Al-mp-3	-	-	1	4.16 × 4.65					
2-Cu-ep-3	-	-	1	5.54 × 3.76					
2-Cu-mp-3	-	-	2	4.16 × 4.95	4.16 × 4.95				
3-Cu-mp-3	-	yes	3	3.86 × 5.35	3.66 × 4.16	4.16 × 4.16*			
1-SS-ep-3	yes	yes	4	2.98 × 4.13†	3.86 × 5.35	2.87 × 5.35	2.63 × 5.87	4.16 × 4.16*	
2-SS-ep-3	-	yes	4	5.35 × 2.77	5.35 × 2.77	3.24 × 3.54	1.49 × 5.84*		
1-SS-mp-3	-	yes	3	4.65 × 4.75	3.27 × 3.86	4.16 × 4.16*			
2-SS-mp-3	-	yes	4	4.26 × 5.15	4.16 × 5.15	4.46 × 4.46	4.46 × 4.16*		
3-SS-mp-3	yes	-	5	3.27 × 5.64†	4.16 × 5.35	4.16 × 5.35	4.55 × 4.65	4.46 × 4.16	0.89 × 4.16

Table 4.4: Results of Kelvin Probe measurements of different samples before and after coating. In addition to $\sigma_{\mathrm{RMS,surface}}$ the CPD values are given for completeness.

	before coating		after coating	
sample	CPD /mV	$\sigma_{\mathrm{RMS,surface}}$ /mV	CPD /mV	$\sigma_{\mathrm{RMS,surface}}$ /mV
Cu mirror	123.4	8.7	45.2	54.1
1-SS-ep-3	-70.7	13.0	279.3	6.5
3-SS-mp-3	-422.4	25.8	258.0	9.4
1-Al-ep-3	79.8	21.6	53.3	18.1
2-Al-mp-3	-554.3	129.7	-46.5	32.4

4.4.5.2 The dependence of σ_{RMS} on the substrate

The CPD of 20 samples is measured after the coating process. The results of these measurements are summarized in table 4.5. The corresponding CPD maps can be found in appendix E. With exception of the gold sheet all measured $\sigma_{\mathrm{RMS,surface}}$ values are below 55 mV. The first two measurements of the gold sheet give $\sigma_{\mathrm{RMS,surface}}$ values of more than 49 V. In contrast to that the $\sigma_{\mathrm{RMS,surface}}$ of the last measurement is only about 63 mV. These very high values are most probably caused by bends in the gold sheet. These bends, which are also visible by eye, cause an inhomogeneous distance between tip and sample which makes a reliable measurement with a Kelvin Probe difficult. The copper mirror has the highest $\sigma_{\mathrm{RMS,surface}}$ of the remaining samples with about 54 mV.

The results of all other samples dependent on their substrate can be summarized as follows:

- **Sapphire:** with the exception of the first measurement of sample Sapphire-6 all measurements have a $\sigma_{\mathrm{RMS,surface}}$ below 18 mV and are therefore within the accepted RMS deviation over the sample surface of KATRIN. A CPD map of this first measurement is shown in figure 4.9 in comparison to the second measurement. As the feature which causes the high $\sigma_{\mathrm{RMS,surface}}$ of 46.1 mV is visible in both plots it is more likely that it is caused by a characteristic of the surface than for example by dust.
- **SiO_2:** there is also one outlier in case of the silicon substrates namely the first measurement of sample SiO_2-6. Just like in the first measurement of sample Sapphire-6, line-like structures can be seen in the CPD map of this measurement. As those lines can also be found in the second scan which is performed at the identical position, this is again not caused by dust or other conditions of the measurement. The associated figures can be found in appendix E.1. All other measurements have $\sigma_{\mathrm{RMS,surface}} \leq 19.6$ mV. But most of the measurements show even smaller values of below 10 mV.
- **Aluminum:** independent from the used polishing and coating techniques 3 of the 5 performed measurements on aluminum samples show $\sigma_{\mathrm{RMS,surface}} > 27$ mV.
- **Copper:** only the copper sample 3-Cu-mp-3 meets the requirements on the homogeneity of the CPD. Its $\sigma_{\mathrm{RMS,surface}}$ is less than 12.8 mV. The other copper samples, which are not coated by sputtering like sample 3-Cu-mp-3 but by galvanization, fail the requirement with $\sigma_{\mathrm{RMS,surface}} \geq 28.0$ mV.
- **Stainless steel:** with the exception of sample 1-SS-mp-3 all tested samples have $\sigma_{\mathrm{RMS,surface}}$ values below 20 mV and therefore meet the requirement on the CPD

Table 4.5: Overview of measured CPD and $\sigma_{\mathrm{RMS,surface}}$ of all samples tested with the ambient air Kelvin Probe. Not listed in this table are results of measurements prior to the coating and after the bake-out. In addition to the name, the CPD and the $\sigma_{\mathrm{RMS,surface}}$ values the coating procedure is given for clarity. This is the case, as this sample characteristic cannot be found in the name of the samples. The abbreviations v, g and s in the second column mean: vapor deposited, galvanically coated and sputter coated. Note, that the measurements of sample SiO_2-3 or SiO_2-4 are measured on one day. The splitting into several measurements is only due to the size of these samples.

sample	coating	CPD /mV	$\sigma_{\mathrm{RMS,surf.}}$ /mV	CPD /mV	$\sigma_{\mathrm{RMS,surf.}}$ /mV	CPD /mV	$\sigma_{\mathrm{RMS,surf.}}$ /mV	CPD /mV	$\sigma_{\mathrm{RMS,surf.}}$ /mV
goldsheet	-	573.2	49508.0	12717.4	136875.0	-9.8	62.7		
Cu mirror	v	45.2	54.1						
Sapphire-5	-	327.8	10.2						
Sapphire-6	-	205.3	46.1	237.0	17.8	284.3	15.3	399.9	8.9
SiO_2-3	e	218.3	9.2	224.9	6.7				
SiO_2-4	e	219.0	12.9	228.9	6.3	222.5	6.1	220.1	4.5
SiO_2-5	e	303.1	18.3	353.9	9.8				
SiO_2-6	e	202.8	51.5	236.6	19.6	244.6	8.8	357.9	8.9
1-Al-ep-3	g	53.3	18.1						
4-Al-ep-3	s	210.4	13.0	343.4	38.6				
2-Al-mp-3	g	-46.5	32.4						
3-Al-mp-3	s	264.1	27.9						
2-Cu-ep-3	g	-77.6	46.8						
2-Cu-mp-3	g	30.7	28.8	38.3	28.0				
3-Cu-mp-3	s	232.8	10.4	298.9	12.8				
1-SS-ep-3	s	279.3	6.5	288.8	7.5	302.4	7.9		
2-SS-ep-3	g	11.5	12.5	15.4	12.9	126.0	19.3		
1-SS-mp-3	g	-28.1	46.6	49.7	37.5				
2-SS-mp-3	s	309.9	11.5	324.6	10.3	339.4	12.0		
3-SS-mp-3	s	258.0	9.4	270.0	8.0	338.3	13.2		

homogeneity over the whole surface. Comparing the other samples, sputtered samples have slightly lower $\sigma_{\mathrm{RMS,surface}}$: the mean $\sigma_{\mathrm{RMS,surface}}$ of the all measurements on sputtered samples is (9.4 ± 2.3) mV compared to that of the galvanized samples of (14.1 ± 3.5) mV without and (23.4 ± 15.0) mV with sample 1-SS-mp-3.
In addition the samples 2-SS-mp-3 and 3-SS-mp-3 have the same mean RMS deviation. This is mentioned particularly as these samples are produced in exactly the same way.

By comparing samples with same surface treatment but different coating procedures it can be noticed that the sputtered samples always provide a higher CPD homogeneity and lower $\sigma_{\mathrm{RMS,surface}}$ values compared to their counterparts coated by galvanization. The difference spans from only 4.5 mV to 36.3 mV, if the first measurements after the production are compared.

In conclusion the best results are found at sample 1-SS-ep-3 with

$$\sigma_{\mathrm{RMS,surface,1-SS-ep-3}} \leq 7.9\,\mathrm{mV} \tag{4.14}$$

or

$$\overline{\sigma}_{\mathrm{RMS,surface,1-SS-ep-3}} = (7.4 \pm 0.8)\,\mathrm{mV} \tag{4.15}$$

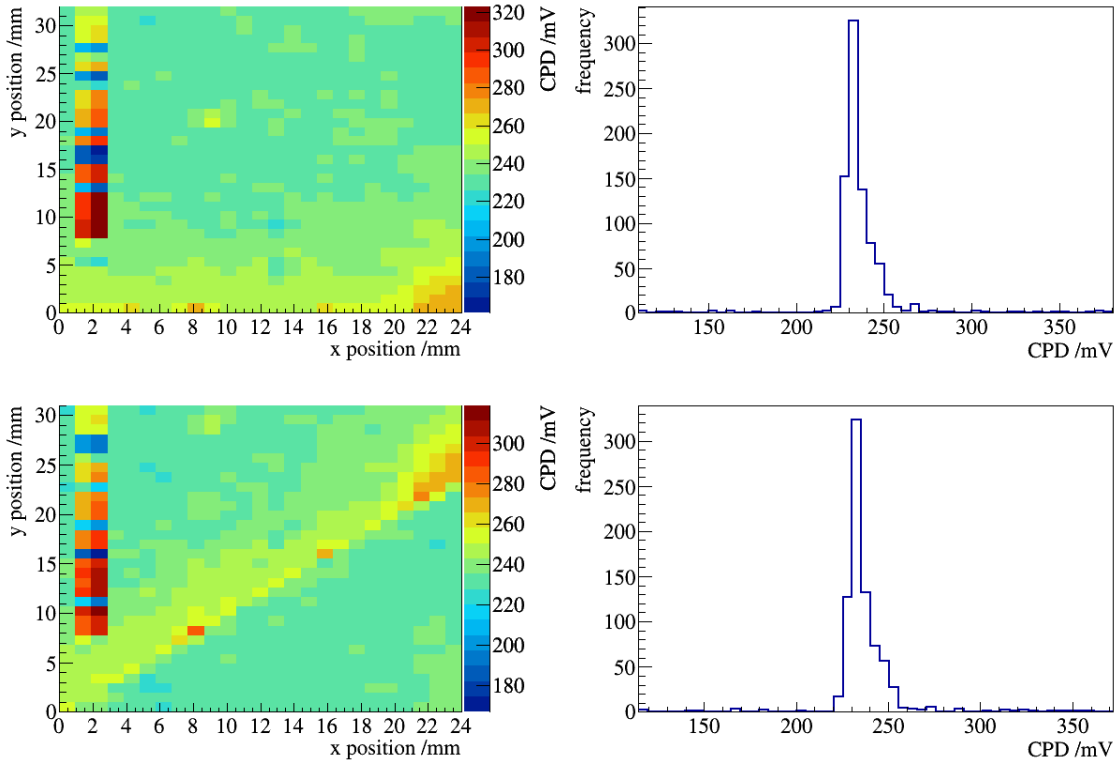

Figure 4.9: Comparison of the CPD maps of the 1st and 2nd measurement of sample Sapphire-6. Top: here both the CPD map of the first measurement of sample Sapphire-6 and the appropriate histogram are shown. The line of increased CPD values in the CPD map in the area from 1 mm to 3 mm in x-direction and 8 mm to 32 mm in y-direction could be caused either by a characteristic of the sample, e.g. a scratch, or by dust which sticks on the tip and is browsed over the sample surface. Bottom: the CPD map and the histogram of the second measurement are plotted. Again a line of higher CPD values is visible in the left plot. This scan and the first scan are performed at exactly the same position of the sample, which makes both shown CPD maps comparable: the line with increased CPD is at the same position. Due to that it is unlikely that the line is caused by dust.

and at sample SiO_2-3 with

$$\overline{\sigma}_{\mathrm{RMS,surface,SiO_2-3}} = (7.5 \pm 3.7)\,\mathrm{mV}. \tag{4.16}$$

Note, that in case of SiO_2-3 only a mean value is given. This is the mean value of 4 measurements performed at the 6-inch sample on the same day. All scans are performed at different areas of the sample.

4.5.5.3 Stability of homogeneity over time

To investigate the long-term stability of the CPD homogeneity the $\sigma_{\mathrm{RMS,surface}}$ results of those samples which are measured more than twice are plotted against the measurement number. This plot can be found in figure 4.10.

In case of sample Sapphire-6 and SiO_2-6 the plotted measurements are performed over a period of 3 months. Between the first and the second measurement a decrease of more

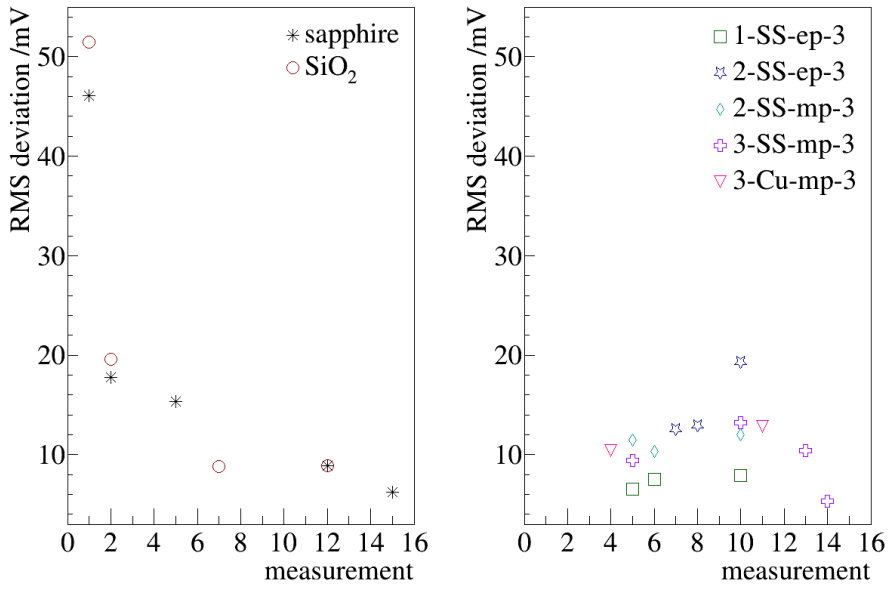

Figure 4.10: Change of the $\sigma_{\mathrm{RMS,surface}}$ over time. For clarity the samples Sapphire-6 and SiO_2-6 are plotted in the diagram on the left side and the samples 1-SS-ep-3, 2-SS-ep-3, 2-SS-mp-3, 3-SS-mp-3 and 3-Cu-mp-3 in the diagram on the right side. Each measurement is related to a date, namely: (1) 28.05.2013; (2) 28.05.2013; (3) 29.05.2013; (4) 16.07.2013; (5) 17.07.2013; (6) 17.07.2013; (7) 18.07.2013; (8) 18.07.2013; (9) 19.07.2013; (10) 14.08.2013; (11) 15.08.2013; (12) 16.08.2013; (13) 27.08.2013; (14) 27.08.2013; (15) 29.08.2013.

than a factor of 2 can be found. That the large $\sigma_{\mathrm{RMS,surface}}$ values of the first measurement of both samples are most likely not caused by dust has already been discussed in the last section. This is additionally supported by the fact, that the later $\sigma_{\mathrm{RMS,surface}}$ values are further reduced.

In case of the results of the stainless steel and the copper samples, which are also plotted in figure 4.10 a more stable behavior of $\sigma_{\mathrm{RMS,surface}}$ is found. With exception of sample 2-SS-ep-3, a sample coated by galvanization, no sample has obvious tendencies towards smaller or lower $\sigma_{\mathrm{RMS,surface}}$ values. The values of 2-SS-ep-3 continuously increase by 7.8 mV within the period of about 1 month. In this time 4 scans are performed.

4.5.5.4 Dependence of homogeneity on a bake-out

The results for $\sigma_{\mathrm{RMS,surface}}$ of the samples SiO_2-6, 1-SS-ep-3, 2-SS-ep-3, 1-SS-mp-3, 2-SS-mp-3 and 3-Co-mp-3 before and after the bake-out are given in table 4.6. The samples SiO_2-5 and 3-SS-mp-3 are identically produced as the SiO_2-6 and 2-SS-mp-3 sample, but not baked-out. These samples function as reference for the baked samples.

For the baked sample 1-SS-ep-3 and 3-Co-mp-3 a decreasing $\sigma_{\mathrm{RMS,surface}}$ is found. It decreases by values ranging from 0.1 mV to 2.7 mV. The other baked samples have increased $\sigma_{\mathrm{RMS,surface}}$ values after the bake-out. The largest absolute increase of 24.8 mV to $\sigma_{\mathrm{RMS,surface}} = 62.3$ mV happens on sample 3-Co-mp-3. But note that this sample already had an RMS deviation over the surface larger than the Rear Wall requirement before the

Table 4.6: Comparison of the $\sigma_{\mathrm{RMS,surface}}$ values before and after the bake-out at 160 °C for about 60 hours. The measurements before the bake-out are performed about 2 weeks prior to those after the bake-out.

		before bake-out		after bake-out	
sample	bake-out	CPD /mV	$\sigma_{\mathrm{RMS,surface}}$ /mV	CPD /mV	$\sigma_{\mathrm{RMS,surface}}$ /mV
SiO_2-5	-	303.1	18.3	353.9	9.8
SiO_2-6	160°C 60 h	357.9	8.9	281.9	27.2
1-SS-ep-3	160°C 60 h	302.4	7.9	179.0	7.8
2-SS-ep-3	160°C 60 h	126.0	19.3	-51.9	20.0
1-SS-mp-3	160°C 60 h	49.7	37.5	-71.7	62.3
2-SS-mp-3	160°C 60 h	339.4	12.0	180.9	15.2
3-SS-mp-3	-	258.0	9.4	359.7	10.4
3-Co-mp-3	160°C 60 h	298.9	12.8	144.1	10.1

bake-out. The largest relative change can be observed for sample SiO_2-6. In case of this sample the $\sigma_{\mathrm{RMS,surface}}$ value increases by a factor of 3.1. That means, that this sample, which met the $\sigma_{\mathrm{RMS,surface}}$ requirement before the bake-out, seems not to be suitable anymore after the bake-out. This is further supported by the fact that the $\sigma_{\mathrm{RMS,surface}}$ of the unbaked reference sample SiO_2-5 decreases at the same time. It is also supported by the CPD maps presented in figure 4.11.

To verify the unsteady CPD distribution over the surface an additional measurement of sample SiO_2-6 is performed two days after the first measurement. The result of this measurement is

$$205.5 \pm 16.1\,\mathrm{mV}. \tag{4.17}$$

This means, that $\sigma_{\mathrm{RMS,surface}}$ is decreasing again. The CPD map also looks similar, but the difference between the minimal and maximal CPD value is reduced. This supports the assumption that the CPD homogeneity rises with time.

4.5.6 Discussion of the ambient air Kelvin Probe results

The results of the ambient air Kelvin Probe provide first insights as how the best suitable Rear Wall design looks like. The investigation of the dependence on the surface treatment show no correlation between surface treatment and CPD homogeneity. With exception of the copper mirror all samples have an increased homogeneity concerning CPD after coating. The worse homogeneity of the mirror could be explained by a higher surface roughness: as stated by the manufacturer of the mirror, the mean surface roughness is usually in the range from 1 nm to 5 nm [LTU14]. In case of 316L stainless steel values of about 3.2 nm and 1.5 nm can be found in [Ven06] for mechanical polishing or electropolishing, respectively. However, due to the fact that step-like scratches in the surface can cause work function changes of up to 0.9 mV [Jia97, Jia98a], even small scratches in the surface must be prevented. Therefore, specially produced metals which are plastered with foil are recommended to be used for later samples and Rear Wall candidates. The surface of these metals is protected during the manufacturing process by the foil. These special metals are available at the KIT main workshop. To get rid of possible damages during the processing of the metallic blank discs, an electropolishing process is also recommended.

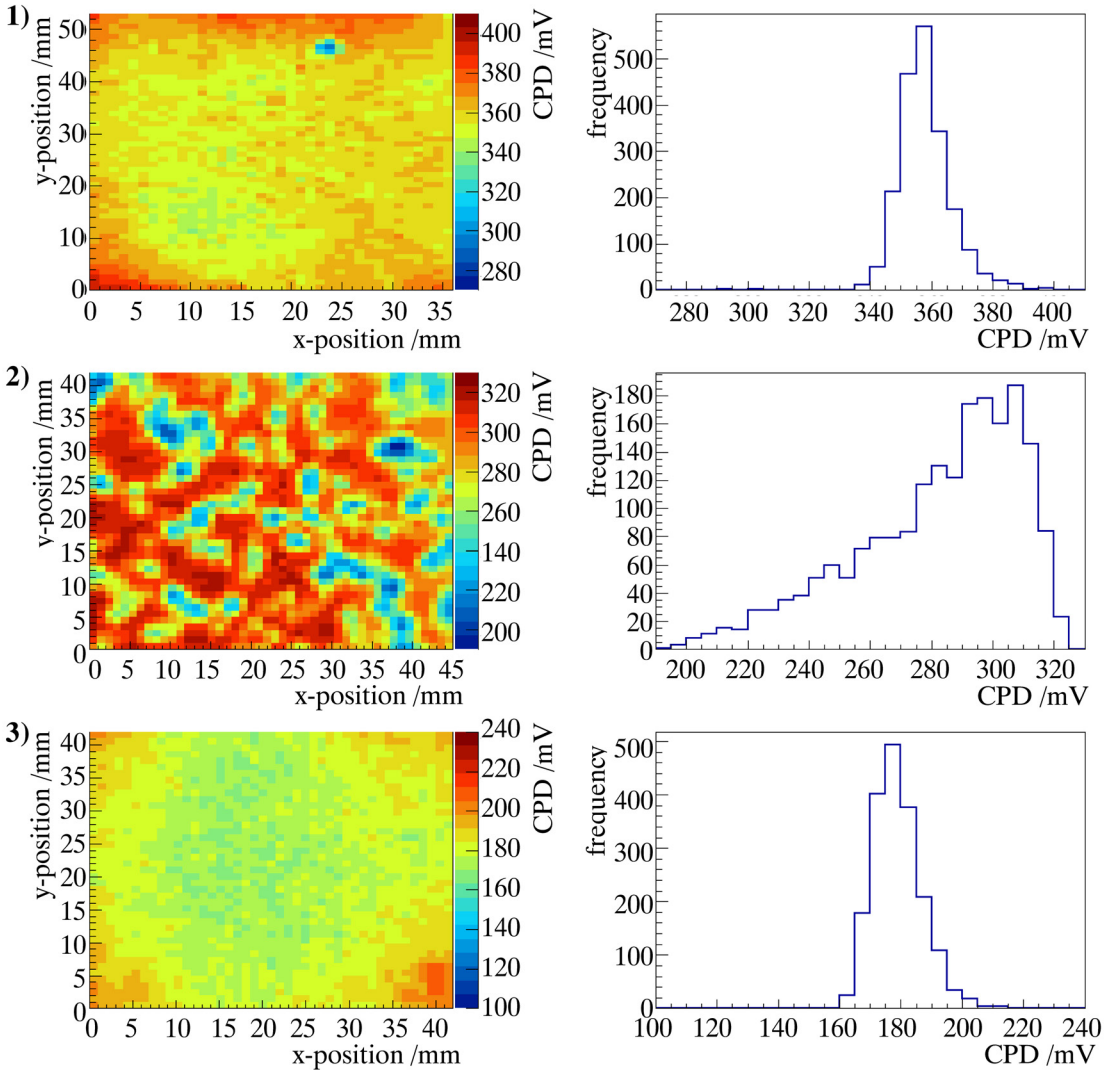

Figure 4.11: Comparison of CPD maps before and after bake-out. On the left side the CPD maps and on the right side the corresponding histograms are plotted. All histograms and maps are plotted with the same difference of minimal and maximal CPD value for better comparison. In (1) the results of sample SiO_2-6 before the bake-out are shown. In (2) those after the bake-out are presented. The CPD value is less steadily distributed over the surface than prior to the bake-out. This can also be detected in the histogram which is broadened after the bake-out. For comparison the results of sample 1-SS-ep-3 after the bake-out are also given in (3). Here no unsteadiness can be observed in the CPD map and the distribution in the histogram is also not as broad as that of sample SiO_2-6.

With these findings the first question of section 4.5 concerning the surface treatment and its dependence on the CPD homogeneity is successfully answered.

During the investigations with the ambient air Kelvin Probe an even larger effect on the homogeneity caused by the coating process is found. All samples with same surface treatment but different coating processes have lower $\sigma_{\mathrm{RMS,surface}}$ values if they are sputter coated. In addition, the evaporated sapphire and silicon samples also provide sufficient results with $\sigma_{\mathrm{RMS,surface}} < 20\,\mathrm{mV}$, at least after a certain time. If this result is combined with the fact, that the samples with the lowest $\sigma_{\mathrm{RMS,surface}}$ values are produced with silicon and stainless steel substrates it is recommended to either produce the Rear Wall candidates using sputter coated stainless steel or silicon wafers coated by evaporation. As neither stainless steel samples coated by evaporation nor SiO_2 samples coated by sputtering were tested, a statement on the possible suitability of such samples is not possible.

The long-term investigation of the $\sigma_{\mathrm{RMS,surface}}$ values indicates that a change in the uppermost surface layer of the samples with silicon and sapphire substrate happens. These layers, which at ambient air usually consist of adsorbed water molecules, smear out possible inhomogeneities of the work function and also reduce the work function [Hec12]. If this is the case, a decrease in CPD homogeneity is expected after a bake-out, as adsorbed water layers are removed. And indeed, this increase is found after a bake-out of the silicon sample SiO_2-6. Also the fact that $\sigma_{\mathrm{RMS,surface}}$ is again decreased two days after the first measurement of the baked sample, can be explained by the formation of new water layers on the surface. But the long-term stability of the Rear Wall's $\sigma_{\mathrm{RMS,surface}}$ must be ensured during the KATRIN measurements. This is of particular interest, as the work function homogeneity cannot be measured anymore, after the Rear Wall is installed. Therefore, samples with an unstable long-term behavior must be excluded. This also extends to samples with a work function homogeneity of more than 20 meV after a bake-out: it is planned to bake-out the Rear Section at least once before the start of the KATRIN experiment. As the silicon samples show an unstable behavior over several months and have an increased $\sigma_{\mathrm{RMS,surface}}$ after the bake-out, they are not suitable for usage as a Rear Wall.

In contrast to the results of the silicon and sapphire samples the stainless steel samples do neither show a temporal nor a bake-out effect. This could be explained by a faster adsorption of water for those surfaces. In that case a removal or reduction of the adsorbed layers would not be detectable with the Kelvin Probe setup working at ambient air: even if the samples are baked out directly at the University of Mainz, the sample must be exposed to ambient air for at least 12 to 24 hours to achieve the equilibrium in the optical enclosure. Therefore, measurements at vacuum are required. These measurements are described in section 4.6 and section 4.7.

Based on all these results an answer to the second question from section 4.5 can be given. The recommended Rear Wall design consists of:

- a **stainless steel** substrate of 2 mm thickness which is cut out of **foil plastered raw material** and afterwards **electropolished**
- 100 nm of **sputtered titanium** as an adhesion layer
- 1 µm of **sputtered gold**.

The comparatively large gold layer thickness is chosen, to prevent the gold from completely diffusing into the other layers during the bake-out of the Rear Section. In addition, the probability that the gold layer is removed completely by the ion bombardment from the tritium source is reduced. In the following experiments the focus is on samples which are produced with regard to these recommendations.

Furthermore, the need of vacuum compatible measurement techniques gets obvious: the Rear Wall will be installed in a vacuum environment with a pressure of about 10^{-5} mbar. In addition, the Rear Wall will be baked out in this environment. It is also planned to irradiate the Rear Wall with high intensity UV light to prevent the source from getting positively charged. But as UV light irradiation enables the desorption of adsorbed molecules from the surface, it can affect the work function homogeneity similar to a bake-out. For that reason measurement techniques, which enable the simulation of these conditions, are needed to verify the suitability of the recommended Rear Wall design. An investigation of the impact of the central hole must also be possible. Therefore, photoelectron spectroscopy measurements are performed at the monitor spectrometer of KATRIN which enable the investigation of all aspects: the impact of the vacuum environment, bake-outs, UV irradiation and of the hole on the work function and its homogeneity over the surface. These measurements and their results are presented in the following section.

4.6 Absolute work function measurements by photoelectron spectroscopy

The photoelectron spectroscopy measurements at the monitor spectrometer enable the absolute measurement of the work function of Rear Wall samples. Due to the results of the ambient air Kelvin Probe bare stainless steel and 3-inch samples based on stainless steel substrates are investigated during these measurements. In addition the usage of the Rear Wall as an electrode in the source part of a MAC-E filter (compare 2.1.3) can be tested in the experimental setup. In doing so the suitability or the failing of the recommended sample design can be examined.

The ambient air Kelvin Probe measurements were not able to give a final answer on the third question from the beginning of this chapter

3. How does a bake-out or UV irradiation affect the work function and its homogeneity?

Especially the impact of UV irradiation could not be addressed at all. With photoelectron measurements at the monitor spectrometer information about the impact of both, a bake-out and UV irradiation, can be gained. In addition, a Kelvin Probe is in general incapable of investigating the region of the hole or the area directly next to it[16]. For that reason the question

4. How does the central hole effect the work function at the center of the flux tube?

from the beginning of this chapter can only be addressed by the measurements at the monitor spectrometer.

The experimental setup which is used for the investigation of the stainless steel samples is described in the following section 4.6.1. The measurement procedure and the analysis method are then discussed in sections 4.6.2 and 4.6.3, respectively. Afterwards the results of previous measurements at the monitor spectrometer and the experiences gained during those measurements are summarized (section 4.6.4). The execution of new measurements and their results are presented in the sections 4.6.5 and 4.6.6. The final discussion of the results concerning photoelectron measurements in the last section (4.6.7) reconnects with this introductory section and gives answers to the questions posed.

[16] During the Kelvin Probe measurements space of about 1 mm is left to the hole.

4.6.1 Experimental setup at the Monitor Spectrometer

The photoelectron measurements are performed at the source part of the monitor spectrometer. The monitor spectrometer was briefly introduced in section 2.2.3 already. A drawing of its setup is shown in figure 4.12 together with some technical information on it.

Besides the monitor spectrometer itself, the setup of the photoelectron measurements consists mainly of two parts which were both developed at the University of Mainz and are shown in figure 4.13: the sample holder acting as a high voltage electrode and an optical setup providing the required UV light.

The light source of the optical system is a deuterium lamp. Its light is focused by a lens with 3.5 mm focal length into a prism spectrometer. The prism spectrometer filters the light of the deuterium lamp to a certain wavelength. The particular wavelength must be adjusted manually. This extends to the slit width of the prism spectrometer as well. The specifications of this spectrometer can be found in [Lei]. After the prism spectrometer another lens of the type LA4148 from Thorlabs with 5 mm focal length collimates the light. A lens of the type LA4158 from Thorlabs with a focal length of 25 cm focuses the light. The long focal length make a small spot size at the sample possible. A mirror of the type PF10-03-F01 from Thorlabs is used to redirect the focused light through a CF-40 sapphire window into the source vacuum chamber on the sample. Due to the fact that the optical setup is well aligned the light intensity was so large that too many electrons are produced and the detector was swamped by electrons. For that reason a pinhole aperture is inserted in front of the prism spectrometer. This reduces the light intensity and enables a measurement.

The sample holder is based on a two-part design which makes the installation of 2- and 3-inch samples possible. Larger samples cannot be tested due to space restrictions. The sample is clamped between the two parts by the usage of insulating PEEK rods and nuts. These rods are made of PEEK to insulate the sample from the rest of the sample holder construction and the vacuum system. Together with an additional KAPTON foil the sample holder is insulated by more than 10 kV from the other components of the setup. As the holder also acts as electrode, it is shaped in a way that the resulting fields focus the emitted electrons to a parallel beam. If an electrode is built with this special shape, it is called a Pierce electrode [Pie49]. To minimize the production of background electrons from the sample holder, it is platinized. As the work function of polycrystalline platinum is 5.64 V [Hay14] and therefore higher than that of gold[17], close to the threshold of gold no electrons can be emitted from the sample holder. To enable the positioning of the sample, the actual sample holder is mounted on top of two plates of which each have two parallel elongated holes. These make a change in x- and y-position of the sample possible. The height and the dumping of the sample can be changed, as the sample holder and the plates are connected by threaded rods and nuts. All components mentioned so far are mounted on a CF flange which can be connected to the vacuum chamber. In the center of this flange there is a high voltage feed-through. The connection between the sample and the feed-through is established by a KAPTON insulated wire.

As both, the model of the deuterium lamp and its specifications, are unknown, the optical setup has been calibrated at the University of Mainz. In doing so the optical power at the position of the sample has been measured dependent on the wavelength selected at

[17] The maximum work function of gold is 5.47 in case of monocrystalline Au(100) [Hay14].

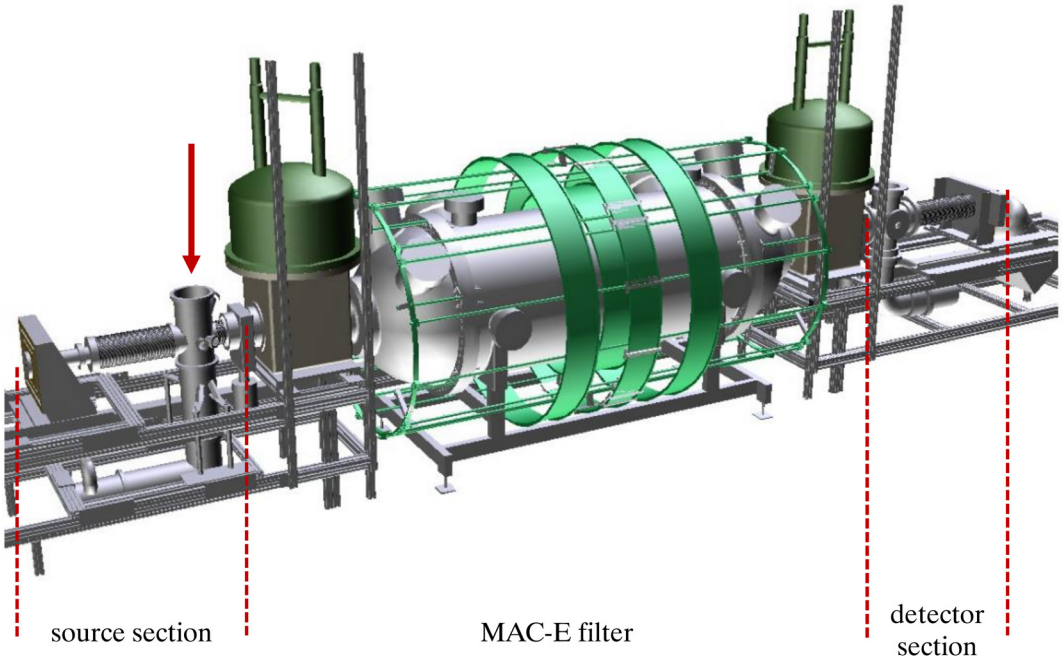

Figure 4.12: The monitor spectrometer of KATRIN. The setup of the monitor spectrometer can be divided into 3 main parts: the source section, the detector section and the actual MAC-E filter. The later consists of 2 solenoids (the domes of the solenoids are marked by dark green color) with a maximum magnetic field of 6.014 T at both ends of a vacuum tank. The diameter of this spectrometer vessel is 1 m. The distance from center to center of the solenoids is about 4 m. At the analyzing plane of the MAC-E filter the magnetic field drops to 309 μT. 4 air coils improve the magnetic field at the analyzing plane and 2 further coils in horizontal direction compensate for the earth's magnetic field (both shown in light green in the figure). The retarding potential can be applied to a system of cylindrical and conical full metal and wire electrodes. The energy resolution of the monitor spectrometer is $\Delta E = 0.93$ eV at 18.6 keV. In the detector section at the right side of the figure a circular silicon PIN-diode is installed as detector. The sensitive area of the detector is 1.5 cm^2. Around the detector 4 further auxiliary PIN-diodes are arranged. In the source section, at the left side of the MAC-E filter, the radioactive sources are usually placed which are used to monitor the high voltage stability of KATRIN. In case of the photoelectron measurements the large bellow and everything left of it is removed. The vacuum chamber marked by the red arrow is the place where the samples are installed (adapted from [Erh14]).

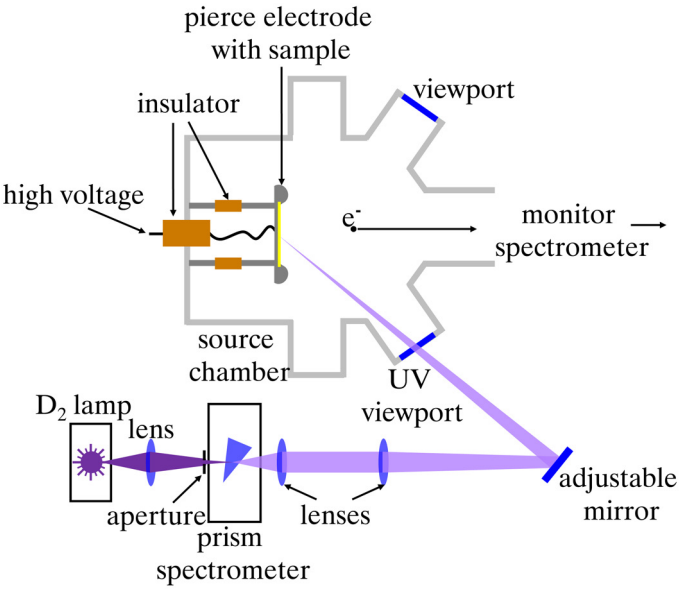

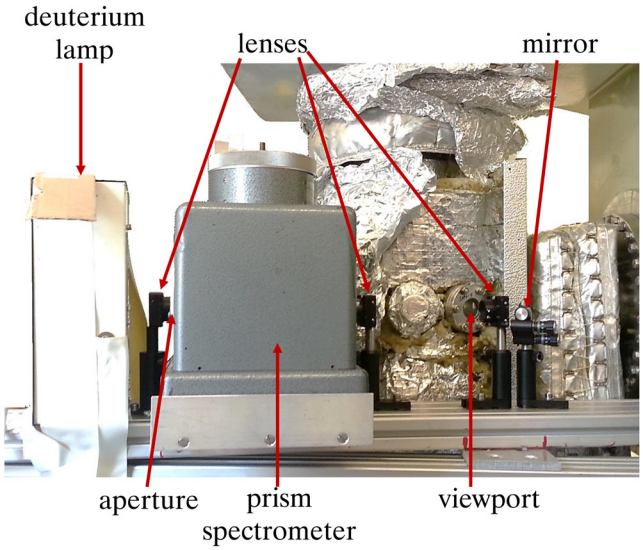

Figure 4.13: Scheme and photography of the setup of the photoelectron measurements at the monitor spectrometer. Top: here a schematic drawing of the setup at the source part of the monitor spectrometer is shown. The light of the optical system is focused in the vacuum chamber of the monitor spectrometer source region. Here the Pierce electrode with the sample is installed. In addition to the flange where the piece electrode can be installed and the port with the sapphire window, the vacuum chamber has 2 further used ports. On one of these a viewport is installed, which enables the visual control of the light spot position on the surface of the sample. On the other port a pressure sensor is installed. Bottom left: a photography of the optical setup is shown. All optical components are mounted to an aluminum profile. Bottom right: a photography of the Pierce electrode with installed sample is shown. The electrode is mounted on two plates with elongated holes for x-y-z positioning which are mounted on a CF-flange (in accord with [Bab14]).

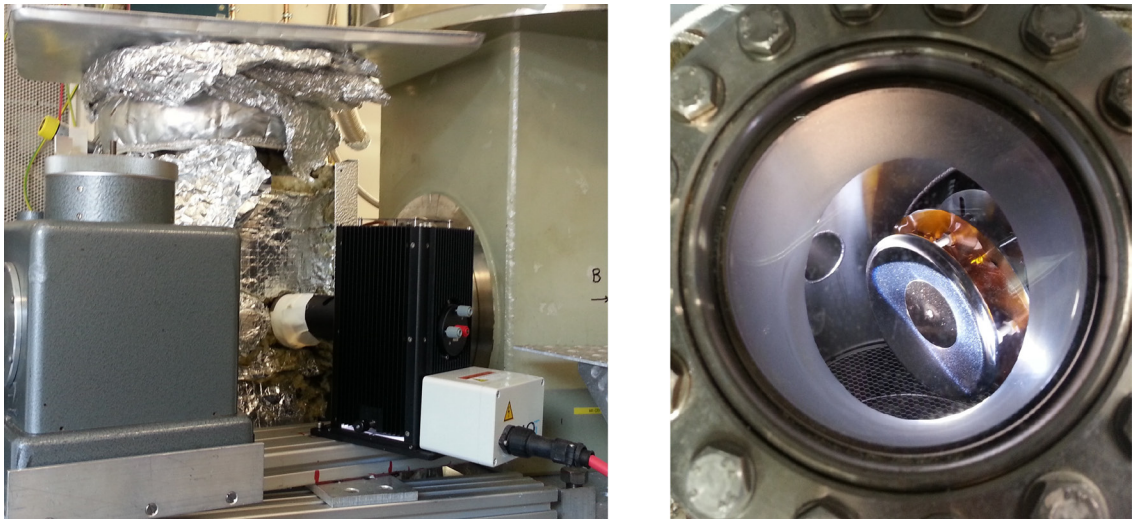

Figure 4.14: Photography of the UV irradiation setup with a high intensity xenon lamp at the source part of the monitor spectrometer. Left: the xenon lamp is directly mounted to the sapphire window of the vacuum chamber. To reduce the amount of produced ozone, the area between the lamp and the viewport is closed up by tape. The light spot is collimated by the integrated optics at the front of the lamp. Right: the light spot of the xenon lamp on the surface of the sample can be seen. The sample is completely irradiated.

the prism spectrometer. The results of this calibration can be found in [Bab14]. The optical setup can be replaced by a 300 W xenon lamp. This lamp is used to determine the effect of high intensity UV irradiation on the work function of the sample. It is mounted directly in front of the sapphire viewport (see figure 4.14).

The flange with the sample holder and the high voltage feed-through are installed at the end of the source vacuum chamber of the monitor spectrometer. The monitor spectrometer is used in a pass through mode for the measurements. That means, that the retarding potential of the MAC-E filter is below the acceleration potential which is applied to the Pierce electrode. Therefore, all electrons produced at the cathode are reaching the detector at the other side of the monitor spectrometer and are counted there. The chosen value of the acceleration potential is about 10 kV to improve the detection efficiency and signal to noise ratio of the monitor spectrometer. In addition to the main setup of the monitor spectrometer its corresponding infrastructure for bake-outs can also be used during the measurement period.

The present electric fields in combination with the magnetic fields of the superconducting magnets generate a Penning trap [Bla06] for electrons. To deplete this Penning trap a wire sweeper is installed in the beam tube. This wire sweeper consists of a grounded wire installed in a ring. This ring can be clamped into the beam tube between the source section and the spectrometer vessel. The wire sweeper prevents the filling of the Penning trap and associated discharges efficiently.

All parts of the just described setup are used to measure the work function by photoelectron emission. The procedure of these measurements is described in the following section.

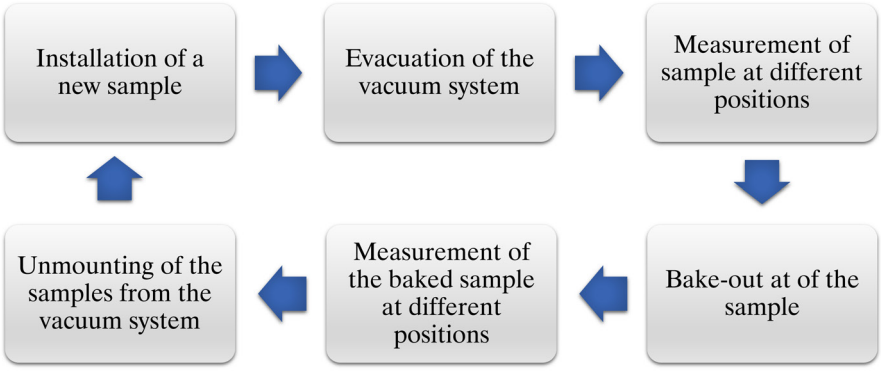

Figure 4.15: Measurement procedure during photoelectron spectroscopy at the monitor spectrometer. Every measurement starts with the installation of a new sample. To enable an unscattered motion of the electrons through the spectrometer the vacuum chamber is evacuated afterwards. Only if the pressure in the source vacuum chamber is below 10^{-8} mbar the connection to the monitor spectrometer vessel is opened. After the measurements at different positions of the sample, the vacuum chamber is baked out for at least a day at the target temperature of 180 °C and the sample is measured again. The last part of each measurement cycle is the dismounting of the sample. A new cycle starts again with the installation of a new sample.

4.6.2 Measurement procedure

A rough overview of the necessary steps during the photoelectron measurements is given in figure 4.15: a new sample is installed at the source vacuum chamber and a first measurement is performed. After a bake-out of the system, the sample is measured again. The dismounting of the sample from the vacuum chamber is the last necessary step before this procedure restarts with another sample.

To be able to mount a new sample at the source vacuum chamber, it must be installed in the sample holder prior to that. This also includes the installation of a defined surface behind the sample to cover the sample holder surface. The defined surface acts as a background at the hole position of the actual sample. In addition, the sample and the voltage feed-through must be electrically connected. Afterwards the flange, on which the sample holder is installed, is mounted on the source vacuum chamber of the monitor spectrometer.

During the measurement the wavelength dependent photoelectron rate is measured. This is performed by deactivating the filter spectrometer. That means that a retarding potential of $U_{\mathrm{MS}} \approx -9.98\,\mathrm{kV}$ is applied at the MAC-E filter of the monitor spectrometer. The cathode on the other hand is put on a potential of $U_{\mathrm{C}} \approx 10\,\mathrm{kV} < U_{\mathrm{MS}}$. As a result even emitted electrons with vanishing kinetic energy can pass the electrostatic filter.

The photon energy of the optical setup defines the kinetic energy of the emitted electrons. The wavelength is changed in the range from 205 nm to 320 nm, always starting at the longest and going down to the shortest wavelength. A complete scan through this range is called a measurement in the following. The distance of the wavelength at which a measurement is performed is either $\Delta\lambda = 5\,\mathrm{nm}$ or $\Delta\lambda = 1\,\mathrm{nm}$. The smaller steps are only used in the range from 320 nm to 280 nm to detect the exponential rise of the electron rate close to the work function more precisely. But note, that not all measurements are performed with these finer steps. The broadness of the wavelength distribution is

determined by the slit width N at the prism spectrometer. This can be manually set to arbitrary values from 2 to 90. For most of the measurements a value of $N = 5$ is used. The wavelength distribution is linked to N by a wavelength dependent proportional factor. This factor can be taken from graphs given in the manual of the prism spectrometer [Lei]. The resulting wavelength distribution at $N = 5$ is between $\sim$0.3 nm at 205 nm and $\sim$1.5 nm at 320 nm.

By analyzing the wavelength dependent electron rate, the work function of the sample can be calculated. These measurements are performed for each sample at least 5 times: at top, bottom, left, right and hole position. For those samples where the hole position is not equal with the central position the center position is also measured. By calculating the mean value of these measurements the $\sigma_{\mathrm{RMS,surface}}$ can be estimated. The analysis method to calculate the work function from the measured data is presented in the following section.

4.6.3 Analysis method

The determination of the sample work function is achieved by the analysis of the increase in the electron rate in dependence of the incident photon energy. For this the derivative of the Fowler function [Fow31]:

$$\begin{aligned} A \cdot \left(\frac{\pi^2}{6} + \frac{1}{2}\mu^2 - \left(\exp^{-\mu} - \frac{\exp^{-2\mu}}{2^2} + \frac{\exp^{-3\mu}}{3^3} \right) \right) + C \text{ for } \mu > 0, \\ A \cdot \left(\exp^{\mu} - \frac{\exp^{2\mu}}{2^2} + \frac{\exp^{3\mu}}{3^3} \right) + C \text{ for } \mu \leq 0, \end{aligned} \tag{4.18}$$

is fitted to the experimental data. In the fit function A is a constant of proportionality, C is the background and

$$\mu = e^{\frac{E_\gamma - \Phi}{k_\mathrm{B} T}}, \tag{4.19}$$

where E_γ is the photon energy, Φ is the work function, k_B is the Boltzmann constant and T is the temperature.

To take the wavelength dependent intensity of the optical setup into account, the calibration of the optical setup is also included in the analysis. At energies where no calibration data is available a cubic spline interpolation is performed [Gal09].

By knowing the energy dependent quantum yield [Jia98b] and the free mean path of electrons in gold [Sea79] the expected shape of the spectrum can be calculated. If the experimental data is compared with this theoretical shape of the spectrum it can be found that both generally match at energies close to the work function (compare figure 4.16). Both have a maximum at energies about 1 eV above the threshold energy as well. But in contrast to the experimental data the calculated data is not reduced to the background rate. A systematic effect causing this decrease could be excluded by measuring the wavelength dependent electron rate at the monitor spectrometer with a completely different setup, namely the Münster e-gun [Val11]. The data of this measurement can be found in appendix E.3 on page 258.

The rapidly decreasing rate can be explained by the coincidence of several effects: a free electron cannot absorb light due to the violation of the conservation of momentum during

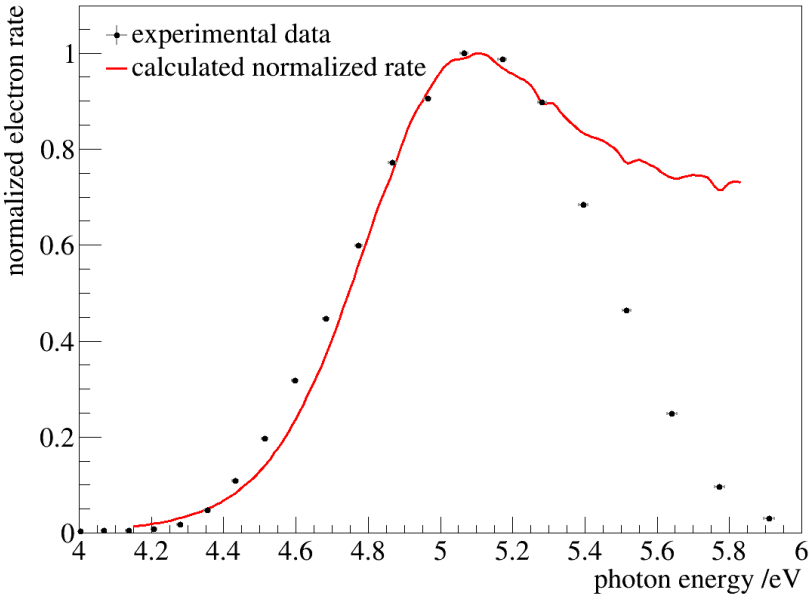

Figure 4.16: Comparison of calculated and measured data of the photoelectron spectroscopy. The black points mark the experimental data of sample 3-SS-ep-3 with gold background at the top position. The data of this sample is used, as its work function is about 4.2 eV. This is important as the quantum yield assumed for the red line, which is the calculated electron rate, is based on data of a gold surface with a work function of about 4.2 eV given in [Jia98b]. Besides the quantum yield the decreasing free mean path in gold with increasing photon energy is used to calculate the rate [Sea79]. As one can see, for both the calculated and the measured data, the electron rate rises until the maximum at about 5.1 eV with the photon energy. From this point on the measured data decreases until it reaches the background rate. In contrast to this the calculated electron rate only drops to a value of about 70 % of the maximum value.

this process[18]. In a material the momentum conservation is achieved by interactions with the potential of the bulk (volume effect) or the surface (surface effect) [Tho57]. In case of the volume effect the electrons lose energy through collisions, e.g. with other electrons in the conductive band or by the excitation of plasma vibrations which are also-called phonons. The latter is only possible from a certain energy on and its probability is increasing with the kinetic energy of the electron [Sea79]. Both, collisions and excitations, decrease the number of electrons as the electrons do not leave the bulk material anymore. A surface effect involved in photoelectron emission is selective transparency [Fre31]. If the surface field includes a transition from one potential energy level U_1 inside of the material to another level U_2 outside of it, the reflection coefficient of the electron reflection is dependent on the electron energy. The transition increases with the kinetic energy of the electron after a first drop. This results in a peak in the spectrum. In addition, the density of states, both of the bulk and the surface, is limited. At certain material specific energies there are even gaps in these densities [Feu76]. These gaps cause that despite of a sufficient number of photons no more electrons can be emitted in a capped region.

[18] At higher energies a partial energy transfer from a photon to a free electron is possible, but only with a small wavelength change of the photon in the order of $\Delta\lambda/\lambda \approx 10^{-5}$. This is the so-called Compton effect [May57].

All these effects are frequently investigated. Therefore, a more detailed description can be found in [Mit36, Mit34, Tho57, May57, Met57, Fre31]. Nevertheless, an inclusion of these effects into the fit of the analysis of the measured data is unrewarding. The introduction of more fit parameters would increase the uncertainty of all fit parameters including the work function. For that reason the fit is restricted to energies close to the work function instead. The used energy range starts from an energy below the work function (about 3.8 eV to 4.2 eV) to approximately 1 eV above the work function. The exact values are dependent on each spectrum. In this region the described effects can be neglected.

Before data of the measurements which were performed in the course of this thesis are analyzed, previous measurements of Rear Wall samples at the monitor spectrometer are briefly described in the following section.

4.6.4 Previous results of measurements at the monitor spectrometer

First results of photoelectron measurement at the monitor spectrometer have been presented in [Bab14]. One of the main results of these measurements was the fact, that the work function of gold coated samples is significantly lower than given in literature: In literature a work function of 5.31 eV in case of Au(111), 5.37 eV in case of Au(110), 5.47 eV in case of Au(100) [Hay14] and 4.8 eV to 5.5 eV in case of amorphous and polycrytalline gold [And59, Hay14] can be found. The work function values determined at the monitor spectrometer are about 1 eV lower than these values. Mostly values in the range of 4.2 eV to 4.4 eV are measured.

This discrepancy between literature and measurement can be explained by the physisorption of water molecules on the surface of the samples. The water molecules are condensed from the humidity of the air the samples are exposed to. The samples in literature are usually produced and measured in the same vacuum chamber and therefore not exposed to air. If that is not the case, a work function value of about 4.2 eV for gold surfaces can be found in the literature as well [Sav95, Jia98b].

Another important result was, that no significant degradation or change can be found in the work function if a gold layer, coated on sapphire or silicon, is irradiated by electrons. For this test 10 keV electrons were used to simulate the electron bombardment from the tritium source. Although the energy of the electrons is less than the maximum energy achievable from tritium decay, it is more than the mean value of 5.73 keV [Pil61]. The used current also exceeds the expected current during the KATRIN run time of 5 years.

The results obtained after bake-out of the samples based on sapphire and silicon were different. In case of the sapphire sample only an insignificant change in the mean work function of about 5 mV could be found, while the work function of the silicon sample was shifted by 300 mV. This shift was associated with a color change in the gold layer. The explanation for this is the diffusion of the titanium adhesion layer into the gold driven by the elevated temperature during the bake-out [Mar10].

Furthermore, another measurement method was used during the first photoelectron spectroscopy: instead of changing the wavelength, the potential of the monitor spectrometer was changed. The potential increases from a value where no electrons can pass the analyzing plane to a value where all electrons pass the filter. By analyzing the broadness of the kinetic energy distribution of the emitted electrons at several wavelengths an extrapolation to a vanishing energy distribution can be performed. The photon energy at that point is equal to the work function. But these measurements need a comparatively long

time of up to several days for the determination of the work function at one position of the sample, if suitable uncertainties should be achieved. Therefore, this kind of measurement is not recommended for the development of the Rear Wall. Only the measurement method already described is used during the measurements presented in this thesis. A description of the execution of the measurements can be found in the next section.

4.6.5 Execution of measurements

The measurements at the monitor spectrometer are performed over 4 weeks. Overall 4 different samples, namely sample 2-SS-ep-3, 3-SS-ep-3, 4-SS-ep-3 and 5-SS-ep-3 are measured. All of these samples with the exception of sample 2-SS-ep-3 are produced by sputter coating of an electropolished substrate with a central 4 mm hole. Although the substrate of sample 2-SS-ep-3 is also electropolished, it is not coated by sputtering but by galvanization and the off-center hole is only 3 mm in diameter.

The background behind the hole is varied only in case of sample 3-SS-ep-3. Both stainless steel and gold are installed behind this sample at consecutive measurements. To be able to compare the measurements at the hole position with measurements of the background material, a measurement of the stainless steel back plate of the sample holder is also performed before and after a bake-out. Since it is necessary that all measurements are reproducible for this comparison, the reproducibility over time and after the motion of the mirror has been successfully proven (compare appendix C). In case of all other samples a gold surface is installed in the background. In case of sample 2-SS-ep-3 the gold surface of sample 3-SS-el-3 and in case of the other samples the gold surface of sample 2-SS-ep-3 is used as background.

All samples are first measured at the 5 to 6 defined measurement positions and then baked out at 180 °C for different duration. During heating up and cooling down of the system the temperature gradient is adjusted to 0.2 °C/min. After the bake-out, a measurement at each position is performed again. Sample 5-SS-ep-3 is additionally irradiated with high intensity UV-light of the xenon lamp. This irradiation is done after the first measurement of all positions. Afterwards these positions are measured again, before the sample is baked out. A summary of the measured samples, the materials installed behind these samples and their treatment can be found in table 4.7. A more detailed list of actions performed during the 4 weeks of measurement time, e.g. including details like the monitor spectrometer run numbers of performed voltage scans, can be found in appendix E on page 246 ff.

4.6.6 Results of the measurements by photoelectron spectroscopy

In this section the results of the photoelectron spectroscopy at the monitor spectrometer are presented. For clarity only the results of the analysis are shown here. The spectrum of each individual measurement can be found in appendix E.2 on page 248.

The results are divided in two parts: section 4.6.6.1 investigates the work function homogeneity over the sample surface and the effect of a bake-out or UV irradiation. section 4.6.6.2 deals with the work function at the hole position and its dependence on the background material.

Table 4.7: Summary of sample treatment during the photoelectron measurement. Stainless steel refers to the back plate of the sample holder. The duration of a bake-out starts, when 180 °C is reached, and ends as soon as the temperature is reduced again. In case of the bake-out marked with *, one of the three heating sleeves installed at the monitor spectrometer reaches only 170 °C.

sample	background	bake-out /h	UV irradiation /h
3-SS-ep-3	stainless steel	49	-
3-SS-ep-3	2-SS-ep-3	15	-
stainless steel	-	33	-
2-SS-ep-3	3-SS-ep-3	40	-
4-SS-ep-3	2-SS-ep-3	34	-
5-SS-ep-3	2-SS-ep-3	33*	0.5

4.6.6.1 The work function homogeneity over the sample surface and the effect of a bake-out or UV irradiation

Each of the tested samples have been measured at 5 to 6 positions before and after any treatment. Therefore, it is not possible to calculate either a $\sigma_{\mathrm{RMS,surface}}$ or a $\sigma_{\mathrm{RMS,pixel}}$ value (compare section 4.1). Instead, the mean value $\overline{\Phi}$ and the RMS deviation of the measurements $\sigma_{\mathrm{RMS},\overline{\Phi}}$ is calculated. The measurements at the hole position are not included in the averaging. As it is assumed, that the measurements are uniformly distributed over the surface, at least an assumption on the homogeneity over the surface is possible. The values of $\overline{\Phi}$ and $\sigma_{\mathrm{RMS},\overline{\Phi}}$ are given in table 4.8 for all samples. The individual Φ values and the error of each measurement can be found in appendix E.2 on page 256 ff.

By comparing the $\overline{\Phi}$ values before any treatment 3 things are apparent:

- All $\overline{\Phi}$ values are below 4.7 eV.
- The $\overline{\Phi}$ values vary between (4.168 ± 0.011) eV in case of sample 3-SS-ep-3 and (4.683 ± 0.044) eV in case of sample 5-SS-ep-3.
- $\sigma_{\mathrm{RMS},\overline{\Phi}}$ of the sample 2-SS-ep-3, 3-SS-ep-3 and 4-SS-ep-3 is below 20 meV, while that of sample 4-SS-ep-3 and 5-SS-ep-3 is above 20 meV.

After the bake-out, the $\overline{\Phi}$ values of all samples are reduced with exception of sample 3-SS-ep-3 with stainless steel background. This decrease is larger than 500 mV. It also affects each of the work function values in a similar way independent of the measurement position (compare figure 4.17). On the contrary, $\overline{\Phi}$ of sample 3-SS-ep-3 decreases only by 72 mV during the measurements with gold background. This comparatively small change could be caused by bake-out time which was more than a factor of 2 shorter than in case of all other bake-outs. After the bake-out of sample 3-SS-ep-3 with stainless steel background $\overline{\Phi}$ increases by 26 mV. Therefore, $\overline{\Phi}$ values of the measurements with steel background before and after the bake-out are compatible within $2\,\sigma$. But note, that the difference in the change of $\overline{\Phi}$ cannot be caused by the background material as the results of the hole position are not included in the averaging. The hole position is the only position which can be affected by the background material.

In addition to the bake-out sample 5-SS-ep-3 is irradiated by high intensity UV light, too. As this irradiation took place before the bake-out, $\overline{\Phi}$ after the irradiation must be compared with $\overline{\Phi}$ of the unbaked sample. The resulting change is 36 meV. That means the result of $\overline{\Phi}$ before and after the UV irradiation are compatible within the errors.

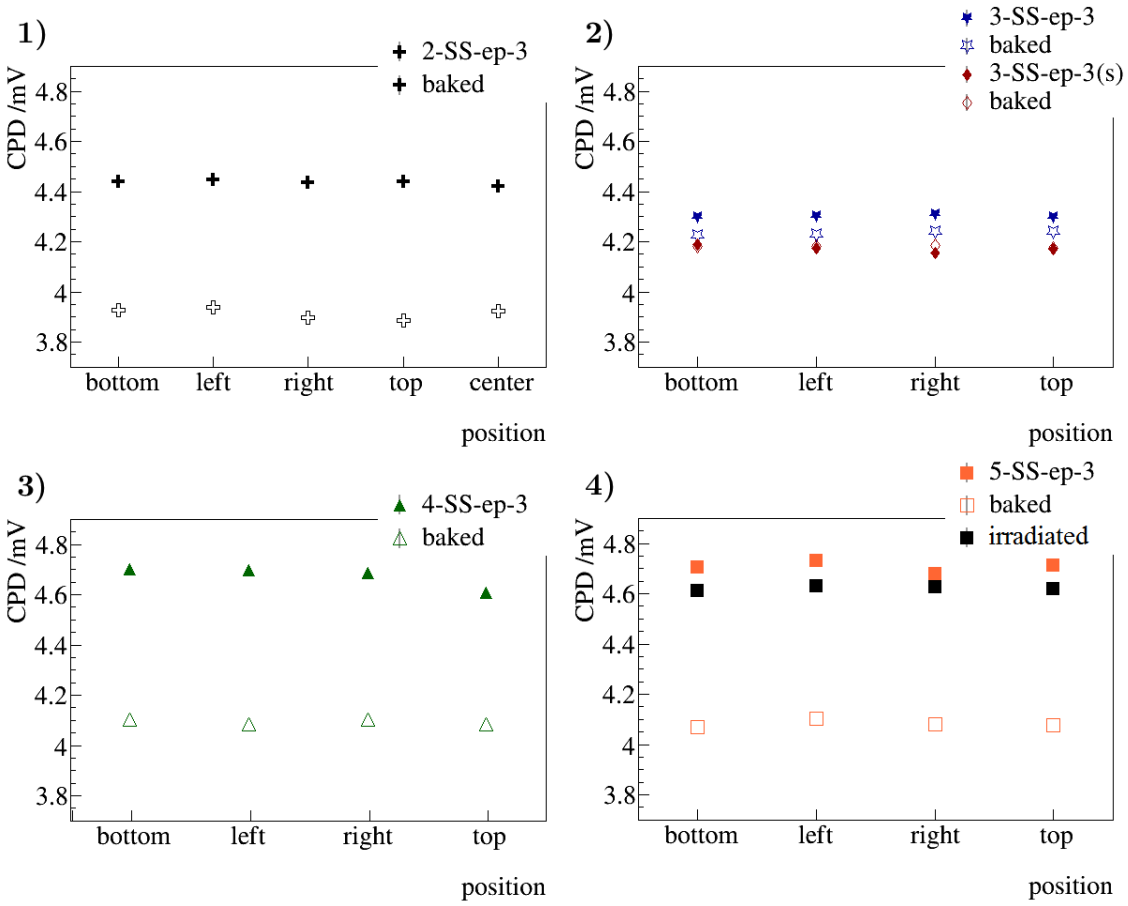

Figure 4.17: Effect of a bake-out and UV-irradiation on the work function. Here the work function results of the measurements at different positions on the sample are plotted. Filled markers are always used for unbaked samples and unfilled ones for measurements performed at baked samples. The error bars of the work function values are plotted, but they are too small to be seen. (1): the measurements of sample 2-SS-ep-3 are plotted. The change of $\overline{\Phi}$ due to the bake-out is (524 ± 24) meV, which is compatible with the mean change at the individual positions of (522 ± 23) meV, (2): here both the work function values of sample 3-SS-ep-3 with stainless steel (red rhombus) and with gold background (blue star) are shown. The difference of $\overline{\Phi}$ before and after the bake-out of (-26 ± 16) mV or (72 ± 8) meV is equal with the mean change of the work function at the different positions of (-9 ± 17) meV or (70 ± 7) meV, respectively. (3): in case of sample 4-SS-ep-3 the mean work function change at the different positions is (580 ± 39) meV, whereas the difference of $\overline{\Phi}$ before and after bake-out is (585 ± 42) meV. (4): in this diagram both treatments of sample 5-SS-ep-3 are plotted together, the bake-out and the UV irradiation. The mean change due to the UV irradiation is (63 ± 38) meV. The work function values after the bake-out are further decreased by (540 ± 10) meV. The changes of $\overline{\Phi}$ are (36 ± 51) meV and (564 ± 32) meV, respectively.

Table 4.8: Mean work functions of the samples measured by photoelectron spectroscopy. In addition to $\overline{\Phi}$ and $\sigma_{\mathrm{RMS},\overline{\Phi}}$ the material behind the sample, the treatment and the number of measurement positions are given. If a certain position is measured more than once, the mean value of these measurements is for the calculation of $\overline{\Phi}$ and $\sigma_{\mathrm{RMS},\overline{\Phi}}$.

sample	background	treatment	measured positions	$\overline{\Phi}$ /eV	$\sigma_{\mathrm{RMS},\overline{\Phi}}$ /eV
2-SS-ep-3	gold	-	5	4.436	0.009
3-SS-ep-3	steel	-	5	4.168	0.011
3-SS-ep-3	gold	-	4	4.302	0.005
4-SS-ep-3	gold	-	4	4.679	0.041
5-SS-ep-3	gold	-	4	4.683	0.044
5-SS-ep-3	gold	UV	4	4.647	0.027
2-SS-ep-3	gold	baked	5	3.912	0.022
3-SS-ep-3	steel	baked	4	4.194	0.011
3-SS-ep-3	gold	baked	4	4.230	0.006
4-SS-ep-3	gold	baked	4	4.094	0.010
5-SS-ep-3	gold	baked	4	4.083	0.017

Table 4.9: Difference of the mean work function $\overline{\Phi}$ and the work function at the hole position. In case of the UV irradiated sample 5-SS-ep-3, the work function difference is calculated by comparison with the unbaked sample. In contrast to that the value given for the baked sample 5-SS-ep-5 is the difference between the UV irradiated and the baked sample.

sample	background	treatment	Φ_{hole} /meV	$\overline{\Phi} - \Phi_{\mathrm{hole}}$ /meV
2-SS-el-3	gold	-	4.442 ± 0.008	-6 ± 12
3-SS-el-3	steel	-	4.163 ± 0.005	5 ± 5
3-SS-el-3	gold	-	4.279 ± 0.003	23 ± 11
4-SS-el-3	gold	-	4.517 ± 0.004	162 ± 41
5-SS-el-3	gold	-	4.575 ± 0.006	107 ± 44
5-SS-el-3	gold	UV	4.472 ± 0.005	175 ± 27
2-SS-el-3	gold	baked	3.925 ± 0.004	-13 ± 23
3-SS-el-3	steel	baked	4.019 ± 0.002	175 ± 11
3-SS-el-3	gold	baked	3.802 ± 0.017	428 ± 19
4-SS-el-3	gold	baked	4.095 ± 0.004	-1 ± 11
5-SS-el-3	gold	baked	4.076 ± 0.002	7 ± 17

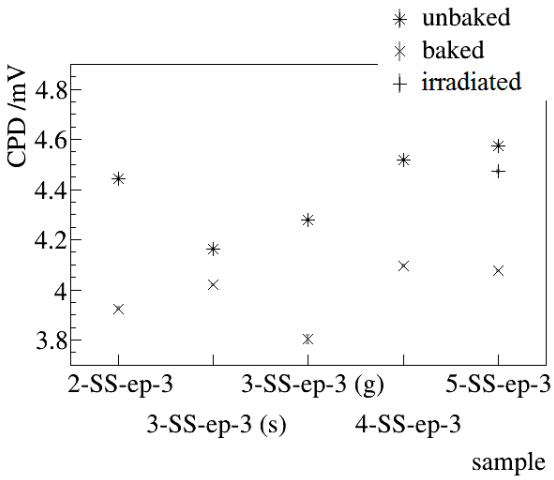

Figure 4.18: Work function at the hole position before and after bake-out and UV irradiation. The corresponding error bars are plotted but not visible due to their smallness.

In these considerations the work function at the hole position is not included. The effect due to the hole is discussed in the following section instead.

4.6.6.2 The work function at the hole position and its dependence on the background material

In table 4.9 the difference of $\overline{\Phi}$, the mean work function of all measurement positions with exception of the hole position, and the work function at the hole Φ_{hole} are given. This difference varies before the bake-out from a value which is compatible with 0 meV to more than 160 meV. With exception of sample 3-SS-ep-3 the work function at the position of the hole is always smaller than the work function of the remaining surface.

After the bake-out the work function at the hole position is reduced for all samples (compare figure 4.18). But this reduction is not equally large for the different samples: it is largest in case of sample 2-SS-ep-3 with (517 ± 9) meV and smallest at sample 3-SS-ep-3 with stainless steel background with (144 ± 6) meV. As result of this, the work functions measured at the hole position becomes equal to the work function at the remaining surface (compare table 4.9). For most samples the work function difference after the bake-out is even compatible with 0 meV, but not in case of sample 3-SS-ep-3. With both background materials the work function difference gets larger after the bake-out.

The UV irradiation affects the work function at the hole position similar to a bake-out. It also decreases the work function at this position. But the difference between the work function of the surface and that at the hole position is further increased.

4.6.7 Discussion of the measurements by photoelectron spectroscopy

During the photoelectron spectroscopy at the monitor spectrometer further knowledge is gained to develop a final Rear Wall. A general observation is that the work function measured at any position of any sample is up to 1 eV smaller than expected from the literature [Hay14]. The largest work function values before the bake-out are only in the

order of 4.6 eV and the lowest just about 4.1 eV. This discrepancy between the measured and the literature value was already detected in [Bab14] for differently produced samples. The explanation for this is known: even at vacuum conditions a condensed film of water molecules is both physisorbed and chemisorbed at any gold surface [Nov03, Wel72]. This film cannot be removed by pumping and can be easily polarized. The latter can affect measurements of the potential [Ono01]. In addition, the work function can be decreased by 1 eV due to the adsorbed water depending on the packing of the water molecules at the surface [Hec12].

Furthermore, a comparatively large variation of the mean work function $\overline{\Phi}$ of different samples is observed. The difference between the sample with the highest work function and that with the lowest work function is more than 500 meV. A difference of sample 2-SS-ep-3 can be explained by the coating procedure, as it is the only tested sample which is coated by galvanization. The fact that samples 4-SS-ep-3 and 5-SS-ep-3 provide similar results can also be explained: both samples are produced in the same way and in the same batch. However, it is not explainable, that sample 3-SS-ep-3 has the lowest mean work function value of all samples, although it is also produced in the batch of sample 4-SS-ep-3 and 5-SS-ep-3. But as the absolute values of the work function are of minor interest compared with the homogeneity and long-term stability for the later Rear Wall, these differences do not cause a modification in the recommended layer design.

This statement is further underlined by the homogeneity of $\overline{\Phi}$. The values $\sigma_{\mathrm{RMS},\Phi}$ of the sputtered samples after the bake-out are all below 20 meV. The largest variation found is 17 meV in case of sample 5-SS-ep-3. But it must be noted, that $\sigma_{\mathrm{RMS},\Phi}$ is not measured over the whole surface and it is not equal to $\sigma_{\mathrm{RMS,surface}}$ of the requirement. However, the small RMS deviations imply a good homogeneity. This is even underlined by the fact that photoelectron spectroscopy does not average over the light spot area: it measures the microscopic work function in this area. These work functions are assumed to vary more than macroscopic, averaged ones, e.g. due to impurities in or at the surface of the gold layer.

In addition to the improvement of the homogeneity of $\overline{\Phi}$, the bake-out also affects $\overline{\Phi}$ itself: the work function of all samples is shifted towards lower energies, in case of sample 5-SS-ep-3 by even more than 500 meV. The only exception is sample 3-SS-ep-3 with gold background. For this sample the mean work function is increased by 26 meV, but this shift is compatible within 2σ of the measured uncertainties. The decrease of the work function after the bake-out is rather unexpected. By the bake-out the adsorbed water molecules are desorbed, which should cause an increase in the work function [Wel72]. Eventually the titanium intermediate layer is diffused into the gold layer during the bake-out [Mar10] as it happened for the SiO_2 sample during the first measurement time at the monitor spectrometer. But this is not expected for several reasons: there is no color change observable as it was the case for the SiO_2 sample, the gold layer is much thicker, namely 1 µm, which makes the diffusion through the complete gold layer to the surface within about 40 hours unlikely, and the decrease is also observable at sample 2-SS-ep-3 which does not have a titanium layer. Another possibility is, that additional adsorbed layers are formed at the gold surface. In spite of the bake-out, this is possible if the temperature of the gold surface is much lower than the temperature of the vacuum chamber walls. In that case the desorbed adsorbates from the surface of the chamber walls could be adsorbed at the gold surface. As the heating sleeve directly heats up the chamber walls but the sample holder and the sample itself are mostly heated by thermal radiation, a lower temperature

of the sample holder is possible[19]. Therefore, this is the most probable explanation of the observed work function reduction. However, as discussed already a change in the absolute work function is not as important as the homogeneity and the long-term stability of it.

At the hole position there is also a decrease in Φ observable by the bake-out. But the value of the shift is different from that at the other positions of the sample: in case of the samples 4-SS-ep-3 and 5-SS-ep-3 the shift to lower work functions is by 28 % or 17 %, in case of sample 3-SS-ep-3 it is by a factor of more than 5 larger and in case of sample 2-SS-ep-3 the values are compatible within the errors. The different shifts of the three sputtered samples can either be explained by the shift of the background material or by a different coating thickness at the inner surface of the hole. But it is not possible to distinguish between these reasons or to exclude that both contribute to the shift. The fact that $\overline{\Phi}$ and Φ_{hole} are compatible in case of sample 2-SS-ep-3 can on the one hand be explained by the smallness of the hole at this sample. As the hole diameter is only 3 mm the light cannot enter the hole as it does in the case of the other samples. On the other hand the galvanization process deposits the gold at every position of the sample including the inner surface of the hole. In addition, it must be mentioned that no harsh reduction of the work function of up to 0.9 eV compared to the surface are detected. Shifts in this order of magnitude were detected by another working group at steps and edges at the surface [Jia97, Jia98a].

Concerning the high intensity UV irradiation no significant effect on $\overline{\Phi}$ itself is detected, but on its homogeneity. The latter is improved by 17 meV to 27 meV. Contrary to that, at the hole position the work function is reduced by more than 100 meV. Similar to the bake-out, an increase instead of a reduction was expected, as adsorbed molecules are removed which reduce the work function at ambient air.

In conclusion one can state, that the recommended layer design of the Rear Wall is successfully tested within a MAC-E filter for the first time during the photoelectron measurements. In addition, the work function homogeneity of the recommended layer design[20] is proven to be equal to or below 20 meV. Concerning the question about the effect of a bake-out on the work function and its homogeneity from the beginning of this chapter further knowledge is gained: the bake-out does reduce the work function of the gold surface but increases its homogeneity. But for a final answer long-term measurements on the work function of baked samples are necessary. If the work function remains stable at the lower work function value with smaller RMS deviation, the effect of the bake-out is even positive with regard to KATRIN. Concerning the question about the effect of a UV irradiation, no change of the work function over the surface but only at the hole position is measurable. Therefore, further investigations with longer irradiation time and long-term measurements afterwards are recommended.

In contrast to this, the question about the work function at the hole position can be answered: the work function can be different compared to the remaining surface and it can also be differently affected by a bake-out. Both depends not on the step at the hole or the edge of the hole as assumed prior to these measurements, but either on the material behind the hole or the inner surface of the hole. Therefore, it is recommended to coat the inner surfaces more carefully so that there is no difference in the thickness of the gold layer at the inner surface of the hole compared to the that at the surface. In addition,

[19] Note, that the Rear Wall will be actively heated in the Rear Section. This is enabled by thermocouples installed at the backside of the Rear Wall holder.

[20] Note, that only the layer design and not the complete design was proved to be suitable. The used substrate was not the foil plastered stainless steel.

a matching of the work function of the surface behind the Rear Wall to the Rear Wall work function is recommended. In doing so a different work function at the hole position is prevented.

To find further approaches for an answer to the question about the effect of a bake-out and UV irradiation on the work function and its homogeneity, long-term measurements and measurements over the whole surface under KATRIN-like conditions are needed. But neither the ambient air Kelvin Probe nor the photoelectron measurements are suitable for these investigations. Also, a final characterization of Rear Wall candidates at vacuum conditions and the possibility to bake the candidate in the same vacuum chamber as they are measured in are required. For that reason a third setup is build up which enables all these measurements: a scanable, vacuum compatible Kelvin Probe. This setup and the results obtained at it are the content of the following section.

4.7 Work function measurements with a UHV Kelvin Probe

From the previously presented experiments the need for a further experimental setup can be concluded. At this setup the following requirements are imposed:

- The complete surface of a Rear Wall candidate must be scannable to measure the homogeneity of the work function over the surface.
- Long-term measurements must be possible, automatically by preference.
- The measurement must be possible in a pressure of 10^{-5} mbar to simulate the pressure conditions at KATRIN.
- A bake-out of the sample at 150 °C must be possible within the measurement chamber. This is needed to investigate the effect of the bake-out on the homogeneity without exposing the sample to ambient air before measuring.
- The irradiation of the sample with UV light is also required inside of the measurement chamber for the same reason.

In addition to these requirements the experimental setup must have measurement uncertainties, which enable the measurement of $\sigma_{\mathrm{RMS,surface}}$ and $\sigma_{\mathrm{RMS,pixel}}$ if they are equal to or smaller than 20 mV. To decide, if a system is suitable for this, the overall uncertainty σ_{tot} of the system must be considered: σ_{tot} consists of the homogeneity of the work function over the surface of the sample, $\sigma_{\mathrm{RMS,surface}}$ or $\sigma_{\mathrm{RMS,pixel}}$, and the systematic and statistic uncertainties

$$\sigma_{\mathrm{exp}} = \sqrt{\sigma_{\mathrm{sys}}^2 + \sigma_{\mathrm{stat}}^2} \tag{4.20}$$

of the measurement technique (compare also figure 4.19):

$$\sigma_{\mathrm{tot}} = \sqrt{\sigma_{\mathrm{RMS,surface/pixel}}^2 + \sigma_{\mathrm{exp}}^2}. \tag{4.21}$$

It must be noted, that the calculation of the RMS deviation over a scan of a surface does not directly give $\sigma_{\mathrm{RMS,surface}}$ or $\sigma_{\mathrm{RMS,pixel}}$, but σ_{tot}. A first approach to the required uncertainties of the experiment is

$$\sigma_{\mathrm{exp}} \leq 20\,\mathrm{mV}. \tag{4.22}$$

Otherwise a distribution of the work function of 20 meV is not detectable. But of course $\sigma_{\mathrm{exp}} = 20$ mV is the absolute maximum value which could be accepted. To improve the sensitivity for the work function homogeneity of the Rear Wall measurements stricter

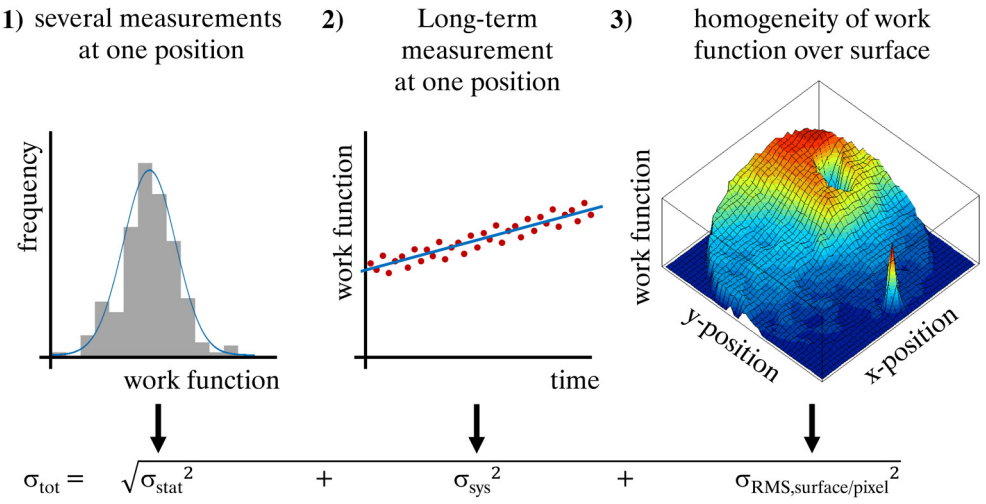

Figure 4.19: Uncertainties of the work function measurement. The overall uncertainty σ_{tot} which can be determined experimentally consists of the statistic uncertainty σ_{stat}, the systematic uncertainty σ_{sys} and the work function distribution over a certain surface $\sigma_{\mathrm{RMS,surface/pixel}}$. σ_{stat} can be determined by measuring several times at the same position of the sample. As the work function of the material does not change within short times, the deviation of the resulting distribution is equal with σ_{stat} (1). In long-term measurements at one position of the sample drifts of the signal can be detected. These drifts are described by σ_{sys} (2). In addition to the uncertainties before there is also the sample specific uncertainty $\sigma_{\mathrm{RMS,surface/pixel}}$ involved in the measurement. This uncertainty describes the homogeneity of the work function independent from the experiment (3).

requirements are defined: the contribution of σ_{exp} to σ_{tot} must be smaller than 30 %[21] of the contribution of $\sigma_{\mathrm{RMS,surface/Pixel}}$. That means that in case of $\sigma_{\mathrm{RMS,surface/Pixel}} = 20\,\mathrm{meV}$ the upper limit of the experimental uncertainties must not exceed

$$\sigma_{\mathrm{exp}} \leq 10.95\,\mathrm{mV}. \tag{4.23}$$

Therefore the desired experimental setup needs to have smaller uncertainties than 10.95 meV. In addition, it could be the case, that σ_{exp} and $\sigma_{\mathrm{RMS,surface/pixel}}$ are intact in a way which minimizes σ_{tot}. Therefore, the 20 meV limit must also be fulfilled for σ_{tot} in this worst case. As a consequence

$$\sigma_{\mathrm{tot}} = \sqrt{\sigma^2_{\mathrm{RMS,surface/pixel}} + \sigma^2_{\mathrm{exp}}} \leq 20\,\mathrm{mV} \tag{4.24}$$

must be fulfilled as well. As a distinction between $\sigma_{\mathrm{RMS,surface/pixel}}$ and σ_{tot} is not possible, the name $\sigma_{\mathrm{RMS,surface/pixel}}$ is used for the combination of both uncertainties in the following.

As no experimental setup was available which meets all these requirements, a new one had to be built up: a vacuum compatible, scanning Kelvin Probe, which in the following will be called UHV Kelvin Probe. This measurement device is designed and built up during the course of this thesis. Although no absolute but only CPD measurements are possible with this setup, all requirements given above can be met (see section 4.7.1 and appendix D.6).

[21] The 30 % requirement is an additional requirement defined by the experimentalist.

The aim which needs to be achieved with the UHV Kelvin Probe is to give further answers to the questions about the long-term stability of the homogeneity and the effect of a bake-out or UV irradiation on the homogeneity. First results on this are given in this thesis. Furthermore, Rear Wall candidates must be characterized and qualified concerning their homogeneity and the CPD distribution over the surface.

The experimental setup of the UHV Kelvin Probe is described in the following section 4.7.1. The used measurement procedure and the analysis of the consequent data are described in sections 4.7.2 and 4.7.3. Details on the execution of the measurements presented in this thesis are given in section 4.7.4, before the results of these measurements are presented in section 4.7.5. Conclusively these results are discussed and the posed questions are answered in section 4.7.6.

4.7.1 Experimental setup of the UHV Kelvin Probe

The experimental setup of the Kelvin Probe is self-built from components of various manufactures such as McAllister[22], AML[23] and Vacom to name but a few. A picture of the complete setup is shown in figure 4.20. The main component is the vacuum compatible Kelvin Probe head of the type KP6500 from McAllister at whose end the tip is installed. Different tip sizes with varying sensitivities dependent on the specific capacities (compare equation (4.11)) are available. But for all measurements presented in this thesis a stainless steel tip with 5 mm diameter is used. The Kelvin Probe head is installed at the top flange of a 5-way cross with 5 CF250 flanges produced by Vacom. This cross functions as a vacuum chamber for the Kelvin Probe. A picture of the Kelvin Probe head can be found in figure 4.21 where the components inside of the vacuum chamber are shown.

Below the Kelvin Probe head the sample is installed in a sample holder. This sample holder consists of a base holder and an additional holder for specific samples. The base holder has a diameter of 160 mm and 44 threaded holes. These threaded holes can be used to mount almost any sample fixed by clamps. For the most common Rear Wall samples and Rear Wall candidates specific sample holders are available. These can be installed on top of the base holder. All holders are made of stainless steel as it does not oxidize like copper or aluminum. This oxidization would cause a degradation of the electrical contact. To minimize virtual leaks[24] by the stacking of the sample holders, slits enabling the gas to stream out are integrated in the design of all sample holders and the base holder.

The height of the Kelvin Probe above the sample can be adjusted in two different ways: a z-stage of type BLT026-2 from McAllister driven by a Schneider electronic[25] MDrive 34 intelligent motor enables a rough positioning. The vacuum compatible connection of the linear stage is made by a CF40 membran bellow. Two limit switches make sure that the Kelvin Probe cannot move further than a certain position in both directions. The fine adjustment of the height is realized by the coil in the Kelvin Probe head which drives the vibration of the tip. This is done by applying an additional static voltage to the periodic signal on the coil. The travel range of the coil at a certain applied voltage is dependent on the used coil itself. In the case of the here described setup, the travel range is ± 0.12 mm.

[22] McAllister Technical Services, West 280 Prairie Avenue, Coeur d'Alene, ID 83815, USA

[23] Arun Microelectronics Limited, Fitzalan Road, ARUNDEL, BN18 9JS, United Kingdom

[24] Virtual leaks are volumes which enclose gas. This gas cannot be easily pumped out. Therefore, the driblets of gas which escape from the virtual leak cause the pressure in the vacuum system to rise similar to a real leak in the system.

[25] Schneider Electric SA, 43-45, bd Franklin Roosevelt, 92500 Rueil Malmaison, France

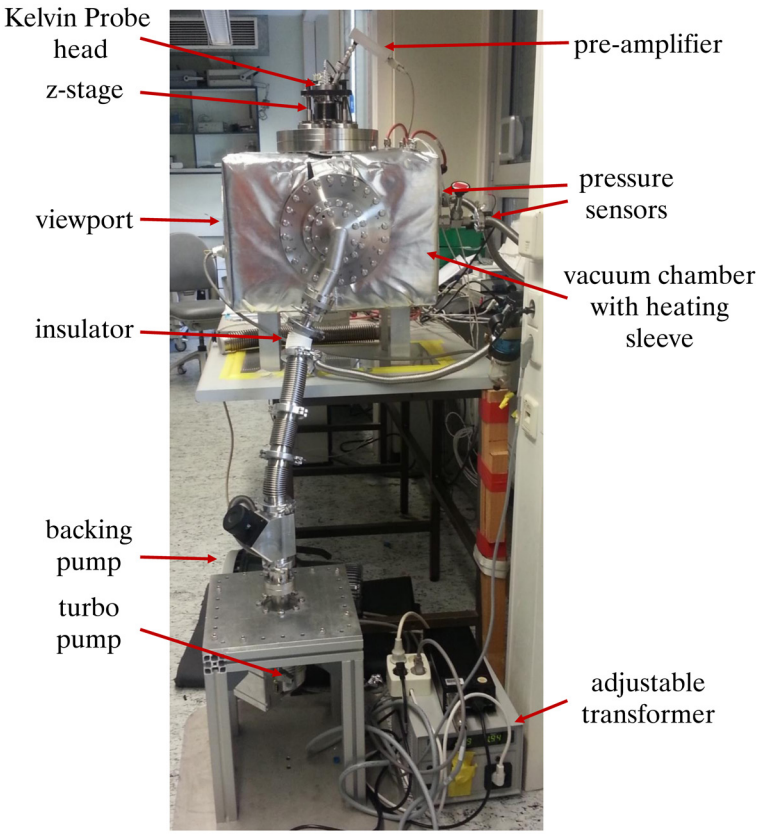

Figure 4.20: Setup of the UHV-Kelvin Probe. In the photography the corresponding electronics and the flange opened to exchange samples cannot be seen as they are hidden by the setup.

The scanning over the complete surface of a Rear Wall candidate is realized by a rotary table of the type CRS10K stacked on a LTVL150L linear stage. Both components are vacuum compatible, bakeable and produced by the manufacturer AML. Due to the usage of a rotary table, a travel range of about 73 mm would be required to scan over the complete surface of a Rear Wall candidate. But the installed linear stage has a travel range of 150 mm. This makes a more comfortable exchange of the samples possible, as it can be moved closer to the flange used for that purpose. To enable the installation of the motor in the vacuum chamber a base plate is welded in the 5-way cross, on which the motors are fastened in place.

Neither the linear stage nor the rotary table have an encoder which would provide information about the actual relative position of the Kelvin Probe to the sample. In case of the linear stage a calibration of the position by a limit switch is possible. But this is not possible in case of the rotary table, as it can move endlessly in one direction. For that reason it cannot be compensated if the motor of the rotary table loses steps.

The electrical connection of the Kelvin Probe head with the sample must be realized via the vacuum chamber, the linear stage, the rotary table and the sample holder. But as the table of the rotary table is electrically isolated from its housing, this connection cannot be established just by the contact of these components. Furthermore the connection of the vacuum chamber with the sample holder by a simple vacuum compatible cable is also not possible as the rotary table can in principle rotate endlessly. For that reason the

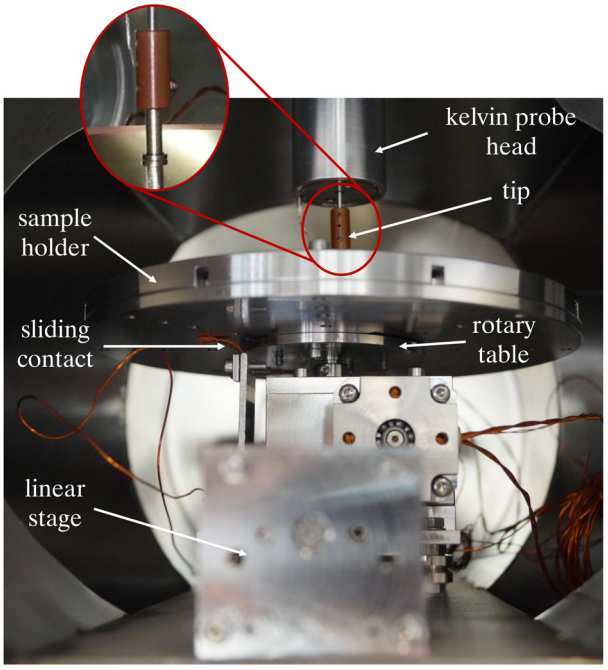

Figure 4.21: View into the vacuum chamber of the UHV-Kelvin Probe. The linear stage, the rotary table, the sample holder and the sliding contacts, which electrically connect sample and Kelvin Probe, can be seen. In addition, the bottommost part of the Kelvin Probe head is in view. As the tip itself is covered by the sample holder, a magnified view of it is added in the left corner of the photography.

electrical contact is realized by sliding contacts. For redundancy in case of the failure of a sliding contact, two of them are installed.

The visual control of the Kelvin Probe is possible through a CF63 viewport of the type HVP-2500 from Hositrad[26]. In addition, a potassium fluoride window (VPCF40CAF2-L) produced by Vacom is installed at the top flange of the vacuum system. Through this flange a temperature measurement by an IR thermometer is possible.

To be able to irradiate the Rear Wall with UV light a mercury arc lamp is also installed at the top flange of the vacuum system. This lamp has an optical power of about 76 $\mu W\,cm^{-2}$ at the position of the sample after warm up. The measurement of the optical power is described in appendix D.6 about the commissioning of the UHV Kelvin Probe.

To evacuate the system a Pfeiffer[27] HiPace 80 is connected to the vacuum chamber by an insulator and bellows. The insulator is needed to electrically disconnect the pump from the remaining system to avoid disturbing the measurement signal. The bellows mechanically decouple the pump and the vibration of the Kelvin Probe. The pressure at the outlet of the turbo pump is reduced by a baking pump of the type SCROLLVAC SC 15 D of Oerlikon Leybold[28]. To make sure that the electrical circuits of both pumps are not coupled with the electrical circuit of the Kelvin Probe, an adjustable transformer is installed at the pumps as well. This is required as the Kelvin Probe is grounded by the fuse of the power outlet. With the described combination of pumps a pressure in the

[26]Hositrad Holland B.V., Postbus 114, 3870 CC Hoevelaken, Netherlands
[27]Pfeiffer Vacuum GmbH, Berliner Strasse 43, 35614 Asslar, Germany
[28]Oerlikon Leybold Vacuum, Bonner Str. 498, 50968 Köln, Germany

order of 10^{-5} mbar can be reached. In this way the pressure conditions at the Rear Wall position in the KATRIN experiment are simulated.

The monitoring of the pressure is achieved by a combination of a Pirani pressure sensor THERMOVAC TR 212 KF from Leybold and a cold cathode sensor Penningvac PR36 from the same manufacturer. The first pressure sensor covers pressure from $5 \cdot 10^{-4}$ mbar to 1 000 mbar, the second from $1 \cdot 10^{-9}$ mbar to $1 \cdot 10^{-2}$ mbar. Therefore, the complete pressure range of interest can be monitored. But as the cold cathode causes a disturbance of the Kelvin Probe if both are measuring at the same time (compare appendix D.6), the cold cathode can be disconnected by a valve from the vacuum chamber. To avoid a direct line of sight between cold cathode and Kelvin Probe tip, the pressure sensor is additionally mounted by a corner piece to the chamber.

In order to bake-out the system a heating sleeve is installed around the vacuum chamber. This heating sleeve enables the bake-out at 150 °C, which is the Rear Wall baking temperature at the Rear Section. That means, that a bake-out of the sample directly in the Kelvin Probe measurement chamber is also possible.

For the operation of the described hardware several dedicated controllers are needed, which are mostly controlled by a LabView software especially designed for the usage at the UHV Kelvin Probe by M. Babutzka: the KP controller 6500 from McAllister powers and controls the Kelvin Probe head, meaning that it controls the backing potential and the vibration of the coil inside of the Kelvin Probe. In addition, it passes the signals from the pre-amplifier, which is directly mounted to the Kelvin Probe head via a BNC connector, to the signal processing. This further signal processing is realized by a proprietary link to the LabView connector box SCB-68 and a DAQ module of the type NI USB-6212. The DAQ module is finally connected to the PC on which the control software is running. The z-stage is controlled by the dedicated controller produced by McAllister. It controls the movement of the motor and stops it if a limit switch is pushed. The connection to the PC is realized by a RS232-to-RS485 converter, as the controller only provides a RS485 interface. The movement of the rotary table and the linear stage is controlled by the dedicated AML 2-stage motor controller. In addition, it monitors the temperature of the motors and the limit switches. Note, that only one motor can be driven at once. It provides both, an automatic control via a RS232 bus connected to the PC and manual control directly at the controller.

Not controlled by the LabView software is the pressure sensor controller COMBIVAC CM 32 from Leybold. This controller automatically changes between the cold cathode and the pirani sensor dependent on the pressure in the vacuum chamber. The heating controller is also not controlled by the software. The desired temperature must be manually adjusted. The controller works using the bang-bang principle. To enable a safe operation the controller includes a limiter, which switches the heating off, if a certain temperature is exceeded.

The LabView software itself allows controlling of all parameters of the measurement, e.g. amplitude of the coil vibration and position of the Kelvin Probe head with respect to the sample and distance between sample and tip by using the Gradient (compare section 4.4). In addition, it enables manual and automatic measurements with these parameters.

In the commissioning phase of the UHV Kelvin Probe setup the functionality of the setup and of all related components is proven. In addition, the software is tested and improved if necessary. The overall uncertainty of measurements of 3-inch samples is determined to

$$\sigma_{\mathrm{exp,3inch}} = 5.5 \pm 0.5\,\mathrm{mV} \tag{4.25}$$

and of Rear Wall candidates to

$$\sigma_{\mathrm{exp,RW}} = 9.8 \pm 2.3\,\mathrm{mV}. \tag{4.26}$$

A detailed description of the commissioning can be found in appendix D.6.

In conclusion the presented UHV Kelvin Probe setup meets all requirements described in the last section. Therefore, principle effects caused by the parameters of KATRIN can be investigated in more detail. The same is true for a qualification of Rear Wall candidates for the usage in KATRIN. The measurement procedure during both kinds of measurements is described in the following section.

4.7.2 Measurement procedure

All measurements of a sample are consecutively performed without opening the vacuum system and with running pumps including the time periods of bake-out and UV irradiation. Before the actual scan can start, the sample and the corresponding sample holder must be installed. To make this simpler, the sample can be automatically moved to the so-called exchange position using the LabView software. After the installation it must be checked that the connection of the sample and the Kelvin Probe allows measurements. The resistance between both must be below

$$R_{\mathrm{tip-sample}} = 5\,\Omega. \tag{4.27}$$

In addition, it is necessary to adjust the positions of the limit switches at the z-stage and the z-limit which is implemented in the software. Both prevent the Kelvin Probe during a scan from getting damaged by a too low position. In order to adjust the software limit, the z-position at several outermost positions of the sample must be determined by manual measurements. The minimal measured z-position plus a safety margin is set as z-limit.

After these installation related operations, the vacuum system can be closed and the baking and later the turbo pump can be started. During the evacuation both pressure sensors are connected to the system. Conditions stable enough for measurements are achieved about 1.5 days after the beginning of the evacuation due to desorption processes. Before a scan is started, the cold cathode sensors must be disconnected from the vacuum chamber by the valve in between (compare appendix D.4).

To perform a scan the following measurement parameters must be set: the Gradient G, the baking potential V_b and the number of measurements at $\pm V_\mathrm{b}$ used to determine the work function. In addition, a file must be provided to the software in which the r- and ϕ-coordinates of the measurement positions are given. After starting the scan the software controls the Kelvin Probe and all motors automatically: the first approach of the tip is done by the increase of the measurement signal with decreasing distance between tip and sample. As soon as a certain peak-to-peak signal is exceeded, the approach stops. From this position on the height adjustment is based on the current value of the Gradient. During the complete measurement G is stabilized within 2 % of its value to keep the distance between sample and tip constant. The scan is stopped either if the end of the positioning file is reached or, in case of repeated measurements, if the scan is manually interrupted.

The measurement positions of the scan are arranged in circles with increasing radius r. Between two consecutive circles the radius is increased by $\Delta r = 2.5\,\mathrm{mm}$, which is equal

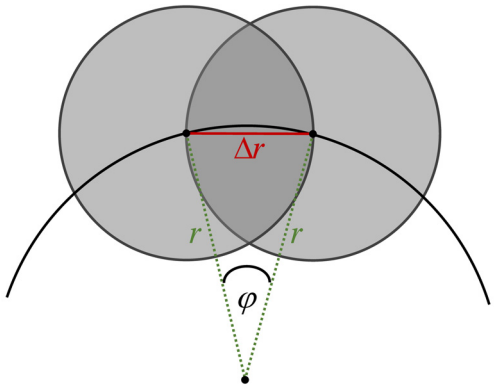

Figure 4.22: Scheme explaining the calculation of $\Delta\varphi$. $\Delta\varphi$ is dependent not only on Δr but also on the radius of the current measurement circle. The chord is in this case equal to Δr (marked in red). By using the dependence between the chord and the angle φ, the latter can be calculated.

to the radius of the tip. Meaning, the measurement points overlap. This ensures, that the complete surface is covered despite the round area of the tip. The same applies to the position change within each circle: $\Delta\varphi$ is chosen in a way that the chord is equal to Δr, namely 2.5 mm (compare 4.22). To meet this requirement $\Delta\varphi$ must be

$$\Delta\varphi = 2 \cdot \arcsin\left(\frac{\Delta r}{2 \cdot r}\right) \tag{4.28}$$

in the radian measure. The resulting measurement grid and the order of position changes is described in figure 4.23. At each of the grid positions 5 work function measurements are performed. To ensure that the Kelvin Probe does not touch the surface during the positioning it is moved upwards by

$$\Delta z = \frac{\sqrt{|\Delta r| + |r \cdot \Delta\varphi|}}{25}. \tag{4.29}$$

For all measurements the vacuum system must be heated up to temperatures slightly above the room temperature. In doing so, it is ensured, that temperature changes in the laboratory do not affect the measurements. In case of a bake-out at higher temperature all connectors to the Kelvin Probe head and also the z-motor and its limit switches must be removed. In addition to the bake-out using the heating sleeve, it is possible to directly heat up the motor of the rotary table and therefore the sample. The motor can achieve a temperature between 150 °C and 175 °C. The usage of this additional heating makes sure that gas desorbed at the vacuum chamber walls is not adsorbed at the cooler Kelvin Probe surface. Especially during the ramp down of the temperature this is important.

The irradiation with the UV light source can be performed without any change at the system. To enable the best possible irradiation of the sample surface, the sample must be moved to a r-position of ∼-60 mm.

The analysis of the measurements performed according to the described procedure is presented in the following section.

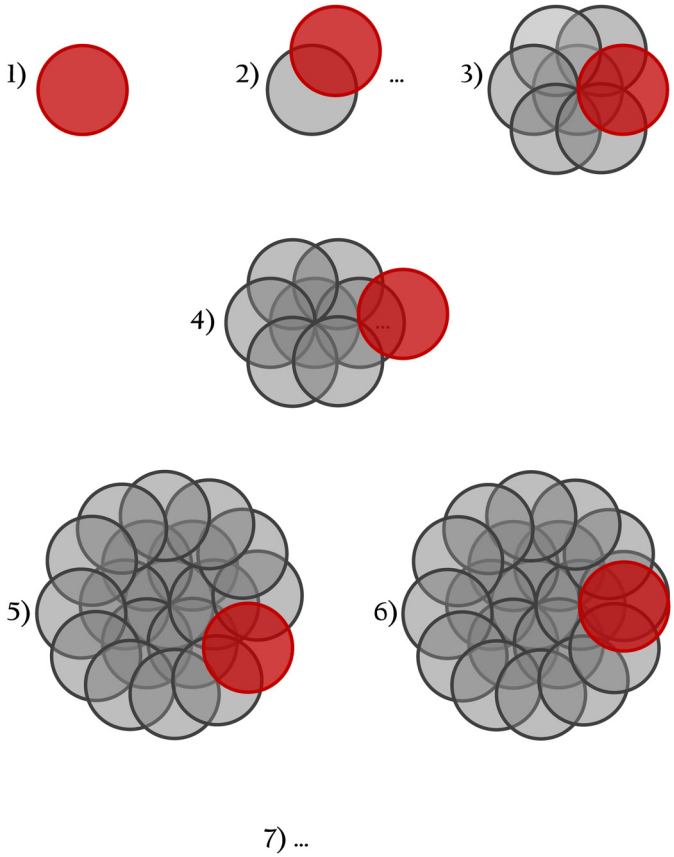

Figure 4.23: Grid of the scans performed with the UHV Kelvin Probe measurements using the example of a sample without central hole. Each circle represents the area of the Kelvin Probe tip. The red colored circles are the current measurement points, grey marked circles give the positions where the Kelvin Probe has already measured before. During the measurement the r-coordinate is always increased by half of the tip diameter and the ϕ-coordinate by a value which is dependent on the current radius. This $\Delta\varphi$ value is constant for a complete circle with the corresponding radius (compare fig 4.22). (1) The first measurement point is the center. (2) The r-position r_2 is changed using the linear stage. Afterwards the ϕ-position is changed by the rotary table. As soon as the new coordinates are reached, the Kelvin Probe measures. (3) The circle with radius r_2 is completed by the current measurement. After this measurement, the rotary table is turned back by 360°. (4) Again the radius is increased to r_3. After the new ϕ-position is also reached, the measurement takes place. (5) As a result of the fact, that the angle φ between two measurements is always the same, the current measurement position is the last one with $\varphi < 360°$. That means the circle would usually not be closed. (6) For that reason an additional measurement point at the $\phi = 360°$ is added to the circle. (7) This procedure of first increasing the radius by half of the tip size, then changing the ϕ-position until the circle is completed, rotating the rotary table 360° backwards and increasing the radius again is continued until the complete sample surface is measured.

4.7.3 Analysis method

The analysis of the data is in principle done similarly to the data of the ambient air Kelvin Probe described in section 4.5.2. But since in case of the UHV Kelvin Probe each measurement position is not only measured once but 5 times, the mean values and their σ_{RMS} are calculated for each measurement point. Then the mean CPD value and the $\sigma_{\mathrm{RMS,surface}}$ is calculated as it is in the analysis of the ambient air Kelvin Probe. But different from the ambient air Kelvin Probe, the actual mean CPD values can also be used for the analysis. This is possible as the work function of both, the sample and the tip, is not or only insignificantly affected by the measurement conditions at vacuum. The CPD values of all measurements, where the vacuum chamber was not opened in the meantime, are comparable. Therefore, not only can the effect of a bake-out on $\sigma_{\mathrm{RMS,surface}}$ be detected, but also on the CPD value itself: an absolute measurement of the work function is admittedly not possible but the change of the CPD value before and after a bake-out or UV irradiation can be detected.

The CPD distribution over the surface is investigated using the CPD maps also introduced in section 4.5.2. But due to the comparability of the CPD values at the UHV Kelvin Probe, these CPD maps can also be used to detect spatial changes of the CPD distribution.

In addition to this analysis the stricter requirement on the Rear Wall work function, $\sigma_{\mathrm{RMS,pixel}}$, can also be addressed by the analysis of the UHV Kelvin Probe data. For this, all measurement points are selected, which are within the area of a specific detector pixel of the Focal Plane Detector projected on the surface of the Rear Wall candidate (compare figure 4.24). Then the mean CPD and $\sigma_{\mathrm{RMS,pixel}}$ within this detector pixel is calculated. This is successively done for all 148 detector pixels. But since the possibility, that the flux tube is rotated on its way through KATRIN can not be excluded, the projection of the detector pixels must be analyzed after any possible rotation. This means that the outer detector pixel projections must be rotated by up to 30° and the four inner ones by up to 90°. The rotation is performed in 1° steps. The maximum of all pixels and possible rotations, $\sigma_{\mathrm{RMS,pixel,max}}$, is also the maximum $\sigma_{\mathrm{RMS,pixel}}$ of the Rear Wall candidate:

$$\sigma_{\mathrm{RMS,pixel}} = \sigma_{\mathrm{RMS,pixel,max}} \leq 20\,\mathrm{mV}. \tag{4.30}$$

The mean CPD values of the detector pixels and the corresponding $\sigma_{\mathrm{RMS,pixel}}$ values are again visualized in so-called CPD and $\sigma_{\mathrm{RMS,pixel}}$ pixel maps. The projected area of each detector pixel is plotted in a color representing the individual mean CPD or $\sigma_{\mathrm{RMS,pixel}}$ value. Using the color scale the diagram makes the distribution of both values over the surface visible. Usually the distribution leading to the maximum $\sigma_{\mathrm{RMS,pixel,max}}$ of all rotation angles, is used for the presented plots.

Based on the measurement procedure described in the last section the measurements performed with the UHV Kelvin Probe are described in the following.

4.7.4 Execution of measurements

During the measurements described in the course of this thesis, 4 different samples are used, namely the samples 6-SS-ep-3, 7-SS-ep-3, 3-SS-ep-6 and 5-SS-ep-6. All of these samples are produced in the way recommended in section 4.5.6. Sample 6-SS-ep-3 is the only sample, which does not have a hole in the center. Both 6-inch samples are Rear Wall candidates.

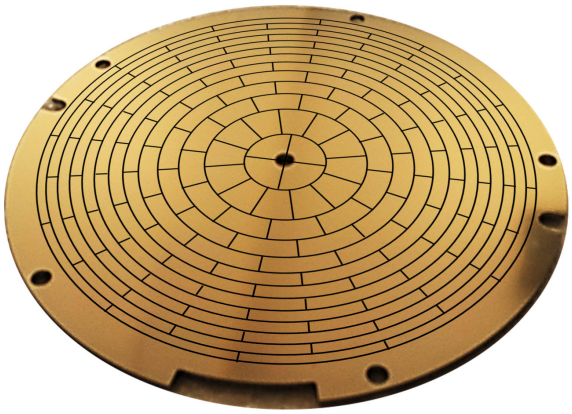

Figure 4.24: Rear Wall with projection of the pixels of the focal plane detector on its surface. The detector pixels are arbitrarily rotated and projected on the surface of the Rear Wall candidate. Overall the detector has 148 detector pixels, organized in 12 rings of 12 pixels and 4 center pixels. Each pixel has the same area. The outer radius of the projection of the largest detector ring is about 64 mm assuming 1.6 T at the Rear Wall design z-position.

The order of measurements and treatments are basically the same for all samples: they are measured after the evacuation of the vacuum system and prior to the bake-out several times. After the bake-out, the samples are again measured several times. In case of sample 6-SS-ep-3 and sample 3-SS-ep-6 a second bake-out is performed. The latter is also exposed to UV irradiation of the discharge lamp for 69 hours. The number of scans after a certain treatment varies from sample to sample. The number of scans is given in table 4.10 for all samples.

But there are also sample specific deviations from this general procedure:

- Sample 6-SS-ep-3 is baked out twice. But after the 4. measurement after the first bake-out the system is vented completely. Afterwards the system is evacuated and baked-out a second time to restore the conditions after bake-out. The sample is not measured between venting and second bake-out.
- Sample 7-SS-el-3 is accidentally vented to 1.2 mbar during ramping up the temperature due to an open fuse. During the sudden breakdown the turbo pump is damaged. After the exchange of the pump, the ramping up of the temperature is continued without measuring the sample again. As several software issues caused interruptions of most scans before the first bake-out, this data is not used for further analysis.
- Sample 5-SS-ep-6 is also baked twice consecutively. During ramping down of the temperature after the first bake-out, the system was vented to 3.2 mbar due to a total blackout in the laboratory. Therefore, the system was baked again. No measurements took place between these bake-outs.
- In case of sample 3-SS-ep-6 the measurements of the Kelvin Probe were disturbed after the first bake-out most likely by damages at the surface of the sample. Due to that the measured CPD values are too low, e.g. in the order of -1 V and even below. For that reason the first 5 measurements after the first bake-out are not used for further analysis.

The duration of the bake-outs and how long the heating with the rotary table is used, is given in table 4.11.

Table 4.10: Overview of performed scans per sample. If there are several numbers given, they are ordered by the date of the measurement, the earlier scan is represented by the first number. As incomplete scans are also counted, in the brackets the number of completed scans is additionally given. The outer radius which defines a full scan is given in the second column from the left.

sample	radius /mm	scans before bake-out	scans after bake-out	scans after UV irradiation
6-SS-ep-3	27.5	5 (3)/0	4(2)/22 (18)	
7-SS-ep-3	30.5	17(7)/21(20)	18(14)	
5-SS-ep-5	62.5	6 (5)	6 (5)	
3-SS-ep-5	62.5	8 (6)	11(10)/17(16)	7(6)

Table 4.11: Overview on the performed bake-outs. The duration of the motor heating is varying so much as the motor controller tends to break down during operation.

sample	duration of bake out with heating sleeve /h	duration of bake out with motor heating /h
6-SS-el-3	155	-
6-SS-el-3	157	14
7-SS-el-3	161	32
3-SS-el-5	161	51
3-SS-el-5	140	51
5-SS-el-5	164	4
5-SS-el-5	182	186

The pressure in the system is in the order of 10^{-5} mbar for each measurement. To enable stable temperature conditions the temperature is elevated to about 45 °C at the outside of the vacuum chamber with the heating sleeve.

The Gradient describing the distance between sample and tip is adjusted to -0.07 ± 2 % for all measurements. As the relation between Gradient and distance is non-trivial the exact distance is unknown. The baking potential in most cases is set to ± 1 V, but a few of the measurements are also performed at ± 1.2 V. The number of measurements at $\pm V_b$ used to determine the CPD is 10 for each scan.

The results of these measurements are presented in the following section.

4.7.5 Results of the measurements with the UHV Kelvin Probe

The CPD and corresponding $\sigma_{\mathrm{RMS,surface}}$ values of all samples are plotted in figure 4.25. In this figure the data points, which are not used for the following analysis, are also marked. For clarity only a few exemplary CPD maps are shown in the following. But a collection of all CPD maps and corresponding mean CPD and $\sigma_{\mathrm{RMS,surface}}$ values can be found in appendix E.4 on page 259 ff.

During the analysis of the data three topics are investigated: the bake-out effect on the CPD, the effect of an irradiation with UV light on the CPD and the suitability of two Rear Wall candidates as a final Rear Wall. Each of these topics is addressed in the following paragraphs.

4.7.5.1 Investigation of bake-out effects on several samples

By looking at the mean CPD results of each scan, comparing those scans before and those after a bake-out, it is conspicuous that the mean CPD is decreased by the treatment (compare figure 4.25). This decrease is about several 10 mV to several 100 mV. It is either caused by an increase of the mean work function $\overline{\Phi}_\mathrm{S}$ of the sample relative to the work function Φ_p of the tip or by a decrease of Φ_p compared to $\overline{\Phi}_\mathrm{S}$. This is a consequence of the relation

$$\Phi_\mathrm{S} = \Phi_\mathrm{P} - U_\mathrm{CPD} \tag{4.31}$$

deduced from equation (4.13). But it is not possible to distinguish between a change of Φ_S or Φ_p or of a simultaneous change of both work functions.

After this first rapid decrease the mean CPD value increases again by about 50 mV. The shape of the increase is exponential. To characterize it, a function of the form

$$f(t) = -\left(C_1 - C_2 \cdot \mathrm{e}^{-\tau \cdot t}\right) \tag{4.32}$$

is fitted to the data. Here C_1 describes the saturation value of the mean CPD over the surface and C_2 is a constant of proportionality. The time dependence of the exponential increase is represented by τ.

The results of these fits are:

$$\begin{aligned}
f_{3-\mathrm{SS}-\mathrm{el}-6}(t) &= -\left((350.4 \pm 4.8)\,\mathrm{mV} + (-45.9 \pm 17.4)\,\mathrm{mV} \cdot \mathrm{e}^{-(0.7 \pm 0.5)\,\mathrm{d}^{-1} \cdot t}\right) \\
f_{5-\mathrm{SS}-\mathrm{el}-6}(t) &= -\left((340.2 \pm 68.9)\,\mathrm{mV} + (-64.8 \pm 64.7)\,\mathrm{mV} \cdot \mathrm{e}^{-(0.3 \pm 0.5)\,\mathrm{d}^{-1} \cdot t}\right) \\
f_{7-\mathrm{SS}-\mathrm{el}-3}(t) &= -\left((493.4 \pm 7.8)\,\mathrm{mV} + (-60.1 \pm 20.0)\,\mathrm{mV} \cdot \mathrm{e}^{-(2.9 \pm 3.0)\,\mathrm{d}^{-1} \cdot t}\right).
\end{aligned}$$

Note that the fit is not successful in case of sample 6-SS-ep-3 and the first bake-out of sample 3-SS-ep-6. The corresponding fit graphs are presented in figure 4.26. In case of sample 5-SS-ep-6 it must be taken into account, that this is the only sample, which was not measured within 3 to 4 hours after the temperature at the heating sleeve again reached the measurement temperature. Instead, the measurement was started after more than 15 hours. This could cause the comparatively small τ value.

However, the absolute CPD value over the surface is not of such big interest as its fluctuation over the surface and its long-term stability. For that reason the mean value $\overline{\mathrm{CPD}}$ of all mean CPD values over the surface is calculated. The deviation of these values reflects the stability of the work function over time. This also extends to the mean RMS deviation $\overline{\sigma}_\mathrm{RMS,surface}$ and its deviation $\sigma_{\overline{\sigma}_\mathrm{RMS,surface}}$ averaged from the $\sigma_\mathrm{RMS,surface}$ of the single scans. These values are given in table 4.12. With exception of sample 6-SS-ep-3 the stability of the $\overline{\mathrm{CPD}}$ is improved after the bake-out. The same is true for $\overline{\sigma}_\mathrm{RMS}$. This is of particular interest in case of sample 3-SS-ep-6: here the measurements after bake-out are performed over about 3 weeks, which is the longest measurement duration without changing the conditions presented in this thesis. In addition, the exponential fit parameters C_1, the saturation value, and the $\overline{\mathrm{CPD}}$ values given in table 4.12 are compatible within the errors.

Besides the mean CPD over the surface and $\sigma_\mathrm{RMS,surface}$, also their spatial distribution over the surface is of great interest. Therefore, some exemplary CPD maps before and after the bake-out are shown in figure 4.27. The corresponding histograms are presented in figure 4.28. Overall in the three shown comparisons three different behaviors are noticeable:

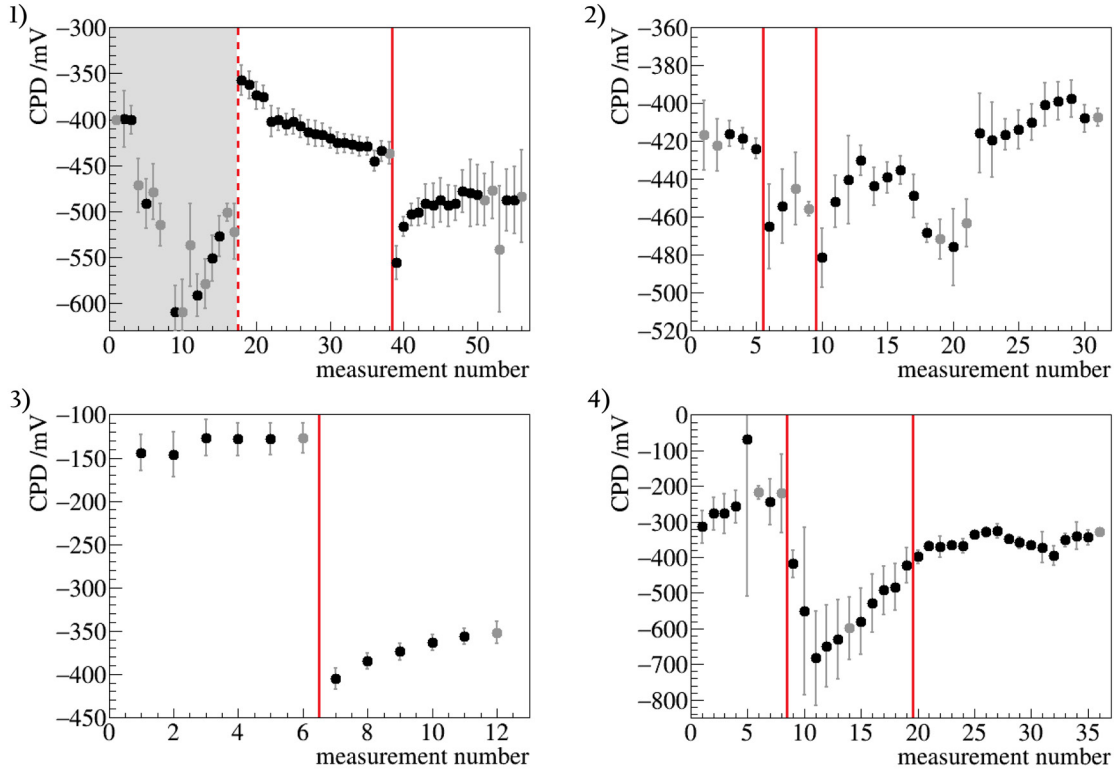

Figure 4.25: Overview on results of all measurements performed with the UHV Kelvin Probe. For all samples the mean CPD values are plotted together with the $\sigma_{\mathrm{RMS,surface}}$ as error bars against the measurement number. Data points which are grayed out are incomplete scans. The red lines in the diagrams mark the time of the bake-outs. (1) Here the results of sample 7-SS-ep-3 are plotted. The data in the gray area is not used for further analysis. This is a consequence of software related issues during the data collection. The dashed line marks the moment of the first bake-out of the sample. The sample is exposed to ambient air at a pressure of 1.2 mbar after this bake-out. The solid red line represents the time of the second bake-out. (2) The diagram shows the results of sample 6-SS-ep-3. Before the second bake-out, the system is vented. (3) The mean CPD values of the scans of sample 5-SS-ep-6 are plotted. (4) The data points represent the mean CPD values of sample 3-SS-ep-6. During the measurements performed between the two bake-outs the Kelvin Probe is not working properly (data points are blank). This is most likely caused by the damages on the surface of the sample. Therefore, only the last 4 measurements can be used for the further analysis although the scans before are also completed.

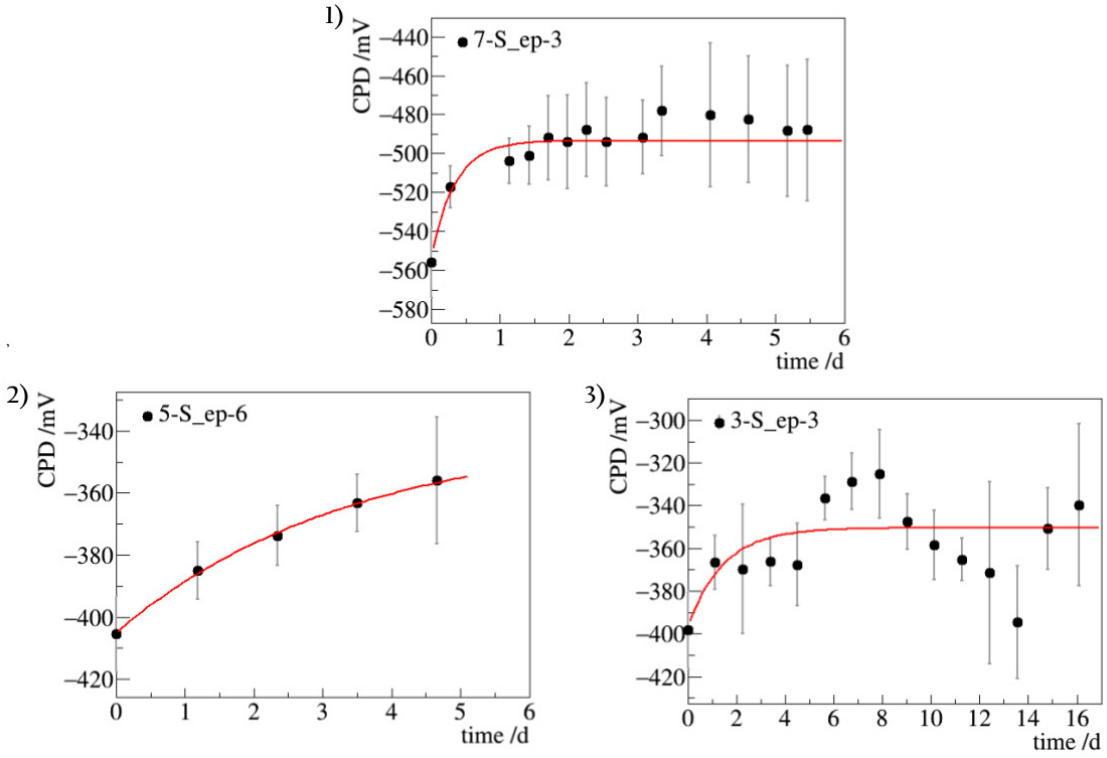

Figure 4.26: Exponential behavior of CPD after the bake-out. The mean CPD values over the sample of the surface are plotted against the time starting at the beginning of the first measurement after the bake-out. The difference in the time between 2 scans is caused by the different sizes of the samples and the resulting longer duration of 1 scan. The red lines are the fit graphs. The results of sample 7-SS-ep-3 are presented in diagram (1), those of sample 5-SS-ep-6 in diagram (2) and those of sample 3-SS-ep-6 in diagram (3). Note that only the mean CPD values over the sample surface and the corresponding $\sigma_{\mathrm{RMS,surface}}$ values of completed scans are plotted and used for the fit.

- Before and after the bake-out the CPD values are higher towards the edge of the sample.
- Before the bake-out the edge has a lower and afterwards a higher CPD compared to the center of the samples.
- The basic distribution is not changed.

It is still possible to state from these results, that regions of higher/lower CPD before a bake-out also have a different CPD compared to the remaining surface after a bake-out. However it is possible for regions of lower CPD to be higher after the bake-out and vice versa.

4.7.5.2 Investigation of the effect of UV irradiation on the contact potential difference

Sample 3-SS-ep-6 is irradiated by UV light after the second bake-out. The first scan after the UV irradiation is started about 2 minutes after the light source is switched off. At the beginning of the measurement the CPD value is increased from a negative value by about 800 mV to above 400 mV. That means that the sample has a lower work function

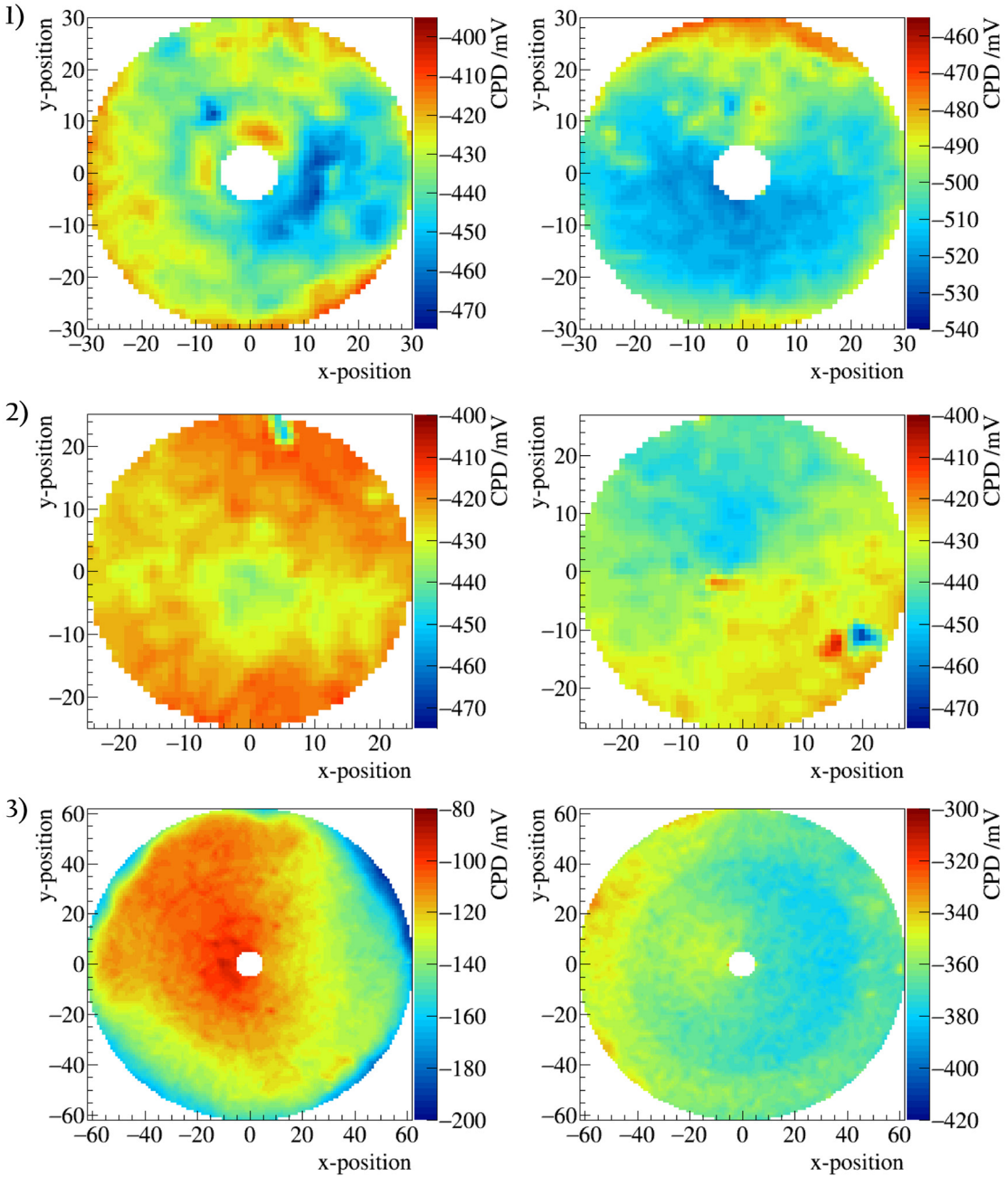

Figure 4.27: Effect of bake-out on the CPD distribution over surface. On the left side of the figure the CPD maps before the bake-out and on the right side after the bake-out are shown. Within each row the difference from maximum to minimum of the color scale is the same but not the scale itself. Otherwise, the distribution over the surface would not be visible anymore due to the change of the CPD after the bake-out. Note, that in case of the CPD maps in (2) also the same scale is used. (1): both CPD maps belong to sample 7-SS-ep-3. The CPD rises from the center to the edges of the sample in both cases. (2): exemplary CPD maps of sample 6-SS-ep-3 are shown. The CPD is homogeneously distributed over the surface. (3): the distribution of the 6-inch sample 5-SS-ep-6 is presented here. In contrast to the CPD maps of (1) the CPD values are decreasing towards the edges of the sample before the bake-out. This changes after the bake-out: The CPD values at the edge are higher after the bake-out compared with those of the surface.

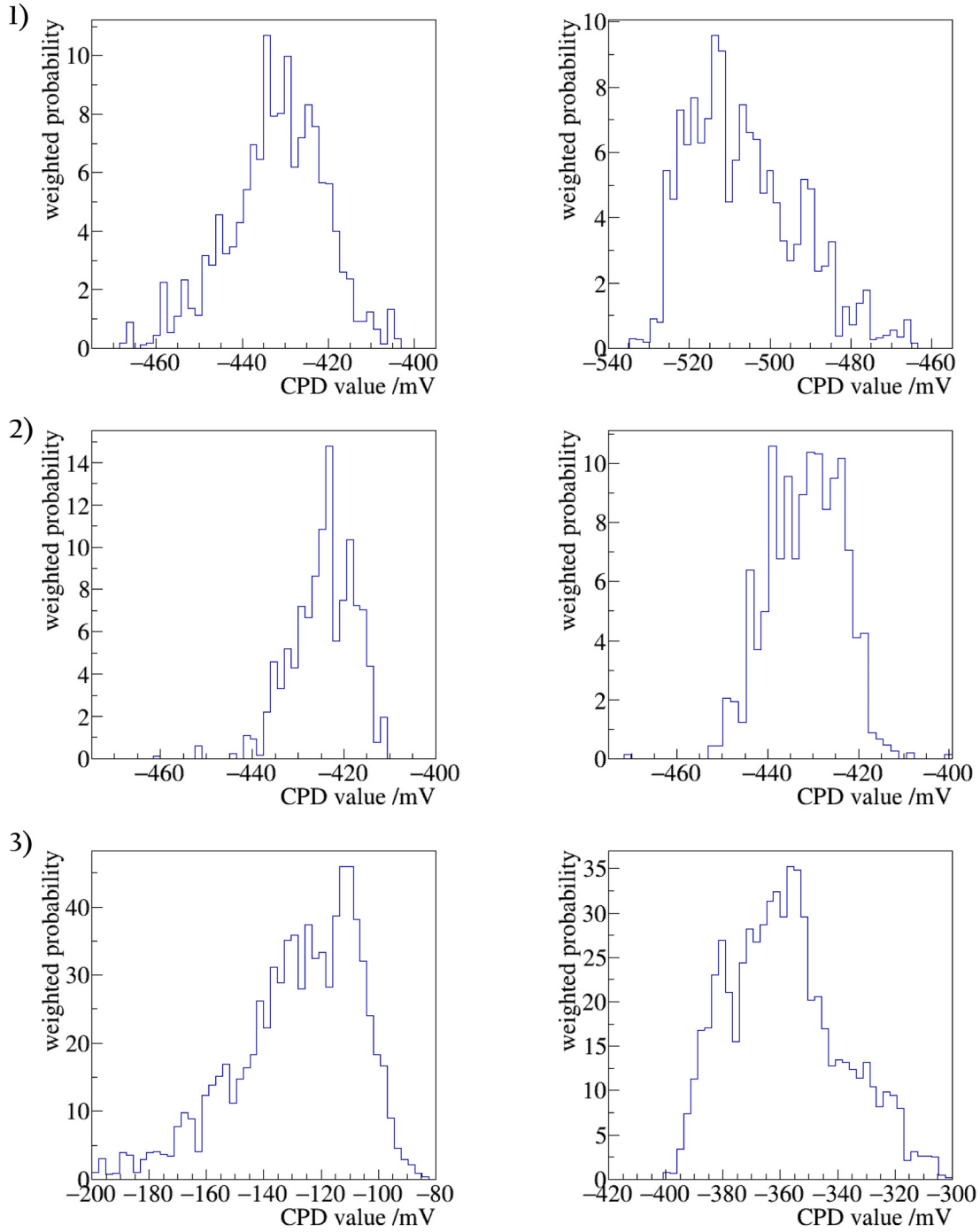

Figure 4.28: Effect of bake-out on the CPD distribution over surface - histograms. The histograms that correspond to the CPD maps given in figure 4.27 are shown in the same arrangement as the CPD maps: on the left side those histograms of the scans before and on the right side those after the bake-out are shown. In (1) the values of sample 7-SS-ep-3, in (2) those of sample 6-SS-ep-3 and in (3) those of sample 5-SS-ep-6 are presented. The relative range of the x-axis before and after the bake-out is equalized for better comparability. The absolute range is equal only in case of the histograms shown in (2).

Table 4.12: $\overline{\text{CPD}}$ and $\overline{\sigma}_{\text{RMS,surface}}$ before and after bake-out. For the calculation of values before the measurements which are not excluded from the analysis are used. In case of the values after the bake-out, the values of the first and the second scan are not included.

sample	note	$\overline{\text{CPD}}$ /mV	$\overline{\sigma}_{\text{RMS,surface}}$ /mV
3	-	-270.8 ± 79.4	116.5 ± 144.9
3	after 2.bake-out	-352.9 ± 18.5	20.8 ± 9.9
5	-	-133.9 ± 8.5	20.9 ± 2.5
5	after bake-out	-364.2 ± 7.3	9.4 ± 0.2
6	-	-419.8 ± 3.3	6.0 ± 0.6
6	after 2.bake-out	-428.1 ± 22.7	11.8 ± 5.4
7	-	-491.5 ± 70.3	24.5 ± 7.8
7	-	-413.2 ± 21.2	12.2 ± 1.9
7	after bake-out	-492.3 ± 7.4	25.0 ± 7.8

Table 4.13: CPD and $\sigma_{\text{RMS,surface}}$ results after UV irradiation. The seventh scan, which is marked with * is not completed.

scan	CPD /mV	$\sigma_{\text{RMS,surface}}$ /mV
1	200.1	60.1
2	121.4	15.3
3	96.9	12.7
4	83.4	12.0
5	72.9	11.3
6	68.2	10.7
7*	63.4	9.2

than the tip.

After this sudden rise, the CPD values decreases exponentially. After the first scan, meaning about 1 day later, the exponential decrease change into an almost linear acting one (compare figure 4.30). The values of the mean CPD over the surface and the corresponding values of $\sigma_{\text{RMS,surface}}$ after the UV irradiation are given in table 4.13.

4.7.5.3 Characterization of a Rear Wall candidates

In the last 2 sections more general investigations on the effects of a bake-out and UV irradiation on the CPD are presented. In this section the specific characterization of 2 Rear Wall candidates is described, namely of sample 3-SS-ep-6 and 5-SS-ep-6.

Sample 3-SS-ep-6 is not suitable as Rear Wall. Over the surface of the sample there are several scratches with sizes in the order of several millimeters. These scratches influence both the work function of the sample at their position and the CPD measurement with the UHV Kelvin Probe. The latter is most probably caused by heaped up material at the edges of the scratches. This material reduces the distance to the tip inhomogeneously and therefore disturb the measurement. The RMS deviation of the mean CPD values over the sample surface varies between almost 50 mV and 10 mV. All values can be found

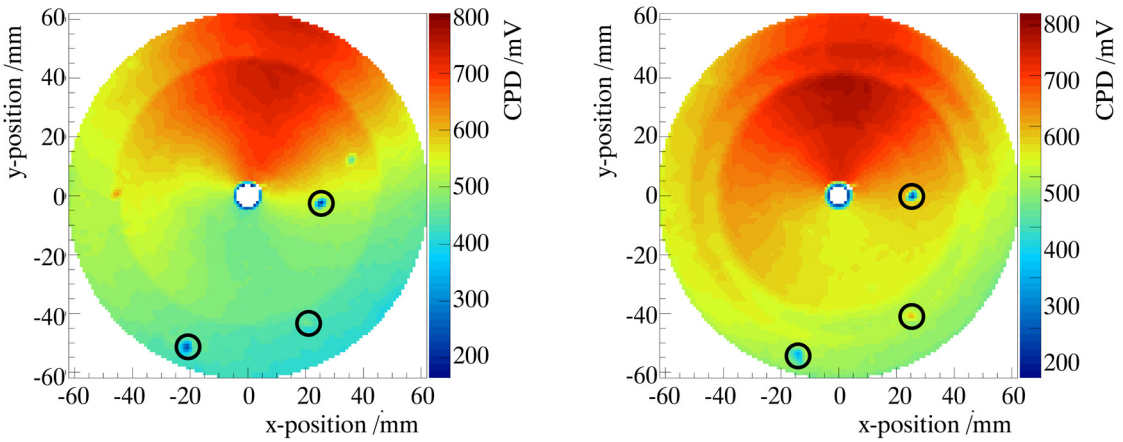

Figure 4.29: Defects on sample 3-SS-ep-5. The defects are marked with black circles. The change in the position from one to the next scan is caused by a rotation of the sample. This rotation is due to the fact, that the stepper motor of the rotary table loses steps during motion.

in appendix E.4. This also extends to the CPD maps and corresponding histograms. 3 of the scratches are marked in the CPD maps presented in figure 4.29. At most of the performed scans these or even other points can be found. But due to their position on the surface of the sample an identification of the single scratches is possible.

Nevertheless, sample 3-SS-ep-6 is used to investigate the long-term behavior of the CPD after the bake-out. The $\overline{\text{CPD}}$ values can be found in table 4.12. The deviation of 18.5 mV over a time of 3 weeks even with this sample, implies that the work function stability of Rear Wall candidates without scratches is of equal size or even lower than this value.

However, sample 5-SS-ep-6 does not have any visible scratches on the surface. But the highest $\sigma_{\text{RMS,tot}}$ measured at this sample is 25.7 mV. The highest value of a reliable scan is 20.7 mV. In any case, especially after the bake-out, these values are even smaller, namely in the range of 10 mV to 12 mV. In table 4.14 the mean CPD values over the sample and the $\sigma_{\text{RMS,tot}}$ for all scans are given.

If the mean values $\overline{\text{CPD}}$ and $\overline{\sigma}_{\text{RMS}}$ are calculated from the values given in table 4.14, they are:

$$\begin{aligned} \overline{\text{CPD}}_{\text{before}} &= 132.6 \pm 8.2\,\text{mV} \quad & \overline{\sigma}_{\text{RMS,before}} &= 20.3 \pm 2.7\,\text{mV} \\ \overline{\text{CPD}}_{\text{after}} &= 372.2 \pm 18.3\,\text{mV} \quad & \overline{\sigma}_{\text{RMS,after}} &= 10.4 \pm 1.5\,\text{mV}. \end{aligned} \tag{4.33}$$

Before the bake-out the requirement for the homogeneity is not met in case of a rigid interpretation of the requirement. After the bake-out $\overline{\sigma}_{\text{RMS,after}}$ is clearly below the limit of 20 mV. In contrast to this the stability of $\overline{\text{CPD}}$ is worse after the bake-out. But it must be noted, that this is a worst case calculation including an unreliable scan and the first scan after the bake-out. More realistic values are:

$$\begin{aligned} \overline{\text{CPD}}_{\text{before}} &= 127.6 \pm 0.6\,\text{mV} \quad & \overline{\sigma}_{\text{RMS,before}} &= 18.9 \pm 1.2\,\text{mV} \\ \overline{\text{CPD}}_{\text{after}} &= 364.2 \pm 7.3\,\text{mV} \quad & \overline{\sigma}_{\text{RMS,after}} &= 9.4 \pm 0.2\,\text{mV}. \end{aligned} \tag{4.34}$$

Here both, the values before and after the bake-out, meet the requirement concerning homogeneity. By interpreting the uncertainty of $\overline{\text{CPD}}$ as temporal stability, the total uncertainty of the CPD over the surface of the sample after the bake-out is therefore

$$\sqrt{18.3^2 + (10.4 \pm 1.5)^2} = (21.0 \pm 0.7)\,\text{mV} \tag{4.35}$$

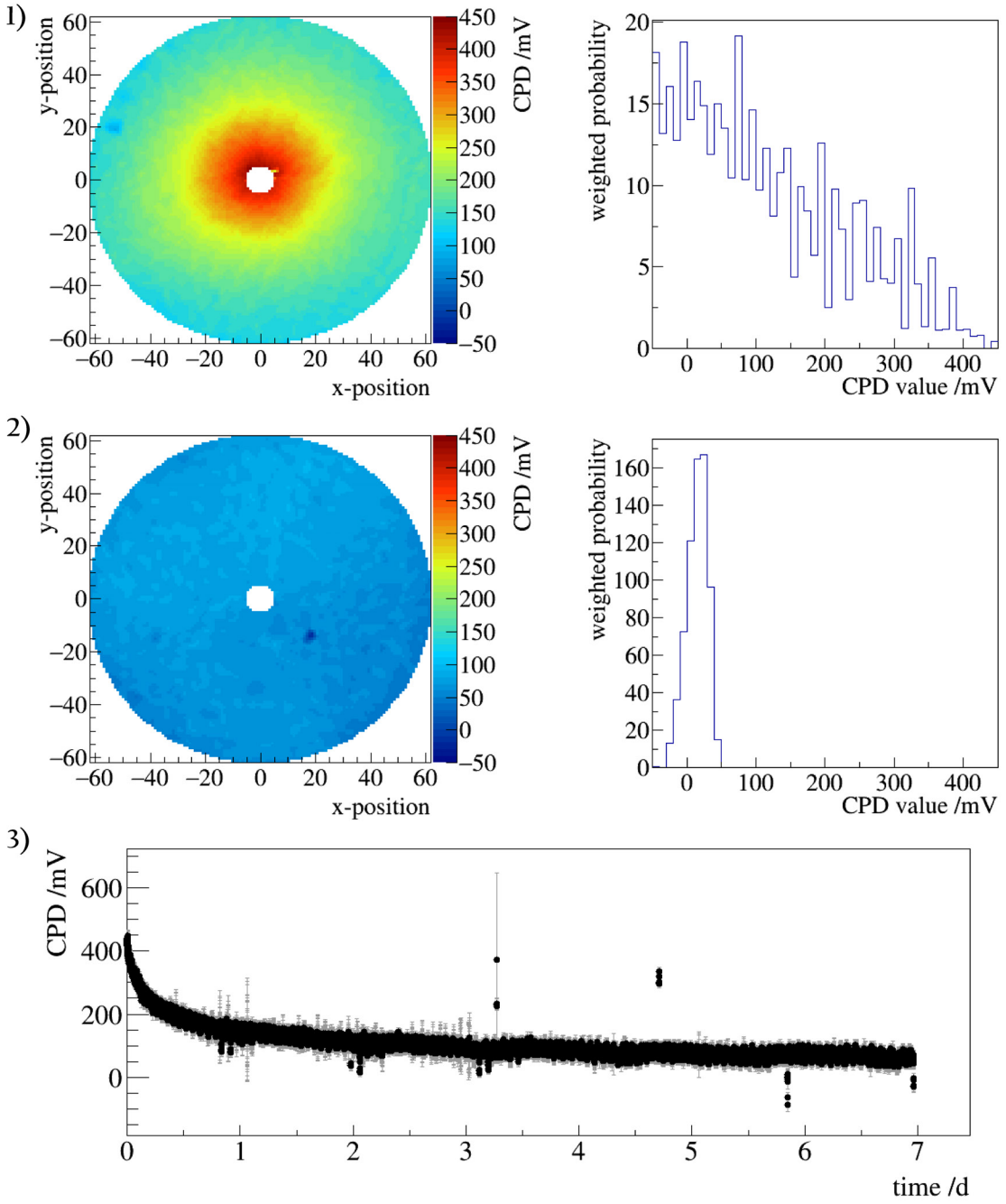

Figure 4.30: CPD maps and CPD behavior of sample 3-SS-ep-6 after UV irradiation. (1) Here the first scan after the UV irradiation can be seen. On the left side the CPD map is presented. The scan starts near the hole at the center with a CPD of about 450 mV with time and increasing radius the CPD drops down. On the right side the corresponding histogram is plotted. As the frequency is increasing with decreasing CPD value, the reduction of the CPD is slowing down with time. (2) The CPD map of the last completed scan, scan 6 after UV irradiation, is shown on the left side. The color scale is adapted to the scale of the first measurement for easier comparability. On the right the histogram of the same data is plotted. (3) The temporal progress in the CPD value is shown. The CPD first decreases exponentially. After about one day, the decrease changes more into a linear one.

Table 4.14: CPD and $\sigma_{\mathrm{RMS,surface}}$ over the whole samples 5-SS-ep-5. * marks uncompleted scans.

scan	baked	CPD /mV	$\sigma_{\mathrm{RMS,surface}}$ /mV
1	no	-143.4	20.7
2	no	-145.9	25.7
3	no	-127.5	20.7
4	no	-128.3	18.9
5	no	-128.4	18.5
6*	no	-128.0	17.5
7	yes	-405.4	12.2
8	yes	-385.1	9.3
9	yes	-373.8	9.7
10	yes	-363.2	9.2
11	yes	-356.0	9.3
12*	yes	-352.1	12.7

with the values of the worst case and

$$\sqrt{7.3^2 + (9.4 \pm 0.2)^2} = (11.9 \pm 0.2)\,\mathrm{mV} \tag{4.36}$$

in the more realistic case. In the realistic case both, the requirements for $\sigma_{\mathrm{RMS,surface}}$ concerning stability and homogeneity, are met. In the worst case scenario the Rear Wall candidate barely fail to meet the latter requirement.

The distribution of the CPD over the surface of the sample is examined, to decide whether the sample is suitable as a Rear Wall or not. One exemplary CPD map of sample 5-SS-ep-6 before and after the bake-out was shown already in figure 4.27 and the corresponding histograms in 4.28. In both cases the CPD has a gradient from the center to the edge of the sample. As mentioned in section 4.1, such a radial distribution is suitable for the Rear Wall.

The results of the pixelwise analysis for this Rear Wall candidate are given in table 4.15. Note that the given values in the fourth column are the maximum values found in all detector pixel and in any rotation of the detector projection on the surface of the sample. With exception of the first 2 measurements the requirement on $\sigma_{\mathrm{RMS,pixel}}$ is met in every scan even in case of $\sigma_{\mathrm{RMS,pixel,max}}$. The mean values of $\overline{\sigma}_{\mathrm{RMS,pixel}}$ and $\overline{\sigma}_{\mathrm{RMS,pixel,max}}$ averaged over all scans are

$$\begin{aligned} \overline{\sigma}_{\mathrm{RMS,pixel,before}} &= 5.9 \pm 2.8\,\mathrm{mV} \quad & \overline{\sigma}_{\mathrm{RMS,pixel,max,before}} &= 22.8 \pm 9.6\,\mathrm{mV} \\ \overline{\sigma}_{\mathrm{RMS,pixel,after}} &= 3.4 \pm 0.7\,\mathrm{mV} \quad & \overline{\sigma}_{\mathrm{RMS,pixel,max,after}} &= 10.0 \pm 1.0\,\mathrm{mV}. \end{aligned} \tag{4.37}$$

Before the bake-out the numeric value of $\overline{\sigma}_{\mathrm{RMS,pixel,max}}$ is higher than the required value. After the bake-out the homogeneity requirement of $\sigma_{\mathrm{RMS,pixel}} < 20\,\mathrm{mV}$ is clearly met.

An exemplary CPD pixel map and the corresponding $\sigma_{\mathrm{RMS,pixel}}$ pixel map are presented in figure 4.31. In these diagrams the tendency of higher CPD values at the edges is visible. But in addition there is a bisection of the sample over the complete surface. This regular distribution is not as easy to compensate during analysis as the radial distribution but it might still be possible. In the $\sigma_{\mathrm{RMS,pixel}}$ pixel map it can be seen that the edge is not only the position with the higher CPD values but also with higher $\sigma_{\mathrm{RMS,pixel}}$ values. But again the distribution is more or less regular. All CPD pixel and $\sigma_{\mathrm{RMS,pixel}}$ pixel maps can be

Table 4.15: $\overline{\text{CPD}}_{\text{pixel}}$, $\sigma_{\text{RMS,pixel,max}}$ and $\overline{\sigma}_{\text{RMS,pixel}}$ of all pixels after every possible rotation of the projection of the detector pixels on the surface of the Rear Wall. Maximum means in this context, that the given values are the maximum values which can be found in any of the 148 detector pixels and in any possible rotation. As scan 6 and 12 are not completed they are not included in the analysis.

measurement	$\overline{\text{CPD}}_{\text{pixel}}$	$\overline{\sigma}_{\text{RMS,pixel}}$ /mV	$\sigma_{\text{RMS,pixel,max}}$ /mV
1	141.4 ± 19.6	7.2 ± 4.1	30.5
2	143.9 ± 22.3	9.9 ± 8.4	37.8
3	123.8 ± 20.3	5.2 ± 2.6	14.7
4	124.7 ± 18.6	5.0 ± 2.8	14.7
5	124.0 ± 18.0	5.1 ± 3.3	16.2
7	406.7 ± 11.6	3.8 ± 1.9	10.9
8	385.8 ± 8.7	3.5 ± 1.6	10.0
9	364.1 ± 8.7	3.2 ± 1.0	9.9
10	374.7 ± 9.3	3.3 ± 1.3	8.2
11	356.8 ± 8.7	3.4 ± 1.5	10.9

found in appendix E.4. In the following section the results presented in this section are discussed in more detail.

4.7.6 Discussion of the UHV Kelvin Probe results

In the described results, changes of the CPD due to both, a bake-out and UV irradiation, are observed. In case of a bake-out the CPD values are decreased after the bake-out by several 100 mV. But due to the measurement principle of a Kelvin Probe, it is not possible to distinguish between an increase of the sample work function, a reduction of the tip work function or a combination of both. From the literature it is expected, that the gold work function is increased [Wel72] and the stainless steel work function of the tip is decreased by the removal of adsorbates from the surface during bake-out. That the gold work function is actually changed, at least in case of sample 5-SS-ep-6, can be seen from the CPD distribution. This distribution is changed after the bake-out by about 100 mV[29]. For that reason the minimal change of the gold work function is in the order of this value. Following the explanation of removed adsorbates from the surface, the limited exponential increase of the CPD after the bake-out is explainable by adsorption on the surface [Bab14]. But it is again not possible to distinguish between changes of the tip and the sample work function.

In the last section limited exponential functions are fitted on the mean CPD results of several scans. These fit functions include the fit parameters C_1, which reflect the saturation value of the increase, and the time constants τ, describing the temporal behavior. The parameters τ of all fit functions are consistent within the errors. On the one hand this could be a result of their large errors, especially in case of $f_{7-\text{SS}-\text{ep}-3}(t)$, the fit function of sample 7-SS-ep-3. Here the error on τ is large enough that the value is compatible with zero. On the other hand the consistence could be caused by a reproducible behavior of all equally produced and treated gold surfaces. In case of the latter explanation an estimation of the time to reach the saturation values of the work function after a bake-out

[29] The difference between the center work function and the edge work function is about 60 mV before and -40 mV after the bake-out.

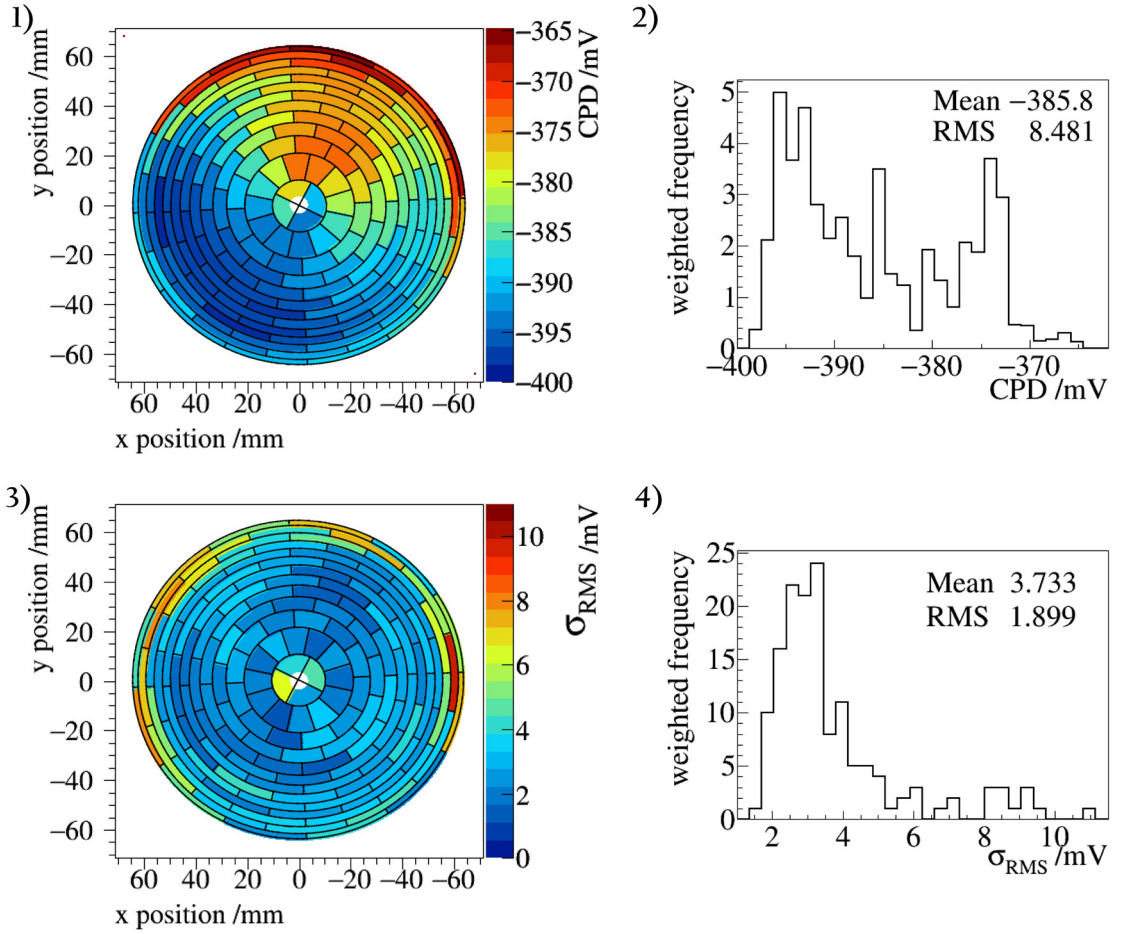

Figure 4.31: CPD pixel and $\sigma_{\mathrm{RMS,pixel}}$ pixel maps of sample 5-SS-ep-6. Both the maps on the left side and the corresponding histograms on the right side present data from the second scan after the bake-out. (1) The CPD pixel map is shown here. From the left bottom corner (at about position 40 mm/50 mm) of the diagram to the right top corner (at about position -20 mm/60 mm) the CPD increases over the complete surface of the sample. In addition, higher CPD values are found in the outer rings of the detector projection on the sample. (2) The corresponding histogram to the CPD map in (1) is plotted here. The distribution is rather broad and not normally distributed. (3) The $\sigma_{\mathrm{RMS,pixel}}$ pixel map is presented here. In the outer rings the highest RMS deviations can be found. (4) The histogram contains the $\sigma_{\mathrm{RMS,pixel}}$ values. Most pixels have values between 2 mV and 5 mV RMS deviation.

is possible. The time to achieve 95 % of the saturation value is given by

$$t = \frac{\log\left(\frac{0.05 \cdot C_1}{C_2}.\right)}{-k} \tag{4.38}$$

By setting the fit parameters to the values given in equation (4.33) the following time scales are obtained

$$\begin{aligned} t_{3-\mathrm{SS}-\mathrm{el}-6} &= 1.4 \pm 1.1\,\mathrm{d} \\ t_{5-\mathrm{SS}-\mathrm{el}-6} &= 4.5 \pm 9.0\,\mathrm{d} \\ t_{7-\mathrm{SS}-\mathrm{el}-3} &= 3.0 \pm 0.3\,\mathrm{d}. \end{aligned} \tag{4.39}$$

That means, that under the assumption of equally behaving gold surfaces after a bake-

out, 95 % of the saturation value is latest achieved after about 2 weeks. This effect must be taken into account at KATRIN measurements. As a bake-out of the Rear Section is not planned regularly but only in the beginning of KATRIN and eventually on request at a later moment, it is feasible to wait this time.

In addition to the change of the mean CPD value over the surface, the CPD homogeneity is improved after the bake-out for all tested 6-inch samples. This improvement is in the order of a factor of 2 or even larger. Besides that, the distribution of the CPD value can be changed due to the bake-out. But this is sample specific, as different behaviors have been observed at the different samples. Therefore, the change of the work function distribution after a bake-out must be investigated for each Rear Wall candidate during its characterization process.

A completely different behavior of the CPD is observable after the UV irradiation: The CPD value is increased by about 800 mV after the irradiation. Again, it is most probable that both, the work function of the tip and the sample, are shifted. However, as discussed before this behavior is not expected in case of a cleaning of the surface from adsorbates. Therefore more measurements and a detailed investigation of this effect are recommended.

The results of Rear Wall candidates demonstrate the importance of a careful manufacturing and handling of the final Rear Wall. Sample 3-SS-ep-3 has clearly visible scratches on the surface. These scratches result in a $\sigma_{\mathrm{RMS,surface}}$ of up to 50 mV. For that reason the sample is not suitable for KATRIN.

The results after the bake-out of the Rear Wall candidate 5-SS-ep-6 can be summarized as follows:

$$
\begin{array}{lll}
\sigma_{\mathrm{RMS,surface,max}} = 12.2 & & \text{mV for completed scan} \\
\overline{\sigma}_{\mathrm{RMS,surface}} = 9.4 & \pm 0.2 \pm 7.3_{\mathrm{stability}} & \text{mV averaged over all } \sigma_{\mathrm{RMS,surface}} \\
\sigma_{\mathrm{RMS,pixel,max}} = 10.9 & & \text{mV for completed scan} \\
\overline{\sigma}_{\mathrm{RMS,pixel,max}} = 10.0 & \pm 1.0 \pm 4.2_{\mathrm{stability}} & \text{mV averaged } \sigma_{\mathrm{RMS,pixel,max}} \\
\overline{\sigma}_{\mathrm{RMS,pixel}} = 3.4 & \pm 0.7 \pm 4.2_{\mathrm{stability}} & \text{mV averaged over all } \sigma_{\mathrm{RMS,pixel}}.
\end{array}
\tag{4.40}
$$

The given stability values are the fluctuations of the $\overline{\mathrm{CPD}}$ over time. As both, the change of the tip and the change of the sample work function with time, is included in the stability value, it is an upper limit for the stability. All these σ values are below the surface and pixel requirement of 20 mV RMS deviation. Concerning the CPD distribution it must be stated, that the work function at the edge is higher after the bake-out. The higher work function result in a higher endpoint energy in the β-spectrum of KATRIN in the outer detector pixels compared to that of the inner pixels. In addition, a gradient of the work function in the detector pixel projection on the Rear Wall is found. This gradient covers the complete surface of the Rear Wall. In the analysis of the KATRIN data these differences must be considered.

Concluding the following results are obtained by the presented measurements with the UHV Kelvin Probe:

- The work function of gold surfaces is changed by a bake-out. The specific value of the change cannot be quantified.
- The distribution of the work function can be changed by a bake-out, but this is sample specific and must therefore be investigated during the characterization process of Rear Wall candidates.
- The homogeneity of the work function over the surface is increased after a bake-out.

- UV irradiation changes the CPD measured with the Kelvin Probe. The reason for this is so far unknown. Therefore further investigations are required.
- The Rear Wall candidate 3-SS-ep-6 is not suitable as a Rear Wall. But its results demonstrate the necessity of careful manufacturing and handling of Rear Wall candidates and the later Rear Wall.
- A long-term measurement of sample 3-SS-ep-6 over 3 weeks after a second bake-out implies that the work function stability within this time range is possible to be in the order of 19 mV or even smaller.
- A first final Rear Wall is found: sample 5-SS-ep-6. This sample meets all requirements after the bake-out. The homogeneity over the surface is 9.4 ± 0.2 mV with a stability of $\leq$7.3 mV in one week. The averaged maximum RMS deviation within one pixel ($\overline{\sigma}_{\mathrm{RMS,pixel,max}}$) is found to be 10 ± 1.0 mV with a stability of $\leq$4.2 mV in one week. The average RMS deviation within the 148 detector pixels is 3.4 ± 0.7 mV.
- The CPD values of sample 3-SS-ep-5 follow a radial distribution combined with a distribution covering the complete surface. But as these distributions are not random, their consideration in the analysis of the KATRIN data seems to be possible.

These results also answer some of the questions mentioned in the beginning of this chapter. In the last section of the chapter the results of all experiments, which are performed to find a final Rear Wall meeting all the KATRIN requirements, are collected again. The consequences of these results on the Rear Section are also considered.

4.8 Consequences for the Rear Section

In the previous sections the development of the Rear Wall and the setups related to its development were presented, namely the ambient air Kelvin Probe, the photoelectron spectroscopy at the KATRIN monitor spectrometer and the UHV Kelvin Probe. The results obtained with these setups answer the questions from the beginning of this chapter:

1. Which Rear Wall layer design is most qualified for KATRIN? - Based on the results of the ambient air Kelvin Probe the most qualified layer design was found: a stainless steel substrate of 2 mm thickness, which is cut out of foil plastered raw material, electropolished and sputter coated with 100 nm titanium and 1 µm gold. The later tests in the other presented experiments confirmed that samples produced according to this recommendation are suitable for KATRIN (see especially last question). Besides that, the layer design has already been successfully used as an electrode in the source region of the monitor spectrometer MAC-E filter. In addition, the importance of a careful manufacturing and handling of the sample was demonstrated by the results of sample 3-SS-ep-6 at the UHV Kelvin Probe. Therefore, the decision for foil plastered raw material as a substrate is justified. To prevent changes in the work function at the position of the central hole this part of the Rear Wall must be coated with special diligence (see also question 4).

2. Is the work function and its distribution stable over several weeks? - The results of the ambient air Kelvin Probe showed that samples with stainless steel substrate have $\sigma_{\mathrm{RMS,surface}}$ values of below 20 mV over 1.5 months. But in this time only 3 to 4 measurements of the sample were performed. In addition, the samples were stored at ambient conditions between the measurements. Nevertheless, it was possible to deduced, that the $\sigma_{\mathrm{RMS,surface}}$ stays below 20 mV over this time. An exact value for the long-term stability cannot be given. But with the UHV Kelvin Probe long-term measurements were possible under stabilized conditions. Sample 3-SS-ep-6 was measured for 3 weeks after the sample

is baked out. The stability of $\overline{\text{CPD}}$ over the surface in this time was 18.5 mV. But it must be noted, that the sample was difficult to measure due to scratches on its surface which cause issues in the measurement with the UHV Kelvin Probe. Therefore, the given values are suspected to be a conservative estimate of the stability of $\overline{\text{CPD}}$ during 3 weeks of measurement.

3. How does a bake-out or UV light irradiation affect the work function and its homogeneity? - Concerning the bake-out different results are found. During the photoelectron measurements a decrease in the work function of gold due to the bake-out was found for most of the sample. But this reduction could have also been caused by a further adsorption on the surface due to a lower temperature of the sample compared to the vacuum chamber walls. The measurements at the UHV Kelvin Probe indicated an increase of the work function. This result is in agreement with other results in the literature. However, both experiments give the same result concerning the homogeneity of the work function over the surface: The work function homogeneity is improved after the bake-out. In addition, it was found that a bake-out can also have an effect on the distribution of the work function over the surface. But this effect is sample specific and must be investigated during the characterization process of the individual Rear Wall candidate.
Concerning the UV irradiation no significant effect on the work function value could be found during photoelectron measurements. But similar to a bake-out the UV irradiation improved the work function homogeneity.

4. How does the central hole effect the work function at the center region of the flux tube? - It was found, that the work function at the central hole can be different compared to the remaining surface. In addition, a different behavior of the hole after a bake-out or UV-irradiation is possible. The reason for the different behavior can either be the material behind the hole or the inner surface of the hole. With the performed measurements a distinction between these two causes was not possible.

5. How large are the work function deviations of final Rear Wall candidates and how is the work function distributed over the sample? - Two final Rear Wall candidates were tested so far. Of these sample 3-SS-ep-6 is not suitable as Rear Wall due to scratches on its surface. In the contrary sample 5-SS-ep-6 was found to be suitable. That means, it is the first final Rear Wall which was found. The $\overline{\sigma}_{\text{RMS,surface}}$ is 9.4 ± 0.2 mV and $\overline{\sigma}_{\text{RMS,pixel,max}}$ is 10.0 ± 1.0 mV with a stability of $\leq$7.3 mV or $\leq$4.2 mV in one week. The maximum values of $\sigma_{\text{RMS,surface,max}}$ and $\overline{\sigma}_{\text{RMS,pixel,max}}$ after bake-out are 12.2 mV or 10.9, respectively. All these values meet the requirements concerning homogeneity over the whole surface and within a detector pixel. The work function distribution over the surface was found to be a mixed distribution of a radial distribution and a non-symmetric distribution over the whole surface. The work function is not randomly distributed over the surface.

Although each of the questions could be answered, further investigates of Rear Wall related effects are advisable. One of these investigations is related with the UV irradiation of the Rear Wall and its effect on the work function. It must be investigated, why the CPD value is increased by about 800 mV. Therefore, further measurements after an UV irradiation are required.

Also, the long-term stability of the Rear Wall needs further investigation. A measurement over 60 days is required, as this is the duration of one KATRIN measurement run. In addition, it must be verified, if there are differences in the long-term stability of various samples which are produced in the same way.

Despite of the fact, that the final Rear Wall is found during the Rear Wall development phase another tested Rear Wall candidate is not suitable. Due to the fact that 3 Rear Wall

candidates are produced so far, only one further candidate is remaining. Therefore, the production of further Rear Wall candidates is highly recommended. In case of damage of the Rear Wall surface during installation another already qualified and characterized Rear Wall candidate must be available. For that reason the qualification of further Rear Wall candidates is needed. As consequence of the results presented in the scope of this chapter, this qualification must also include an investigation of changes of the work function distribution caused by a bake-out.

Another consequence of the presented results is that a careful matching of the Rear Wall and the small cover, which is installed behind the Rear Wall to cover the Rear Wall hole, is required. This matching process will be performed at the UHV Kelvin Probe: several covers will be installed together with a Rear Wall candidate. By comparing the CPD values of the covers and the Rear Wall candidate, the best matching cover for the individual Rear Wall candidate can be found. This requirement results from the photoelectron spectroscopy at the position of the hole. In addition, these measurements have shown, that the absolute work function values of identically produced samples can be very different.

Due to the results of the UHV Kelvin Probe it is also required to wait after a bake-out before measurements at KATRIN are performed. This must be considered in the measurement plan of KATRIN. It is recommended to wait for about 2 weeks before a KATRIN measurement run is started. By that changes of the Rear Wall work function are minimized.

But the most important consequence of the presented results is, that after a development phase of several years, a first final Rear Wall is found. This Rear Wall meets all KATRIN requirements and is fully characterized concerning its spatial work function distribution.

Chapter 5

Summary and outlook

This thesis set out to answer a number of questions regarding the setup of the Karlsruhe Tritium Neutrino experiment, which aims to measure the mass of the neutrino with an unpresedented sensitivity. The stage for the efforts of measuring the neutrino mass was set by the discovery of the neutrino oscillation. Since then all previous experiments were limited in their ability to pinpoint the neutrino's mass, permitting them only to set an upper limit. The Karlsruhe Tritium Neutrino experiment KATRIN is designed to improve the current sensitivity on the neutrino mass by 1 order of magnitude.

To be able to achieve this sensitivity the measurement parameters of KATRIN must be known and monitored precisely in order to minimize the systematic uncertainties of the measurement. This is the purpose of the Calibration and Monitoring System (CMS) of the tritium related components of KATRIN. The Rear Section as one important part of this system combines different monitoring tools in one component. It provides monitoring of the source activity by β-induced X-ray spectrometry (BIXS) and an angular selective electron gun. The e-gun is essential for several purposes such as the measurement of the column density in the tritium source and of the transmission of KATRIN's main spectrometer. In addition, the Rear Section provides the gold coated Rear Wall which dominantly defines the source potential with its work function.

Great progress in the development of the Rear Section components has been achieved already. But there are still some open questions, which cover a highly diverse range of subjects. These must be answered in order to provide a fully functional Rear Section to KATRIN. Answering these questions was the objective of the thesis in hand. A summary of the obtained answers is given in the following.

1. Are all components, which are planned to be used, tritium compatible concerning aspects of safety and their performance?
Three components were tested in a tritium atmosphere in the course of this thesis: a piezo motor, a fiber feed-through and an optical fiber. None of them have been operated in a tritum atmosphere before. To qualify these components three different experimental setups were developed and built up. All components tested were found to be suitable for usage in a tritium atmosphere both concerning safety aspects and their performance:

- In the Piezotest a custom made piezo motor based on the N-310K176 motor was developed in cooperation with the company Physik Instrumente. This motor was successfully tested concerning its performance in a tritium atmosphere. The required driving cycles of 100 000 were found to be exceeded by more than a factor of 2. While

the motor's performance degraded, this does not affect its suitability for KATRIN since only driving operations from one limit switch to the other are required. In addition, it was shown that the motor can be baked out at 150 °C. That means, that the motor can be used in the KATRIN experiment due to the qualification process presented in this thesis.

- The suitability of a fiber feed-through installed in a vacuum flange was successfully demonstrated in the Fibertest I for the first time. The leak rate through such a fiber feed-through was measured in a test experiment. The fiber feed-through divided two chambers, one with a tritium partial pressure in the order of 10^{-1} mbar and one with 0 mbar tritium partial pressure. The leak rate through the fiber feed-through was determined to be $L = (3.65 \pm 0.08) \cdot 10^{-13}\,\mathrm{mbar\,l\,s^{-1}}$. This leak rate is expected to be about 7 orders of magnitude lower at the Rear Section. This is a consequence of the linear pressure dependence of a diffusion process and the fact, that the tritium partial pressure in the Rear Section will be about 7 orders of magnitude lower than it was in the Fibertest I. It was therefore demonstrated, that the safety limit of $10^{-9}\,\mathrm{mbar\,l\,s^{-1}}$ is maintained and that the fiber feed-through can be used for a tritium containing system.
- The effect of a tritium atmosphere on the optical transmission of fibers was investigated in the Fibertest II. Here no significant change of the optical properties caused by the tritium exposure could be found: the detected changes of the respective parameters were all within 3σ compatible with the initial values before the tritium exposure. In addition, these changes were found to cause no degradation of the transmission but rather an improvement. Although the fibers were only exposed to tritium for a minimum of 7 days these results are applicable to the whole KATRIN lifetime of 5 years: due to the linear dependence of the activity and the diffusion on the tritium partial pressure, 1 second in the Fibertest II is equivalent to more than 100 days under KATRIN conditions. This is a consequence of the 7 orders of magnitude larger tritium partial pressure in the Fibertest II compared to the partial pressure at the Rear Section e-gun. Therefore, the optical transmission properties of the tested fibers under tritium conditions were found to be suitable for KATRIN.

2. How can the optical setup, used to produce the electrons at the e-gun, be designed to prevent misalignment of optical components inside of a glove box and to meet the required electron rate of at least $10^4\,\mathrm{s^{-1}}$?

In this thesis the final optical setup of the e-gun was designed. The main components of the optical setup are a laser driven light source, an automatable monochromator, a fiber feed-through, a splitter fiber and a focusing system consisting of 2 lenses. All these components were chosen in a way that the transmitted light is maximized and the probability of a misalignment especially inside of the Rear Section glove box is minimized. The former was accomplished (among other things) by carefully selecting the utilized lenses based on a detailed analysis of the losses of different candidate lenses. The latter was achieved by using fiber (coupled) components wherever possible, e.g. a beam splitter which is integrated into a fiber and therefore cannot be misaligned.

The electron rate of this optical setup was calculated and shown to be sufficient for KATRIN. The calculated electron rate was found to exceed the required rate by up to 1 order of magnitude at the design wavelength of 275 nm. Assuming a work function of 4.2 eV, the electron rate is $7.26{\cdot}10^5\,\mathrm{s^{-1}}$ at the maximum slit width of the monochromator. The maximum achievable rate (for this slit width and gold work function) is $2.27{\cdot}10^6\,\mathrm{s^{-1}}$ at 238 nm. The contribution of the optical system to the energy distribution width σ_E was calculated to be approximately 0.07 eV at the design wavelength of 275 nm using the

maximum slit width. Therefore the contribution of the optical system was found to be lower than the required value of less than 0.2 eV. All in all an optical setup was developed which meets all the KATRIN requirements.

3. What is the most suitable design of the Rear Wall to achieve a homogeneous and long-term stable surface potential, how is the surface potential effected by a bake-out or UV irradiation and how large is the resulting inhomogeneity of a final Rear Wall?
Thanks to the experiments performed in the course of this thesis it was possible to determine the most suitable layer design for Rear Wall candidates. This design uses foil plastered stainless steel as a substrate, which is electropolished after the cutting process. On this 100 nm titanium and 1µm gold are coated by sputtering. This layer design was successfully tested as a cathode in a MAC-E (Magnetic Adiabatic Collimation combined with an Electrostatic) filter already.
A precise knowledge of the effects of a bake-out and of UV irradiation is essential for the KATRIN experiment. Therefore, detailed investigations of the work function dependence on these treatments were performed in this thesis: both, a bake-out and UV irradiation, were found to improve the homogeneity of the work function over the surface. But a general quantification of this improvement is not possible as it is sample specific. However, the improvement seems to be mostly in the order of a factor of 2 measured against the work function homogeneity before the bake-out/UV irradiation. A bake-out additionally can change the work function distribution over the surface. But again this effect is found to be sample specific. For that reason, bake-out effects are recommended to be characterized in the qualification process of the final Rear Walls as well.
Also the impact of the central hole of the Rear Wall on the work function is of great interest for KATRIN. If the work function fluctuations at this position exceed the 20 meV requirement, the 4 central detector pixels of KATRIN can hardly be used for the determination of the neutrino mass. Investigations of this Rear Wall region were performed in this thesis for the first time. It was found, that the inner surface of the hole and the plate behind the hole affect the work function at the hole position. But it was not possible to distinguish their different effects.
All in all the efforts of this thesis lead to a first final Rear Wall (which can in principle be installed in the Rear Section). This Rear Wall was fully characterized concerning the KATRIN requirements. Its $\overline{\sigma}_{\mathrm{RMS,surface}}$ was determined to be 9.4 ± 0.2 mV and its $\overline{\sigma}_{\mathrm{RMS,pixel,max}}$ to be 10.0 ± 1.0 mV. The stability of these values was found to be $\leq$7.3 mV and $\leq$4.2 mV in one week. The maximum values $\sigma_{\mathrm{RMS,surface,max}}$ and $\overline{\sigma}_{\mathrm{RMS,pixel,max}}$ after one bake-out were 12.2 mV and 10.9, respectively. Examination of the contact potential difference (CPD) distribution after a bake-out showed a combination of a radial distribution and an asymmetric distribution from one side to the other side over the complete surface. As the CPD distribution is not random, it can be compensated by later KATRIN analysis. That means, that a Rear Wall which meets all homogeneity requirements on the work function has been determined.
Finally, a first investigation of the long-term stability of the gold surface CPD in a vacuum atmosphere was performed for the first time. This investigation indicates a stability of at least 18.5 mV over 3 weeks. Therefore, the stability requirement on the work function of the Rear Wall is most probably also met. But further investigations are required for a more definitive statement.
As its most important result the work of this thesis has therefore enabled the development of a first final Rear Wall which meets all the KATRIN requirements.

In spite of great effort, concerning questions 2 and 3 there are still open tasks which must

be completed:

- The optical setup of the e-gun must be built up. The experience gained during the Fibertest II implies that the intensity of the light could decrease with time due to the formation of color centers. These effects will be investigated and quantified if existing.
- Further investigations on the long-term stability of the work function are needed. This includes the measurement of several equally manufactured samples to investigate if the stability is sample specific. Besides that a long-term measurement of at least 60 days, which is the duration of a KATRIN run, is recommended.
- The effect of UV irradiation on the Rear Wall will be investigated further. In particular a measurement strategy to do so at the UHV Kelvin Probe is required.
- Further Rear Wall candidates must be fabricated and characterized. In addition, several plates, which can be used to cover the central Rear Wall hole from the backside, will be fabricated. For each final Rear Wall a plate must be found, which has a matching work function.

All these tasks are currently approached or will be in near future by the Rear Section group. The optical system of the e-gun is being set up in winter 2015. Also, the qualification of further Rear Walls is ongoing. The Rear Wall and the plate behind it are installed at the latest in August 2016. After a final test of all components the Rear Section is planned to be ready for operation at KATRIN at the end of 2016.

Appendix A

Additional data of tritium related experiments

This appendix presents additional data of the experiments described in chapter 3. This data is not absolutely necessary to arrive at the results of the experiments but it supports the conclusions drawn in the given chapter.

A.1 Additional data of the Piezotest

In this section additional data both, of the automatic and the manual measurements, are presented. No new takeaways from these plots are possible but they support the already draw conclusions from the plots shown in section 3.1.

First the data of the manual measurements with the laser rangefinder are presented. In each plot the blue areas mark the time in which the TRAP fume hood was needed for other experiments and therefore the Piezotest was suspended. The red areas mark the time periods of the bake-outs. The straight lines plotted in the diagrams represent the mean value of the measurements before the tritium exposure and the dotted lines mark the error of the mean value. The last to diagrams present the data of the automatic measurements where the motor moves towards the negative limit.

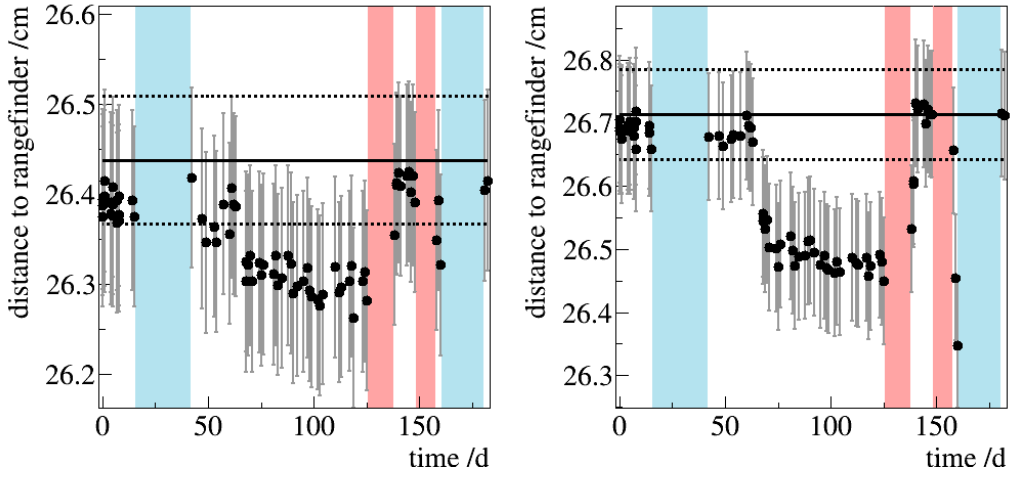

Figure A.1: Plot of data taken during manual measurements with 100 and 300 steps. Left: here the data with 100 steps is plotted. Right: diagram if the motor is moved by 300 steps.

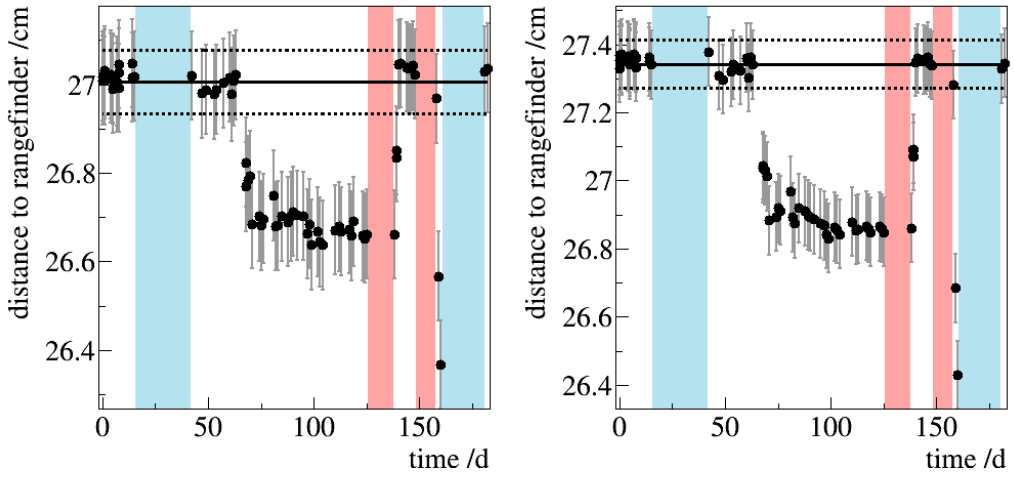

Figure A.2: Plot of data taken during manual measurements with 500 and 700 steps. Left: here the data with 500 steps is plotted. Right: diagram if the motor is moved by 700 steps.

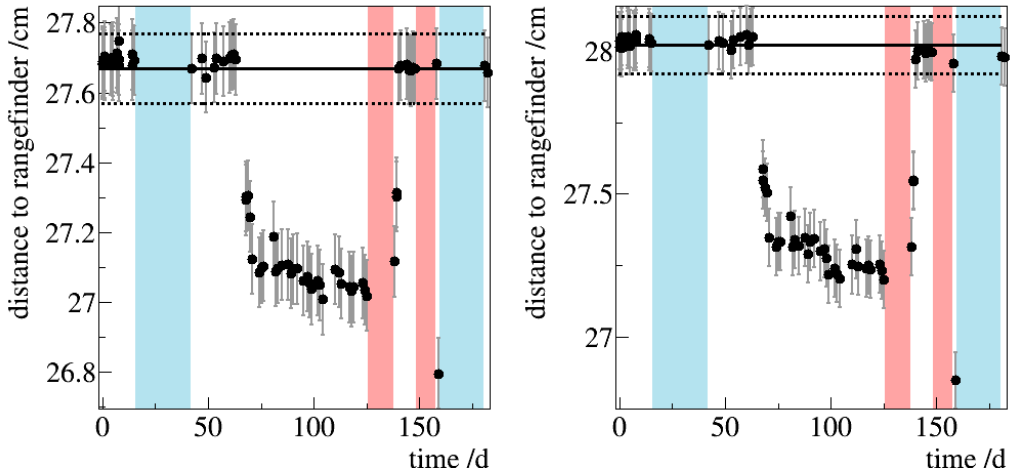

Figure A.3: Plot of data taken during manual measurements with 900 and 1 100 steps. Left: here the data with 900 steps is plotted. Right: diagram if the motor is moved by 1 100 steps.

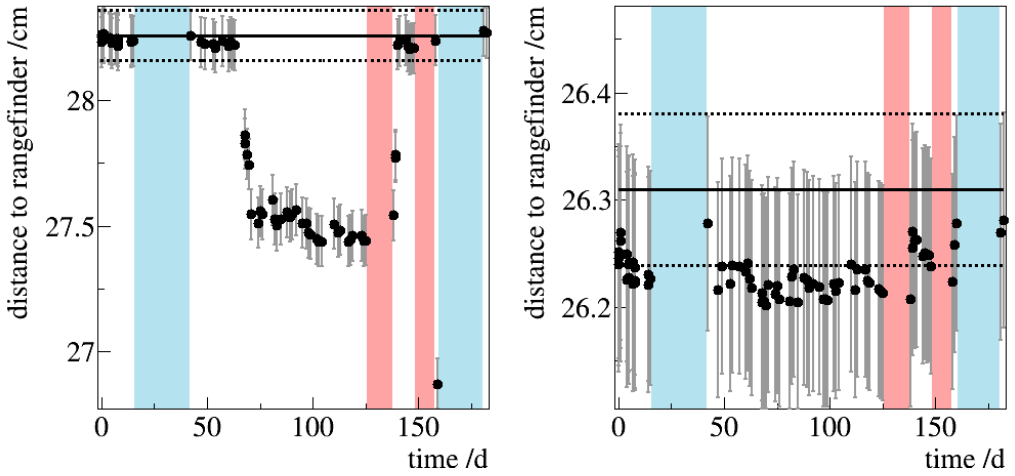

Figure A.4: Plot of data taken during manual measurements with 1 300 steps and moving towards the negative limit. Left: here the data with 1 300 steps is plotted. Right: diagram if the motor is moved towards the negative limit.

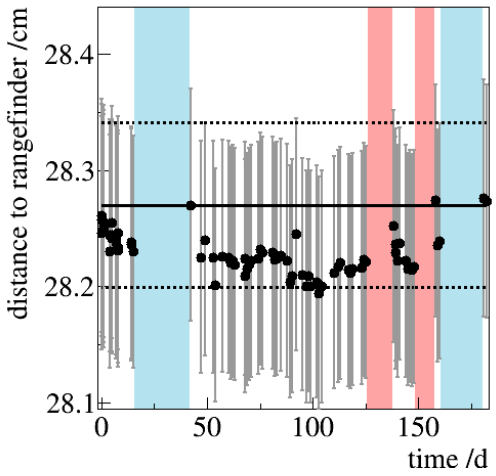

Figure A.5: Plot of data taken during manual measurements towards the positive limit.

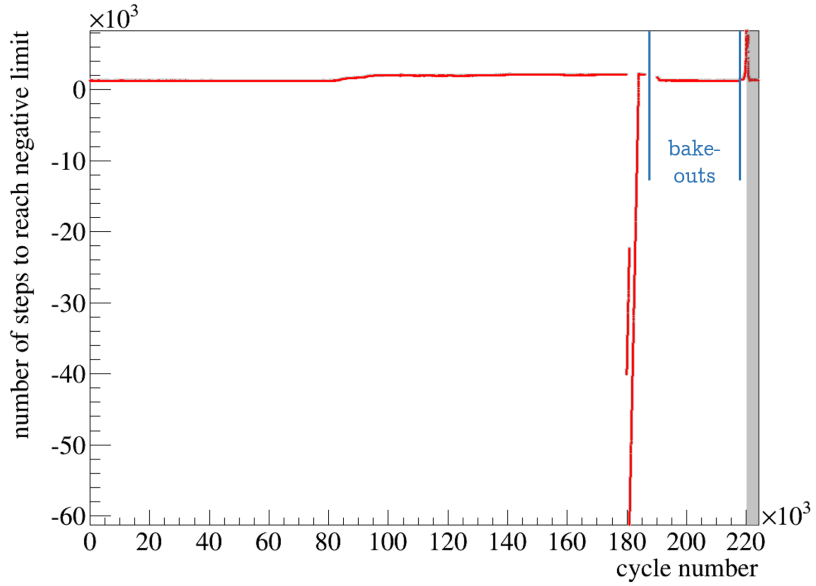

Figure A.6: Plot of data taken during automatic measurements to negative limit. The steps needed to move from the positive limit to the negative limit are plotted against the driving cycles. In addition the bake-outs are marked by the vertical blue lines. The gray area at the right side of the diagram marks the time when the system is filled with ambient air. In the remaining time the system is filled with tritium gas. Note that the motor reached the negative limit at each cycle.

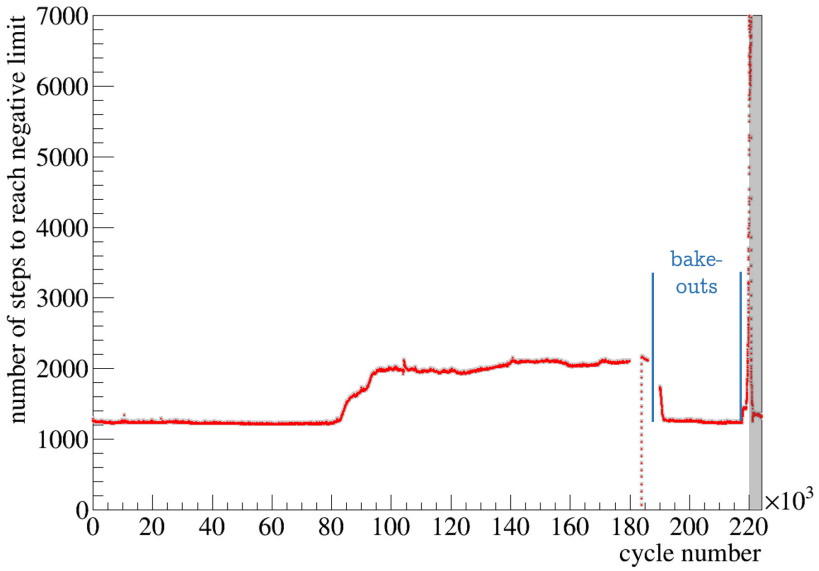

Figure A.7: Detailed plot of the data taken during automatic measurements to negative limit. This is a magnified section ot the figure A.6. The markers (blue line and gray area) have the same meaning as they do in that figure. In direction of the x-axis the same range is covered, but at the y-axis only steps in the positive range are shown.

A.2 Limit finding of fits in the Fibertest I

Here the analysis leading to the most suitable time, when the signal of the Fibertest I ionization chamber switches from a signal describable with the linear function f_2 to a signal describable with exponential function f_3, is presented. In addition the lower limit of f_2 must be found. To do so, more than 150 000 fittings with different limits were performed. The decision which time is most suitable is made by the minimization of the summed up mean residuals of both fits. The results for the most suitable times are given in table A.1.

Table A.1: List of the most suitable limits for the functions describing the Fibertest I signals. In the first column the time, when the description with f_2 stops and the description with f_3 starts, is given. Then the residuals of f_3 are given. In the third column the lower limit from where the signal is suitably described by f_2 is indicated. The residuals of f_2 and the sum of both the residuals of f_2 and f_3 are given in the last two columns. By looking at the limits one can see that the time range for which the two fits are most suitable is very narrow.

upper limit f_2/lower limit f_3 /days	residuals of f_3	lower limit f_2 /days	residuals of f_2	added residuals
28.951	$7.18750 \cdot 10^{-17}$	10.980	$7.23421 \cdot 10^{-17}$	$1.44217 \cdot 10^{-16}$
28.950	$7.18747 \cdot 10^{-17}$	10.980	$7.23430 \cdot 10^{-17}$	$1.44218 \cdot 10^{-16}$
28.951	$7.18750 \cdot 10^{-17}$	10.981	$7.23443 \cdot 10^{-17}$	$1.44219 \cdot 10^{-16}$
28.958	$7.18753 \cdot 10^{-17}$	10.980	$7.23442 \cdot 10^{-17}$	$1.44219 \cdot 10^{-16}$
28.950	$7.18747 \cdot 10^{-17}$	10.981	$7.23453 \cdot 10^{-17}$	$1.44220 \cdot 10^{-16}$
28.951	$7.18750 \cdot 10^{-17}$	10.979	$7.23449 \cdot 10^{-17}$	$1.44220 \cdot 10^{-16}$
28.952	$7.18761 \cdot 10^{-17}$	10.980	$7.23436 \cdot 10^{-17}$	$1.44220 \cdot 10^{-16}$
28.953	$7.18777 \cdot 10^{-17}$	10.980	$7.23420 \cdot 10^{-17}$	$1.44220 \cdot 10^{-16}$
28.949	$7.18754 \cdot 10^{-17}$	10.980	$7.23456 \cdot 10^{-17}$	$1.44221 \cdot 10^{-16}$
28.950	$7.18747 \cdot 10^{-17}$	10.979	$7.23459 \cdot 10^{-17}$	$1.44221 \cdot 10^{-16}$
28.954	$7.18772 \cdot 10^{-17}$	10.980	$7.23434 \cdot 10^{-17}$	$1.44221 \cdot 10^{-16}$
28.956	$7.18752 \cdot 10^{-17}$	10.980	$7.23462 \cdot 10^{-17}$	$1.44221 \cdot 10^{-16}$
28.951	$7.18750 \cdot 10^{-17}$	10.982	$7.23470 \cdot 10^{-17}$	$1.44222 \cdot 10^{-16}$
28.952	$7.18761 \cdot 10^{-17}$	10.979	$7.23464 \cdot 10^{-17}$	$1.44222 \cdot 10^{-16}$
28.952	$7.18761 \cdot 10^{-17}$	10.981	$7.23458 \cdot 10^{-17}$	$1.44222 \cdot 10^{-16}$
28.953	$7.18777 \cdot 10^{-17}$	10.981	$7.23442 \cdot 10^{-17}$	$1.44222 \cdot 10^{-16}$
28.957	$7.18741 \cdot 10^{-17}$	10.980	$7.23481 \cdot 10^{-17}$	$1.44222 \cdot 10^{-16}$
28.958	$7.18753 \cdot 10^{-17}$	10.979	$7.23470 \cdot 10^{-17}$	$1.44222 \cdot 10^{-16}$
28.958	$7.18753 \cdot 10^{-17}$	10.981	$7.23464 \cdot 10^{-17}$	$1.44222 \cdot 10^{-16}$
28.959	$7.18752 \cdot 10^{-17}$	10.980	$7.23471 \cdot 10^{-17}$	$1.44222 \cdot 10^{-16}$
28.949	$7.18754 \cdot 10^{-17}$	10.981	$7.23479 \cdot 10^{-17}$	$1.44223 \cdot 10^{-16}$

Table A.2: Slope of the measurements performed at different pressures. The measurements are ordered not chronologically but with increasing pressure.

pressure /mbar	slope /(10^{-10} s)
1	-8.83±0.05
3	2.58±0.05
10	1.55±0.05
200	20.11±0.05
400	21.46±0.05
600	23.46±0.05

A.3 Pressure effect on transmission through optical fibers

During the investigation of the second fiber with the Fibertest II the primary system is accidentally filled with a pressure larger than 3.4 mbar (but still with a maximum tritium partial pressure of 0.59 mbar or maximum activity of below 10^{10} Bq). This pressure caused an increase in the ratio of the two photodiodes. As it is not expected that the signal of the monitoring photodiode is suddenly decreased for no reason, this increase is caused by an increase of the monitoring photodiode's signal. Similar effects are described in [Ste93, SZ08, Bur00].

To check for the pressure dependence a reference measurement at 10^{-2} mbar is performed at first. Before this measurement the light source was turned off for 20 days. Afterwards the primary system is filled first with 200 mbar, then with 400 mbar and finally with 600 mbar. In between the system is not evacuated only after the 600 mbar measurement. For the following measurements at 1 mbar, 10 mbar and 3 mbar the system is evacuated before each measurement. The light source is turned on 4 hours before each measurement, which means that the optics are irradiated for this period of time before the actual measurement starts. The pressure is increased directly before a measurement starts.

For the analysis the reference measurement is subtracted from the other data to see changes in the behavior more precisely. The obtained data is plotted in figure A.8. A linear fit is performed for it. The resulting slopes are given in table A.2.

What attracts attention is, that the only negative slope is for the 1 mbar measurement, which is below the limit stated in [Ste93], where the transmission decrease starts. The data at 3 mbar and 10 mbar have a positive but relatively small slope and the measurements at even higher pressures have a slope which is about 1 order of magnitude larger.

The large and positive slope of the obtained data with 200 mbar, 400 mbar and 600 mbar can be explained by a higher transmission through the measurement photodiode due to the higher pressure in the primary system. The higher pressure cause the ratio to be increased compared to the reference measurement. That means that a regeneration of the silica and its transmission takes place. An explanation for the increasing slope from the 200 mbar to the 600 mbar measurement is that the color center formation of the monitoring photodiode slows down due to the exponential behavior of the color center formation.

The three measurements below 10 mbar behave differently, their slope is negative and by a one order of magnitude smaller than the ratios taken at measurements above this pressure. This is evidence that the pressure has an impact on the transmission through the fiber, indeed: below 10 mbar the transmission through the fiber is reduced.

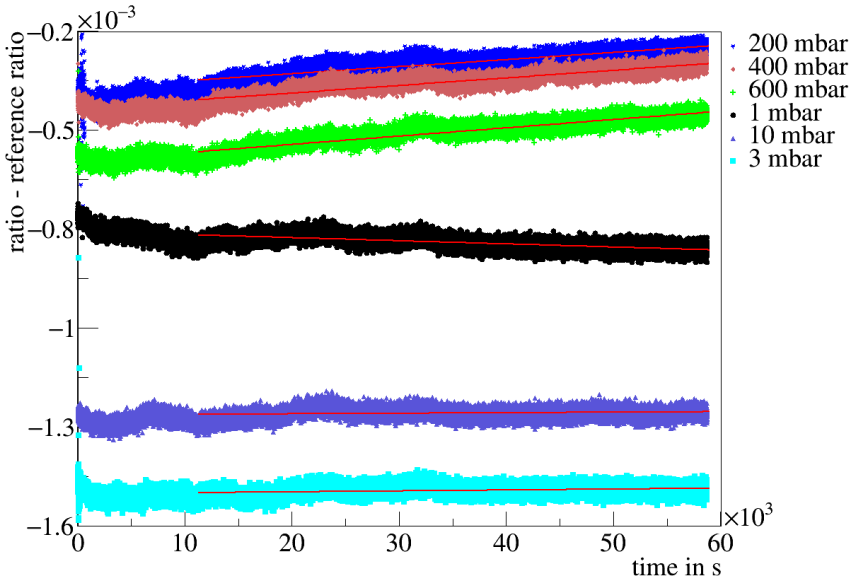

Figure A.8: Plot of the measurements at different pressures. From top to bottom the pressures are 200 mbar, 400 mbar, 600 mbar, 1 mbar, 10 mbar and 3 mbar. This is also the chronological order. As the ratio decreases from measurement to measurement, the values of the ratio substracted by the reference ratio become more negative as well.

Appendix B

Additional calculations on optics

In this appendix additional calculations on optics are presented, namely: the e-gun rate calculations of the e-gun test setup at the University of California Santa Barbara (UCSB) and the effect of irradiation on the acceptance angle due to a change in the refractive indices of the fiber which is installed in the primary system.

B.1 E-gun rate calculation of the e-gun test setup at UCSB

B.1.1 The optical setup

As the setup of the e-gun has been tested at UCSB before shipping, the measured count rates can be used to test the count rate calculations shown in section 3.2.1. But before the calculations and their results are discussed in more detail, the optical setup and its properties are presented.

The optical setup used for the test measurements is shown in figure B.1. It was originally planned to use this optical setup at the final e-gun but due to the better handling of the fiber coupled setup described in section 3.2.1 this plan was altered. Nevertheless the optical setup of the test experiments can help to improve the calculations of the electron rate of the final setup by comparing the calculated with the measured e-gun rate.

The optical setup described in this appendix consists of the following parts:

- **Light source**: the light source is of the type EQ-99X from Energetiq[1]. The spectral radiance of the light source is given in figure B.2 and its NA value is 0.47. In contrast to the final setup the light source is not directly coupled to a fiber in this case.
- **Lenses:** all lenses are of the type LA4052 from Thorlabs[2]. The transmission curve is shown in figure B.2. All lenses are uncoated. The front focal length is 35.1 mm, and the back focal length (BFD) is 29.5 mm at the design wavelength of 587.6 nm. The actual focal length and BFD can be calculated by [Hec13]

$$\frac{1}{f(\lambda)} = (n(\lambda) - 1)\left(\frac{1}{R_1} - \frac{1}{R_2} + \frac{(n(\lambda) - 1) \cdot d_1}{n(\lambda) \cdot R_1 \cdot R_2}\right) \tag{B.1}$$

[1]Energetiq Technology, Inc.,7 Constitution Way, Woburn, MA 01801, USA (Corporate Headquarters)
[2]Thorlabs Inc, 56 Sparta Avenue, Newton, New Jersey, 07860, USA

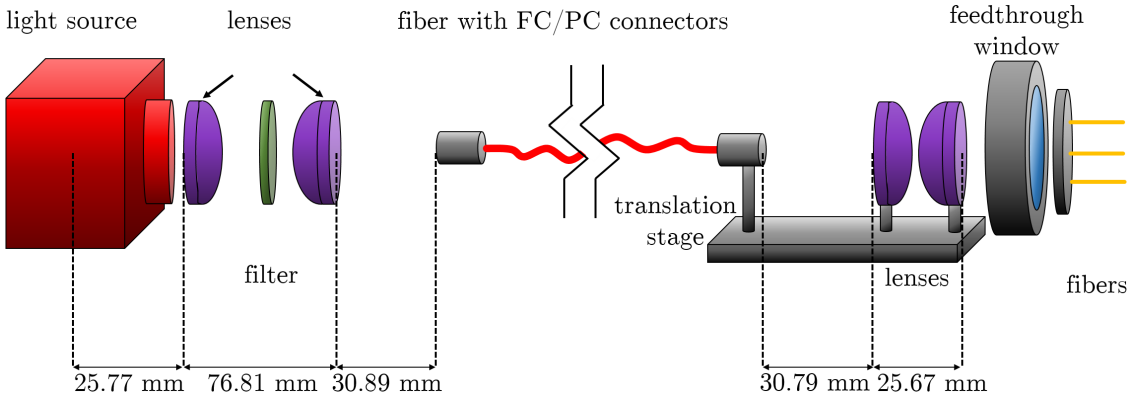

Figure B.1: Optical setup used during the e-gun test measurements. The numbers given in the lower part of the scheme are the distances between the optical components.

Table B.1: Specifications of the different filters used during the e-gun test at UCSB

filter wheel position	filter part number	center wavelength /nm	transmission at peak	FWHM /nm
1	Edmund Optics 67-802	$220\ ^{+3}\ /\ _{-0}$	> 0.12	10 ± 2
2	Edmund Optics 67-804	$232\ ^{+3}\ /\ _{-0}$	> 0.15	11 ± 2
3	Edmund Optics 67-806	$248\ ^{+3}\ /\ _{-0}$	> 0.12	12 ± 2
4	Edmund Optics 67-812	$270\ ^{+3}\ /\ _{-0}$	> 0.12	13 ± 2
5	Edmund Optics 67-815	$297\ ^{+3}\ /\ _{-0}$	> 0.15	14 ± 2

and

$$BFD(\lambda) = f \cdot \left(1 - \frac{(n(\lambda) - 1) \cdot d}{n(\lambda) \cdot R_1}\right) \tag{B.2}$$

where f is the focal length, $n(\lambda)$ is the refractive index of the lens material, $R_1 = 16.1\,\text{mm}$ and $R_2 = \infty$ are the radii of the lens at the side of the light source or of the other side and $d = 2\,\text{mm}$ is the thickness of the lens without the thickness of the curvature.

- **Filters:** a selection of five different filters produced by Edmund Optics[3] is available and can be chosen by a filter wheel. The specifications of the filters are given in table B.1. The transmission curves are given in figure B.2.
- **Fiber (outside vacuum):** the fiber is of the type FG550UEC from Thorlabs. The core size is 550 µm, the NA value is 0.22, and the length is 1 m. At both sides the fiber is terminated by a FC/PC connector which usually has an insertion loss of 0.2 dB. The attenuation caused by the length of the fiber is wavelength dependent and is given in figure B.2.
- **Feedthrough window:** the feedthrough window is of the type 9712000 from MDC Vacuum Products, LLC[4]. The transmission of this sapphire window is shown in figure B.2.
- **Fiber (inside vacuum):** the fibers are of type Edmund Optics #57-074, have a core size of 200 µm and a length of 16.4 cm. The attenuation caused by the length of the fiber is wavelength dependent and is given in figure B.2.

[3]Edmund Optics Inc.— 101 East Gloucester Pike, Barrington, NJ 08007-1380, USA
[4]MDC Vacuum Products, LLC, 23842 Cabot Blvd, Hayward, CA, 94545-1661, USA

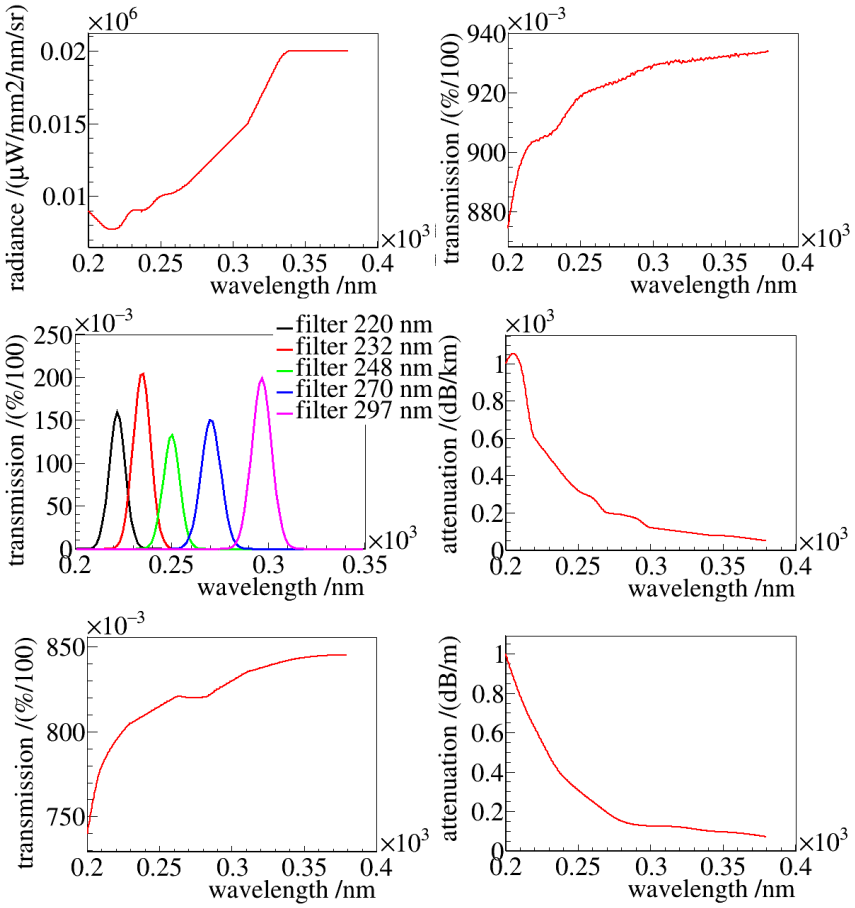

Figure B.2: Properties of the optical components. In this figure the optical properties of the light source, the lenses, the filters, the different fibers and the feedthrough window are shown. Top left: the diagram is showing the spectral radiance of the light source. The graph is interpolated from data points taken from a diagram provided by the manufacturer [Ene14]. Top right: the transmission curve of the lenses, which is interpolated from data given by the manufacturer [Tho15b], is shown. Middle left: here the transmission curves of the five filters with center wavelengths at 220 nm, 232 nm, 248 nm, 270 nm and 297 nm are shown. The curves are interpolated from data points taken from a diagram provided by the manufacturer [Edm14]. Middle and bottom right: the attenuation of the fiber outside (middle) and inside (bottom) of the vacuum system is shown. The attenuation is interpolated from data points taken from a diagram provided by the manufacturer [Tho15a, Edm14]. Bottom left: the given transmission through the feedthrough window is interpolated from data points taken from a diagram provided by the manufacturer [MDC15].

Table B.2: Absorption coefficients of titanium and gold. The absorption coefficients are taken from [Joh74].

wavelength /nm	absorption coefficient of Ti /cm^{-1}	absorption coefficient of Au /cm^{-1}
220	$9.4933 \cdot 10^5$	$8.0870 \cdot 10^5$
232	$9.1359 \cdot 10^5$	$8.1341 \cdot 10^5$
248	$9.2221 \cdot 10^5$	$8.2217 \cdot 10^5$
270	$9.7007 \cdot 10^5$	$8.4228 \cdot 10^5$
297	$1.0220 \cdot 10^6$	$7.9712 \cdot 10^5$

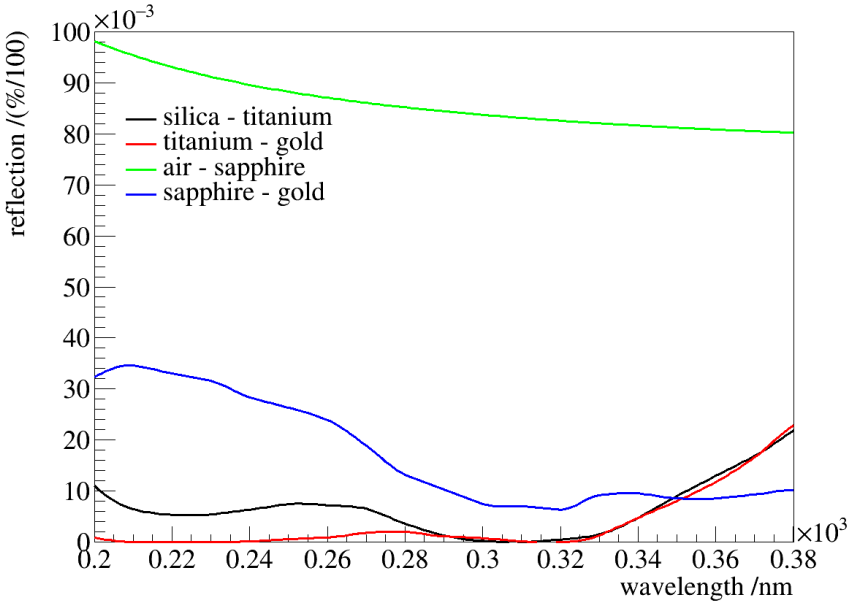

Figure B.3: Reflection curves of the different material junctions of the e-gun cathode. As Jiang at al. [Jia98b] measured the quantum yield of thin films of gold coated on sapphire, the reflection at air-sapphire and sapphire-gold junctions must be known. In addition the reflection at a silica-titanium and titanium-gold junction is needed, as the e-gun is build out of these materials. In the left diagram the reflection at these four junctions calculated by data of [Mal65, Joh74] is shown.

- **Gold layer:** the gold layer has a thickness of 37 nm and is coated on a 3 nm intermediate layer of titanium. The work function Γ of the gold layer is unknown, but is expected to be about $\Gamma = 4.2\,\text{eV}$. The reflection at the silica titanium and the titanium gold junction is shown in figure B.3. The absorption coefficients of the titanium and the gold layer are listed in table B.2.

B.1.2 The calculation of the electron rate

The calculation of the electron flux has two main parts: the spectral flux $\Phi(\lambda)$ reaching the gold layer of the cathode and the probability $\Gamma(\lambda)$ to produce an electron which leaves the gold layer. By integration of the product of both parts the electron rate Ξ of the e-gun can be calculated

$$\Xi = \int_{-\infty}^{\infty} \Phi(\lambda) \cdot \Gamma(\lambda)\, d\lambda. \tag{B.3}$$

Both parts are separately discussed in the following.

B.1.3 The spectral flux in the gold layer

The formula

$$\Phi(\lambda) = I(\lambda) \cdot E \cdot T_{\text{lens}}(\lambda)^4 \cdot T_{\text{filter}}(\lambda) \cdot L_{\text{fiber1}}(\lambda) \cdot T_{\text{window}}(\lambda) \cdot L_{\text{fiber2}}(\lambda) \cdot R(\lambda) \cdot L_{\text{align}}(\lambda) \tag{B.4}$$

is used to calculate the spectral flux of the light directly after entering the gold layer (which means after the reflection on the silica gold junction and before absorption takes place). The parameters of this formula are:

- $I(\lambda)$**:** spectral radiance of the light source (compare figure B.2).
- E**:** etendue of the light source. In case of the used light source with NA of 0.47 the etendue can be extrapolated from data given by the manufacturer [Ene14]:

$$E = 0.0244\,\text{mm}^2\text{sr}. \tag{B.5}$$

- $T_{\text{lens}}(\lambda)$**:** transmission of the lenses divided by 100 (compare figure B.2).
- $T_{\text{filter}}(\lambda)$**:** transmission of the filter divided by 100 (compare figure B.2).
- $L_{\text{fiber1/2}}(\lambda)$**:** losses in the fiber caused by the insertion loss $L_{\text{i,fiber1/2}}$ and the attenuation inside the fiber $L_{\text{att,fiber1/2}}(\lambda)$ (compare figure B.2):
  - $L_{\text{i,fiber1/2}}$: the insertion loss for the used fibers is 0.2 dB or

$$L_{\text{i,fiber1/2}} = 10^{\frac{-0.2}{10}}. \tag{B.6}$$

  - $L_{\text{att,fiber1}}(\lambda)$: the length l of the fibers is 1 m or 0.16 m, respectively. The attenuation can be calculated with

$$L_{\text{att,fiber1/2}}(\lambda) = 10^{\frac{-attenuation(\lambda)\cdot l}{10}}. \tag{B.7}$$

    The values of $attenuation(\lambda)$ are shown in figure B.2.
- $T_{\text{window}}(\lambda)$**:** transmission of the feed-through window divided by 100 (compare figure B.2).
- $R(\lambda)$**:** the reflection at the entrance of the gold film is part of every quantum yield measurement. As the quantum yield data used in these calculations was taken of a gold film coated on sapphire, the quantum yield must be adapted to the e-gun setup. Therefore the reflection at the junctions silica-titanium and titanium-gold (in case of the e-gun setup) and air-sapphire and sapphire-gold must be calculated. The reflection of these junctions are shown in figure B.3. The resulting correction factor $R(\lambda)$ caused by the different reflection factors compared to the measured quantum yield data is also shown in figure B.3. The formula used to calculate the correction factor is

$$R(\lambda) = \frac{(1 - R_{\text{SiO}_2-\text{Ti}}) \cdot (1 - R_{\text{Ti-Au}})}{(1 - R_{\text{air-sapphire}}) \cdot (1 - R_{\text{sapphire-Au}})}. \tag{B.8}$$

- $L_{\text{align}}(\lambda)$: this factor combines all losses due to the alignment of the optics. It consists of four different factors $L_{\text{align,lens1}}$, $L_{\text{align,lens2}}(\lambda)$, $L_{\text{align,fiber1}}(\lambda)$ and $L_{\text{align,fiber2}}(\lambda)$. All are described in more detail in the following (compare figure B.1 for all distances and figure B.4 for notations):
  - $L_{\text{align,lens1}}$**:** $L_{\text{align,lens1}}(\lambda)$ describes the losses at the first lens of the setup directly after the light source. As the NA_{ls} of the light source is 0.47 and the distance x_1 is 25.77 mm, the radius r_1^* of the light cone at position of the first lens is
  $$r_1^* = \tan(\vartheta_1) \cdot x_1 = 13.72\,\text{mm}. \tag{B.9}$$
  But the radius r_1 of the lens is only 12.7 mm. Therefore the losses at the first lens are given by
  $$L_{\text{align,lens1}} = \frac{r_1^2}{r_1^{*2}} = 92.6\,\% \tag{B.10}$$
  - $L_{\text{align,lens2}}(\lambda)$**:** the light collimated by the first lens is not perfectly parallel. Therefore, the light cone increases on its way to the second lens. The angle of this widening is
  $$\vartheta_2(\lambda) = \arcsin\left(\frac{r_1}{f_1(\lambda)}\right), \tag{B.11}$$
  where $f_1(\lambda)$ is the wavelength dependent focal length of the lens given in equation (B.1). So the light cone radius at the position of the second lens is
  $$r_2^*(\lambda) = r_1 + \tan(\vartheta_2(\lambda)) \cdot x_2, \tag{B.12}$$
  with $x_2 = 76.81$ mm. The losses at the second lens are calculated by
  $$L_{\text{align,lens2}}(\lambda) = \frac{r_2^2}{r_2^*(\lambda)^2}, \tag{B.13}$$
  where r_1 is the radius of the lens, namely 12.7 mm.
  - $L_{\text{align,fiber1}}(\lambda)$**:** $L_{\text{align,fiber1}}(\lambda)$ describes the losses due to the light injection into the fiber outside of the second containment. As the fiber end was moved out of the back focal point of the second lens on purpose to reduce the electron rate the light path looks like it is shown in the upper part of figure B.4. The losses can be calculated with
  $$L_{\text{align,fiber1}}(\lambda) = \frac{r_3^2}{r_3^*(\lambda)^2}, \tag{B.14}$$
  with $r_3 = 550\,\text{nm}/2$ and
  $$r_3^*(\lambda) = \tan(\varphi(\lambda)) \cdot x_4(\lambda) = \tan\left(\arctan\left(\frac{r_2}{BFD(\lambda)}\right)\right) \cdot (y_1 - BFD(\lambda)). \tag{B.15}$$
  $BFD(\lambda)$ can be calculated with equation (B.2) and $y_1 = 30.89$ mm.
  - $L_{\text{align,fiber2}}(\lambda)$**:** the losses at the fiber in the primary system depend on whether the distance y_2 between the second lens and the fiber end is larger or smaller than $BFD(\lambda)$. Additionally there are two different contributions to the losses: the light spot being to large and the angle of the light spot exceeding the acceptance angle $\vartheta = \arcsin(NA_f)$ of the fiber, with $NA_f = 0.22$. Therefore one has to distinguish between the following cases:
  Case 1: y_2 is larger than $BFD(\lambda)$ (as in the upper part of figure B.4). If r_3^* is

larger than the radius of the fiber ($r_3 = 100\,\mu\text{m}$), the loss due to a too large light cone is given by

$$L_{\text{align,fiber2}}(\lambda) = \frac{r_3^2}{r_3^*(\lambda)^2} = \frac{r_3^2}{\left(\tan(\varphi)\cdot(y_1 - BFD(\lambda))\right)^2}, \tag{B.16}$$

with $\tan(\varphi(\lambda)) = r_2(\lambda)/BFD(\lambda)$, $r_2(\lambda) = \tan(\vartheta)\cdot x_5 + \tan(\arcsin(r_\text{f}/f(\lambda)))\cdot x_4$, $x_5 = 30.79\,\text{mm}$, $r_\text{f} = 275\,\mu\text{m}$, $x_4(\lambda) = y_1 - BFD(\lambda)$ and y_1 is not known exactly but expected to be 21 mm (compare figure B.5). In addition, it must be checked, if the angle $\varphi(\lambda)$ exceeds the acceptance angle ϑ. If this is the case, $L_{\text{align,fiber2}}(\lambda)$ must be multiplied by $r_{\text{acc}}(\lambda)^2/r_3(\lambda)^2$, where $r_{\text{acc}}(\lambda) = x_4(\lambda)\cdot\tan(\vartheta)$ is the acceptance radius of the cone with acceptance angle ϑ.
Case 2: y_2 is equal or smaller than $BFD(\lambda)$ (as in the lower part of figure B.4). Then $L_{\text{align,fiber2}}(\lambda)$ is given by

$$L_{\text{align,fiber2}}(\lambda) = \frac{r_6^2}{r_6^*(\lambda)^2} = \frac{r_6^2}{\left(\tan(\varphi_2(\lambda))\cdot(BFD(\lambda) - y_2)\right)^2}, \tag{B.17}$$

with $r_6 = 100\,\mu\text{m}$, $\tan(\varphi_2(\lambda)) = r_5/BFD(\lambda)$ and $r_5(\lambda) = r_4 + x_6\cdot\tan(\vartheta_5(\lambda)) = r_4 + x_6\cdot\tan(\arcsin(r_\text{f}/f(\lambda)))$. As already mentioned, the value of y_2 is unknown but expected to be 21 mm (see figure B.5). As in the last case, it must be checked if the angle $\varphi_2(\lambda)$ is larger than the acceptance angle of the fiber ϑ. If this is the case, $L_{\text{align,fiber2}}(\lambda)$ must be multiplied by $r_{\text{acc}}(\lambda)^2/r_\varphi(\lambda)^2$, where $r_{\text{acc}} = BFD(\lambda)\cdot\tan(\vartheta)$ and $r_\varphi(\lambda) = BFD(\lambda)\cdot\tan(\varphi_2(\lambda))$.

B.1.4 Probability of electron production and leaving of gold layer

The probability that a produced electron leaves the gold layer is given by

$$P = \int_0^t A(x)\cdot P_{\text{leaving}}(x)dx \cdot P_{\text{quantumyield}}(\lambda), \tag{B.18}$$

where t is the thickness of both the titanium and gold layer taken together, $A(x)$ is the absorption of the light in the titanium and the gold layer, $P_{\text{leaving}}(x)$ is the probability that a produced electron leaves the gold layer and $P_{\text{quantumyield}}(\lambda)$ is the probability to produce an electron. The factors of this formula are discussed in more detail in section 3.2.1.

B.1.5 Results of the calculations and discussion

As already mentioned above the electron rate $\Xi(\lambda)$ can be calculated by using equation (B.3).

The resulting spectra for each filter dependent on the work function of the gold layer is shown in figure B.5. According to the calculations the maximum achievable rate is $3.1\cdot10^5$ electrons s^{-1} with the 232 nm filter and a work function of 3.8 eV. As long as the work function is not exceeding a value of about 4.52 eV the maximum value is always achieved with this filter. At higher work functions the highest possible rates are reached with the 220 nm filter. Generally by comparing the ratio of the calculated rates of the different filters with the ratios of the measured rates one should be able to determine the actual work function of the gold layer. The measured rates and the ratios are listed

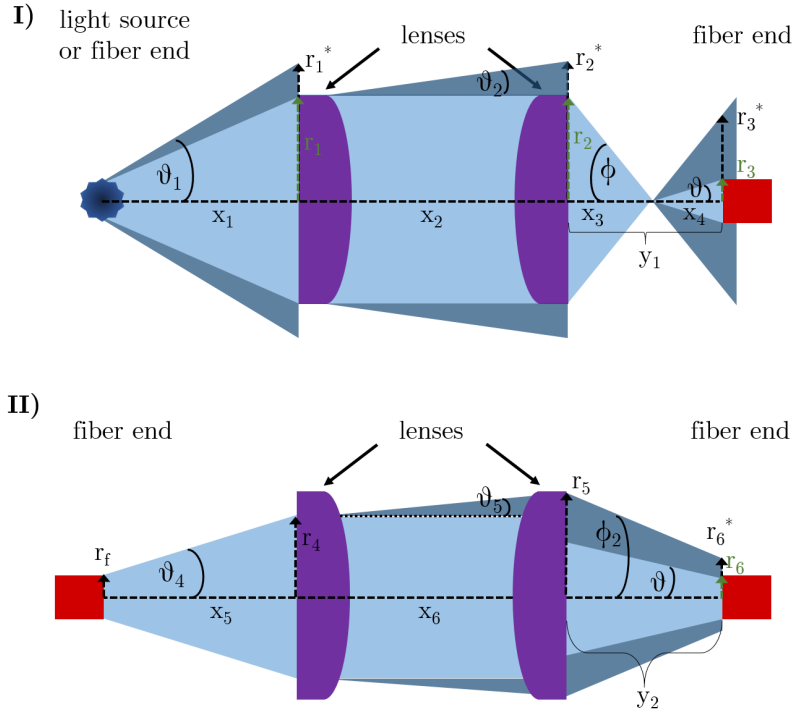

Figure B.4: Sketch to clarify the loss calculations. In the upper scheme (I) the situation of the light injection into the fiber outside of the second containment is shown. The dark blue light cannot be injected into the fiber. If the distance between the lens and the in-vacuum fiber is larger than $BFD(\lambda)$ the sketch also represents the situation at the fiber injection inside of the primary system. If this is not the case, sketch (II) can be used for clarification.

in table B.3. But the measured ratios cannot be made consistent with the calculated ratios. The main reason for that is, that the measured rate of the 220 nm filter is higher than measured rate with the 232 nm filter at 4.2 eV work function. According to the calculations that can only be the case, if the work function is higher than 4.6 eV. But in this case, no electrons should be produced with the 297 nm filter and almost none with the 270 nm filter. For that reason it is expected, that the optical system has lost more transmission due to the UV irradiation at the measurement with the 232 nm filter already. If that is the case the transmission is highly effected by the UV irradiation, indeed. As this degradation is wavelength dependent, it would also explain the different factors between experiment and calculation at each filter.

Nevertheless the rates given by this calculation seems to be in the correct order of magnitude and allow an estimate of the expected electron rate with the final optical system of the e-gun.

B.2 Injection intensity changes due to refractive index changes

Both radiation and UV irradiation are known to densify fused silica and consequently change the refractive index [Nat04, Dev94]. The effect of this change on the acceptance angle and the critical angle for total-reflection Φ_C are calculated in the following.

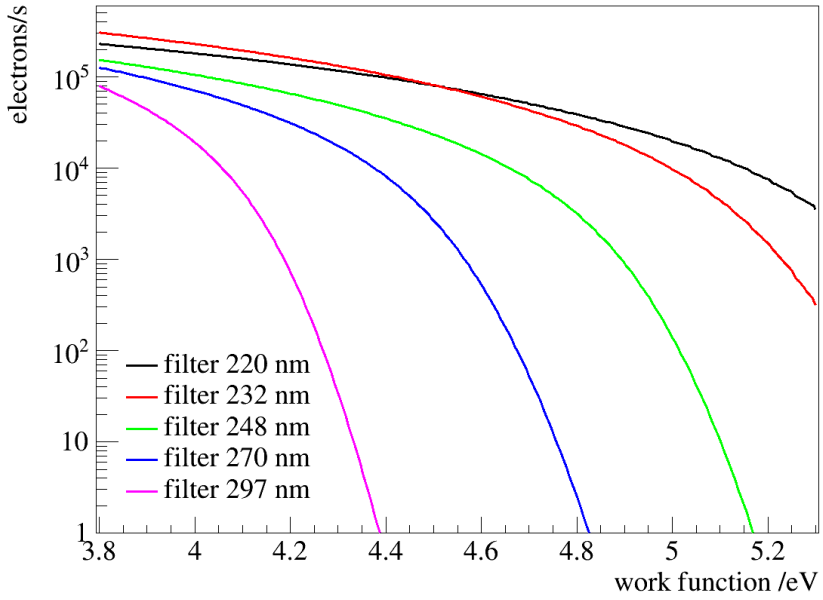

Figure B.5: Electron spectra of the different filters. From top left to bottom the spectra of the filters with 220 nm, 232 nm, 248 nm, 270 nm and 297 nm center wavelength are shown. As expected the rate drops down to $0\,s^{-1}$ if the energy of the photon does not exceed the expected work function.

The the critical angle is [Gha98]

$$\Phi_C = \arcsin\left(\frac{n_2}{n_1}\right) \tag{B.19}$$

and the acceptance angle of a fiber is given by

$$\vartheta_{max} = \arcsin\left(1/n_0 \cdot \sqrt{n_1^2 - n_2^2}\right), \tag{B.20}$$

where n_0 is the refractive index of the material surrounding the fiber, n_1 is the refractive index of the core and n_2 of the cladding. In case of the used fiber at the e-gun the manufacturer gives the following values for the refractive indices for the used fiber:

$$n_1 = 1.458 \text{ and } n_2 = 1.441. \tag{B.21}$$

As the fiber is surrounded by vacuum, n_0 is equal to 1 by definition. With these values the acceptance angle and the critical angle are

$$\Phi_C = 56.6° \tag{B.22}$$

$$\vartheta_{max} = 12.8°. \tag{B.23}$$

By UV irradiation the maximum change in the refractive index is about 10^5 [Nat04] and the change caused by ionizing radiation is 1 %[Dev94]. The change in Φ_C and ϑ_{max} caused by this depends on the fact which refractive index is affected by the irradiation: in case of the UV irradiation the cladding is usually not irradiated which is why a change of the refractive index n_2 is unlikely. In case of the ionizing radiation a change of the cladding is more likely as the electrons do not reach the core. Only at the end of the fiber facing the

Table B.3: Measured electron rates at the e-gun test setup at UCSB. For each filter the electron rates Ξ are listed, both the measured rates with reduced light source power and accordingly estimated maximum rates. In the fourth column the calculated electron rate at a cathode work function of 4.2 eV is given for comparison.

center wavelength of filter /nm	measured electron rate Ξ /s^{-1}	estimated electron rate /s^{-1}	calculated electron rate /s^{-1}
220	36 058	$4.5 \cdot 10^5$	$1.4 \cdot 10^5$
232	29 779	$3.7 \cdot 10^5$	$1.6 \cdot 10^5$
248	9 258	$1.2 \cdot 10^5$	$6.6 \cdot 10^4$
270	1 888	$2.4 \cdot 10^4$	$3.1 \cdot 10^4$
297	423	$5.3 \cdot 10^3$	$7.3 \cdot 10^2$

Table B.4: Summary of the changes on $\vartheta_{\max}$ and Φ_C by irradiation.

	effected refractive indices	change in $\vartheta_{\max}$	change in Φ_C
electron irradiation	n_2	-7.8	0.6
electron irradiation	n_1 and n_2	0.13	-
UV irradiation	n_1	0.004	-0.0004
UV irradiation	n_1 and n_2	0.00005	0.000005

feed through window and if tritium is diffused into the fiber do the electrons have direct contact with the core.

Nevertheless the changes for both scenarios (at the first the refractive index of the cladding and in the second of the cladding and the core is changed) are calculated. The results can be found in table B.4. The UV irradiation and the electron irradiation affecting both indices cause only minor changes in the parameters. In contrast the electron irradiation with an increased n_2 changes $\vartheta_{\max}$ by 5° which is almost a 40 % change.

The losses due to the change in the acceptance angle can be calculated by

$$\mathfrak{L} = \frac{r_f}{r_i} = \frac{\tan(\vartheta_{\max,f}) \cdot f}{\tan(\vartheta_{\max,i}) \cdot f}, \tag{B.24}$$

where r is the radius of the accepted light cone at the last lens of the focusing system, $f = 27.8$ mm is the focal length of the lens if the refraction at the feed-through window is neglected[5], the index i stands for the initial values before irradiation and the index f for those after irradiation. The losses caused by electron irradiation in case of an unchanged n_1 are

$$\mathfrak{L} = 0.85. \tag{B.25}$$

For the three other possibilities no additional losses occur, as the acceptance angle is increased.

[5]Neglecting the feed-through window is possible as it only redirects the light path twice and therefore increases the distance between lens and fiber by about 0.3 mm. The angle of the light cone before and after the window is the same.

Appendix C

Reproducibility of the photoelectron measurements at the monitor spectrometer

To be able to compare different measurements of the photoelectron spectroscopy at the monitor spectrometer, the reproducibility of those measurements must be proven first. Therefore, measurements are performed verifying the reproducibility at the same position over time without moving the mirror in between. In addition it is tested whether the work function results are comparable when the mirror is moved in between two measurements. For these measurement the top position of the unbaked sample 5-SS-ep-3 is used.

Initially the reproducibility of the measurements in short time scales is verified. For this the same position is measured twice with a period of 1 hour in between. Note, that the mirror is not moved during this time. The work function results of the first measurement are

$$\Phi_1 = 4.704 \pm 0.007\,\text{eV} \tag{C.1}$$

and of the second

$$\Phi_2 = 4.711 \pm 0.008\,\text{eV}. \tag{C.2}$$

Both values are equal within the errors. This is also supported by a look at the spectra presented in figure C.1.

To test if the comparability is also achieved over longer time scales, two additional measurements are performed. The time between these measurements is 14 hours. The work function results of these measurements are

$$\Phi_3 = 4.696 \pm 0.006\,\text{eV} \tag{C.3}$$

and

$$\Phi_4 = 4.700 \pm 0.007\,\text{eV}. \tag{C.4}$$

Again, the work function values are equal within the errors. The corresponding spectra presented in C.2 have also the same shape.

As a movement of the mirror can have even larger effects on the results of the measurements, it must be verified if the same position can be reproduced. For that reason the mirror is moved between the first and the second reproducibility tests presented above.

That means that a comparison of Φ_2 and Φ_3 indicates whether the reproducibility is achieved or not (the corresponding spectra are plotted together in C.3 for better comparison). The result is that the change caused by the movement is larger than the errors of the measurements. Nevertheless, the values match within 2σ. Therefore no significant change can be detected and the reproducibility is also proven in case of a mirror movement, as supported by the spectra themselves.

in conclusion, the reproducibility of the photoelectron spectroscopy at the monitor spectrometer is proven.

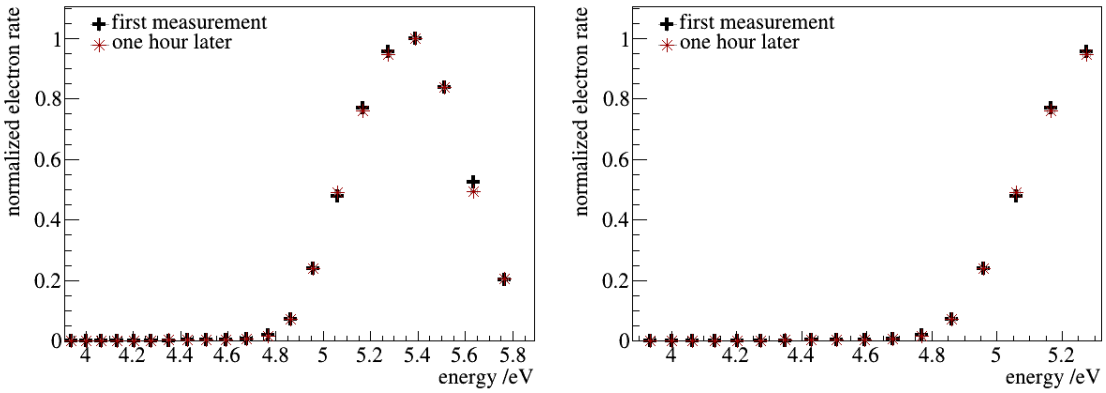

Figure C.1: Comparison of measurements with 1 hours time difference. The mirror is not moved in between the measurements. Left: the complete spectrum of both measurements is plotted. Right: the region of interest for the analysis is shown enlarged.

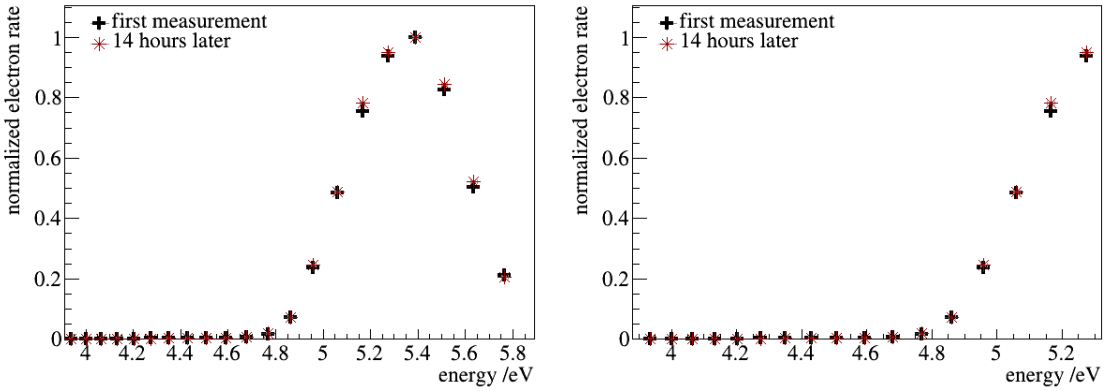

Figure C.2: Comparison of measurements with 14 hours time difference. The mirror is not moved in between the measurements. Left: the complete spectrum of both measurements is plotted. Right: the region of interest for the analysis is shown enlarged.

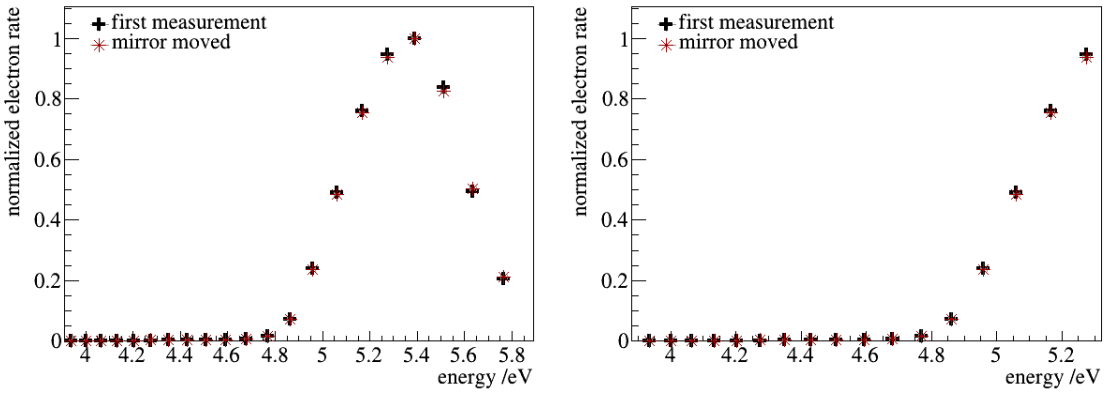

Figure C.3: Comparison of measurements after the movement of the mirror
Left: the complete spectrum of both measurements is plotted. Right: the region of interest for the analysis is shown enlarged.

Appendix D

Commissioning of the UHV Kelvin Probe

In this appendix the commissioning of the UHV Kelvin Probe which is described in section 4.7 is presented. The commissioning includes the tests of individual components: The optical power of the installed discharge lamp (see section D.1) is measured and a good electrical contact between the tip and the sample is insured (compare section D.2). Besides that, the best parameters for the measurements are defined during the commissioning and can be found in section D.3. The influence of the cold cathode on the measurement signal is presented in section D.4 and the long-term stability of the system is presented in section D.5. In the last section of this appendix, D.6, the uncertainties of the measurements based on the commissioning results are discussed.

D.1 Measurement of the optical power of the installed discharge lamp

The discharge lamp is used to simulate the planned UV irradiation at the Rear Wall. By irradiating the Rear Wall with UV light of suitable energy electrons are produced by the photoelectric effect [Ein05]. The emitted electrons can compensate an eventual positive charging of the source.

To test the optical power per area a power meter is used. The optical power per area is not a constant but dependent on the distance to the light source. For that reason a bellow with a length which is approximately equal to the distance between discharge lamp and power meter is used. On one side of the bellow a plate is mounted to which the light source can be fastened. On the other side an equal plate with the power meter is used to close the system. The closing is needed as the light source produces ozone by ionizing the oxygen atoms in the air.

The measurement of the optical power per area is performed at ambient air. After the discharge lamp is switched on the optical power increases. After about 6 minutes the saturation value of $76\,\mu W\,cm^{-2}$ is reached.

As the light source used at the Rear Wall is not yet fully specified and designed a comparison of the measured optical power per area with the expected typical power per area at the Rear Wall is not yet possible.

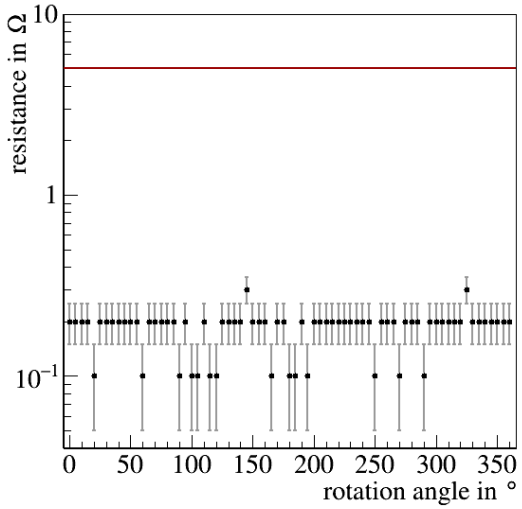

Figure D.1: Resistance between Kelvin Probe tip and sample. The resistance is well below the required value of 5 Ω which is marked by the red line in the diagram.

D.2 Verification of contact quality between tip and sample

The Kelvin Probe method is based on the electrical connection of the sample and the Kelvin Probe tip. In case of the UHV Kelvin Probe this electrical connection is established over the vacuum system: the Kelvin Probe head is connected with the vacuum chamber by its flange. The linear stage, which is made of conductive stainless steel, is mounted on the plate which is welded into the vacuum system. That way the connection remains. But the rotary table poses two problems. On the one side it is insulted against its motor housing. For that reason a Kapton insulated copper wire is used for the connection. On the other side the rotary table could in principle be rotating endlessly. Therefore for safety reasons it is not possible to connect the sample holder directly with the wire. The solution is to use two sliding contacts which are connected to the wire and are sliding over the bottom side of the sample holder. In principle one of these contacts would be enough, but as the connection is of such importance for the measurement a second sliding contact is added for redundancy.

To make sure that the connection at any position of the rotary table is below the maximum defined resistance of 5 Ω[1], this resistance is measured with a common multimeter with a resolution of 0.1 Ω. The rotation angle is changed by $\Delta\varphi$=1° per measurement. The rotary table is turned by 360° over the measurement.

The results of this measurement are plotted in figure D.1. As one can see the resistance between the sample and the tip is far below the 5 Ω requirement. The mean resistance is 183 ±44 mΩ. The resistance must be verified again after each exchange of a sample.

[1]This is not a limit given by the manufacturer, but a limit set by the experimentators.

D.3 The best parameters for measurement with the UHV Kelvin Probe

In order to measure accurately, the best parameters of the Kelvin probe must be found. All parameters must be chosen in a way, that the measurement is as stable as possible. That means, that the deviation of the mean CPD values of several measurements at the same position is minimized.

At the UHV Kelvin Probe there are 4 main parameters which can be chosen:

- The amplitude of the tip vibration
- The frequency of the tip vibration
- The Gradient G during the measurement (which is correlated in a non-trivial way with the distance between tip and sample)
- The backing potential $\pm V_\mathrm{b}$ which is applied between tip and sample during the measurements

For the amplitude 125 is chosen as this is the recommended value provided by the manufacturer. The frequency is set to 165 Hz. This frequency is chosen as it is far enough from a resonance frequency of the coil. The resonance frequencies of the coil are determined by a frequency scan (compare figure D.2 (1)). This frequency scan is performed with the dedicated McAllister software. The other two parameters, G and $\pm V_\mathrm{b}$, must be determined experimentally so that the deviation of the measured CPD values is minimized. The principle dependence of the CPD on these parameters can be found in the diagrams (2) and (3) of figure D.2.

To reduce the effort caused by the search for the best values for the parameters G and $\pm V_\mathrm{b}$ the parameter regions are limited: in case of the Gradient values between -0.05 and -0.1 are tested. Values above these region cause a large distance between tip and sample. The resulting measurement signal is too noisy to measure reliable. In case of even lower gradients the distance between tip and sample gets very small (a precise distance information is not possible due to the non-trivial correlation of G and the distance). But to enable a scan over the surface the sample must be moved below the tip. To make sure that the tip is not scratching over the surface during a scan the gradient is limited to values of -0.1 or above. That means, that the Gradient is limited to

$$-0.05 \geq G \geq -0.1. \tag{D.1}$$

In case of the backing potential the lowest possible value is given by the measured sample: U_b should not be chosen smaller than the CPD value. Otherwise the measurement signal is too noisy to give reliable results: if for example U_b=0.45 V and the CPD value is -0.4 V the signal is almost zero. In addition no values larger than 2 V are tested although the signal is increased with the backing potential. This is the result of the analysis by a fit. If the two points through which the line is fitted are to far away from each other outliers and uncertainties have more of an effect on the fit and therefore on the result of the measurement. Hence the limited parameter range of U_b is:

$$2\,V \geq U_\mathrm{b} \geq 0.5\,V. \tag{D.2}$$

To find the best parameters within these limited parameter ranges, G and U_b are changed with a step width of ΔG=0.005 and ΔU_b=0.05 V. At every possible combination within

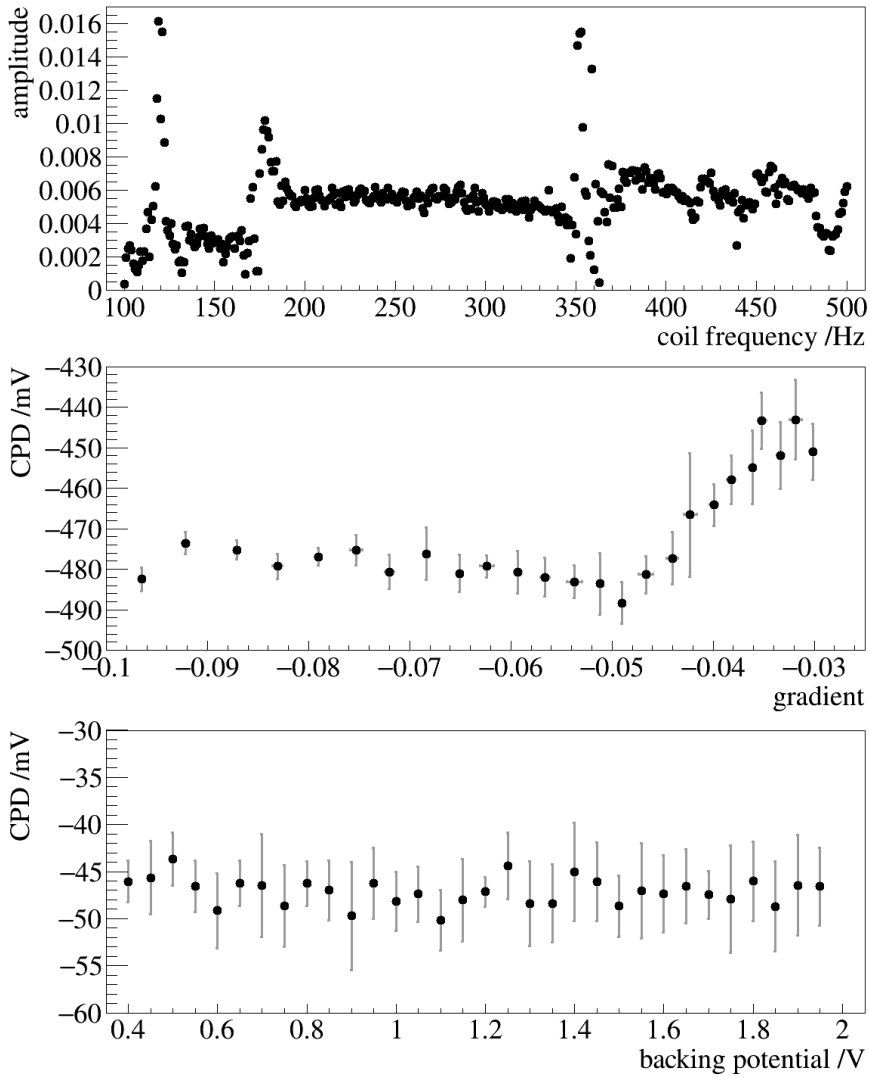

Figure D.2: Frequency scan and dependence of CPD on G and $\pm V_\mathrm{b}$. (1) a frequency scan of the coil in the Kelvin Probe head is shown. The unit of the amplitude is not given by the manufacturer. (2) The CPD value measured with $V_\mathrm{b} = 1\,\mathrm{V}$ is measured for different G values. At each position 10 measurements are performed. From these the mean gradient and the mean CPD are calculated. The change in the CPD value due to a change in G is clearly visible. At gradients of about -0.03 (which is far away from the sample) the CPD values are larger than at lower gradients (which means a smaller distance between tip and sample). A minimum in the CPD value is reached around $G = $ -0.05. At even lower gradients the effect on the CPD due to a change in G is reduced. (3) The diagram visualizes the dependence of the CPD on the backing potential $\pm V_\mathrm{b}$. All measurements are performed at $G = $ -0.07. At each potential 10 measurements are performed. No dependence of the CPD on $\pm V_\mathrm{b}$ can be found. The errors vary between 1.5 mV and more than 5 mV.

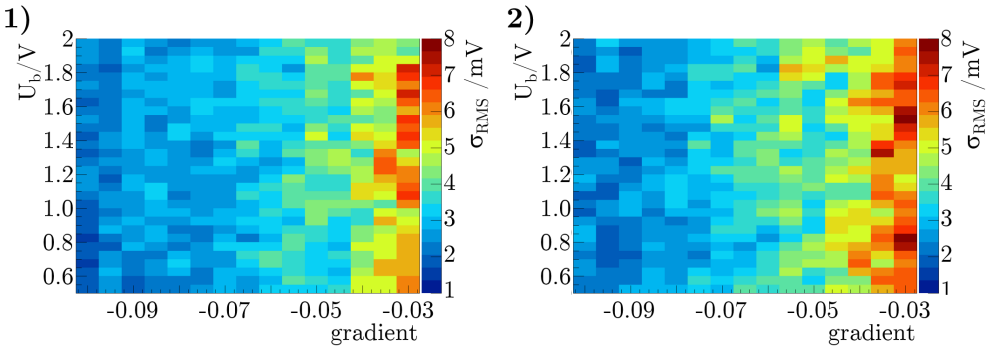

Figure D.3: Results of the best parameter search at UHV Kelvin Probe. In both parts of the figure σ_{RMS} is plotted by color in a diagram with the backing potential on the y-axis and the Gradient on the x-axis. (1) Here the diagram of the best parameter search at the central position of sample 6-SS-ep-3 at ambient air is shown. (2) These are the results of a measurement performed not at the center of the same sample in vacuum. Both the backing and the turbo pump are running during the measurement.

the parameter ranges 20 CPD measurements are performed. The required σ_{RMS} is calculated out of these measurements. To make sure that the parameters do not change if the conditions of the measurement change, these measurements are performed at several conditions: at ambient air, at vacuum both with pumps running and without and at different positions of the sample.

Two exemplary diagrams resulting from these measurements are presented in figure D.3. In both cases the highest detected σ_{RMS} is below 8 mV. The highest values are obtained at high gradients above -0.05. For gradients below -0.07 σ_{RMS} is equal or smaller than 4 mV. A dependence on the backing potential is not detectable.

Although the smallest σ_{RMS} values are obtained at the smallest gradient (smallest distances between tip and sample) the standard for measurements with the UHV Kelvin Probe is set to

$$G = -0.07 \tag{D.3}$$

and

$$U_{\mathrm{b}} = 1\,V. \tag{D.4}$$

By increasing the distance between the tip and the sample the risk that the tip could scratch over the surface during a scan is taken into account. With only a few exceptions these parameter values are used for all measurements presented in section 4.7 and all following measurements discussed in this appendix.

D.4 The influence of the cold cathode on the measurement signal

During the first long-term measurements performed with the UHV Kelvin Probe a behavior of the measured values as shown in figure D.4 is observed: the CPD value increases by more than 100 mV within the measurement time of about 1.5 days. The shape of the increase is in the beginning similar to an exponential increase. After about 5 000 measurement points this increase is slowed down but still steady.

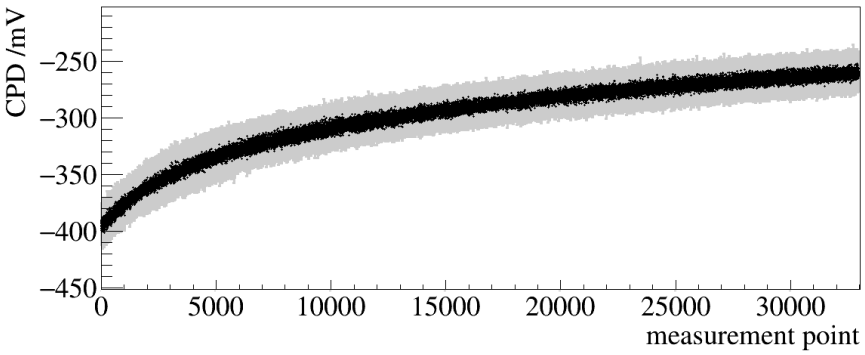

Figure D.4: Long-term measurement performed with the UHV Kelvin Probe with cold cathode running. The measurement is performed at a pressure of $2{\cdot}10^{-5}$ mbar. Both the backing and the turbo pumps are running during the measurement. The duration of the measurement is about 1.5 days.

After the exclusion of almost any other possible reason for the behavior of the CPD with time, the cold cathode, which is installed at the vacuum chamber, is found as the cause: ions produced by the cathode disturb the measurement with the UHV Kelvin Probe. If the cold cathode is not sparked the signal shows no indications for the described behavior.

For that reason it is decided, that the cold cathode is turned off for any measurement with the UHV Kelvin Probe. In addition the direct line of sight between potentially produced ions in the cathode and the sample is disrupted by the installation of a corner piece between vacuum chamber and pressure sensor. A long-term measurement performed after this improvement of the setup is described in the following section.

D.5 Long-term stability of the UHV Kelvin Probe measurements

To determine the statistical fluctuation of the measurement signal and possible systematic drifts long-term measurements are performed. To also simulate the position change of the sample during a scan these measurements are done at 2 different positions. At each of these positions 5 measurements are performed before the sample is moved to another position. To improve the stability of the measurement it is performed at elevated temperatures of about 45 °C. In doing so the temperature of the Kelvin Probe is decoupled from the temperature of the laboratory.

The longest of these long-term measurements is presented in figure D.5. The duration of the measurement is 69 hours. The system is pumped. The pumping started more than one week prior to the measurement.

The CPD signal shows a slight decrease with increasing measurement point numbers. This decrease can be fitted by a line, resulting in the fit functions:

$$\begin{aligned} f_1(x) &= (-423.2 \pm 0.4)\,\mathrm{mV} + (-9.9 \pm 0.7) \cdot 10^{-4}\,\mathrm{mV} \cdot x \\ f_2(x) &= (-420.4 \pm 0.4)\,\mathrm{mV} + (-6.5 \pm 0.6) \cdot 10^{-4}\,\mathrm{mV} \cdot x \end{aligned} \tag{D.5}$$

That means that the mean drift per measurement point is

$$(8.1 \pm 2.4) \cdot 10^{-4}\,\mathrm{mV}. \tag{D.6}$$

With this value the expected drift during the scan of a Rear Wall can be calculated: during a Rear Wall scan with 5.5 mm inner diameter and 62.5 mm outer diameter the CPD value is determined at 2 079 measurement positions. To compensate for outliers each of these positions is measured 5 times. So each scan consists of 10 395 measurement points. The expected drift is:

$$\sigma_{\text{drift}} = (8.4 \pm 2.5)\,\text{mV}. \tag{D.7}$$

In addition it is possible to determine the statistical uncertainty of a measurement by the data given in figure D.5:

$$\begin{aligned} \sigma_{\text{RMS},1} &= 5.3\,\text{mV} \\ \sigma_{\text{RMS},2} &= 4.9\,\text{mV} \\ \rightarrow\ \overline{\sigma}_{\text{RMS}} &= (5.1 \pm 0.3)\text{mV} \end{aligned}$$

This values of $\overline{\sigma}_{\text{RMS}}$ is consistent with the errors measured for the used measurement parameters during the best parameter search.

The overall measurement uncertainty of the UHV Kelvin Probe is calculated in the following section based on the results presented in this section.

D.6 Discussion on the uncertainties of the UHV Kelvin Probe measurements

As described in detail in the beginning of section 4.7 the uncertainty of the Kelvin Probe measurements is given by

$$\sigma_{\text{tot}} = \sqrt{\sigma^2_{\text{RMS,surface/pixel}} + \sigma^2_{\text{exp}}}, \tag{D.8}$$

where $\sigma_{\text{RMS,surface/pixel}}$ is the work function fluctuation over the surface of the sample and σ_{exp} are the measurement uncertainties of the Kelvin Probe setup. The latter consists of both the systematic and the statistic uncertainties of the Kelvin Probe measurements:

$$\sigma_{\text{exp}} = \sqrt{\sigma^2_{\text{sys}} + \sigma^2_{\text{stat}}}. \tag{D.9}$$

With the values

$$\sigma_{\text{stat}} = \overline{\sigma}_{\text{RMS}} = 5.1\,\text{mV} \tag{D.10}$$

and

$$\sigma_{\text{sys}} = \sigma_{\text{drift}} = (8.4 \pm 2.5)\,\text{mV}. \tag{D.11}$$

which are given in the last section the uncertainty of the Kelvin Probe can be calculated:

$$\sigma_{\text{exp}} = 9.8 \pm 2.3\,\text{mV}. \tag{D.12}$$

That means that the requirement of an uncertainty is achieved with the UHV Kelvin Probe setup.

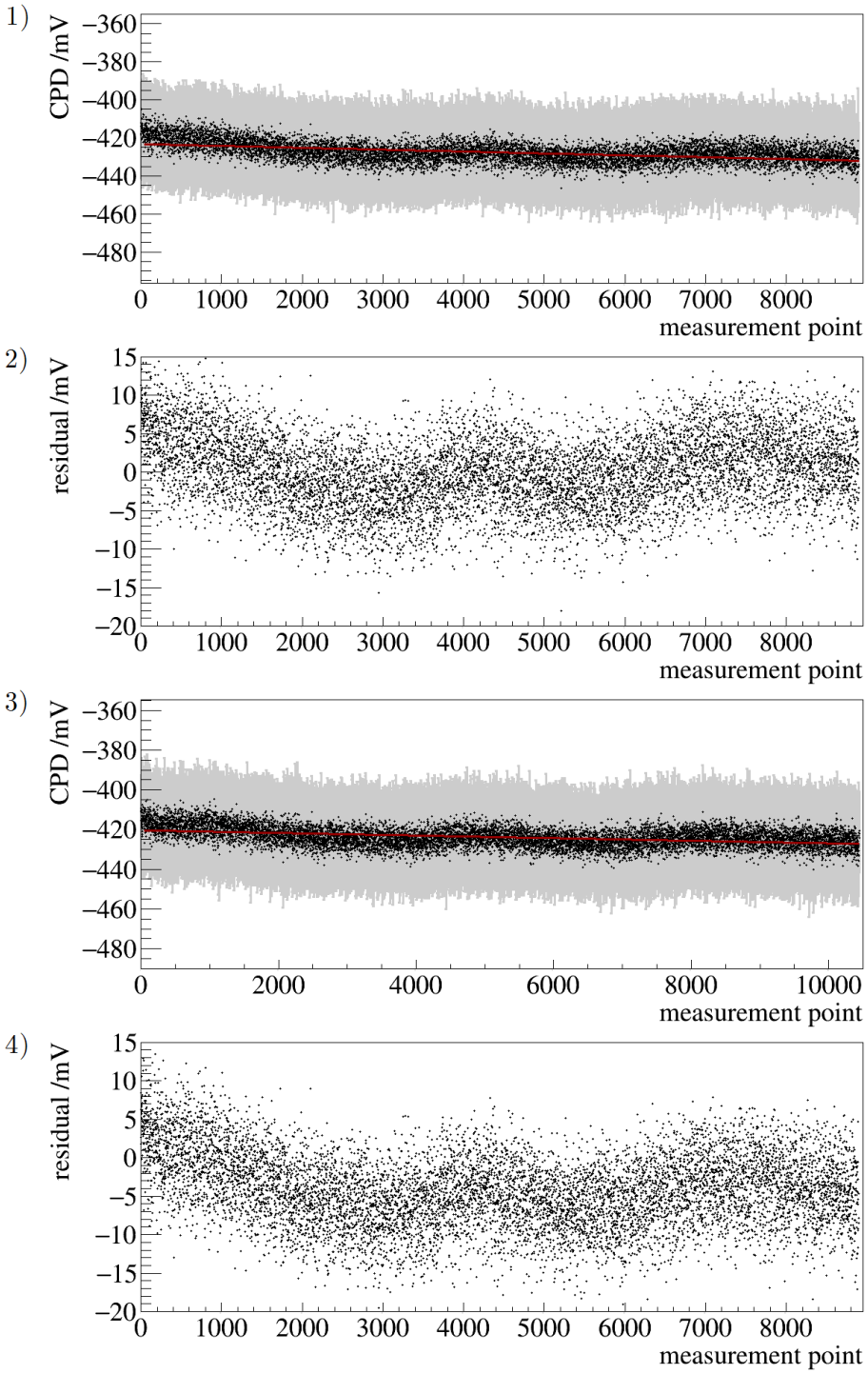

Figure D.5: Long-term stability of the UHV Kelvin Probe. In (1) and (3) the measured CPD values are plotted against the measurement point number. The red lines are the fits performed on the data. The mean CPD values are (-427.5±5.3) mV or (-423.8±4.9) mV, respectively. the difference in the number of measurement points is caused by faults in the positioning file, which defines the measurement positions. This causes some of the measurement positions to be measured not only 5 but 6 times. In (2) and (4) the corresponding residuals are plotted. These are arranged around 0, which means that the linear fit assumption suitably describes the behavior of the data.

Appendix E

Additional information on Rear Wall related experiments

This appendix present additional data of the experiments described in chapter 4. This data is not necessary to get a result of the experiment but it supports the conclusions drawn in the given chapter.

E.1 Additional data taken by the ambient air Kelvin Probe

In this section the CPD maps of all measurements performed with the ambient air Kelvin Probe are presented. In addition the corresponding histograms to the CPD maps are given. The ranges of both the CPD maps and the histograms are optimized for the respective measurement. This must be considered by the comparison of different measurements.

Goldsheet

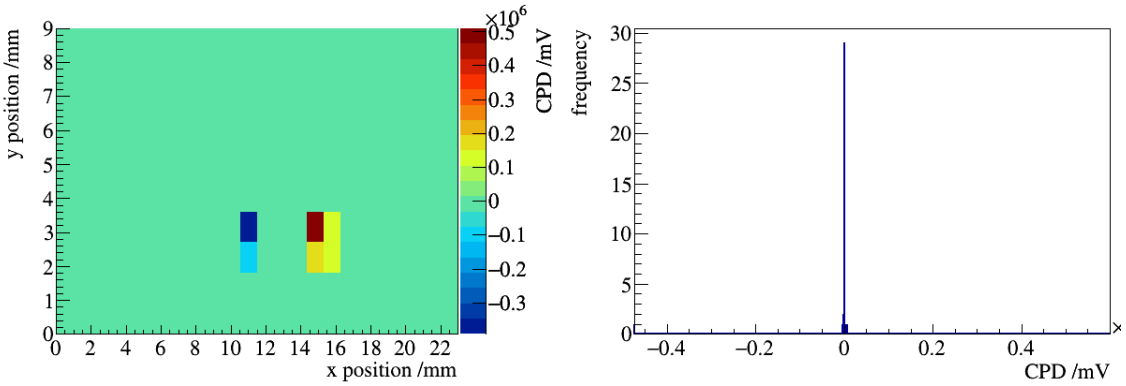

Figure E.1: CPD map and histogram of the 1. measurement of the goldsheet. The date of the measurement is the 27.05.2013. The mean CPD value of this scan is $(573.2 \pm 49\,508.0)$ mV.

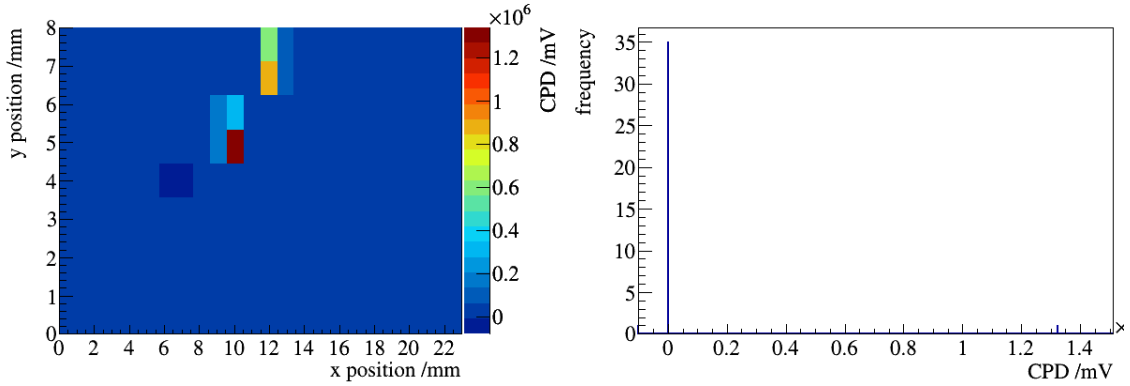

Figure E.2: CPD map and histogram of the 2. measurement of the goldsheet. The date of the measurement is the 27.05.2013. The position and the scan area is not changed between this and the first measurement. The mean CPD value of this scan is $(12\,717.4 \pm 136\,875.0)$ mV.

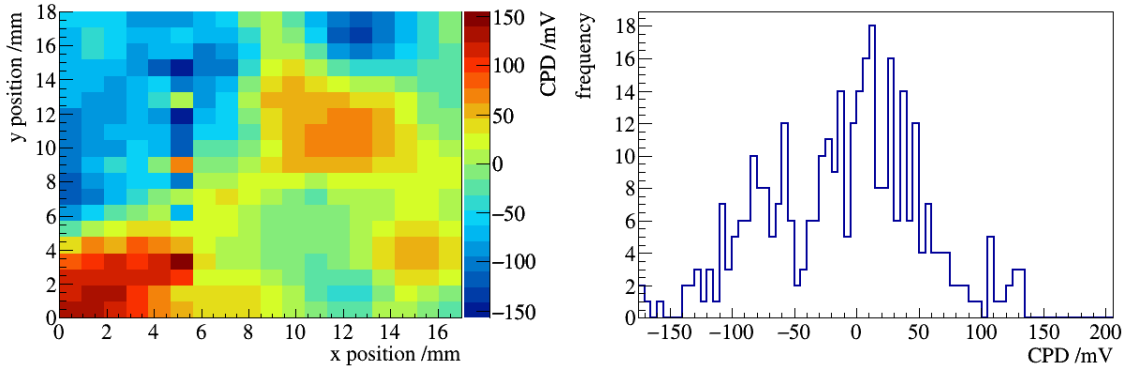

Figure E.3: CPD map and histogram of the 3. measurement of the goldsheet. The date of the measurement is the 29.05.2013. The mean CPD value of this scan is (-9.8 ± 62.7) mV.

Cu mirror

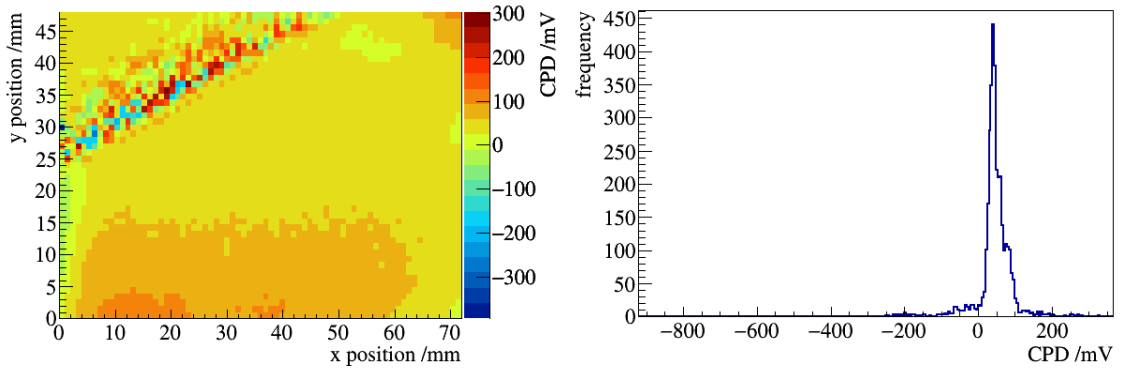

Figure E.4: CPD map and histogram of the measurement of the gold coated Cu mirror. The date of the measurement is the 27.05.2013. The mean CPD value of this scan is (45.2 ± 54.1) mV.

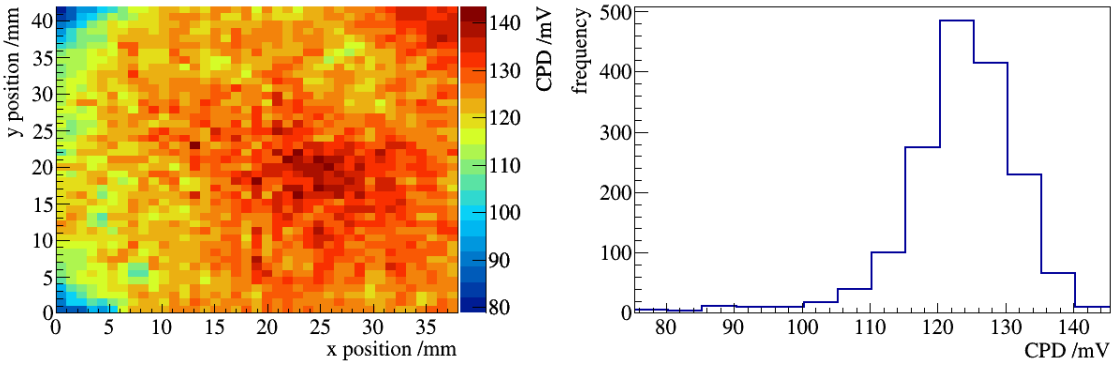

Figure E.5: CPD map and histogram of the measurement of the uncoated copper mirror. The date of the measurement is the 15.08.2013. The mean CPD value of this scan is (123.4 ± 8.7) mV.

Sapphire-5

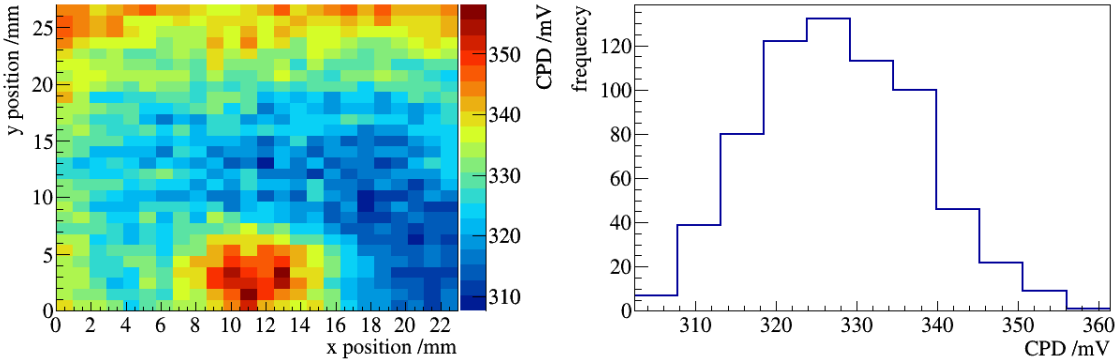

Figure E.6: CPD map and histogram of the 1. measurement of sample Sapphire-5. The date of the measurement is the 13.08.2013. The mean CPD value of this scan is (327.8 ± 10.2) mV.

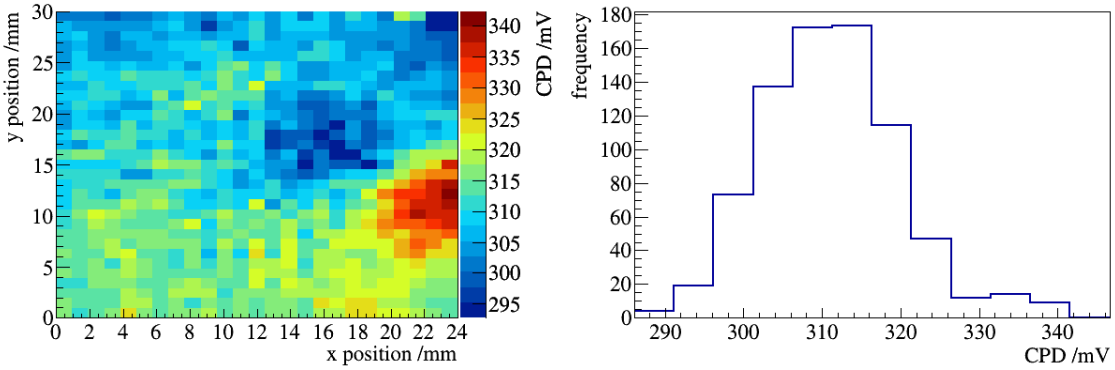

Figure E.7: CPD map and histogram of the 2. measurement of sample Sapphire-5. The date of the measurement is the 29.08.2013. The mean CPD value of this scan is (311.1 ± 8.8) mV.

Sapphire-6

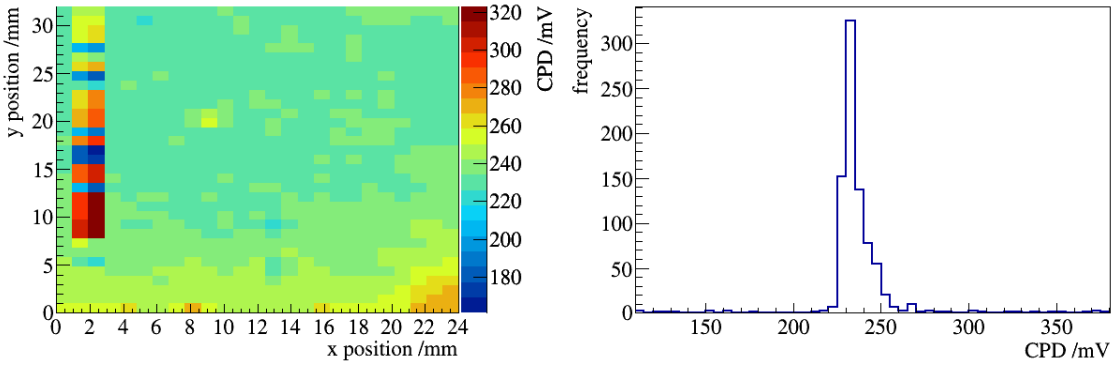

Figure E.8: CPD map and histogram of the 1. measurement of sample Sapphire-6. The date of the measurement is the 28.05.2013. The mean CPD value of this scan is (205.3 ± 46.1) mV.

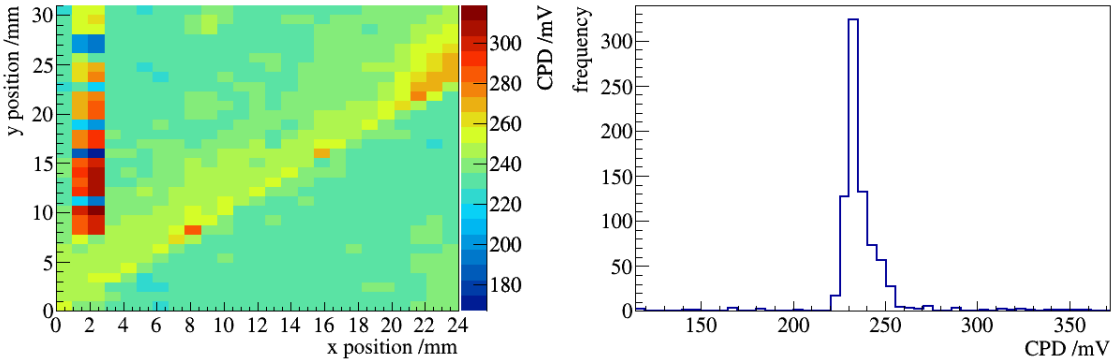

Figure E.9: CPD map and histogram of the 2. measurement of sample Sapphire-6. The date of the measurement is the 28.05.2013. The position and the scan area is not changed between this and the first measurement. The mean CPD value of this scan is (237.0 ± 17.8) mV.

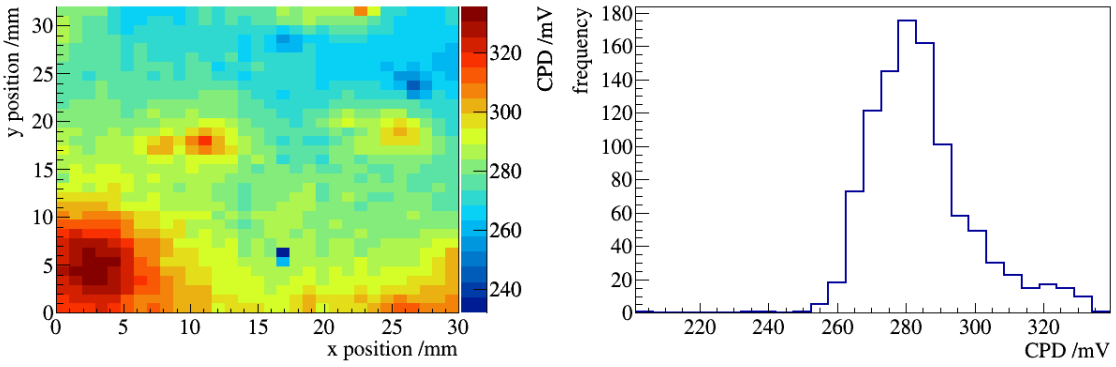

Figure E.10: CPD map and histogram of the 3. measurement of sample Sapphire-6. The date of the measurement is the 17.07.2013. The mean CPD value of this scan is (284.3 ± 15.3) mV.

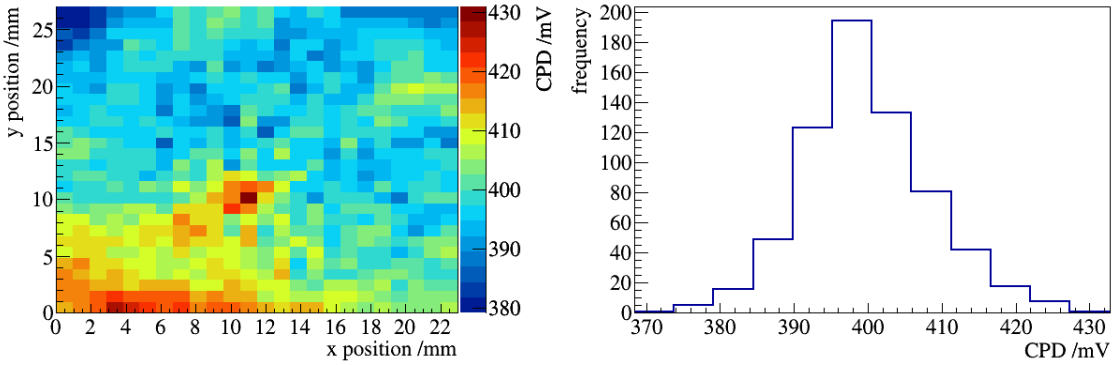

Figure E.11: CPD map and histogram of the 4. measurement of sample Sapphire-6. The date of the measurement is the 16.08.2013. The mean CPD value of this scan is (399.9 ± 8.9) mV.

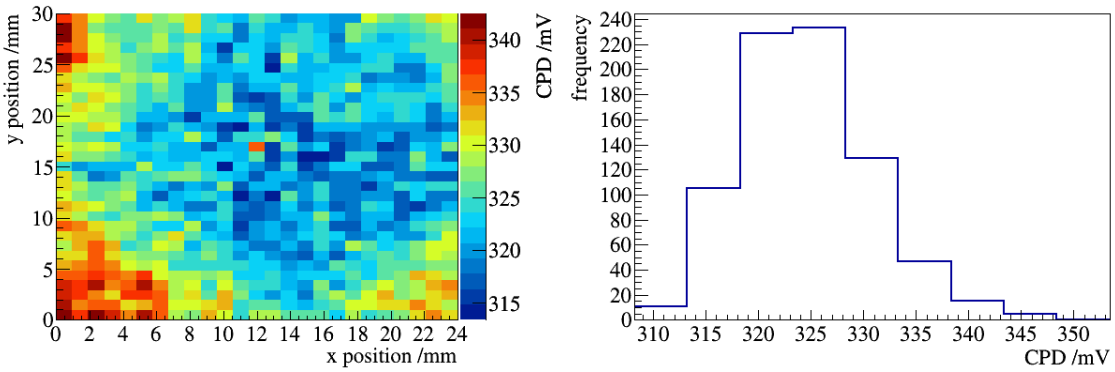

Figure E.12: CPD map and histogram of the 5. measurement of sample Sapphire-6. The date of the measurement is the 29.08.2013. The mean CPD value of this scan is (324.6 ± 6.2) mV.

SiO_2-3

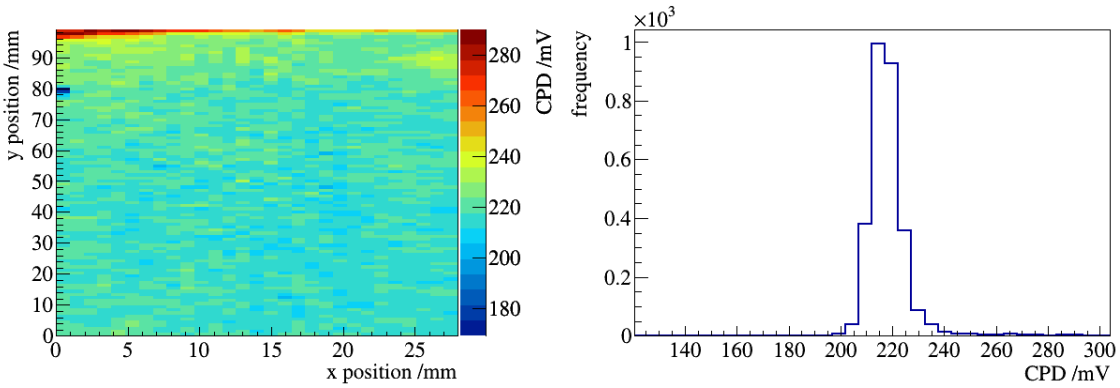

Figure E.13: CPD map and histogram of the 1. measurement of sample SiO_2-3. The date of the measurement is the 21.08.2013. The mean CPD value of this scan is (218.3 ± 9.2) mV.

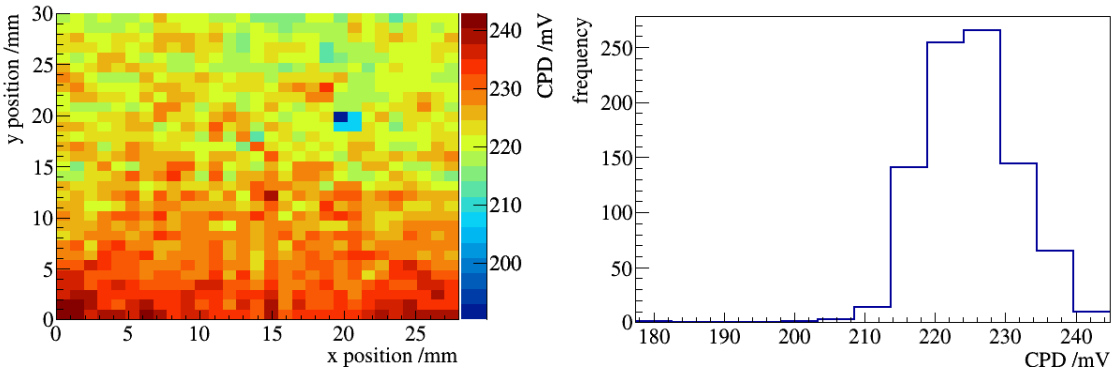

Figure E.14: CPD map and histogram of the 2. measurement of sample SiO_2-3. The date of the measurement is the 21.08.2013. The measurement is performed directly after the first measurement but at a different position of the sample. The mean CPD value of this scan is (224.9 ± 6.7) mV.

SiO_2-4

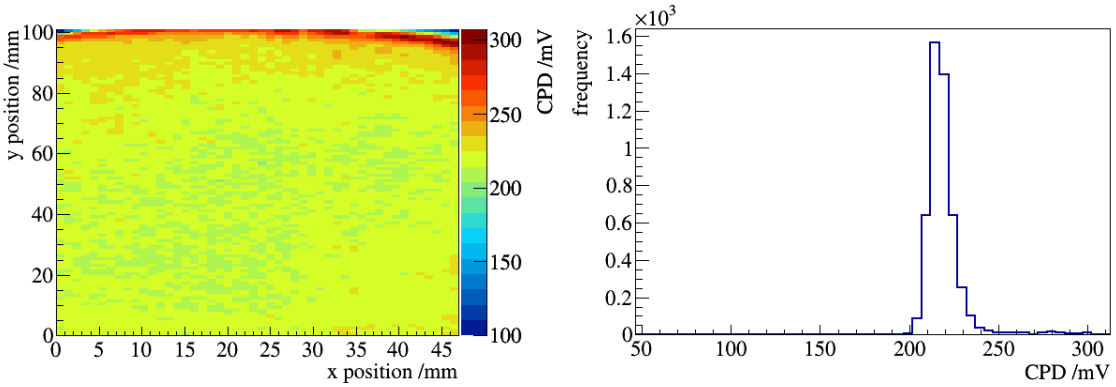

Figure E.15: CPD map and histogram of the 1. measurement of sample SiO_2-4. The date of the measurement is the 22.08.2013. The mean CPD value of this scan is (219.0 ± 12.9) mV.

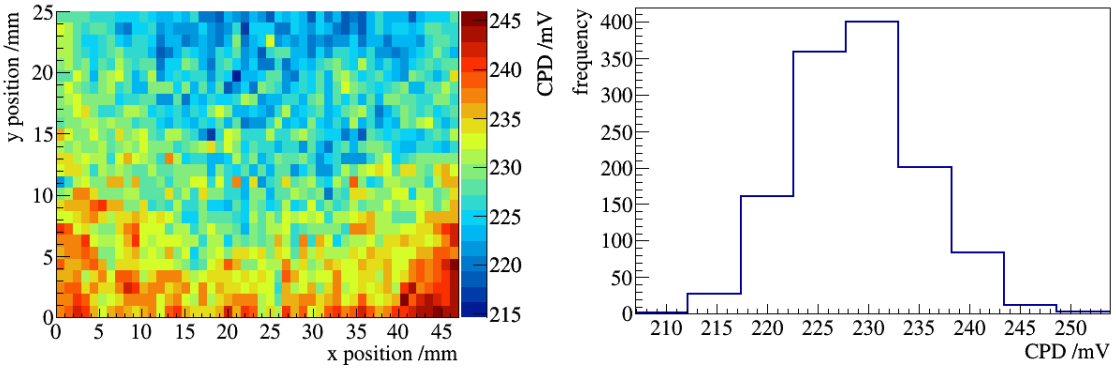

Figure E.16: CPD map and histogram of the 2. measurement of sample SiO_2-4. The date of the measurement is the 22.08.2013. The measurement is performed directly after the first measurement but at a different position of the sample. The mean CPD value of this scan is (228.9 ± 6.3) mV.

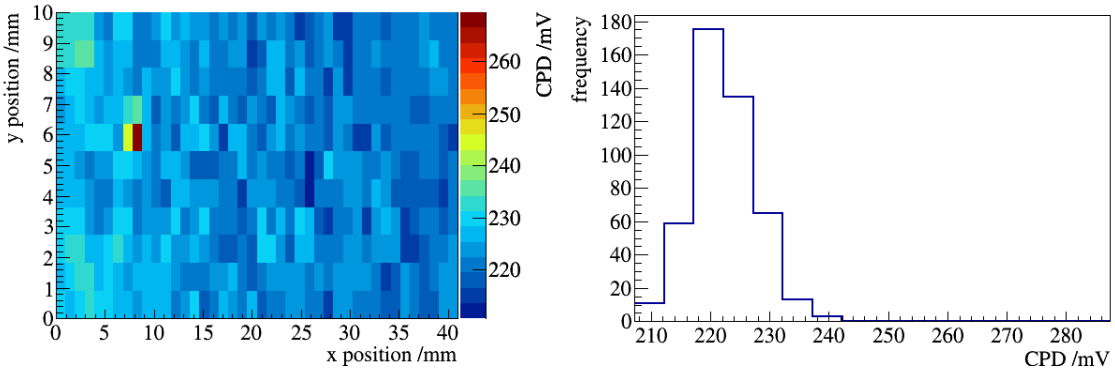

Figure E.17: CPD map and histogram of the 3. measurement of sample SiO_2-4. The date of the measurement is the 22.08.2013. The measurement is performed directly after the first measurement but at a different position of the sample. The mean CPD value of this scan is (222.5 ± 6.1) mV.

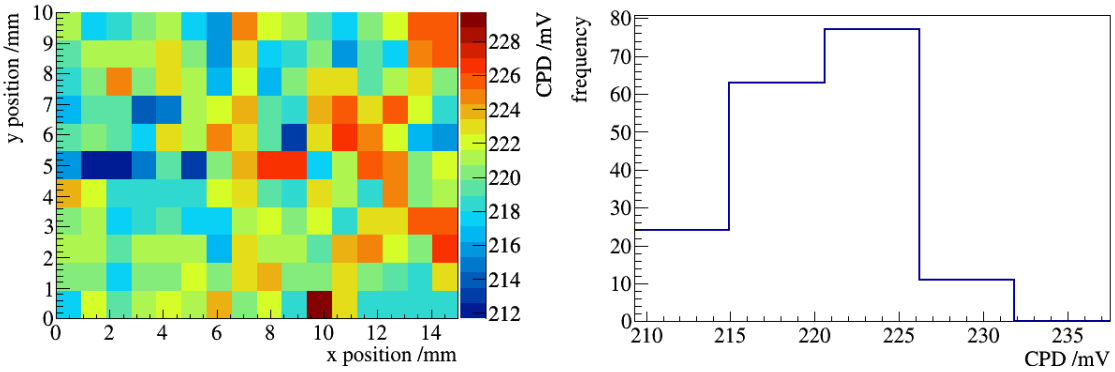

Figure E.18: CPD map and histogram of the 4. measurement of sample SiO_2-4. The date of the measurement is the 22.08.2013. The measurement is performed directly after the first measurement but at a different position of the sample. The mean CPD value of this scan is (220.1 ± 4.5) mV.

SiO_2-5

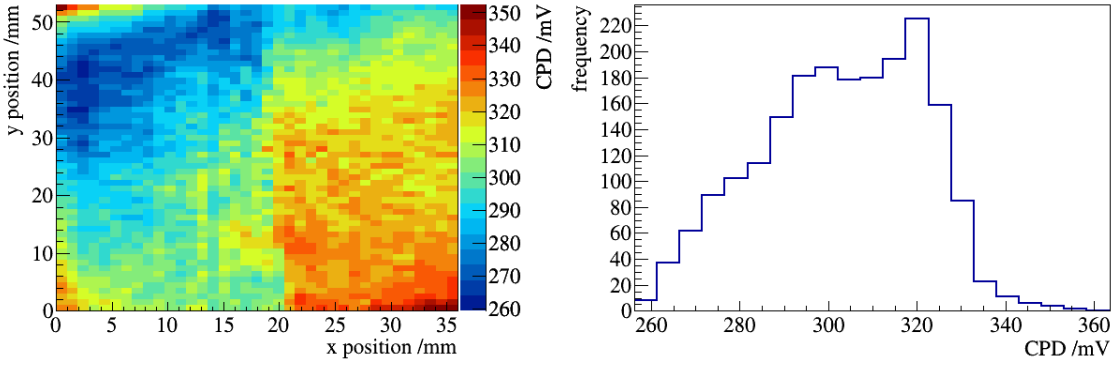

Figure E.19: CPD map and histogram of the 1. measurement of sample SiO_2-5. The date of the measurement is the 16.08.2013. The mean CPD value of this scan is (303.1 ± 18.3) mV.

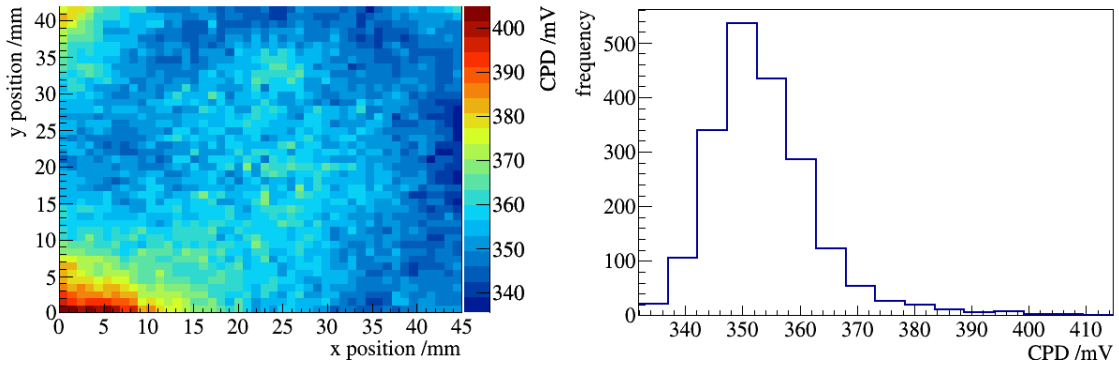

Figure E.20: CPD map and histogram of the 2. measurement of sample SiO_2-5. The date of the measurement is the 27.08.2013. The mean CPD value of this scan is (353.9 ± 9.8) mV.

SiO_2-6

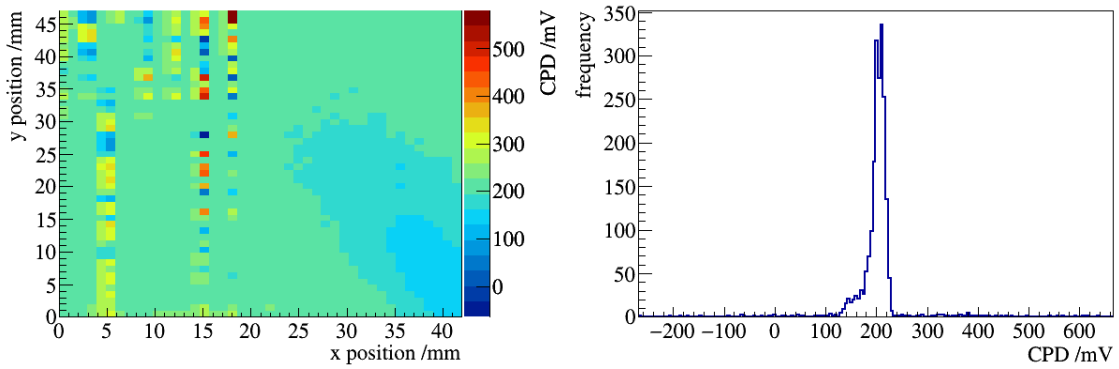

Figure E.21: CPD map and histogram of the 1. measurement of sample SiO_2-6. The date of the measurement is the 28.05.2013. The mean CPD value of this scan is (202.8 ± 51.5) mV.

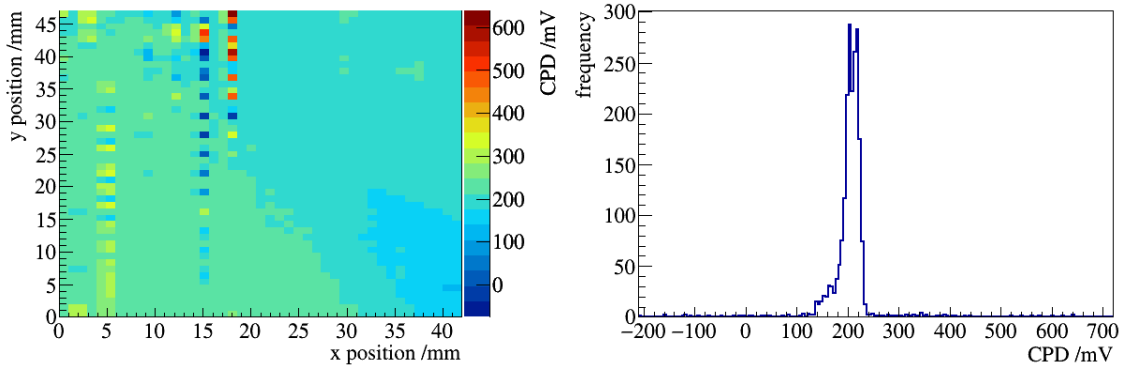

Figure E.22: CPD map and histogram of the 2. measurement of sample SiO_2-6. The date of the measurement is the 28.05.2013. The position and the scan area is not changed between this and the first measurement. The mean CPD value of this scan is (236.6 ± 19.6) mV.

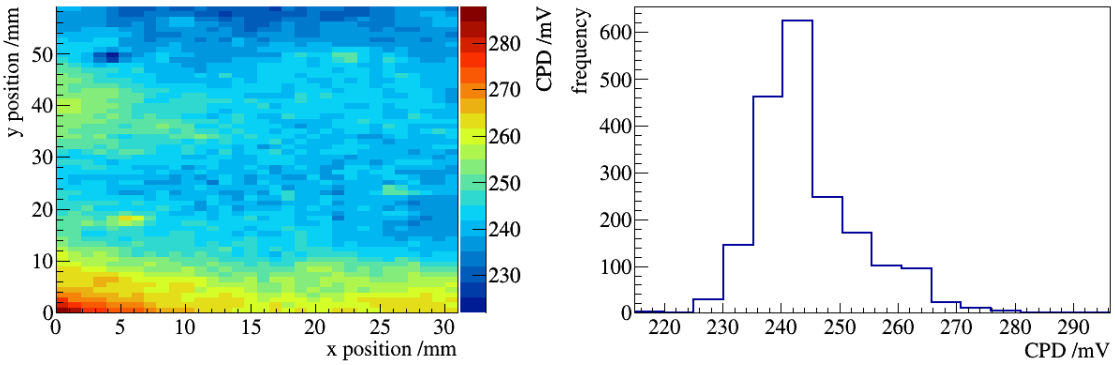

Figure E.23: CPD map and histogram of the 3. measurement of sample SiO_2-6. The date of the measurement is the 18.07.2013. The mean CPD value of this scan is (244.6 ± 8.8) mV.

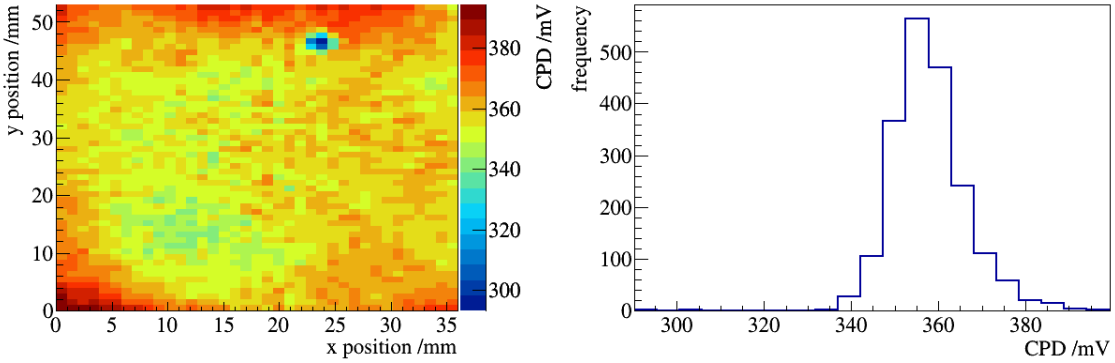

Figure E.24: CPD map and histogram of the 4. measurement of sample SiO_2-6. The date of the measurement is the 16.08.2013. The mean CPD value of this scan is (357.9 ± 8.9) mV.

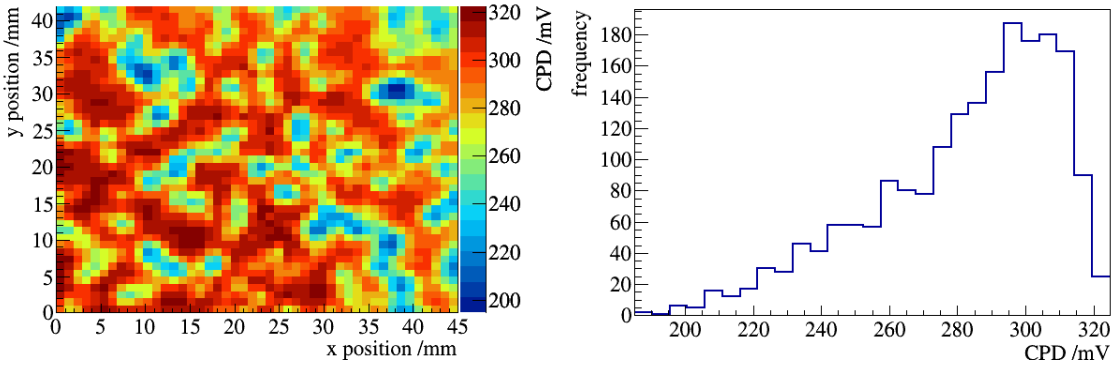

Figure E.25: CPD map and histogram of the 5. measurement of sample SiO_2-6. The date of the measurement is the 27.08.2013, which is after the bake-out of this sample. The mean CPD value of this scan is (281.9 ± 27.2) mV.

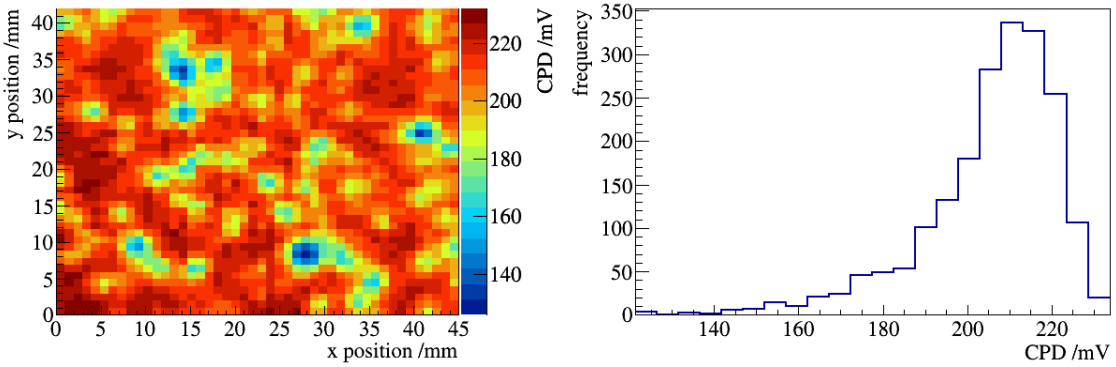

Figure E.26: CPD map and histogram of the 6. measurement of sample SiO_2-6. The date of the measurement is the 29.08.2013, which is after the bake-out of this sample. The mean CPD value of this scan is (205.5 ± 16.1) mV.

1-Al-ep-3

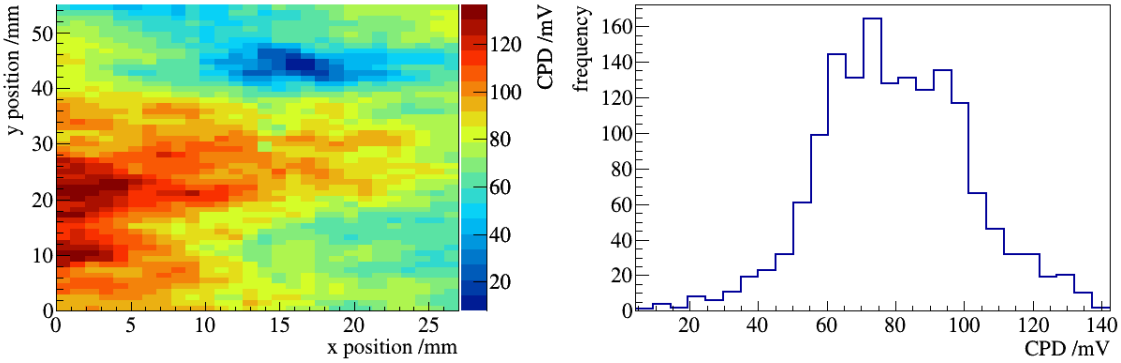

Figure E.27: CPD map and histogram of the 1. measurement of sample 1-Al-ep-3. The date of the measurement is the 29.05.2013. The sample is not coated at the time of the measurement. The mean CPD value of this scan is (79.8 ± 21.6) mV.

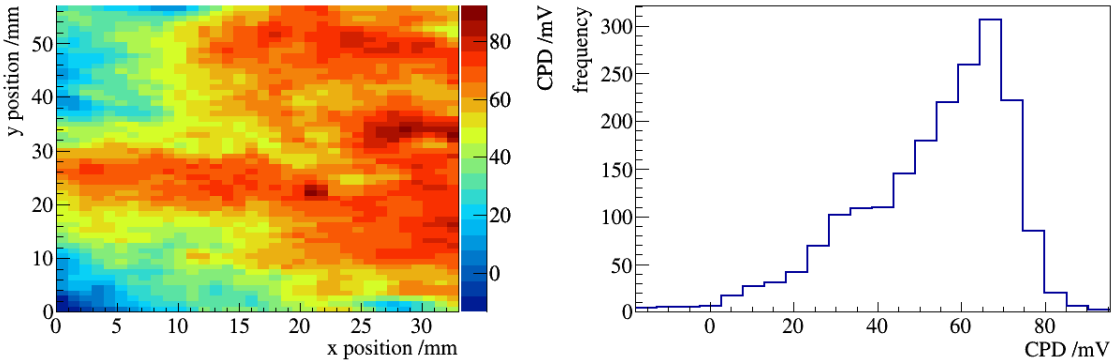

Figure E.28: CPD map and histogram of the 2. measurement of sample 1-Al-ep-3. The date of the measurement is the 19.07.2013. The mean CPD value of this scan is (53.3 ± 18.1) mV.

4-Al-ep-3

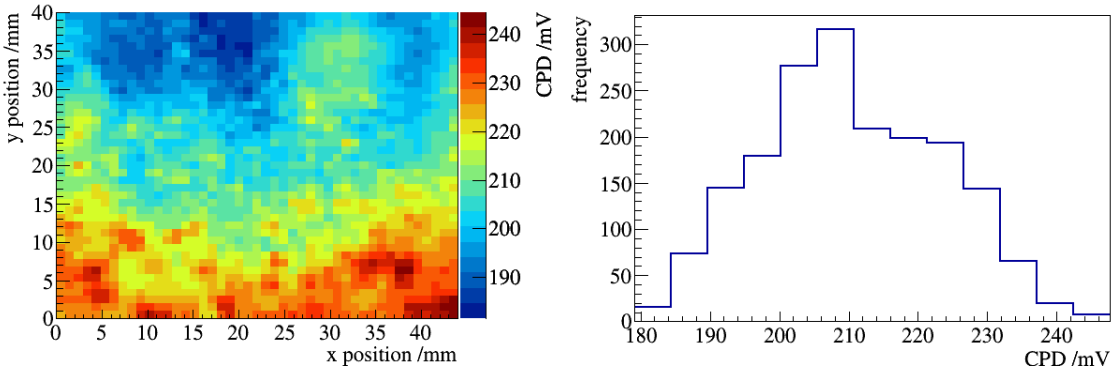

Figure E.29: CPD map and histogram of the 1. measurement of sample 4-Al-ep-3. The date of the measurement is the 16.07.2013. The mean CPD value of this scan is (210.4 ± 13.0) mV.

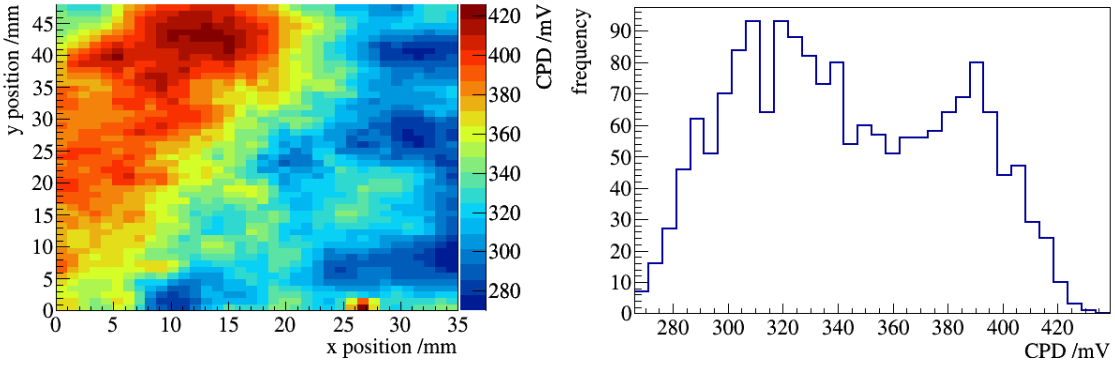

Figure E.30: CPD map and histogram of the 2. measurement of sample 4-Al-ep-3. The date of the measurement is the 15.08.2013. The mean CPD value of this scan is (343.4 ± 38.6) mV.

2-Al-mp-3

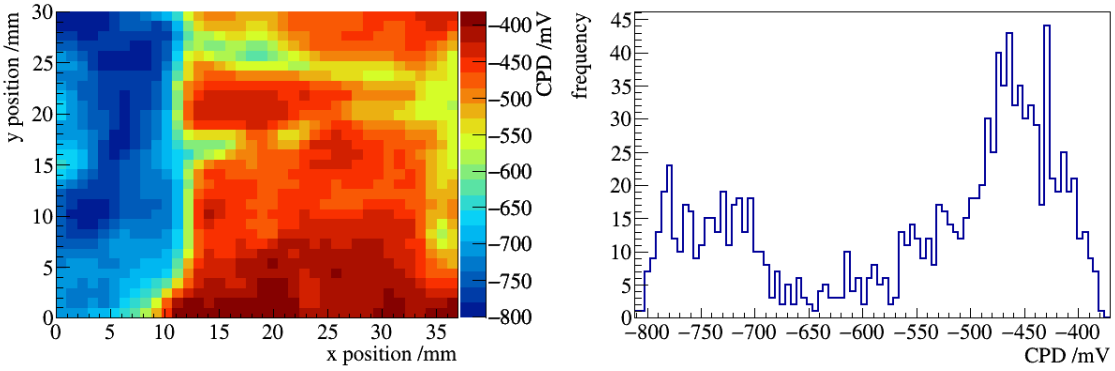

Figure E.31: CPD map and histogram of the 1. measurement of sample 2-Al-mp-3. The date of the measurement is the 28.05.2013. The sample is not coated at the time of the measurement. The mean CPD value of this scan is (-554.3 ± 129.7) mV.

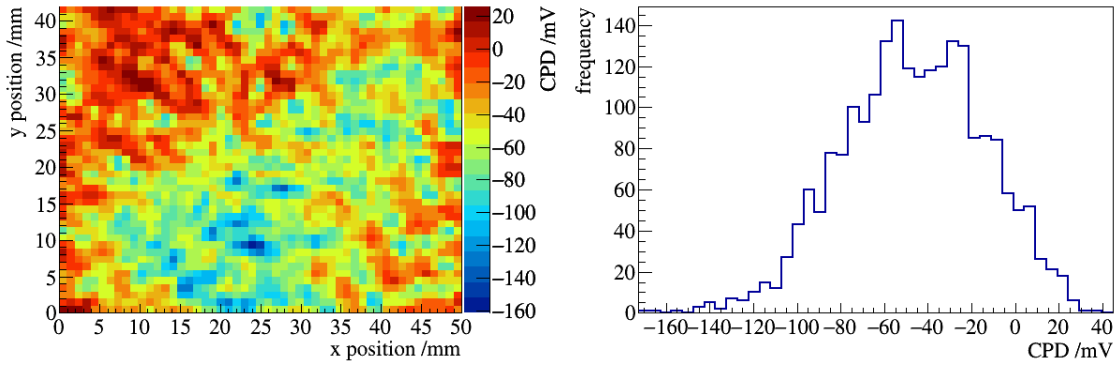

Figure E.32: CPD map and histogram of the 2. measurement of sample 2-Al-mp-3. The date of the measurement is the 19.07.2013. The mean CPD value of this scan is (-46.5 ± 32.4) mV.

3-Al-mp-3

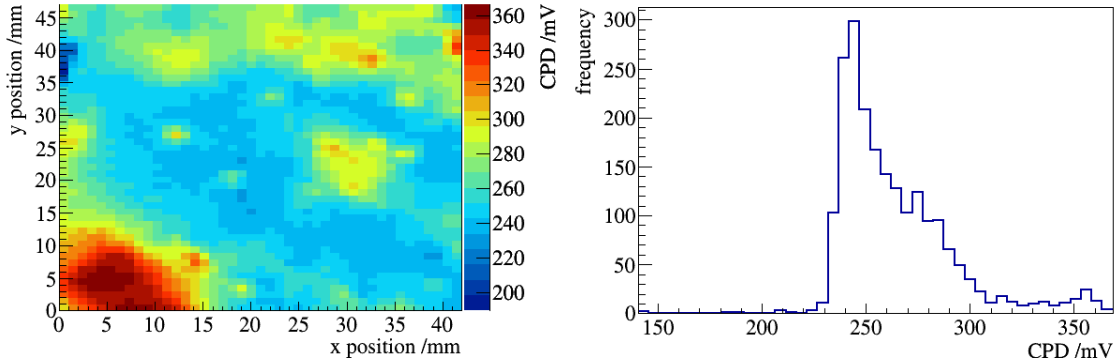

Figure E.33: CPD map and histogram of the 1. measurement of sample 3-Al-mp-3. The date of the measurement is the 16.07.2013. The mean CPD value of this scan is (264.1 ± 27.9) mV.

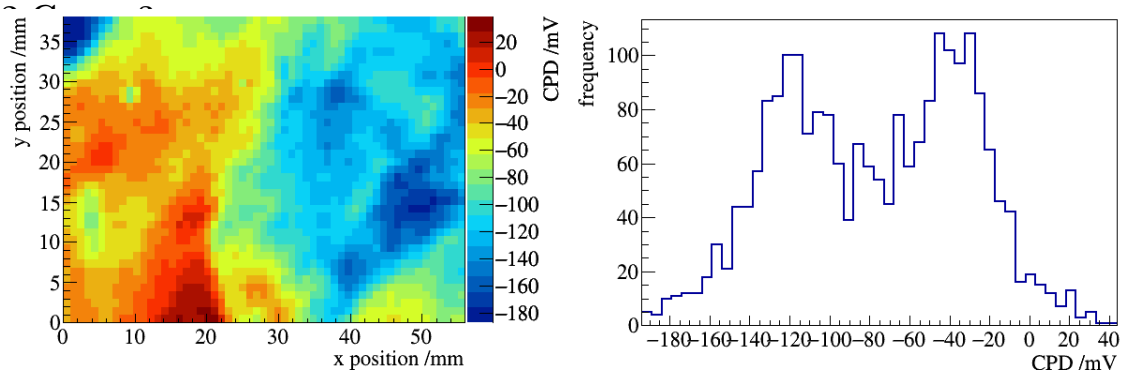

Figure E.34: CPD map and histogram of the 1. measurement of sample 3-Cu-ep-3. The date of the measurement is the 18.07.2013. The mean CPD value of this scan is (-148.0 ± 35.0) mV.

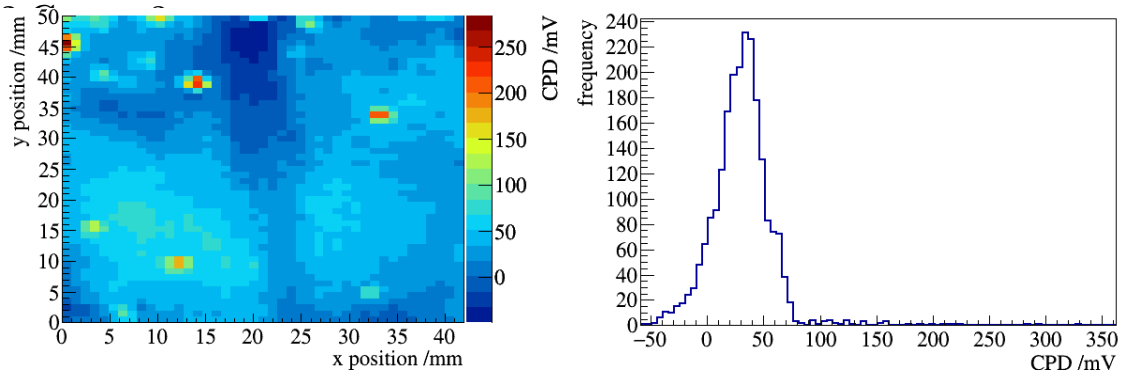

Figure E.35: CPD map and histogram of the 1. measurement of sample 2-Cu-mp-3. The date of the measurement is the 18.07.2013. The mean CPD value of this scan is (30.7 ± 28.8) mV.

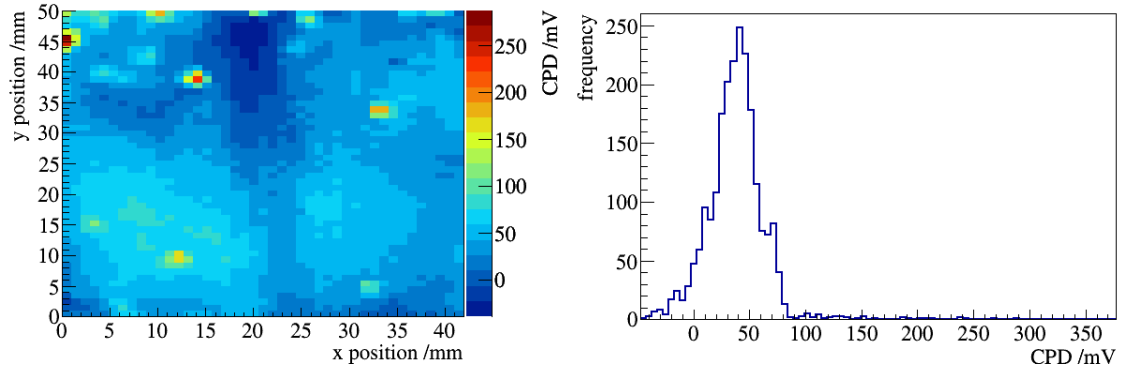

Figure E.36: CPD map and histogram of the 2. measurement of sample 2-Cu-mp-3. The date of the measurement is the 18.07.2013. The position and the scan area is not changed between this and the first measurement. The mean CPD value of this scan is (38.3 ± 28.0) mV.

3-Cu-mp-3

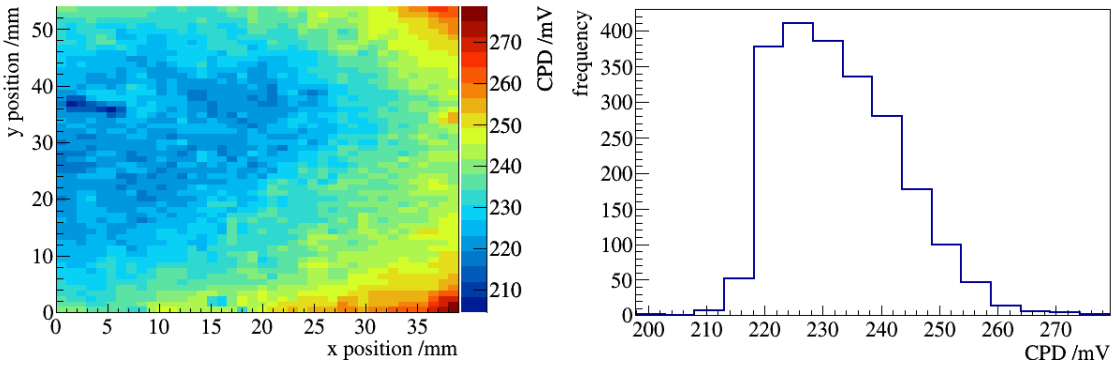

Figure E.37: CPD map and histogram of the 1. measurement of sample 3-Cu-mp-3. The date of the measurement is the 16.07.2013. The mean CPD value of this scan is (232.8 ± 10.4) mV.

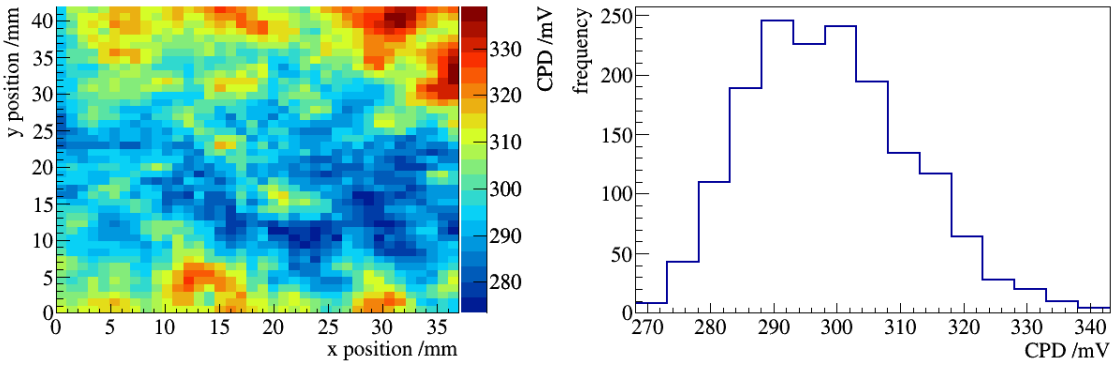

Figure E.38: CPD map and histogram of the 2. measurement of sample 3-Cu-mp-3. The date of the measurement is the 15.08.2013. The mean CPD value of this scan is (298.9 ± 12.8) mV.

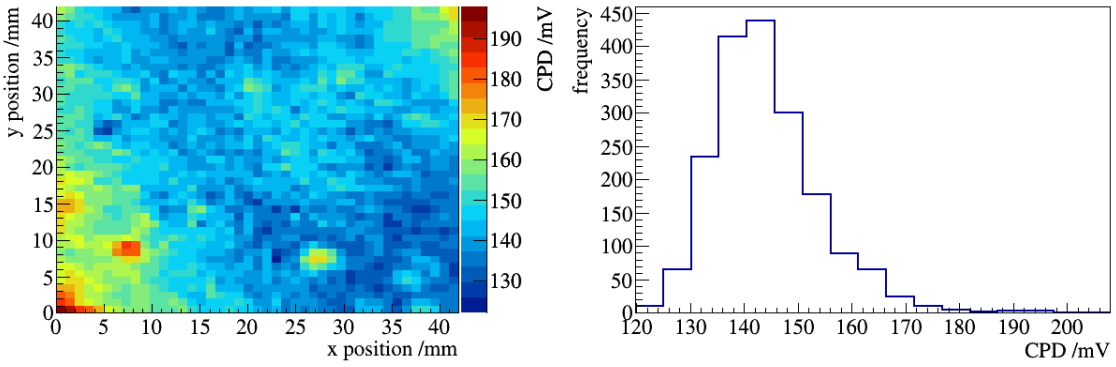

Figure E.39: CPD map and histogram of the 3. measurement of sample 3-Cu-mp-3. The date of the measurement is the 28.07.2013, which is after the bake-out of this sample. The mean CPD value of this scan is (144.1 ± 10.1) mV.

1-SS-ep-3

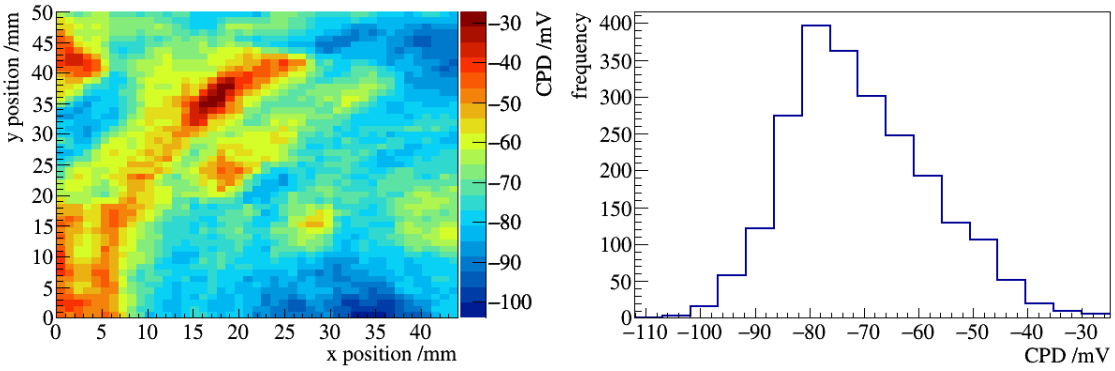

Figure E.40: CPD map and histogram of the 1. measurement of sample 1-SS-ep-3. The date of the measurement is the 29.05.2013. The sample is not coated at the time of the measurement. The mean CPD value of this scan is (-70.7 ± 13.0) mV.

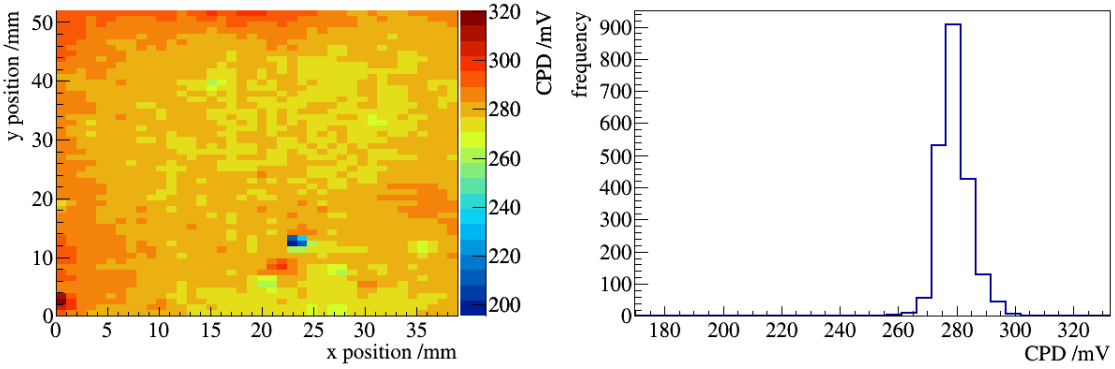

Figure E.41: CPD map and histogram of the 2. measurement of sample 1-SS-ep-3. The date of the measurement is the 17.07.2013. The mean CPD value of this scan is (279.3 ± 6.5) mV.

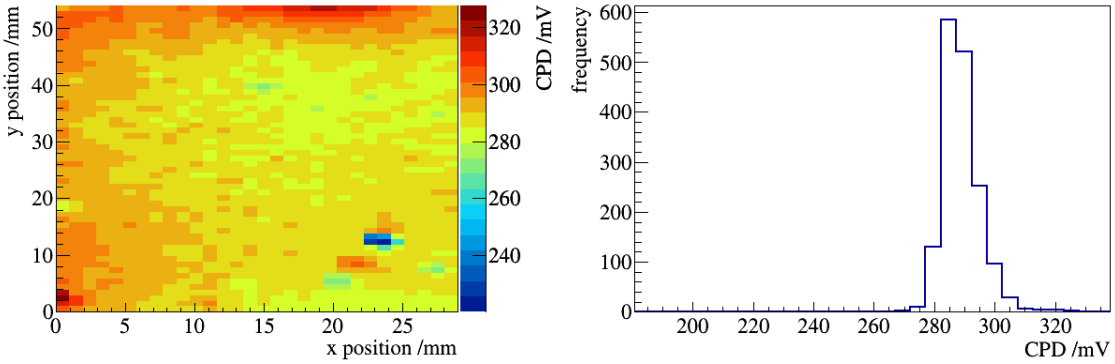

Figure E.42: CPD map and histogram of the 3. measurement of sample 1-SS-ep-3. The date of the measurement is the 17.07.2013. The position and the scan area is not changed between this and the first measurement. The mean CPD value of this scan is (288.8 ± 7.5) mV.

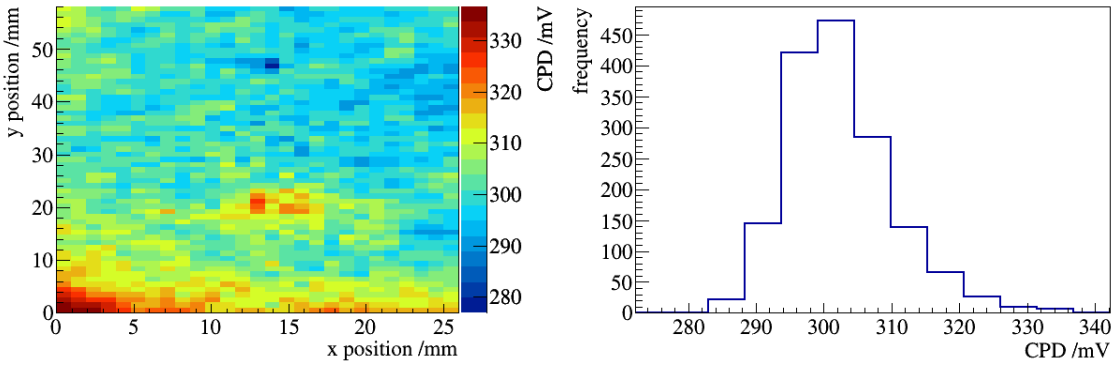

Figure E.43: CPD map and histogram of the 4. measurement of sample 1-SS-ep-3. The date of the measurement is the 14.08.2013. The mean CPD value of this scan is (302.4 ± 7.9) mV.

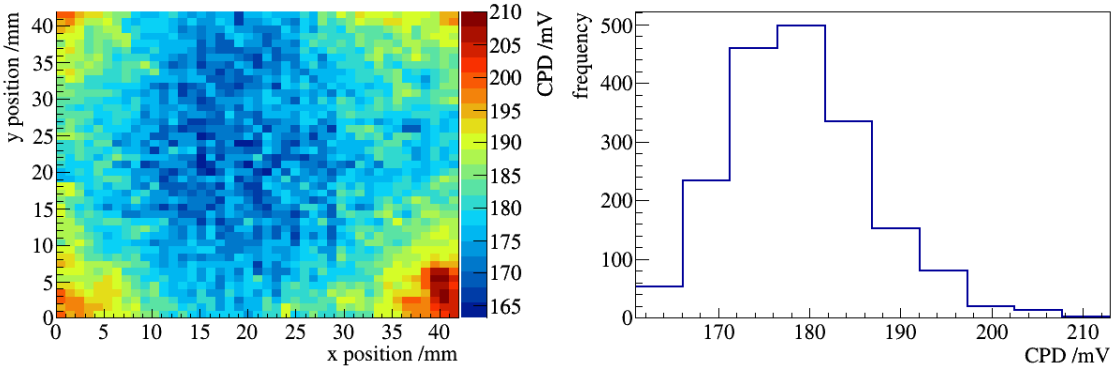

Figure E.44: CPD map and histogram of the 5. measurement of sample 1-SS-ep-3. The date of the measurement is the 28.08.2013, which is after the bake-out of this sample. The mean CPD value of this scan is (179.0 ± 7.8) mV.

2-SS-ep-3

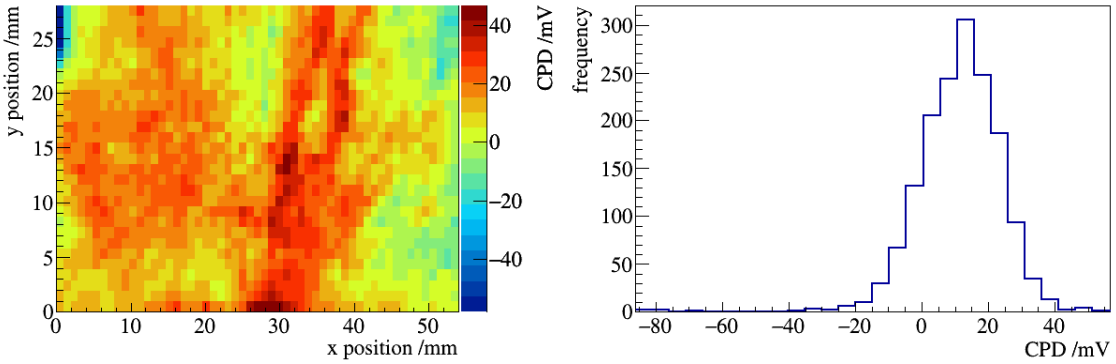

Figure E.45: CPD map and histogram of the 1. measurement of sample 2-SS-ep-3. The date of the measurement is the 18.07.2013. The mean CPD value of this scan is (11.5 ± 12.5) mV.

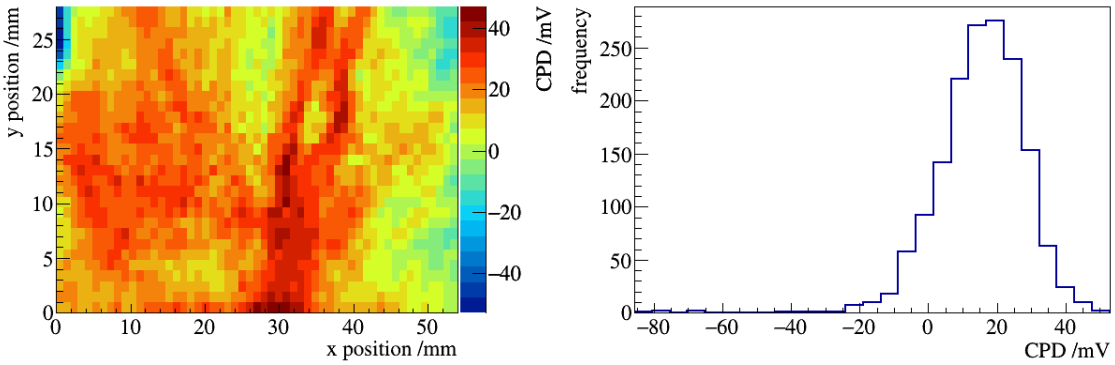

Figure E.46: CPD map and histogram of the 2. measurement of sample 2-SS-ep-3. The date of the measurement is the 18.07.2013. The position and the scan area is not changed between this and the first measurement. The mean CPD value of this scan is (15.4 ± 12.9) mV.

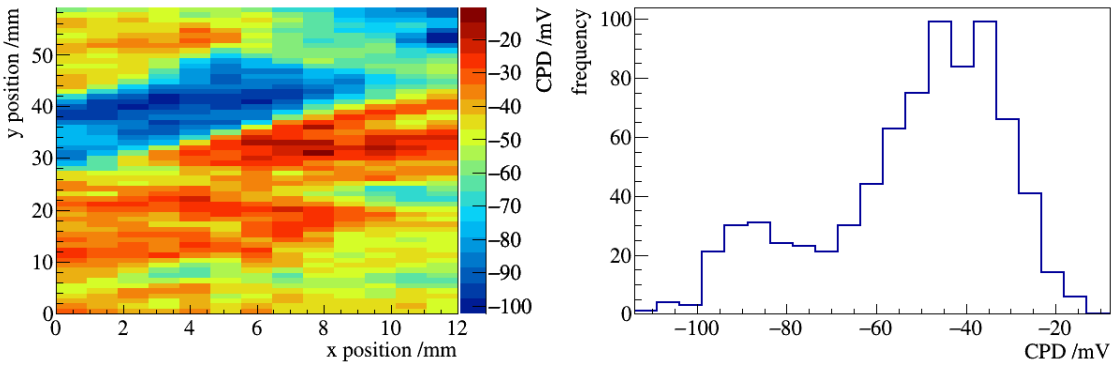

Figure E.47: CPD map and histogram of the 3. measurement of sample 2-SS-ep-3. The date of the measurement is the 13.08.2013. The mean CPD value of this scan is (126.0 ± 19.3) mV.

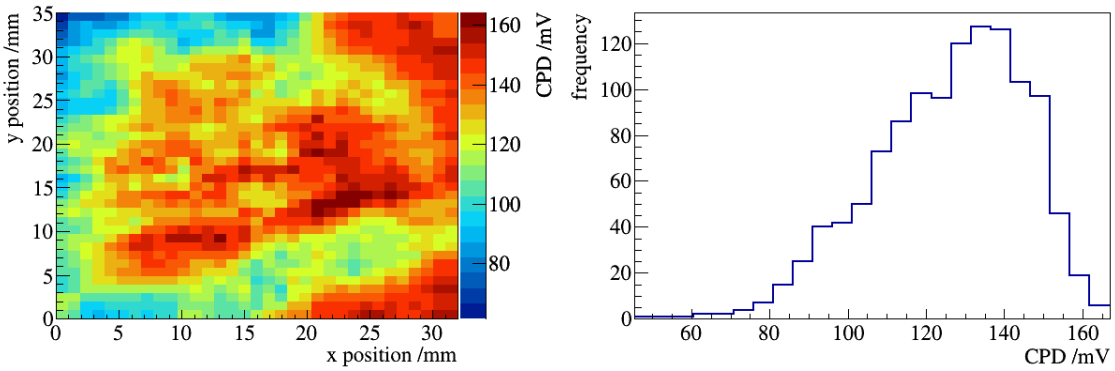

Figure E.48: CPD map and histogram of the 4. measurement of sample 2-SS-ep-3. The date of the measurement is the 28.08.2013, which is after the bake-out of this sample. The mean CPD value of this scan is (-51.9 ± 20.0) mV.

1-SS-mp-3

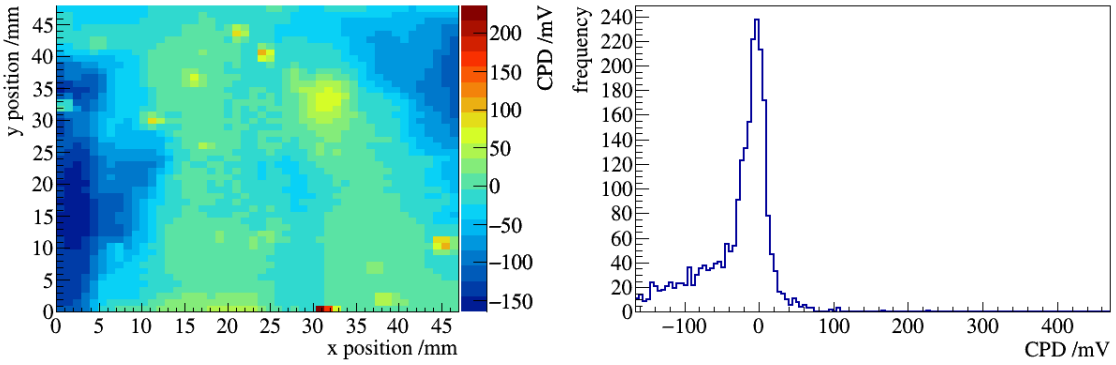

Figure E.49: CPD map and histogram of the 1. measurement of sample 1-SS-mp-3. The date of the measurement is the 19.07.2013. The mean CPD value of this scan is (-28.1 ± 46.6) mV.

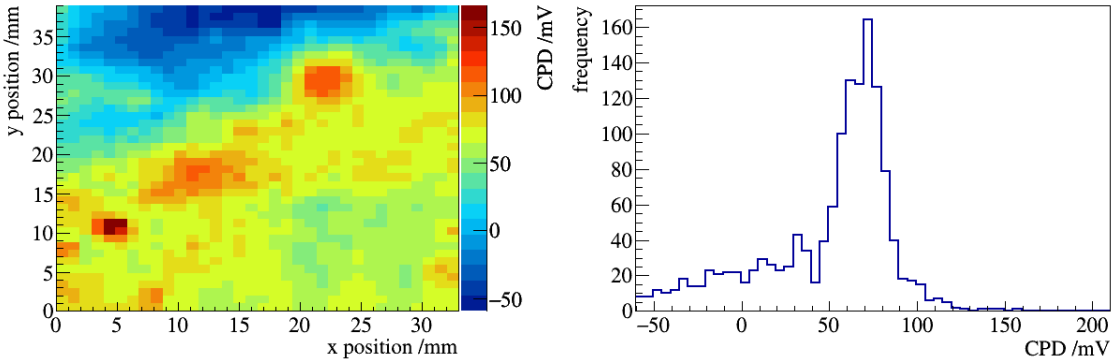

Figure E.50: CPD map and histogram of the 2. measurement of sample 1-SS-mp-3. The date of the measurement is the 15.08.2013. The mean CPD value of this scan is (49.7 ± 37.5) mV.

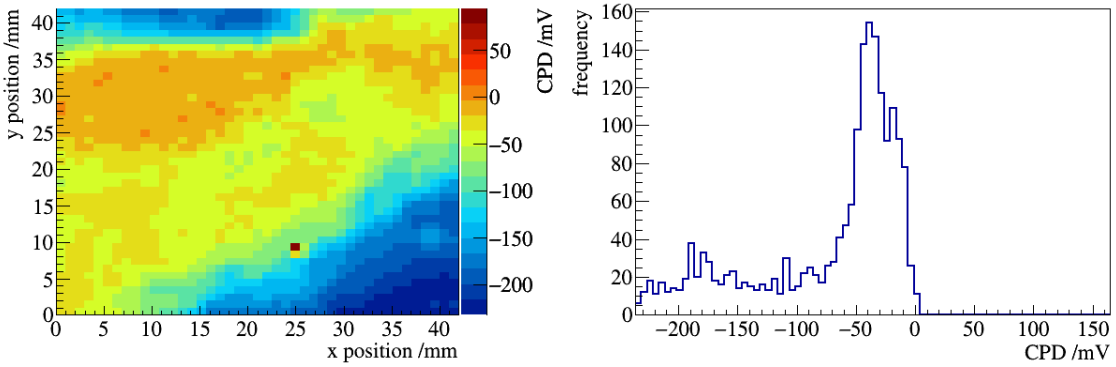

Figure E.51: CPD map and histogram of the 3. measurement of sample 1-SS-mp-3. The date of the measurement is the 28.08.2013, which is after the bake-out of this sample. The mean CPD value of this scan is (-71.7 ± 62.3) mV.

2-SS-mp-3

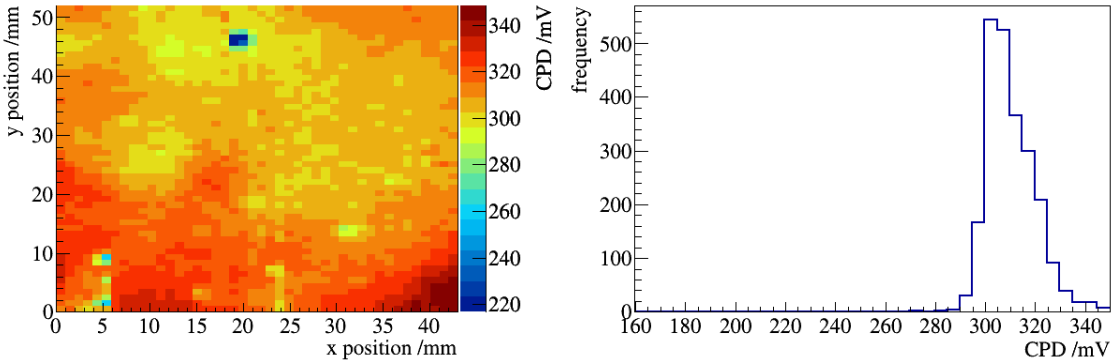

Figure E.52: CPD map and histogram of the 1. measurement of sample 2-SS-mp-3. The date of the measurement is the 17.07.2013. The mean CPD value of this scan is (309.9 ± 11.5) mV.

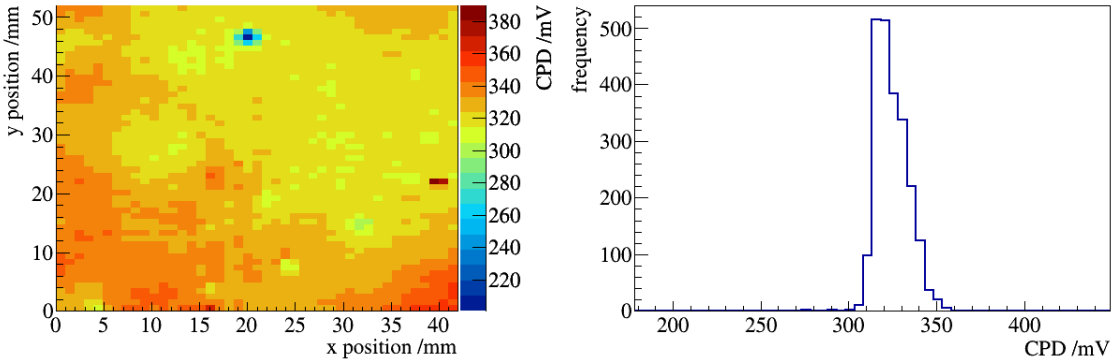

Figure E.53: CPD map and histogram of the 2. measurement of sample 2-SS-mp-3. The date of the measurement is the 17.07.2013. The position and the scan area is not changed between this and the first measurement. The mean CPD value of this scan is (324.6 ± 10.3) mV.

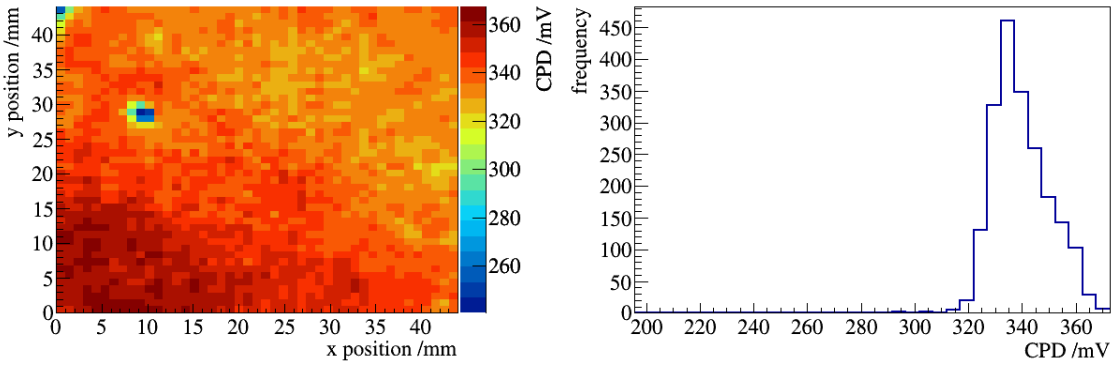

Figure E.54: CPD map and histogram of the 3. measurement of sample 2-SS-mp-3. The date of the measurement is the 14.08.2013. The mean CPD value of this scan is (339.4 ± 12.0) mV.

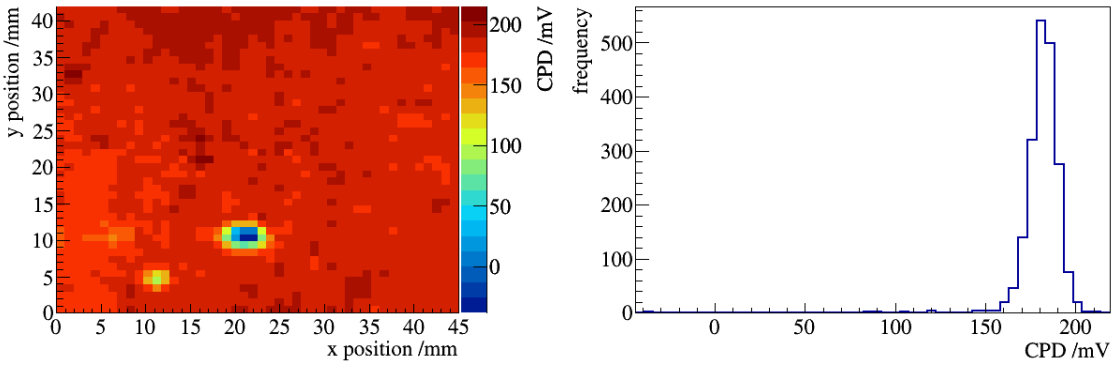

Figure E.55: CPD map and histogram of the 4. measurement of sample 2-SS-mp-3. The date of the measurement is the 27.08.2013, which is after the bake-out of this sample. The mean CPD value of this scan is (180.9 ± 15.2) mV.

3-SS-mp-3

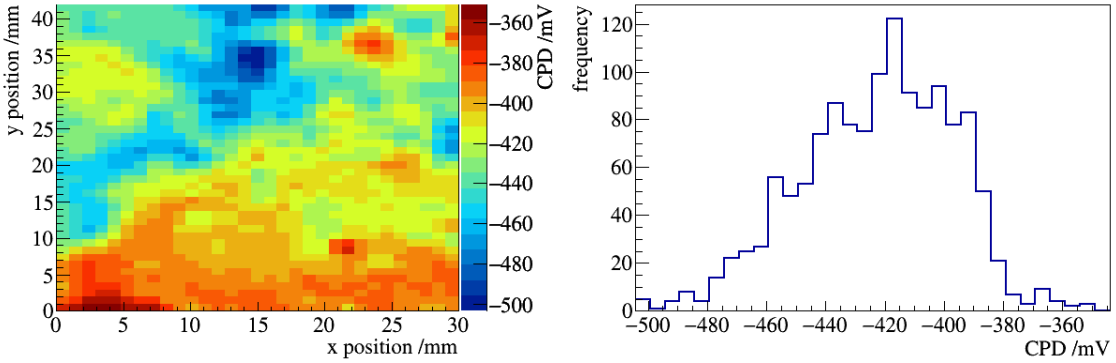

Figure E.56: CPD map and histogram of the 1. measurement of sample 3-SS-mp-3. The date of the measurement is the 28.05.2013. The sample is not coated at the time of the measurement. The mean CPD value of this scan is (-422.4 ± 25.8) mV.

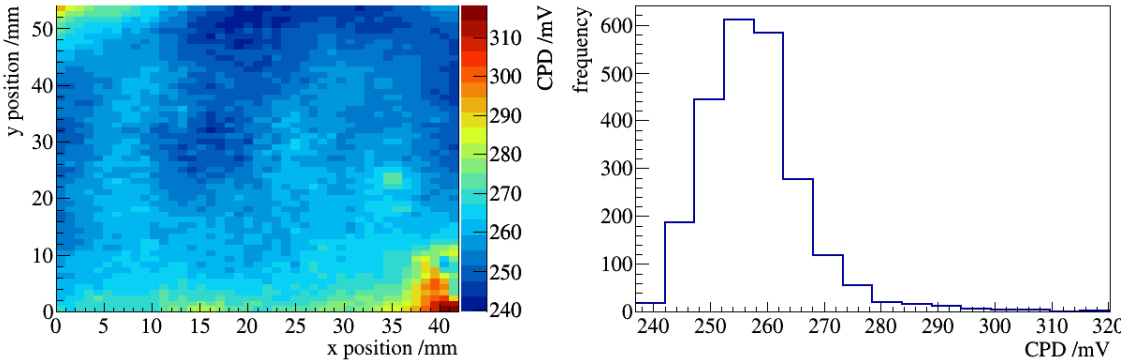

Figure E.57: CPD map and histogram of the 2. measurement of sample 3-SS-mp-3. The date of the measurement is the 17.07.2013. The mean CPD value of this scan is (258.0 ± 9.4) mV.

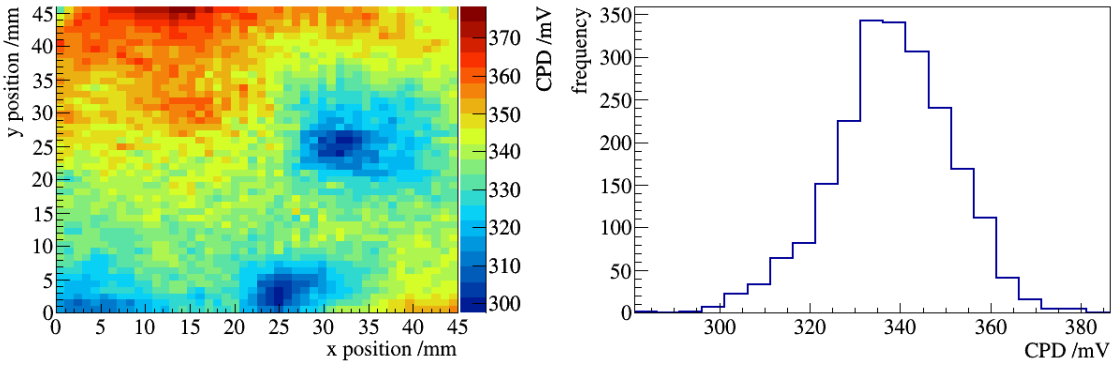

Figure E.58: CPD map and histogram of the 3. measurement of sample 3-SS-mp-3. The date of the measurement is the 14.08.2013. The mean CPD value of this scan is (338.3 ± 13.2) mV.

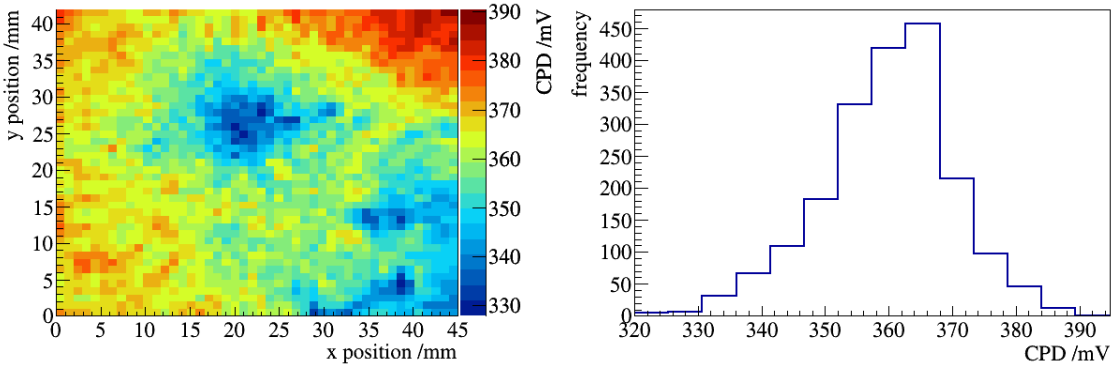

Figure E.59: CPD map and histogram of the 4. measurement of sample 3-SS-mp-3. The date of the measurement is the 27.08.2013. The mean CPD value of this scan is (359.7 ± 10.4) mV.

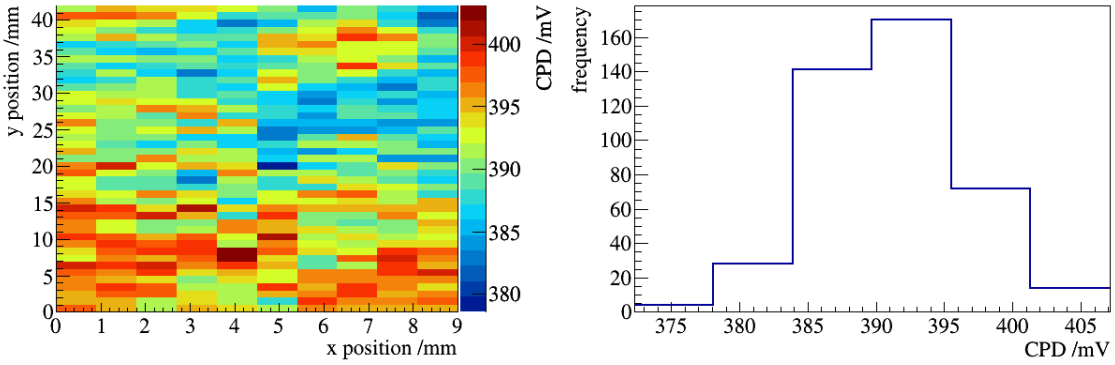

Figure E.60: CPD map and histogram of the 5. measurement of sample 3-SS-mp-3. The date of the measurement is the 27.08.2013. The position and the scan area is not changed between this and the first measurement. The mean CPD value of this scan is (391.2 ± 5.3) mV.

E.2 Raw data and additional information on the photoelectron measurements

In this section the raw data of the photoelectron measurements is presented first. The fit results of these measurements are summarized in the second paragraph of this section. In addition, further information is provided concerning the actions during the measurements in the last part of this section.

Detailed description of the performed actions during photoelectron measurements

In this section a detailed chronological description of all action performed during the photoelectron measurements at the KATRIN monitor spectrometer is given. Due to the quantity of actions the list is divided in two tables (see tables E.1 and E.2).

Table E.1: List of actions during the photoelectron measurements at the monitor spectrometer.

date	actions
21.04.2014	Pickup of all the components provided by University of Mainz.
22.04.2014	Modification of the monitor spectrometer, setting up and adjusting the optical setup.
23.04.2014	Optimization of the optical setup by using a sheet of paper inside the pierce electrode. Integration of a pinhole aperture to reduce the electron flux on the detector. Performance of filter scans to find the voltage at which the electrons reach the detector (runs 167622 - 167623). Installation of sample 3-SS-el-3; no other sample is installed behind this sample so that the stainless steel back plate of the pierce electrode can be seen through the centered hole of the sample. First measurements of sample 3-SS-el-3.
24.04.2014	Measurements of sample 3-SS-el-3. At 15:45 power-up of heating; the set value of the temperature is 120 °C and the temperature rise 0.2 °C/min.
25.04.2014	At 8:45 raising temperature to 180 °C. At 13:30 system reaches 180 °C.
27.04.2014	At 14:10 reducing temperature to room temperature.
29.04.2014	Performance of filter scans to find the voltage at which the electrons reach the detector (runs 167629 - 167631). Measurements of baked sample 3-SS-el-3. Modification: sample 2-SS-el-3 is installed behind sample 3-SS-el-3. Through the hole of sample 3-SS-el-3 the gold surface of sample 2-SS-el-3 can be seen, as sample 2-SS-el-3 has a non-centered hole.
30.04.2014	Measurements of sample 3-SS-el-3 on top of sample 2-SS-el-3. Performance of filter scans to find the voltage at which the electrons reach the detector (runs 167633 - 167637). At 12:15 power-up of heating: the set value of the temperature is 180 °C.

Table E.2: List of actions during the photoelectron measurements at the monitor spectrometer - continuation of table E.1.

date	actions
01.05.2014	At 2:30 system reaches 180 °C. At 17:45 reducing temperature to room temperature.
02.05.2014	Measurements of baked sample 3-SS-el-3 on top of sample 2-SS-el-3. Modification: all samples are removed. The back plate of the pierce electrode act as a substitute of a blank stainless steel sample. Measurements of stainless steel back plate. At 16:25 power-up of heating: the set value of the temperature is 180 °C.
03.05.2014	At 5:25 system reaches 180 °C.
04.05.2014	At 14:50 reducing temperature to room temperature.
05.05.2014	Measurements of baked stainless steel back plate. Modification: sample 2-SS-el-3 is installed in front of sample 3-SS-el-3. Through the hole of sample 2-SS-el-3 the gold surface of sample 3-SS-el-3 can be seen, as sample 2-SS-el-3 has a non-centered hole.
06.05.2014	Measurements of sample 2-SS-el-3 on top of sample 3-SS-el-3. At 10:25 power-up of heating; the set value of the temperature is 180 °C. At 23:40 system reaches 180 °C.
08.05.2014	At 15:15 reducing temperature to room temperature
09.05.2014	Measurements of baked sample 2-SS-el-3 on top of sample 3-SS-el-3. Modification: sample 4-SS-el-3 is installed in front of sample 2-SS-el-3. Through the hole of sample 4-SS-el-3 the gold surface of sample 2-SS-el-3 can be seen, as sample 2-SS-el-3 has a non-centered hole. Measurements of sample 4-SS-el-3 on top of sample 2-SS-el-3. At 16:55 power-up of heating; the set value of the temperature is 180 °C.
10.05.2014	At 6:00 system reaches 180 °C.
11.05.2014	At 16:00 reducing temperature to room temperature.
12.05.2014	Measurements of baked sample 4-SS-el-3 on top of sample 2-SS-el-3. Modification: sample 5-SS-el-3 is installed in front of sample 2-SS-el-3. Through the hole of sample 5-SS-el-3 the gold surface of sample 2-SS-el-3 can be seen, as sample 2-SS-el-3 has a non-centered hole.
13.05.2014	Test for reproducibility on sample 5-SS-el-3. Measurements of sample 5-SS-el-3 on top of sample 2-SS-el-3. Installation of a 300 W xenon lamp in front of the vacuum chamber. At about 15:35 begin of irradiation wit xenon lamp. At about 16:05 end of irradiation wit xenon lamp. Measurement of UV irradiated sample 5-SS-el-3 on top of sample 2-SS-el-3.
14.05.2014	At 17:30 power-up of heating: the set value of the temperature is at all heaters 180 °C at the beginning; as the heater directly at the elipot turns off several times, the set value of this heater is set to 170 °C. At 6:25 system reaches 180 °C or 170 °C respectively.
15.05.2014	At 15:00 reducing temperature to room temperature.
16.05.2014	Measurements of baked sample 5-SS-el-3 on top of sample 2-SS-el-3. Performance of several filter scans to find the voltage at which the electrons reach the detector (runs 167638 - 167674).

Spectra of the photoelectron measurements

In this section the raw data of the photoelectron measurements at the monitor spectrometer is presented. To be able to compare different raw data spectra in each diagram different spectra are combined: First the spectra of all positions of a specific sample are plotted. The treatment of the sample before data taking is the same for all spectra within a diagram. In the second paragraph the spectra within a diagram are measured at the same position of a sample but after different treatments. The results of all fits on the presented data can be found in the last paragraph of this section.

Photoelectron spectra of each sample after a certain treatment

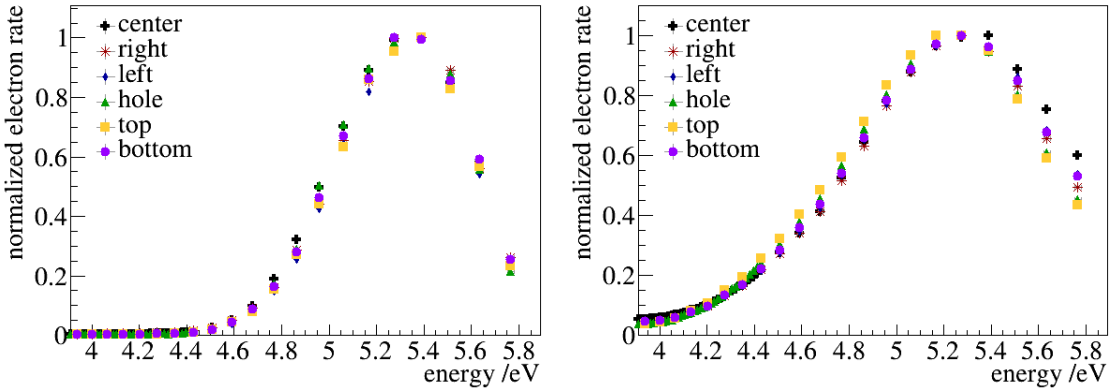

Figure E.61: Photoelectron measurements at sample 2-SS-ep-3 before and after bake-out. In the background of the sample a gold surface is installed. Left: in the unbaked spectra of all positions of sample 2-SS-ep-3 are plotted. Right: the spectra taken after a bake-out are shown here.

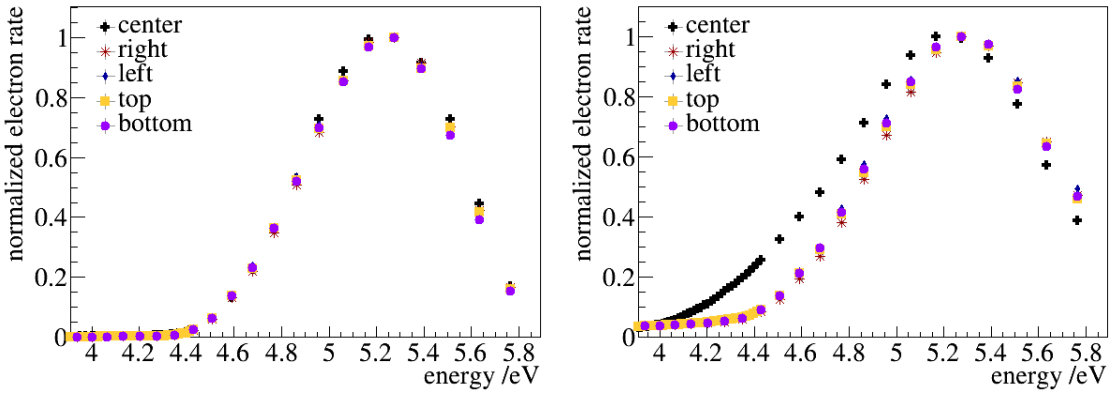

Figure E.62: Photoelectron measurements at sample 3-SS-ep-3 before and after bake-out. In the background of the sample a gold surface is installed. Left: in the unbaked spectra of all positions of sample 3-SS-ep-3 are plotted. Right: the spectra taken after a bake-out are shown here.

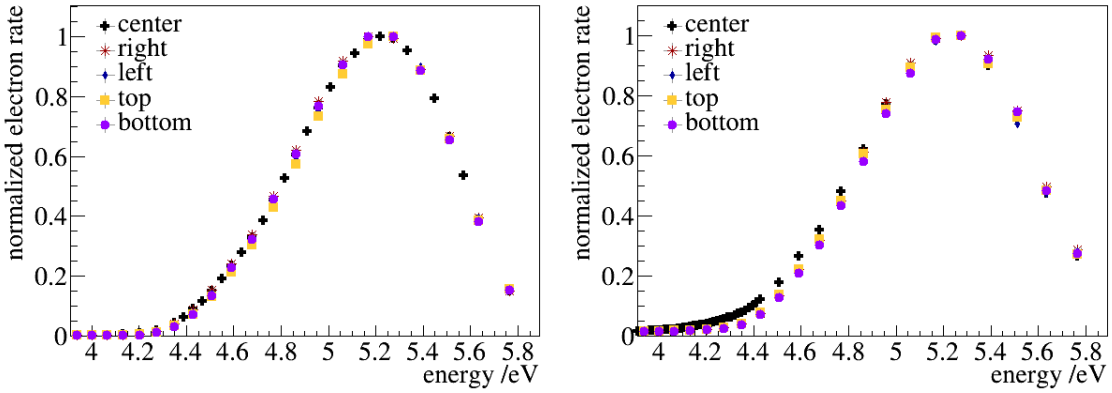

Figure E.63: Photoelectron measurements at sample 3-SS-ep-3 before and after bake-out. In the background of the sample a gold surface is installed. Left: in the unbaked spectra of all positions of sample 3-SS-ep-3 are plotted. Right: the spectra taken after a bake-out are shown here.

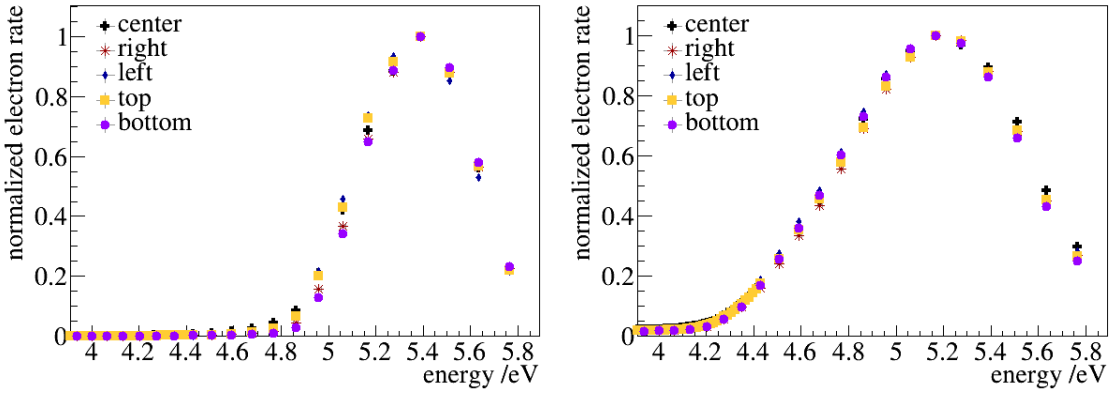

Figure E.64: Photoelectron measurements at sample 4-SS-ep-3 before and after bake-out. In the background of the sample a gold surface is installed. Left: in the unbaked spectra of all positions of sample 4-SS-ep-3 are plotted. Right: the spectra taken after a bake-out are shown here.

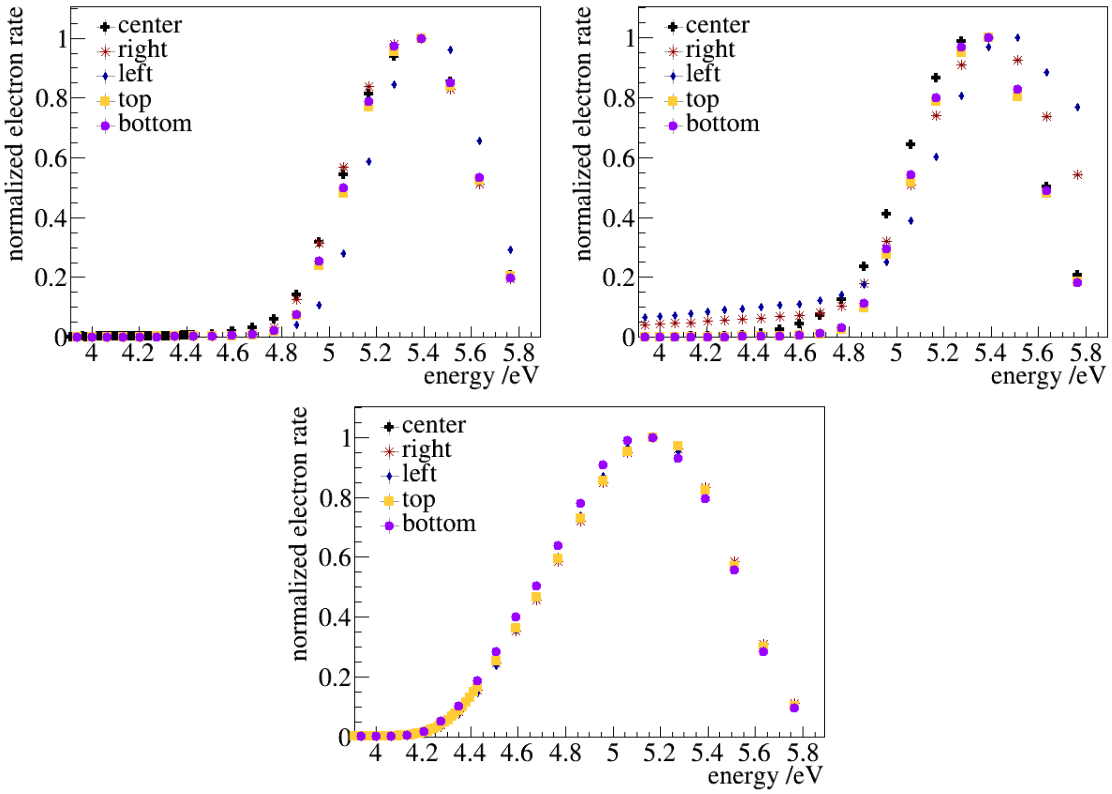

Figure E.65: Photoelectron measurements at sample 5-SS-ep-3 before and after bake-out. In the background of the sample a gold surface is installed. Top left: the spectra before bake-out of all positions of sample 5-SS-ep-3 are plotted. Top right: spectra after the UV irradiation are plotted. Bottom center: the spectra taken after a bake-out are shown here.

Photoelectron spectra at each position

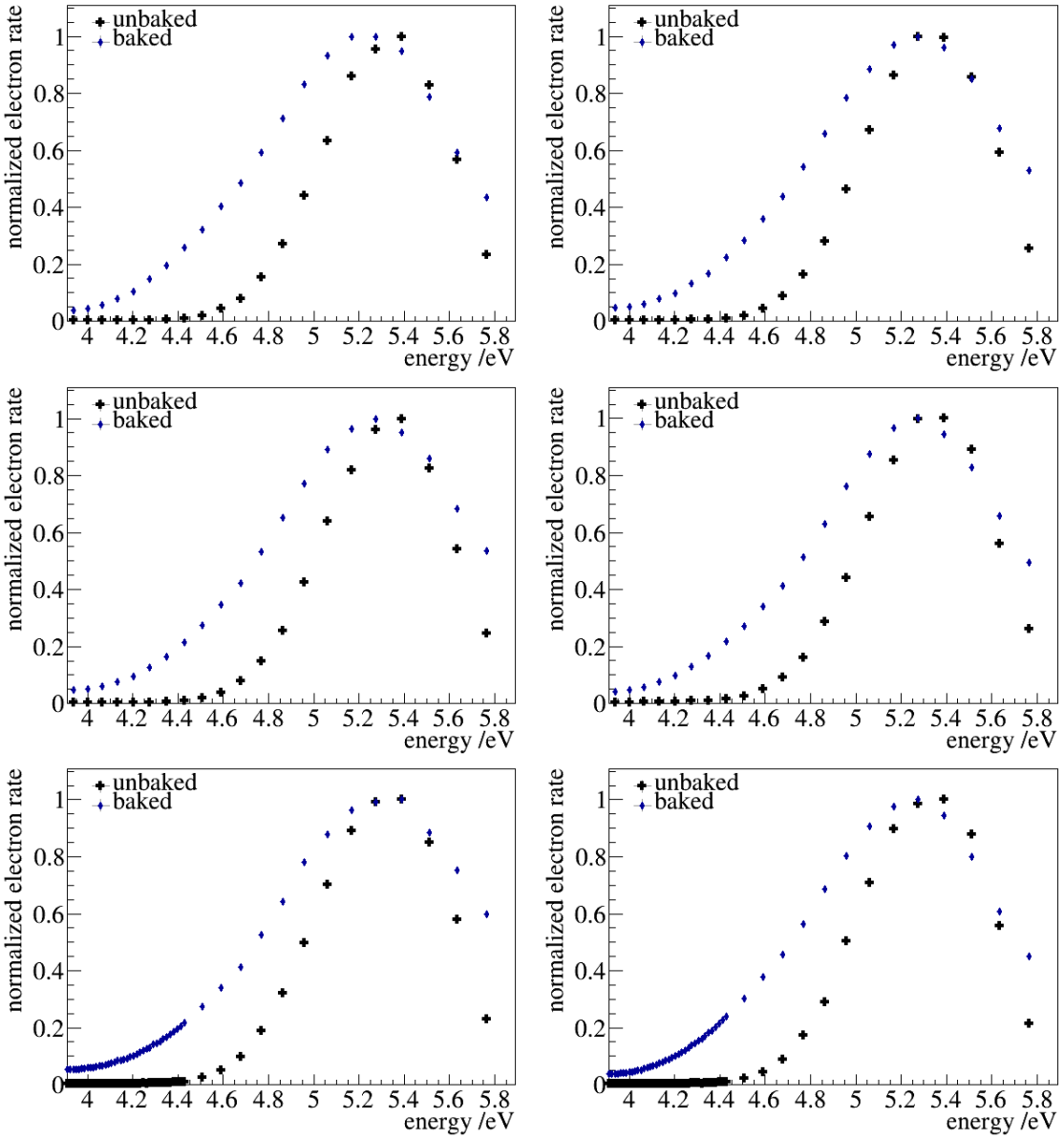

Figure E.66: Photoelectron spectra of sample 2-SS-ep-3 at different positions of the sample with gold background. In the background of the sample 2-SS-ep-3 sample 3-SS-ep-3 is installed. Top left: the spectra of the top position are plotted here. Top right: the presented spectra belong to the bottom measurement position. Middle left: the spectra of the measurements performed at the left position of the sample is shown. Middle right: the electron rate emitted from the right position of the sample is plotted. Bottom left: the measured spectra of the center position is presented here. In contrast to all other samples the center position of the sample is not equal to the position of the hole. Bottom right: the electron rate emitted from the position of the hole is drawn in the diagram.

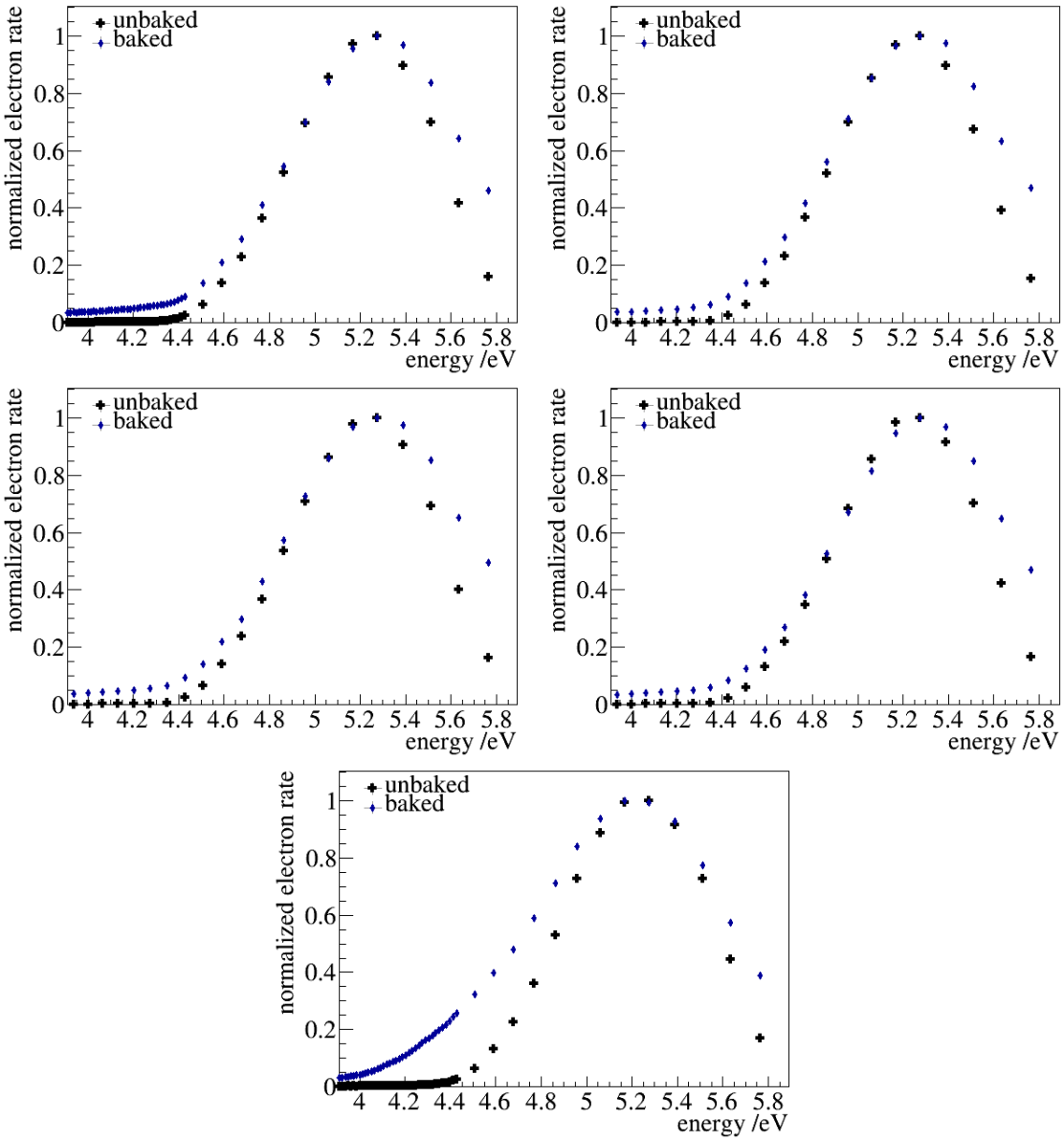

Figure E.67: Photoelectron spectra of sample 3-SS-ep-3 at different positions of the sample with gold background. In the background of the sample 3-SS-ep-3 sample 2-SS-ep-3 is installed. Therefore a gold surface can be seen through the central hole. Top left: the spectra of the top position are plotted here. Top right: the presented spectra belong to the bottom measurement position. Middle left: the spectra of the measurements performed at the left position of the sample is shown. Middle right: the electron rate emitted from the right position of the sample is plotted. Bottom center: the electron rate emitted from the position of the hole is drawn in the diagram.

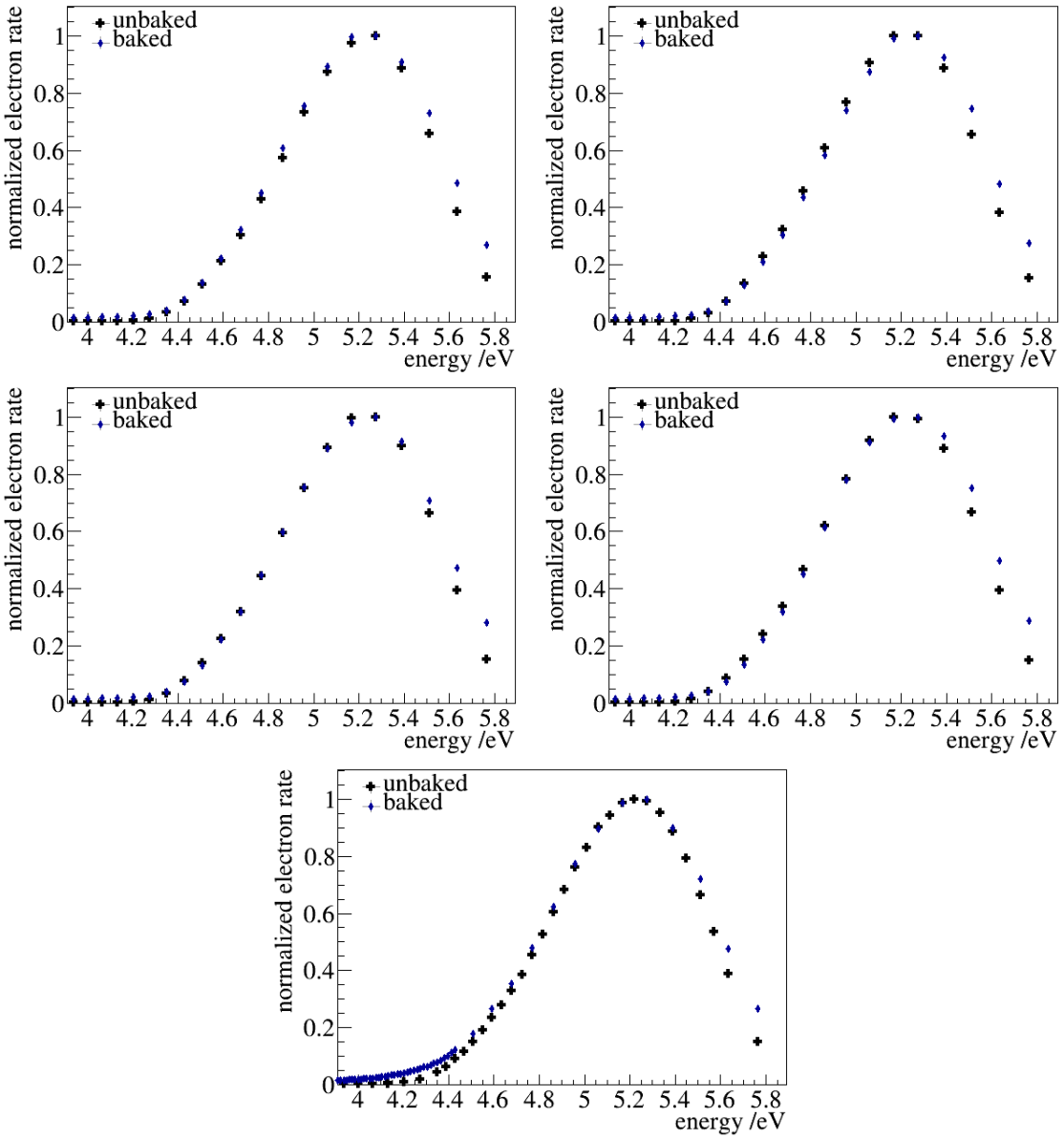

Figure E.68: Photoelectron spectra of sample 3-SS-ep-3 at different positions of the sample with steel background. In the background no further sample is installed. Therefore a stainless steel surface can be seen through the central hole. Top left: the spectra of the top position are plotted here. Top right: the presented spectra belong to the bottom measurement position. Middle left: the spectra of the measurements performed at the left position of the sample is shown. Middle right: the electron rate emitted from the right position of the sample is plotted. Bottom center: the electron rate emitted from the position of the hole is drawn in the diagram.

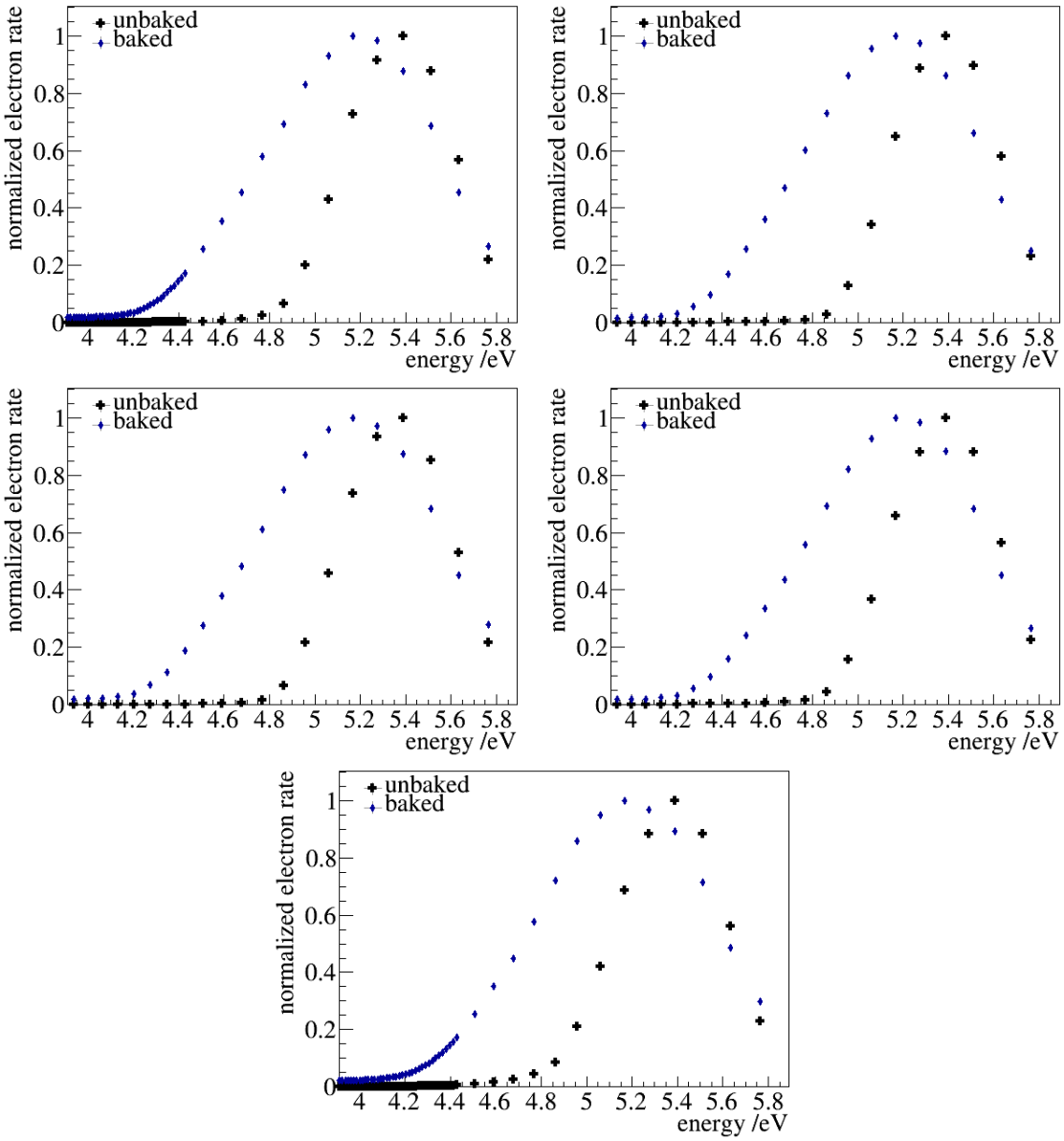

Figure E.69: Photoelectron spectra of sample 4-SS-ep-3 at different positions of the sample with gold background. In the background of the sample 4-SS-ep-3 sample 2-SS-ep-3 is installed. Therefore a gold surface can be seen through the central hole. Top left: the spectra of the top position are plotted here. Top right: the presented spectra belong to the bottom measurement position. Middle left: the spectra of the measurements performed at the left position of the sample is shown. Middle right: the electron rate emitted from the right position of the sample is plotted. Bottom center: the electron rate emitted from the position of the hole is drawn in the diagram.

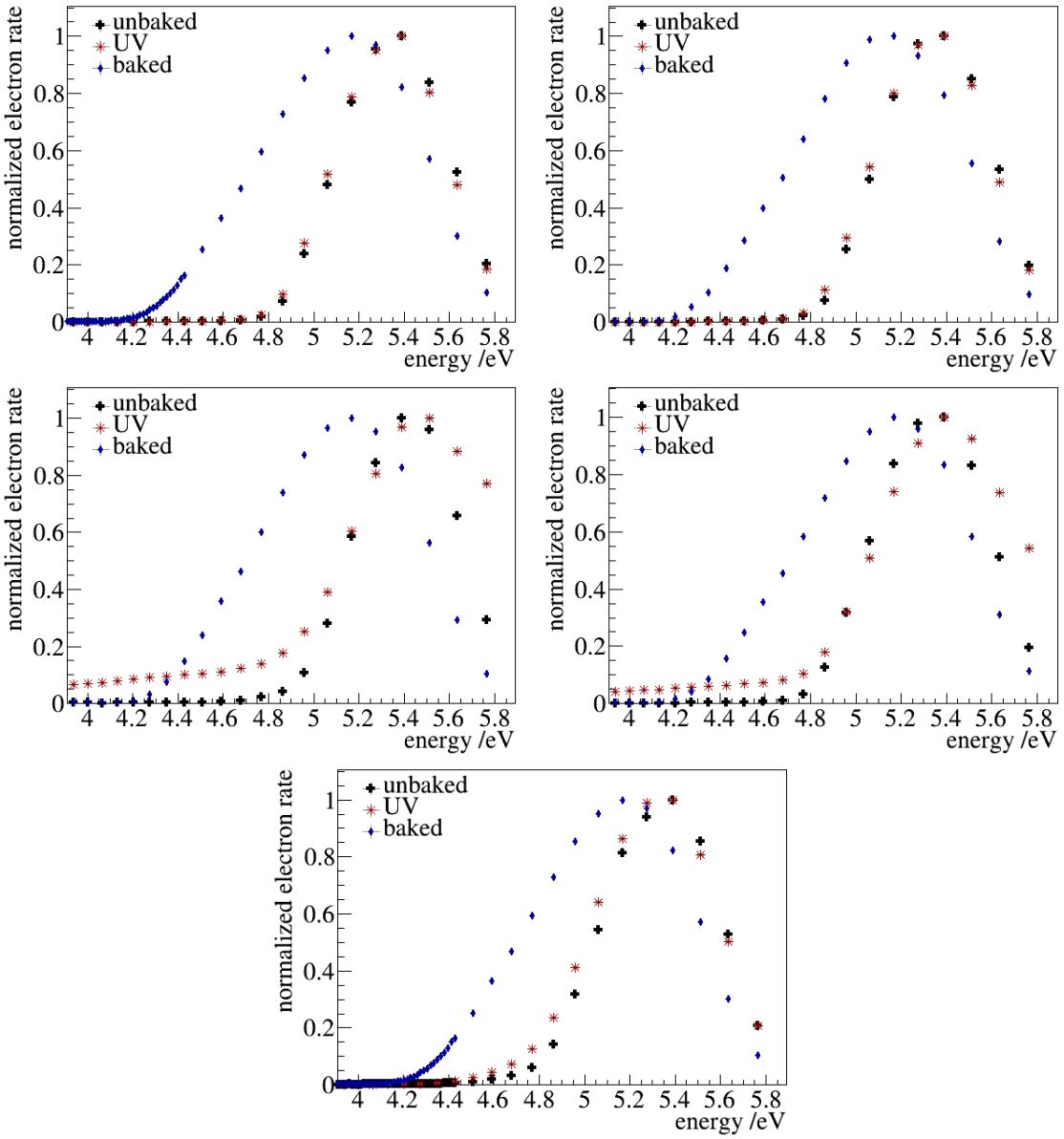

Figure E.70: Photoelectron spectra of sample 5-SS-ep-3 at different positions of the sample with gold background. In the background of the sample 5-SS-ep-3 sample 2-SS-ep-3 is installed. Therefore a gold surface can be seen through the central hole. Top left: the spectra of the top position are plotted here. Top right: the presented spectra belong to the bottom measurement position. Middle left: the spectra of the measurements performed at the left position of the sample is shown. Middle right: the electron rate emitted from the right position of the sample is plotted. Bottom center: the electron rate emitted from the position of the hole is drawn in the diagram.

Work function results of photoelectron measurements

In this section all results of the photoelelectron spectroscopy at the monitor spectrometer are presented. Due to the large number of measurements the results are split in 2 tables (see tables E.3 and E.4).

Table E.3: Results of the fits on the photoelectron spectra of sample 2-SS-ep-3 and 5-SS-ep-3 performed at the monitor spectrometer.

sample	back-ground	position	comment	Φ /V	σ_Φ /V	P	σ_P	B	σ_B
2-SS-ep-3	Au	bottom	unbaked	4.438	0.009	36	1	104	7
		center	unbaked	4.422	0.009	41	1	140	7
		left	unbaked	4.448	0.007	35	1	102	6
		Loch	unbaked	4.442	0.008	42	1	131	6
		right	unbaked	4.437	0.009	38	1	191	9
		top	unbaked	4.439	0.008	38	1	103	7
2-SS-ep-3	Au	bottom	baked	3.926	0.007	170	4	8314	116
		center	baked	3.925	0.004	135	2	8276	50
		left	baked	3.938	0.006	167	4	8301	104
		Loch	baked	3.902	0.004	218	3	8296	79
		right	baked	3.899	0.007	167	4	7938	152
		top	baked	3.886	0.008	228	6	8036	245
5-SS-ep-3	Au	bottom	UV	4.612	0.006	222	9	268	12
		center	UV	4.472	0.005	184	5	1152	38
		left	UV	4.629	0.008	187	7	9554	74
		left 2	UV	4.687	0.006	133	5	159	7
		right	UV	4.628	0.010	405	20	9916	82
		right 2	UV	4.633	0.010	313	15	397	22
		top	UV	4.618	0.006	318	12	332	13
5-SS-ep-3	Au	bo	unbaked	4.704	0.007	328	17	325	13
		bottom	unbaked	4.629	0.009	202	10	152	6
		center	unbaked	4.575	0.006	131	4	528	25
		center 2	unbaked	4.570	0.006	128	4	578	26
		left	unbaked	4.731	0.008	87	4	164	8
		right	unbaked	4.677	0.009	362	22	359	14
		top 2	unbaked	4.711	0.008	346	20	339	13
		top 3	unbaked	4.696	0.006	315	15	333	13
		top 4	unbaked	4.700	0.007	330	17	330	13
5-SS-ep-3	Au	bottom	baked	4.068	0.005	860	20	1111	21
		center	baked	4.076	0.002	813	13	1308	11
		left	baked	4.104	0.005	726	17	971	18
		right	baked	4.080	0.004	780	16	1247	21
		top	baked	4.076	0.002	813	13	1308	11

Table E.4: Results of the fits on the photoelectron spectra of sample 3-SS-ep-3 with different background material, sample 4-SS-ep-3 and stainless steel performed at the monitor spectrometer.

sample	background	position	comment	Φ /V	σ_Φ/V	P	σ_P	B	σ_B
		bottom	unbaked	4.299	0.005	360	9	470	16
		center	unbaked	4.279	0.003	282	5	455	7
3-SS-ep-3	Au	left	unbaked	4.300	0.005	365	9	498	16
		right	unbaked	4.308	0.006	368	10	514	16
		top	unbaked	4.297	0.003	383	8	520	7
		bottom	baked	4.224	0.006	395	10	11283	86
		center	baked	3.802	0.017	247	7	4242	1653
3-SS-ep-3	Au	left	baked	4.226	0.006	378	9	11309	85
		right	baked	4.236	0.005	391	9	11354	81
		top	baked	4.236	0.004	408	8	12844	83
		bottom	unbaked	4.188	0.006	461	13	658	14
		center	unbaked	4.163	0.005	425	9	1177	30
		center 15	unbaked	4.143	0.003	1642	29	4440	75
3-SS-ep-3	steel	left	unbaked	4.174	0.006	480	12	872	17
		left 2	unbaked	4.149	0.004	469	9	848	17
		c.t. center	unbaked	4.164	0.006	493	13	1285	63
		c.t. center 2	unbaked	4.176	0.005	478	10	1166	46
		right	unbaked	4.156	0.004	520	11	864	17
		top	unbaked	4.169	0.006	404	10	798	16
		bottom	baked	4.181	0.005	396	9	4359	35
		center	baked	4.019	0.002	266	3	4861	27
		center 15	baked	4.080	0.004	1524	27	23604	547
3-SS-ep-3	steel	left	baked	4.180	0.005	398	9	4325	35
		right	baked	4.186	0.005	409	10	4378	35
		top	baked	4.175	0.006	410	10	4609	37
		top 2	baked	4.223	0.003	475	10	5797	33
		bottom	unbaked	4.700	0.005	618	21	513	16
		center	unbaked	4.517	0.004	305	7	887	23
4-SS-ep-3	Au	left	unbaked	4.699	0.007	803	33	552	17
		right	unbaked	4.687	0.005	755	26	1052	24
		top	unbaked	4.608	0.004	557	15	890	32
		bottom	baked	4.103	0.005	712	18	7758	107
		center	baked	4.095	0.004	546	13	9312	177
4-SS-ep-3	Au	left	baked	4.085	0.006	606	17	8016	136
		right	baked	4.101	0.006	666	17	8262	110
		top	baked	4.084	0.003	632	11	8208	49
stainless steel		center	unbaked	4.535	0.008	33	1	123	4
		top	unbaked	4.523	0.008	43	2	170	8
stainless steel		center	baked	4.141	0.004	124	2	8166	45
		top	baked	4.149	0.007	107	2	8143	86

E.3 Photoelectron measurements performed with the Münster e-gun

In addition to the photoelectron measurements performed in the context of the Rear Wall development, a photoelectron spectrum is taken with the Münster E-gun. The reason of this measurement is the verification of the basic shape of the spectra, especially at wavelengths below 240 nm. At these wavelengths the electron rate drops down to the background rate.

For the measurement the same light source and prism spectrometer as for the other photoelectron measurements is used. But the cathode is not a Rear Wall sample but the e-gun cathode. The measurements are also performed at the KATRIN monitor spectrometer.

The resulting spectra can be found in figure E.71. By comparing this spectrum with the other photoelectron measurements no difference in the basic shape of the spectrum can be identified.

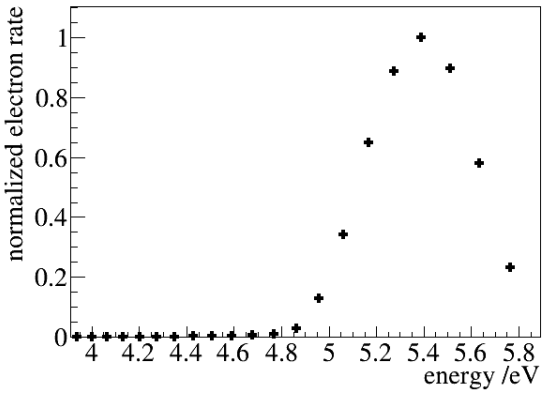

Figure E.71: Spectrum of the photoelectron measurements with the Münster e-gun. The spectrum has a maximum at about 5.4 eV. To higher and lower photon energies the electron rate drops down.

E.4 CPD maps taken by the UHV Kelvin Probe and their results

In this section additional information on the results of the UHV Kelvin Probe is given. The results are sorted by the samples. For each sample all CPD maps and also the calculated CPD and $\sigma_{\mathrm{RMS,surface}}$ values are given. In case of sample 5-SS-ep-6 the CPD and $\sigma_{\mathrm{RMS,pixel}}$ pixel maps and the corresponding value are given as well.

Measurements performed at sample 6-SS-ep-3

In this section the results sample 6-SS-ep-3 are presented. First the CPD maps are plotted and then the numeric values of CPD and $\sigma_{\mathrm{RMS,surface}}$ are summarized subsequently. Both are presented in chronological ordering.

CPD maps of the measurements performed on sample 6-SS-ep-3

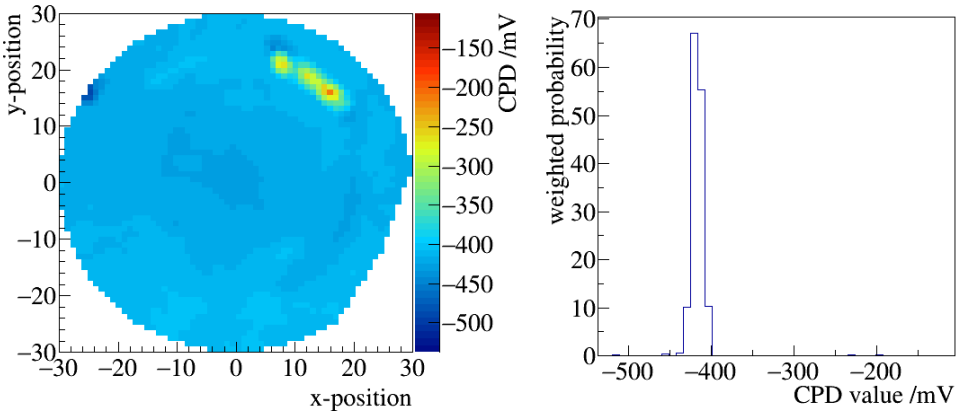

Figure E.72: CPD map and histogram of the 1. scan of sample 6-SS-ep-3.

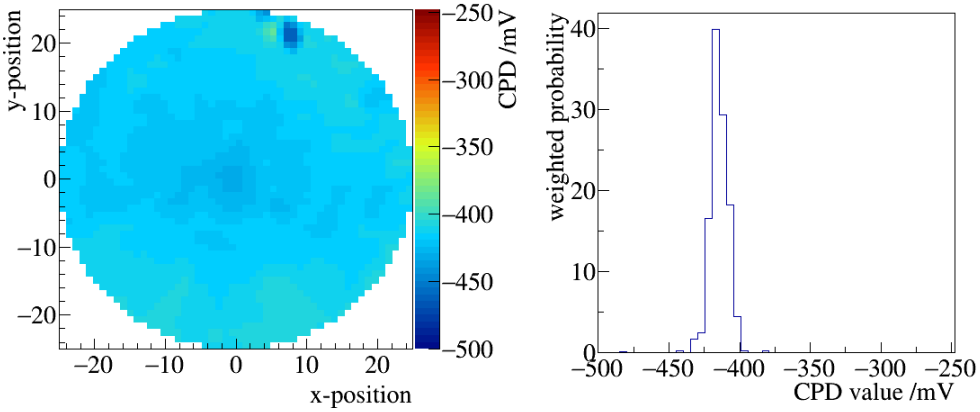

Figure E.73: CPD map and histogram of the 3. scan of sample 6-SS-ep-3.

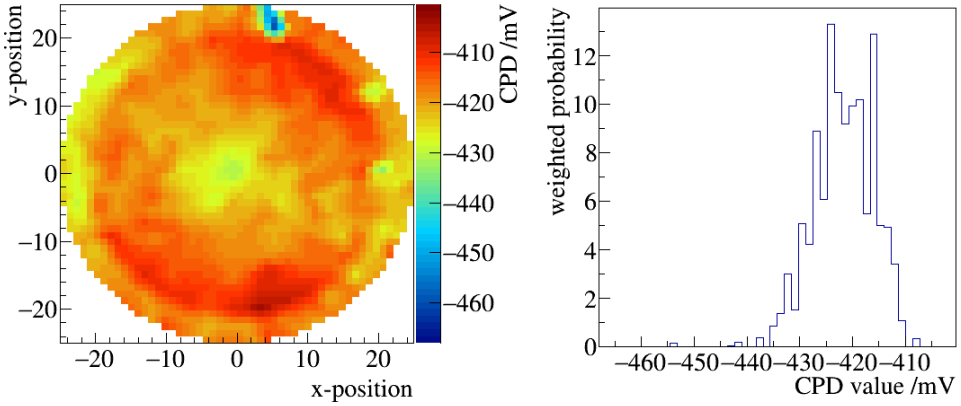

Figure E.74: CPD map and histogram of the 4. scan of sample 6-SS-ep-3.

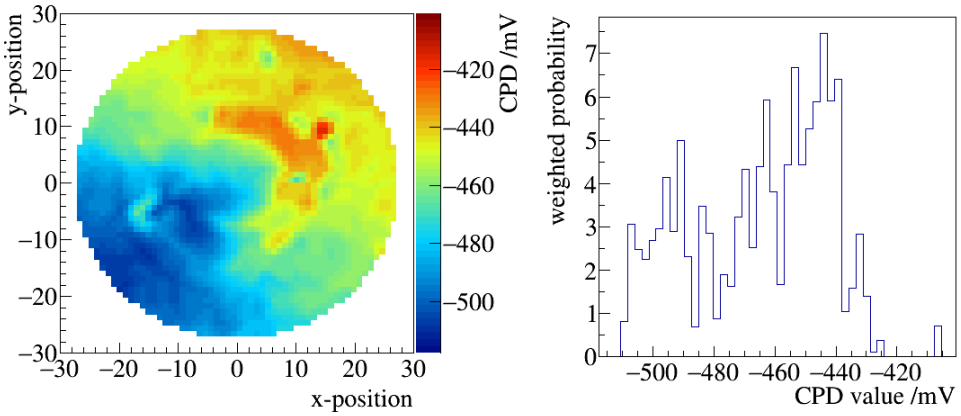

Figure E.75: CPD map and histogram of the 1. scan of sample 6-SS-ep-3 after 1. bake-out.

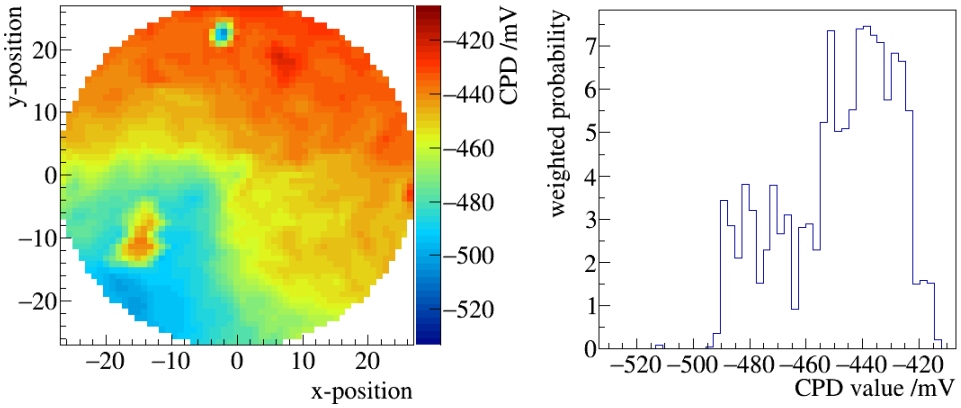

Figure E.76: CPD map and histogram of the 2. scan of sample 6-SS-ep-3 after 1. bake-out.

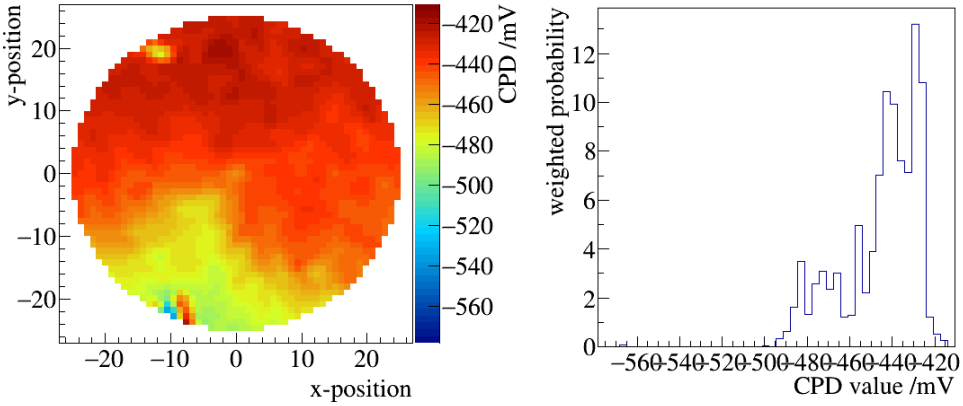

Figure E.77: CPD map and histogram of the 3. scan of sample 6-SS-ep-3 after 1. bake-out.

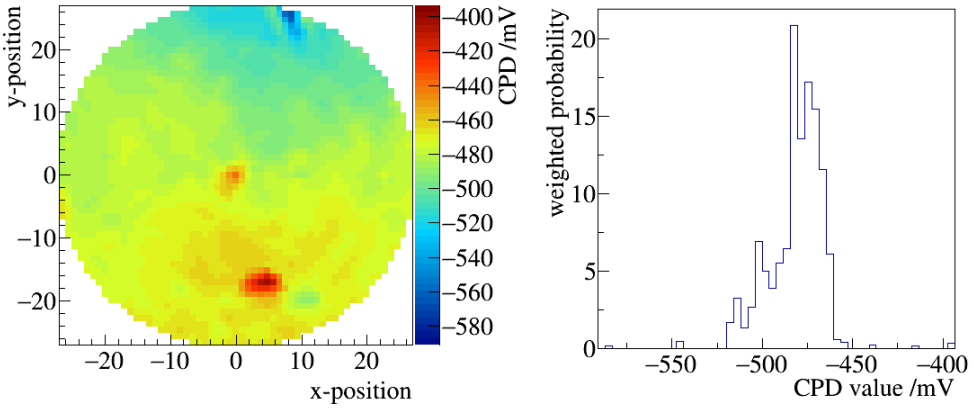

Figure E.78: CPD map and histogram of the 1. scan of sample 6-SS-ep-3 after 2. bake-out.

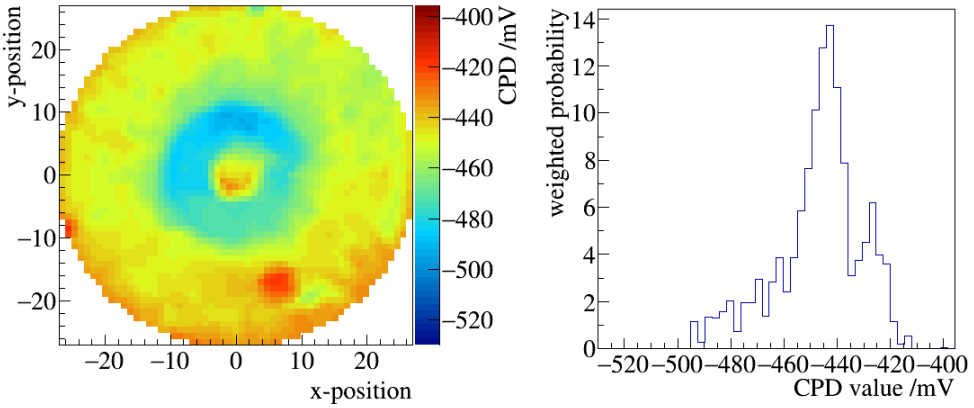

Figure E.79: CPD map and histogram of the 2. scan of sample 6-SS-ep-3 after 2. bake-out.

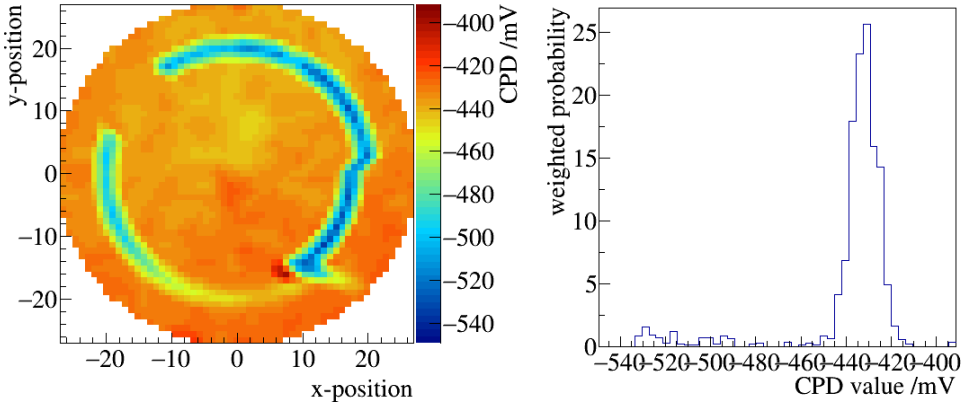

Figure E.80: CPD map and histogram of the 3. scan of sample 6-SS-ep-3 after 2. bake-out. As the ring of lower CPD (blue) is following the scanning behavior of the Kelvin Probe, it is most probably caused by a particle between tip and sample.

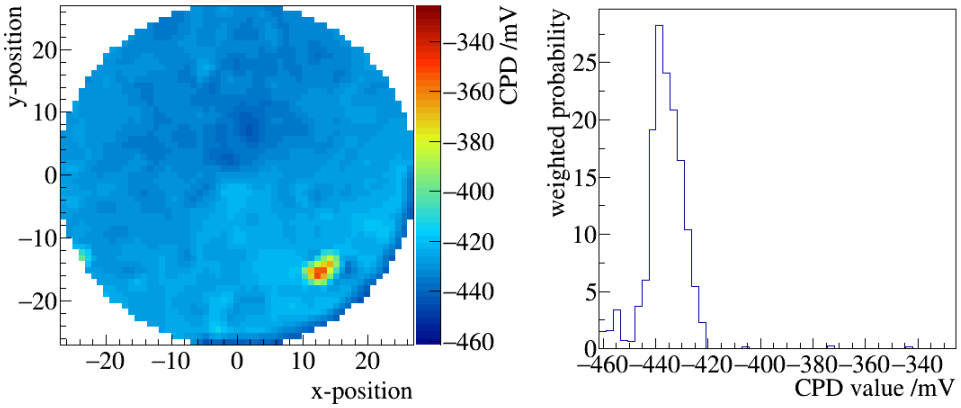

Figure E.81: CPD map and histogram of the 4. scan of sample 6-SS-ep-3 after 2. bake-out.

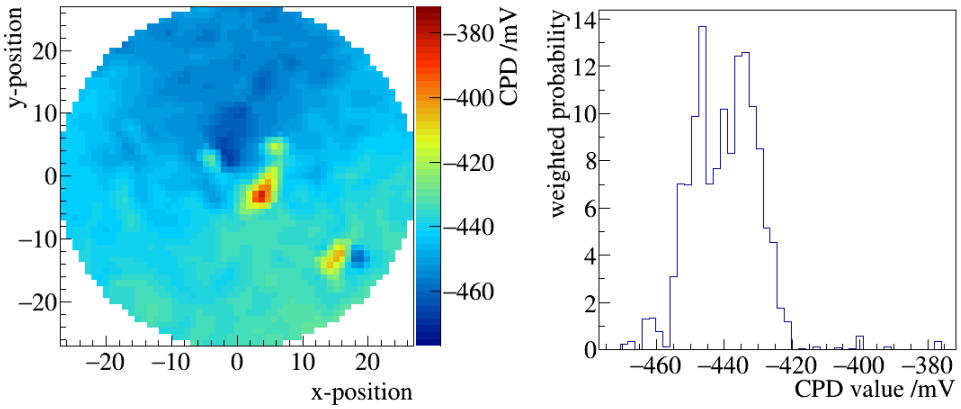

Figure E.82: CPD map and histogram of the 5. scan of sample 6-SS-ep-3 after 2. bake-out.

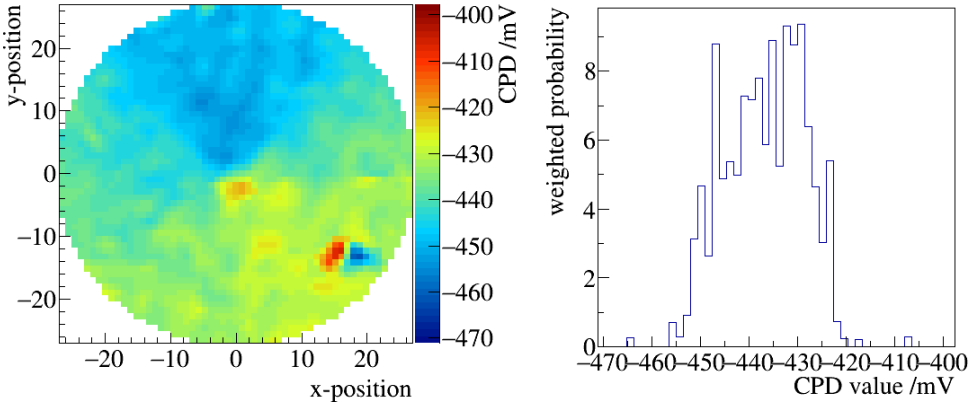

Figure E.83: CPD map and histogram of the 6. scan of sample 6-SS-ep-3 after 2. bake-out.

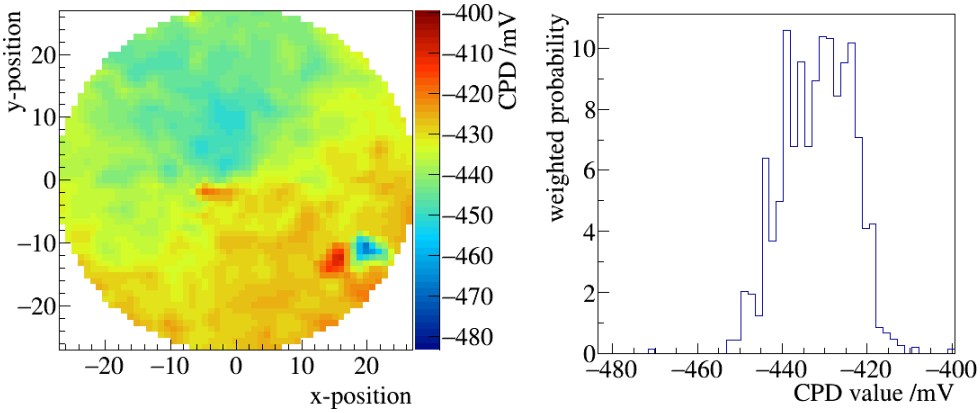

Figure E.84: CPD map and histogram of the 7. scan of sample 6-SS-ep-3 after 2. bake-out.

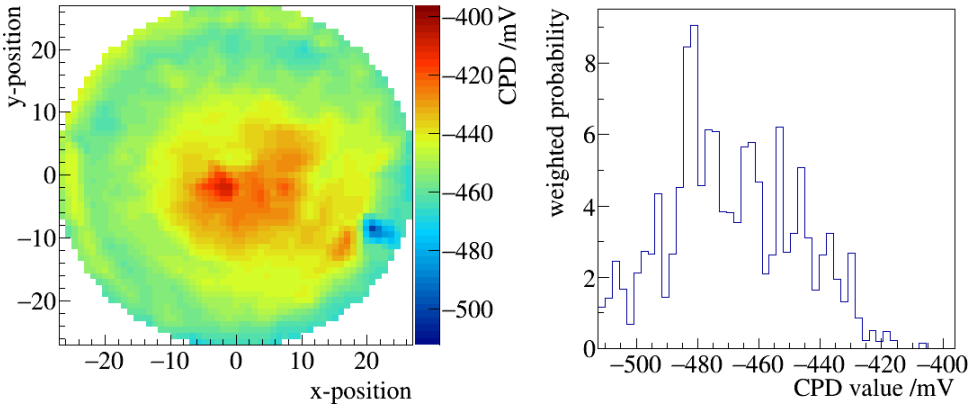

Figure E.85: CPD map and histogram of the 8. scan of sample 6-SS-ep-3 after 2. bake-out.

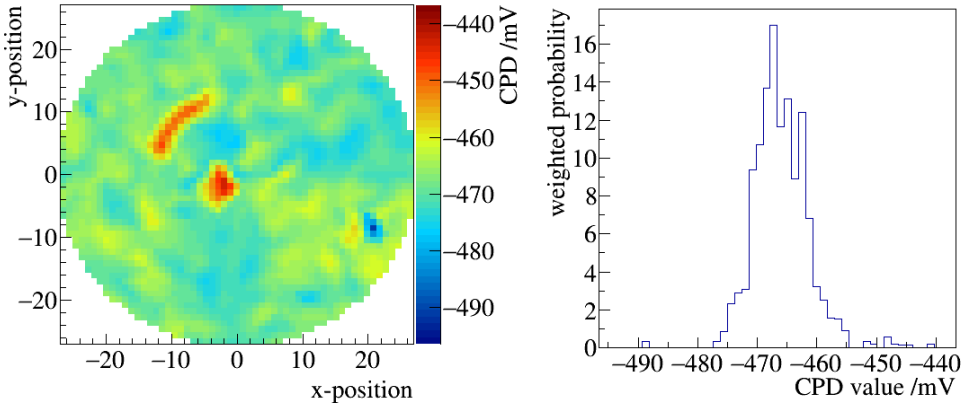

Figure E.86: CPD map and histogram of the 9. scan of sample 6-SS-ep-3 after 2. bake-out.

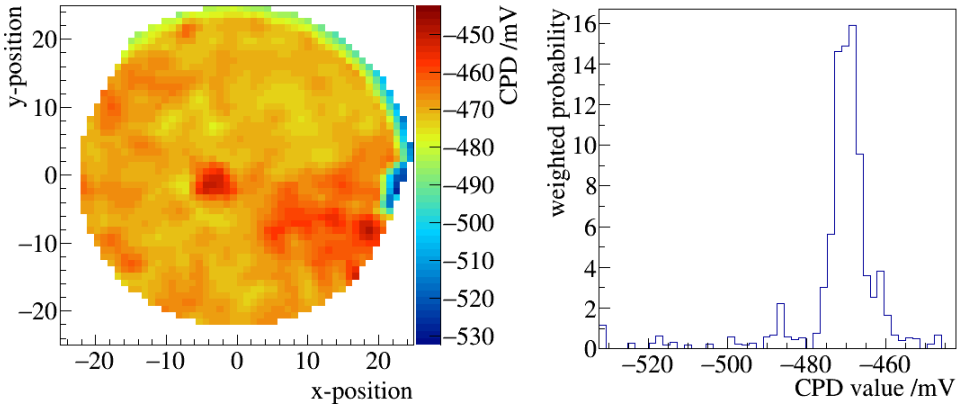

Figure E.87: CPD map and histogram of the 10. scan of sample 6-SS-ep-3 after 2. bake-out.

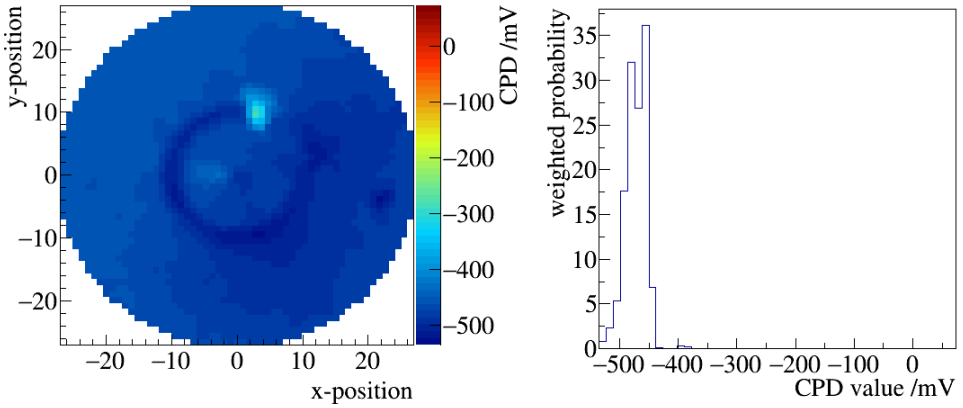

Figure E.88: CPD map and histogram of the 11. scan of sample 6-SS-ep-3 after 2. bake-out.

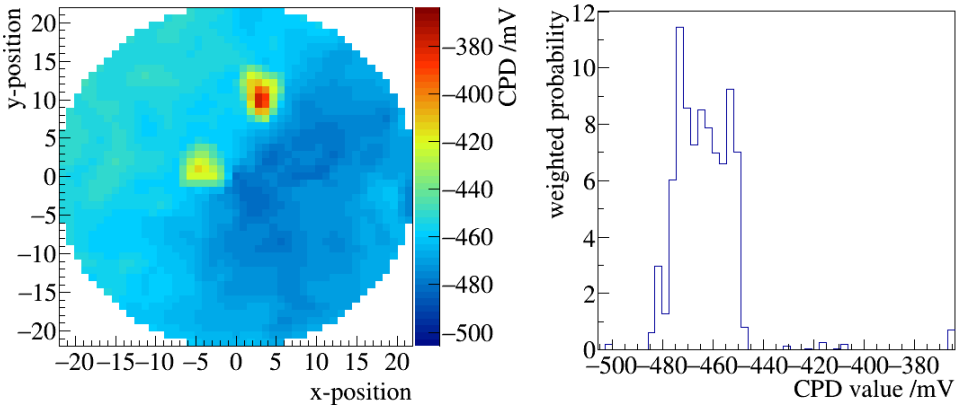

Figure E.89: CPD map and histogram of the 12. scan of sample 6-SS-ep-3 after 2. bake-out.

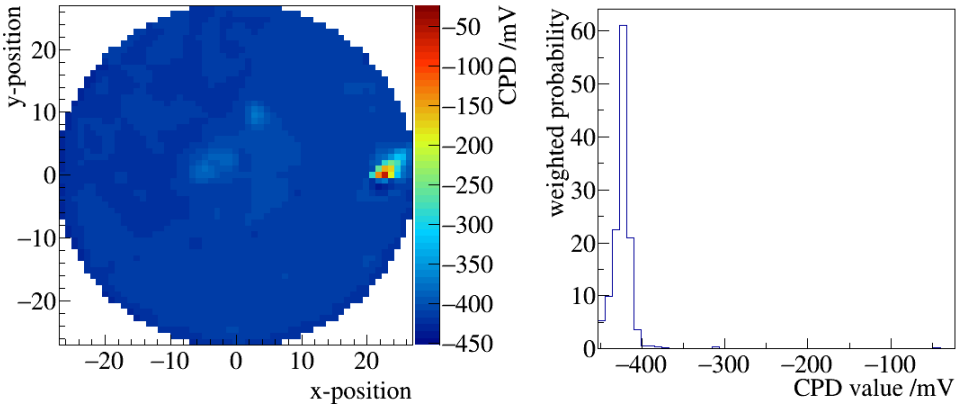

Figure E.90: CPD map and histogram of the 13. scan of sample 6-SS-ep-3 after 2. bake-out. The point of higher CPD is probably caused by a scratch as it can be found in several scans from now on. This scratch is the result of a contact between tip and sample and can be seen by eye.

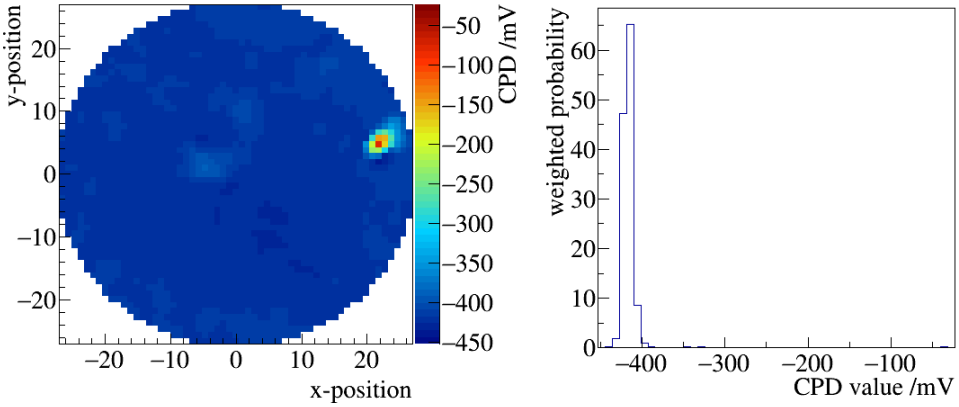

Figure E.91: CPD map and histogram of the 14. scan of sample 6-SS-ep-3 after 2. bake-out. The point of higher CPD is probably caused by a scratch as it can be found in several scans. This scratch is the result of a contact between tip and sample and can be seen by eye.

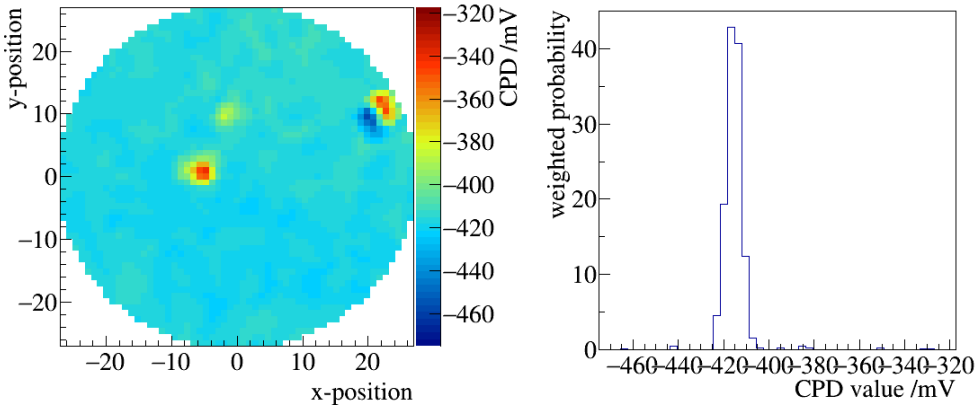

Figure E.92: CPD map and histogram of the 15. scan of sample 6-SS-ep-3 after 2. bake-out. The points of higher CPD are probably caused by scratches as they can be found in several scans. These scratches are the result of a contact between tip and sample and can be seen by eye.

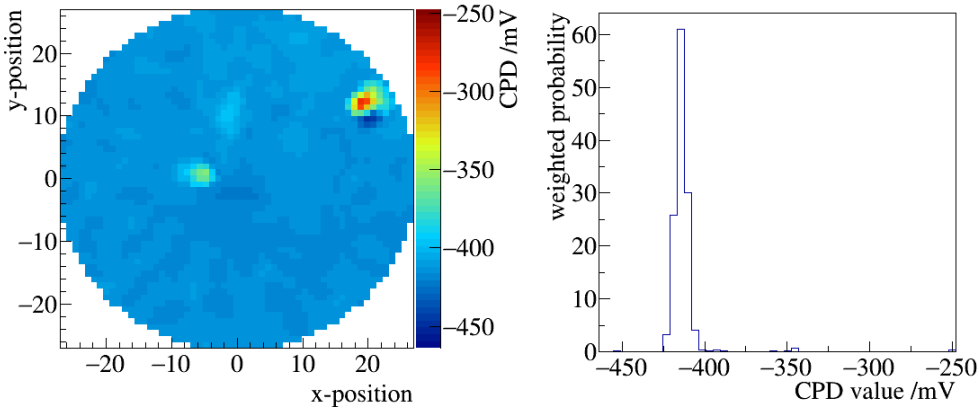

Figure E.93: CPD map and histogram of the 16. scan of sample 6-SS-ep-3 after 2. bake-out. The points of higher CPD are probably caused by scratches as they can be found in several scans. These scratches are the result of a contact between tip and sample and can be seen by eye.

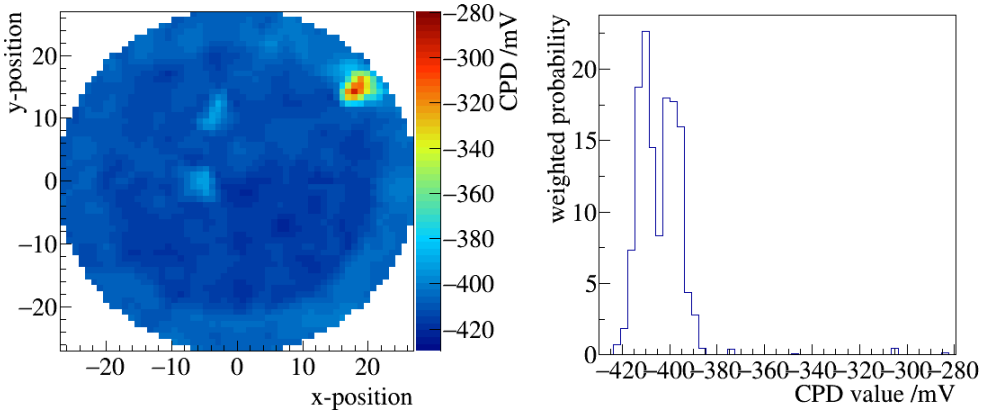

Figure E.94: CPD map and histogram of the 17. scan of sample 6-SS-ep-3 after 2. bake-out. The points of higher CPD are probably caused by scratches as they can be found in several scans. These scratches are the result of a contact between tip and sample and can be seen by eye.

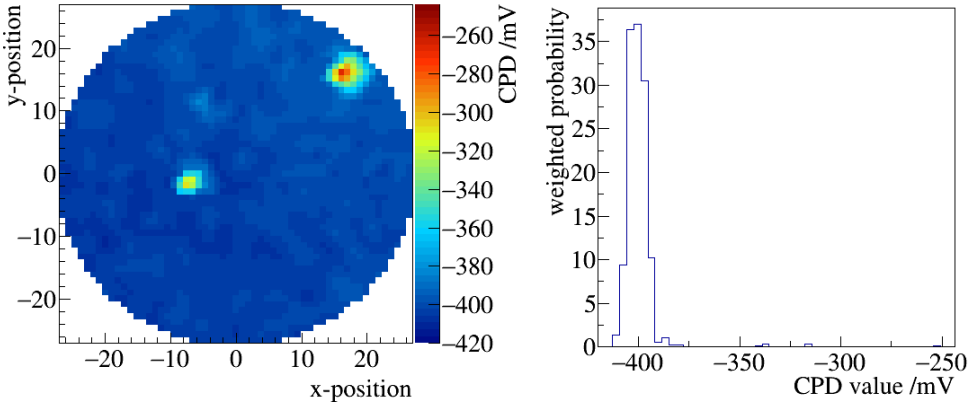

Figure E.95: CPD map and histogram of the 18. scan of sample 6-SS-ep-3 after 2. bake-out. The points of higher CPD are probably caused by scratches as they can be found in several scans. These scratches are the result of a contact between tip and sample and can be seen by eye.

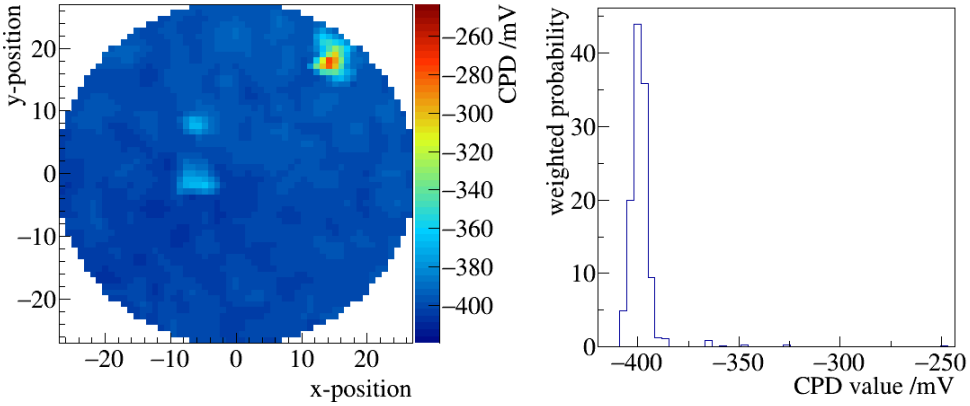

Figure E.96: CPD map and histogram of the 19. scan of sample 6-SS-ep-3 after 2. bake-out. The points of higher CPD are probably caused by scratches as they can be found in several scans. These scratches are the result of a contact between tip and sample and can be seen by eye.

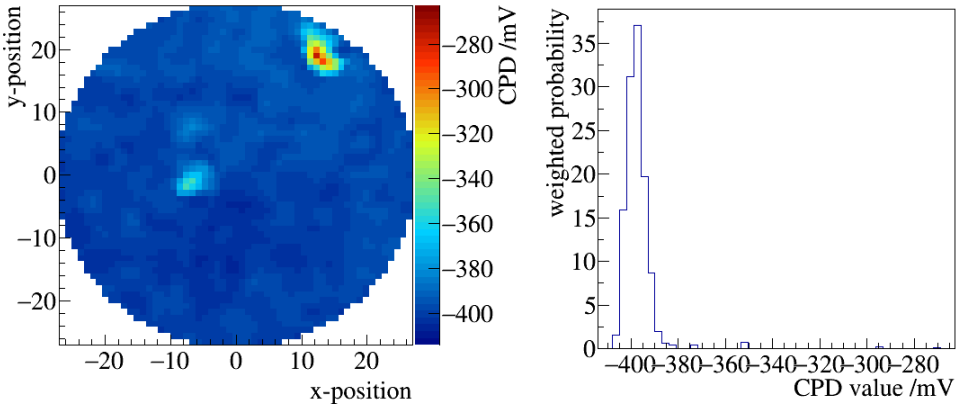

Figure E.97: CPD map and histogram of the 20. scan of sample 6-SS-ep-3 after 2. bake-out. The points of higher CPD are probably caused by scratches as they can be found in several scans. These scratches are the result of a contact between tip and sample and can be seen by eye.

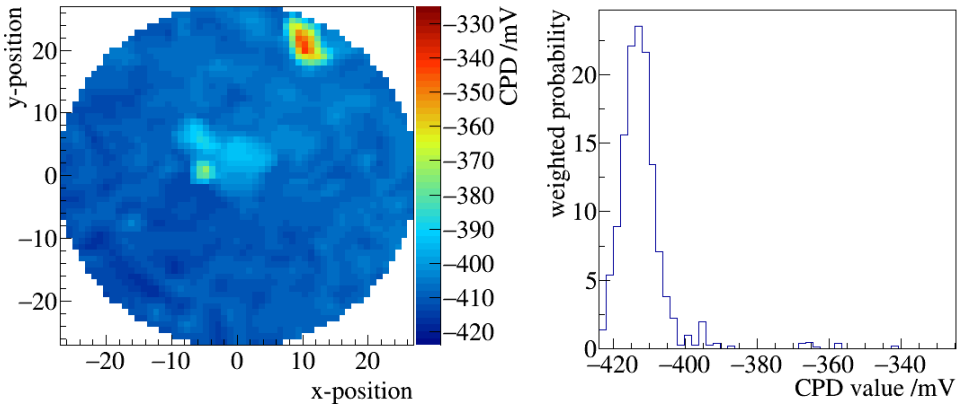

Figure E.98: CPD map and histogram of the 21. scan of sample 6-SS-ep-3 after 2. bake-out. The points of higher CPD are probably caused by scratches as they can be found in several scans. These scratches are the result of a contact between tip and sample and can be seen by eye.

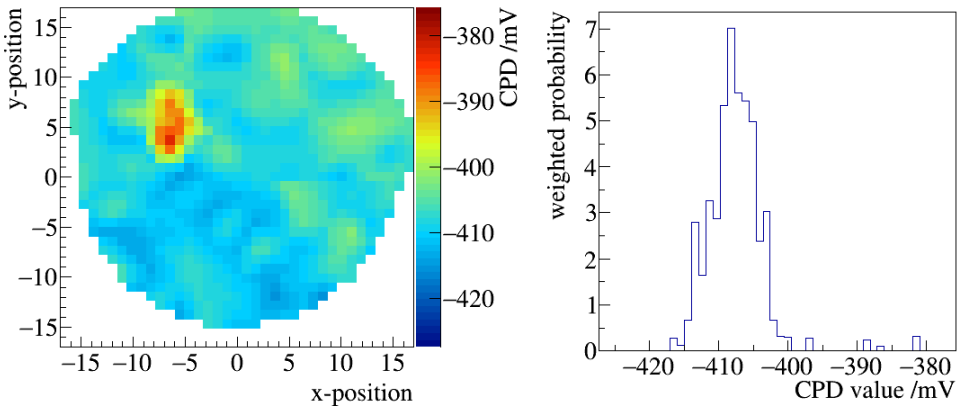

Figure E.99: CPD map and histogram of the 22. scan of sample 6-SS-ep-3 after 2. bake-out. The point of higher CPD is probably caused by a scratch as it can be found in several scans. This scratch is the result of a contact between tip and sample and can be seen by eye.

Results of the measurements performed on sample 6-SS-ep-3

Table E.5: CPD and $\sigma_{\mathrm{RMS,surface}}$ over the whole samples 6-SS-el-3. * marks uncompleted scans.

scan	baked	mean CPD of whole sample /mV	$\sigma_{\mathrm{RMS,surface}}$ /mV
1*	-	-416.7	18.4
2*	-	-422.0	13.8
3	-	-416.0	6.8
4	-	-418.5	5.8
5	-	-424.0	5.4
1	once	-465.1	22.3
2	once	-454.2	19.6
3*	once	-445.1	19.1
4*	once	-455.9	3.8
1	twice	-481.5	15.6
2	twice	-451.8	13.9
3	twice	-440.5	23.4
4	twice	-430.1	8.0
5	twice	-443.8	9.9
6	twice	-439.1	8.1
7	twice	-435.2	7.6
8	twice	-449.0	11.3
9	twice	-468.4	4.9
10*	twice	-471.8	10.3
11	twice	-476.0	20.4
12*	twice	-463.3	12.5
13	twice	-415.7	21.0
14	twice	-419.2	19.8
15	twice	-416.4	8.3
16	twice	-413.8	10.4
17	twice	-409.9	9.7
18	twice	-400.6	11.5
19	twice	-398.8	9.9
20	twice	-397.5	9.7
21	twice	-407.8	7.2
22*	twice	-407.4	4.6

Measurements performed at sample 7-SS-ep-3

In this section the results of sample 7-SS-ep-3 are presented. First the CPD maps are plotted and then the numeric values of CPD and $\sigma_{\mathrm{RMS,surface}}$ are summarized subsequently. Both are presented in chronological ordering.

CPD maps of the measurements performed on sample 7-SS-ep-3

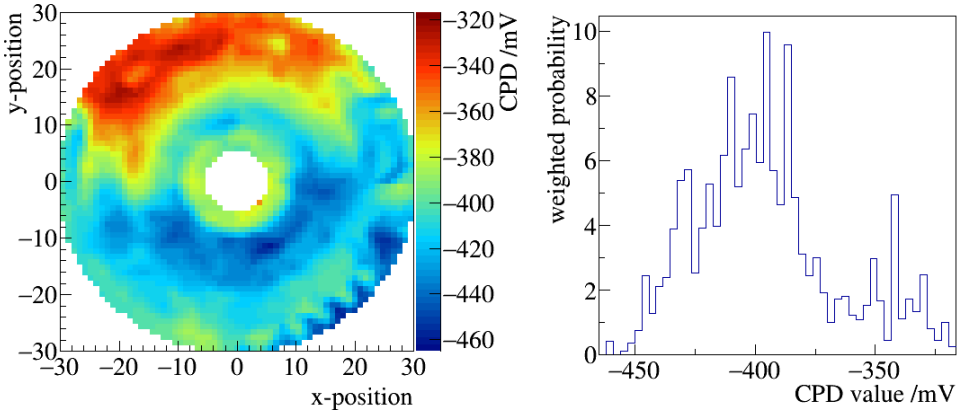

Figure E.100: CPD map and histogram of the 2. scan of sample 7-SS-ep-3.

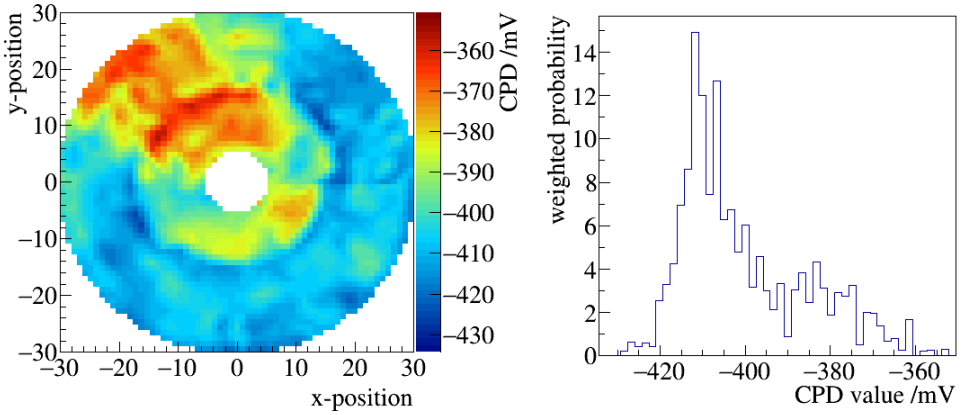

Figure E.101: CPD map and histogram of the 3. scan of sample 7-SS-ep-3.

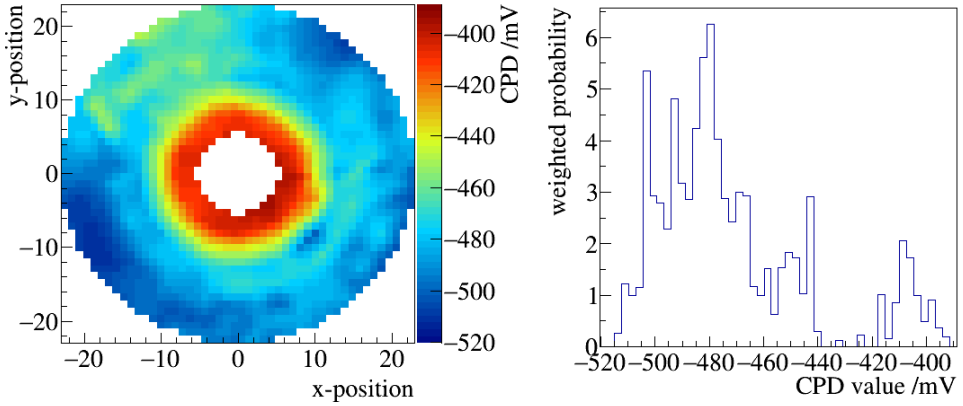

Figure E.102: CPD map and histogram of the 4. scan of sample 7-SS-ep-3.

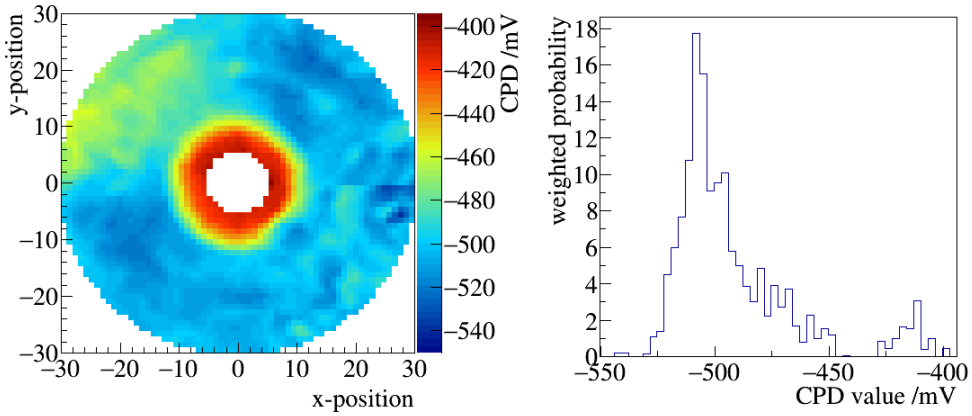

Figure E.103: CPD map and histogram of the 5. scan of sample 7-SS-ep-3.

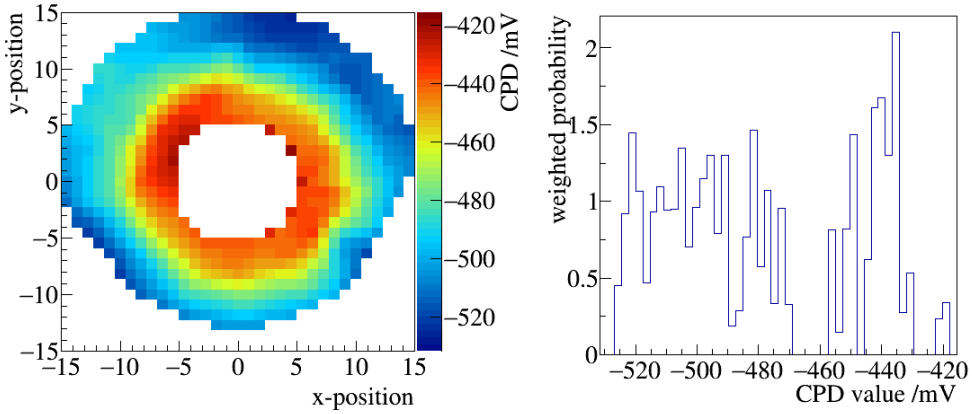

Figure E.104: CPD map and histogram of the 6. scan of sample 7-SS-ep-3.

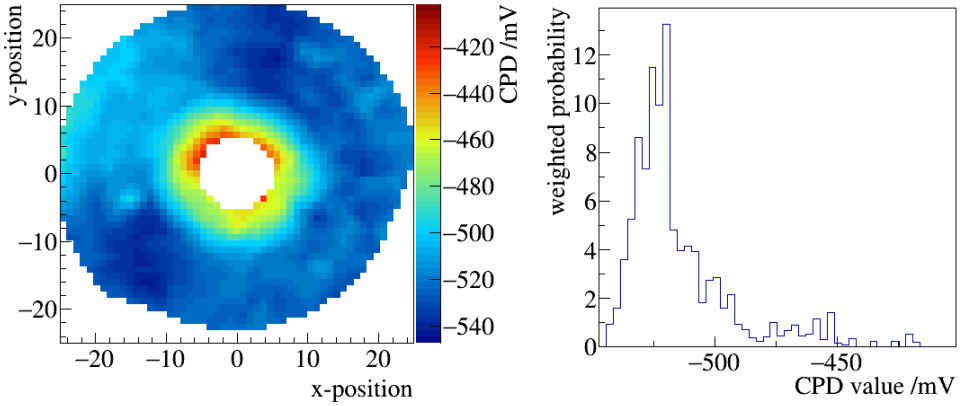

Figure E.105: CPD map and histogram of the 7. scan of sample 7-SS-ep-3.

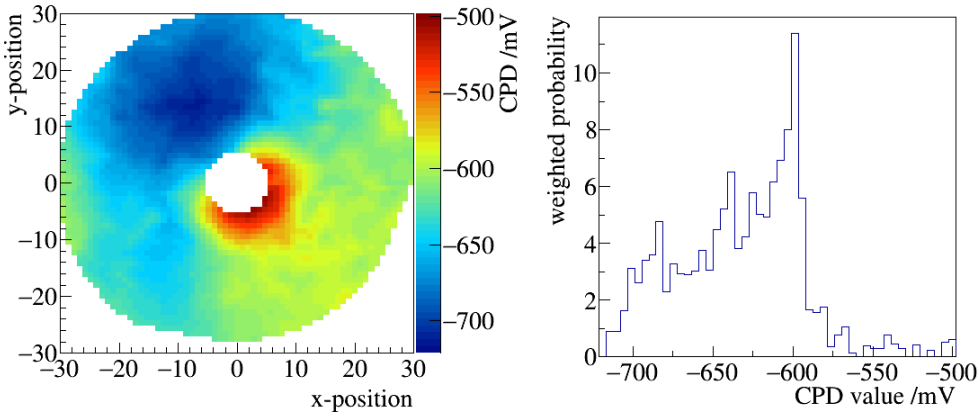

Figure E.106: CPD map and histogram of the 8. scan of sample 7-SS-ep-3.

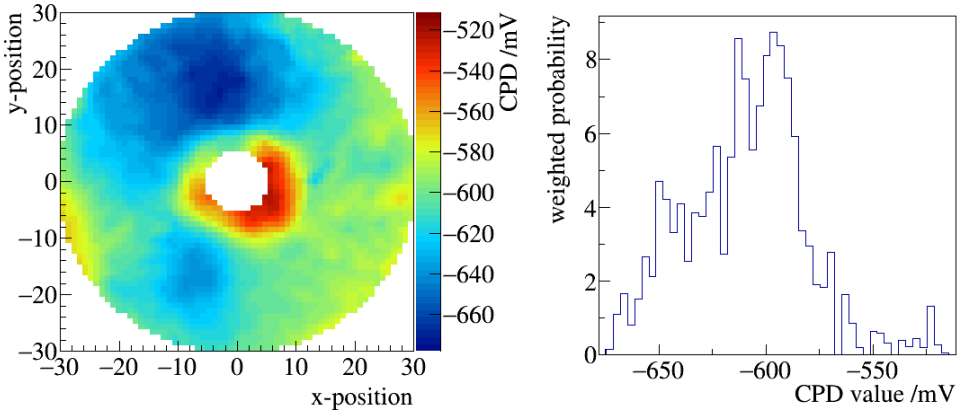

Figure E.107: CPD map and histogram of the 9. scan of sample 7-SS-ep-3.

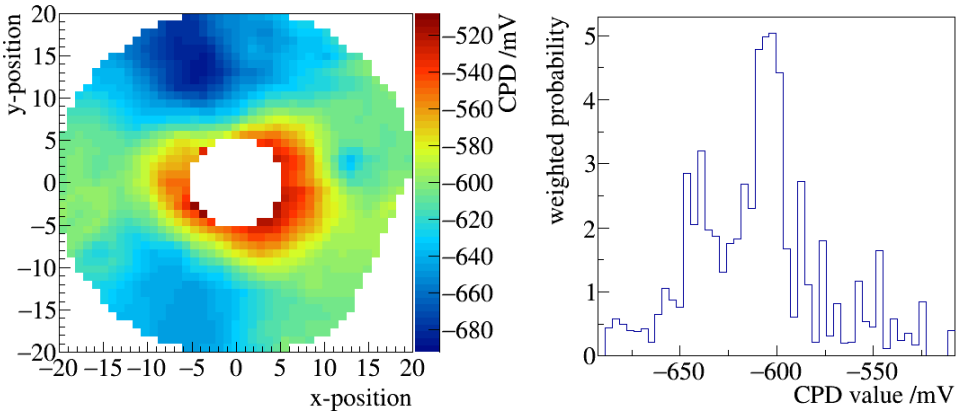

Figure E.108: CPD map and histogram of the 10. scan of sample 7-SS-ep-3.

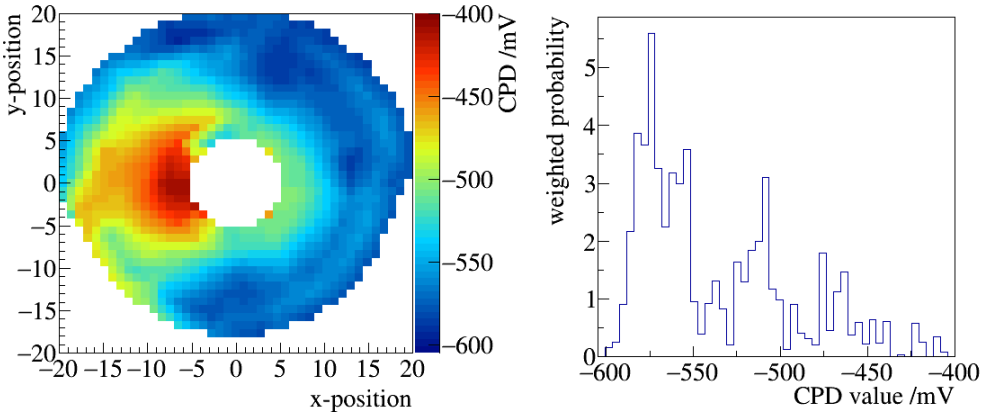

Figure E.109: CPD map and histogram of the 11. scan of sample 7-SS-ep-3.

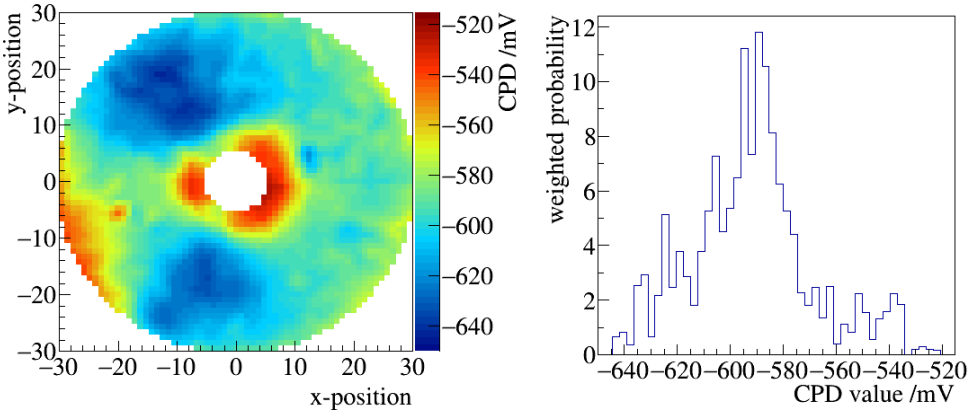

Figure E.110: CPD map and histogram of the 12. scan of sample 7-SS-ep-3.

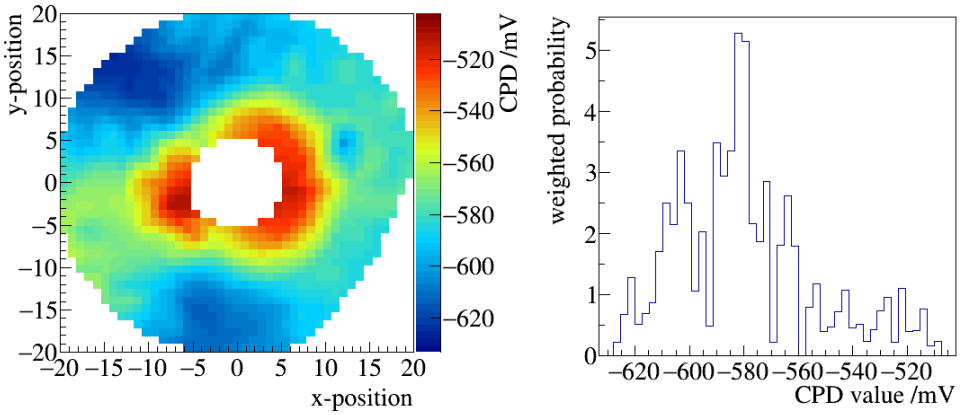

Figure E.111: CPD map and histogram of the 13. scan of sample 7-SS-ep-3.

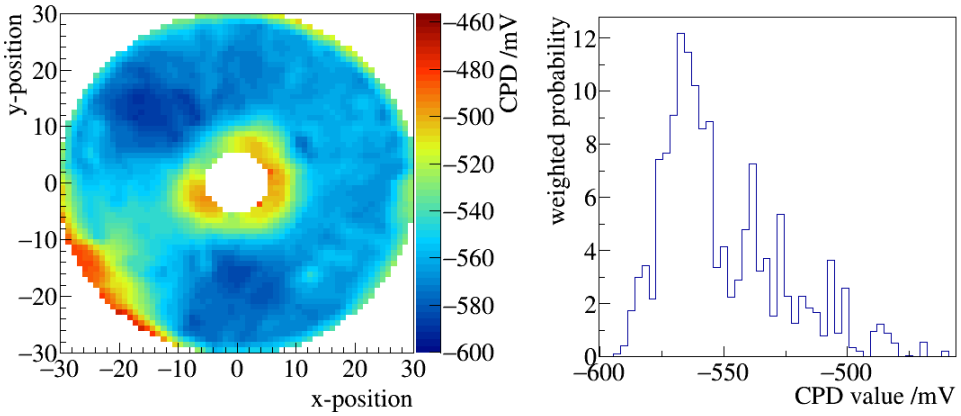

Figure E.112: CPD map and histogram of the 14. scan of sample 7-SS-ep-3.

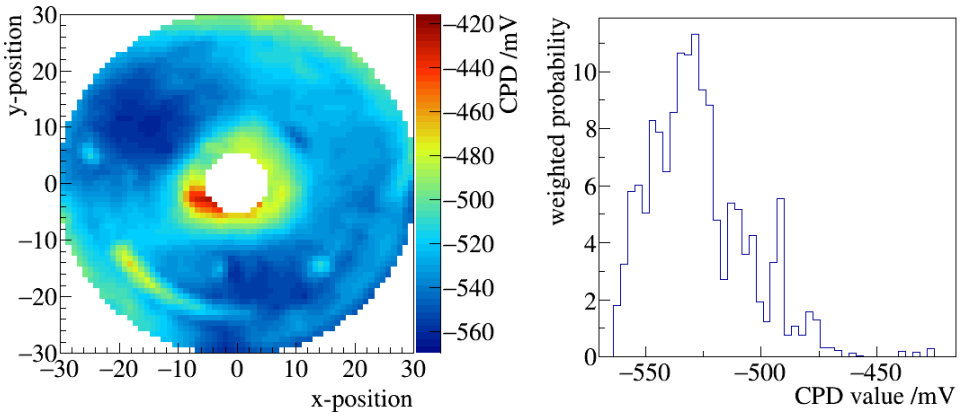

Figure E.113: CPD map and histogram of the 15. scan of sample 7-SS-ep-3.

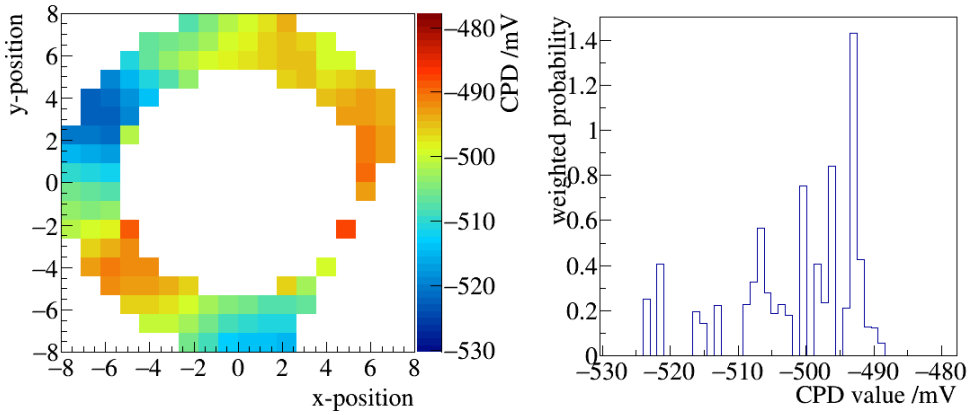

Figure E.114: CPD map and histogram of the 16. scan of sample 7-SS-ep-3.

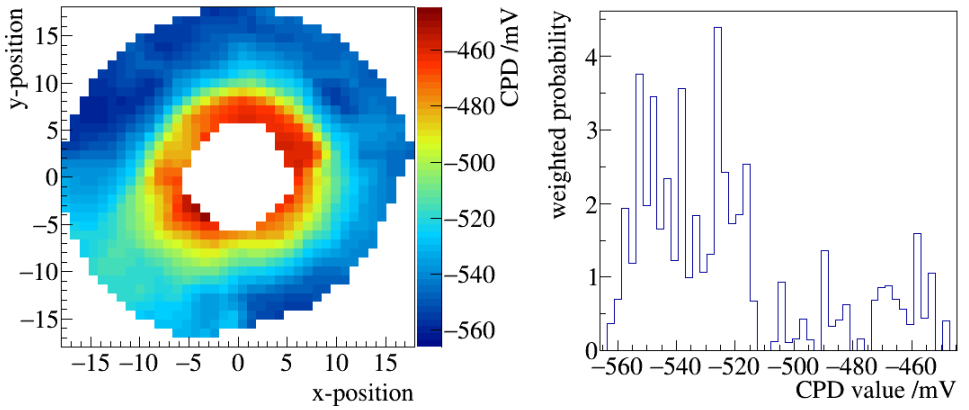

Figure E.115: CPD map and histogram of the 17. scan of sample 7-SS-ep-3.

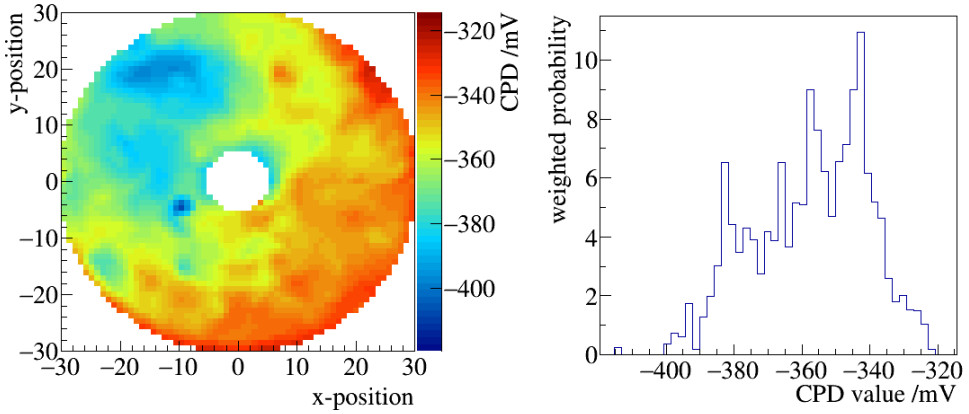

Figure E.116: CPD map and histogram of the 1. scan of sample 7-SS-ep-3 after venting.

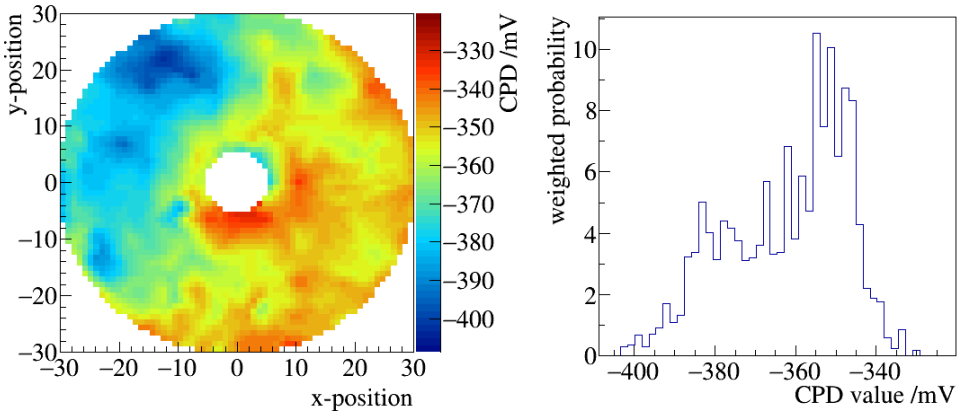

Figure E.117: CPD map and histogram of the 2. scan of sample 7-SS-ep-3 after venting.

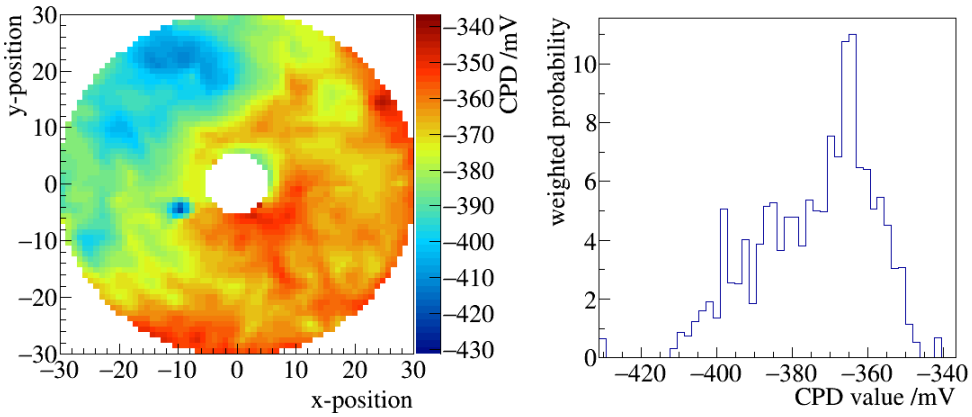

Figure E.118: CPD map and histogram of the 3. scan of sample 7-SS-ep-3 after venting.

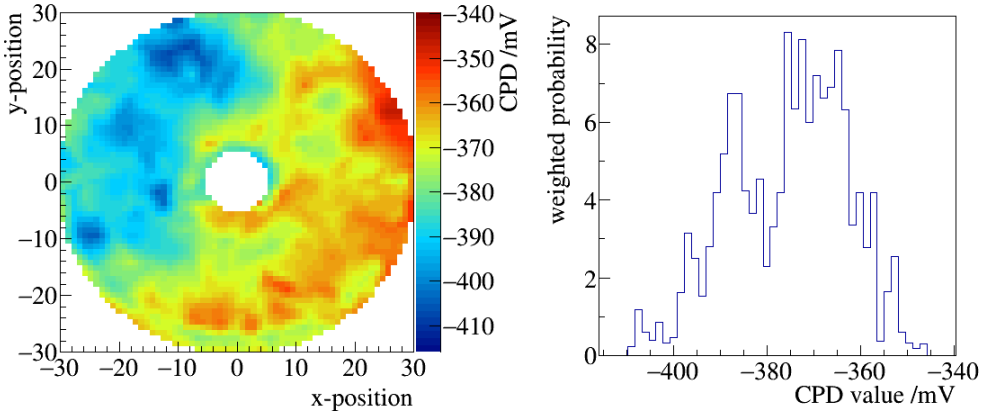

Figure E.119: CPD map and histogram of the 4. scan of sample 7-SS-ep-3 after venting.

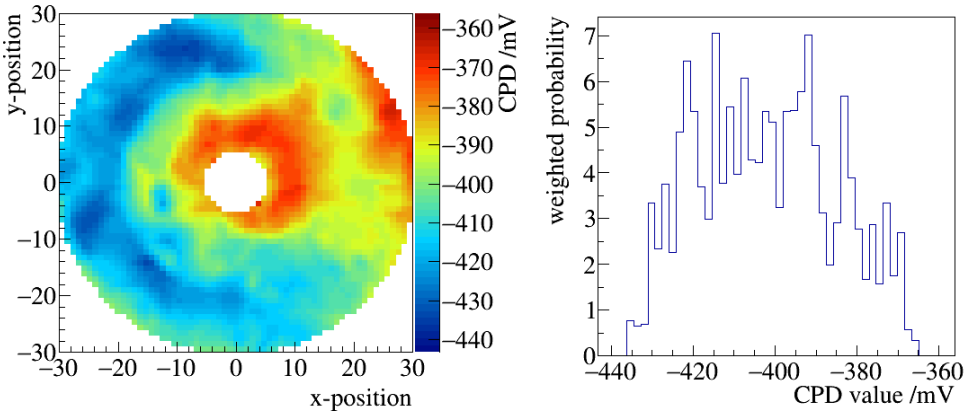

Figure E.120: CPD map and histogram of the 5. scan of sample 7-SS-ep-3 after venting.

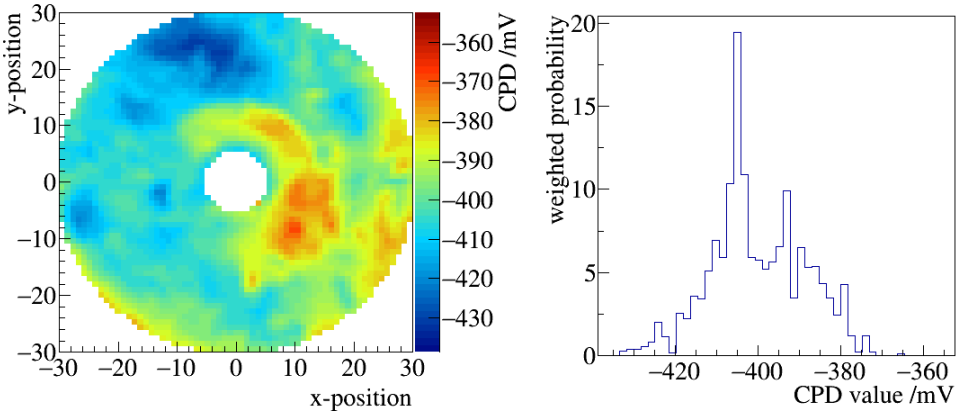

Figure E.121: CPD map and histogram of the 6. scan of sample 7-SS-ep-3 after venting.

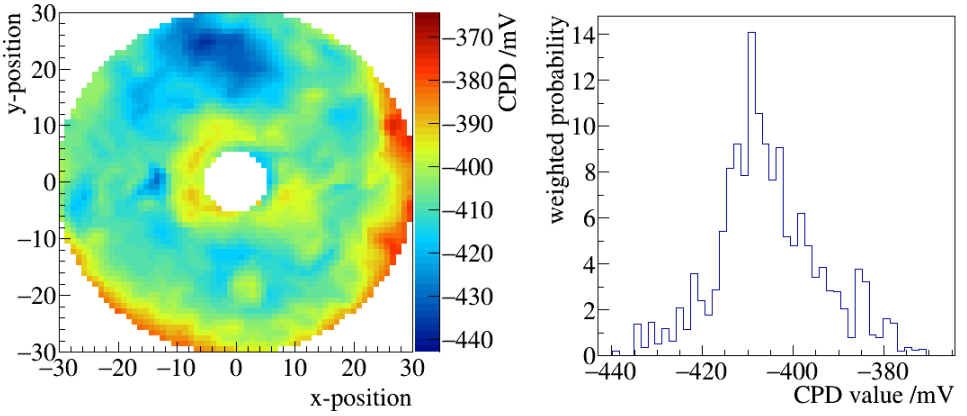

Figure E.122: CPD map and histogram of the 7. scan of sample 7-SS-ep-3 after venting.

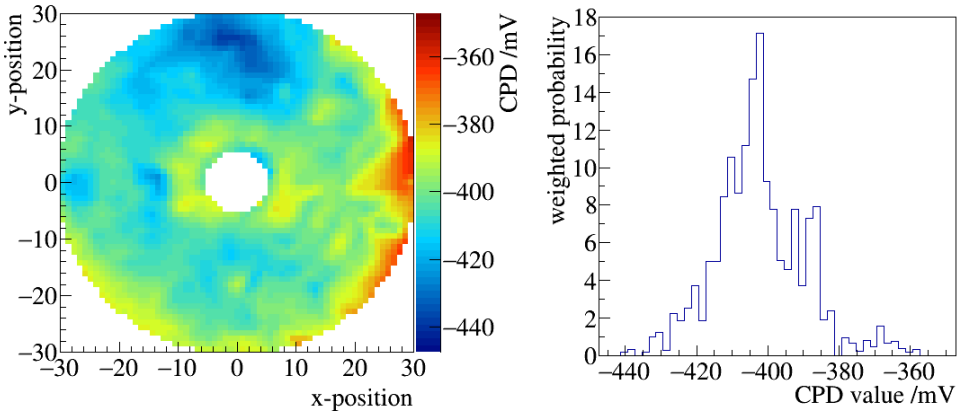

Figure E.123: CPD map and histogram of the 8. scan of sample 7-SS-ep-3 after venting.

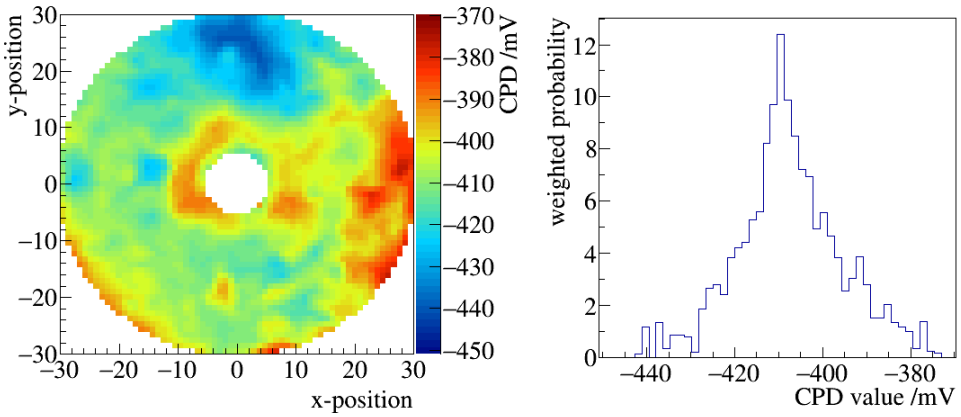

Figure E.124: CPD map and histogram of the 9. scan of sample 7-SS-ep-3 after venting.

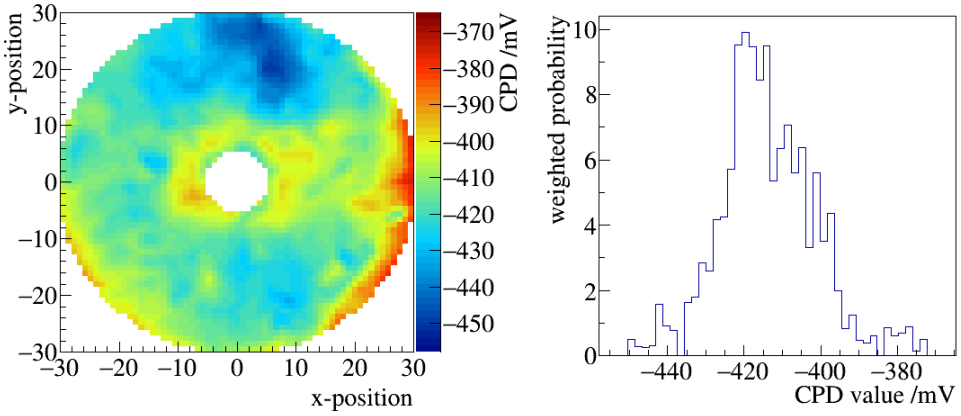

Figure E.125: CPD map and histogram of the 10. scan of sample 7-SS-ep-3 after venting.

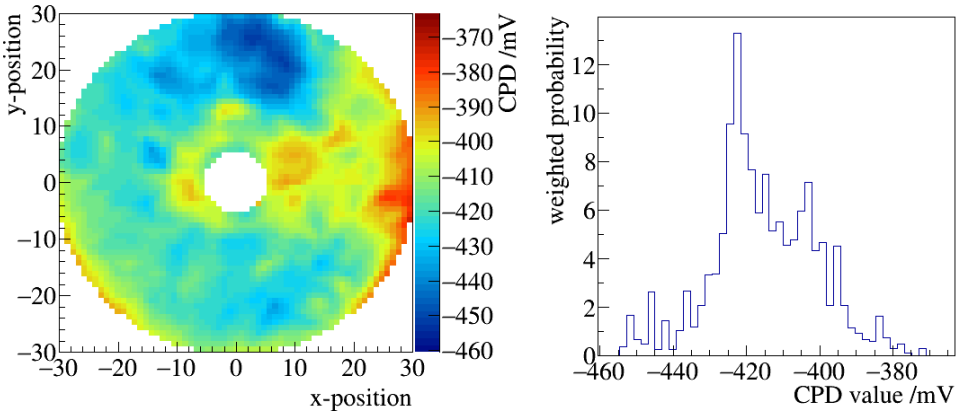

Figure E.126: CPD map and histogram of the 11. scan of sample 7-SS-ep-3 after venting.

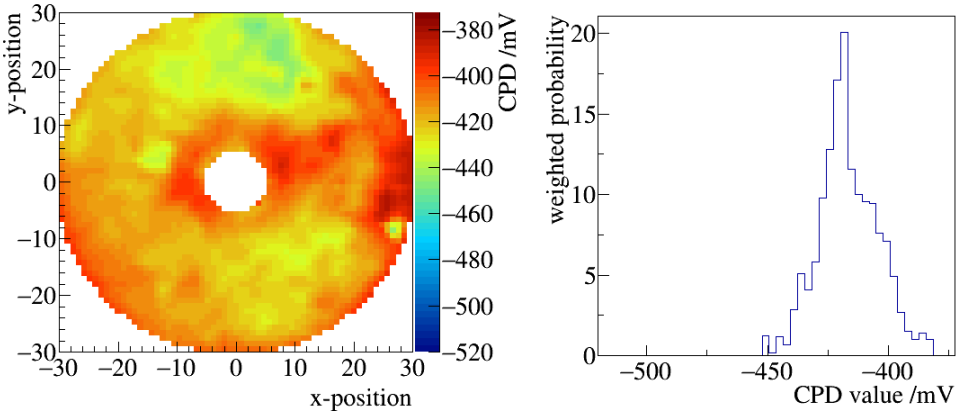

Figure E.127: CPD map and histogram of the 12. scan of sample 7-SS-ep-3 after venting.

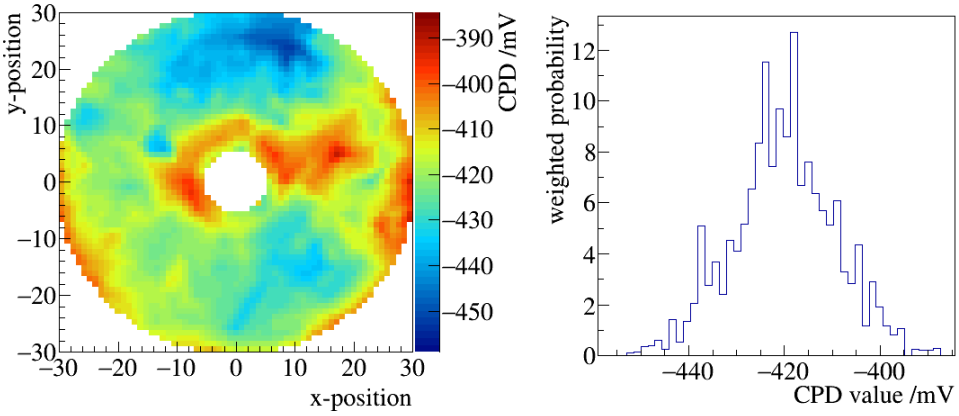

Figure E.128: CPD map and histogram of the 13. scan of sample 7-SS-ep-3 after venting.

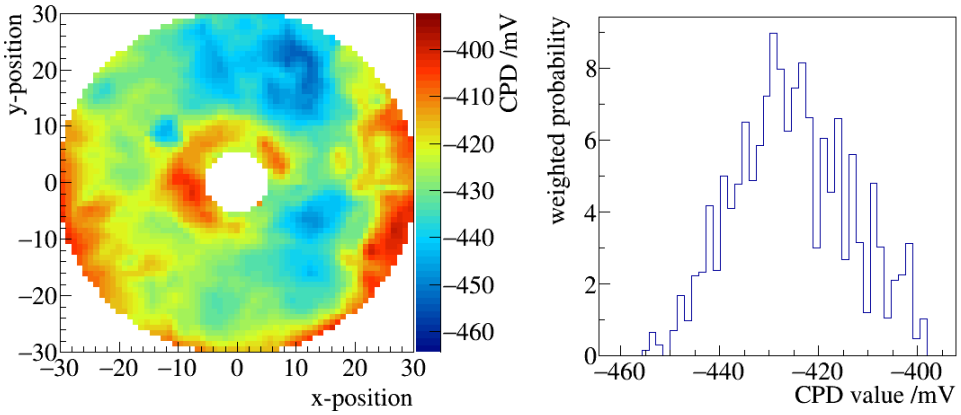

Figure E.129: CPD map and histogram of the 14. scan of sample 7-SS-ep-3 after venting.

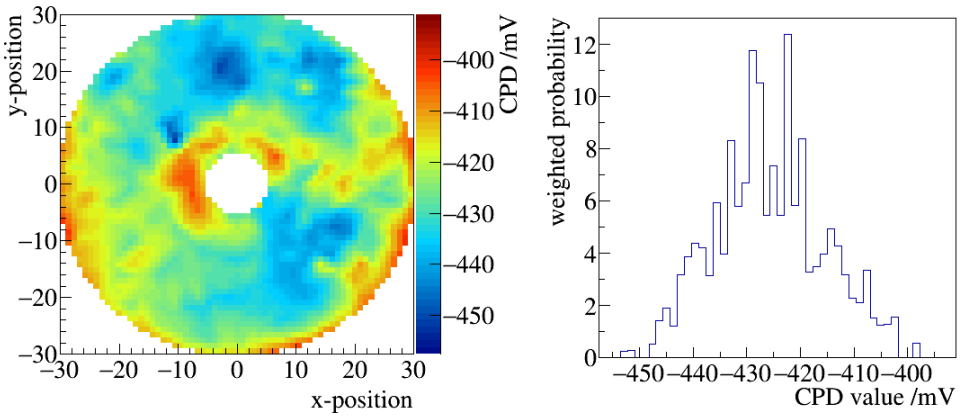

Figure E.130: CPD map and histogram of the 15. scan of sample 7-SS-ep-3 after venting.

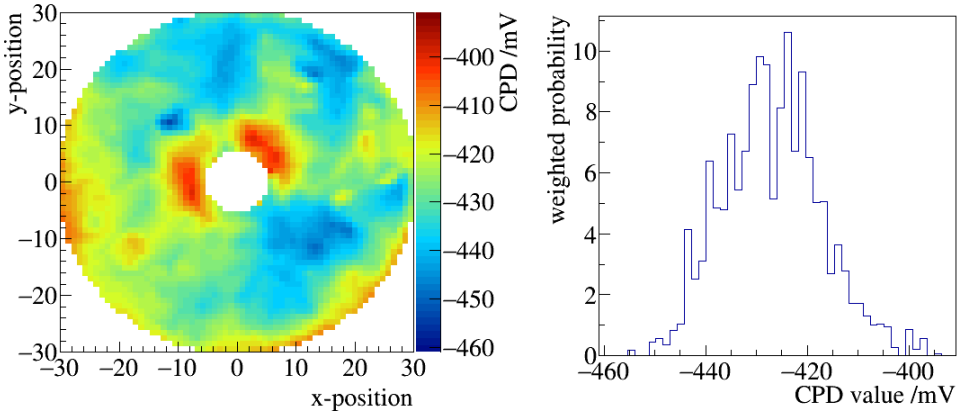

Figure E.131: CPD map and histogram of the 16. scan of sample 7-SS-ep-3 after venting.

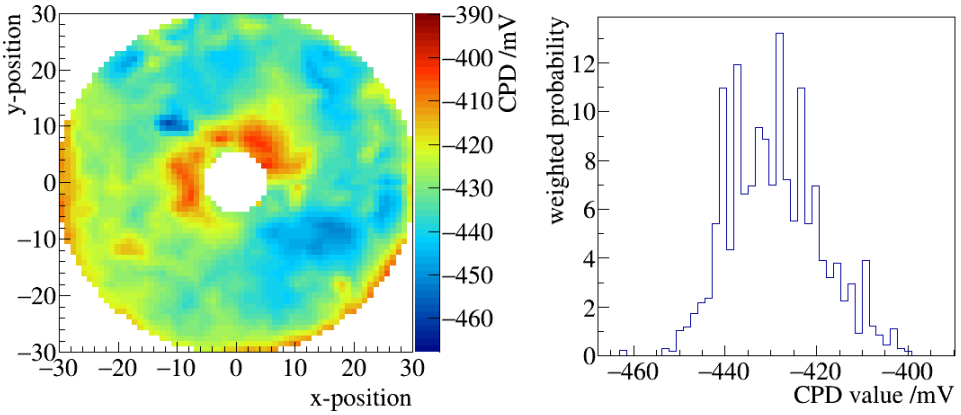

Figure E.132: CPD map and histogram of the 17. scan of sample 7-SS-ep-3 after venting.

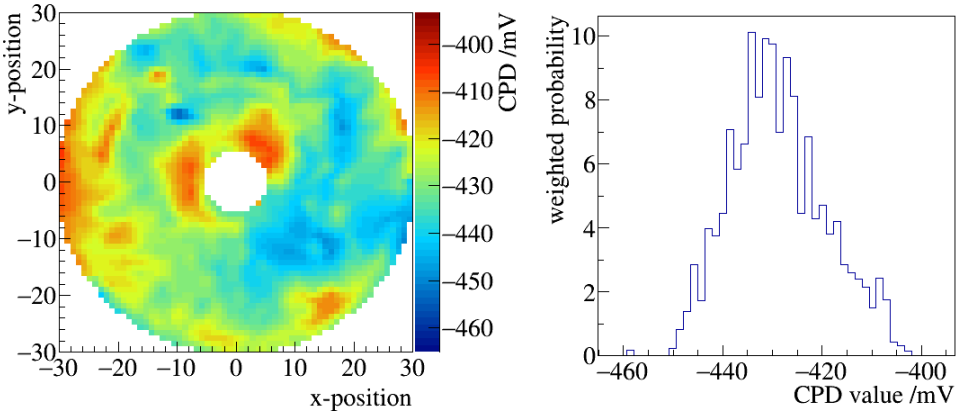

Figure E.133: CPD map and histogram of the 18. scan of sample 7-SS-ep-3 after venting.

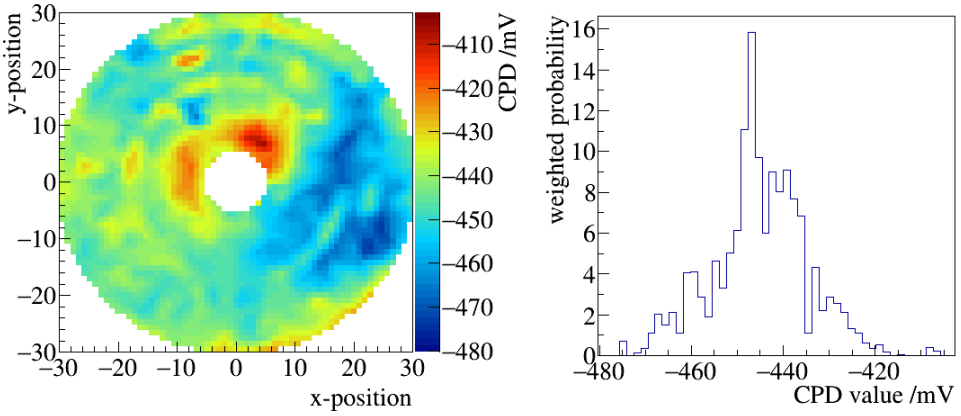

Figure E.134: CPD map and histogram of the 19. scan of sample 7-SS-ep-3 after venting.

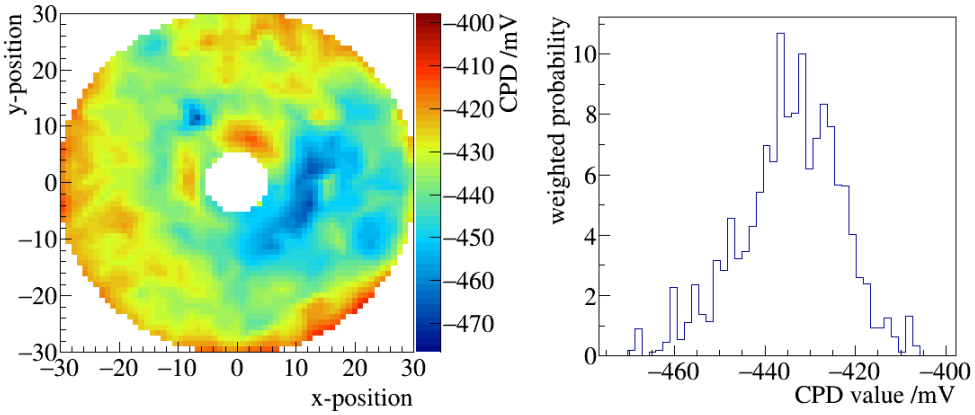

Figure E.135: CPD map and histogram of the 20. scan of sample 7-SS-ep-3 after venting.

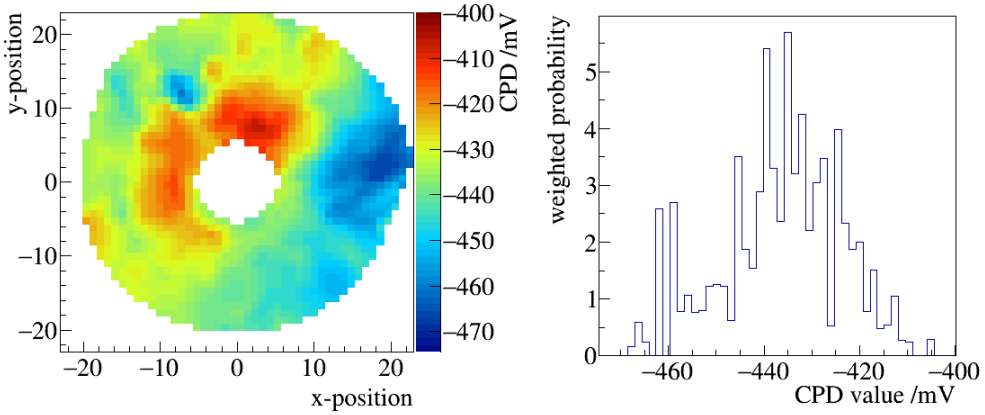

Figure E.136: CPD map and histogram of the 21. scan of sample 7-SS-ep-3 after venting.

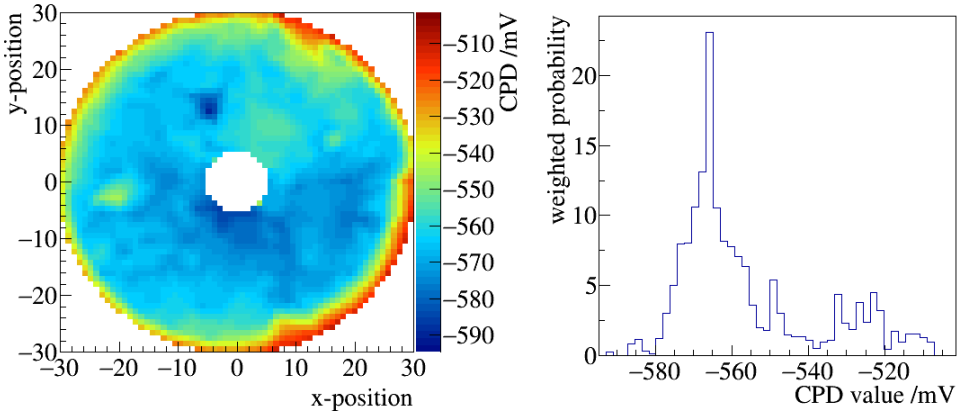

Figure E.137: CPD map and histogram of the 1. scan of sample 7-SS-ep-3 after bake-out.

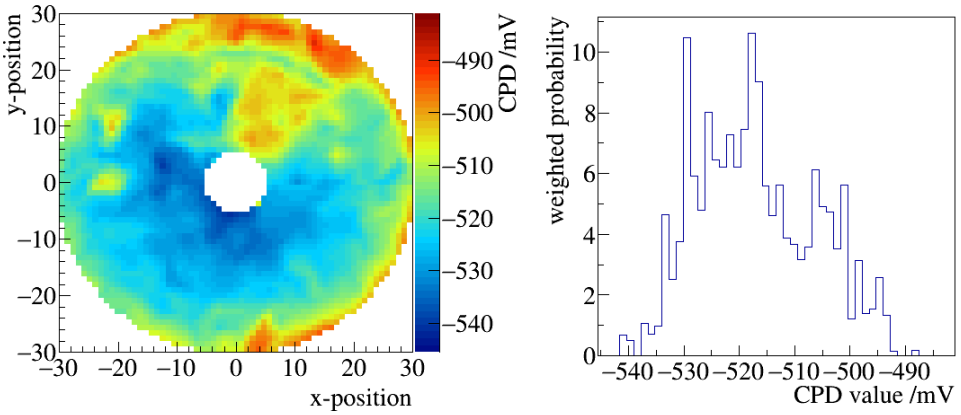

Figure E.138: CPD map and histogram of the 2. scan of sample 7-SS-ep-3 after bake-out.

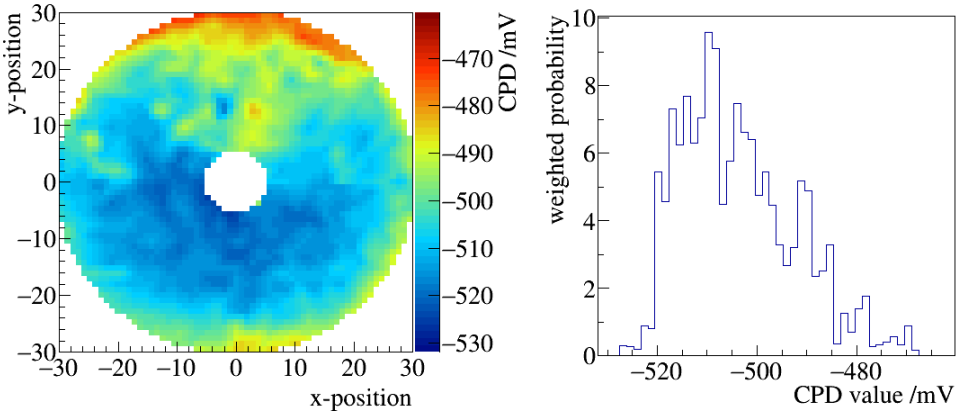

Figure E.139: CPD map and histogram of the 3. scan of sample 7-SS-ep-3 after bake-out.

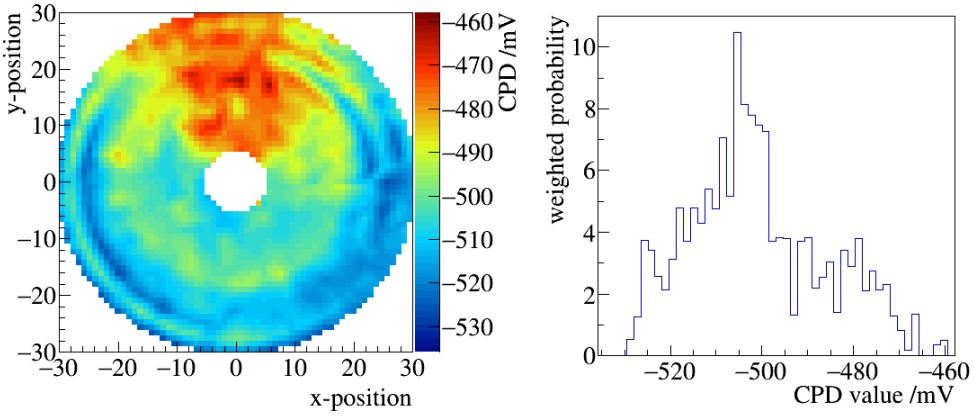

Figure E.140: CPD map and histogram of the 4. scan of sample 7-SS-ep-3 after bake-out.

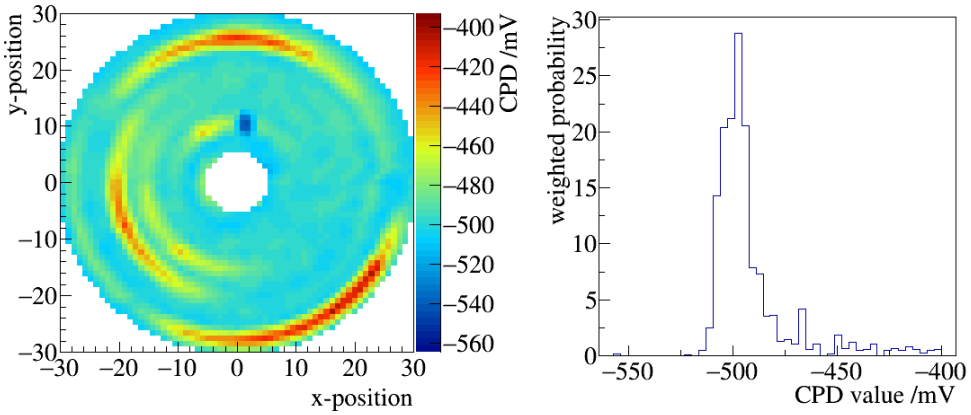

Figure E.141: CPD map and histogram of the 5. scan of sample 7-SS-ep-3 after bake-out. The ring like structures with higher CPD are caused by a damage of the surface. The tip is scratched over the surface for a complete circle by mistake. In doing so the gold is scrapped away. Similar rings can be found in all scan from now on due to that.

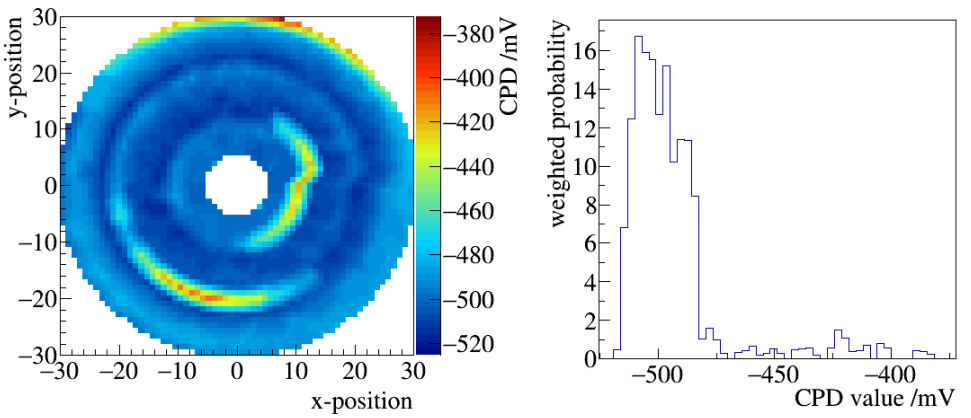

Figure E.142: CPD map and histogram of the 6. scan of sample 7-SS-ep-3 after bake-out. The ring like structures with higher CPD are caused by a damage of the surface (compare figure E.141).

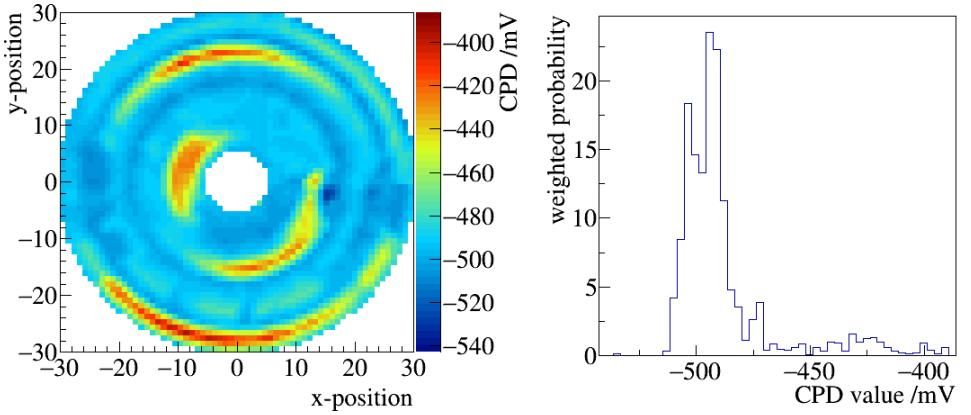

Figure E.143: CPD map and histogram of the 7. scan of sample 7-SS-ep-3 after bake-out. The ring like structures with higher CPD are caused by a damage of the surface (compare figure E.141).

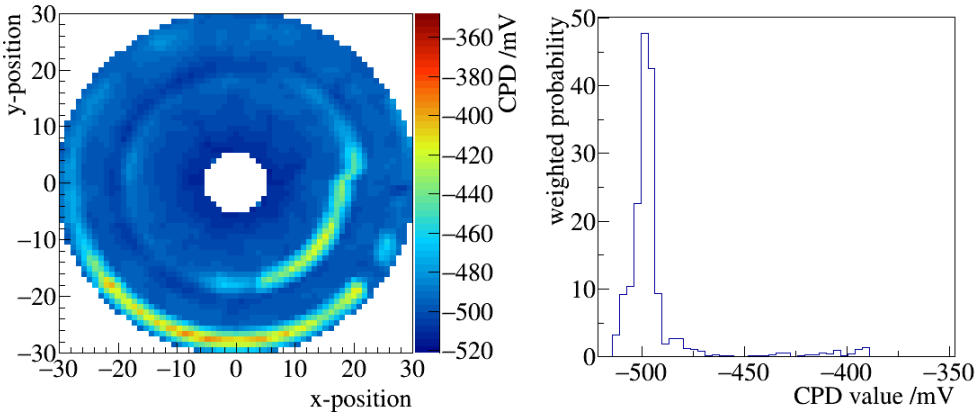

Figure E.144: CPD map and histogram of the 8. scan of sample 7-SS-ep-3 after bake-out. The ring like structures with higher CPD are caused by a damage of the surface (compare figure E.141).

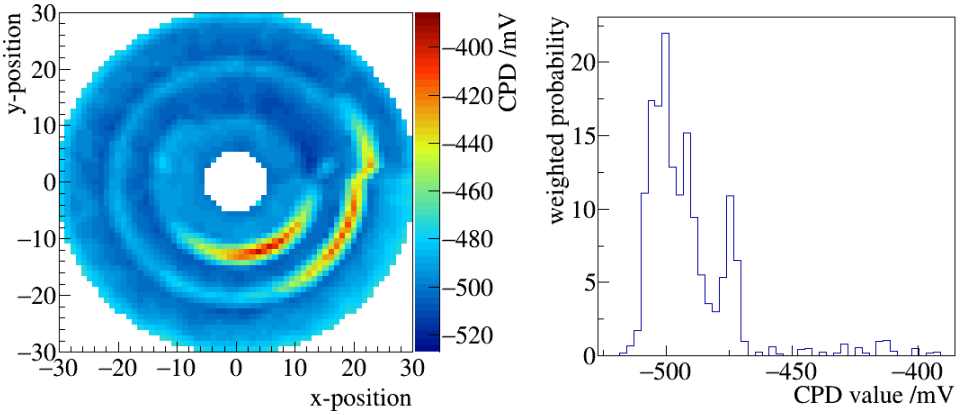

Figure E.145: CPD map and histogram of the 9. scan of sample 7-SS-ep-3 after bake-out. The ring like structures with higher CPD are caused by a damage of the surface (compare figure E.141).

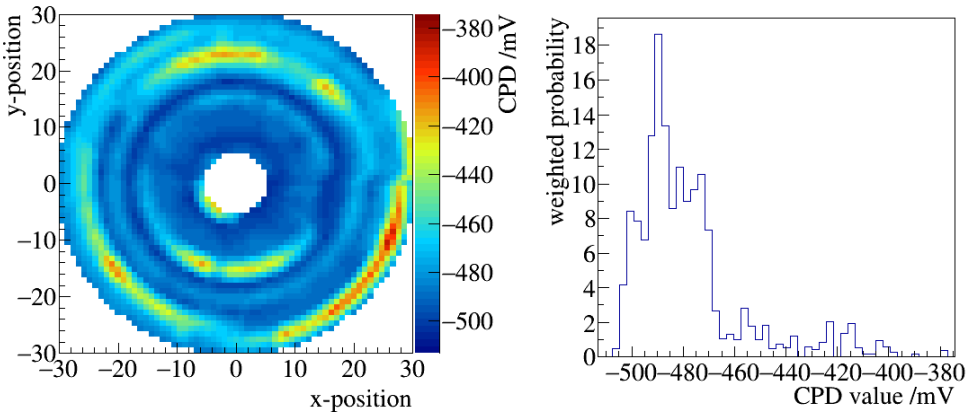

Figure E.146: CPD map and histogram of the 10. scan of sample 7-SS-ep-3 after bake-out. The ring like structures with higher CPD are caused by a damage of the surface (compare figure E.141).

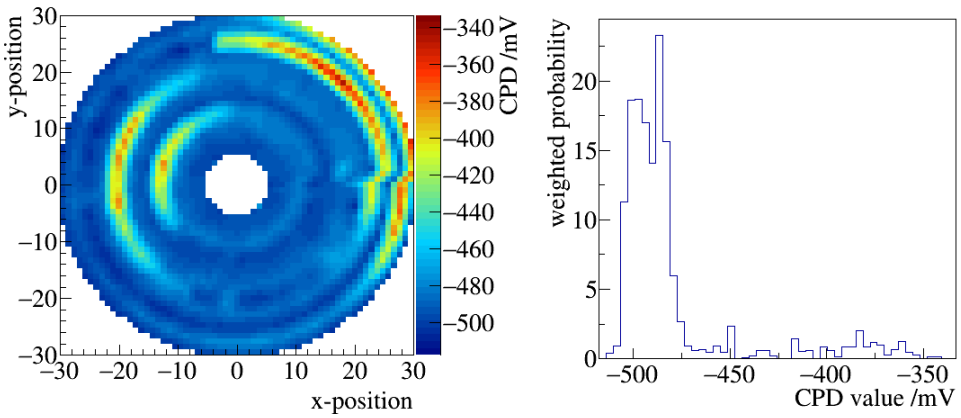

Figure E.147: CPD map and histogram of the 11. scan of sample 7-SS-ep-3 after bake-out. The ring like structures with higher CPD are caused by a damage of the surface (compare figure E.141).

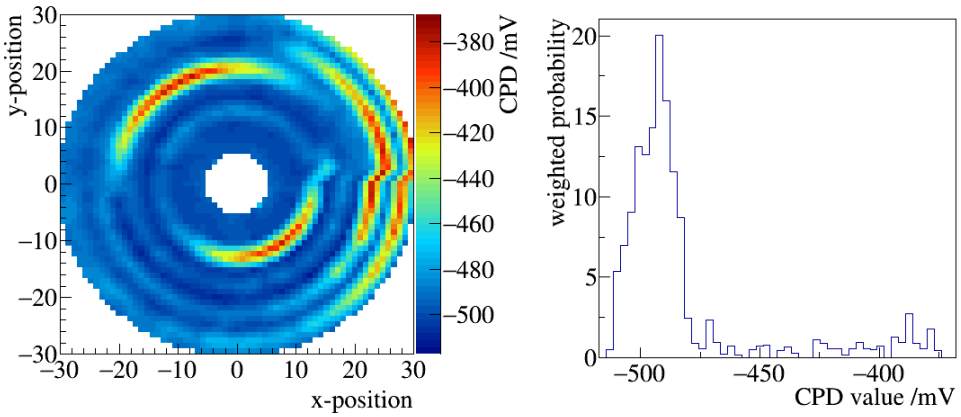

Figure E.148: CPD map and histogram of the 12. scan of sample 7-SS-ep-3 after bake-out. The ring like structures with higher CPD are caused by a damage of the surface (compare figure E.141).

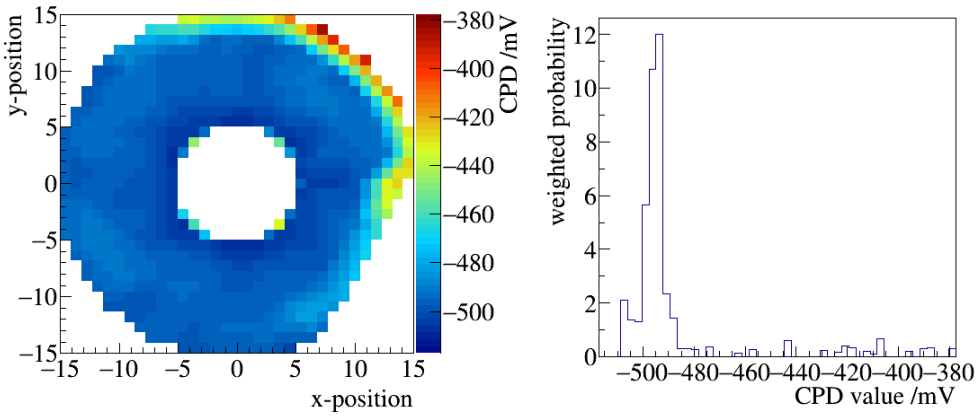

Figure E.149: CPD map and histogram of the 13. scan of sample 7-SS-ep-3 after bake-out. The ring like structures with higher CPD are caused by a damage of the surface (compare figure E.141).

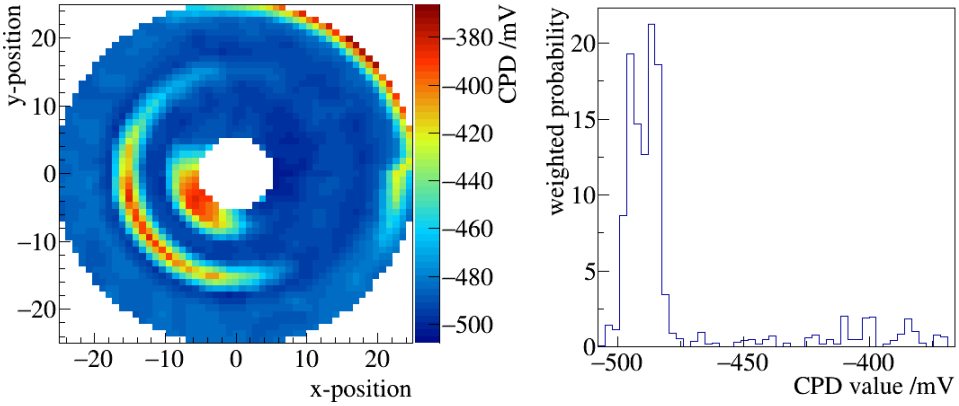

Figure E.150: CPD map and histogram of the 14. scan of sample 7-SS-ep-3 after bake-out. The ring like structures with higher CPD are caused by a damage of the surface (compare figure E.141).

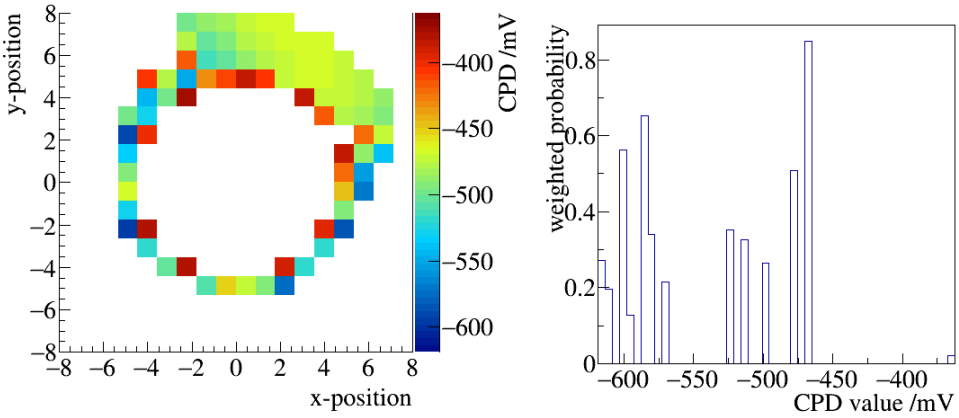

Figure E.151: CPD map and histogram of the 15. scan of sample 7-SS-ep-3 after bake-out.

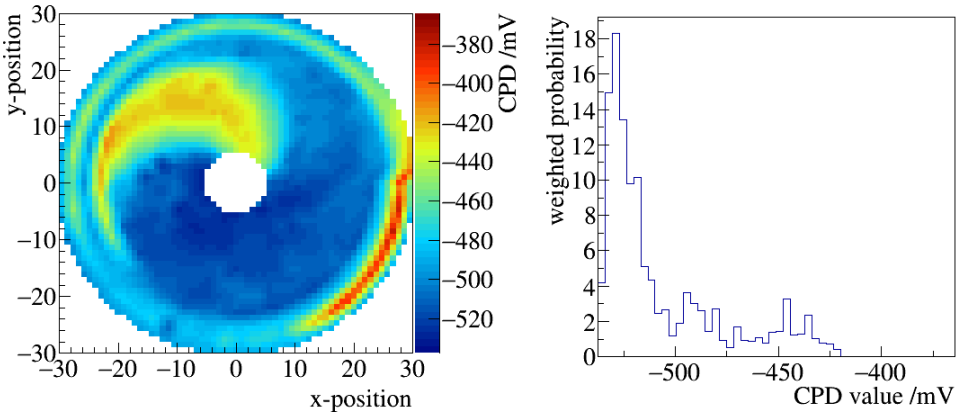

Figure E.152: CPD map and histogram of the 16. scan of sample 7-SS-ep-3 after bake-out. The ring like structures with higher CPD are caused by a damage of the surface (compare figure E.141).

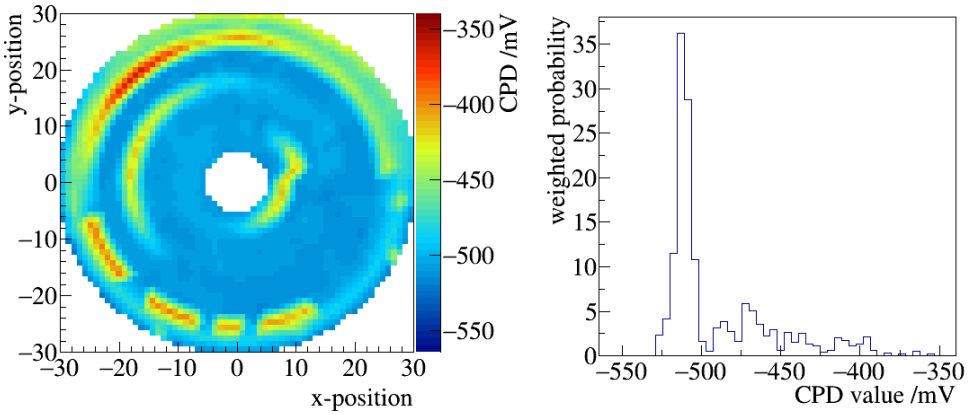

Figure E.153: CPD map and histogram of the 17. scan of sample 7-SS-ep-3 after bake-out. The ring like structures with higher CPD are caused by a damage of the surface (compare figure E.141).

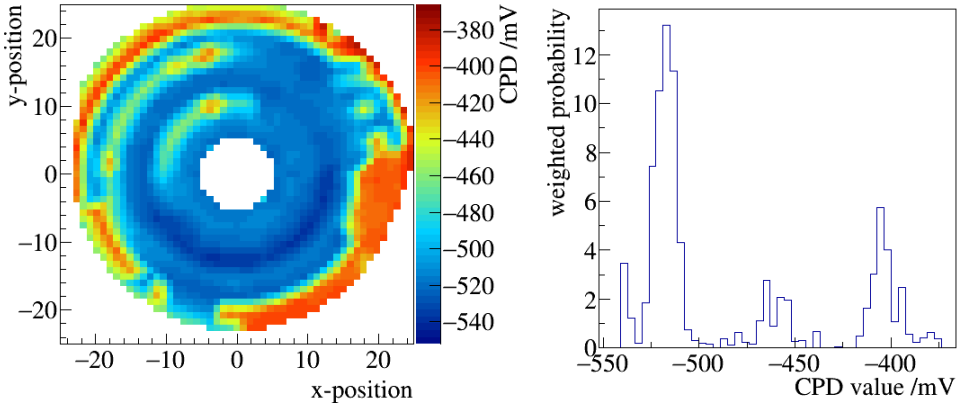

Figure E.154: CPD map and histogram of the 18. scan of sample 7-SS-ep-3 after bake-out. The ring like structures with higher CPD are caused by a damage of the surface (compare figure E.141).

Results of the measurements performed on sample 7-SS-ep-3

Table E.6: CPD and $\sigma_{\mathrm{RMS,surface}}$ over the whole samples 7-SS-el-3. * marks uncompleted scans.

scan	baked	CPD /mV	$\sigma_{\mathrm{RMS,surface}}$ /mV
1	no	-399.5	30.6
2	no	-471.9	29.4
3	no	-491.7	27.2
4	no	-357.4	16.5
5	no	-362.2	14.9
6	no	-374.0	14.8
7	no	-375.5	12.7
8	no	-402.0	16.6
9	no	-400.1	11.8
10	no	-405.4	11.3
11	no	-402.2	13.2
12	no	-407.5	12.0
13	no	-413.8	13.1
14	no	-415.5	14.1
15	no	-416.6	12.7
16	no	-420.2	11.3
17	no	-425.3	11.7
18	no	-425.7	10.1
19	no	-426.9	9.9
20	no	-429.2	10.2
21	no	-428.9	9.6
22	no	-445.2	10.8
23	no	-434.5	11.1
24	no	-436.5	12.1
25	yes	-556.1	17.9
26	yes	-517.0	10.7
27	yes	-503.7	11.6
28	yes	-501.0	15.0
29	yes	-491.9	21.6
30	yes	-493.9	24.0
31	yes	-487.9	24.1
32	yes	-493.9	22.7
33	yes	-491.6	18.8
34	yes	-478.2	23.1
35	yes	-480.2	36.8
36	yes	-482.3	32.5
37	yes	-487.6	28.5
38	yes	-477.2	30.7
39	yes	-541.4	68.6
40	yes	-488.3	33.6
41	yes	-487.9	36.2
42	yes	-483.7	50.6

Measurements performed at sample 3-SS-ep-6

In this section the results sample 3-SS-ep-6 are presented. First the CPD maps are plotted and then the numeric values of CPD and $\sigma_{\mathrm{RMS,surface}}$ are summarized subsequently. Both are presented in chronological ordering.

CPD maps of the measurements performed on sample 3-SS-ep-6

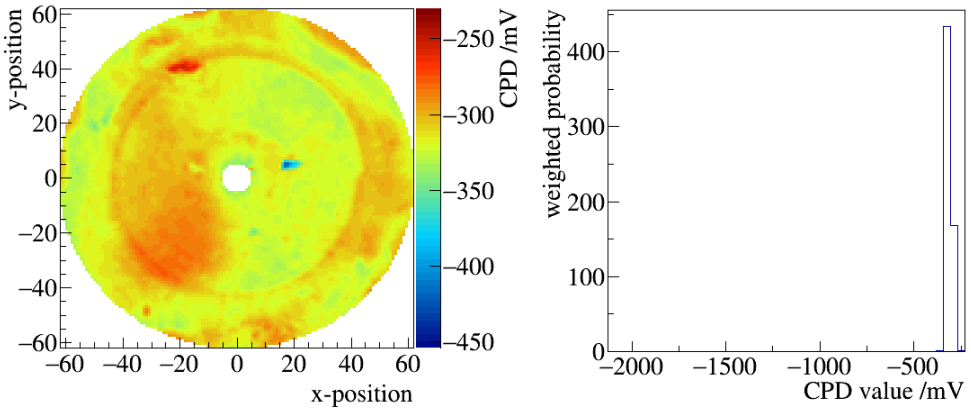

Figure E.155: CPD map and histogram of the 1. scan of sample 3-SS-ep-6.

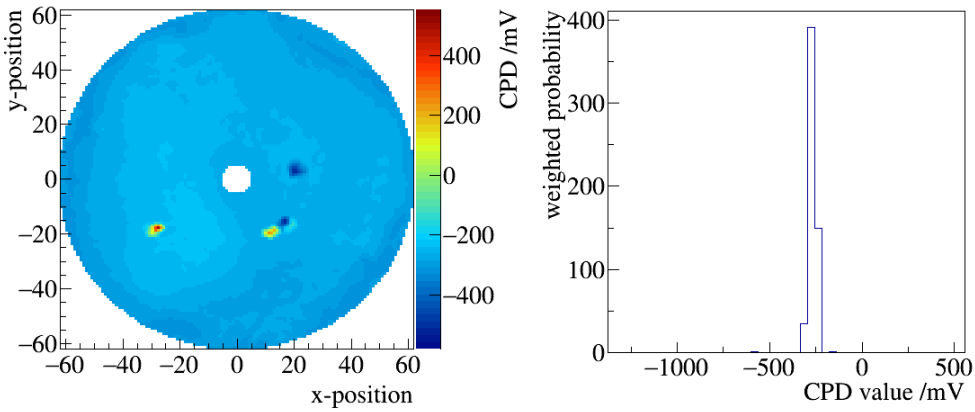

Figure E.156: CPD map and histogram of the 2. scan of sample 3-SS-ep-6.

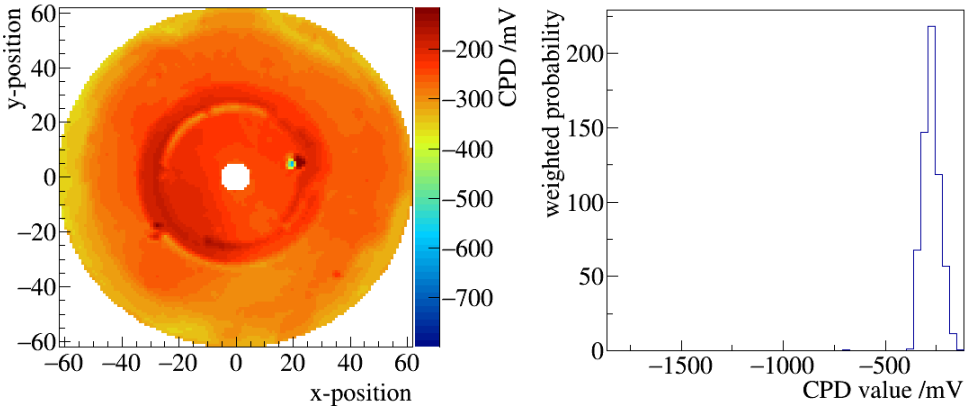

Figure E.157: CPD map and histogram of the 3. scan of sample 3-SS-ep-6.

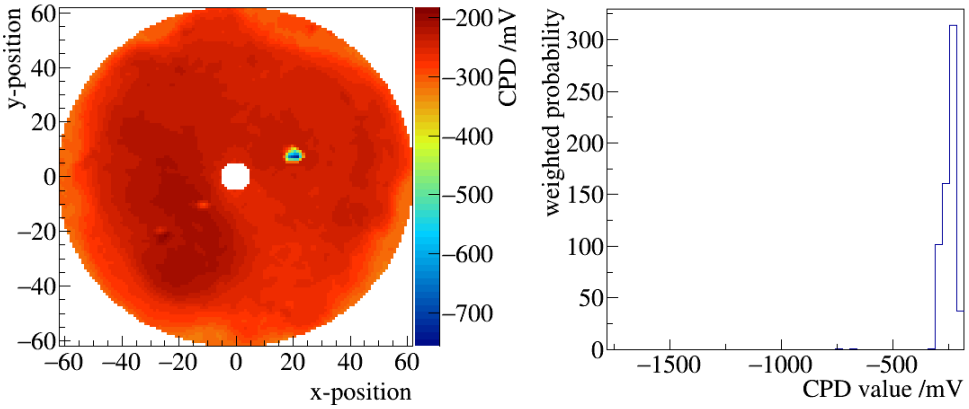

Figure E.158: CPD map and histogram of the 4. scan of sample 3-SS-ep-6.

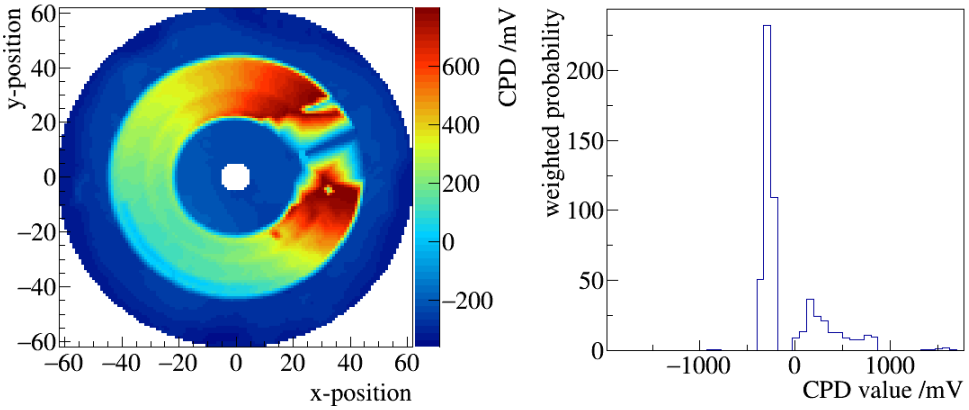

Figure E.159: CPD map and histogram of the 5. scan of sample 3-SS-ep-6.

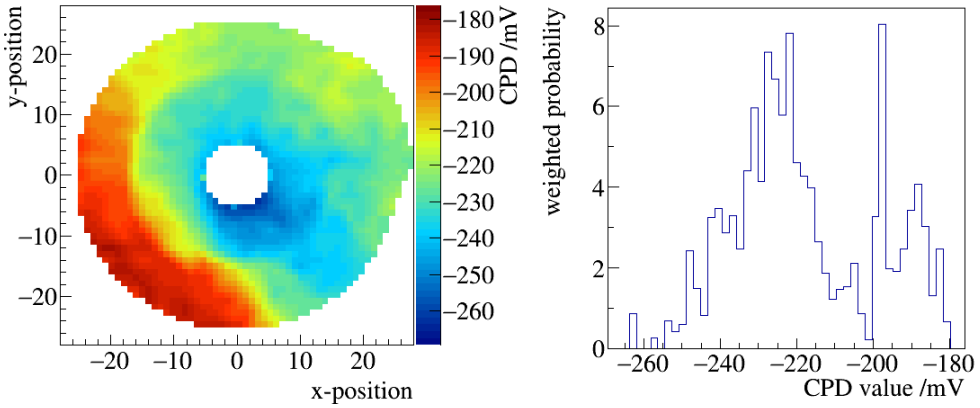

Figure E.160: CPD map and histogram of the 6. scan of sample 3-SS-ep-6.

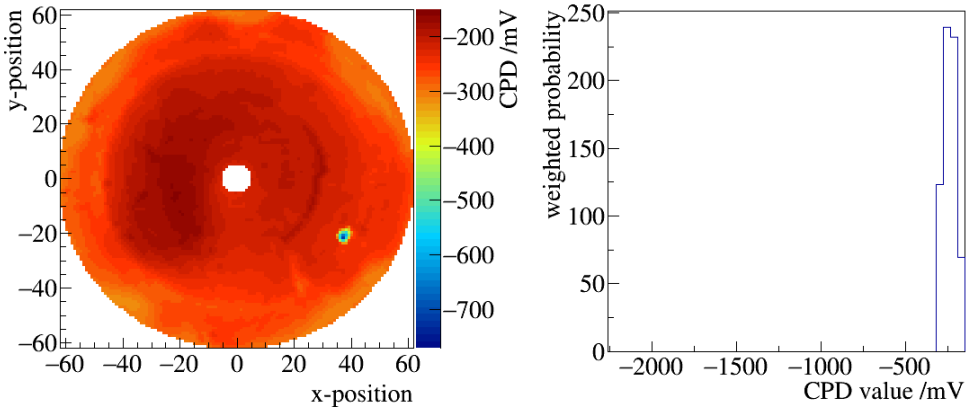

Figure E.161: CPD map and histogram of the 7. scan of sample 3-SS-ep-6.

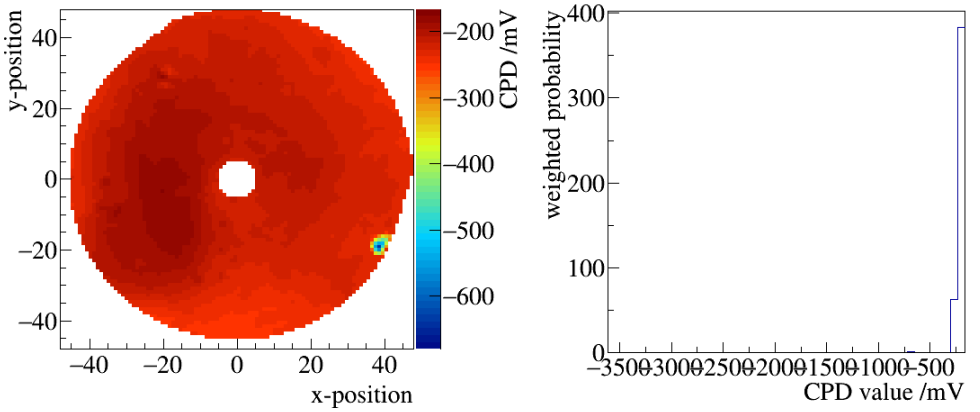

Figure E.162: CPD map and histogram of the 8. scan of sample 3-SS-ep-6.

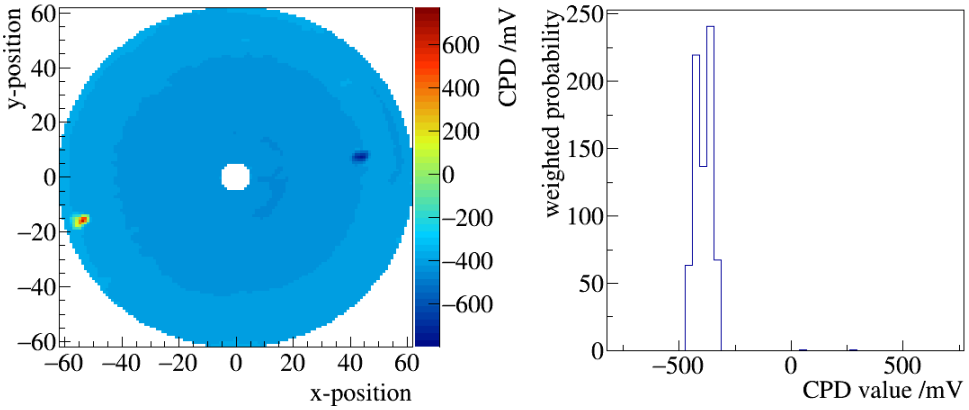

Figure E.163: CPD map and histogram of the 1. scan of sample 3-SS-ep-6 after 1. bake-out.

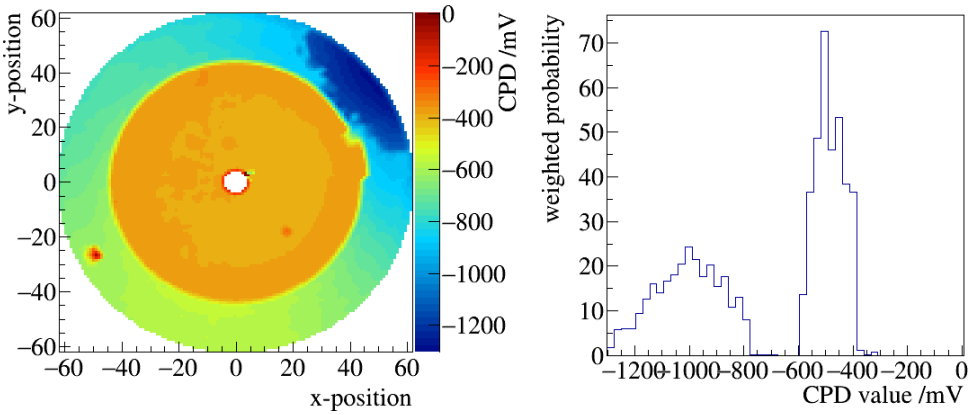

Figure E.164: CPD map and histogram of the 2. scan of sample 3-SS-ep-6 after 1. bake-out.

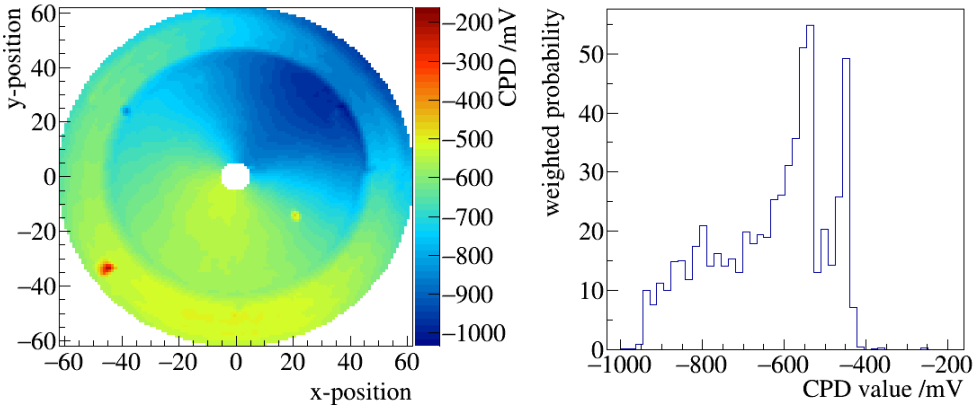

Figure E.165: CPD map and histogram of the 3. scan of sample 3-SS-ep-6 after 1. bake-out.

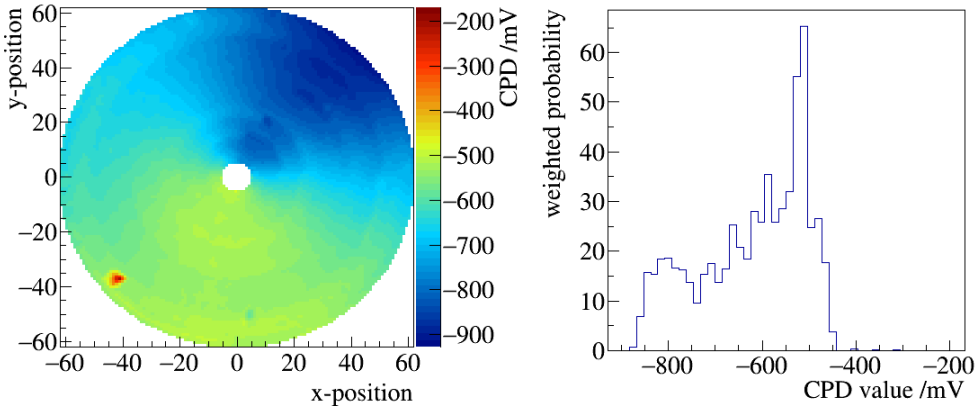

Figure E.166: CPD map and histogram of the 4. scan of sample 3-SS-ep-6 after 1. bake-out.

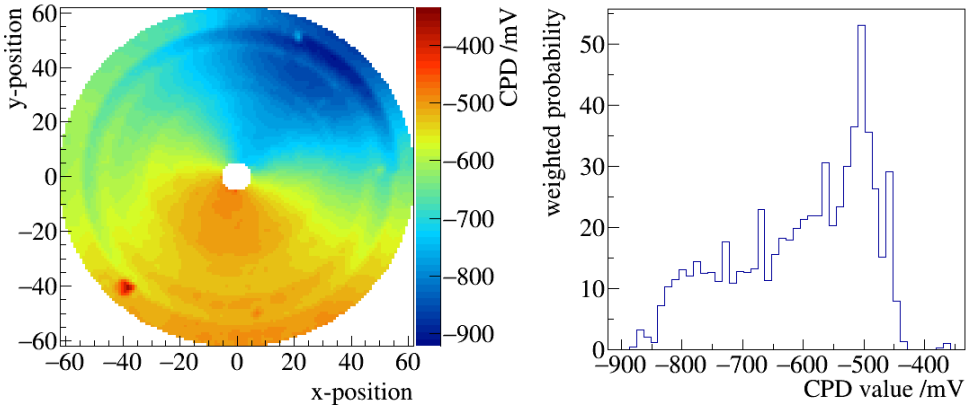

Figure E.167: CPD map and histogram of the 5. scan of sample 3-SS-ep-6 after 1. bake-out.

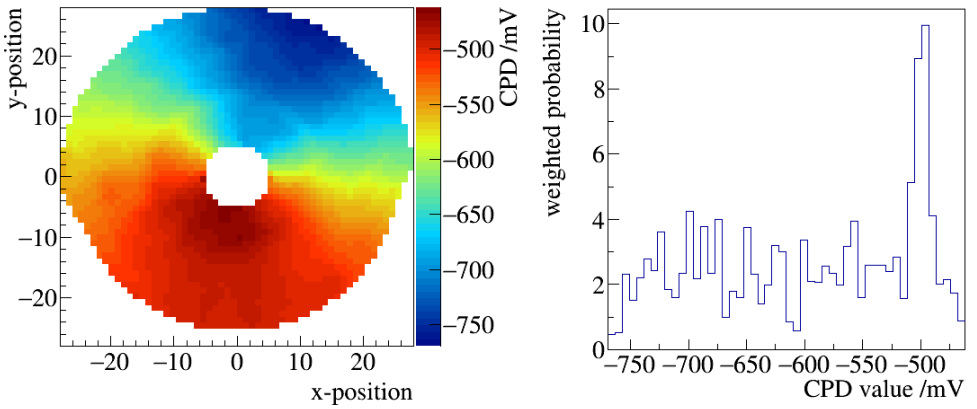

Figure E.168: CPD map and histogram of the 6. scan of sample 3-SS-ep-6 after 1. bake-out.

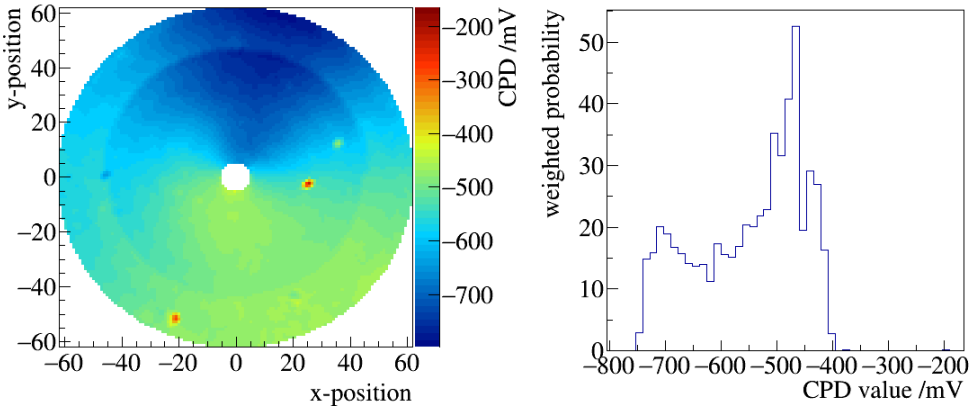

Figure E.169: CPD map and histogram of the 7. scan of sample 3-SS-ep-6 after 1. bake-out.

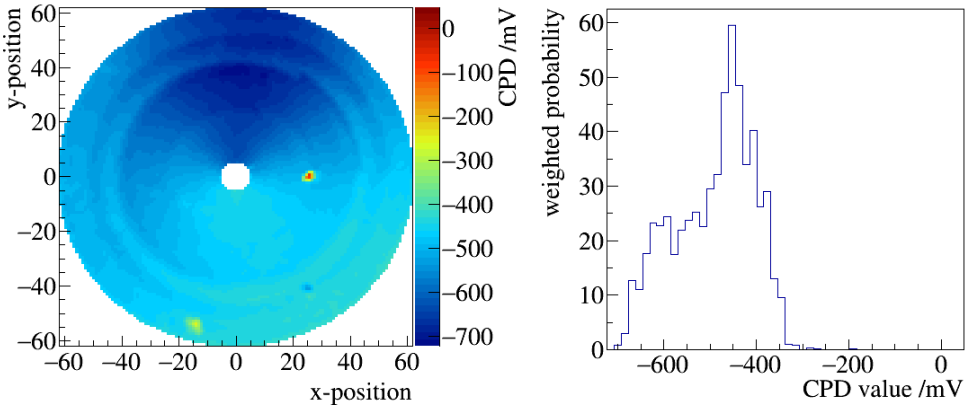

Figure E.170: CPD map and histogram of the 8. scan of sample 3-SS-ep-6 after 1. bake-out.

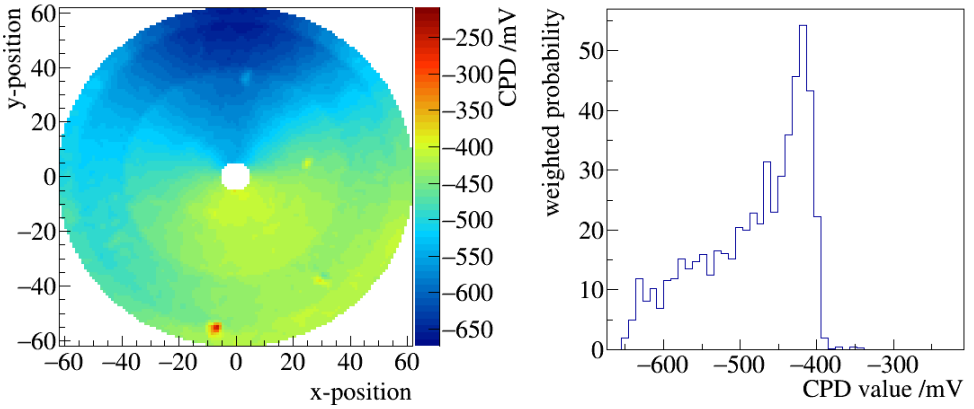

Figure E.171: CPD map and histogram of the 9. scan of sample 3-SS-ep-6 after 1. bake-out.

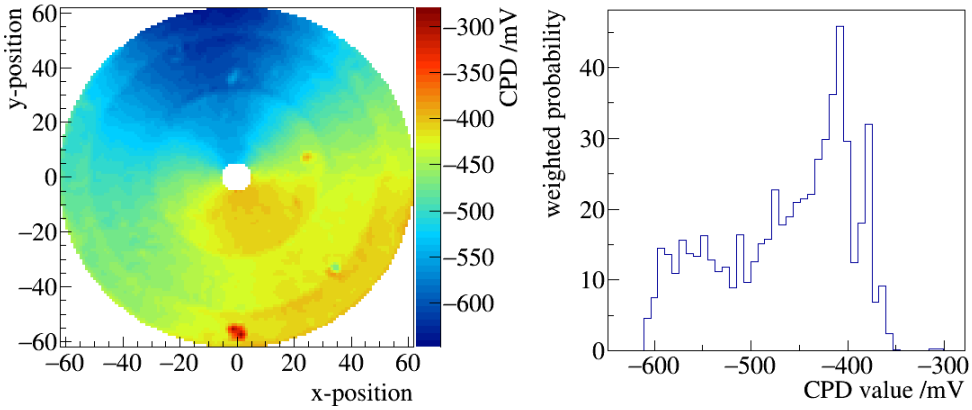

Figure E.172: CPD map and histogram of the 10. scan of sample 3-SS-ep-6 after 1. bake-out.

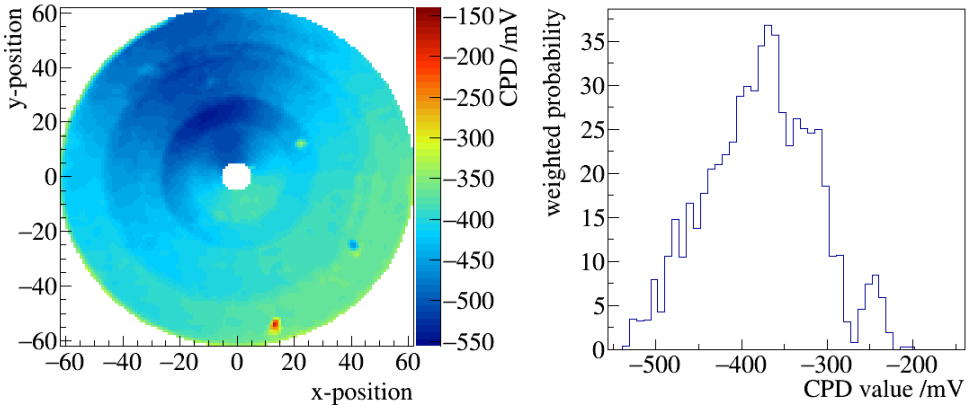

Figure E.173: CPD map and histogram of the 11. scan of sample 3-SS-ep-6 after 1. bake-out.

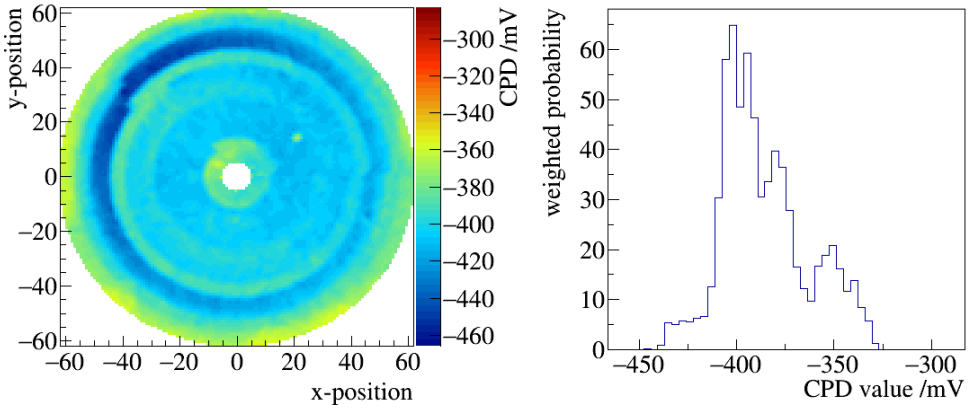

Figure E.174: CPD map and histogram of the 1. scan of sample 3-SS-ep-6 after 2. bake-out.

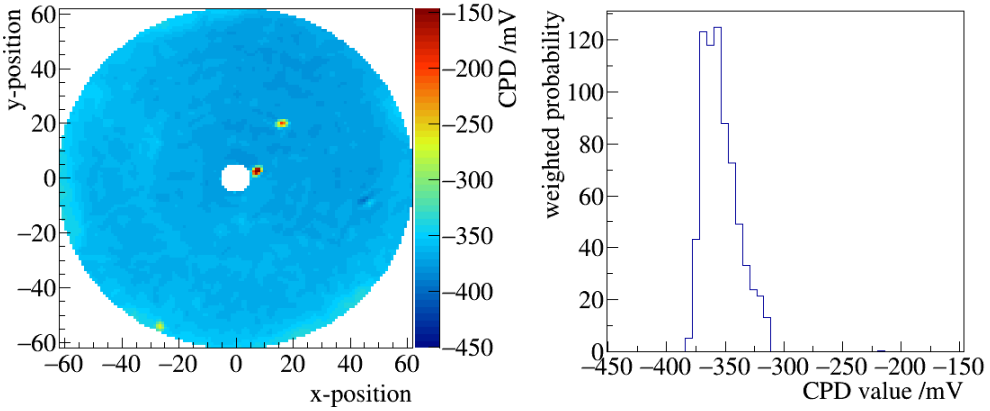

Figure E.175: CPD map and histogram of the 2. scan of sample 3-SS-ep-6 after 2. bake-out.

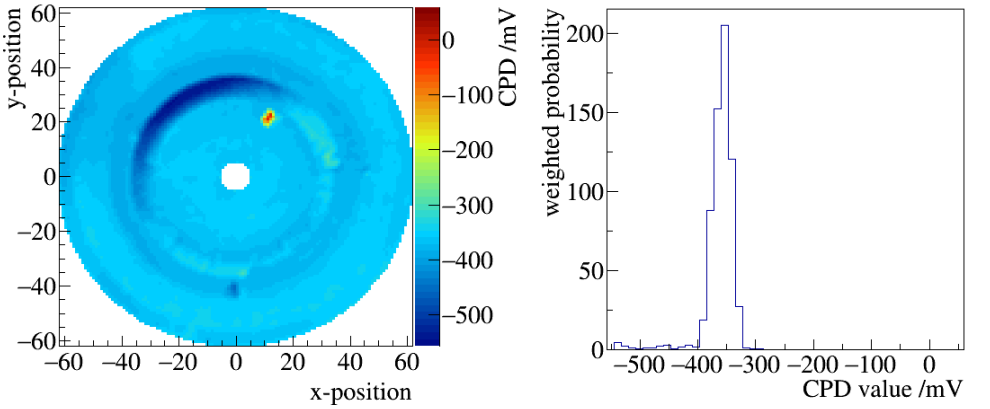

Figure E.176: CPD map and histogram of the 3. scan of sample 3-SS-ep-6 after 2. bake-out.

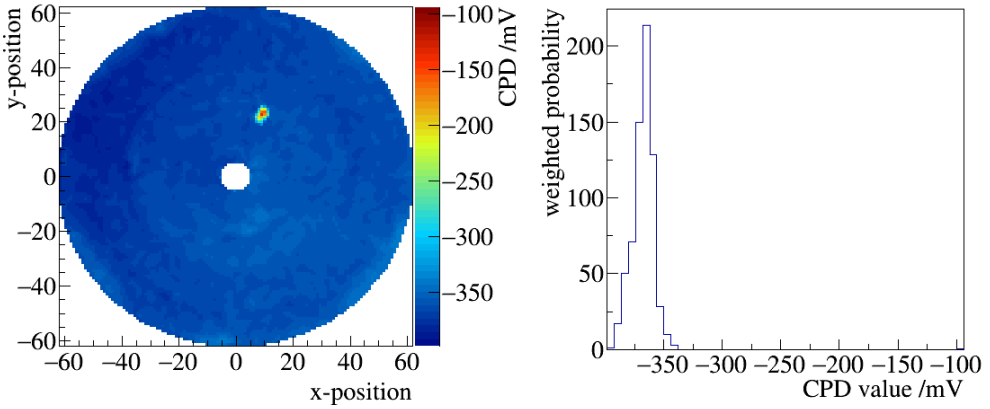

Figure E.177: CPD map and histogram of the 4. scan of sample 3-SS-ep-6 after 2. bake-out.

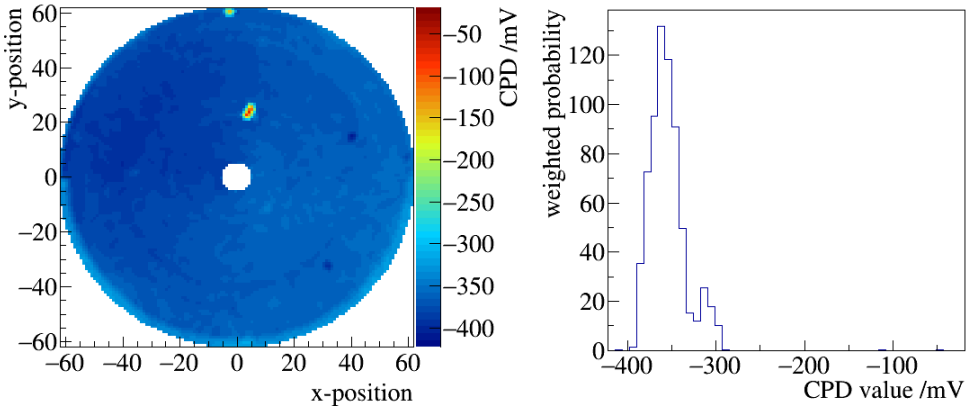

Figure E.178: CPD map and histogram of the 5. scan of sample 3-SS-ep-6 after 2. bake-out.

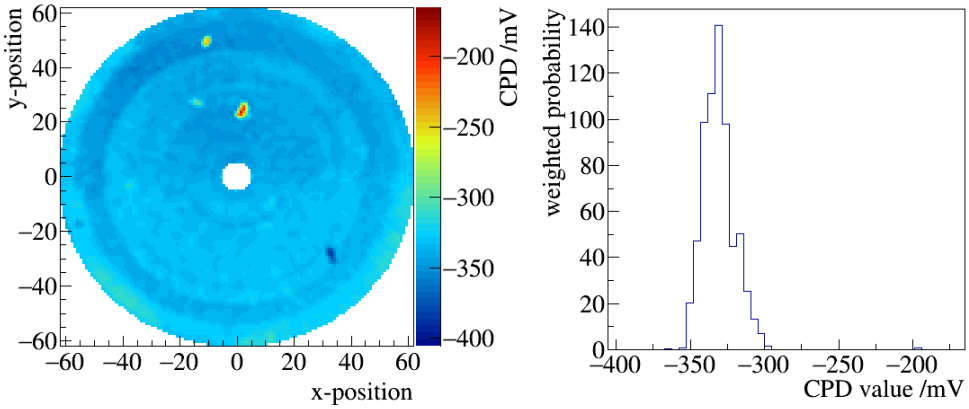

Figure E.179: CPD map and histogram of the 6. scan of sample 3-SS-ep-6 after 2. bake-out.

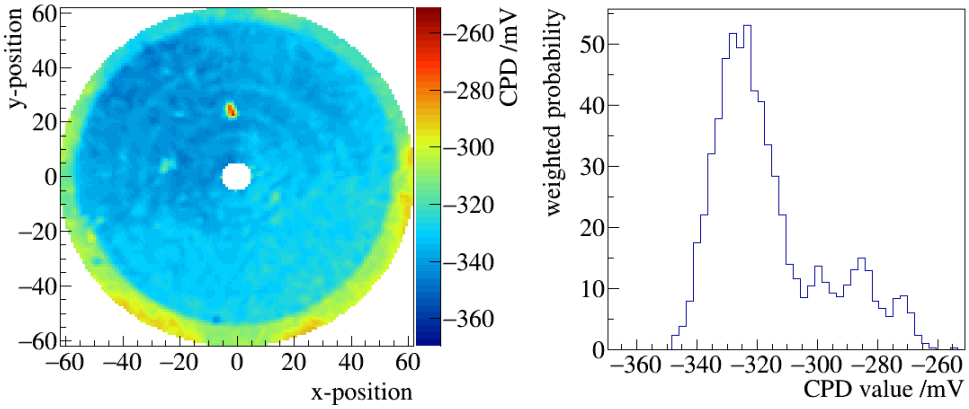

Figure E.180: CPD map and histogram of the 7. scan of sample 3-SS-ep-6 after 2. bake-out.

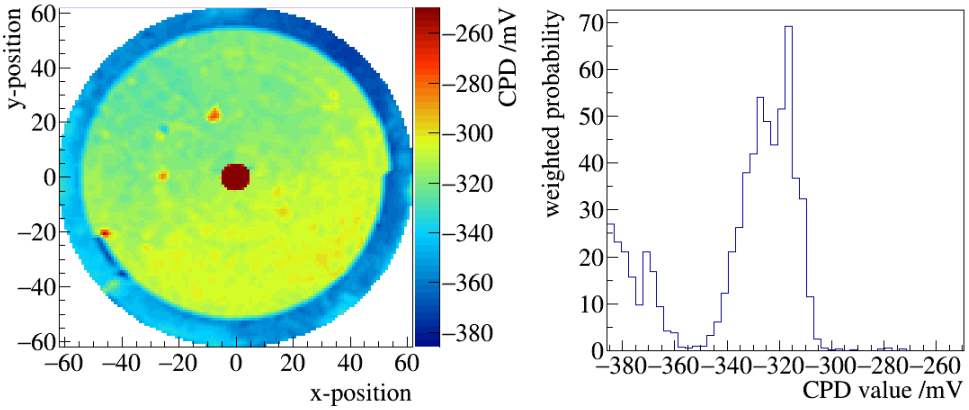

Figure E.181: CPD map and histogram of the 8. scan of sample 3-SS-ep-6 after 2. bake-out.

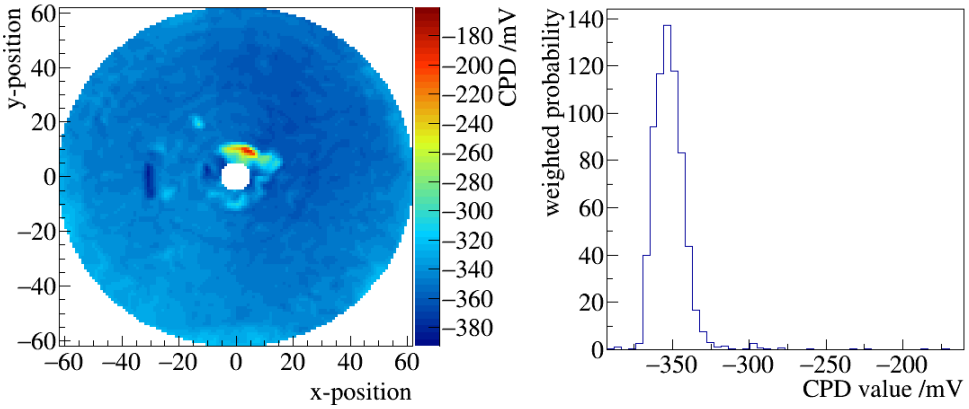

Figure E.182: CPD map and histogram of the 9. scan of sample 3-SS-ep-6 after 2. bake-out.

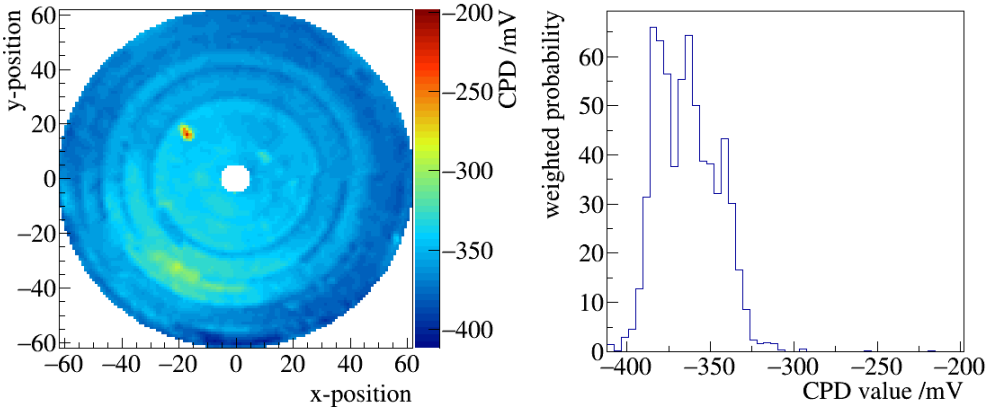

Figure E.183: CPD map and histogram of the 10. scan of sample 3-SS-ep-6 after 2. bake-out.

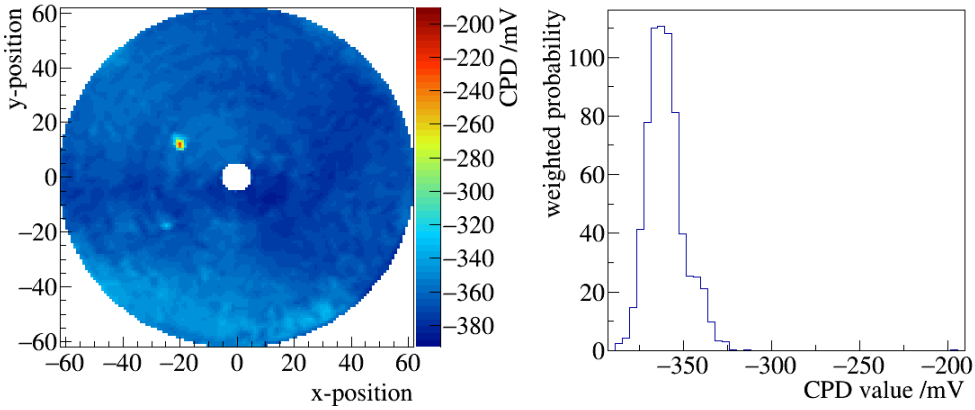

Figure E.184: CPD map and histogram of the 11. scan of sample 3-SS-ep-6 after 2. bake-out.

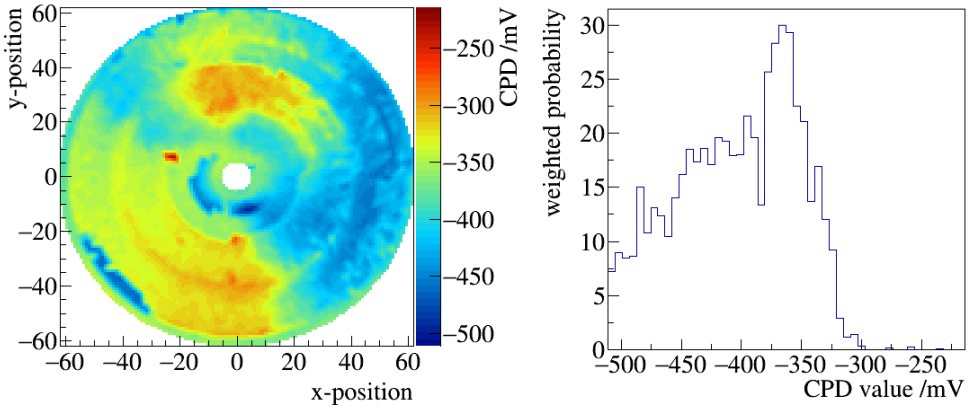

Figure E.185: CPD map and histogram of the 12. scan of sample 3-SS-ep-6 after 2. bake-out.

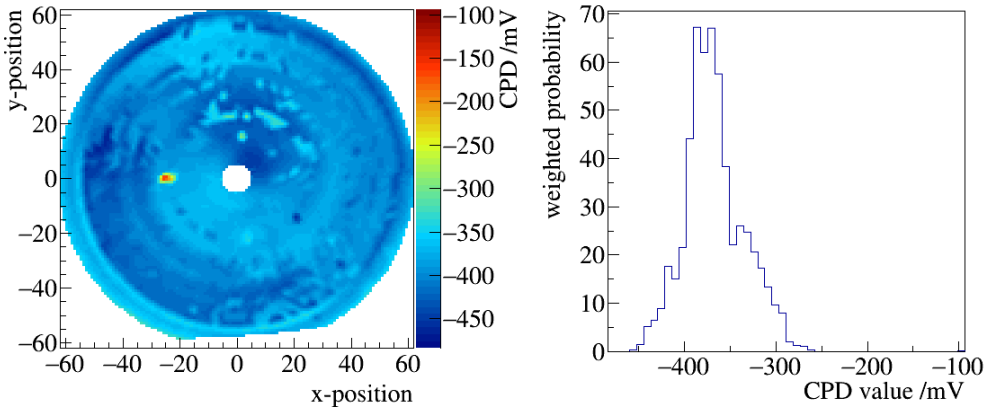

Figure E.186: CPD map and histogram of the 13. scan of sample 3-SS-ep-6 after 2. bake-out. The missing area of the Rear Wall was measured. But during the measurement an error occurred, which prevents the data taking

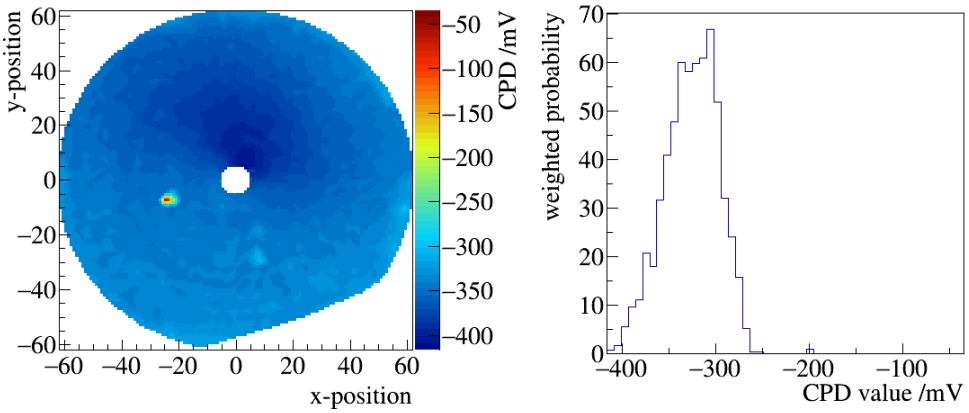

Figure E.187: CPD map and histogram of the 14. scan of sample 3-SS-ep-6 after 2. bake-out. The missing area of the Rear Wall was measured. But during the measurement an error occurred, which prevents the data taking.

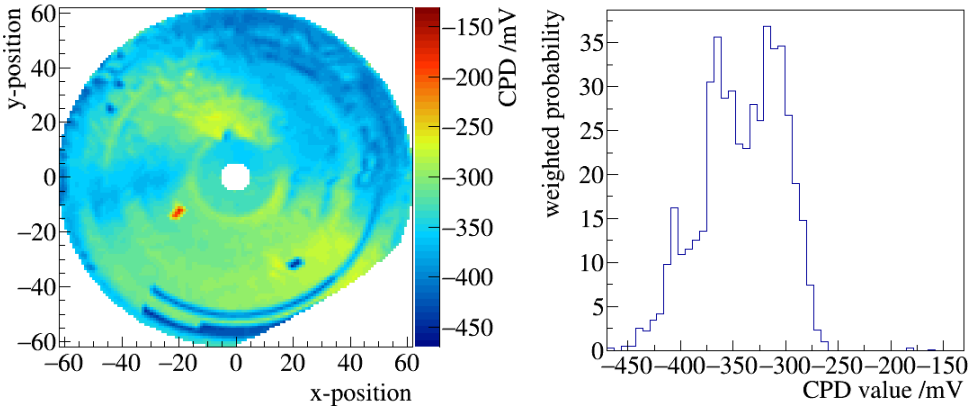

Figure E.188: CPD map and histogram of the 15. scan of sample 3-SS-ep-6 after 2. bake-out. The missing area of the Rear Wall was measured. But during the measurement an error occurred, which prevents the data taking.

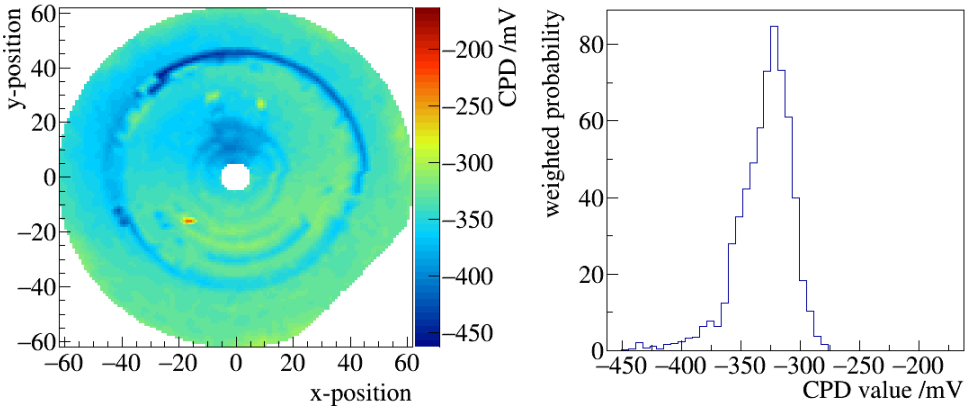

Figure E.189: CPD map and histogram of the 16. scan of sample 3-SS-ep-6 after 2. bake-out. The missing area of the Rear Wall was measured. But during the measurement an error occurred, which prevents the data taking.

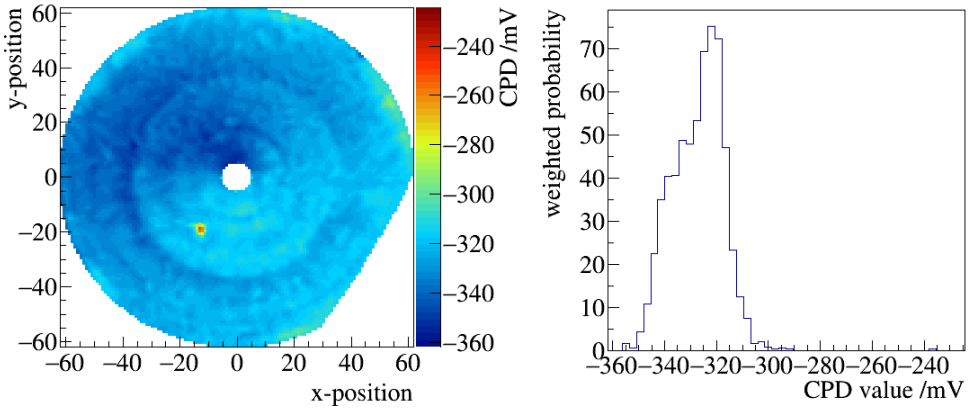

Figure E.190: CPD map and histogram of the 17. scan of sample 3-SS-ep-6 after 2. bake-out. The missing area of the Rear Wall was measured. But during the measurement an error occurred, which prevents the data taking.

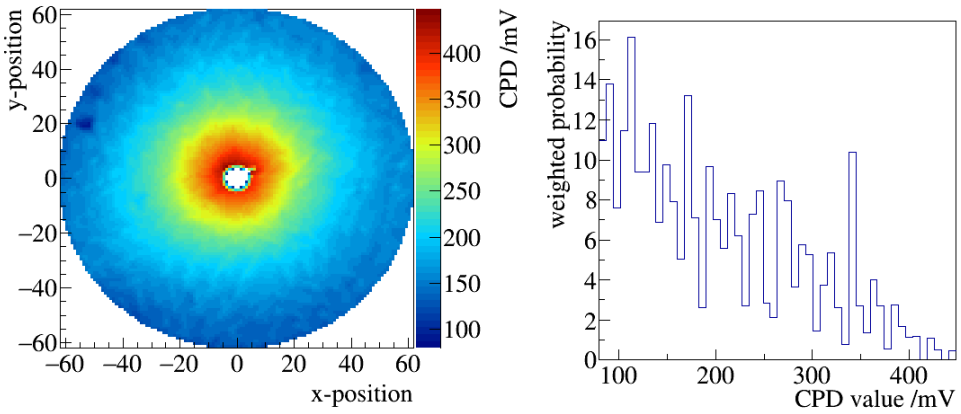

Figure E.191: CPD map and histogram of the 1. scan of sample 3-SS-ep-6 after UV irradiation.

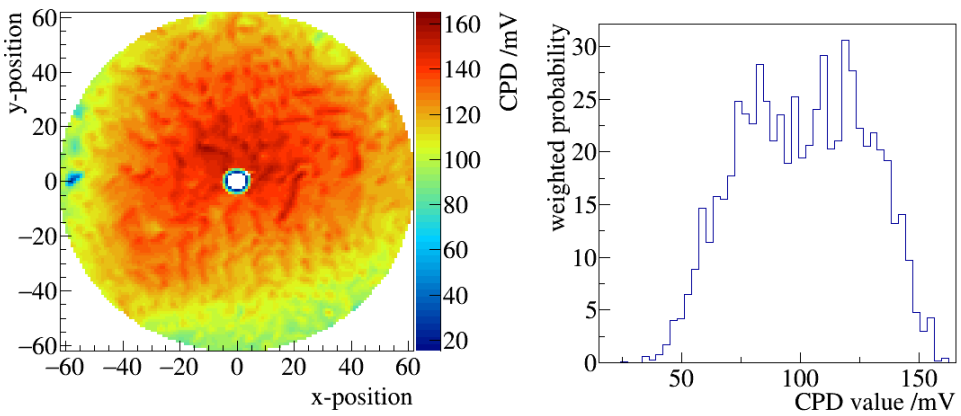

Figure E.192: CPD map and histogram of the 2. scan of sample 3-SS-ep-6 after UV irradiation.

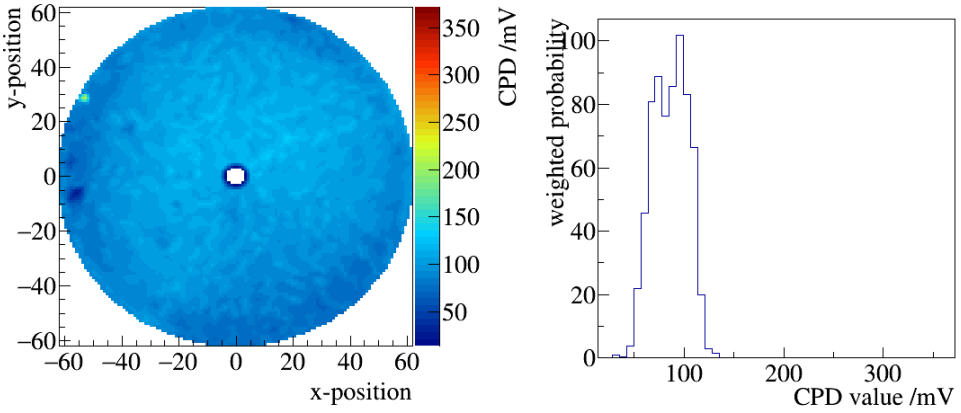

Figure E.193: CPD map and histogram of the 3. scan of sample 3-SS-ep-6 after UV irradiation.

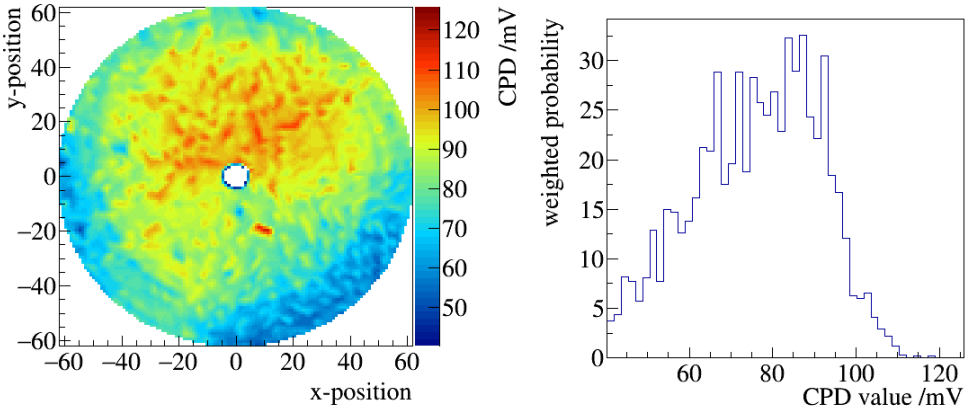

Figure E.194: CPD map and histogram of the 4. scan of sample 3-SS-ep-6 after UV irradiation.

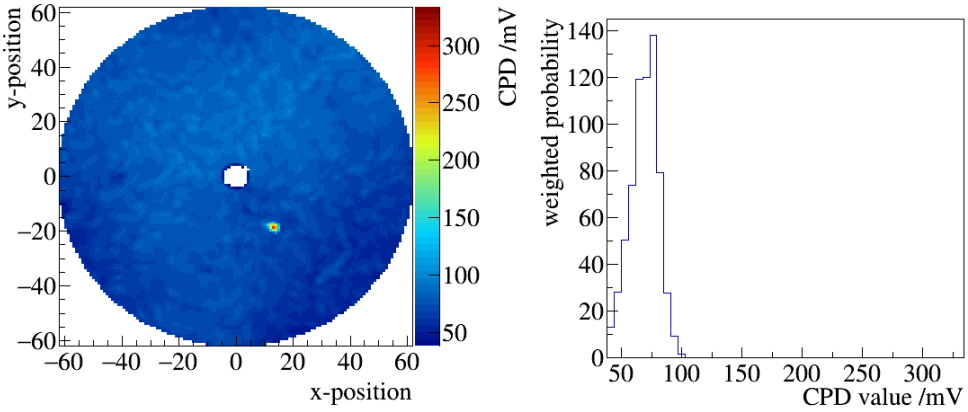

Figure E.195: CPD map and histogram of the 5. scan of sample 3-SS-ep-6 after UV irradiation.

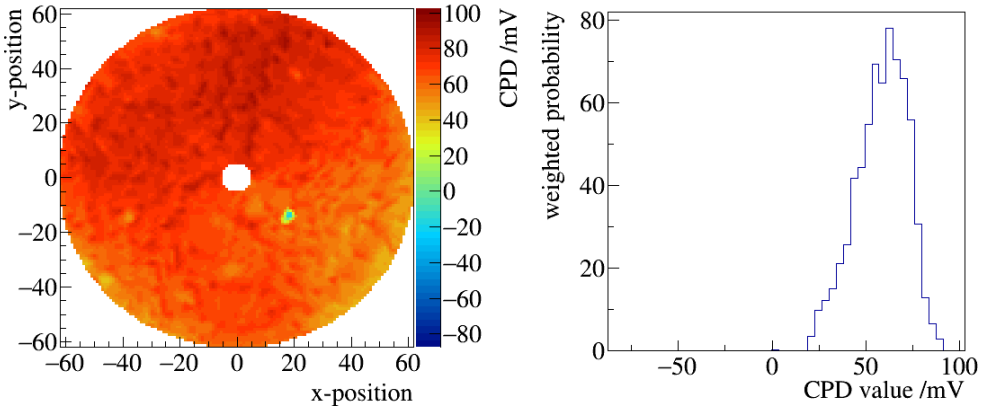

Figure E.196: CPD map and histogram of the 6. scan of sample 3-SS-ep-6 after UV irradiation.

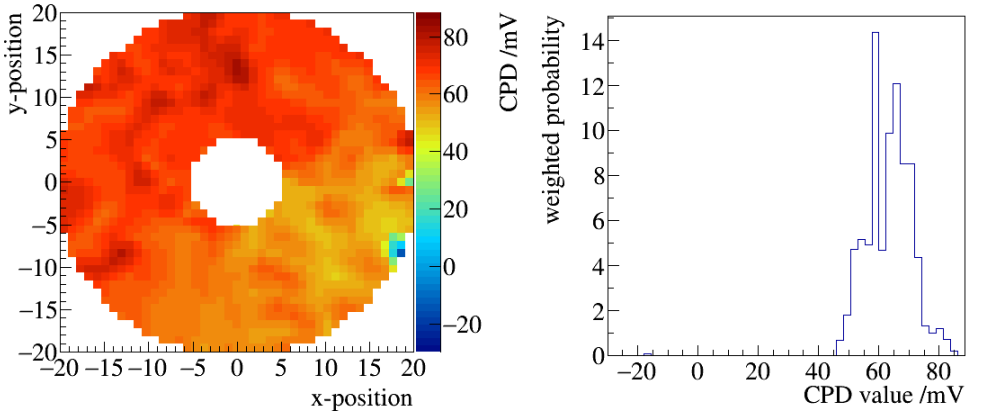

Figure E.197: CPD map and histogram of the 7. scan of sample 3-SS-ep-6 after UV irradiation.

Results of the measurements performed on sample 3-SS-ep-6

Table E.7: CPD and $\sigma_{\mathrm{RMS,surface}}$ over the whole sample 3-SS-el-5. * marks uncompleted scans.

scan	baked	CPD over the surface /mV	$\sigma_{\mathrm{RMS,surface}}$ /mV
1	-	-313.9	45.7
2	-	-276.5	46.2
3	-	-276.8	56.0
4	-	-257.5	46.2
5	-	-68.8	440.1
6 *	-	-217.9	18.3
7	-	-243.0	64.5
8 *	-	-219.4	110.4
1	once	-418.3	39.1
2	once	-550.0	234.8
3	once	-682.4	132.6
4	once	-648.7	115.0
5	once	-630.0	111.8
6*	once	-598.7	88.4
7	once	-579.3	93.8
8	once	-528.1	81.3
9	once	-492.4	69.1
10	once	-482.7	65.4
11	once	-421.7	49.7
1	twice	-398.3	18.3
2	twice	-366.7	12.6
3	twice	-369.7	30.2
4	twice	-366.1	11.3
5	twice	-367.7	19.2
6	twice	-336.5	10.2
7	twice	-328.8	13.2
8	twice	-325.3	20.6
9	twice	-347.5	12.8
10	twice	-358.5	16.2
11	twice	-365.2	10.0
12	twice	-371.5	42.7
13	twice	-394.5	26.5
14	twice	-350.8	18.9
15	twice	-339.7	37.9
16	twice	-343.8	21.4
17	twice	-327.2	10.0

Measurements performed at sample 5-SS-ep-6

In this section the results sample 5-SS-ep-3 are presented. In the following the CPD maps are plotted. Then the pixel maps of CPD and $\sigma_{\mathrm{RMS,pixel}}$ are presented. All diagrams are presented in chronological ordering.

CPD maps of the measurements performed on sample 5-SS-ep-6

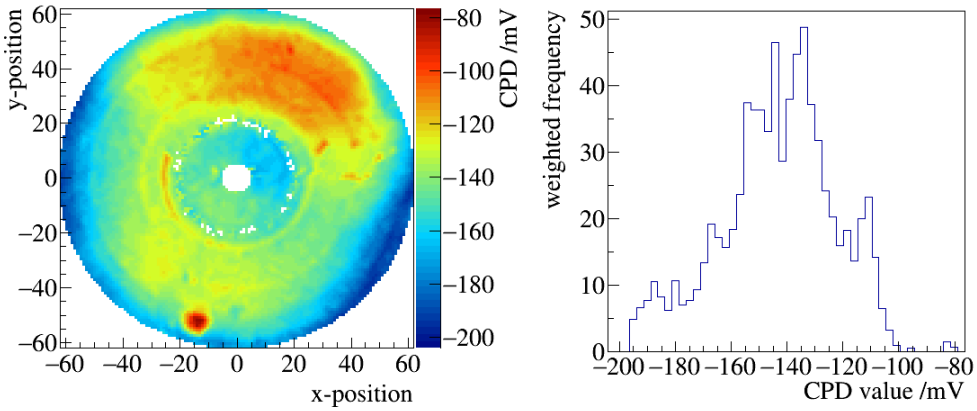

Figure E.198: CPD map and histogram of the 1. scan of sample 5-SS-ep-6.

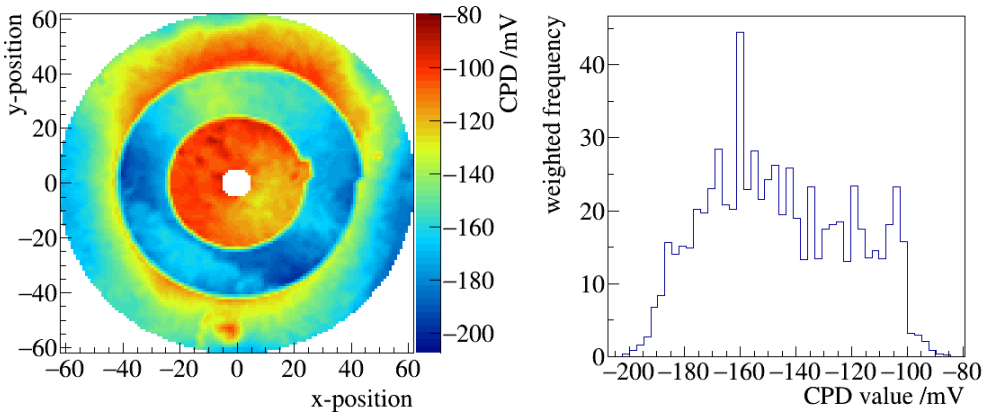

Figure E.199: CPD map and histogram of the 2. scan of sample 5-SS-ep-6.

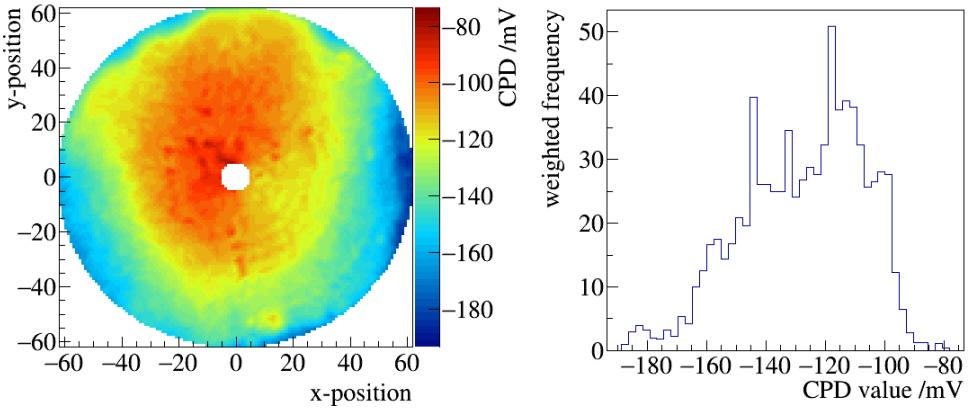

Figure E.200: CPD map and histogram of the 3. scan of sample 5-SS-ep-6.

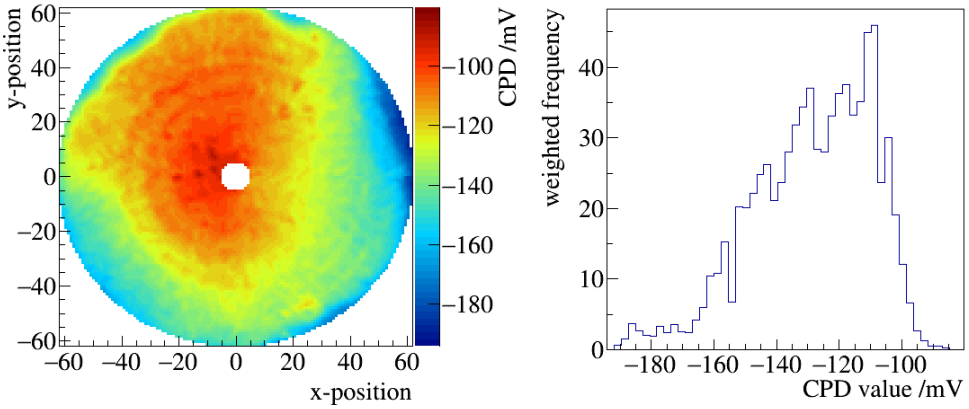

Figure E.201: CPD map and histogram of the 4. scan of sample 5-SS-ep-6.

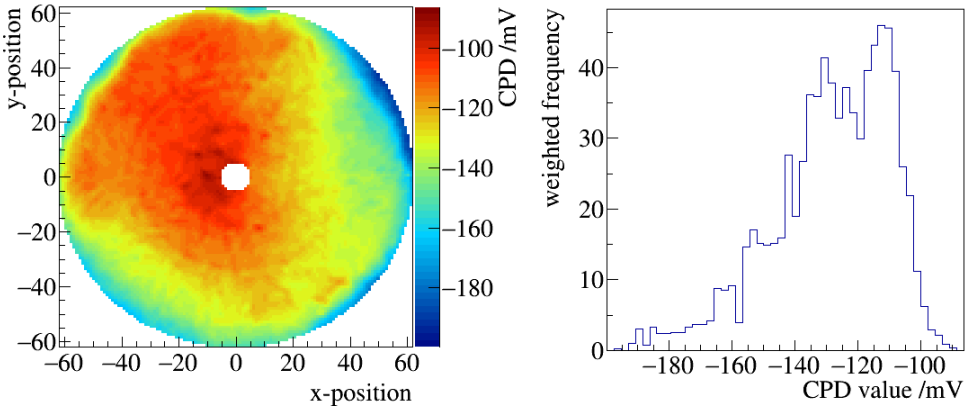

Figure E.202: CPD map and histogram of the 5. scan of sample 5-SS-ep-6.

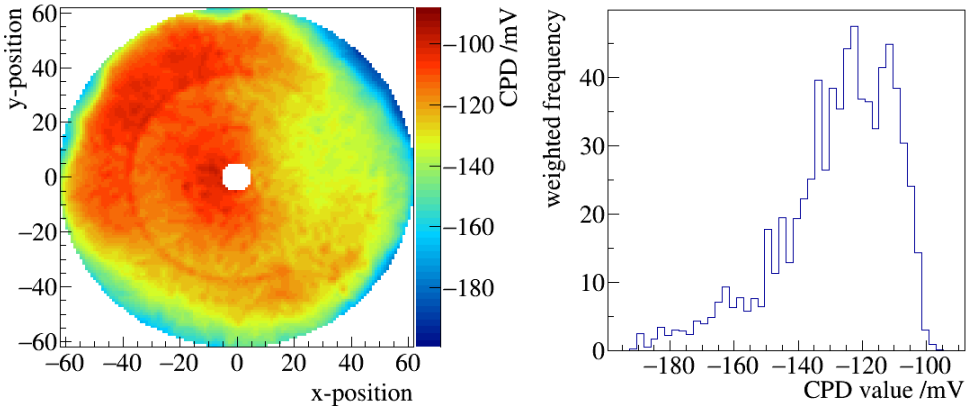

Figure E.203: CPD map and histogram of the 6. scan of sample 5-SS-ep-6.

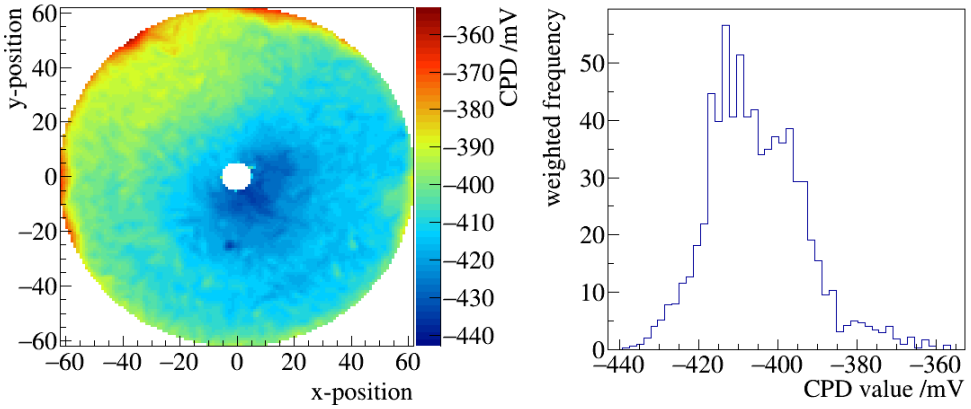

Figure E.204: CPD map and histogram of the 1. scan of sample 5-SS-ep-6 after bake-out.

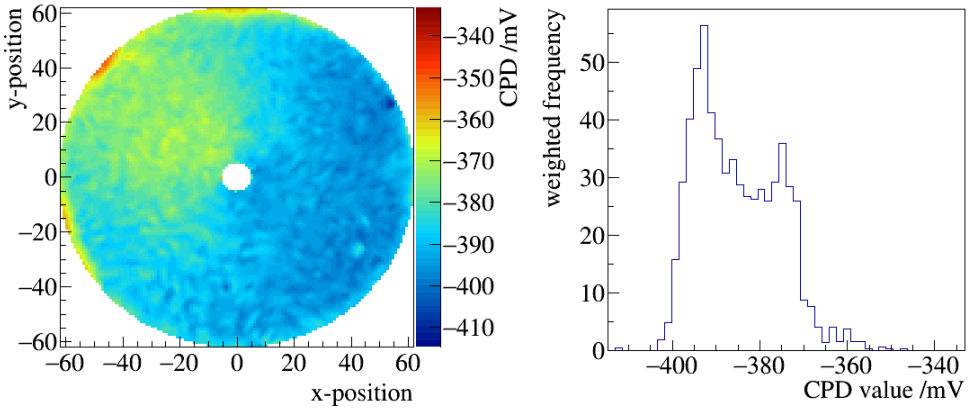

Figure E.205: CPD map and histogram of the 2. scan of sample 5-SS-ep-6 after bake-out.

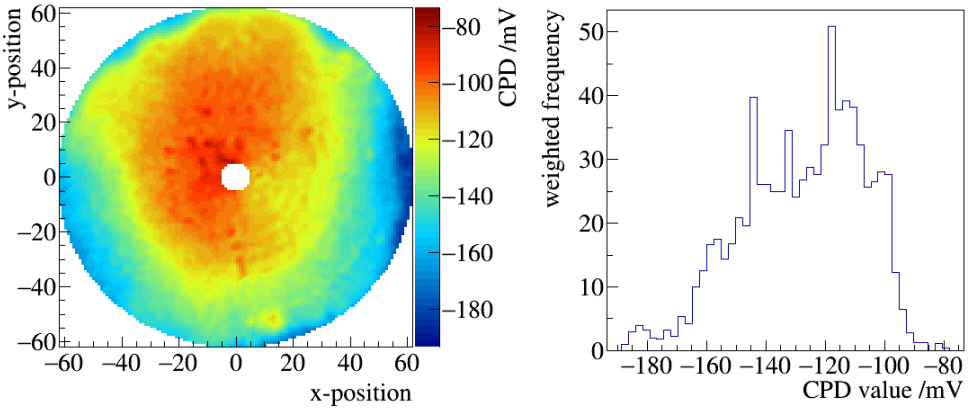

Figure E.206: CPD map and histogram of the 3. scan of sample 5-SS-ep-6.

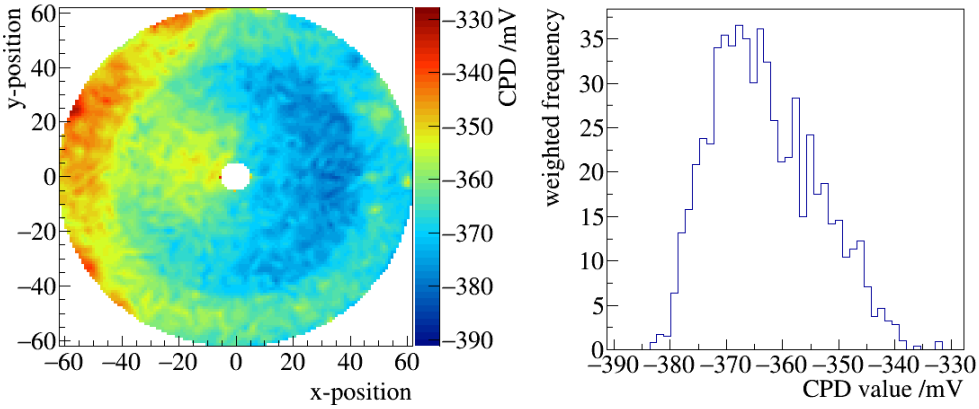

Figure E.207: CPD map and histogram of the 4. scan of sample 5-SS-ep-6 after bake-out.

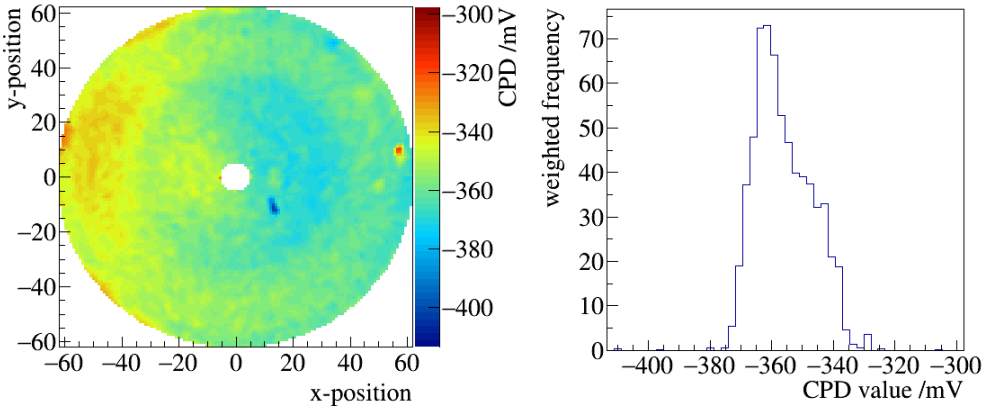

Figure E.208: CPD map and histogram of the 5. scan of sample 5-SS-ep-6 after bake-out.

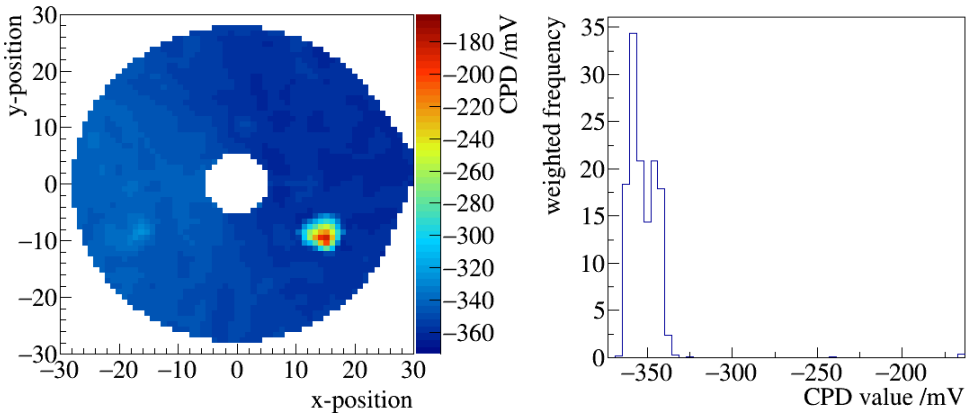

Figure E.209: CPD map and histogram of the 6. scan of sample 5-SS-ep-6 after bake-out.

Pixel maps of the measurements performed on sample 5-SS-ep-6

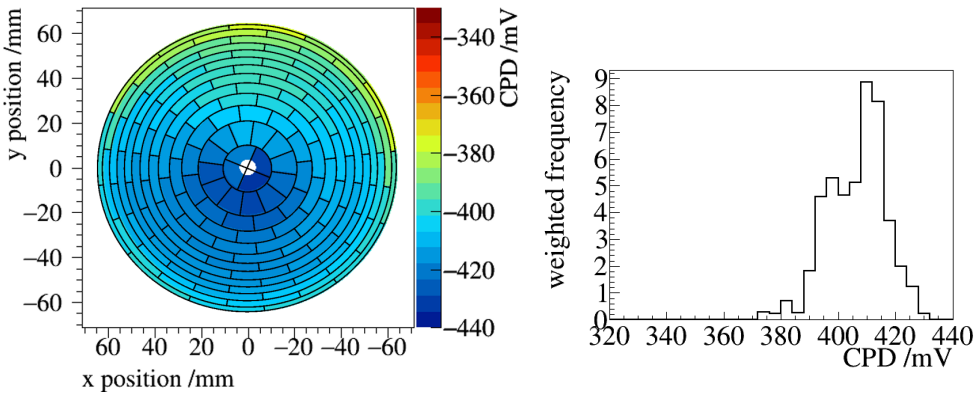

Figure E.210: CPD pixel map and histogram of the 1. scan of sample 5-SS-ep-6 after bake-out.

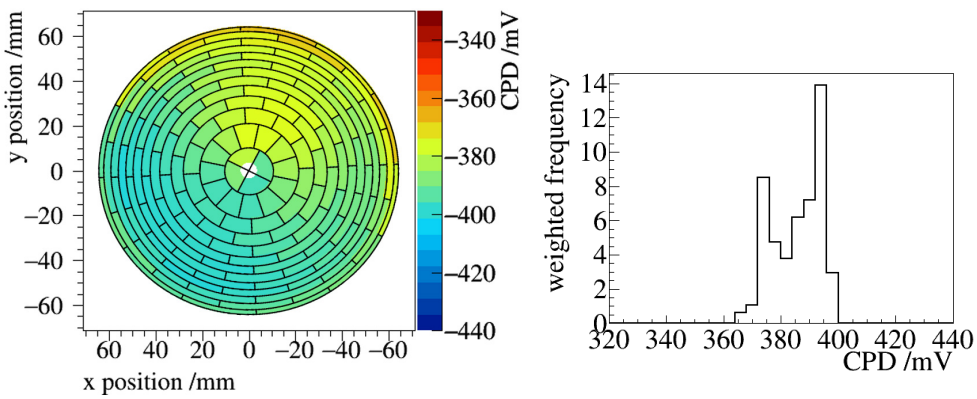

Figure E.211: CPD pixel map and histogram of the 2. scan of sample 5-SS-ep-6 after bake-out.

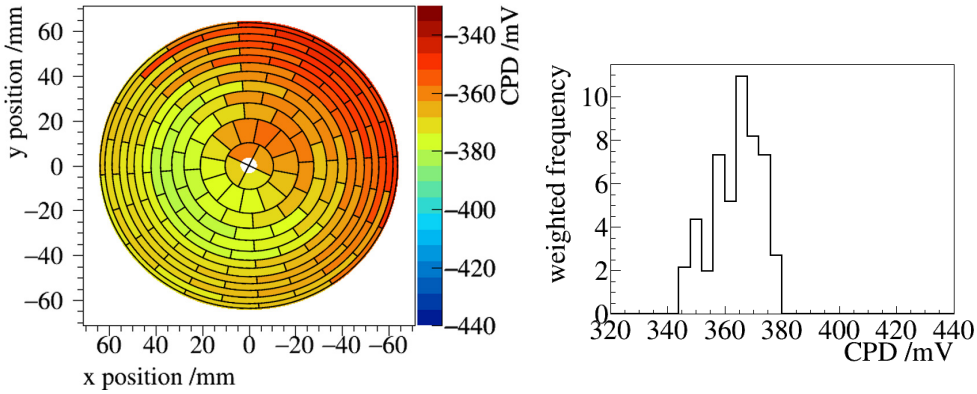

Figure E.212: CPD pixel map and histogram of the 3. scan of sample 5-SS-ep-6 after bake-out.

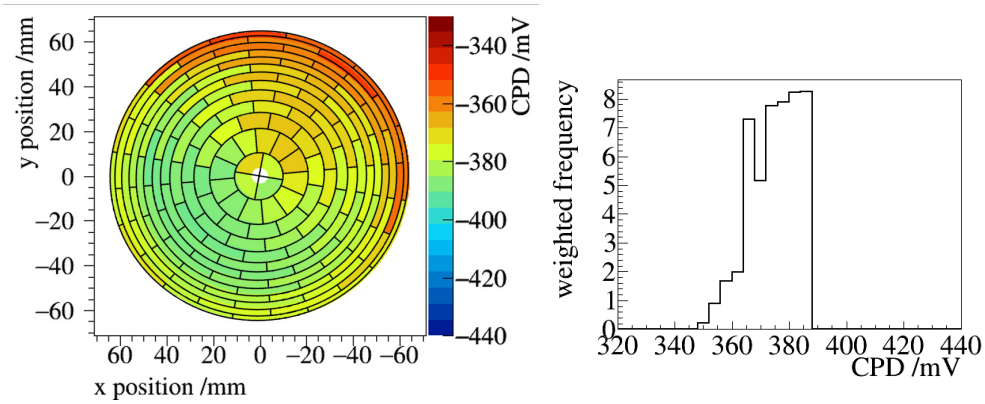

Figure E.213: CPD pixel map and histogram of the 4. scan of sample 5-SS-ep-6 after bake-out.

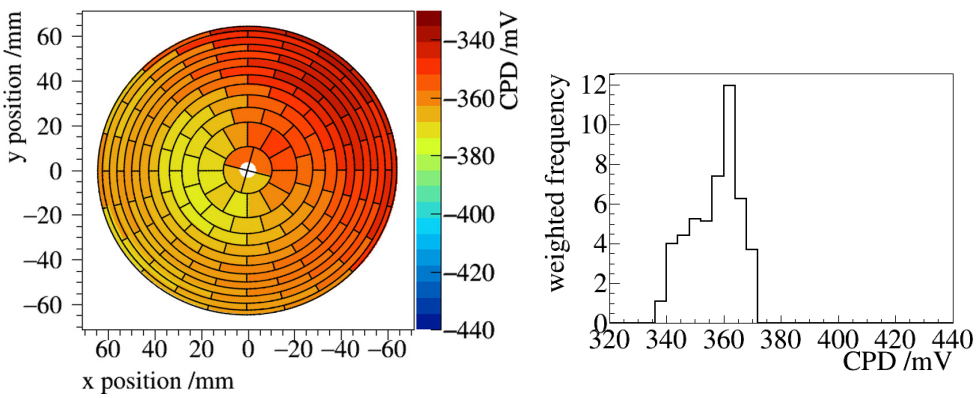

Figure E.214: CPD pixel map and histogram of the 5. scan of sample 5-SS-ep-6 after bake-out.

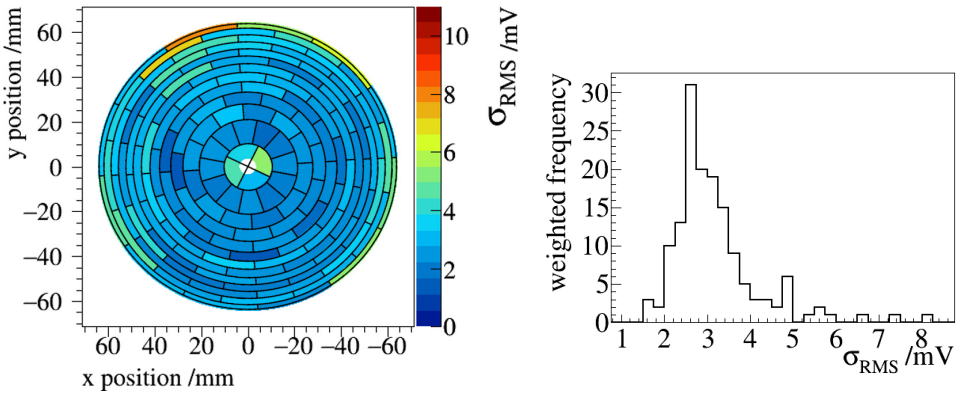

Figure E.215: $\sigma_{\mathrm{RMS,pixel}}$ pixel map and histogram of the 1. scan of sample 5-SS-ep-6 after bake-out.

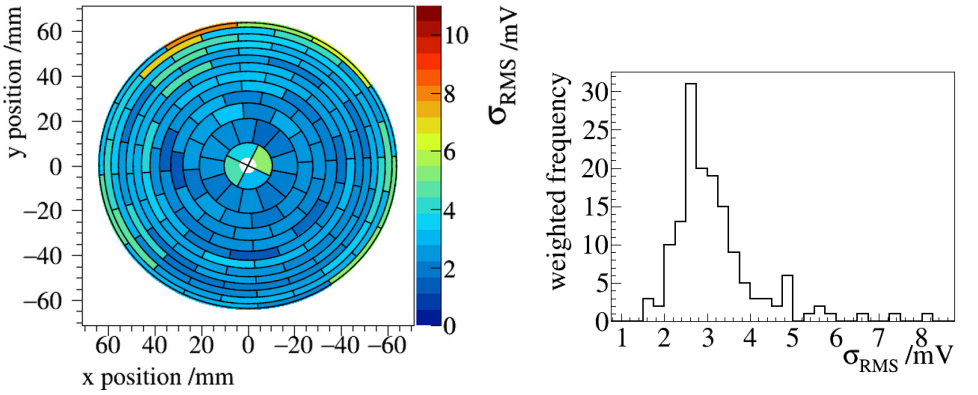

Figure E.216: $\sigma_{\mathrm{RMS,pixel}}$ pixel map and histogram of the 2. scan of sample 5-SS-ep-6 after bake-out.

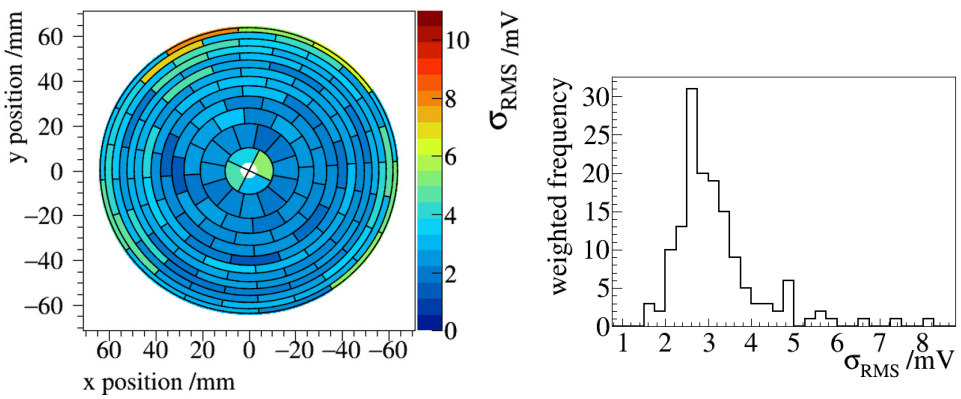

Figure E.217: $\sigma_{\mathrm{RMS,pixel}}$ pixel map and histogram of the 3. scan of sample 5-SS-ep-6 after bake-out.

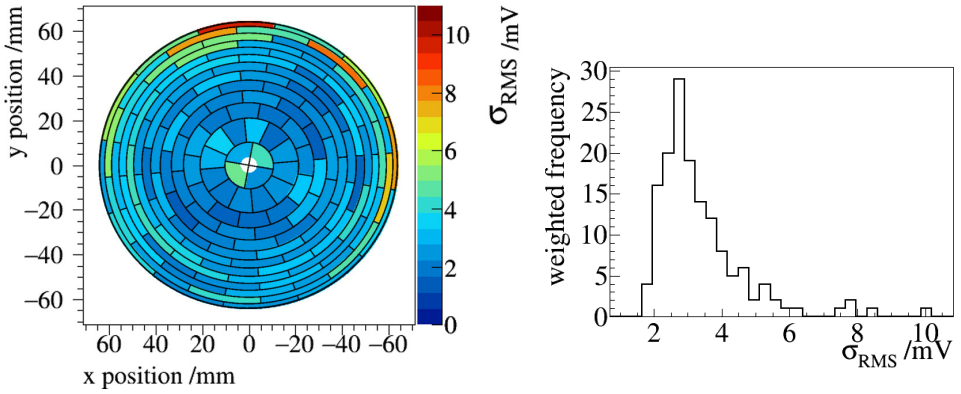

Figure E.218: $\sigma_{\mathrm{RMS,pixel}}$ pixel map and histogram of the 4. scan of sample 5-SS-ep-6 after bake-out.

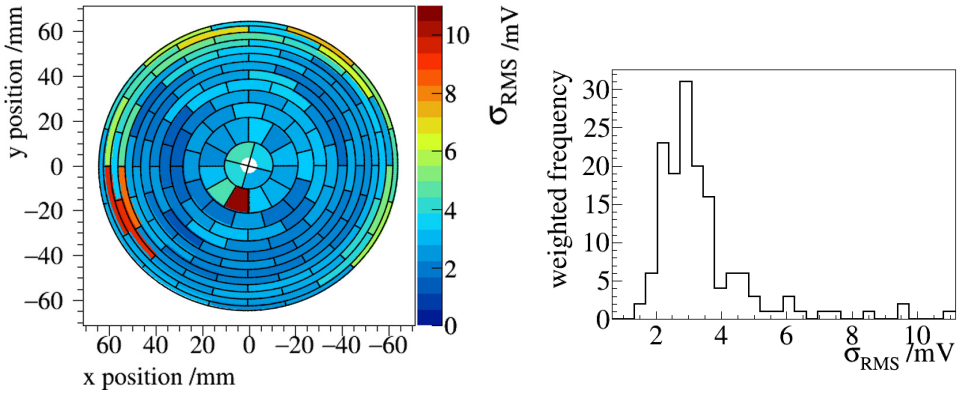

Figure E.219: $\sigma_{\mathrm{RMS,pixel}}$ pixel map and histogram of the 5. scan of sample 5-SS-ep-6 after bake-out.

Bibliography

[Aar14] M. G. Aartsen and others (IceCube PINGU Collaboration). *Letter of Intent: The Precision IceCube Next Generation Upgrade (PINGU)* (2014).

[Abd94] J. N. Abdurashitov et al.. *Results from SAGE (The Russian-American gallium solar neutrino experiment).* Physics Letters B, **328** 1, 234–248 (1994).

[Abd02] J. N. Abdurashitov and others (SAGE Collaboration). *Solar neutrino flux measurements by the Soviet-American Gallium Experiment (SAGE) for half the 22 year solar cycle.* J. Exp. Theor. Phys., **95**, 181–193 (2002).

[Abe08] S. Abe and others (KamLAND Collaboration). *Precision Measurement of Neutrino Oscillation Parameters with KamLAND.* Physical Review Letters, **100** (2008).

[Abe11] K. Abe and others (Super-Kamiokande Collaboration). *Search for Differences in Oscillation Parameters for Atmospheric Neutrinos and Antineutrinos at Super-Kamiokande.* Physical Review Letters, **107** (2011).

[Abe12] Y. Abe and others (Double Chooz Collaboration). *Reactor $\overline{\nu}_e$ disappearance in the Double Chooz experiment.* Physical Review D, **86** (2012).

[Abe13] K. Abe and others (T2K Collaboration). *Evidence of Electron Neutrino Appearance in a Muon Neutrino Beam.* Physical Review, **D88** 3 (2013).

[Abe14] Y. Abe and others (T2K Collaboration). *Observation of Electron Neutrino Appearance in a Muon Neutrino Beam.* Physical Review Letters, **112** (2014).

[Ada13a] C. Adams and others (LBNE Collaboration). *The Long-Baseline Neutrino Experiment: Exploring Fundamental Symmetries of the Universe* (2013).

[Ada13b] P. Adamson and others (MINOS Collaboration). *Measurement of Neutrino and Antineutrino Oscillations Using Beam and Atmospheric Data in MINOS.* Physical Review Letters, **110** (2013).

[Ada14] P. Adamson et al.. *Combined Analysis of ν_μ Disappearance and $\nu_\mu \to \nu_e$ Appearance in MINOS Using Accelerator and Atmospheric Neutrinos.* Physical Review Letters, **112** (2014).

[Ade14] P. A. R. Ade and others (Planck Collaboration). *Planck 2013 results. XVI. Cosmological parameters.* Astronomy and Astrophysics, **571**, A16 (2014).

[Aga11] S. Agarwal and H. A. Feldman. *The effect of massive neutrinos on the matter power spectrum.* Monthly Notices of the Royal Astronomical Society, **410** 3, 1647–1654 (2011).

[Ago13] M. Agostini and others (GERDA Collaboration). *Results on Neutrinoless Double-β Decay of ^{76}Ge from Phase I of the GERDA Experiment.* Physical Review Letters, **111** (2013).

[Aha07] B. Aharmim and others (SNO Collaboration). *Determination of the ν_e and total ^{8}B solar neutrino fluxes using the Sudbury Neutrino Observatory Phase I data set.* Physical Review C, **75** (2007).

[Aha08] B. Aharmim and others (SNO Collaboration). *An Independent Measurement of the Total Active B-8 Solar Neutrino Flux Using an Array of He-3 Proportional Counters at the Sudbury Neutrino Observatory.* Physical Review Letters, **101** (2008).

[Aha13] B. Aharmim and others (SNO Collaboration). *Combined analysis of all three phases of solar neutrino data from the Sudbury Neutrino Observatory.* Physical Review C, **88** (2013).

[Ahm01] Q. R. Ahmad and others (SNO Collaboration). *Measurement of the Rate of $\nu_e + d \rightarrow p + p + e^-$ Interactions Produced by ^8B Solar Neutrinos at the Sudbury Neutrino Observatory.* Physical Review Letters, **87** (2001).

[Ahm02] Q. R. Ahmad and others (SNO Collaboration). *Direct evidence for neutrino flavor transformation from neutral current interactions in the Sudbury Neutrino Observatory.* Physical Review Letters, **89** (2002).

[Ahm14] S. Ahmed. *Physics and Engineering of Radiation Detection.* Elsevier Science (2014).

[Ahn06] M. Ahn and others (K2K Collaboration). *Measurement of neutrino oscillation by the K2K experiment.* Physical Review D, **74** (2006).

[Ahn12] J. K. Ahn and others (RENO Collaboration). *Observation of Reactor Electron Antineutrinos Disappearance in the RENO Experiment.* Physical Review Letters, **108** (2012).

[Akh99] E. K. Akhmedov. *Neutrino physics.* 103–164 (1999).

[Alb04] C. H. Albright, others (Neutrino Factory and Muon Collider Collaboration). *The neutrino factory and beta beam experiments and development* (2004).

[Alb14] J. B. Albert and others (EXO-200 Collaboration). *Improved measurement of the $2\nu\beta\beta$ half-life of ^{136}Xe with the EXO-200 detector.* Physical Review, **C89** 1 (2014).

[Alf81] H. Alfvèn. *Cosmic Plasma.* Astrophysics and Space Science Library: a series of books on the recent developments of space science and of general geophysics and astrophysics. Springer (1981).

[Alt05] M. Altmann and others (GNO Collaboration). *Complete results for five years of GNO solar neutrino observations.* Physics Letters, **B616**, 174–190 (2005).

[Ams15] J. F. Amsbaugh et al.. *Focal-plane detector system for the KATRIN experiment.* Nuclear Instruments and Methods in Physics Research Section A: Accelerators, Spectrometers, Detectors and Associated Equipment (2015).

[An13] F. P. An and others (Daya Bay Collaboration). *Improved Measurement of Electron Antineutrino Disappearance at Daya Bay.* Chinese Physics, **C37** (2013).

[An14] F. P. An and others (Daya Bay Collaboration). *Spectral Measurement of Electron Antineutrino Oscillation Amplitude and Frequency at Daya Bay.* Physical Review Letters, **112** (2014).

[And59] P. A. Anderson. *Work Function of Gold.* Physical Review, **115**, 553–554 (1959).

[Ang05] J. Angrik et al.. *KATRIN design report 2004.* Wissenschaftliche Berichte FZKA, 7090 (2005).

[Ans92] P. Anselmann et al.. *Solar neutrinos observed by GALLEX at Gran Sasso.* Physics Letters B, **285** 4, 376–389 (1992).

[Arn04] C. Arnaboldi et al.. *CUORE: a cryogenic underground observatory for rare events.* Nuclear Instruments and Methods in Physics Research Section A: Accelerators, Spectrometers, Detectors and Associated Equipment, **518** 3, 775 – 798 (2004).

[Ase11] V. Aseev et al.. *Upper limit on the electron antineutrino mass from the Troitsk experiment.* Physical Review D, **84** (2011).

[Ass96] K. Assamagan et al.. *Upper limit of the muon-neutrino mass and charged-pion mass from momentum analysis of a surface muon beam.* Physical Review D, **53**, 6065–6077 (1996).

[Att13] Attocube systems AG. *ANPx101/RES.* datasheet, unpublished (2013). Http://marketing.attocube.com/acton/attachment/4434/f-00d9/0/-/-/-/-/file.pdf (last accessed November 24, 2015).

[Ava15] Avantes. *Avantes homepage - Solarization Resistant Fibers for Deep UV applications.* unpublished (2015). Http://www.avantes.com/products/fiber-optics/item/262-fiber-optic-cables (last accessed November 24, 2015).

[Avd12] S. Avdiaj and B. Erjavec. *Outgassing of hydrogen from a stainless steel vacuum chamber.* Materiali in tehnologije, **46** 2, 161–167 (2012).

[Ayr04] D. S. Ayres and others (NOvA Collaboration). *NOvA: Proposal to build a 30 kiloton off-axis detector to study nu(mu) → nu(e) oscillations in the NuMI beamline.* Fermilab Technical Publications: proposal, 0929 (2004).

[Bab12] M. Babutzka et al.. *Monitoring of the operating parameters of the KATRIN Windowless Gaseous Tritium Source.* New Journal of Physics, **14** 10 (2012).

[Bab13] M. Babutzka et al.. *Katrin rearsection system specification document.* internal document (2013).

[Bab14] M. Babutzka. *Design and development for the Rearsection of the KATRIN experiment.* Ph.D. thesis, Karlsruhe Institute of Technology (2014).

[Bab15] S. Babar and J. H. Weaver. *Optical constants of Cu, Ag, and Au revisited.* Applied Optics, **54** 3, 477–481 (2015).

[Bac85] A. Bachtin. *A very short response time electronic system for the measurement of surface potential changes by means of a static capacitor method.* Vacuum, **35** 12, 519 – 521 (1985).

[Bah64] J. N. Bahcall. *Solar Neutrino Cross Sections and Nuclear Beta Decay.* Physical Review, **135**, B137–B146 (1964).

[Bah76] J. N. Bahcall and R. Davis. *Solar Neutrinos - a Scientific Puzzle.* Science, **191**, 264–267 (1976).

[Bah87] J. N. Bahcall, A. Dar and T. Piran. *Neutrinos and neutrino mass from a supernova.* Nature, **326**, 135–136 (1987).

[Bah01] J. N. Bahcall, M. H. Pinsonneault and S. Basu. *Solar models: Current epoch and time dependences, neutrinos, and helioseismological properties.* The Astrophysical Journal, **555**, 990–1012 (2001).

[Bah05] J. N. Bahcall, A. M. Serenelli and S. Basu. *New solar opacities, abundances, helioseismology, and neutrino fluxes.* The Astrophysical Journal, **621**, L85–L88 (2005).

[Bai89] I. D. Baikie, K. O. van der Werf, H. Oerbekke, J. Broeze and A. van Silfhout. *Automatic kelvin probe compatible with ultrahigh vacuum.* Review of Scientific Instruments, **60** 5, 930–934 (1989).

[Bai91] I. D. Baikie, S. Mackenzie, P. J. Z. Estrup and J. A. Meyer. *Noise and the Kelvin method.* Review of Scientific Instruments, **62** 5, 1326–1332 (1991).

[Bai99] I. Baikie, U. Petermann and B. Lägel. *UHV-compatible spectroscopic scanning Kelvin probe for surface analysis.* Surface Science, **433 - 435** 0, 249 – 253 (1999).

[Bai01] I. D. Baikie, U. Peterman, B. Lägel and K. Dirscherl. *Study of high- and low-work-function surfaces for hyperthermal surface ionization using an absolute Kelvin probe.* Journal of Vacuum Science & Technology A, **19** 4, 1460–1466 (2001).

[Bar41] R. M. Barrer. *Diffusion in and Through Solids.* Cambridge series of physical chemistry. Macmillan (1941).

[Bar98] R. Barate et al.. *An upper limit on the τ neutrino mass from three- and five-prong tau decays.* The European Physical Journal C - Particles and Fields, **2** 3, 395–406 (1998).

[Bar00] V. D. Barger, S. Geer, R. Raja and K. Whisnant. *Long baseline study of the leading neutrino oscillation at a neutrino factory.* Physical Review, **D62** (2000).

[Bar11] A. S. Barabash and V. B. Brudanin. *Investigation of double beta decay with the NEMO-3 detector.* Physics of Atomic Nuclei, **74**, 312–317 (2011).

[Bel10] G. Bellini and others (Borexino Collaboration). *Observation of Geo-Neutrinos.* Physics Letters, **B687**, 299–304 (2010).

[Bel14] G. Bellini and others (Borexino Collaboration). *Final results of Borexino Phase-I on low-energy solar neutrino spectroscopy.* Phys. Rev. D, **89** (2014).

[Bet34] H. Bethe and R. Peierls. *Experimental investigation of geologically produced antineutrinos with KamLAND.* Nature, **133** (1934).

[Beu11] F. Beutler et al.. *The 6dF Galaxy Survey: baryon acoustic oscillations and the local Hubble constant.* Oxford Journals, **416**, 3017–3032 (2011).

[Bil80] S. Bilenky, J. Hošek and S. Petcov. *On the oscillations of neutrinos with Dirac and Majorana masses.* Physics Letters B, **94** 4, 495 – 498 (1980).

[Bio87] R. M. Bionta et al.. *Observation of a Neutrino Burst in Coincidence with Supernova SN 1987a in the Large Magellanic Cloud.* Physical Review Letters, **58**, 1494 (1987).

[Bla06] *High-accuracy mass spectrometry with stored ions.* Physics Reports, **425** 1, 1–78 (2006).

[Bog85] D. Bogdan, A. Faessler, A. Petrovici and S. Holan. *neutrino masses and right-handed current in the neutrinoless double beta decay Ge-76 → Se-76 + 2e⁻.* Physics Letters, **B150**, 29–34 (1985).

[Boi03] B. Boizot, S. Agnello, B. Reynard, R. Boscaino and G. Petite. *Raman spectroscopy study of β-irradiated silica glass.* Journal of non-crystalline solids, **325** 1, 22–28 (2003).

[Boo96] N. Booth, B. Cabrera and E. Fiorini. *Low-temperature particle detectors.* Annual Review of Nuclear and Particle Science, **46**, 471–532 (1996).

[Bru97] R. Brun and F. Rademakers. *ROOT - An object oriented data analysis framework.* Nuclear Instruments and Methods in Physics Research Section A: Accelerators, Spectrometers, Detectors and Associated Equipment, **389** 1–2, 81–86 (1997).

[Bru98] A. S. Brun, S. Turck-Chieze and P. Morel. *Standard solar models in the light of new helioseismic constraints. 1. The Solar core.* The Astrophysical Journal, **506**, 913–925 (1998).

[Bur00] A. K. Burnham, M. J. Runkel, S. G. Demos, M. R. Kozlowski and P. J. Wegner. *Effect of vacuum on the occurrence of UV-induced surface photoluminescence, transmission loss, and catastrophic surface damage.* Proceedings of SPIE, **4134**, 243–252 (2000).

[Bus09] G. Buscarino, S. Agnello, F. M. Gelardi and R. Boscaino. *Polyamorphic transformation induced by electron irradiation in a-SiO_2 glass.* Physical Review B, **80** (2009).

[Bus10] G. Buscarino, S. Agnello, F. Gelardi and R. Boscaino. *The role of impurities in the irradiation induced densification of amorphous SiO2.* Journal of Physics: Condensed Matter, **22** 25 (2010).

[Cal90] J. G. Calvert. *Glossary of atmospheric chemistry terms (Recommendations 1990).* Pure and Applied Chemistry, **62** 11, 2167–2219 (1990).

[Cha14] J. Chadwick. *The intensity distribution in the magnetic spectrum of beta particles from radium (B + C).* Verhandlungen der Physikalischen Gesellschaft, **16**, 383–391 (1914).

[Chu09] C. Chung and W. Chang. *Comparison of methods for sensing contact potential difference of nanocrystalline alloy films using a kelvin actuating capacitor*. 274–277 (2009).

[Cla34] É. Clapeyron. *Mémoire sur la puissance motrice de la chaleur*. Journal de lÉcole Royale Polytechnique XIV, 153–190 (1834).

[Cle98] B. Cleveland et al.. *Measurement of the Solar Electron Neutrino Flux with the Homestake Chlorine Detector*. The Astrophysical Journal, **496** 1, 505 (1998).

[Cof88] D. O. Coffin, S. P. Cole and R. C. Wilhelm. *A tritium-compatible piezoelectric valve for the tokanak fusion test reactor*. Fusion Science and Technology, **14** 2P2B, 972–976 (1988).

[Cor15] N. Corporation. *Optical Materials*. homepage, unpublished (2015). Http://www.newport.com/Optical-Materials/144943/1033/content.aspx (last accessed December 1, 2015).

[Cou67] C. E. Council and U. S. O. of Naval Research. *Nuclear Science and Technology for Ceramists: Proceedings of a Symposium, April 7-12, 1966*. No. Bd. 13 in Miscellaneous publication - Department of Commerce Bureau of Standards. U.S. Department of Commerce, National Bureau of Standards (1967).

[Cow56] C. L. Cowan, F. Reines, F. B. Harrison, H. W. Kruse and A. D. McGuire. *Detection of the free neutrino: A Confirmation*. Science, **124**, 103–104 (1956).

[Cox82] J. Cox. *Notation for states and processes, significance of the word standard in chemical thermodynamics, and remarks on commonly tabulated forms of thermodynamic functions*. Pure and Applied Chemistry, **54** 6, 1239–1250 (1982).

[Cra75] J. Crank et al.. *The mathematics of diffusion*, vol. 2. Clarendon press Oxford (1975).

[Dan62] G. Danby et al.. *Observation of High-Energy Neutrino Reactions and the Existence of Two Kinds of Neutrinos*. Physical Review Letters, **9**, 36–44 (1962).

[Dav55] R. Davis, Jr. *Attempt to detect the antineutrinos from a nuclear reactor by the Cl37(anti-nu,e-) A37 reaction*. Physical Review, **97**, 766–769 (1955).

[Dav68] R. Davis, D. S. Harmer and K. C. Hoffman. *Search for Neutrinos from the Sun*. Physical Review Letters, **20**, 1205–1209 (1968).

[Dav79] R. Davis, Jr., J. C. Evans and B. T. Cleveland. *The solar neutrino problem*. AIP Conf. Proc., **52**, 17–27 (1979).

[Dav94] R. Davis. *A review of the Homestake solar neutrino experiment*. Progress in Particle and Nuclear Physics, **32**, 13–32 (1994).

[Dec04] M. Decreton, T. Shikama and E. Hodgson. *Performance of functional materials and components in a fusion reactor: the issue of radiation effects in ceramics and glass materials for diagnostics*. Journal of Nuclear Materials, **329–333, Part A** 0, 125 – 132 (2004).

[Dem12] D. Demange et al.. *Overview of R and D at TLK for process and analytical issues on tritium management in breeder blankets of ITER and DEMO.* Fusion Engineering and Design, **87** 7–8, 1206–1213 (2012). Tenth International Symposium on Fusion Nuclear Technology (ISFNT-10).

[Dem14] W. Demtröder. *Experimentalphysik 2: Elektrizität und Optik.* Springer-Lehrbuch (2014).

[Dev90] R. Devine. *Radiation damage and the role of structure in amorphous SiO2.* Nuclear Instruments and Methods in Physics Research Section B: Beam Interactions with Materials and Atoms, **46** 1-4, 244 – 251 (1990).

[Dev94] R. Devine. *Macroscopic and microscopic effects of radiation in amorphous SiO2.* Nuclear Instruments and Methods in Physics Research Section B: Beam Interactions with Materials and Atoms, **91** 1-4, 378 – 390 (1994).

[Doi85] M. Doi, T. Kotani and E. Takasugi. *Double Beta Decay and Majorana Neutrino.* Progress of Theoretical Physics Supplement, **83**, 1–175 (1985).

[Dom74] M. Domke, G. Jähnig and M. Drechsler. *Measurement of the adsorption energy on single crystal faces by field emission (hydrogen on tungsten).* Surface Science, **42** 2, 389 – 403 (1974).

[Dre13] G. Drexlin, V. Hannen, S. Mertens and C. Weinheimer. *Current Direct Neutrino Mass Experiments.* Advances in High Energy Physics, **2013** (2013).

[Ede66] G. Eder. *Terrestrial neutrinos.* Nuclear Physics, **78** 3, 657 – 662 (1966).

[Edm14] Edmund Optics Inc. *Homepage of Edmund Optics Inc.* homepage, unpublished (2014). Http://www.edmundoptics.com/ (last accessed November 24, 2015).

[Efr94] B. Efron and R. Tibshirani. *An Introduction to the Bootstrap.* Chapman & Hall/CRC Monographs on Statistics & Applied Probability. Taylor & Francis (1994).

[Ein05] A. Einstein. *Ueber einen die Erzeugung und Verwandlung des Lichtes betreffenden heuristischen Gesichtspunkt.* Annalen der Physik, **322** 6, 132 – 148 (1905).

[Ene14] Energetiq Technology, Inc. *EQ-99XFC LDLS.* datasheet, unpublished (2014). Http://www.energetiq.com/DataSheets/EQ99XFC-Data-Sheet.pdf (last accessed November 24, 2015).

[Eng13] J. Engle et al.. *Evaluation of 163Ho production options for neutrino mass measurements with microcalorimeter detectors.* Nuclear Instruments and Methods in Physics Research Section B: Beam Interactions with Materials and Atoms, **311**, 131 – 138 (2013).

[Erh14] M. Erhard et al.. *High-voltage monitoring with a solenoid retarding spectrometer at the KATRIN experiment.* Journal of Instrumentation, **9** 6, P06022 (2014).

[Fer34] E. Fermi. *Versuch einer Theorie der β-Strahlen.* Zeitschrift für Physik, **88** 3–4, 161–177 (1934).

[Feu76] B. Feuerbacher and R. F. Willis. *Photoemission and electron states at clean surfaces.* Journal of Physics C: Solid State Physics, **9** 2, 169 (1976).

[Fey58] R. P. Feynman and M. Gell-Mann. *Theory of the Fermi Interaction.* Physical Review, **109**, 193–198 (1958).

[Fis11] S. Fischer et al.. *Monitoring of tritium purity during long-term circulation in the KATRIN test experiment LOOPINO using laser Raman spectroscopy.* Fusion Science and Technology, **60** 3, 925–930 (2011).

[Fis14] S. Fischer. *Commissioning of the KATRIN Raman system and durability studies of optical coatings in glove box and tritium atmospheres.* Ph.D. thesis, Karlsruhe Institute of Technology (2014).

[Fla11] R. L. Flack. *NEMO-3 and SuperNEMO: A search for zero neutrino double beta decay.* Nuclear Physics B - Proceedings Supplements, **217** 1, 53 – 55 (2011).

[Fle05] A. Fleischmann, C. Enss and G. Seidel. *Metallic Magnetic Calorimeters.* In C. Enss (Ed.), *Cryogenic Particle Detection*, vol. 99 of *Topics in Applied Physics*, 151–216. Springer Berlin Heidelberg (2005).

[For12] J. Formaggio et al.. *Solving for micro- and macro-scale electrostatic configurations using the robin hood algorithm.* Progress In Electromagnetics Research B, **39**, 1–37 (2012).

[Fow28] R. H. Fowler and L. Nordheim. *Electron emission in intense electric fields.* **119** 781, 173–181 (1928).

[Fow31] R. H. Fowler. *The Analysis of Photoelectric Sensitivity Curves for Clean Metals at Various Temperatures.* Physical Review, **38**, 45–56 (1931).

[Fre31] J. Frenkel. *Some Remarks on the Theory of the Photoelectric Effect.* Physical Review, **38**, 309–320 (1931).

[Fuk94] Y. Fukuda and others (Kamiokande Collaboration). *Atmospheric ν_μ/ν_e ratio in the multi-GeV energy range.* Physics Letters, **B335**, 237–245 (1994).

[Fuk96] Y. Fukuda and others (Kamiokande Collaboration). *Solar neutrino data covering solar cycle 22.* Physical Review Letters, **77**, 1683–1686 (1996).

[Fuk98] Y. Fukuda and others (Super-Kamiokande Collaboration). *Evidence for oscillation of atmospheric neutrinos.* Physical Review Letters, **81**, 1562–1567 (1998).

[Fuk01] S. Fukuda and others (Super-Kamiokande Collaboration). *Solar B-8 and hep neutrino measurements from 1258 days of Super-Kamiokande data.* Physical Review Letters, **86**, 5651–5655 (2001).

[Gal09] M. Galassi et al.. *GNU Scientific Library Reference Manual-(v1. 12).* Network Theory Ltd, **83** (2009).

[Gan13] A. Gando and others (KamLAND-Zen Collaboration). *Limit on Neutrinoless $\beta\beta$ Decay of ^{136}Xe from the First Phase of KamLAND-Zen and Comparison with the Positive Claim in ^{76}Ge.* Physical Review Letters, **110** 6 (2013).

[Gas09] L. Gastaldo et al.. *Low Temperature Magnetic Calorimeters For Neutrino Mass Direct Measurement.* AIP Conference Proceedings, **1185** 1, 607–611 (2009).

[Gat01] F. Gatti. *Microcalorimeter measurements.* Nuclear Physics B - Proceedings Supplements, **91**, 293–296 (2001).

[Gha98] A. Ghatak and K. Thyagarajan. *An Introduction to Fiber Optics* (1998).

[Gil83] J. T. Gill, B. E. Anderson, R. A. Watkins and C. W. Pierce. *Tritium storage/delivery and associated cleanup systems for TFTR.* Journal of Vacuum Science & Technology A, **1** 2, 856–864 (1983).

[Gil10] W. Gil et al.. *The Cryogenic Pumping Section of the KATRIN Experiment.* IEEE Transactions on Applied Superconductivity, **20** 3, 316–319 (2010).

[Glö04] R. Glöss and H. Marth. *Verstellantrieb aus Bimorphelementen* (2004).

[GM00] M. García-Matos, A. Moroño and E. Hodgson. *KU1 quartz glass for remote handling and LIDAR diagnostic optical transmission systems.* Journal of Nuclear Materials, **283–287, Part 2** 0, 890 – 893 (2000).

[Gol58] M. Goldhaber, L. Grodzins and A. W. Sunyar. *Helicity of Neutrinos.* Physical Review, **109**, 1015–1017 (1958).

[Gos78] O. Goscinski. *Principles of Ultraviolet Photoelectron Spectroscopy. J. W. Rabalais. Wiley-Interscience Monographs in Chemical Physics, New York, 1977.* International Journal of Quantum Chemistry, **13** 2 (1978).

[Gri69] V. N. Gribov and B. Pontecorvo. *Neutrino astronomy and lepton charge.* Physics Letters, **B28**, 493 (1969).

[Gri85] D. L. Griscom. *Diffusion of radiolytic molecular hydrogen as a mechanism for the post-irradiation buildup of interface states in SiO2-on-Si structures.* Journal of Applied Physics, **58** 7, 2524–2533 (1985).

[Gri91] D. L. Griscom. *Optical Properties and Structure of Defects in Silica Glass: Optical Materials.* Journal of the Ceramic Society of Japan, **99** 1154, 923–942 (1991).

[Gri14] S. Grimnes and O. Martinsen. *Bioimpedance and Bioelectricity Basics.* Elsevier Science (2014).

[Gro13] S. Grohmann et al.. *The thermal behaviour of the tritium source in KATRIN.* Cryogenics, **55-56** 0, 5–11 (2013).

[Güd05] J. Güdde and U. Höfer. *Femtosecond time-resolved studies of image-potential states at surfaces and interfaces of rare-gas adlayers.* Progress in Surface Science, **80** 3, 49–91 (2005).

[Hal12] R. Halmshaw. *Industrial Radiology: Theory and practice.* Non-Destructive Evaluation Series. Springer Netherlands (2012).

[Ham99] W. Hampel and others (GALLEX Collaboration). *GALLEX solar neutrino observations: Results for GALLEX IV.* Physics Letters, **B447**, 127–133 (1999).

[Har12] J. Hartnell and SNO+ Collaboration. *Neutrinoless Double Beta Decay with SNO+.* Journal of Physics Conference Series, **375** 4 (2012).

[Hay14] W. Haynes. *CRC Handbook of Chemistry and Physics, 95th Edition*. CRC Press (2014).

[Hec12] G. Hechenblaikner et al.. *Energy distribution and quantum yield for photoemission from air-contaminated gold surfaces under ultraviolet illumination close to the threshold*. Journal of Applied Physics, **111** 12 (2012).

[Hec13] F. Hecht. *Verwendung der Radioaktivität in der Mikrochemie*. Handbuch der Mikrochemischen Methoden. Springer Berlin Heidelberg (2013).

[Hei15] F. Heizmann. *Optimization of a katrin source analysis tool and investigations of the relic neutrino discovery potential*. Master thesis, Karlsruhe institute of Technology, Institute of experimental particle physics (2015).

[Her87] H. Hertz. *Ueber einen Einfluss des ultravioletten Lichtes auf die electrische Entladung*. Annalen der Physik, **267** 8, 983 – 1000 (1887).

[Hig64] P. W. Higgs. *Broken Symmetries and the Masses of Gauge Bosons*. Physical Review Letters, **13**, 508–509 (1964).

[Hii10] K.-F. Hii, R. R. Vallancea and M. P. Mengüç. *Design, operation, and motion characteristics of a precise piezoelectric linear motor*. Precision Engineering, **34** 2, 231–241 (2010).

[Hin13] G. Hinshaw and others (WMAP Collaboration). *Nine-Year Wilkinson Microwave Anisotropy Probe (WMAP) Observations: Cosmological Parameter Results*. The Astrophysical Journal Supplement Series, **208**, 19 (2013).

[Hir88] K. S. Hirata et al.. *Observation in the Kamiokande-II Detector of the Neutrino Burst from Supernova SN 1987a*. Physical Review, **D38**, 448–458 (1988).

[Hir89] K. S. Hirata and others (Kamiokande Collaboration). *Observation of B-8 solar neutrinos in the Kamiokande-II detector*. Phys. Rev. Lett., **63**, 16 (1989).

[Hir04] M. Hirsch and J. W. F. Valle. *Supersymmetric origin of neutrino mass*. New Journal of Physics, **6**, 76 (2004).

[Hir05] S. Hirsch, H. Klein and P. Jung. *Dimensional changes of silica-, borosilicate- and germania-glasses and quartz under irradiation*. Journal of Non-Crystalline Solids, **351** 40-42, 3279 – 3288 (2005).

[Hol66] A. A. Holscher. *A field emission retarding potential method for measuring work functions*. Surface Science, **4**, 89–102 (1966).

[Hol70] J. M. Hollander and W. L. Jolly. *X-ray photoelectron spectroscopy*. Accounts of Chemical Research, **3** 6, 193–200 (1970).

[Höt12] M. Hötzel. *Simulation and analysis of source-related effects for KATRIN*. Ph.D. thesis, Karlsruher Institut für Technologie (KIT) (2012).

[Hub31] E. Hubble and M. Humason. *The Velocity-Distance Relation among Extra-Galactic Nebulae*. Astrophysical Journal, **74**, 43 (1931).

[Hub95] A. Hubbard. *The Handbook of Surface Imaging and Visualization*. Taylor & Francis (1995).

[Hüf03] S. Hüfner. *Photoelectron Spectroscopy: Principles and Applications.* Advanced Texts in Physics. Springer (2003).

[Hum97] J. Humpenöder. *Gaspermeation von Faserverbunden mit Polymermatrices.* Forschungszentrum Karlsruhe: Wissenschaftliche Berichte. Forschungszentrum Karlsruhe GmbH (1997).

[Hum98] J. Humpenöder. *Gas permeation of fibre reinforced plastics.* Cryogenics, **38** 1, 143 – 147 (1998).

[Iba07] A. Ibarra, A. Muñoz-Martín, P. Martín, A. Climent-Font and E. Hodgson. *Radiation effects on the deuterium diffusion in SiO2.* Journal of Nuclear Materials, **367–370, Part B**, 1003 – 1008 (2007).

[Ina10] U. Inan and M. Golkowski. *Principles of Plasma Physics for Engineers and Scientists.* Cambridge University Press (2010).

[ISO96] *Natural gas – Standard reference conditions.* Standard, International Organization for Standardization, Geneva, CH (1996).

[Jan07] H.-T. Janka, K. Langanke, A. Marek, G. Martinez-Pinedo and B. Mueller. *Theory of Core-Collapse Supernovae.* Physics Reports, **442**, 38–74 (2007).

[Jia97] J. F. Jia, K. Inoue, Y. Hasegawa, W. S. Yang and T. Sakurai. *Local work function for Cu (111)-Au surface studied by scanning tunneling microscopy.* Journal of Vacuum Science & Technology B, **15** 6, 1861 – 1864 (1997).

[Jia98a] J. F. Jia, K. Inoue, Y. Hasegawa, W. S. Yang and T. Sakurai. *Variation of the local work function at steps on metal surfaces studied with STM.* Physical Review B, **58**, 1193 – 1196 (1998).

[Jia98b] X. Jiang, C. N. Berglund, A. E. Bell and W. A. Mackie. *OS3: Photoemission from gold thin films for application in multiphotocathode arrays for electron beam lithography.* Journal of Vacuum Science & Technology B, **16** 6, 3374–3379 (1998).

[Joh74] P. B. Johnson and R. W. Christy. *Optical constants of transition metals: Ti, V, Cr, Mn, Fe, Co, Ni, and Pd.* Physical Review B, **9**, 5056–5070 (1974).

[Käs02] G. Kästle et al.. *Growth of thin, flat, epitaxial (1 1 1) oriented gold films on c-cut sapphire.* Surface Science, **498** 1–2, 168 – 174 (2002).

[Kaz08] O. Kazachenko et al.. *TRAP - a cryo-pump for pumping tritium on precondensed argon.* Nuclear Instruments and Methods in Physics Research Section A: Accelerators, Spectrometers, Detectors and Associated Equipment, **587** 1, 136 – 144 (2008).

[KB08] S. Kraft-Bermuth et al.. *Development and Characterization of Microcalorimeters for a Next Generation 187Re Beta-Decay Experiment.* Journal of Low Temperature Physics, **151** 3-4, 619–622 (2008).

[Kel98] L. Kelvin. *V. Contact electricity of metals.* Philosophical Magazine Series 5, **46** 278, 82–120 (1898).

[Kib67] T. W. B. Kibble. *Symmetry breaking in nonAbelian gauge theories.* Physical Review, **155**, 1554–1561 (1967).

[Kla04] H. V. Klapdor-Kleingrothaus, I. V. Krivosheina, A. Dietz and O. Chkvorets. *Search for neutrinoless double beta decay with enriched Ge-76 in Gran Sasso 1990-2003*. Physics Letters, **B586**, 198–212 (2004).

[Kla06] H. V. Klapdor-Kleingrothaus and I. V. Krivosheina. *The evidence for the observation of 0nu beta beta decay: The identification of 0nu beta beta events from the full spectra*. Moderne Physics Letters, **A21**, 1547–1566 (2006).

[Kla13] H. V. Klapdor-Kleingrothaus and K. Zuber. *Teilchenastrophysik*. Teubner Studienbücher Physik. Vieweg+Teubner Verlag (2013).

[Kna73] A. Knapp. *Surface potentials and their measurement by the diode method*. Surface Science, **34** 2, 289 – 316 (1973).

[Koc59] H. W. Koch and J. W. Motz. *Bremsstrahlung Cross-Section Formulas and Related Data*. Reviews of Modern Physics, **31**, 920–955 (1959).

[Kod01] K. Kodama and others (DONUT Collaboration). *Observation of tau neutrino interactions*. Physics Letters, **B504**, 218–224 (2001).

[Kon11] G. E. Konrad. *Measurement of the proton recoil spectrum in neutron β-decay with the spectrometer aSPECT: Study of systematic effects*. Ph.D. thesis, Johannes Gutenberg Universität Mainz (2011).

[Kop07] S. E. Kopp. *Accelerator-based neutrino beams*. Physics Reports, **439**, 101–159 (2007).

[Kor13] J. Koryta, H. Bazantova, J. Dvorak and V. Bohackova. *Lehrbuch der Elektrochemie*. Springer Vienna (2013).

[Kos12] A. Kosmider. *Tritium Retention Techniques in the KATRIN Transport Section and Commissioning of its DPS2-F Cryostat*. Ph.D. thesis, Karlsruher Institut für Technologie (KIT) (2012).

[Kra23] H. A. Kramers. *XCIII. On the theory of X-ray absorption and of the continuous X-ray spectrum*. Philosophical Magazine Series 6, **46** 275, 836–871 (1923).

[Kra05] C. Kraus et al.. *Final results from phase II of the Mainz neutrino mass search in tritium β decay*. The European Physical Journal C - Particles and Fields, **40** 4, 447–468 (2005).

[Kuc16] L. Kuckert. *Simulation of the KATRIN tritium source and first measurements with the windowless gaseous tritium source*. Ph.D. thesis, Karlsruhe Institute of Technology (2016). (forthcoming).

[Lan71] N. D. Lang and W. Kohn. *Theory of Metal Surfaces: Work Function*. Physical Review B, **3**, 1215–1223 (1971).

[Lec01] P. Lechner et al.. *Silicon drift detectors for high count rate X-ray spectroscopy at room temperature*. Nuclear Instruments and Methods in Physics Research Section A: Accelerators, Spectrometers, Detectors and Associated Equipment, **458** 1–2, 281 – 287 (2001).

[Lee62] R. W. Lee, R. C. Frank and D. E. Swets. *Diffusion of Hydrogen and Deuterium in Fused Quartz*. The Journal of Chemical Physics, **36** 4, 1062–1071 (1962).

[Lee63] R. W. Lee. *Diffusion of Hydrogen in Natural and Synthetic Fused Quartz.* The Journal of Chemical Physics, **38** 2, 448–455 (1963).

[Leh11] J. Lehto and X. Hou. *Chemistry and Analysis of Radionuclides: Laboratory Techniques and Methodology.* Wiley (2011).

[Lei] Leitz. *Geradsicht-Spiegelmonochromator.* unpublished.

[Leo09] M. Leon, P. Martín, A. Ibarra and E. Hodgson. *Gamma irradiation induced defects in different types of fused silica.* Journal of Nuclear Materials, **386 - 388** 0, 1034 – 1037 (2009).

[Les12] J. Lesgourgues and S. Pastor. *Neutrino mass from Cosmology.* Advances in High Energy Physics, **2012** (2012).

[Li14] Y.-F. Li. *Overview of the Jiangmen Underground Neutrino Observatory (JUNO).* International Journal of Modern Physics Conference Series, **31** (2014).

[Lob85] V. Lobashev and P. Spivak. *A method for measuring the electron antineutrino rest mass.* Nuclear Instruments and Methods in Physics Research Section A: Accelerators, Spectrometers, Detectors and Associated Equipment, **240** 2, 305–310 (1985).

[Lor02] T. J. Loredo and D. Q. Lamb. *Bayesian analysis of neutrinos observed from supernova SN 1987A.* Physical Review D, **65** (2002).

[LTU14] LT ULTRA. *Metalloptiken Gesamtübersicht Optiken.* product catalogue, unpublished (2014). Http://www.lt-ultra.de/wp-content/uploads/2014/05/LT_Ultra_Metalloptik_Gesamt_deutsch.pdf (last accessed November 24, 2015).

[Luc00] L. Lucas and M. Unterweger. *Comprehensive review and critical evaluation of the half-life of Tritium.* Journal of research-national institute of standards and technology, **105** 4, 541–550 (2000).

[Lüt14] H. Lüth. *Solid Surfaces, Interfaces and Thin Films.* Graduate Texts in Physics. Springer International Publishing (2014).

[Mak62] Z. Maki, M. Nakagawa and S. Sakata. *Remarks on the unified model of elementary particles.* Progress of Theoretical Physics, **28**, 870–880 (1962).

[Mal65] I. H. Malitson. *Interspecimen Comparison of the Refractive Index of Fused Silica.* Journal of the Optical Society of America, **55** 10, 1205–1208 (1965).

[Man93] F. Mannone and C. of the European Communities. *Safety in Tritium Handling Technology.* Developments in Environmental Biology of Fishes. Springer Netherlands (1993).

[Mar97] C. D. Marshall, J. A. Speth and S. A. Payne. *Induced optical absorption in gamma, neutron and ultraviolet irradiated fused quartz and silica.* Journal of Non-Crystalline Solids, **212** 1, 59 – 73 (1997).

[Mar07] C. S. Marchi, B. Somerday and S. Robinson. *Permeability, solubility and diffusivity of hydrogen isotopes in stainless steels at high gas pressures.* International Journal of Hydrogen Energy, **32** 1, 100 – 116 (2007).

[Mar09] H. Marth and B. Lula. *Advancements in linear piezoelectric actuator mechanisms.* **7424** (2009).

[Mar10] W. E. Martinez, G. Gregori and T. Mates. *Titanium diffusion in gold thin films.* Thin Solid Films, **518** 10, 2585 – 2591 (2010).

[Mar13] J. Martin. *Physics for Radiation Protection.* Wiley (2013).

[May57] H. Mayer and H. Thomas. *Zum äusseren lichtelektrischen Effekt der Alkalimetalle.* Zeitschrift für Physik, **147** 4, 419–441 (1957).

[May07] P. Mayles, A. Nahum and J. Rosenwald. *Handbook of Radiotherapy Physics: Theory and Practice.* Taylor & Francis (2007).

[MDC15] MDC Vacuum Products LLC. *MDC Vacuum Products LLC Homepage.* unpublished (2014 (last accessed November 24, 2015)). Http://www.mdcvacuum.com/DisplayContentPage.aspx?cc=d60c2d6a-4233-407c-8538-ac7de62366b9.

[Mer12a] S. Mertens. *Study of Background Processes in the Electrostatic Spectrometers of the KATRIN experiment.* Ph.D. thesis, Karlsruher Institut für Technologie (KIT) (2012).

[Mer12b] S. Mertens et al.. *Stochastic Heating by ECR as a Novel Means of Background Reduction in the KATRIN spectrometers.* Journal of Instrumentation, **7** (2012).

[Mes08] D. Meschede. *Optics, Light and Lasers: The Practical Approach to Modern Aspects of Photonics and Laser Physics.* Physics textbook. Wiley (2008).

[Met57] S. Methfessel. *Zum äußeren lichtelektrischen Effekt der Alkalimetalle.* Zeitschrift für Physik, **147** 4, 442–464 (1957).

[Mik85] S. P. Mikheev and A. Yu. Smirnov. *Resonance Amplification of Oscillations in Matter and Spectroscopy of Solar Neutrinos.* Soviet Journal of Nuclear Physics, **42**, 913–917 (1985).

[Mit34] K. Mitchell. *The Theory of the Surface Photoelectric Effect in Metals. I.* Proceedings of the Royal Society of London. Series A, containing papers of a mathematical and physical character, 442–464 (1934).

[Mit36] K. Mitchell. *The Theory of the Surface Photoelectric Effect in Metals. II.* Proceedings of the Royal Society of London. Series A, Mathematical and Physical Sciences, **153** 880, 513–533 (1936).

[Moh80] R. N. Mohapatra and G. Senjanović. *Neutrino Mass and Spontaneous Parity Nonconservation.* Physical Review Letters, **44**, 912–915 (1980).

[Moh81] R. N. Mohapatra and G. Senjanovic. *Neutrino Masses and Mixings in Gauge Models with Spontaneous Parity Violation.* Physical Review, **D23**, 165 (1981).

[Moh15] P. J. Mohr, D. B. Newell and B. N. Taylor. *CODATA Recommended Values of the Fundamental Physical Constants: 2014.* ArXiv e-prints (2015).

[Mon91] H. Monjushiro, I. Watanabe and Y. Yokoyama. *Ultraviolet Photoelectron Yield Spectra of Thin Gold Films Measured in Air.* Analytical Sciences, **7** 4, 543–547 (1991).

[Mon09] B. Monreal and J. A. Formaggio. *Relativistic Cyclotron Radiation Detection of Tritium Decay Electrons as a New Technique for Measuring the Neutrino Mass.* Physical Review, **D80** (2009).

[Mor77] G. Morris. *Methane formation in tritium gas exposed to stainless steel.* Tech. Rep., California Univ., Livermore (USA). Lawrence Livermore Lab (1977).

[Mor03] T. Morita. *Miniature piezoelectric motors.* Sensors and Actuators, A: Physical, **103** 3, 291–300 (2003).

[Nat04] U. Natura, O. Sohr, R. Martin, M. Kahlke and G. Fasold. *Mechanisms of radiation-induced defect generation in fused silica.* Proceedings of SPIE, **5273**, 155–164 (2004).

[Nev85] E. Nevis. *Alteration of the Transmission Characteristics of Fused Silica Optical Fibers by Pulsed Ultraviolet Radiation.* 421–426 (1985).

[Non91] M. Nonnenmacher, M. P. OḂoyle and H. K. Wickramasinghe. *Kelvin probe force microscopy.* Applied Physics Letters, **58** 25, 2921 – 2923 (1991).

[Nor57] F. J. Norton. *Permeation of Gases through Solids.* Journal of Applied Physics, **28** 1, 34–39 (1957).

[Nor74] C. B. Norris and E. P. EerNisse. *Ionization dilatation effects in fused silica from 2 to 18 keV electron irradiation.* Journal of Applied Physics, **45** 9, 3876–3882 (1974).

[Nov03] S. N. Novikov and S. P. Timoshenkov. *Measurements of contact potential difference (work functions) of metals and semiconductors surface by the static ionized capacitor method.* Advances in Colloid and Interface Science, **105** 1-3, 329–339 (2003).

[Oli14] K. Olive and P. D. Group. *Review of Particle Physics.* Chinese Physics C, **38** 9 (2014).

[Ono01] S. Ono, M. Takeuchi and T. Takahashi. *Kelvin probe force microscopy on InAs thin films grown on GaAs giant step structures formed on (110) GaAs vicinal substrates.* Applied Physics Letters, **78** 8, 1086–1088 (2001).

[OPE14] OPERA collaboration. *The fourth transformation of neutrinos.* Press release (2014).

[O'R83] E. P. O'Reilly and J. Robertson. *Theory of defects in vitreous silicon dioxide.* Physical Review B, **27**, 3780–3795 (1983).

[Ott08] E. Otten and C. Weinheimer. *Neutrino mass limit from tritium β decay.* Reports on Progress in Physics, **71** 8 (2008).

[Ott12] E. Otten. *WGTS plasma potential under influence of patch effect potentials at rear plate.* internal document (2012).

[Pac00] G. Pacchioni. *Ab initio theory of point defects in SiO2.* In G. Pacchioni, L. Skuja and D. Griscom (Eds.), *Defects in SiO2 and Related Dielectrics: Science and Technology*, vol. 2 of *NATO Science Series*, 161–195. Springer Netherlands (2000).

[Pan12] T. Pan and L. Sun. *Sub-microscopic phenomena of metallic corrosion studied by a combined photoelectron spectroscopy in air (PESA) and scanning Kelvin probe force microscopy (SKPFM) approach.* International Journal of Electrochemical Science, **7**, 9325–9344 (2012).

[Pat12] R. B. Patterson. *The NOvA Experiment: Status and Outlook.* Proceedings, 25th International Conference on Neutrino Physics and Astrophysics (Neutrino 2012) (2012).

[Pau64] W. Pauli, R. Kronig and V. Weisskopf. *Collected scientific papers - Offener Brief an die Gruppe der Radioaktiven bei der Gauvereinstagung zu Tübingen (datiert 4. Dez. 1930).* Interscience, New York, NY (1964).

[Per09] D. Perkins. *Particle Astrophysics.* Oxford Master Series in Condensed Matter Physics. Oxford University Press, 2 edn. (2009).

[Pfe85] R. L. Pfeffer. *Damage center formation in SiO2 thin films by fast electron irradiation.* Journal of Applied Physics, **57** 12, 5176–5180 (1985).

[Phi12] D. G. Phillips, II et al.. *The Majorana experiment: an ultra-low background search for neutrinoless double-beta decay.* Journal of Physics Conference Series, **381** (2012).

[Phy13] Physik Instrumente (PI) GmbH und Co. KG. *Quote on custom-made piezo motor.* unpublished (2013).

[Phy15] Physik Instrumente (PI) GmbH und Co. KG. *NEXACT OEM Miniature Linear Motor / Actuator.* datasheet, unpublished (2015). Http://www.physikinstrumente.com/download/PI_DataSheet_N-310_42132.pdf (last accessed November 24, 2015).

[Pic92] A. Picard et al.. *A solenoid retarding spectrometer with high resolution and transmission for keV electrons.* Nuclear Instruments and Methods in Physics Research Section B: Beam Interactions with Materials and Atoms, **63** 3, 345–358 (1992).

[Pie49] J. Pierce. *Theory and design of electron beams.* Bell Telephone Laboratories series. Van Nostrand Co. (1949).

[Pil61] W. L. Pillinger, J. J. Hentges and J. A. Blair. *Tritium Decay Energy.* Physical Review, **121**, 232–233 (1961).

[Pit86] J. Pitts and A. Czanderna. *Reduction of silica surfaces with particle beams.* Nuclear Instruments and Methods in Physics Research Section B: Beam Interactions with Materials and Atoms, **13** 1–3, 245 – 249 (1986).

[Pon57] B. Pontecorvo. *Mesonium and anti-mesonium.* Soviet Physics JETP, **6**, 429 (1957).

[Pon58] B. Pontecorvo. *Inverse beta processes and nonconservation of lepton charge.* Soviet Physics JETP, **7**, 172–173 (1958).

[Pon68] B. Pontecorvo. *Neutrino experiments and the problem of conservation of leptonic charge.* Soviet Physics JETP, **26** 984, 25 (1968).

[Pov13] B. Povh, K. Rith, C. Scholz, F. Zetsche and W. Rodejohann. *Teilchen und Kerne: Eine Einführung in die physikalischen Konzepte.* Springer-Lehrbuch. Springer Berlin Heidelberg (2013).

[Pra12] M. Prall et al.. *The KATRIN pre-spectrometer at reduced filter energy.* New Journal of Physics, **14** 7 (2012).

[Pri13a] F. Priester. *Tritiumtechnologie für die fensterlose Quelle WGTS von KATRIN.* Ph.D. thesis, Karlsruher Institut für Technologie (KIT) (2013).

[Pri13b] F. Priester and B. Bornschein. *TriToP - A compatibility experiment with turbomolecular pumps under tritium atmosphere.* Vacuum, **98** 0, 22–28 (2013).

[Pri15] F. Priester, M. Sturm and B. Bornschein. *Commissioning and detailed results of KATRIN inner loop tritium processing system at Tritium Laboratory Karlsruhe.* Vacuum, **116**, 42 – 47 (2015).

[Ran12] P.-O. Ranitzsch et al.. *Development of Metallic Magnetic Calorimeters for High Precision Measurements of Calorimetric 187Re and 163Ho Spectra.* Journal of Low Temperature Physics, **167** 5-6, 1004–1014 (2012).

[Rei53] F. Reines and C. Cowan. *Detection of the Free Neutrino.* Physical Review, **92**, 830–831 (1953).

[Rei97] F. Reines and C. Cowan. *The Reines-Cowan experiments: detecting the poltergeist.* Los Alamos Science, 25, 4–6 (1997).

[Rei98] L. Reimer. *Scanning Electron Microscopy: Physics of Image Formation and Microanalysis.* Springer Series in Optical Sciences. Springer (1998).

[RG13] M. Ribeiro Gomes et al.. *Status of the MARE Experiment.* IEEE Transactions on Applied Superconductivity, **23** 3 (2013).

[Rob91] R. Robertson et al.. *Limit on $\overline{\nu}_e$ mass from observation of the β decay of molecular tritium.* Physical Review Letters, **67**, 957–960 (1991).

[Rob15] Robert Bosch GmbH. *Produktdatenblatt Laser-Entfernungsmesser GLM 150.* datasheet, unpublished (2015). Http://www.bosch-professional.com/de/de/ocs/pdf/productdata/glm-150-sheet.pdf (last accessed November 24, 2015).

[Rod11] W. Rodejohann. *Neutrino-less Double Beta Decay and Particle Physics.* Int. J. Mod. Phys., **E20**, 1833–1930 (2011).

[Rog54] W. A. Rogers, R. S. Buritz and D. Alpert. *Diffusion Coefficient, Solubility, and Permeability for Helium in Glass.* Journal of Applied Physics, **25** 7, 868–875 (1954).

[Röl13] M. Röllig et al.. *Activity monitoring of a gaseous tritium source by beta induced X-ray spectrometry.* Fusion Engineering and Design, **88** 6-8, 1263–1266 (2013).

[Röl15] M. Röllig. *Tritium analytics by beta induced X-ray spectrometry.* Ph.D. thesis, Karlsruhe Institute of Technology (2015).

[Rom15] L. Romano, V. Privitera and C. Jagadish. *Defects in Semiconductors.* Semiconductors and Semimetals. Elsevier Science (2015).

[Roy01] S. Roy. *Thermal Physics and Statistical Mechanics*. Basic physics through problems series. New Age International (2001).

[Rub13] A. Rubbia. *LAGUNA-LBNO: design of an underground neutrino observatory coupled to long baseline neutrino beams from CERN*. Journal of Physics Conference Series, **408** 1 (2013).

[Sal11] R. Salh. *Crystalline Silicon - Properties and Uses* (2011).

[Sar96] S. Sarkar. *Big bang nucleosynthesis and physics beyond the standard model*. Reports on Progress in Physics, **59**, 1493–1610 (1996).

[Sav95] G. F. Saville, P. M. Platzman, G. Brandes, R. Ruel and R. L. Willett. *Feasibility study of photocathode electron projection lithography*. Journal of Vacuum Science & Technology B, **13** 6, 2184–2188 (1995).

[Sch95] P. Schmüser. *Feynman - Graphen und Eichtheorien Für Experimentalphysiker*. Lecture notes in physics. Springer Berlin Heidelberg (1995).

[Sch97] N. Schmitz. *Neutrinophysik*. Teubner Studienbücher Physik. Vieweg+Teubner Verlag (1997).

[Sch00] S. Schmitt, J.-M. Breguet, A. Bergander and R. Clavel. *Stick and Slip Actuators (SA)*. **4194** 65 (2000).

[Sch06] S. Schael et al.. *Precision electroweak measurements on the Z resonance*. Physics Reports, **427**, 257–454 (2006).

[Sch08] D. Schultheiß. *Permeation barrier for lightweight liquid hydrogen tanks*. VDM Publishing (2008).

[Sch11] W. Schomburg. *Introduction to Microsystem Design*. RWTH edition. Springer (2011).

[Sch12] C. Schmidt. *Investigation of the work function fluctuations for the precision experiments aSPECT and KATRIN*. Master thesis, Johannes Gutenberg-Universität Mainz, Institut für Physik (2012).

[Sea79] M. P. Seah and W. A. Dench. *Quantitative electron spectroscopy of surfaces: A standard data base for electron inelastic mean free paths in solids*. Surface and Interface Analysis, **1** 1, 2–11 (1979).

[Sli15] V. M. Slipher. *Spectrographic Observations of Nebulae*. Popular Astronomy, **23**, 21–24 (1915).

[Spa06] K. Spanner. *Survey of the Various Operting Principles of Ultrasonic Piezomotors* (2006).

[Spe09] Spectral Products. *Spectral Products Catalog*. product catalogue, unpublished (2009). Http://www.spectralproducts.com/pdf/SP_Catalog_2009_Proto_Final.pdf, (last accessed November 24, 2015).

[Ste83] S. Steward and L. L. N. Laboratory. *Review of Hydrogen Isotope Permeability Through Materials*. Lawrence Livermore National Laboratory (1983).

[Ste93] T. M. Stephan, B. Van Zyl and R. C. Amme. *Degradation of vacuum-exposed SiO2 laser windows.* Proceedings of SPIE, **1848**, 106–110 (1993).

[Str73] R. Strayer, W. Mackie and L. Swanson. *Work function measurements by the field emission retarding potential method.* Surface Science, **34** 2, 225 – 248 (1973).

[Stu10a] M. Sturm. *Aufbau und Test des Inner-Loop-Systems der Tritiumquelle von KATRIN.* Ph.D. thesis, Karlsruher Institut für Technologie (KIT) (2010).

[Stu10b] M. Sturm et al.. *Monitoring of all hydrogen isotopologues at tritium laboratory Karlsruhe using Raman spectroscopy.* Laser Physics, **20** 2, 493–507 (2010).

[Sud58] E. C. G. Sudarshan and R. e. Marshak. *Chirality invariance and the universal Fermi interaction.* Physical Review, **109**, 1860–1860 (1958).

[Swa02] P. L. Swart and A. A. Chtcherbakov. *Study of hydrogen diffusion in boron/germanium codoped optical fiber.* Journal of lightwave technology, **20** 11, 1933 (2002).

[SZ08] X. Shi-Zhen et al.. *Effects of vacuum on fused silica UV damage.* Chinese Physics Letters, **25** 1, 223 (2008).

[Tho57] H. Thomas. *Zum äusseren lichtelektrischen Effekt der Alkalimetalle.* Zeitschrift für Physik, **147** 4, 395–418 (1957).

[Tho15a] Thorlabs. *Multimode fiber attenuation.* data plot, unpublished (2015). Https://www.thorlabs.com/images/TabImages/Hard_Clad_Silica_022_ TEQS_Large.gif (last accessed November 24, 2015).

[Tho15b] Thorlabs. *Uncoated_UVFS_Transmission.* data file, unpublished (2015). Http://www.thorlabs.de/images/TabImages/Uncoated_UVFS_ Transmission.xlsx (last accessed November 24, 2015).

[Thü09] T. Thümmler, R. Marx and C. Weinheimer. *Precision high voltage divider for the KATRIN experiment.* New Journal of Physics, **11** 10 (2009).

[TLK13] TLK manager's office. *Technische Liefer- und Abnahmebedingungen des Tritiumlabor Karlsruhe (TLA).* internal document (2013).

[Vac08] R. Vaccarone et al.. *The Design of a Frequency Multiplexed Ir-Au TES Array.* Journal of Low Temperature Physics, **151** 3-4, 921–926 (2008).

[Val11] K. Valerius et al.. *Prototype of an angular-selective photoelectron calibration source for the KATRIN experiment.* Journal of Instrumentation, **6** 1 (2011).

[Ven06] R. Venugopalan. *Medical Device Materials Iii.* ASM International (2006).

[Vij12] S. Vijaya. *Piezoelectric Materials and Devices: Applications in Engineering and Medical Sciences.* Taylor and Francis (2012).

[Wal91] T. P. Walker, G. Steigman, D. N. Schramm, K. A. Olive and H.-S. Kang. *Primordial nucleosynthesis redux.* The Astrophysical Journal, **376**, 51–69 (1991).

[Wea99] B. Weaver and W. R. Wall. *Tritium Handling and safe storage.* DOE Handbook 1129-99 (1999).

[Wei35] C. F. V. Weizsacker. *Zur Theorie der Kernmassen.* Zeitschrift für Physik, **96**, 431–458 (1935).

[Wei05] C. Weinheimer. *Direct determination of the neutrino masses.* Comptes Rendus Physique, **6** 7, 768–777 (2005).

[Wel72] R. L. Wells and T. F. Jr. *Adsorption of water on clean gold by measurement of work function changes.* Surface Science, **32** 3, 554 – 560 (1972).

[Wil88] *Limit on ν_e mass from free molecular tritium beta decay.* Nuclear Physics A, **478**, 439 – 446 (1988).

[Win11] R. A. Windhorst et al.. *The Hubble Space Telescope Wide Field Camera 3 Early Release Science Data: Panchromatic Faint Object Counts for 0.2-2 μm Wavelength.* The Astrophysical Journal Supplement Series, **193** 2, 27 (2011).

[Wol78] L. Wolfenstein. *Neutrino Oscillations in Matter.* Physical Review, **D17**, 2369–2374 (1978).

[Woo88] D. Woodruff and T. Delchar. *Modern Techniques of Surface Science.* Cambridge Solid State Science Series. Cambridge University Press (1988).

[Woo05] S. Woosley and T. Janka. *The physics of core-collapse supernovae.* Nature Physics, **1**, 147 (2005).

[Wor05] L. Worth, R. Pearce, J. Bruce, J. Banks and S. Scales. *Development of a novel contamination resistant ion chamber for process tritium measurement and use in the JET first trace tritium experiment.* Fusion science and technology, **48** 1, 370–373 (2005).

[Yas96] M. Yasutake, D. Aoki and M. Fujihira. *Surface potential measurements using the Kelvin probe force microscope.* Thin Solid Films, **273** 1-2, 279–283 (1996).

[Zha08] L. Zhan, Y. Wang, J. Cao and L. Wen. *Determination of the Neutrino Mass Hierarchy at an Intermediate Baseline.* Physical Review, **D78** (2008).

[Zha09] L. Zhan, Y. Wang, J. Cao and L. Wen. *Experimental requirements to determine the neutrino mass hierarchy using reactor neutrinos.* Physical Review D, **79** 7 (2009).

[Zim00] O. Zimmer, J. Byrne, M. van der Grinten, W. Heil and F. Glück. *"aspect" – a new spectrometer for the measurement of the angular correlation coefficient a in neutron beta decay.* Nuclear Instruments and Methods in Physics Research Section A: Accelerators, Spectrometers, Detectors and Associated Equipment, **440** 3, 548 – 556 (2000).

[Zis32] W. A. Zisman. *A methode of measuring contact potential differences in metals.* Review of Scientific Instruments, **3** 7, 367–370 (1932).

[Zub11] K. Zuber. *Neutrino Physics, Second Edition.* Series in High Energy Physics, Cosmology and Gravitation. Taylor & Francis (2011).

Danksagung

Zum Abschluss bleibt mir nur noch den vielen Personen zu danken, ohne die diese Arbeit nicht möglich gewesen wäre.

Zuerst möchte ich Prof. Dr. Guido Drexlin dafür danken, dass er mir die Möglichkeit zu dieser Arbeit gegeben hat und sich gerade gegen Ende der Arbeit immer Zeit für mich genommen hat. Prof. Dr. Bernhard Holzapfel möchte ich dafür danken, dass er sich als Zweitkorrektor der Arbeit zur Verfügung gestellt hat.

Dr. Beate Bornschein gilt mein Dank, da sie mir ermöglicht hat meine Experimente am TLK durchzuführen. Für selbiges möchte ich mich auch bei Dr. Uwe Besserer bedanken. Er war mir während meiner Arbeit ein Mentor und Freund, der mich in schwierigen Zeiten aufgebaut und mir Mut zugesprochen hat. Auch sein fachliches Wissen und sein kritisches Nachfragen haben mir bei der Durchführung meiner Arbeiten immer wieder geholfen und mir neue Denkanstöße gegeben.

Martin Babutzka möchte ich für die Unterstützung bei meinen Experimenten, das offene Ohr für all meine Fragen und die Diskussionen über gewonnene Ergebnisse danken. Zudem kann ich mich gar nicht genug für die ausgezeichnete Software der Kelvinsonde bedanken, die auf meinen Wunsch vielfach verändert wurde.

Der Rear Section Gruppe (Martin Babutzka, Sylvia Ebenhöch, Florian Priester, Marco Röllig sowie den Kollegen von der UCSB Matt Bahr, Greg Courville, Marian Ghilea, Prof. Ben Monreal, Dean White, Luiz de Viveiros) möchte ich für die gute Zusammenarbeit in den letzten 4 Jahren danken.

Dem CAPER-Team (Dr. David Demange, Elenore Fanghänel, Thanh-Long Le und Karl-Heinz Simon) danke ich für die Bereitstellung der tritiierten Gasmischungen. Der TLK-Infrastruktur (Hans-Dieter Adami, Uwe Besserer, Adalbert Braun, Frank Kramer, Nancy Lohr, Stefan Welte) sowie Marco Röllig, Florian Priester und Siegfried Horn möchte ich für ihre technische Unterstützung danken. Vor allem Hans-Dieter Adami gebührt hier mein Dank für seine Lehrstunden in der Werkstatt.

Bei der Mittagsessensrunde (Sylvia Ebenhöch, Robin Größle, Bennet Krasch, Nancy Lohr, Sebastian Mirz, Dirk Osenberg, Stefan Welte) bedanke ich mich für lustige Stunden und interessante Gespräche abseits der Arbeit. Diese sorgten dafür, dass ich nach der Mittagspause erholt an meine Arbeit zurückkehren konnte.

Eva Porter und Sylvia Krieger danke ich für ihre Unterstützung bei (für mich teilweise undurchsichtigen) administrativen Aufgaben.

Da ich vermutlich viele Personen vergessen habe, die auch auf die eine oder andere Art und Weise zum Gelingen dieser Arbeit beigetragen haben, möchte ich generell allen TLK-Mitarbeitern und KATRIN-Kollegen für die Zusammenarbeit in den letzten Jahren

danken: Ich habe mich in eurem Umfeld immer wohlgefühlt und gerne mit euch allen zusammengearbeitet!

Prof. Dr. Mathias Noe, Prof. Dr. Bernhard Holzapfel und Dr. Beate Bornschein möchte ich außerdem dafür danken, dass sie mir die Wichtigkeit der Ausbildung des wissenschaftlichen Nachwuchses aufgezeigt haben und mich bei dessen Ausbildung immer unterstützt haben.

Den Korrekturlesern dieser Arbeit (Martin Babutzka, Uwe Besserer, Beate Bornschein, Sylvia Ebenhöch, Sebastian Mirz, Sebastian Fischer, Marco Röllig) danke ich herzlich für ihre Mühe. Besonders Martin Babutzka und Marco Röllig möchte ich hierbei danken, da sie große Teile der Arbeit gelesen haben, obwohl sie nicht mehr am KIT arbeiten bzw. sich im wohlverdienten Urlaub nach ihrer eigenen Promotionsprüfung befunden haben. Vielen Dank!

Der Carl-Zeiss-Stiftung möchte ich für die Förderung und Finanzierung meiner Arbeit über 3 Jahre hinweg danken.

Zu Guter Letzt möchte ich noch meiner Familie und meinem Freund für ihre Unterstützung danken. Außerdem wäre ohne das Interesse für astrophysikalische Fragestellungen meiner Mutter und das mathematisch naturwissenschaftliche Verständnis meines Vaters diese Arbeit niemals möglich gewesen. Meinem Bruder möchte ich zudem für das unermüdliche Korrekturlesen der Arbeit danken. Danke, dass du die Arbeit auch noch gelesen hast, als ich sie schon nicht mehr sehen konnte! Mein besonderer Dank gilt außerdem meinem Freund Pierre Hufschmidt. Er hat mich während der gesamten Zeit der Arbeit unterstützt, mich in schlechten Zeiten aufgebaut und mir Mut zugesprochen. Besonders in der Endphase meiner Arbeit hat er mit einem schier unendlichen Verständnis all meine Launen mit einem Lächeln auf den Lippen ertragen und war mir eine Stütze, ohne die ich den Stress nicht ausgehalten hätte.